Maxwell-Klein-Gordon Fields in Black Hole Spacetimes

by

Roman J. W. Petryk

Bachelor of Science, The University of Manitoba, 1996
Certificate of Advanced Study in Mathematics, The University of Cambridge, 1997
Master of Science, The University of British Columbia, 2000

A THESIS SUBMITTED IN PARTIAL FULFILMENT OF
THE REQUIREMENTS FOR THE DEGREE OF

DOCTOR OF PHILOSOPHY

in

THE FACULTY OF GRADUATE STUDIES

(Physics)

THE UNIVERSITY OF BRITISH COLUMBIA

November, 2005

In presenting this thesis in partial fulfilment of the requirements for an advanced degree at the University of British Columbia, I agree that the Library shall make it freely available for reference and study. I further agree that permission for extensive copying of this thesis for scholarly purposes may be granted by the head of my department or by his or her representatives. It is understood that copying or publication of this thesis for financial gain shall not be allowed without my written permission.

(Signature) ______________________________

Department of Physics and Astronomy

The University Of British Columbia
Vancouver, British Columbia
Canada

Date ______________________________

ABSTRACT

In this thesis I present results for the evolution and dynamics of massive electromagnetically coupled Maxwell-Klein-Gordon fields in black hole spacetimes. The first part of my investigation for gravitationally and electromagnetically self-interacting fields in spherical symmetry reveals two distinct types of solution at the threshold of black hole formation. For fields with relatively small mass parameter I observe Type II discretely self-similar behaviour for the critical solutions and obtain the black hole mass and charge scaling relations. However, when the mass parameter is sufficiently large a different type of critical solution is obtained. This new solution is periodic and resembles a perturbed charged boson star solution. This new solution exhibits Type I critical behaviour and its lifetime obeys a well-defined scaling law.

The second aspect of investigation involves massive electromagnetically coupled scalar field perturbations in axial symmetry on a Kerr black hole spacetime. Here, results show that both the mass and charge coupling parameters play a significant role in the field dynamics on the spacetime background. For relatively weak parameter values the perturbations exhibit strong gravitational interaction through the phenomenon of orbiting resonances. In the case of pure electromagnetic perturbation there is also evidence of superradiant scattering when the black hole rotation is large. When the parameter values are large both the physics and complexity of the dynamics change. For intermediate values of the mass and charge parameter, the perturbations exhibit trapping and a preference for scattering along the axis of black hole rotation. Finally, all electromagnetically coupled solutions generically display charge separation and dynamo-like behaviour.

CONTENTS

LIST OF TABLES

LIST OF FIGURES

ACKNOWLEDGEMENTS

I would like to express gratitude to my advisor Matthew Choptuik, and thesis committee members Kristin Schleich, Douglas Scott and William Unruh for their efforts and assistance. Thanks are also forwarded to Frans Pretorius for use of his parallel adaptive mesh refinement routine library. And I especially thank Andrea and Anastazia Petryk, along with family and friends for their encouragement and support.

Results presented in this thesis were computed primarily on the vn, vnp4 and WestGrid Glacier clusters located at the University of British Columbia. Substantial use was also made of the WestGrid Network Storage Facility at Simon Fraser University. The vn and vnp4 clusters are funded and supported by the British Columbia Knowledge Development Fund, the Canada Foundation for Innovation, the Canadian Institute of Advanced Research, the Natural Sciences and Engineering Research Council of Canada and the University of British Columbia. Funding and support for Westgrid Glacier and the Westgrid Network Storage Facility is provided by the Alberta Science and Research Authority, the British Columbia Knowledge Development Fund, the Canada Foundation for Innovation, the University of British Columbia, Simon Fraser University and TRIUMF. I also thank the Natural Sciences and Engineering Research Council of Canada, the R. Howard Webster Foundation and the University of British Columbia for their support.

CHAPTER 1

INTRODUCTION

> Of all conceptions of the human mind perhaps the most fantastic is the black hole. Black holes are neither bodies nor radiation. They are clots of gravity.[1]

This dissertation concerns the numerical study of black hole formation from charged, massive scalar fields in spherical symmetry, and the axially symmetric scattering and accretion of such matter onto rotating black holes. In the gravitational collapse to a black hole, and in accretion onto black holes, astrophysically realistic matter will likely be magnetohydrodynamic (MHD)—fluid-like, and ionized. Only in very few highly symmetric cases has the fully general relativistic problem (where matter sources dynamically influence the curvature of spacetime) been completely studied. Even then, computational techniques are required. Shock formation in fluid systems further complicates the details. Numerical simulation of general relativistic MHD systems is in its infancy, and insight gained through the study of MHD analogues like the charged, massive scalar field is required for progress. Furthermore, scalar field models can represent the pions π^0, π^+ and π^-, and have been proposed as candidates for early universe and dark matter. The study of charged, massive scalar fields is therefore interesting in and of itself. Finally, there is the connection to matter models in which critical behaviour has been studied at the threshold of gravitational collapse and open questions in that regard.

Essential to a complete understanding of the physics are both: (1) spherically symmetric investigation of the general relativistic problem; and (2) analysis of the dynamics in axial symmetry. While the spherically symmetric investigation provides information on how the matter dynamically influences spacetime curvature, the effects of magnetic fields and electromagnetic radiation can not be extracted until the imposed symmetry is (at most) axial. The charged, massive scalar field system has not been studied in much detail in these regards, so any additional insight regarding its physics will certainly be useful.

1.1 Scalar Field Critical Collapse

In 1993 Choptuik published the results of an interesting phenomenon in gravitational collapse [23]. There he gave answers to the questions "What happens at the threshold of gravitational collapse?" and "What happens in the limit of increasingly small mass black hole formation?" The system in which he first observed these *critical phenomena* was the massless scalar field minimally coupled to gravity. Since that time, critical phenomena have been observed in a variety of different matter models. Those I will mention are but a small subset of those studied, but they do form the set most important to the discussions which follow. Specifically, I will mention works by Hod and Piran [66], [68], Brady, Chambers and Goncalves [12], [16], Hawley and Choptuik [63], [64], [65], as well as an analysis by Gundlach and Martin-Garcia [57]. Finally, relatively complete overviews of critical phenomena in gravitational collapse have also been provided by Gundlach in [59] and [60].

In brief, for the minimally coupled massless Klein-Gordon field in spherical symmetry, Choptuik considered families of solutions $S[p]$ with the property that the *critical value* of the parameter $p = p^*$ separates solutions which form black holes from those which do not [23]. He found evidence that supported two conjectures. First, he obtained numerical evidence supporting the *universality* of the solution $p \to p^*$ and that it forms structure on arbitrarily small spatiotemporal scales. That

[1] Quoted from [116].

is, not only were all solutions approaching criticality “the same”, but they also exhibited a type of self-similarity in space and time as the evolution proceeded. Second, he observed that there exists a mass-relation for the solutions which formed black holes. Specifically, that the mass of the black hole obeyed a power law

$$m_{\mathrm{BH}} \propto |p - p^*|^{\gamma_m} \ , \tag{1.1}$$

where $\gamma_m \approx 0.37$, is a universal exponent. In principle, the mass of the black hole can be made arbitrarily small (i.e., there is no mass gap in the black hole spectrum). In analogy to phase transitions in condensed matter systems, this continuous scaling of the black hole mass has since been identified as Type II critical behaviour in black hole formation.

Key to the discussion of his results was the observation that, expressed in the usual (t, r, θ, ϕ) spherical coordinates, his system was invariant under the rescalings

$$t \rightarrow kt \ , \tag{1.2}$$

$$r \rightarrow kr \ , \tag{1.3}$$

k being an arbitrary positive constant. Expressing his variables in terms of the form-invariant quantities $X(t, r)$ and $Y(t, r)$, he found there exists a unique sequence of this set of variables $[X, Y]$ in the limit of the exactly critical solution $[X, Y] \rightarrow [X^*, Y^*]$. Expressing this sequence in terms of the logarithmic spatial and temporal variables $\tau = \tau(t)$ and $\rho = \rho(r)$, Choptuik found that for $[X, Y] \rightarrow [X^*, Y^*]$

$$[X^*(\tau - \Delta_\tau, \rho - \Delta_\rho), Y^*(\tau - \Delta_\tau, \rho - \Delta_\rho)] \simeq [X^*(\tau, \rho), Y^*(\tau, \rho)] \ , \tag{1.4}$$

where $\Delta_\tau \simeq \Delta \simeq \Delta_\rho$ is a universal constant with approximate value $\Delta \approx 3.4$. Specifically, Choptuik found

$$\Delta_\tau \approx 3.43 \ , \ \Delta_\rho \approx 3.44 \ . \tag{1.5}$$

This means that every time the profiles X, Y are re-examined after evolution of geometric time interval δT_0, $T_0 = T_0(t)$ being the proper time of a stationary observer at $r = 0$, the solutions essentially appear rescaled by a factor of $\exp(\Delta) \approx 30$. Therefore, there exists a discrete self-similarity in the solution in the form of a series of ever-decreasing echoes as the scalar field evolves on the threshold of black hole formation.

The universality of critical phenomena can be understood in terms of perturbation theory. Consider linear perturbations of the exactly critical solution. The perturbed critical solution will have a number of modes, both stable and unstable. The stable modes decay, thus driving the perturbed solution to the critical solution. The unstable modes, however, drive the system away from the exactly critical solution. In the case at hand, the unstable modes would drive the system to either black hole formation or dispersal. The exactly critical solution has only one unstable mode. It is through the existence of this single mode that the universality of the solution can be explained—tuning similar families of initial data to the critical solution, the system is driven to the same critical point. Furthermore, perturbation theory analysis explains how the eigenvalue of the unstable mode is directly correlated with the black hole scaling exponent γ_m, and correctly predicts its value.

In subsequent research, Brady, Chambers and Goncalves examined critical phenomena in the case of a minimally coupled massive scalar field [12], [16]. Their results showed that, for the massive case, when the radial extent of the initial pulse λ is less than the Compton wavelength of the scalar field m^{-1}, then Type II critical behaviour is observed. The critical solution observed in this case is exactly that which was found by Choptuik. However, they also observed that there exists a minimum mass black hole that can be formed when the radial extent of the initial pulse is much greater than the Compton wavelength (that is, a mass gap exists in the black hole spectrum when $\lambda \gg m^{-1}$). Again, in analogy to condensed matter systems, such behaviour has come to be known as Type I critical phenomena.[2] In the regime of Type I solutions, the exactly critical solutions are unstable soliton stars rather than the naked singularities of the Type II case. In fact, it is the presence of the mass parameter m which destroys the scaling of the system under transformations (1.3) and (1.2). Hence, a different type of critical solution is expected and observed. Noting similarities between the soliton stars examined by Brady, Chambers and Goncalves, and boson stars composed of massive complex scalar fields, Hawley and Choptuik investigated the behaviour of boson stars driven to the brink of black hole formation [63], [64], [65]. Hawley and Choptuik thereby found Type I critical behaviour for massive complex scalar fields, the exactly critical solutions being perturbed and periodically oscillating boson stars, their lifetimes obeying a well-defined scaling relation as $p \to p^*$.

Finally, Gundlach and Martin-Garcia [57] discussed the possibility that, as in the case of the massive minimally coupled scalar field, the presence of a parameter breaking the invariance under transformations (1.3) and (1.2) could lead to behaviour in the electromagnetically coupled complex scalar field different from that first found by Choptuik. The parameter in the electromagnetically coupled complex scalar field system which breaks this invariance is the charge coupling parameter e. However, Gundlach and Martin-Garcia performed an analysis which showed that, as the system evolves, the effects of charge will play a decreasingly significant role. Specifically, assuming a self-similar solution and also that field equations in this system always contain dominant contributions from e in the combination er, a rescaling $r \to \exp(-\Delta)r$ effectively scales e as $e \to \exp(-\Delta)e$. Therefore, after each echo, the effects of the charge coupling will decrease exponentially with Δ. In fact, they showed that in critical collapse the black hole mass should scale as

$$m_{\rm BH} \propto |p - p^*|^{\gamma_m} \ , \tag{1.6}$$

where $\gamma_m \approx 0.37$ (just as found by Choptuik [23]), and that the charge of the black hole should scale as

$$Q_{\rm BH} \propto |p - p^*|^{\gamma_Q} \ , \tag{1.7}$$

where $\gamma_Q \approx 0.88$. In fact, they predicted that for other charged matter models the relationship between γ_m and γ_Q should obey $\gamma_Q \geq 2\gamma_m$. They also predicted the solutions would be universal. Furthermore, they postulated that if a second dimensionful parameter such as scalar field mass m_Φ is added to the system, then universality will not hold generically, but might be recovered in the limit when $e/m_\Phi \to 0$ or $m_\Phi/e \to 0$. In conclusion, they also suggested the value of $|e|/m_\Phi$ could determine whether the system displays a Type I mass scaling typical of perturbed boson star critical solutions.

Soon after Gundlach and Martin-Garcia published their results, Hod and Piran performed the numerical study of the charged massless minimally coupled scalar field [66], [68]. As predicted by Gundlach and Martin-Garcia, they found mass and charge scaling relations with exponents of about $\gamma_m \approx 0.37$ and $\gamma_Q \geq 2\gamma_m$. They also verified that the infinitesimal mass black holes formed were neutral or obeyed the relationship $Q_{\rm BH} \ll m_{\rm BH}$.

To date, nothing has been published in the way of massive electromagnetically coupled scalar field critical phenomena, and only modest work has been presented in hypothesis of the details. The numerical results presented in Chapter 3 from my study of black hole critical phenomena of charged massive scalar fields are the first of their kind.

1.2 Scattering and Scalar Accretion in Kerr Spacetime

From the Rutherford scattering of alpha particles off atomic nuclei, to modern experiments like those at the Large Hadron Collider and proposed TeV electron-positron experiments at the Next Linear Collider, particle scattering has revealed, and will continue to reveal, the physical nature of

[2] It should be noted that, even before the results of Brady, Chambers and Goncalves, Type I critical phenomena was known to exist for the minimally coupled Yang-Mills field [26].

the subatomic world. Photon scattering in its various forms has also provided much information on the physics of matter—Thomson scattering has shown that atomic constituents can have both positive and negative charge, Rayleigh scattering explains why the sky appears blue, Compton scattering has revealed the corpuscular nature of the photon, Raman scattering provides information on the excited energy states of a target material, and Bragg scattering has determined the lattice spacing of crystalline substances. Particle and photon scattering experiments could, in principle, also be performed on black holes. Under the hypothesis that the details would reveal interesting physics, there has been rather detailed theoretical investigation of black hole wave scattering. While much of the work has involved obtaining closed-form solutions, there recently has been much effort in solving the black hole scattering problem using numerical techniques. Rather than provide a complete overview of the developments I will simply address previous work in the field when it pertains directly to the discussion of my results, and refer the reader to [49] and [51] for general reference.

There are essentially three phases in the dynamics of any matter scattering in a black hole spacetime: (1) an early phase which in many ways resembles the initial dynamics of the same matter in a Minkowski spacetime; (2) an intermediate phase in which curvature effects become apparent; and (3) an asymptotic late phase which can in many cases be described by a power law decay in time. The late phase evolution has been studied in some detail in the context of *quasi-normal* (i.e., damped, complex frequency) black hole modes.[3] Since certain frequencies of the quasi-normal modes should be independent of the process that generates them, these frequencies are characteristic of, and directly connected to, the black hole parameters (mass, charge, and angular momentum). They thereby provide a means of identifying the black hole spacetime.

While, by definition, scattering involves dynamics governed predominantly by interactions over a limited range of space and a relatively short interval of time, the physics of interest in accretion is also over a relatively small region of space but now persists over a prolonged period of time. In black hole accretion, there are basically two modes of flow: (1) Bondi-like flow where angular momenta are low and centrifugal forces are too weak to balance gravitational attraction and provide an equilibrium state; and (2) thin-disc where angular momenta are sufficient to generate a stationary state. Bondi-like flow qualitatively resembles spherical accretion, while thin-disk is typified by matter in Keplerian and super-Keplerian orbits. Consequently, locally dissipated energy, entropy and angular momentum are advected or carried along by the flow and lost to the black hole in Bondi-like accretion. Meanwhile, in thin-disc accretion, matter exists at a fixed radius for many orbits allowing for the opportunity to locally transfer substantial energy, entropy and angular momentum.

In black hole accretion, astronomical evidence shows that a portion of inspiralling plasma and generated electromagnetic radiation collimate into bipolar jets from the black hole. Only modest progress has been made through the study of magnetohydrodynamical systems, and the details are not well understood. It is assumed electromagnetic fields play a significant role in the collimation process, but the details are again vague. Some notable computational simulations of this accretion and collimation process have been presented in [42], [82], [107], [83] and [84]. Since the knowledge is incomplete, there is clearly interest to investigate possible electromagnetic effects in black hole accretion and scattering phenomena through matter models simpler than magnetohydrodynamics. As a step towards this goal, and in order to distinguish between matter and gravitational effects—essential to discussion of the fully general relativistic system—Chapter 4 of this dissertation presents results from my axially symmetric study of charged, massive scalar field (i.e., the Maxwell-Klein-Gordon system) accretion and scattering in rotating black hole spacetimes. In this situation, I treat the scalar field as *test matter* (it evolves about the black hole, but does not itself contribute to the curvature of spacetime) and observe its dynamics. To my knowledge, this study is the first of its kind.

[3] [85] provides a good summary of the research before 1999.

1.3 Outline

In Chapter 2, I present methodology in terms of the Arnowitt-Deser-Misner (ADM) formalism, focusing specifically on the polar areal coordinate system. I then discuss the initial value formalism for electromagnetism and general relativity, and close with brief discussion of regularity conditions.

Chapter 3 presents the study of critical solutions for massive charged scalar fields in spherical symmetry, beginning with a presentation of the system of equations. Among the results are both Type I and Type II solutions and the scaling relations associated with each.

By far the most voluminous is Chapter 4 where I present the investigation of massive electromagnetically coupled scalar field dynamics in Kerr spacetime. I provide discussion of the effective potential formalism and its implications. Following that, I provide the system of equations, and then proceed with presentation of my results. Included in the results are electromagnetically uncoupled (i.e., $e = 0$) Klein-Gordon field dynamics, Maxwell field dynamics, and finally, electromagnetically coupled Maxwell-Klein-Gordon equation dynamics in Kerr spacetime. These results cover a range of scalar field mass, electromagnetic coupling, and black hole angular momentum parameters. Among the results shown are orbiting resonances, superradiant scattering and trapping of fields in the black hole spacetime. Also included are solutions demonstrating the preference for Maxwell-Klein-Gordon fields to scatter along the axis of black hole rotation under a certain set of conditions, and also the generic emergence of charge separation and dynamo-like behaviour when the Maxwell and Klein-Gordon fields are coupled electromagnetically through charge.

Chapter 5 provides a summary and outlook, Appendix A provides a glossary of notation, and Appendix B provides a summary of finite difference and discrete operators used throughout the dissertation. Appendix C provides discussion of the numerical and computational techniques used to obtain all the presented results. Finally, Appendix D provides a detailed account of Maxwell-Klein-Gordon dynamics in Minkowski spacetime. There I discuss the Monotonically Increasingly Boosted (MIB) coordinate system and its utility in treating outer boundary conditions. Along with a presentation of the equations, I provide results to compare and contrast flatspace dynamics to those for the black hole background. These results include Klein-Gordon fields, Maxwell fields, and the Maxwell-Klein-Gordon system for a variety of field mass and charge coupling parameter values.

1.4 Conventions and Units

Throughout this dissertation I employ the index notation, where, for example,

$$T^{abc...}_{def...} \tag{1.8}$$

designates the $abc...$ contravariant components and $def...$ covariant components of tensor T. Indices $a, b, c, d, e, f, ...$ take on values $0, 1, 2, 3$, where 0 typically designates the temporal component and $1, 2, 3$ designate the spatial components in a given coordinate system. In a situation where indices are repeated, the Einstein summation convention is implied as per

$$T^{abc...}_{daf...} \equiv \sum_{a=0}^{3} T^{abc...}_{daf...} \ . \tag{1.9}$$

I also employ the metric signature $(-, +, +, +)$, and use Planckian units where $\hbar = G = c = 1$. A quantity with dimension length^m $\times$ mass^n $\times$ time^p in ordinary units is therefore dimensionless in Planckian units. To retrieve an equation valid in ordinary units one simply multiplies each quantity in Planckian units by its conversion factor

$$c^p \left(\frac{G}{c^2}\right)^n \left(\frac{c^3}{G\hbar}\right)^{(m+n+p)/2} . \tag{1.10}$$

In SI units the fundamental constants have values $c = 3.00 \times 10^8 \mathrm{m\ s^{-1}}$, $G = 6.67 \times 10^{-11} \mathrm{m^3\ kg^{-1}\ s^{-2}}$, and $\hbar = 6.626 \times 10^{-34} \mathrm{J\ s}$.

1.5 Significant Figures and Uncertainties

Finally, where other's numerical results are quoted, all significant figures are assumed accurate. For example, Choptuik's original result, $\Delta_\rho \approx 3.44$, is accurate in all three digits. My numerically computed results, however, are usually accurate in all figures but the last significant digit. Thus, my $\Delta \approx 3.47$ is accurate in the first two digits but uncertain in the last. The exception is in cases where my result has but one significant digit. The quantity is then accurate in that single digit. For example, in my $k \approx 1 \times 10^{-2}$, uncertainties would enter at the level of subsequent figures.

1.6 Web References

In the body of this thesis there are a number of references to files found in the World Wide Web. While the availability of all files cannot be guaranteed in the future, efforts will be made to maintain access to those whose Uniform Resource Locator (URL) currently has `laplace.physics.ubc.ca` for host. While there will be a change in file URL in the event of a host change, the path should be preserved. Thus, file URLs like `http://$WWW/People/petryk/animations/9.mpeg` will still be valid in the future, but `$WWW` may differ from its current value `laplace.physics.ubc.ca` .

CHAPTER 2

PHYSICAL FORMALISM

2.1 The 3+1 or Arnowitt-Deser-Misner (ADM) Formalism

In this section I introduce the so-called 3+1 or *Arnowitt-Deser-Misner* (ADM) formulation of relativity. Relevant historical references are [47], [33], [4], and [148]. While the 3+1 formalism was originally developed for use in quantum gravity (see [4]), this approach has perhaps seen its greatest successes in numerical relativity. I employ the 3+1 approach in my investigations and now just briefly cover some of its key points. The following exposition is based upon [27] which is itself a reworking of the results in [148].

2.1.1 Foliations

Start with a spacetime manifold $\mathcal{M}$ endowed with a metric g_{ab}. Assume the metric is expressed in coordinates, where t is the *temporal* parameter. The spacetime can always be foliated as a sequence $\{\Sigma_t\}$ which are isosurfaces to t. These spacelike hypersurfaces are locally described by the dual vector field Ω_a defined

$$\Omega_a = \nabla_a t, \tag{2.1}$$

and has norm

$$g^{ab}\Omega_a\Omega_b = -\alpha^{-2}, \tag{2.2}$$

where α is known as the *lapse function* (or simply the *lapse*). Given this, I can construct a unit-norm dual vector, n_a, as per

$$n_a = -\alpha\Omega_a = -\alpha\nabla_a t, \tag{2.3}$$

where the sign is chosen so that the related unit-norm vector, n^a,

$$n^a = g^{ab}n_b \tag{2.4}$$

is future-directed. n^a can be viewed as the four-velocity of an observer moving orthogonally to the hypersurfaces of Σ_t. Finally, such an observer will have a four-acceleration, a^a, according to

$$a^a = n^b\nabla_b n^a. \tag{2.5}$$

2.1.2 Projections

In the 3+1 formalism I aim to decompose tensors into their single *temporal* (hypersurface-normal) and three *spatial* (hypersurface-tangential) parts. To extract the temporal part of vector W^a I simply contract with n_a as per

$$W^{\hat{n}} = -W^a n_a. \tag{2.6}$$

For a covector W_a I contract with n^a

$$W_{\hat{n}} = +W_a n^a. \tag{2.7}$$

There are two items to note in the preceding pair of equations. First, the superscripts and subscripts $\hat{n}$ designate the original tensor index has been contracted with n_a or n^a. Second, the choice of sign $-$ or $+$ is a convention adopted directly from that of [148]. Meanwhile, partial components are extracted with the rank-two *projection tensor*

$$\perp^a{}_b \equiv \delta^a{}_b + n^a n_b. \tag{2.8}$$

Then any tensor $T^{abc\ldots}_{def\ldots}$ which has had all its free indices projected out with $\perp^a{}_b$ in the manner

$$\perp T^{abc\ldots}_{def\ldots} \equiv \perp^a{}_g \perp^b{}_h \perp^c{}_i \cdots \perp^j{}_d \perp^k{}_e \perp^l{}_f \cdots T^{jkl..}_{ghi\ldots} \tag{2.9}$$

is referred to as a *spatial* tensor. Above and onwards $\perp$ (with no indices) is shorthand to designate that spatial projection is applied to all free indices in the trailing tensor.

When applied to all free indices of the metric tensor, g_{ab}, projection yields the spatial metric γ_{ab},

$$\gamma_{ab} = \perp g_{ab} = g_{ab} + n_a n_b. \tag{2.10}$$

By extension, the contravariant spatial metric is given by

$$\gamma^{ab} = \perp g^{ab} = g^{ab} + n^a n^b. \tag{2.11}$$

Note that tensor indices of $T^{abc\ldots}_{def\ldots}$ continue to be raised and lowered with spacetime metric g_{ab}—not with γ_{ab}—as γ_{ab} and γ^{ab} are not inverses in the four-dimensional spacetime manifold. The only time γ_{ab} can be used to raise or lower indices is when the tensor acted upon is *spatial* (i.e., it has no temporal piece).

2.1.3 Covariant Derivatives on the Spacelike Hypersurface

The spatial projection tensor can then be applied to the operator ∇_a to define the natural derivative operator D_a for spatial tensors,

$$D_a \equiv \perp \nabla_a. \tag{2.12}$$

The action of D_a on a spatial tensor $\perp T^{abc\ldots}_{def\ldots}$ would then be

$$D_j \perp T^{abc\ldots}_{def\ldots} \equiv \perp \nabla_j \perp T^{abc\ldots}_{def\ldots}, \tag{2.13}$$

where shorthand $\perp$ again indicates I apply the projection operator to all free tensor indices. Since

$$D_a \gamma_{bc} = \perp \nabla_a \gamma_{bc} = \perp \nabla_a (g_{bc} + n_b n_c) = \perp \nabla_a (n_b n_c) = \perp (n_c \nabla_a n_b + n_b \nabla_a n_c) = \cdots = 0, \tag{2.14}$$

and similarly for $D_a \gamma^{bc}$, D_a is clearly the natural derivative operator for the spatial metric γ_{ab}.

2.1.4 Intrinsic and Extrinsic Curvature

Given the covariant derivative on the spacelike hypersurface D_a, it is natural to define the curvature of the spacelike hypersurface, $\mathcal{R}_{abc}{}^d$, via

$$(D_a D_b - D_b D_a) \perp W_c = \mathcal{R}_{abc}{}^d \perp W_d, \tag{2.15}$$

where W_a is some covariant vector. $\mathcal{R}_{abc}{}^d$ is referred to as the *intrinsic curvature*. $\mathcal{R}_{abc}{}^d$ is itself a spatial tensor and possesses the expected symmetries

$$\mathcal{R}_{(ab)cd} = \mathcal{R}_{ab(cd)} = 0, \tag{2.16}$$

$$\mathcal{R}_{abcd} = \mathcal{R}_{cdab}, \tag{2.17}$$

and

$$\mathcal{R}_{[abc]d} = 0. \tag{2.18}$$

In continuation, the *spatial Ricci* tensor , $\mathcal{R}_{ab}$, and scalar, $\mathcal{R}$, are defined via

$$\mathcal{R}_{ab} = \mathcal{R}_{acb}{}^{c} \tag{2.19}$$

and

$$\mathcal{R} = \mathcal{R}_{a}{}^{a}. \tag{2.20}$$

While the intrinsic curvature describes the geometry of the spacelike hypersurfaces, it is the *extrinsic curvature* that describes how spacelike hypersurfaces are embedded in the spacetime. The extrinsic curvature, K_{ab}, is defined either through covariant differentiation as per

$$K_{ab} = -\perp \nabla_a n_b, \tag{2.21}$$

or equivalently via Lie differentiation along the normal vector field as in

$$K_{ab} = -\frac{1}{2} \perp \pounds_n g_{ab}. \tag{2.22}$$

Using the (easily derived) property

$$\perp \nabla_a n_b = \nabla_a n_b + n_a a_b \tag{2.23}$$

in the first form of K_{ab}, I obtain

$$K_{ab} = -\nabla_a n_b - n_a a_b, \tag{2.24}$$

which makes clear a relationship between the spatial extrinsic curvature tensor, and the four-velocities and four-accelerations of observers moving orthogonally to the spacelike hypersurfaces.

2.1.5 The Spacetime Constraint Equations

Having introduced the necessary elements of the 3+1 formalism, I are now in a position to derive the evolution of spacetime from Einstein's field equations,

$$G_{ab} = R_{ab} - \frac{1}{2} g_{ab} R = 8\pi T_{ab}. \tag{2.25}$$

I begin by defining three projections of the stress-energy tensor, T_{ab},

$$\rho \equiv T_{\hat{n}\hat{n}} = T_{ab} n^a n^b, \tag{2.26}$$

$$j^a \equiv \perp T^{a\hat{n}} = -\perp \left(T^{ab} n_b \right), \tag{2.27}$$

$$S^{ab} \equiv \perp T^{ab}. \tag{2.28}$$

ρ, j^a, and S^{ab}, can respectively be interpreted as the local energy density, momentum density and spatial stress tensor as seen by an observer with four-velocity n^a.

Omitting the detailed algebra, I simply state that contracting Einstein's equations twice with n^a obtains the *Hamiltonian constraint*

$$\mathcal{R} + K^2 - K^a{}_b K^b{}_a = 16\pi\rho \ , \tag{2.29}$$

where $K \equiv \mathrm{Tr} K \equiv K^a{}_a$. Likewise, contracting Einstein's equations once with n^a and then projecting onto the spacelike hypersurface, I obtain the *momentum constraint*

$$D_b K^{ab} - D^a K = 8\pi j^a. \tag{2.30}$$

Notice the preceding two equations contain only spatial tensors and derivatives, and no explicit temporal derivatives, as they are truly equations of constraint. Being constraints, they must be satisfied at every time or hypersurface in the foliation $\{\Sigma_t\}$ by the values of γ_{ab} and K_{ab} (the fundamental 3+1 variables).

2.1.6 Time Derivatives

While the spacetime history could, in principle, be obtained from the constraint equations alone, it is often useful to obtain the solutions from evolutionary equations instead. To this end, I must first define the appropriate time derivatives. It turns out that vector field N^a defined

$$N^a = \alpha n^a \tag{2.31}$$

is a natural vector along which I could Lie differentiate. Since

$$n^a = -\alpha \Omega^a, \tag{2.32}$$

and

$$\Omega^a \Omega_a = 1, \tag{2.33}$$

contracting N^a with Ω^a is a unit norm,

$$N^a \Omega_a = 1. \tag{2.34}$$

However, there is no reason to be so restrictive, and I could, in principle, construct a more general vector field, t^a, appropriate for Lie differentiation,

$$t^a = N^a + \beta^a. \tag{2.35}$$

Providing the *shift vector* β^a is spatial

$$\beta^a n_a = 0, \tag{2.36}$$

I prove $t^a = \frac{\partial}{\partial t}$ is an equally valid choice, since

$$t^a \Omega_a = (N^a + \beta^a)\, \Omega_a = N^a \Omega_a + \beta^a \Omega_a = N^a \Omega_a = 1 \tag{2.37}$$

also has the desired property.

The vector β^a I just introduced can be interpreted as follows. Four-velocity t^a represents a congruence of observers moving in the future direction. In moving from one spacelike hypersurface to the next in foliation $\{\Sigma_t\}$, the observers move into the future an amount n^a perpendicular to the original hypersurface Σ_t. But on the future hypersurface Σ_{t+dt}, the position of the observers has been spatially shifted by an amount β^a. So, only if $\beta^a = 0$ is the propagation purely perpendicular to Σ_t. This scenario is depicted in Figure 2.1 below.

2.1.7 Spacetime Evolution Equations

With all the preliminaries developed, I are now in a position to state the equations of spacetime evolution. The derivation of evolution equations for the spacetime begins with the Lie derivative definition of the extrinsic curvature, K_{ab},

$$K_{ab} = -\frac{1}{2} \pounds_t g_{ab}, \tag{2.38}$$

where for full generality I Lie differentiate along vector t^a rather than n^a. I thus obtain

$$\pounds_t \gamma_{ab} = -2\alpha K_{ab} + \pounds_\beta \gamma_{ab}, \tag{2.39}$$

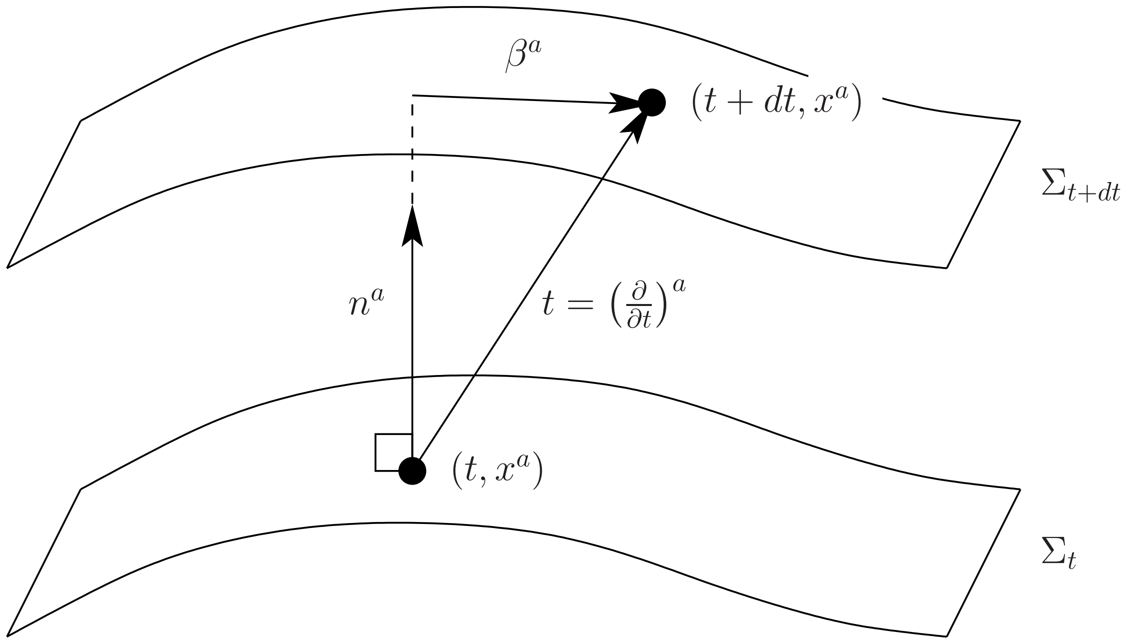

Figure 2.1: A schematic depiction of the 3+1 decomposition. n^a is the unit normal to Σ_t at coordinate (t, x^a). Moving in the future direction amount dt, an observer with four-velocity $\left(\frac{\partial}{\partial t}\right)^a = t^a = N^a + \beta^a = \alpha n^a + \beta^a$ ends up on hypersurface Σ_{t+dt} at coordinate $(t + dt, x^a)$. α is the *lapse function* and measures movement into the future. The *shift vector* β^a measures the spatial displacement of coordinates in going from Σ_t to Σ_{t+dt}.

which are the evolution equations of the spatial metric.

The procedure to obtain the evolution of the extrinsic curvature is somewhat more lengthy and involves, among other things, contractions of Einstein's field equations and projections of the curvature tensor R_{abcd} (and its contractions) onto the spacelike hypersurfaces. For brevity I omit the details and simply state the results.[1] Evolution equations for the extrinsic curvature thus obtained are

$$\pounds_t K_{ab} = \pounds_\beta K_{ab} - D_a D_b \alpha + \alpha \left(\mathcal{R}_{ab} + K K_{ab} - 2 K_{ac} K^c{}_b - 8\pi \left(S_{ab} - \frac{1}{2} \gamma_{ab} \left(S - \rho \right) \right) \right), \quad (2.40)$$

where $S \equiv \mathrm{Tr} S \equiv S^a{}_a$. Finally, raising an index produces the often more useful form

$$\pounds_t K^a{}_b = \pounds_\beta K^a{}_b - D^a D_b \alpha + \alpha \left(\mathcal{R}^a{}_b + K K^a{}_b + 8\pi \left(\frac{1}{2} \perp^a{}_b \left(S - \rho \right) - S^a{}_b \right) \right). \quad (2.41)$$

2.1.8 Spherically Symmetric Spacetime in Polar Areal Coordinates

In a following chapter I study the evolution of spherically symmetric spacetime in the context of critical gravitational collapse of a massive electromagnetically coupled complex scalar field. Since the study employs the 3+1 formalism in the polar areal coordinate system, it is natural now to present the spacetime constraints and evolution equations for that choice of metric.

The most general spherically symmetric spacetime metric in (t, r, θ, ϕ) coordinates is given by line element

$$ds^2 = \left(-\alpha^2 + a^2 \beta^2 \right) dt^2 + 2a^2 \beta dt dr + a^2 dr^2 + r^2 b^2 d\Omega^2, \quad (2.42)$$

where $\alpha = \alpha(t, r)$, $\beta = \beta(t, r)$, $a = a(t, r)$, $b = b(t, r)$, and where

$$d\Omega^2 = d\theta^2 + \sin^2 \theta d\phi^2 \quad (2.43)$$

is the usual metric on the unit sphere. In the special case

$$\beta = 0, \;\; b = 1 \quad (2.44)$$

the line element reduces to that of the *polar areal* coordinate system

$$ds^2 = -\alpha^2 dt^2 + a^2 dr^2 + r^2 d\Omega^2. \quad (2.45)$$

The future-directed unit-norm spatial hypersurface orthogonal vector is $n^a = (1/\alpha, 0, 0, 0)$. The term *polar* is used because of the usual association of r, θ, and ϕ with the polar coordinate system in flat spacetime, while *areal* is used because the proper area of a two-sphere of radius r, centered at $r = 0$, is $4\pi r^2$. r is thus a geometric quantity. This polar slicing condition places a restriction on the trace of the extrinsic curvature tensor, K_{ab},

$$K \equiv \mathrm{Tr} K \equiv K^a{}_a = K^r{}_r. \quad (2.46)$$

It is straightforward to show (algebra omitted) this in turn implies

$$K^\theta{}_\theta = K^\phi{}_\phi = 0. \quad (2.47)$$

Finally, since a generalized Birkhoff's theorem tells us that spherically symmetric electrovac solutions are uniquely Reissner-Nordström, I can identify polar areal metric functions α and a outside

[1] I refer the reader to [148] or [27] for the full procedure.

sources through[2]

$$\alpha^2 = \left(1 - \frac{2m}{r} + \frac{q^2}{4\pi r^2}\right), \tag{2.50}$$

$$a^2 = \left(1 - \frac{2m}{r} + \frac{q^2}{4\pi r^2}\right)^{-1}, \tag{2.51}$$

where parameters $m = m(t,r)$ and $q = q(t,r)$ respectively represent the gravitational mass and electric charge of the source. Then, rewriting (2.51) I obtain

$$m = \frac{r}{2}\left(1 - \frac{1}{a^2} + \frac{q^2}{4\pi r^2}\right), \tag{2.52}$$

the so-called *mass aspect function* [28]. In an evolutionary problem, the divergence of a^2 signals the formation of an apparent horizon—and therefore existence of a black hole—for this choice of coordinates.[3] In the limit $r \to \infty$ the mass aspect function is then interpreted as the *total effective mass* of the black hole, consisting of the usual ADM mass (see [4]) less the difference of total ingoing and outgoing matter flux at the time of apparent horizon formation [56].[4] As noted in [21], this total effective mass is the natural measure in the signal of black hole formation for time-dependent problems. Once a^2 has diverged, I can integrate the charge density to obtain $q(t,r)$. Knowing all the functions on the right hand side of (2.52) I can immediately deduce $m(t,r)$ for the solution.

I now state (without derivation) the values of $D^a D_b \alpha$, $K^a{}_b$, K, $D_b K^{ab}$, $D^a K$, $\mathcal{R}^a{}_b$ and $\mathcal{R}$ required by the equations of spacetime constraint and evolution. The non-vanishing contributions are

$$D^r D_r \alpha = \frac{1}{a}\left(\frac{\alpha'}{a}\right)', \quad D^\theta D_\theta \alpha = D^\phi D_\phi \alpha = \frac{\alpha'}{a^2 r}, \tag{2.57}$$

$$K^r{}_r = -\frac{\dot{a}}{a\alpha}, \tag{2.58}$$

[2]The last term employs a common convention different from those of [62], [145], [40], [49], and [17]. The factor $\frac{1}{4\pi}$ has been inherited by the current term since I use the Maxwell equation convention

$$\nabla^a F_{ab} = -J_b, \tag{2.48}$$

rather than

$$\nabla^a F_{ab} = -4\pi J_b. \tag{2.49}$$

[3]The equation for a trapped surface is [44]

$$\left(\gamma^{ab} - s^a s^b\right)(D_a s_b - K_{ab}) = 0 \ , \tag{2.53}$$

where s^a is a spacelike, outward-pointing, unit-norm to the surface. Using the polar areal coordinate system in spherical symmetry s^a is given by

$$s^a = \left(0, \frac{1}{a}, 0, 0\right) \ . \tag{2.54}$$

In polar areal coordinates, expression (2.53) then evaluates to

$$\frac{2}{ar} = 0 \ . \tag{2.55}$$

Since a becomes arbitrarily large, but never reaches the limit $a \to \infty$, apparent horizons never actually form in this coordinate system. However, apparent horizon formation is imminent as a increases to arbitrarily large values. With some confidence, the location at which a diverges can then be used to estimate the eventual location of the apparent horizon. Finally, if an apparent horizon forms, an event horizon is known to exist at or outside the location of the apparent horizon. It is in this sense that I refer to the formation of a black hole.

[4]As can be seen from results that follow, choosing polar areal coordinates allows the Hamiltonian constraint in the $q = 0$ limit to be rewritten in the suggestive form

$$\frac{dm}{dr} = 4\pi r^2 \rho. \tag{2.56}$$

$$K = -\frac{\dot{a}}{a\alpha}, \tag{2.59}$$

$$D^a K^r{}_a = -\left(\frac{\dot{a}}{a\alpha}\right)' - \frac{2\dot{a}}{ra\alpha}, \tag{2.60}$$

$$D^r K = -\frac{\dot{a}}{a^3\alpha}, \tag{2.61}$$

$$\mathcal{R}^r{}_r = \frac{2a'}{ra^3}, \quad \mathcal{R}^\theta{}_\theta = \mathcal{R}^\phi{}_\phi = \frac{1}{ar^2}\left(a - \left(\frac{r}{a}\right)'\right), \tag{2.62}$$

$$\mathcal{R} = \frac{2}{ar}\left(-2\left(\frac{1}{a}\right)' + \frac{a}{r}\left(1 - \frac{1}{a^2}\right)\right), \tag{2.63}$$

where prime, $'$, designates partial differentiation with respect to radial coordinate r, and overdot, $\dot{}$, designates partial differentiation with respect to time coordinate t. Substituting these quantities into the results of subsections 2.1.5 and 2.1.7 I obtain the *Hamiltonian constraint*

$$\frac{a'}{a} + \frac{a^2 - 1}{2r} - 4\pi r a^2 \rho = 0, \tag{2.64}$$

and the *momentum constraint*

$$\dot{a} - 4\pi r a \alpha j_r = 0. \tag{2.65}$$

Rather than directly using the *evolution equations* for the spatial metric and extrinsic curvature, I find the so-called *slicing condition* more useful in the calculations. This equation can be derived from the evolution equations for K^a_b. First note that, since the spacetime metric is torsion-free, Lie derivatives of K_{ab} with respect to N^c reduce to covariant derivatives as per

$$\pounds_N K^a_b = (D_c K^a_b)\, N^c - K^c_b\,(D_c N^a) + K^a_c\,(D_b N^c)\,. \tag{2.66}$$

For polar areal metric (2.45) this reduces (2.41) to

$$D_t K^a_b = -D^a D_b \alpha + \alpha\left(\mathcal{R}^a{}_b + K K^a{}_b + 8\pi\left(\frac{1}{2}\perp^a{}_b (S - \rho) - S^a{}_b\right)\right)\,. \tag{2.67}$$

Then, using $K^\theta_\theta = \dot{K}^\theta_\theta = 0$, and substituting Hamiltonian constraint (2.64) where appropriate, (2.67) becomes

$$\frac{\alpha'}{\alpha} - \frac{a^2 - 1}{2r} - 4\pi r a^2\left(S - 2S^\theta_\theta\right) = 0\,. \tag{2.68}$$

However, using the Einstein field equations, it is possible to show that here

$$T^\theta{}_\theta = T^\phi{}_\phi\,, \tag{2.69}$$

from which it follows

$$S^\theta{}_\theta = S^\phi{}_\phi\,, \tag{2.70}$$

reducing the slicing condition to

$$\frac{\alpha'}{\alpha} - \frac{a^2 - 1}{2r} - 4\pi r a^2 S^r{}_r = 0\,. \tag{2.71}$$

The set of equations (2.64), (2.65), (2.71) is sufficient to solve for the entire evolution of spacetime geometry. The method by which to choose appropriate data from which to begin evolution is the initial value problem of general relativity. It is the topic of the next section.

2.2 The Initial Value Problem

The *Cauchy problem* of a theory amounts to (1) the determination of a boundary and conditions on that boundary along with (2) equations which yield unique solutions for these boundary conditions. The boundary of the Cauchy problem is known as a *Cauchy surface*. In an evolutionary theory like general relativity or electromagnetism where a $3+1$ formulation has been adopted, the Cauchy surface is the spatial hypersurface $\Sigma_{t=0}$ on which initial conditions are specified, from which the system is deterministically evolved.[5] In fact, the Cauchy problems of electromagnetism and general relativity are remarkably similar. Both the Einstein equations and the Maxwell equations with sources form sets of coupled nonlinear partial differential equations, both sets containing evolutionary equations of hyperbolic character as well as constraint equations of elliptic type. And not only are the same solution methods applicable to the hyperbolic equations of both electromagnetism and general relativity, but also similar are the methods for solving the elliptic constraints and initial value problems of both theories. The next chapter provides a rather detailed account of the numerical techniques used to solve the initial value and evolutionary equations. I now demonstrate well-posedness of the Maxwell equations as discussed in [145] and outline the solution of the initial value problem as developed by [149]. Since this thesis involves only the solutions of Einstein's equations in spherical symmetry, but the Maxwell equations in both spherical symmetry and axial symmetry, I focus discussion primarily on the initial value problem of electromagnetism.

2.2.1 The Initial Value Problem for Electromagnetism

In covariant form the Maxwell's equations for non-polarizable, non-magnetizable media are

$$\begin{aligned} \nabla^a F_{ab} &= -J_b \ , & (2.72) \\ \nabla_a F_{bc} + \nabla_c F_{ab} + \nabla_b F_{ca} &= 0 \ , & (2.73) \end{aligned}$$

where F_{ab} is the electromagnetic field-strength tensor and J_a is the four-current. (2.72) are the inhomogeneous equations and (2.73) are the homogeneous Maxwell equations. Since F_{ab} is anti-symmetric, contracting (2.72) with the covariant derivative obtains

$$0 = \nabla^b \nabla^a F_{ab} = -\nabla^b J_b \ , \tag{2.74}$$

demonstrating J_a is conserved current. I can use

$$F_{ab} = \nabla_a A_b - \nabla_b A_a \tag{2.75}$$

to write them in terms of the four-vector potential A_a as

$$\begin{aligned} \nabla^a(\nabla_a A_b - \nabla_b A_a) &= -J_b \ , & (2.76) \\ \nabla_a(\nabla_b A_c - \nabla_c A_b) + \nabla_c(\nabla_a A_b - \nabla_b A_a) + \nabla_b(\nabla_c A_a - \nabla_a A_c) &= 0 \ . & (2.77) \end{aligned}$$

The inhomogeneous Maxwell equations are exactly what I derive for A_a using the Euler-Lagrange equations. In addition, it is clear that by substituting

$$(\nabla_a \nabla_b - \nabla_b \nabla_a)\, T^{c_1 \ldots c_k}{}_{d_1 \ldots d_l} = -\sum_{i=1}^{k} R_{abe}{}^{c_i} T^{c_1 \ldots e \ldots c_k}{}_{d_1 \ldots d_l} + \sum_{j=1}^{l} R_{abd_j}{}^{e} T^{c_1 \ldots c_k}{}_{d_1 \ldots e \ldots d_l} \tag{2.78}$$

[5]The one caveat is occurrence of a *Cauchy horizon* marking the boundary of the domain of dependence beyond which the evolution will not be determined by data supplied on the Cauchy surface. While Cauchy horizons occur in black hole spacetimes, such as Reissner-Nordström and Kerr, they are typically shrouded by event horizons. Furthermore, as discussed in Chapter 3, the Cauchy horizon is known to be unstable in the case of Reissner-Nordström, and it is also debatable whether one will form during the gravitational collapse of a realistic matter distribution.

into the left hand side of (2.77) I obtain

$$\begin{aligned}
&\nabla_a(\nabla_b A_c - \nabla_c A_b) + \nabla_c(\nabla_a A_b - \nabla_b A_a) + \nabla_b(\nabla_c A_a - \nabla_a A_c) \\
&= -\left(R_{bdac} + R_{adcb} + R_{cdba}\right) A^d \\
&= \left(R_{dbac} + R_{dacb} + R_{dcba}\right) A^d \\
&= 0 \ , \qquad (2.79)
\end{aligned}$$

and so the homogeneous Maxwell's equations hold by construction, by virtue of the vector potential formulation of the theory.[6] However, I have still not discussed the character of these equations.

Because the homogeneous equations hold by construction, there is no need to examine them in any more detail. However, since the inhomogeneous equations must be solved explicitly, it is useful to examine their character, as it will determine how I must solve for the dynamics of the system. First, notice that, because of antisymmetry, the inhomogeneous equations

$$\nabla^a F_{ab} = \nabla^a(\nabla_a A_b - \nabla_b A_a) = -J_b \qquad (2.84)$$

contain no nonvanishing terms $\nabla^i \nabla_i A_i$, where summation over repeated indices is in this instance *not* implied, and index i designates a specific component living in the n-dimensional spacetime. Because of this, (2.84) can only provide evolution equations for $n-1$ of the n components A_a. Specifically, if A_t is the temporal component, then the inhomogeneous equation

$$\nabla^a F_{at} = \nabla^a(\nabla_a A_t - \nabla_t A_a) = -J_t \qquad (2.85)$$

is an elliptic equation of constraint for the electromagnetically coupled system.[7] (2.85) must be satisfied at all times. The question which naturally arises, is, "If (2.85) is satisfied at the initial time, will the evolution equations preserve the solution of (2.85) for all time?" The answer to this question is "yes", and it is reasonably straight-forward to demonstrate. To obtain the answer, I first choose a gauge. For the current purposes, Lorentz gauge

$$\nabla_a A^a = \nabla^a A_a = 0 \qquad (2.87)$$

[6] In electromagnetism texts this proof is typically presented for stationary observers in flat spacetime as follows. In (spatial) three-vector notation the homogeneous Maxwell's equations terms of the magnetic field, $\vec{B}$, and electric field, $\vec{E}$, are written

$$\begin{aligned}
\vec{\nabla} \cdot \vec{B} &= 0 \ , \qquad (2.80) \\
\vec{\nabla} \times \vec{E} + \frac{\partial \vec{B}}{\partial t} &= 0 \ . \qquad (2.81)
\end{aligned}$$

In terms of the three-vector potential $\vec{A}$ and scalar potential φ, the $\vec{B}$ and $\vec{E}$ are

$$\begin{aligned}
\vec{B} &= \vec{\nabla} \times \vec{A} \ , \qquad (2.82) \\
\vec{E} &= -\frac{\partial \vec{A}}{\partial t} - \vec{\nabla}\varphi \ . \qquad (2.83)
\end{aligned}$$

Then, since the divergence of the curl of any vector field is identically zero (i.e., $\vec{\nabla} \cdot \left(\vec{\nabla} \times \vec{A}\right) = 0$) and since the curl of the gradient of any scalar field is also identically zero (i.e., $\vec{\nabla} \times \vec{\nabla}\varphi = 0$) equations (2.80) and (2.81) hold by construction.

[7] Using the (spatial) three-vector nomenclature of flat space, this constraint equation is simply Gauss' law of electrodynamics,

$$\vec{\nabla} \cdot \vec{E} = \rho_Q \ , \qquad (2.86)$$

where ρ_Q is the charge density.

is the most convenient. Then, substituting

$$\nabla^a F_{ab} = \nabla^a(\nabla_a A_b - \nabla_b A_a) = \nabla^a \nabla_a A_b - R^c{}_{acb} A^a = \nabla^a \nabla_a A_b - R^a{}_b A_a \ , \tag{2.88}$$

(which has incorporated in it the Lorentz gauge condition) into (2.76) I obtain the form

$$\nabla^a \nabla_a A_b - R^a{}_b A_a + J_b = 0 \ , \tag{2.89}$$

a wave equation for the field A_b. Since I are generally allowing gravitational back-reaction, the Ricci tensor $R^a{}_b$ will be dependent on the stress-energy tensor. Now, covariantly differentiating (2.89) I obtain

$$\nabla^b \nabla^a \nabla_a A_b - \nabla^a R_{ae} A^e = 0 \ , \tag{2.90}$$

where I have used the symmetries of the Ricci tensor and $\nabla^a J_a = 0$ to get the result. Next, using (2.78) I find that

$$\begin{aligned}
\nabla^b \nabla^a \nabla_a A_b &= \nabla_b \nabla_a \nabla^a A^b \\
&= \nabla_a \nabla_b \nabla^a A^b - R_{bae}{}^a \nabla^e A^b - R_{bae}{}^b \nabla^a A^e \\
&= \nabla^a \nabla_b \nabla_a A^b - R_{bae}{}^a \nabla^e A^b - R_{bae}{}^b \nabla^a A^e \\
&= \nabla^a \nabla_a \nabla_b A^b - \nabla^a R_{bae}{}^b A^e - R_{bae}{}^a \nabla^e A^b - R_{bae}{}^b \nabla^a A^e \\
&= \nabla^a \nabla_a \nabla_b A^b + \nabla^a R_{ae} A^e \ .
\end{aligned} \tag{2.91}$$

Then, substituting (2.91) into (2.90) I find

$$\nabla^a \nabla_a \left(\nabla_b A^b \right) = 0 \ . \tag{2.92}$$

Clearly, the Euler-Lagrange equations for vector potential A_a (i.e., the inhomogeneous Maxwell equations) can be written as a linear, diagonal second-order hyperbolic system. As such, it has a *well-posed* initial value formulation as proven by theorems (see [145] for details). Then, given both an initial data set (A_a, $\frac{\partial A_a}{\partial t}$) satisfying (2.85) and the Lorentz gauge condition on a Cauchy surface $\Sigma_{t=0}$, this system is guaranteed to satisfy the Maxwell equations and Lorentz gauge condition everywhere for all time.

To solve constraint equation (2.85) I implement the procedure outlined by York and Piran [149], described in terms of the electric field[8]

$$E_a = F_{ab} n^b \tag{2.94}$$

as follows. Since the constraint equation is essentially Gauss' law for the electric field, I start by decomposing the electric field into its longitudinal (divergenceful) and transverse (divergenceless) parts, L_a and T_a respectively,

$$E_a = L_a + T_a \ . \tag{2.95}$$

Now, I introduce a scalar field U and define it to be the potential for the electric field,

$$L_a = D_a U \ , \tag{2.96}$$

[8]Here the magnetic field would be expressed

$$B_a = -\frac{1}{2} \epsilon_{ab}{}^{cd} F_{cd} n^b \ , \tag{2.93}$$

where ϵ_{abcd} is the totally antisymmetric tensor of positive orientation.

where D_a is again the spatial covariant derivative operator. Then, clearly,

$$\begin{aligned} D^a E_a &= D^a (L_a + T_a) \\ &= D^a L_a \\ &= D^a D_a U \ , \end{aligned} \tag{2.97}$$

where $D^a D_a$ is the (spatial) 3-dimensional Laplacian operator.[9] Then, since

$$D^a D_a U = D^a E_a = \rho_Q \ , \tag{2.99}$$

where $\rho_Q = -n^a J_a$ is the electric charge density,[10] I recognize this constraint equation as the usual Poisson equation. As expected, it is of elliptic type. Once I have solved elliptic differential equation (2.99) for U, I can determine E_a up to a transverse component T_a as

$$E_a = L_a + T_a = D_a U + T_a \ . \tag{2.100}$$

The electromagnetic initial value problem thus has been reduced to a single equation (2.99). Now, while the longitudinal component L_a is explicitly involved in the solution of U, the transverse component T_a (which represents the radiative degrees of freedom) is freely specifiable. I could just as well choose it to be vanishing at initial time. Thus, given charge density ρ_Q, I can solve for U via (2.99). Having found U, I can then determine L_a via (2.96). Meanwhile, I are free to specify any reasonable (i.e., smooth, differentiable, and satisfying regularity conditions discussed in section 2.4) initial values for any remaining variables not determined by gravitational constraints.

2.2.2 The Initial Value Problem for General Relativity

The Einstein, Einstein-Klein-Gordon and Einstein-Maxwell equations are known to possess well-posed initial value formulations.[11] The initial value problem of the Einstein equations is in many ways analogous to that of electromagnetism. Where in electromagnetism a choice of gauge condition had to be made for four-vector potential A_a, the gauge choice for the Einstein equations amounts to a choice of coordinates along with a slicing condition that determines the embedding of hypersurfaces Σ_t. Furthermore, while the well-posedness of electromagnetism was dependent on the ability to cast the inhomogeneous Maxwell equations as a linear, diagonal second-order hyperbolic system, well-posedness for general relativity requires the reformulation of Einstein's equations as a quasilinear, diagonal second-order hyperbolic system (see [145] for details). Well-posedness of the Einstein equations was first demonstrated in [33]. Further developments of special significance were produced in [34], and [35].

While the inhomogeneous Maxwell equations (2.85) form the initial value constraints of electromagnetism, for Einstein's equations they are furnished by the Hamiltonian constraint (2.29) and momentum constrains (2.30). Then, by theorem, providing an initial data set $(\Sigma_{t=0}, h_{ab}, K_{ab})$ satisfying (2.29) and (2.30) is supplied on a Cauchy surface diffeomorphic to $\Sigma_{t=0}$, the system is guaranteed to satisfy the Einstein equations on subsequent Σ_t. Here γ_{ab} is the spatial three-metric as defined in subsection 2.1.2 and K_{ab} is the extrinsic curvature as defined in subsection 2.1.4.

[9] The 3-dimensional Laplacian in polar areal coordinates acting on $U(t,r)$ is

$$\begin{aligned} D^a D_a U(t,r) &= \left(\frac{1}{a^2}\right)\left[\frac{2}{r}(\partial_r U) - \frac{1}{a}(\partial_r a)(\partial_r U) + (\partial_r \partial_r U)\right] \\ &= \left(\frac{1}{a}\right)\frac{1}{r^2}\partial_r\left[\frac{r^2}{a}(\partial_r U)\right] \ . \end{aligned} \tag{2.98}$$

[10] In polar-areal coordinates, $\rho_Q = -n^a J_a = -\frac{1}{\alpha} J_t$.

[11] The equations of Chapter 3 form an Einstein-Maxwell system where the sources are given by an electromagnetically coupled complex scalar field.

The solution of (2.29) and (2.30) can be carried out by decomposing extrinsic curvature, K_{ab}, into longitudinal and transverse components, and then freely specifying the divergenceless (transverse) component while solving the required elliptic for the divergenceful (longitudinal) part. This is closely analogous to the preceding decomposition and solution of the electric field where the transverse component represented the radiative degrees of freedom for the electromagnetic field. In the case of Einstein's equations, the transverse component of the extrinsic curvature encodes gravitational radiation content of the spacetime.[12]

2.3 Conserved Quantities

If a given tensor $T^{abc\cdots}_{def\cdots}$ is divergenceless, for example

$$\nabla_a T^{abc\cdots}_{def\cdots} = 0, \tag{2.101}$$

it has associated with it zero or more conserved quantities, depending on the symmetries (and thus Killing vectors) of the spacetime. If the divergenceless tensor is the stress-energy, T_{ab}, then the conserved quantities will be energy and a component of the momentum. If the tensor is instead the current four-vector J_a, the conserved quantity will be a charge.

2.3.1 Conservation of Charge

Consider first the case of a conserved current four-vector, J_a,

$$\nabla_a J^a = 0, \tag{2.102}$$

an example being the electromagnetic current. Then, contracting this vector with the hypersurface orthonormal n_a yields charge density, ρ_Q,

$$\rho_Q = -n_a J^a, \tag{2.103}$$

as measured by an observer with four-velocity n_a. Using Gauss' theorem, the total charge, Q, can be obtained by integrating (2.103) over one of the spacelike hypersurfaces Σ_t,

$$Q = -\int_{\Sigma_t} \sqrt{|\gamma|} n_a J^a d^3x, \tag{2.104}$$

where $|\gamma|$ is the determinant of the spacial metric γ_{ab}, and d^3x is the invariant volume element on Σ_t. This integrated charge will then be a constant, regardless of any dynamics. Observe how conservation is manifest for divergenceless four-vectors regardless of spacetime symmetry. The situation is different for tensors of rank-two or more—conservation there depends on the existence of Killing vectors.

2.3.2 Conservation of Energy and Momentum

The (rank-two) stress-energy tensor T_{ab} is by construction divergenceless,

$$\nabla_a T^{ab} = \nabla_a T^{ba} = 0. \tag{2.105}$$

[12] For the spherically symmetric spacetime in polar-areal coordinates, the constraint equations and slicing condition have been reduced to ordinary differential equations (2.64), (2.65) and (2.71) which can easily be integrated. In this case, the system also possesses no radiative degrees of freedom.

In situations where the spacetime possesses a timelike Killing vector field t_a, the contraction

$$\rho_T = n_a t_b T^{ab} \tag{2.106}$$

is the energy density measured by an observer with four-velocity n_a. And when the spacetime possesses a spacelike Killing vector field s_a, the quantity

$$\rho_S = -n_a s_b T^{ab} \tag{2.107}$$

represents the momentum density in the direction of s_a. Then integrals

$$T = \int_{\Sigma_t} \sqrt{|\gamma|} n_a t_b T^{ab} d^3x \tag{2.108}$$

and

$$S = -\int_{\Sigma_t} \sqrt{|\gamma|} n_a s_b T^{ab} d^3x \tag{2.109}$$

respectively represent the total conserved energy and total conserved component of momentum. For instance, S could be the radial, angular, or other-directional momentum, the specifics depending on Killing vector s_a.

2.4 Regularity Conditions

In simulations presented later in this dissertation I employ coordinate systems which become degenerate over finite sets of spatial coordinate values. Specifically, in the spherically symmetric simulation of charged scalar critical collapse in Chapter 3, I use the (t, r, θ, ϕ) polar-areal coordinate system over a range which includes $r = 0$. Similarly, in Chapter 4, I study axially symmetric charged scalar accretion in (t, r, θ, ϕ) Kerr-Schild coordinates over a range which includes $\theta = 0$ and $\theta = \pi$. The system of equations to be evolved sometimes become singular at $r = 0$ for the polar-areal coordinates, and at $\theta = 0$ or $\theta = \pi$ for Kerr-Schild. In cases where the equations do not explicitly diverge, the evolution often becomes numerically unstable at the degenerate points unless the equations are recast in a more appropriate form. The form they take on is determined by so-called *regularity conditions* at the degenerate coordinate values [6], [45].

2.4.1 Regularity at $r = 0$ in Polar-Areal Coordinates

Following [6], I say a tensorial quantity is *regular* at $r = 0$ of the (t, r, θ, ϕ) polar-areal coordinate system if and only if its components can there be expanded in non-negative integer powers of the (x, y, z) spatial Cartesian components defined

$$x = r \sin\theta \cos\phi \; , \tag{2.110}$$

$$y = r \sin\theta \sin\phi \; , \tag{2.111}$$

$$z = r \cos\theta \; . \tag{2.112}$$

Clearly, assuming neither the spacetime nor matter are anywhere singular, I should ensure that all physical quantities are in this sense regular. Once the regularity conditions have been determined for the physical quantities, their consequences should be consistently propagated through the equations of any unphysical auxiliary variables. For example, under this definition, a physical rank-zero tensor quantity such as electric charge density, ρ_Q, or scalar field amplitude, $\Phi = \Phi(t, r)$, would to leading order have to be an even function of radial coordinate at $r = 0$. This would in turn imply that an auxiliary variable such as

$$\Phi_r(t,r) \equiv \partial_r \Phi \tag{2.113}$$

would by consequence have to be an odd function of r and therefore vanishing about $r = 0$. Furthermore, as the electric field is a rank-one tensor, the radial component E_r would have to be odd in r in order to be regular there. Indeed, if I were to integrate charge density ρ_Q over space, I would find that E_r would have to be odd about $r = 0$ by consequence of ρ_Q being even there (cf. Appendix C). This line of argument is similarly applied to determine the nature of each function about $r = 0$ in the evolution leading to critical collapse of charged scalar fields in Chapter 3.

2.4.2 Regularity at $\theta = 0$ and $\theta = \pi$ in Kerr-Schild Coordinates

Extending the definition, I say a tensorial quantity is *regular* at $\theta = 0$ and $\theta = \pi$ of the (t, r, θ, ϕ) Kerr-Schild coordinate system if and only if its components can be expanded in non-negative integer powers of its (x, y, z) spatial Cartesian components at these coordinate values. As a consequence, physical rank-zero tensors such as the scalar field, $\Phi = \Phi(t, r, \theta)$, or charge density, ρ_Q, are to leading order in θ even functions about $\theta = 0$ and $\theta = \pi$. By definition, auxiliary quantity

$$\Phi_\theta(t,r,\theta) \equiv \partial_\theta \Phi \tag{2.114}$$

would then have to be odd at these degenerate coordinate values. The components of a physical rank-one tensor can similarly be determined. For example, regularity requires the radial and axial components, E_r and E_ϕ, of the electric field vector be even to leading order in θ, and the angular component, E_θ, be odd in θ about $\theta = 0$ and $\theta = \pi$. The regularity conditions are obtained and enforced for all functions in Chapter 4.

2.5 The Sommerfeld Condition

When studying a dynamical system—or any system, for that matter—on a finite spatial domain, properties of the system on the domain boundary must be considered. The exact properties may or may not be known. If not known, the only choice is to apply approximate boundary conditions and examine whether they are sufficient for the purpose of current investigation.

As an example of a system where exact boundary conditions can be determined, consider the spherically symmetric massless Klein-Gordon equation

$$\nabla^a \nabla_a \Phi(t,r) = 0 \tag{2.115}$$

in Minkowski spacetime. In the usual (t, r, θ, ϕ) spherical polar coordinates, the spacetime is described by line element

$$ds^2 = -dt^2 + dr^2 + r^2 d\Omega^2 \ , \tag{2.116}$$

where

$$d\Omega^2 = d\theta^2 + \sin^2\theta d\phi^2 \ . \tag{2.117}$$

The spherically symmetric massless Klein-Gordon equation (2.115) can then be written

$$\partial_{tt}(r\Phi) = \partial_{rr}(r\Phi) \ , \tag{2.118}$$

where ∂_{tt} denotes the second partial derivative with respect to temporal coordinate t, and ∂_{rr} designates the second partial derivative with respect to radial coordinate r. There are both ingoing and outgoing solutions to (2.118), the ingoing being given by

$$(r\Phi)(t,r) = f(c_- t + r) \ , \tag{2.119}$$

$f(c_- t + r)$ being an arbitrary function of its single variable, while the outgoing solution is given by

$$(r\Phi)(t, r) = g(c_+ t - r) \ , \tag{2.120}$$

$g(c_+ t - r)$ again being an arbitrary function of just one variable, c_- being the ingoing wave speed and c_+ being the outgoing wave speed. The wave speeds are given by solutions of the radial null geodesic equation, here

$$\left(\frac{dr}{dt}\right)_\pm = c_\pm = \pm 1 \ . \tag{2.121}$$

From (2.119) it follows that ingoing solutions can be written

$$\partial_t(r\Phi) - (c_-)\partial_r(r\Phi) = 0 \ , \tag{2.122}$$

while from (2.120) it can be shown that outgoing solutions have the form

$$\partial_t(r\Phi) + (c_+)\partial_r(r\Phi) = 0 \ . \tag{2.123}$$

A radial inflow boundary condition for (2.115) then is given exactly by (2.122), while radial outflow is given exactly by (2.123). When applied at the domain boundary, equation (2.123) is commonly known as an *outgoing radiation boundary condition* or the *Sommerfeld condition* (cf. [135], [136]).

2.5.1 The Sommerfeld Condition in Polar Areal Coordinates

In the spacetime described by polar areal metric

$$ds^2 = -\alpha^2 dt^2 + a^2 dr^2 + r^2 d\Omega^2 \ , \tag{2.124}$$

where $\alpha = \alpha(t, r)$, $a = a(t, r)$, and $d\Omega^2$ again is given by (2.117), the Sommerfeld condition (2.123) will exactly describe outflow conditions of the massless Klein-Gordon equation when $\alpha = 1$ and $a = 1$ on the boundary. The Sommerfeld condition can still be applied when the spacetime is curved, but the quality of its approximation to perfect outflow will have to be tested. In the case of curved spacetime, radial null geodesics satisfy

$$\left(\frac{dr}{dt}\right)_\pm = c_\pm = \pm\left(\frac{\alpha}{a}\right) \ , \tag{2.125}$$

and so the (now approximate) condition (2.123) becomes

$$\partial_t(r\Phi) + \left(\frac{\alpha}{a}\right)\partial_r(r\Phi) = 0 \ . \tag{2.126}$$

In Chapter 3 (2.126) is used to study the critical gravitational collapse of charged massive complex scalar fields in spherical symmetry. While only approximate, the condition is sufficient for the choices of scalar field parameters and coordinate range, as demonstrably little inflow or reflection is observed from the domain boundary.

2.5.2 The Sommerfeld Condition in Kerr-Schild Coordinates

Suppose, instead, the massless Klein-Gordon equation is evolving in the spacetime of a rotating black hole described by the Kerr metric. In (t, r, θ, ϕ) Kerr-Schild coordinates, this spacetime is described by the line element

$$\begin{aligned} ds^2 &= -\left(1-\frac{2Mr}{\Sigma}\right)dt^2+\left(1+\frac{2Mr}{\Sigma}\right)dr^2+\Sigma d\theta^2+\sin^2\theta\left(r^2+a^2+\frac{2Mra^2\sin^2\theta}{\Sigma}\right)d\phi^2 \\ &\quad +\left(\frac{4Mr}{\Sigma}\right)dtdr-\left(\frac{4Mra\sin^2\theta}{\Sigma}\right)dtd\phi-2a\sin^2\theta\left(1+\frac{2Mr}{\Sigma}\right)drd\phi\ , \end{aligned} \tag{2.127}$$

where

$$\Sigma \equiv r^2+a^2\cos^2\theta\ , \tag{2.128}$$

$$a \equiv \frac{J}{M}\ , \tag{2.129}$$

t is the temporal coordinate, and r, θ and ϕ are respectively the radial and angular spatial coordinates, M represents the total mass of the black hole spacetime and J its total angular momentum. In this case, the radial null geodesics satisfy equation

$$0=-\left(1-\frac{2Mr}{\Sigma}\right)dt^2+\left(\frac{4Mr}{\Sigma}\right)dtdr+\left(1+\frac{2Mr}{\Sigma}\right)dr^2\ , \tag{2.130}$$

and so the wave speeds are

$$\left(\frac{dr}{dt}\right)_{\pm}=c_{\pm}=\left(\frac{-2Mr/\Sigma\pm 1}{1+2Mr/\Sigma}\right)\ . \tag{2.131}$$

Assuming the scalar field wavefronts are nearly spherical at the domain boundary, the approximate Sommerfeld condition can then be written

$$\partial_t(r\Phi)+\left(\frac{-2Mr/\Sigma+1}{1+2Mr/\Sigma}\right)\partial_r(r\Phi)=0\ . \tag{2.132}$$

This approximate boundary condition is used in Chapter 4 when studying the dynamics of electromagnetic radiation and charged massive scalar fields on a Kerr spacetime background. As discussed above, the implementation must be tested for inflow and reflections off the outer boundary. In doing so (2.132) is found sufficient for the purposes of the study.

To conclude, the Sommerfeld condition is often acceptable in practice. The computational boundaries can always be moved sufficiently far from regions of physical interest that partial reflections at late time will add only a tolerably small error to the solution. In situations where more precisely outgoing conditions are required on the boundary of a finite domain, a technique using boosted coordinates in conjunction with numerical dissipation can be applied. However, as the Sommerfeld condition is sufficient for the investigations presented in Chapters 3 and 4, discussion of this boosted coordinate method is reserved for Appendix D.

CHAPTER 3

CHARGED SCALAR CRITICAL COLLAPSE

3.1 Preliminary Discussion

3.1.1 Context of This Study

The near-critical collapse of a charged massive scalar field in spherical symmetry is studied in this chapter. Critical phenomena in gravitational collapse have been briefly discussed in the Chapter 1. More important, the interested reader can access a significant amount of review work on this subject, most notably due to Gundlach [59], [60], along with other detailed accounts of previous studies of critical phenomena in spherical symmetry. The latter include Ph. D. theses of many of Choptuik's former students (specifically, Liebling [93], Neilsen [106], Hawley [64], Honda [77], Pretorius [127], Ventrella [144], Noble [108], Olabarrieta [117] and Lai [92]).

Briefly, the reader is reminded that, in traditional critical behaviour, a *critical solution* has come to be identified as a type of separatrix (in solution space) between solutions modelling collapse to a black hole from those which do not. This separatrix has a small number of unstable modes—indeed, often only a single unstable mode—in perturbation theory. Even within the context of spherical symmetry, in which the bulk of critical phenomena computations—including those in this chapter—have been carried out, critical solutions are characterized by additional symmetry relative to generic solutions admitted for the model. To date, the additional symmetry has been of one of two types, each of which is further sub-typed as to whether the symmetry is discrete or continuous.

This has lead to the following classification hierarchy of critical solutions. In the top of this hierarchy, the phase transition between black hole spacetimes and those that are not are classified first or second order (Type I or Type II respectively) depending on whether or not the minimum black hole mass above threshold is finite or infinitesimal. Historically, this motivation through observation that the mass could be viewed as an order parameter traces back to Christodoulou [36] and Evans [46]. Now, in the second level of this hierarchy, the solutions are further sub-classified as either discrete or continuous, depending on their symmetry. As discussed in Chapter 1, one of the additional symmetries of Type II solutions is spatiotemporal discrete self-similarity (DSS). Continuously self-similar (CSS) and static solutions have also been found for Type II case in spherical symmetry. On the other hand, Type I solutions in spherical symmetry have been found to additionally possess a time-translational symmetry, which manifests as either (discrete) periodic or (continuous) static evolution. This classification hierarchy is presented with examples in Table 3.1.

One of the more novel features of the model studied in this chapter—shared with those of [24], [12] and [16] (for the massive real scalar field), [26] and [29] (for SU(2) Yang-Mills), [9] and [10] (for the SU(2) Skyrme model), [63], [64], [65] and [92] (for massive complex scalar fields), and [114] and [108] (for perfect fluids)—is the existence of both Type I and Type II behaviour. This arises from dimensionful terms in the matter Lagrangian that set a length scale which factors into the type critical solution obtained. In the limit of small scalar field mass m_Φ, and for an appropriate range of electric coupling parameter e, the massive charged scalar field solutions at black hole threshold should observe the Type II scaling relations noted in [66], [68] and [58]. The existence and properties of charged boson star solutions (see [79], [80], [81]), together with the current understanding of massive scalar critical phenomena, suggest that Type I critical solutions resembling perturbed charged boson stars should exist for an appropriate set of initial conditions and range of parameter values e and m_Φ [31]. However, details regarding the emergence and

critical solution	additional symmetry	example (from spherical symmetry)
Type I	continuous (static)	SU(2) Yang-Mills [26], [29]
		SU(2) Skyrme [9]
		perfect fluids [108]
	discrete (periodic)	massive real scalar field [12], [16]
Type II	continuous (static)	SU(2) Skyrme [10]
	continuous (CSS)	perfect fluids [114], [108]
	discrete (DSS)	massive real scalar field [24]
		SU(2) Yang-Mills [26], [29]

Table 3.1: Classification hierarchy of critical solutions. At the top of the hierarchy, the solutions are classified as either Type I or Type II. In Type I, near-critical black hole masses are finite. The spherically symmetric Type I solutions are further sub-typed by additional symmetry as either continuous (static) or discrete (periodic). In Type II, near-critical black hole masses are infinitesimal. The spherically symmetric Type II solutions are further sub-typed by additional symmetry as either continuously self-similar (CSS) or static, or discretely self-similar (DSS). Examples are given from spherically symmetric computations for each of these sub-types. All of the tabulated example models allow both Type I and Type II solutions, depending on parameter values and initial conditions.

properties of such solutions have not been documented elsewhere.

Note that the study described below has much in common with those of Brady, Chambers and Goncalves [12], [16], Hod and Piran [66], [68], Gundlach and Martin-Garcia [57], Hawley and Choptuik [63], [64], [65] and Lai [92]. Also note that, for the case of the Type II behaviour described herein, the results of Hod and Piran [66], [68] are expected to be significantly more accurate, and possessive of better convergence properties due to the fact that they were computed using a high-order unigrid technique, originally due to Garfinkle [52], tailored to the critical solution. The value of this particular study then, has been largely one of providing further confirmation of the view described by Gundlach and Martin-Garcia [57], and Hod and Piran [66], [68] with regards to charge scaling in the model, as well as completeness, as yet another case of critical collapse has been examined and the basic theoretical understanding of the phenomenology found solid. Perhaps most important, this study has provided valuable experience and insight into the nature of critical phenomena. This experience is likely to be vital in the studies of non-spherical charged collapse planned for the future.

3.1.2 Issues Regarding Horizons

Before solving the Einstein-Maxwell-Klein-Gordon equations with electromagnetically coupled complex scalar field sources, it is prudent to first consider what global structure one could expect for the spacetime. Even the spherically symmetric gravitational collapse of simple charged matter is nontrivial. The spacetime that results is one of a spherically symmetric charge-carrying black hole with some dynamic spherically symmetric charged matter distribution in its exterior. However, a generalization of Birkhoff's theorem guarantees the spacetime external to all matter is represented by the static Reissner-Nordström solution. While the maximal analytic extension of Reissner-Nordström spacetime is described by the Penrose diagram 3.1, it does not actually depict the spacetime generated by the realistic collapse of charged matter in spherical symmetry.

The dynamical evolution of a charged spherical shell of dust has been described in detail by

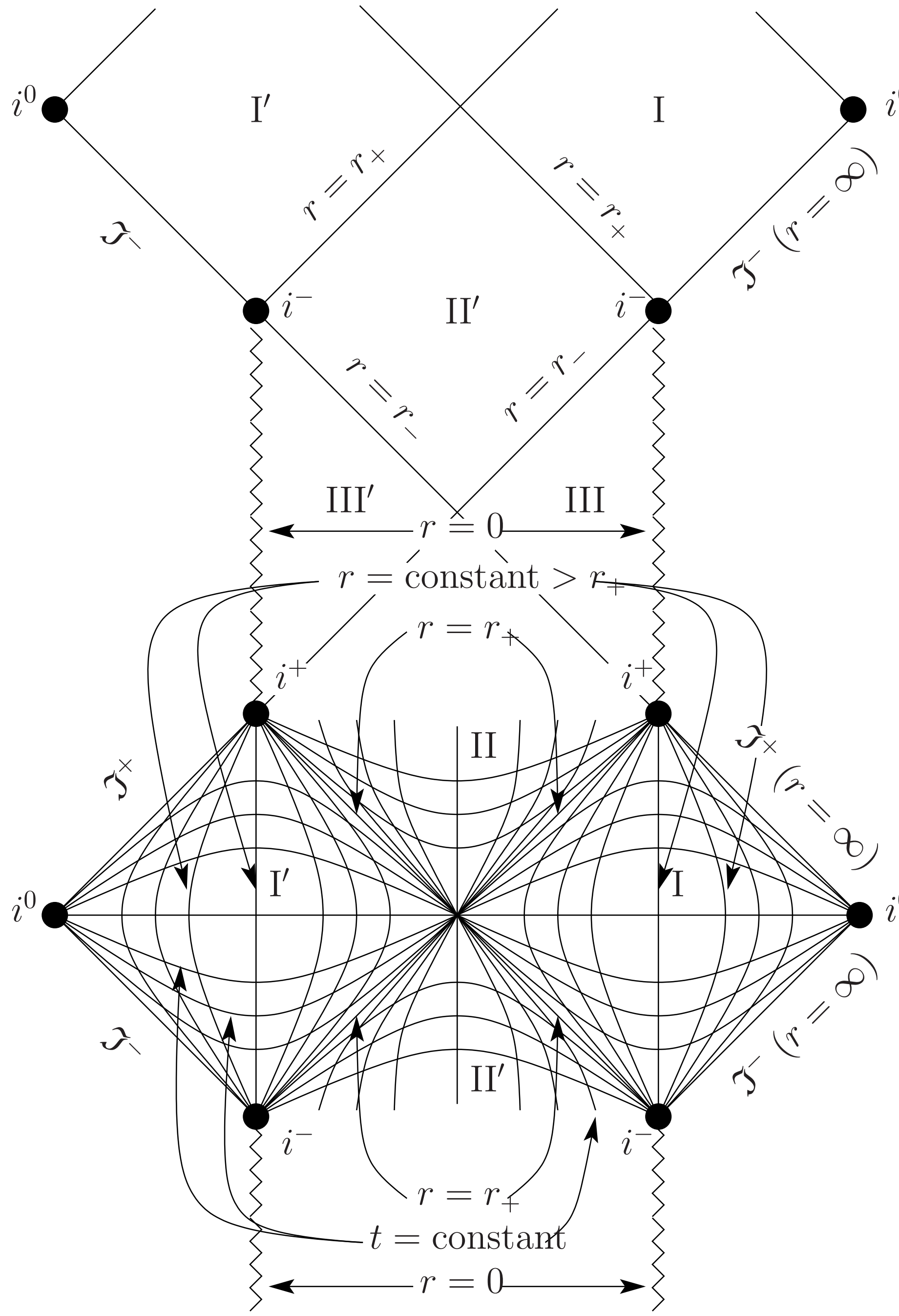

Figure 3.1: Penrose diagram showing causal structure of Reissner-Nordström spacetime (cf. [62]). I and I' depict asymptotically flat regions of the spacetime outside the black hole. II and II' are interior to the event horizon at $r = r_+$, while interior regions III and III' are separated from II and II' by the Cauchy horizons at $r = r_-$. $\mathfrak{I}^+$ represents future null infinity and $\mathfrak{I}^-$ past null infinity, while i^- represents past timelike infinity, i^+ future timelike infinity and i^0 spacelike infinity. The singularity at $r = 0$ is timelike, and can thus be avoided by a timelike trajectory.

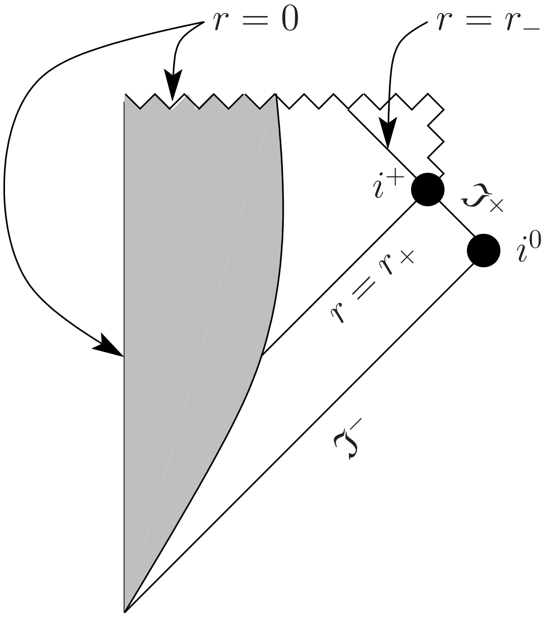

Figure 3.2: Conformal diagram for gravitational collapse and apparent horizon formation for a spherical shell of charged dust when the charge is too small to prevent spacelike singularity formation in its interior (cf. [11]). $\mathfrak{I}^+$ represents future null infinity, $\mathfrak{I}^-$ is past null infinity, i^0 is spacelike infinity, and i^+ represents future timelike infinity. An apparent horizon forms at radial coordinate $r = r_+$, and $r = r_-$ represents a Cauchy horizon. The spacetime singularity is spacelike and appears in the interior at $r = 0$.

Boulware [11] for various values of total mass, M, total charge, Q, and total rest mass $\mathcal{M}$.[1] While the spacetime interior to the spherically symmetric distribution is flat, the complete structure of spacetime is generally complicated and dependent on the values M, Q and $\mathcal{M}$. For example, if the charge carried by the matter is sufficiently small, it will not be able to prevent the formation of a spacelike spacetime singularity in its interior by electrostatic repulsion. In this case, the collapse will follow the evolution shown in Figure 3.2, which is a conformal diagram showing formation of an apparent horizon at radial coordinate value $r = r_+$ during evolution. The spacetime singularity appears in the interior at $r = 0$, and there exists a Cauchy horizon at $r = r_-$ beyond which spacetime is not determined by Einstein's equations with the given initial data. In the case where charge Q is large enough to prevent spacelike singularity formation, the evolution proceeds as depicted in Figure 3.3. An apparent horizon still forms at $r = r_+$, and a Cauchy horizon at $r = r_-$. A singularity again forms within the apparent horizon, but outside the charged matter. This singularity is now timelike and therefore can be avoided by the evolving matter. In fact, once inside $r = r_+$, the matter can pass through $r = r_-$, and, avoiding the singularity, re-expand into a second asymptotically flat region of space.

However, the case where a charged shell collapses to leave a black hole spacetime with timelike singularity is thought to be unrealistic. In fact, Penrose was first to notice that an observer crossing Cauchy horizon $r = r_-$ would see the entire history of asymptotically flat regions in a finite time [122], implying that $r = r_-$ should be unstable to small perturbations as later demonstrated in [100]. Meanwhile, by studying generic self-gravitating charged scalar field collapse, Hod and Piran were the first to demonstrate that in addition to the spacelike singularity at $r = 0$, a null singularity forms along the Cauchy horizon which then contracts and meets the spacelike singularity

[1] Novikov similarly studied the evolution of a shell of charged matter in [115].

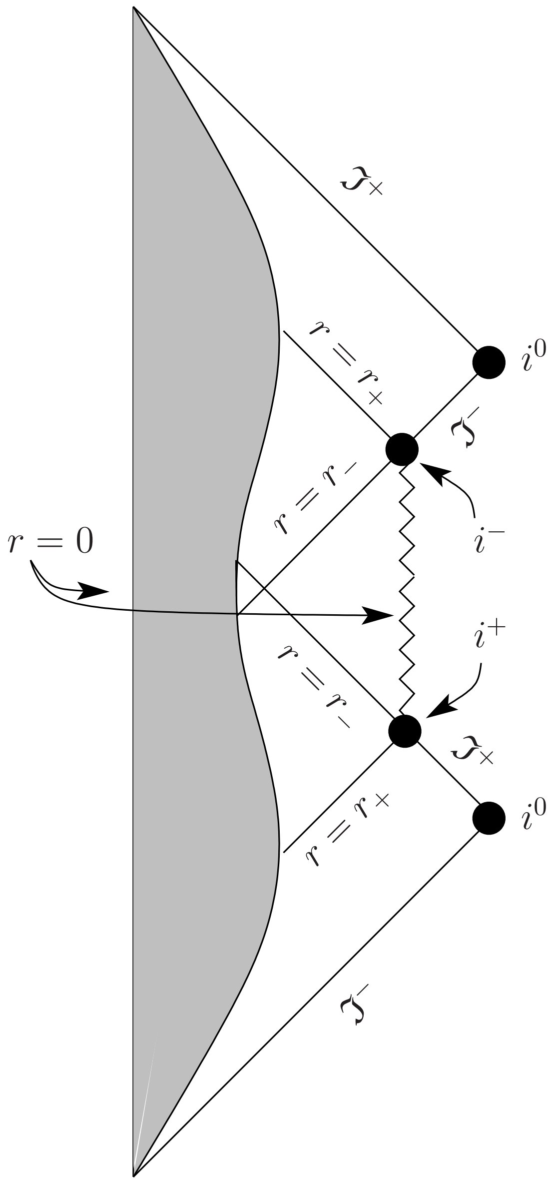

Figure 3.3: Conformal diagram for gravitational collapse and apparent horizon formation for a spherical shell of charged dust when the charge is large enough to prevent spacelike singularity formation in its interior (cf. [11]). $\mathfrak{I}^+$ represents future null infinity, $\mathfrak{I}^-$ is past null infinity, i^0 is spacelike infinity, and i^+ represents future timelike infinity. An apparent horizon forms at radial coordinate $r = r_+$, and $r = r_-$ represents a Cauchy horizon. A spacetime singularity again appears at $r = 0$, but it is now timelike and exterior to the matter.

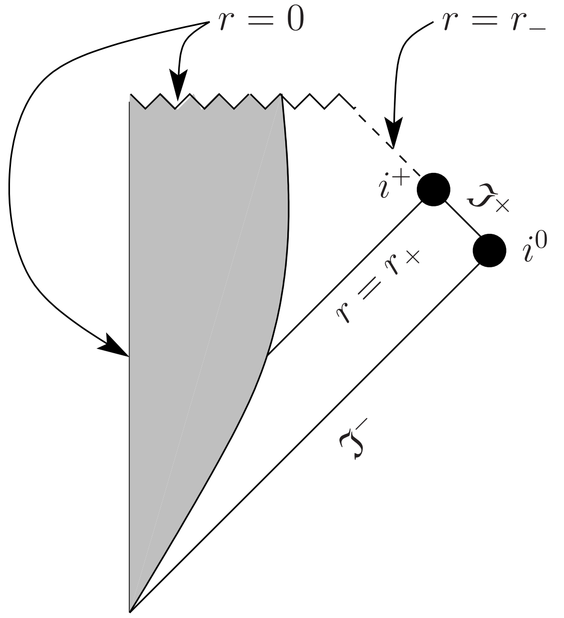

Figure 3.4: Conformal diagram for gravitational collapse and horizon formation for a spherically symmetric distribution of charged scalar field matter (cf. [72], [73]). $\mathfrak{I}^+$ represents future null infinity, $\mathfrak{I}^-$ is past null infinity, i^0 is spacelike infinity, and i^+ represents future timelike infinity. An apparent horizon forms at radial coordinate $r = r_+$, and $r = r_-$ represents a Cauchy horizon. A spacelike singularity forms in the interior at $r = 0$. Meanwhile, a weak null singularity forms along the Cauchy horizon and then contacts to meet the spacelike singularity at $r = 0$.

at $r = 0$ [72], [73]. This scenario is depicted in Figure 3.4. These results were confirmed and analyzed in somewhat greater detail by Oren and Piran [119]. Furthermore, their investigations demonstrated the contracting null singularity is *weak*, in that an observer crossing it will experience only finite tidal forces (cf. [120], [121]). So while their future is unpredictable after crossing $r = r_-$, observers can ultimately still escape to a causally disconnected region of spacetime which may also be asymptotically flat.

The salient feature of all these charged matter collapse scenarios is the appearance of the apparent horizon, outside which the spacetime is still predictable, regardless of any details within the Cauchy horizon. This property is what allows the use of any of a large number of coordinates to model processes leading up to the formation of a black hole by charged matter. Providing I am not interested in evolution beyond apparent horizon formation, non-penetrating coordinates are a completely suitable choice. The system of equations used in simulations of critical gravitational collapse of charged massive scalar fields now follows.

3.2 System of Equations

3.2.1 The Matter Lagrangian and Equations of Motion

The Lagrangian for a massive electromagnetically coupled complex scalar field is given by [62]

$$\mathcal{L}_{\mathcal{M}} = \sqrt{-g}[-(\nabla_a\Phi - ieA_a\Phi)(\nabla^a\Phi^* + ieA^a\Phi^*) - \frac{1}{4}F^{ab}F_{ab} - m_\Phi^2\Phi^*\Phi] \ , \tag{3.1}$$

where m_Φ is the scalar field mass parameter, e sets the strength of electromagnetic coupling between the real and imaginary components of complex scalar field $\Phi = \Phi(t,r)$, the symbol * denotes complex conjugation, $A_a = A_a(t,r)$ is the electromagnetic vector potential, and F_{ab} is the anti-symmetric electromagnetic field strength tensor defined according to

$$F_{ab} = \nabla_a A_b - \nabla_b A_a \ . \tag{3.2}$$

In terms of its real and imaginary components (respectively $\phi_1 = \phi_1(t,r)$ and $\phi_2 = \phi_2(t,r)$) the scalar field is written

$$\Phi = \phi_1 + i\phi_2 \ . \tag{3.3}$$

To make connection with the physical fields, an observer moving with four-velocity n^a would measure an electric field

$$E_a = F_{ab} n^b \tag{3.4}$$

and a magnetic field

$$B_a = -\frac{1}{2}\epsilon_{ab}{}^{cd} F_{cd} n^b \ , \tag{3.5}$$

where ϵ_{abcd} is the totally antisymmetric tensor of positive orientation.[2]

The set of Euler-Lagrange equations for the system described by (3.1),

$$\frac{\partial \mathcal{L}_\mathcal{M}}{\partial \Phi} - \nabla_a \left[\frac{\partial \mathcal{L}_\mathcal{M}}{\partial(\nabla_a \Phi)}\right] = 0 \ , \quad \frac{\partial \mathcal{L}_\mathcal{M}}{\partial \Phi^*} - \nabla_a \left[\frac{\partial \mathcal{L}_\mathcal{M}}{\partial(\nabla_a \Phi^*)}\right] = 0 \ , \tag{3.6}$$

$$\frac{\partial \mathcal{L}_\mathcal{M}}{\partial A_b} - \nabla_a \left[\frac{\partial \mathcal{L}_\mathcal{M}}{\partial(\nabla_a A_b)}\right] = 0 \ , \tag{3.7}$$

yields equations of motion[3]

$$\nabla^a \nabla_a \Phi^* + 2ie(\nabla_a \Phi^*)A^a - e^2 \Phi^* A_a A^a + ie\Phi^* \nabla_a A^a - m_\Phi{}^2 \Phi^* = 0 \ , \tag{3.8}$$

$$\nabla^a \nabla_a \Phi - 2ie(\nabla_a \Phi)A^a - e^2 \Phi A_a A^a - ie\Phi \nabla_a A^a - m_\Phi{}^2 \Phi = 0 \ , \tag{3.9}$$

$$\nabla^a F_{ab} - ie(\Phi^* \nabla_b \Phi - \Phi \nabla_b \Phi^*) - 2e^2 \Phi \Phi^* A_b = 0 \ . \tag{3.10}$$

I have the freedom to choose an electromagnetic gauge condition. I choose the Lorentz gauge condition

$$\nabla_a A^a = 0 \ . \tag{3.11}$$

This provides me with an equation of evolution for the temporal component of A_a.

Furthermore, since it can be demonstrated that

$$\nabla_a J^a = 0 \ , \tag{3.12}$$

where

$$-J^b \equiv \nabla_a F^{ab} = ie(\Phi^* \nabla^b \Phi - \Phi \nabla^b \Phi^*) + 2e^2 \Phi \Phi^* A^b, \tag{3.13}$$

I conclude J^a is a conserved current.[4]

[2] ϵ_{abcd} has norm given by $\epsilon_{abcd}\epsilon^{abcd} = -24$, and $\epsilon_{0123} = 1$ in a right-handed orthonormal basis.
[3] Under decomposition (3.3) it is clear that (3.8) and (3.9) are completely equivalent.
[4] The choice of sign and normalizing factor on J^b are somewhat arbitrary. A different choice of sign would later introduce a factor of -1 in the value of the electric charge density ρ_Q.

3.2.2 The Einstein Lagrangian and Field Equations

The Einstein Lagrangian is

$$\mathcal{L}_{\mathcal{G}} = \sqrt{-g}R \ , \tag{3.14}$$

and the total Lagrangian is given by minimally coupling the matter Lagrangian to the geometry via

$$\mathcal{L} = \mathcal{L}_{\mathcal{G}} + \alpha_{\mathcal{M}}\mathcal{L}_{\mathcal{M}} \ , \tag{3.15}$$

where coupling constant $\alpha_{\mathcal{M}}$ will have to be chosen to give the correct normalization for the stress-energy tensor of the matter field.

The Einstein field equations are obtained by variation of the action

$$\mathcal{S}[g_{ab}, \Phi, \Phi^*, A_a] = \int \mathcal{L} d^4x \tag{3.16}$$

with respect to g_{ab}. They are

$$G_{ab} = R_{ab} - \frac{1}{2} g_{ab} R = 8\pi T_{ab} \ , \tag{3.17}$$

where the stress-energy tensor T_{ab} is given by

$$T_{ab} = \frac{\alpha_{\mathcal{M}}}{8\pi} \frac{1}{\sqrt{-g}} \left(-\frac{\partial \mathcal{L}_{\mathcal{M}}}{\partial g^{ab}} + \frac{1}{2} g_{ab} \mathcal{L}_{\mathcal{M}} \right) \ . \tag{3.18}$$

Using (3.1) and (3.18) I explicitly obtain

$$\begin{aligned} T_{ab} \quad = \quad & \frac{1}{2}\left(\nabla_a\Phi\nabla_b\Phi^* + \nabla_b\Phi\nabla_a\Phi^*\right) - \frac{1}{2} ie \left[\left(\Phi\nabla_b\Phi^* - \Phi^*\nabla_b\Phi\right)A_a + \left(\Phi\nabla_a\Phi^* - \Phi^*\nabla_a\Phi\right)A_b\right] \\ & + e^2\Phi\Phi^* A_a A_b + \frac{1}{2} F_{ac}F_{bd}g^{cd} - \frac{1}{2} g_{ab}[(\nabla_c\Phi - ieA_c\Phi)(\nabla^c\Phi^* + ieA^c\Phi^*) + \frac{1}{4}F^{cd}F_{cd} \\ & + {m_\Phi}^2\Phi^*\Phi] \ , \end{aligned} \tag{3.19}$$

where $\alpha_{\mathcal{M}} = 8\pi$ has been chosen in order that I retrieve the Einstein-Maxwell-Klein-Gordon equations from (3.17).

3.2.3 The Spacetime Metric and Equations

While many coordinate systems could be used to study the critical collapse of a massive charged scalar field, one convenient choice is polar-areal. As presented in subsection 2.1.8, the line element of a spherically symmetric spacetime in polar-areal coordinates is

$$ds^2 = -\alpha^2 dt^2 + a^2 dr^2 + r^2 d\Omega^2, \tag{3.20}$$

where $\alpha = \alpha(t,r)$, $a = a(t,r)$, $d\Omega^2 = d\theta^2 + \sin^2\theta d\phi^2$, t is the temporal coordinate, and r, θ and ϕ are respectively the radial and angular spatial coordinates. Again, the future-directed unit-norm spatial hypersurface orthogonal vector is $n^a = (1/\alpha, 0, 0, 0)$, and the spatial metric is

$$\gamma_{ab} = \mathrm{diag}\left(a^2, r^2, r^2\sin^2\theta\right) . \tag{3.21}$$

Clearly, as the divergence of a^2 marks the formation of an apparent horizon, this coordinate system becomes singular and is therefore horizon non-penetrating. With the choice I've made for normalization of the electromagnetic field Lagrangian density, the mass aspect function takes on the form

$$m = \frac{r}{2}\left(1 - \frac{1}{a^2} + \frac{q^2}{4\pi r^2}\right) , \tag{3.22}$$

where $m = m(t, r)$ is the gravitational mass and $q = q(t, r)$ is the electric charge of the source. Finally, the Hamiltonian constraint is

$$\frac{a'}{a} + \frac{a^2 - 1}{2r} - 4\pi r a^2 \rho = 0, \tag{3.23}$$

the momentum constraint is

$$\dot{a} - 4\pi r a \alpha j_r = 0, \tag{3.24}$$

and the polar slicing condition is

$$\frac{\alpha'}{\alpha} - \frac{a^2 - 1}{2r} - 4\pi r a^2 S^r{}_r = 0, \tag{3.25}$$

where prime, $'$, designated partial differentiation with respect to radial coordinate r, overdot, $\dot{}$, designates partial differentiation with respect to temporal coordinate t.[5] The explicit forms of ρ (energy density), j_r (momentum density) and $S^r{}_r$ (stress tensor) are

$$\begin{aligned}
\rho &= T_{ab} n^a n^b \\
&= \frac{1}{2}\left(\frac{1}{a^2}\right)\left[\Pi_\Phi \Pi_\Phi^* + \left(\Phi_r - ie\Phi A_r\right)\left(\Phi_r^* + ie\Phi^* A_r\right)\right] + \frac{1}{4}\left(\Pi_r\right)^2 + \frac{1}{2} m_\Phi{}^2 \Phi\Phi^* , && (3.26)\\
j_r &= -\perp\left(T_r{}^a n_a\right) \\
&= -\frac{1}{2}\left(\frac{1}{a}\right)\left[\left(\Phi_r^* + ie\Phi^* A_r\right)\Pi_\Phi + \left(\Phi_r - ie\Phi A_r\right)\Pi_\Phi^*\right] , && (3.27)\\
S^r{}_r &= \perp T^r{}_r \\
&= \frac{1}{2}\left(\frac{1}{a^2}\right)\left[\Pi_\Phi \Pi_\Phi^* + \left(\Phi_r - ie\Phi A_r\right)\left(\Phi_r^* + ie\Phi^* A_r\right)\right] - \frac{1}{4}\left(\Pi_r\right)^2 - \frac{1}{2} m_\Phi{}^2 \Phi\Phi^* , && (3.28)
\end{aligned}$$

where $\Pi_\Phi = \Pi_\Phi(t, r)$, $\Phi_r = \Phi_r(t, r)$, and $\Pi_r = \Pi_r(t, r)$ are defined below in equations (3.30), (3.31) and (3.38).

3.2.4 Matter Equations in First-Order Form

I can rewrite equation of motion (3.9) as

$$\nabla^a\left(\nabla_a \Phi - ieA_a \Phi\right) - ieA^a\left(\nabla_a \Phi - ieA_a \Phi\right) - m_\Phi{}^2 \Phi = 0 . \tag{3.29}$$

Then, computing covariant derivatives of (3.29) for metric (3.20), the equation of motion is a relatively simple expression. I choose to re-express it in first order form. Defining

$$\begin{aligned}
\Pi_\Phi(t, r) &\equiv n^a a\left(\nabla_a \Phi - ieA_a \Phi\right) , && (3.30)\\
\Phi_r(t, r) &\equiv \partial_r \Phi , && (3.31)
\end{aligned}$$

[5] However, to eliminate divergences and loss of numerical precision when a and α approach values close to zero, the Hamiltonian constraint and slicing condition are best solved using logarithmic variables $A \equiv \ln a$ and $L \equiv \ln \alpha$.

where ∂_r designates partial differentiation with respect to coordinate r, equation of motion (3.29) becomes the following triplet

$$\dot{\Pi}_\Phi = 3\partial_{r^3}\left[r^2\frac{\alpha}{a}\left(\Phi_r - ieA_r\Phi\right)\right] - ie\left[\frac{\alpha}{a}\left(\Phi_r - ieA_r\Phi\right)A_r - \Pi_\Phi A_t\right] - \alpha a m_\Phi^2\Phi \ , \quad (3.32)$$

$$\dot{\Phi}_r = \partial_r\left[\frac{\alpha}{a}\left(\Pi_\Phi\right) + ieA_t\Phi\right] \ , \quad (3.33)$$

$$\dot{\Phi} = \left[\frac{\alpha}{a}\left(\Pi_\Phi\right) + ieA_t\Phi\right] \ , \quad (3.34)$$

where overdot, $\dot{}$, again designates partial differentiation with respect to t, and I have used the chain rule to rewrite the partial derivative with respect to r as a partial derivative with respect to r^3, designated ∂_{r^3}.[6]

As with the scalar field, I choose to write and evolve the spatial part of A_a in first order form.[7] Defining

$$\Pi_r(t,r) \equiv n^a\frac{1}{a}\left(\nabla_a A_r - \nabla_r A_a\right) \ , \quad (3.38)$$

$$A_{tr}(t,r) \equiv \partial_r A_t \ , \quad (3.39)$$

the Euler-Lagrange equation for the spatial component of A_a becomes the following set of three equations

$$\dot{\Pi}_r = \frac{\alpha}{a}\left(J_r\right) \ , \quad (3.40)$$

$$\dot{A}_r = \left[\alpha a\left(\Pi_r\right) + A_{tr}\right] \ , \quad (3.41)$$

$$A_{tr} = \partial_r\left(A_t\right) \ , \quad (3.42)$$

where (3.13) gives

$$J_r = -ie(\Phi^*\Phi_r - \Phi\Phi_r^*) - 2e^2\Phi\Phi^*A_r \ . \quad (3.43)$$

Finally, while the Lorentz gauge condition is already in first order form, I find it convenient to define

$$\Omega_t(t,r) \equiv n^a a A_a \ , \quad (3.44)$$

$$\Pi_t(t,r) \equiv \dot{\Omega}_t \ , \quad (3.45)$$

[6]By using the chain rule as per

$$\frac{\partial f}{\partial r} = \frac{\partial r^n}{\partial r}\frac{\partial f}{\partial r^n} = nr^{n-1}\frac{\partial f}{\partial r^n} \quad (3.35)$$

numerically unsuitable forms such as

$$\frac{1}{r^2}\frac{\partial f}{\partial r} \quad (3.36)$$

at $r = 0$ can be rewritten more appropriately as

$$\frac{1}{r^2}\frac{\partial f}{\partial r} = 3\frac{\partial f}{\partial r^3}. \quad (3.37)$$

The first appearance in the literature of numerical relativity for this application of the chain rule was [45].

[7]It can be demonstrated that in spherical symmetry the components A_θ and A_ϕ must completely decouple from the system of equations. I am therefore free to set them both to zero for all time.

and recast the gauge condition as the triplet

$$\Pi_t = 3\partial_{r^3}\left[r^2\frac{\alpha}{a}(A_r)\right] , \tag{3.46}$$

$$\dot{\Omega}_t = \Pi_t , \tag{3.47}$$

$$A_t = \frac{\alpha}{a}(\Omega_t) , \tag{3.48}$$

where the chain rule has again been applied to recast the differential equation in a more appropriate form.

3.2.5 Physical and Conserved Quantities

The only non-vanishing electromagnetic field component measured by an observer with four-velocity n^a can be expressed

$$E_r = -a\Pi_r , \tag{3.49}$$

the temporal component of the current four-vector can be written

$$J_t = ie\frac{\alpha}{a}\left(\Phi^*\Pi_\Phi - \Phi\Pi_\Phi^*\right) , \tag{3.50}$$

and the conserved electric charge density expressed

$$\rho_Q = -ie\frac{1}{a}\left(\Phi^*\Pi_\Phi - \Phi\Pi_\Phi^*\right) . \tag{3.51}$$

Outside gravitational sources, where $t^a = (1,0,0,0)$ is a timelike Killing vector field, the quantity

$$\rho_T = \frac{1}{2}\left(\frac{\alpha}{a^2}\right)\left[\Pi_\Phi\Pi_\Phi^* + \left(\Phi_r - ie\Phi A_r\right)\left(\Phi_r^* + ie\Phi^* A_r\right)\right] + \frac{1}{4}\alpha\left(\Pi_r\right)^2 + \frac{1}{2}\alpha {m_\Phi}^2\Phi\Phi^* \tag{3.52}$$

is a conserved energy density. Then, from (2.104), the total charge,

$$Q = \int_{\phi=0}^{2\pi}\int_{\theta=0}^{\pi}\int_{r=0}^{\infty}\rho_Q\left(ar^2\sin\theta\right)drd\theta d\phi , \tag{3.53}$$

will be constant. Similarly, from (2.108), the total energy,

$$T = \int_{\phi=0}^{2\pi}\int_{\theta=0}^{\pi}\int_{r=r_1}^{r_2}\rho_T\left(ar^2\sin\theta\right)drd\theta d\phi , \tag{3.54}$$

will also be constant if no gravitational sources reside within $r_1 \leq r \leq r_2$.

3.2.6 Regularity, Boundary Conditions and Dissipation

According to the definitions of section 2.4 (cf. [6], [45]), the regularity conditions for functions listed above require that matter variables Φ, Π_Φ, A_t, Ω_t, Π_t J_t, ρ_Q and ρ_T are, to leading order, even in r about $r = 0$. Variables Φ_r, A_r, Π_r, A_{tr}, J_r and E_r will to leading order be odd. For the leading-order-even variables I enforce regularity at the grid point corresponding to $r = 0$ by applying a quadratic fix as listed in Appendix C. Meanwhile, the regularity condition of the leading-order-odd variables is enforced by setting the functions equal to zero at the degenerate point.

I apply the (approximate) Sommerfeld outgoing radiation condition to Φ at the computational domain boundary $r = r_{\max}$. As discussed in Chapter 2, this condition adopts the form

$$\partial_t(r\Phi) + \left(\frac{\alpha}{a}\right)\partial_r(r\Phi) = 0 \tag{3.55}$$

for the spherically symmetric metric in polar areal coordinates. Assuming spacetime is essentially flat at $r = r_{\max}$, condition (3.55) reduces to

$$\partial_t(r\Phi) + \partial_r(r\Phi) = 0 \ . \tag{3.56}$$

Observe how (3.55) and (3.56) assume both e and m_Φ have an insignificant effect on scalar field dynamics at the boundary. It can be shown that, under these assumptions, an approximate Sommerfeld condition can also be written for Π_Φ as per

$$\partial_t(r\Pi_\Phi) + \partial_r(r\Pi_\Phi) = 0 \ . \tag{3.57}$$

Assuming $r = r_{\max}$ is sufficiently large, an approximate Sommerfeld condition can similarly be written for Φ_r. I implement the these equations (and all others containing partial derivatives in r) using backwards spatial differencing operators.

Since the Hamiltonian constraint is solved by integrating outwards, I impose the inner boundary condition

$$a(t, 0) = 1 \tag{3.58}$$

on metric function $a(t, r)$. Function a is set to unity here because this is the flat-space value the metric takes interior to a spherically symmetric matter distribution. Meanwhile, for $\alpha(t, r)$ I impose an outer boundary condition

$$\alpha(t, r_{\max}) = \frac{1}{a(t, r_{\max})} \ . \tag{3.59}$$

The condition is for the outer boundary because I solve the slicing condition by integrating inwards from $r = r_{\max}$. Furthermore, the specific choice $a^{-1}(t, r_{\max})$ is used because of the analogy with Reissner-Nordström spacetime in which the temporal and radial metric functions are reciprocal. Finally, regularity for metric functions a and α requires they be even to leading order in coordinate r about $r = 0$.

I employ Kreiss-Oliger dissipation as discussed in Appendix C. The dissipation is added to all functions whose evolutionary equations explicitly include derivatives with respect to t. The complete set is Φ, Φ_r, Π_Φ, A_r, Π_r, Ω_t and a_{mom}, where a_{mom} represents the metric function $a(t, r)$ when solved using the momentum constraint (3.24). Since the Kreiss-Oliger dissipation operator has a stencil[8] five points wide, it is only applied at locations two grid points from the bounds of the computational domain ($r = 0$ and $r = r_{\max}$). Finally, I find the value $\epsilon = 0.5$ a good choice for the adjustable dissipation parameter in all simulations presented. With the choice of Courant factor $\lambda = 0.5$, the system of equations evolves stably under the Crank-Nicholson iterative scheme.

3.3 Results

3.3.1 Initial Data Profiles

The basic idea is to choose a family of initial data parametrized by a single variable p and let the system evolve. Observing the dynamics, I note whether or not the outcome is formation of a black hole at some future time. I then successively adjust the value of p to the critical value p^* which marks the threshold of black hole formation: if $p > p^*$ the system forms a black hole, if $p < p^*$ it does not.

[8] A *stencil* is essentially a list of the set of points on which a finite difference operator is dependent. Details and discussion can be found in Appendix C.

Now, since the scalar field is complex

$$\Phi = \phi_1 + i\phi_2 \ , \tag{3.60}$$

its conjugate momentum must also be complex

$$\Pi_\Phi = \Pi_1 + i\Pi_2 \ , \tag{3.61}$$

where $\Pi_1 = \Pi_1(t,r)$ and $\Pi_2 = \Pi_2(t,r)$. From definition (3.30) it is evident the complex components of Π_Φ are explicitly

$$\Pi_1 = \frac{a}{\alpha}\left(\dot{\phi}_1 + eA_t\phi_2\right) \ , \tag{3.62}$$

and

$$\Pi_2 = \frac{a}{\alpha}\left(\dot{\phi}_2 - eA_t\phi_1\right) \ . \tag{3.63}$$

In terms of the field variables, electromagnetic coupling parameter, and metric components, the electric charge density (3.51) is explicitly

$$\begin{aligned}\rho_Q &= -\frac{2e}{a}\left(\phi_1\Pi_2 - \phi_2\Pi_1\right) \\ &= -\frac{2e}{\alpha}\left(\phi_1\dot{\phi}_2 - \phi_2\dot{\phi}_1 - eA_t(\phi_1^2+\phi_2^2)\right) \ . \end{aligned} \tag{3.64}$$

So while it may be tempting to ascribe positive charge to, say, scalar field component ϕ_1 and negative charge to ϕ_2, the dependencies of Π_1 and Π_2 on both ϕ_1 and ϕ_2 indicates that positive and negative charge must simultaneously be attributed to both scalar field components. Families of initial data can therefore possess a variety of charge density profiles, depending on the choice of ϕ_1, ϕ_2, Π_1, Π_2 and e, and generic initial data will evolve to a state with both positive and negative charge density distributed within some volume of space.[9]

For given values of e and m_Φ, I choose from one of six different initial data families tabulated below and tune a single free parameter to its critical value. Each of the six families are constructed from initial Gaussian profiles for ϕ_1, ϕ_2, Π_1, Π_2, A_t and A_r.[10] That is,

$$\phi_1(t=0,r) = a_1\exp(-((r-r_1)/\delta_1)^2) \ , \tag{3.65}$$

$$\phi_2(t=0,r) = a_2\exp(-((r-r_2)/\delta_2)^2) \ , \tag{3.66}$$

$$\Pi_1(t=0,r) = a_3\exp(-((r-r_3)/\delta_3)^2) \ , \tag{3.67}$$

$$\Pi_2(t=0,r) = a_4\exp(-((r-r_4)/\delta_4)^2) \ , \tag{3.68}$$

$$A_t(t=0,r) = a_t\exp(-((r-r_t)/\delta_t)^2) \ , \tag{3.69}$$

[9] Furthermore, assume that a system is assembled from two species of massive complex scalar field, both with the same charge coupling parameter e, but one having a large mass parameter m_Φ and the other a small one. Data could always be constructed where the field with large mass parameter contributes a positive charge density at initial time, while the field with small mass parameter contributes a negative charge density. However, as evident from equation (3.64), generic evolution of the field with initial positive charge density will soon appear to carry a component of negative charge, while the initially negative charge density field will appear to contribute some amount of positive charge. While total charge of the ensemble will be conserved, neither positive nor negative contributions by either field need remain separately constant. This behaviour is borne out by numerical simulation. It is in this sense that massive charged scalar fields are incapable of modelling the generic behaviour of an ionized gas composed of heavy, always positively charged ions amid a cloud of light, always negatively charged electrons.

[10] From equation (3.43) a nonzero radial electric current requires e, Φ and Φ^* to be nonzero. In addition, the conditions for a nonzero current are either A_r be nonzero, Φ_r be nonzero, or Φ^*_r be nonzero. Clearly, families A, B, C and D of Table 3.2 satisfy the nonzero current condition at initial time if $e \neq 0$. Charge separation in these four cases can therefore be said to originate at initial time $t = 0$. Furthermore, since families E or F do not satisfy the requirements for nonzero radial current at initial time, charge separation can only occur when $t > 0$.

and

$$A_r(t=0,r) = a_r \exp(-((r-r_r)/\delta_r)^2) \ . \tag{3.70}$$

The tuning parameter is always a_1, $a_t = a_r = 0.0132$, and depending on the family, a_2, a_3 and a_4 take on values either 0.0 or 0.0132. For all families

$$r_1 = r_2 = r_3 = r_4 = 10.0 \tag{3.71}$$

and

$$\delta_1 = \delta_2 = \delta_3 = \delta_4 = 2.0 \ . \tag{3.72}$$

The spatial coordinate range is always $0 \le r \le 80$. Finally, all solutions are computed on a finite difference grid with at least $J = 3201$ grid points in the radial direction, and using adaptive mesh refinement as outlined in Appendix C.

family	ϕ_1, ϕ_2, Π_1, Π_2	$\rho_Q(t=0,r;e\neq 0)$
A	$\phi_1(t=0,r) = a_1 \exp(-((r-r_1)/\delta_1)^2)$, $\phi_2(t=0,r) = a_2 \exp(-((r-r_2)/\delta_2)^2)$, $\Pi_1(t=0,r) = a_3 \exp(-((r-r_3)/\delta_3)^2)$, $\Pi_2(t=0,r) = a_4 \exp(-((r-r_4)/\delta_4)^2)$	$\neq 0$
B	$\phi_1(t=0,r) = a_1 \exp(-((r-r_1)/\delta_1)^2)$, $\phi_2(t=0,r) = 0$, $\Pi_1(t=0,r) = a_3 \exp(-((r-r_3)/\delta_3)^2)$, $\Pi_2(t=0,r) = a_4 \exp(-((r-r_4)/\delta_4)^2)$	$\neq 0$
C	$\phi_1(t=0,r) = a_1 \exp(-((r-r_1)/\delta_1)^2)$, $\phi_2(t=0,r) = a_2 \exp(-((r-r_2)/\delta_2)^2)$, $\Pi_1(t=0,r) = a_3 \exp(-((r-r_3)/\delta_3)^2)$, $\Pi_2(t=0,r) = 0$	$\neq 0$
D	$\phi_1(t=0,r) = a_1 \exp(-((r-r_1)/\delta_1)^2)$, $\phi_2(t=0,r) = 0$, $\Pi_1(t=0,r) = a_3 \exp(-((r-r_3)/\delta_3)^2)$, $\Pi_2(t=0,r) = 0$	$= 0$
E	$\phi_1(t=0,r) = a_1 \exp(-((r-r_1)/\delta_1)^2)$, $\phi_2(t=0,r) = a_2 \exp(-((r-r_2)/\delta_2)^2)$, $\Pi_1(t=0,r) = 0$, $\Pi_2(t=0,r) = 0$	$= 0$
F	$\phi_1(t=0,r) = a_1 \exp(-((r-r_1)/\delta_1)^2)$, $\phi_2(t=0,r) = 0$, $\Pi_1(t=0,r) = 0$, $\Pi_2(t=0,r) = 0$	$= 0$

Table 3.2: Critical gravitational collapse initial data families A through F. The first column lists the family and the second column specifies the initial data profiles for ϕ_1, ϕ_2, Π_1 and Φ_2 of that family. The third column lists whether or not the initial data can carry nonzero electric charge density when $e \neq 0$.

3.3.2 Results for $e = 1.0$ with $m_\Phi = 0.0$

As expected, I recover Choptuik's original discretely self-similar and universal solution [23] in the limit $e \to 0$ and $m_\Phi \to 0$. For values $e = 1.0$ with $m_\Phi = 0.0$ I again observe a discretely self-similar and universal solution, but the near-critical solution now carries electric charge.

Discrete Self-Similarity and Universality

The solution represents itself as an infinite series of echoes as the scalar field repeatedly attempts to collapse to a black hole, but never quite makes it. With each failed attempt some scalar field is shed, and the succeeding echo occurs on an exponentially smaller spatial scale after an exponentially shorter interval of time.

The discrete self-similarity of the critical solution is apparent in successive maxima of the quantity

$$2m(t,r)/r = (1 - a^{-2}) + Q^{\ 2}/(4\pi r^2)\ , \tag{3.73}$$

where $Q = Q(t,r)$ is the net charge enclosed by a sphere of radius r at time t. For example, having tuned to $|p - p^*| \sim 10^{-16}$, I take the profile of $2m(t,r)/r$ at the maximum of its third echo for family A and spatially rescale it by a factor $\exp(\Delta)$, $\Delta \approx 3.47$. I then find the rescaled third echo profile matches that of the preceding (second) echo, consistent with the findings of [66] and [68]. This is displayed below in Figure 3.5. Meanwhile, universality of the solution is manifest in the fact that all critical solutions exhibit like profiles and that the scaling exponents Δ are essentially the same for all families A through F.

Mass and Charge Scaling

As the critical solution is approached from above, it would appear the back holes formed become arbitrarily small as $p \to p^*$. This is supported by the results presented in Figure 3.6. Down to machine precision, black hole masses there observe a power-law behavior

$$\ln(m_{\mathrm{BH}}) = \gamma_m \ln\left((p - p^*)/p^*\right) + c_1, \tag{3.74}$$

where c_1 is a family dependent constant. For family A I find a value $\gamma_m \approx 0.385$, consistent with the results of [66], [68] and analysis of [57]. Not only do black hole masses observe a power-law relationship with respect to the critical parameter, but so do the black hole charges. Supporting numerical results are presented in Figure 3.7. Similarly, this power-law has the functional form

$$\ln(|Q_{\mathrm{BH}}|) = \gamma_Q \ln\left((p - p^*)/p^*\right) + c_2, \tag{3.75}$$

where c_2 is another family dependent constant.[11] However, $\gamma_Q > \gamma_m$ so the black hole sheds charge more rapidly than mass with each successive echo as the critical solution is approached from above. For family A I find $\gamma_Q \approx 0.854$, again consistent with [66], [68] and [57], and also their prediction that $\gamma_Q \geq 2\gamma_m$. Explicitly, I show the charge to mass ratio of the black hole solutions in Figure 3.8. Clearly, while the ratio $|Q_{\mathrm{BH}}|/m_{\mathrm{BH}}$ decreases exponentially as $p \to p^*$, it is possible to form black holes with $0 \lesssim |Q_{\mathrm{BH}}|/m_{\mathrm{BH}} \lesssim 1$ when sufficiently far from the critical solution.

[11] The data of Figure 3.7 suggest a small periodic wiggle superimposed on the otherwise straight line fit, consistent with the predictions and results of [57], [66] and [68]. While a similar periodic wiggle is known to exist for the mass scaling relationship of both charged [57], [66], [68] and uncharged [58], [67] massive scalar fields, the behaviour is not apparent in Figure 3.6. The absence of a wiggle can there be attributed to numerical inaccuracy arising with the divergence of polar areal radial metric function $a(t,r)$ just before apparent horizon formation. Of course, the periodic wiggle could be explored further by examining maximum spacetime curvature of subcritical solutions as $p \to p^*$ from below.

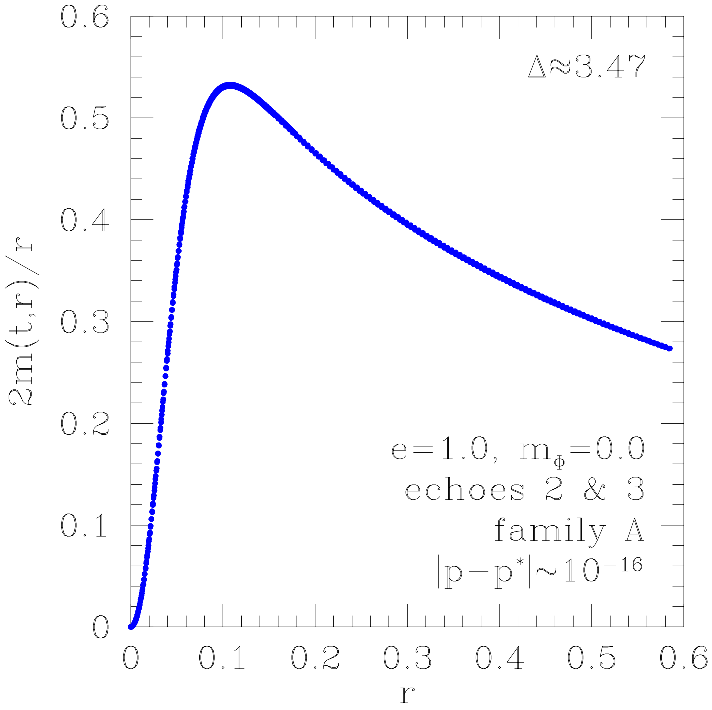

Figure 3.5: Discrete self-similarity for the critical solution of family A with $e = 1.0$, $m_\Phi = 0.0$ as demonstrated by spatially rescaling the third echo of $2m(t,r)/r$ by $\exp(\Delta)$ and comparing it to the unscaled second echo. The two echo profiles agree so closely their differences are not apparent on the scale of this figure.

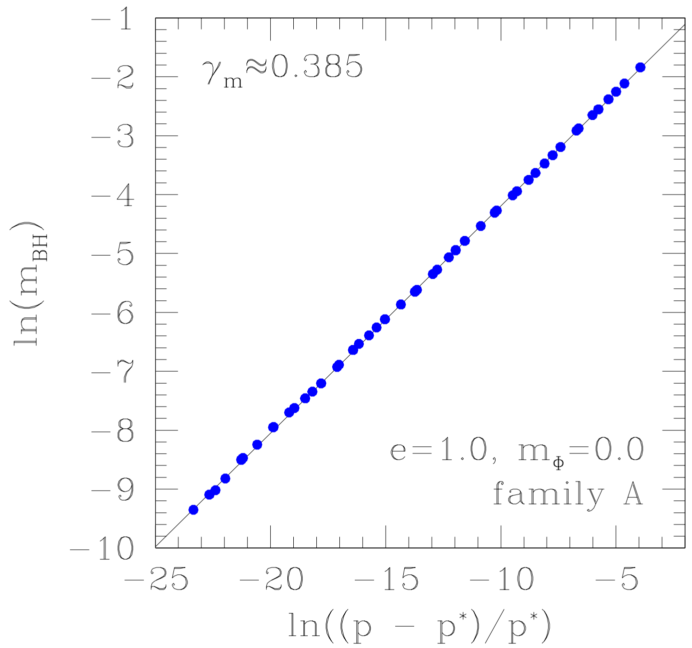

Figure 3.6: Power-law scaling of the black hole mass $m_{\rm BH}$ as the critical solution is approached from above for family A with $e = 1.0$ and $m_\Phi = 0.0$. Here, the scaling exponent is $\gamma_m \approx 0.385$.

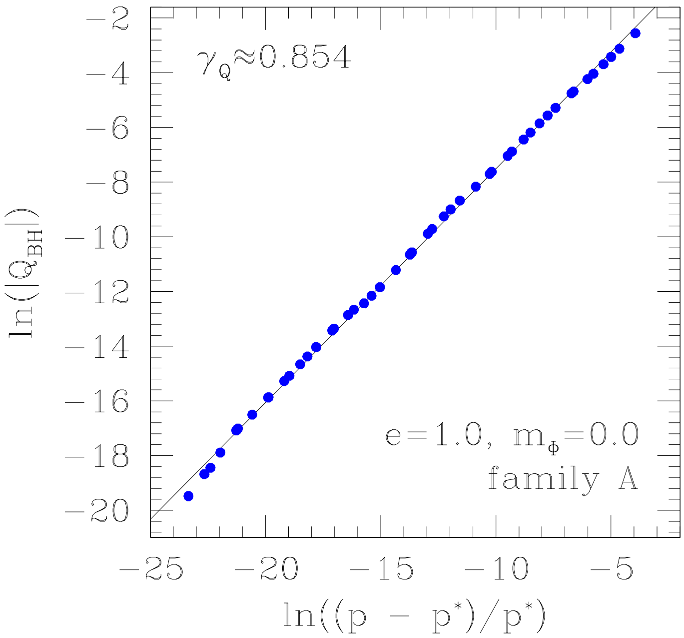

Figure 3.7: Power-law scaling of the black hole charge $Q_{\rm BH}$ as the critical solution is approached from above for family A with $e = 1.0$ and $m_\Phi = 0.0$. Here, the scaling exponent is $\gamma_Q \approx 0.854$.

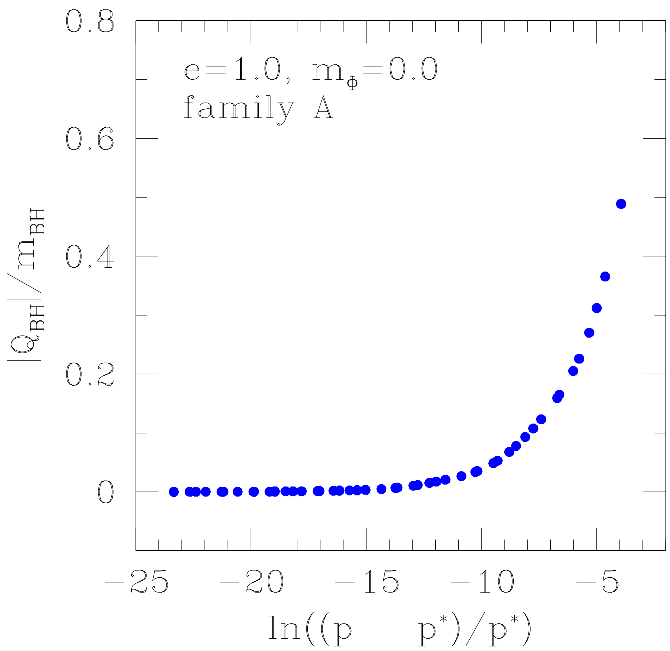

Figure 3.8: Charge to mass scaling of the black hole solutions as the critical solution is approached from above for family A with $e = 1.0$ and $m_\Phi = 0.0$. The charge of black hole solutions decreases more rapidly than black hole mass as $p \to p^*$, indicating the exactly critical solution will be uncharged. Furthermore, solutions with $0 \lesssim |Q_{\rm BH}|/m_{\rm BH} \lesssim 1$ can be obtained when p is sufficiently far from its critical value p^*.

3.3.3 Results for $e = 1.0$ with $m_\Phi = 1.0$

When the scalar field mass parameter m_Φ is sufficiently larger than zero, the critical solution ceases to be discretely self-similar. Rather, it becomes periodic—resembling an oscillating perturbed boson star with nonzero electric charge. Again, the existence of such solutions is not surprising—not only are charged boson star solutions known to exist [79], [80], [81], but the current understanding of massive scalar critical phenomena would also suggest that critical solutions resembling perturbed charged boson stars should exist for an appropriate set of initial conditions and range of parameter values e and m_Φ [31]. However, the emergence and details of such solutions were not previously observed.

Figures 3.9, 3.10 and 3.11 show the maximum of $2m(t,r)/r$ and its location for an $e = 1.0$, $m_\Phi = 1.0$ supercritical evolution of the family F when $|p - p^*| \sim 10^{-16}$. Examining Figures 3.10 and 3.11 it is clear the nearly critical solutions are composed of a high frequency component with period $\approx 4t$ modulated by a lower frequency of period $\approx 40t$. Assuming the results from [63], [64] and [65] carry over to the situation presented here, the low frequency period $\approx 40t$ can likely be attributed to excitation of the first harmonic mode of an unstable boson star. However, the occurrence of an additional higher frequency period ($\approx 4t$ or otherwise) has not been noted in previous studies of critical gravitational collapse in massive complex scalar field systems. But note those previous studies involved perturbation of (static) boson star initial conditions when obtaining critical solutions. It is entirely possible initial conditions of that sort may actually disallow the additional high frequency components as observed in this study. Finally, note the presence of the high frequency mode throughout the entire evolution (not just over the critical phase $140 \lesssim t \lesssim 450$) here indicates it is not unique to the critical solution, and so must be associated with more generic properties of the scalar field evolution.

To investigate further consequences of the additional high frequency mode, the scalar field modulus at $r = 0$ is plotted as a function of time in Figure 3.12. It is there apparent how the maxima of $|\Phi(t,0)|$ follow a low frequency period likely equal to that of the first harmonic mode of an unstable boson star. However, the scalar field amplitude also oscillates with a period $\approx 4t$, dropping to nearly zero with each oscillation.[12] Furthermore, careful examination reveals that while the low frequency maxima of $|\Phi(t,0)|$ occur in phase with the low frequency mode maxima of $\max(2m(t,r)/r)$, the high frequency extrema of $|\Phi(t,0)|$ occur exactly out of phase with those of $\max(2m(t,r)/r)$. This opposing phase correlation is observed throughout evolution, not just during the critical phase $140 \lesssim t \lesssim 450$. Furthermore, the high frequency opposing phase correlation is observed between functions $|\Phi(t,0)|$ and $\max(2m(t,r)/r)$ for (generic) evolution of this family when p is far from p^*.

To examine possible correlation of the two dominant modes of oscillation and electric charge, Figure 3.13 displays $Q(t,r)$, the total charge contained within spheres of r, for family F when $|p - p^*| \sim 10^{-16}$. The chosen values for r are $r = \bar{r}$, $r = 2\bar{r}$, $r = 3\bar{r}$ and $r = 4\bar{r}$, where $\bar{r} \approx 2.7$ is the average radius of $\max(2m(t,r)/r)$ over $150 \lesssim t \lesssim 360$. This figure shows how, just as for $|\Phi(t,0)|$, the low frequency local maxima in $Q(t,\bar{r})$ and $Q(t,2\bar{r})$ correlate with the low frequency local maxima in $\max(2m(t,r)/r)$. Furthermore, a high frequency component is observed in $Q(t,\bar{r})$ and $Q(t,2\bar{r})$, as would be expected from the relationship between charge density and scalar field amplitude. Notice how integration of charge density over larger radii effectively averages the dynamics observed in $Q(t,r)$. Finally, it is clear the average value of $Q(t,r)$ tends towards zero from above, indicating small net leakage of positive charge (or inflow of negative charge) from smaller (larger) radii during critical evolution.

Finally, to investigate whether the additional high frequency mode stems from electromagnetic coupling, the critical solution was obtained for family F when $m_\Phi = 1.0$ and $e = 0.0$. In doing so, it found the high frequency oscillation of period $\approx 4t$ was again present, as was the fundamental

[12] Similar behaviour has been noted for the so-called (uncharged, non-critical) *phase-shifted boson star* solutions documented in Hawley's dissertation [64]. There, numerical evolution suggested the oscillations in scalar field amplitude were likely stable and quasi-periodic.

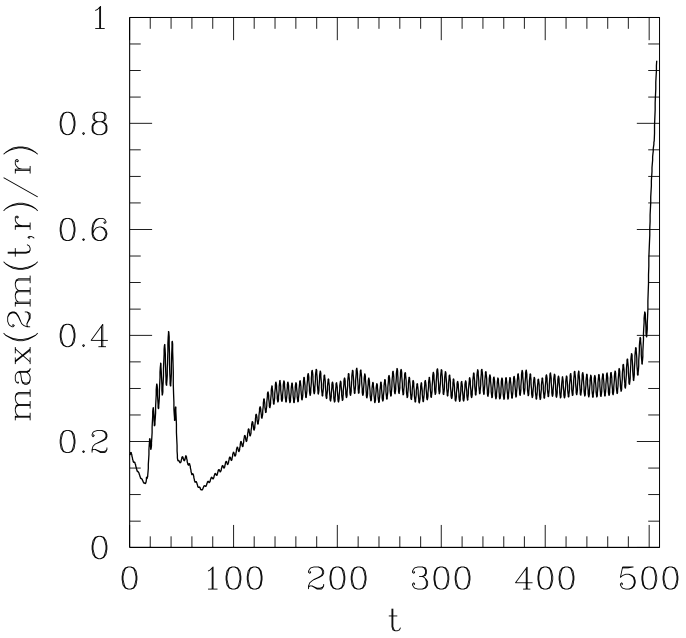

Figure 3.9: $\max(2m(t,r)/r)$ of the critical periodic state for $e = 1.0$, $m_\Phi = 1.0$ Maxwell-Klein-Gordon fields evolved from initial data family F when $|p - p^*| \sim 10^{-16}$. After an initial phase of evolution, the solution enters its critical state which lasts over the period $140 \lesssim t \lesssim 450$. The sharp increase of $\max(2m(t,r)/r)$ at late time corresponds with $a(t,r) \to 1$, the signal of imminent apparent horizon formation. An MPEG animation of $2m(t,r)/r$ over the period $0 \leq t \lesssim 507$ leading to black hole formation is available at `http://$WWW/People/petryk/animations/1.mpeg` where `$WWW` is currently `laplace.physics.ubc.ca` .

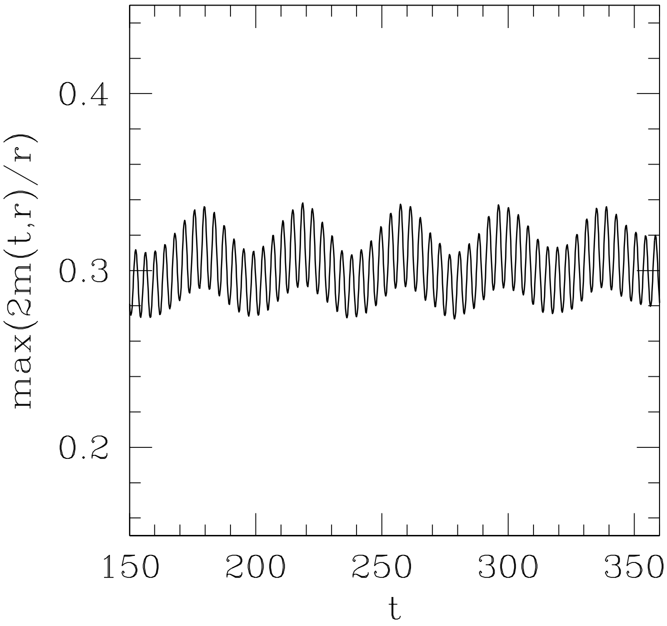

Figure 3.10: A closer view of $\max(2m(t,r)/r)$ showing oscillations within the critical periodic state for $e = 1.0$, $m_\Phi = 1.0$ Maxwell-Klein-Gordon fields evolved from family F when $|p - p^*| \sim 10^{-16}$. The average value of $\max(2m(t,r)/r)$ over $150 \lesssim t \lesssim 360$ is approximately 0.30. The periodicity of the solution is clearly evident as a low frequency component with period $\approx 40t$ along with a high frequency component with periodicity $\approx 4t$.

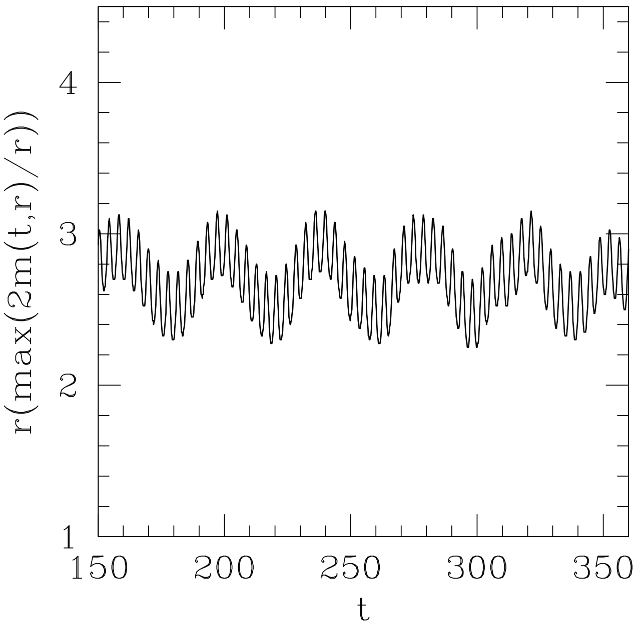

Figure 3.11: A view of $r(\max(2m(t,r)/r))$ within the critical periodic state for $e = 1.0$, $m_\Phi = 1.0$ Maxwell-Klein-Gordon fields evolved from family F when $|p - p^*| \sim 10^{-16}$. Clearly, the location of $\max(2m(t,r)/r)$ oscillates about an average radius of approximately $\bar{r} \approx 2.7$ for $150 \lesssim t \lesssim 360$ during the critical phase of evolution.

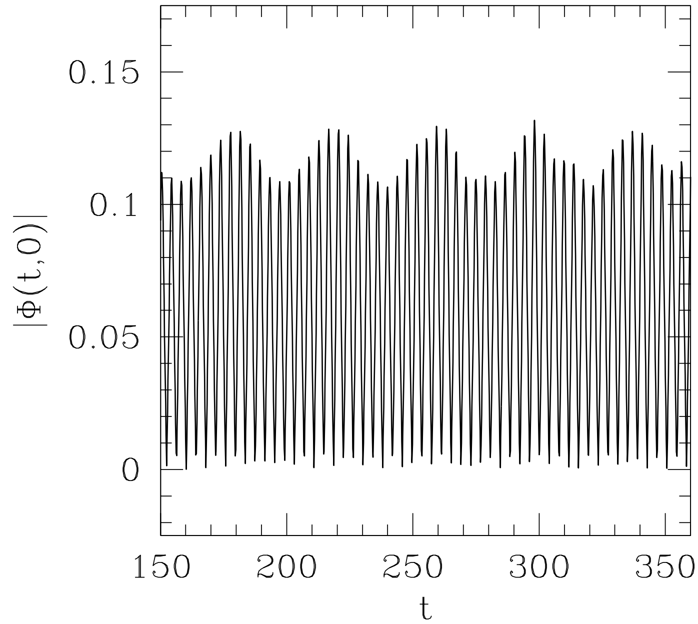

Figure 3.12: Modulus of the scalar field amplitude at $r = 0$ for the critical periodic state of $e = 1.0$, $m_\Phi = 1.0$ Maxwell-Klein-Gordon fields evolved from family F when $|p - p^*| \sim 10^{-16}$. Unlike previously studied boson star critical solutions where just the first harmonic mode is excited and $|\Phi(t, 0)|$ remains far from zero, the central scalar field amplitude of the highly excited periodic critical solution drops to nearly zero with each high frequency oscillation of period $\approx 4t$.[14] Furthermore, while previous perturbed boson star critical solutions displayed coincident peak values of $\max(2m(t, r)/r)$ and $|\Phi(t, 0)|$, just the local maxima associated with the low frequency excitation remain coincident for the solution displayed here. In fact, local maxima associated with the high frequency mode of $|\Phi(t, 0)|$ are precisely coincident with the local minima associated with the high frequency mode of $\max(2m(t, r)/r)$.

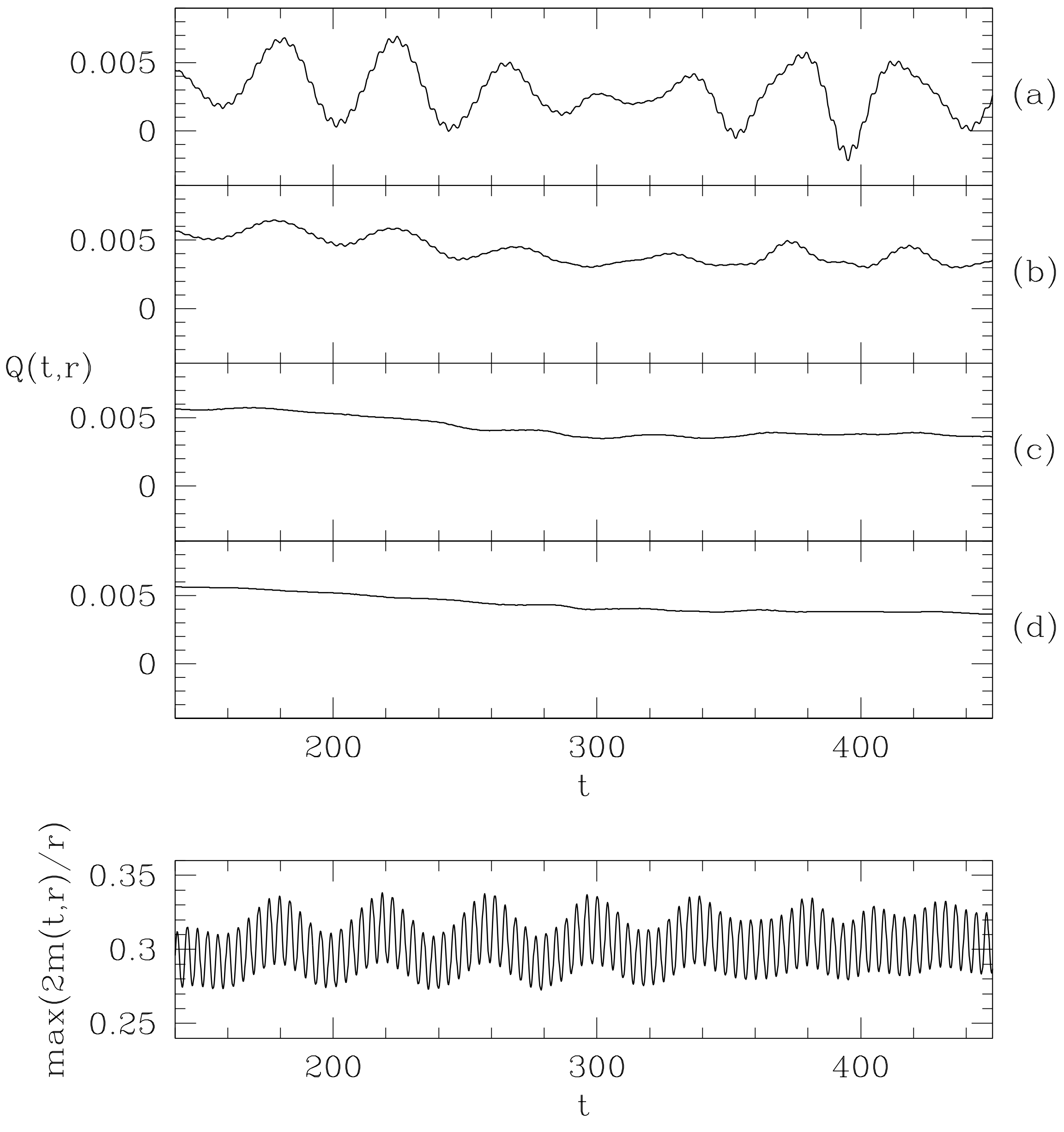

Figure 3.13: Charge contained within spheres of radius r for the critical periodic state from $e = 1.0$, $m_\Phi = 1.0$ Maxwell-Klein-Gordon fields evolved from initial data family F. A frame displaying $\max(2m(t,r)/r)$ is provided for reference. Subfigure (a) displays $Q(t,r)$ for $r = \bar{r}$ where $\bar{r} \approx 2.7$ is the average radius of $\max(2m(t,r)/r)$ over $150 \lesssim t \lesssim 360$. Meanwhile, (b) displays $Q(t,r)$ for $r = 2\bar{r}$, (c) displays $Q(t,r)$ for $r = 3\bar{r}$, and (d) shows $Q(t,r)$ for $r = 4\bar{r}$. From (a) and (b) it is clear that, at small radii, $Q(t,r)$ fluctuates with a low frequency component period $\approx 40t$ and a high frequency component period of $\approx 4t$. While the low frequency mode becomes somewhat irregular at later time, the high frequency component is persistent and very regular throughout evolution. Integration over larger radii effectively averages the fluctuations in $Q(t,r)$. In doing so, it makes clear a tendency for the net charge within $r = 4\bar{r}$ to slowly decrease in time during the critical phase of evolution.

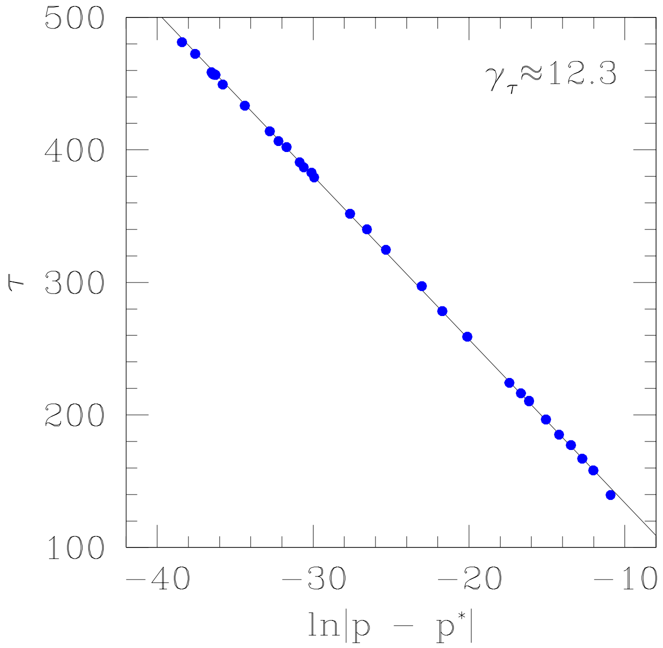

Figure 3.14: Lifetime of the critical periodic state for $e = 1.0$, $m_\Phi = 1.0$ Maxwell-Klein-Gordon fields evolved from initial data family F. The exponential scaling of τ with $|p-p^*|$ is typical of perturbed boson star critical solutions [63], [64], [65], [92], and the scaling exponent is here $\gamma_\tau \approx 12.3$.

harmonic mode of period $\approx 40t$. The critical solutions for family F with $m_\Phi = 1.0$ and $e = 1.0$, and $m_\Phi = 1.0$ and $e = 0.0$ are very similar in all but two regards. The first being the obvious lack of charge for case $e = 0.0$. The second is the lifetime of the critical state for $|p-p^*| \sim 10^{-16}$. While the critical phase of evolution for the $e = 1.0$ charged case was $140 \lesssim t \lesssim 450$, the critical phase of the $e = 0.0$ uncharged case was merely $140 \lesssim t \lesssim 240$, indicating the unstable mode of the charged critical solution appears to grow more slowly than that of the uncharged critical solution when the adjustable parameter of this family is tuned to its critical value to within one part in 10^{-16}.

This brings discussion to the lifetimes of the charged periodic critical solutions. Figure 3.14 displays the scaling of the critical solution lifetime, τ, with $\ln|p-p^*|$. Clearly, the relationship of lifetime with tuning parameter is

$$\tau = -\gamma_\tau \ln|p-p^*| + c_3 \ , \tag{3.76}$$

where γ_τ and c_3 are solution-dependent constants (cf. [63], [64], [65], [92]).[15] The lifetime of the critical solution is measured from the time it takes to form a black hole from the slightly supercritical data. In the present case $\gamma_\tau \approx 12.3$.

[15]This constant is known to be related to the growth factor of unstable modes for uncharged boson stars. The relationship can be verified through perturbation theory analysis about equilibrium boson star solutions. While it is likely that a similar relationship exists for weakly charged boson stars, I am unaware how this relationship could carry over for boson stars with strong electromagnetic coupling. Investigation along these lines are certainly of interest for future calculation.

Typical of such periodic critical solutions is the presence of a mass gap in the black hole spectrum when tuning to p^* from above (i.e., they exhibit Type I critical behaviour). This means there is a minimum mass for the black holes formed from supercritical evolution. This behaviour is clearly depicted in Figure 3.15 where the average black hole mass limit is $m_{\mathrm{BH}} \approx 0.48$. A least-squares fit of the data to $m_{\mathrm{BH}} = c_4 \ln|p - p^*| + c_5$ yields values $c_4 \approx -9.2 \times 10^{-4}$ and $c_5 \approx 4.6 \times 10^{-1}$. Also provided is Figure 3.16 displaying how the average charge of these black holes approaches the limit $Q_{\mathrm{BH}} \approx 0.0032$. A least-squares fit to $Q_{\mathrm{BH}} = c_6 \ln|p-p^*| + c_7$ here yields $c_6 \approx 3.6 \times 10^{-5}$ and $c_7 \approx 4.1 \times 10^{-3}$. These results together imply a charge to mass ratio $Q_{\mathrm{BH}}/m_{\mathrm{BH}} \sim 10^{-2}$ as $p \to p^*$ for this family of solutions. These periodic solutions carrying electric charge represent a new result, because the only critical solutions found prior to this investigation have been uncharged. Finally, the oscillation periods of the critical solution are dependent on e and m_Φ, and the scaling exponent γ_τ depends on the initial data family. Of course, the family dependence of perturbed boson star solutions is well known [63], [64], [65], [92] and means the critical solutions are not universal. Table 3.3 lists the properties of black holes formed from slightly supercritical Type I solutions for each of the families A through F when $e = 1.0$ and $m_\Phi = 1.0$. Each family exhibiting Type I critical behaviour has a scaling exponent $\gamma_\tau \approx 12$ and forms a black hole of mass $m_{\mathrm{BH}} \approx 0.5$. However, the black hole charges vary widely, and the charge to mass ratios of the black holes range from $|Q_{\mathrm{BH}}|/m_{\mathrm{BH}} \sim 0.006$ for family D to $|Q_{\mathrm{BH}}|/m_{\mathrm{BH}} \sim 0.3$ for family B.

family	$\rho_Q(t=0,r)$	$Q(t=0,r)$	γ_τ	$m_{\mathrm{BH}}(p \to p^*)$	$Q_{\mathrm{BH}}(p \to p^*)$
A	–	–	–	–	–
B	< 0	≈ -0.46	≈ 12.4	≈ 0.48	≈ -0.16
C	–	–	–	–	–
D	$= 0$	$= 0$	≈ 11.9	≈ 0.45	≈ 0.0026
E	$= 0$	$= 0$	≈ 12.3	≈ 0.47	≈ 0.0032
F	$= 0$	$= 0$	≈ 12.3	≈ 0.48	≈ 0.0032

Table 3.3: Black hole properties from gravitational collapse of slightly supercritical Type I solutions for families A through F when $e = 1.0$ and $m_\Phi = 1.0$. The first column lists the family (cf. Table 3.2), the second column specifies whether the initial charge density is nonzero and the third column lists the total charge carried by the initial data. The fourth column lists the lifetime scaling exponent for the Type I critical solution. The scaling exponents are all close in value. The fifth and sixth columns respectively list the black hole mass and charge from gravitational collapse of slightly supercritical solutions. The black hole masses are all close in value, but the charges cover a wide range of values. The charge to mass ratio of the black holes range from $|Q_{\mathrm{BH}}|/m_{\mathrm{BH}} \sim 0.006$ for family D to $|Q_{\mathrm{BH}}|/m_{\mathrm{BH}} \sim 0.3$ for family B. The entries for families A and C are left blank, since those initial data profiles do not exhibit Type I critical solutions for any value of tuning parameter ϕ_1.

Concluding discussion of the results, I now comment on the final fate of subcritical periodic solutions. In the earlier studies [63], [64] and [65] it was assumed the subcritical periodic solutions were simply described by dispersal of the scalar field to large distances. Since then it was found that slightly subcritical periodic solutions may actually begin dispersal, only to gravitationally recontract to a more compact distribution at later time [92]. After such recontraction to a more compact state, the scalar field distribution may either collapse to form a black hole or again expand to larger radii. If a second dispersal is attempted, the scalar field distribution will again recontract to a more compact compact state before either collapsing to a black hole or repeating the process of expansion and contraction. The results I now present displaying this behaviour were found

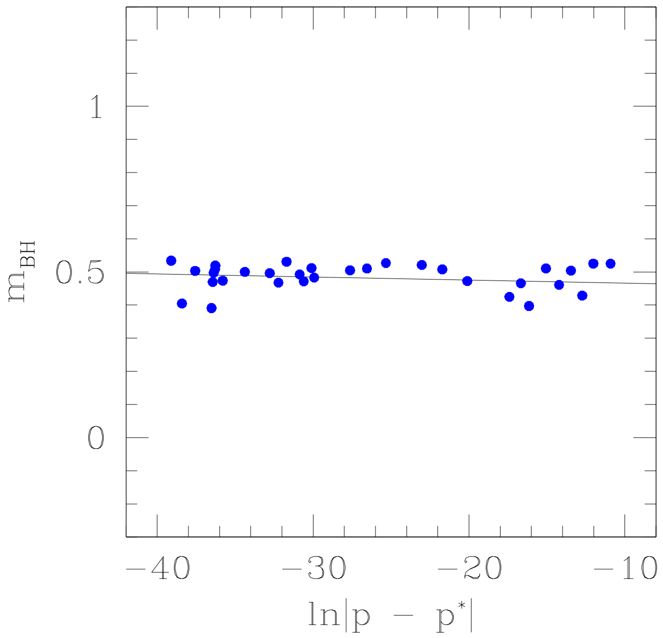

Figure 3.15: Mass gap for (supercritical) black hole solutions for $e = 1.0$, $m_\Phi = 1.0$ Maxwell-Klein-Gordon fields evolved from initial data family F. The average minimum mass of black holes formed from slightly supercritical data remains fairly constant about $m_{\rm BH} \approx 0.48$ as $p \to p^*$. The best fit line is shown for reference.

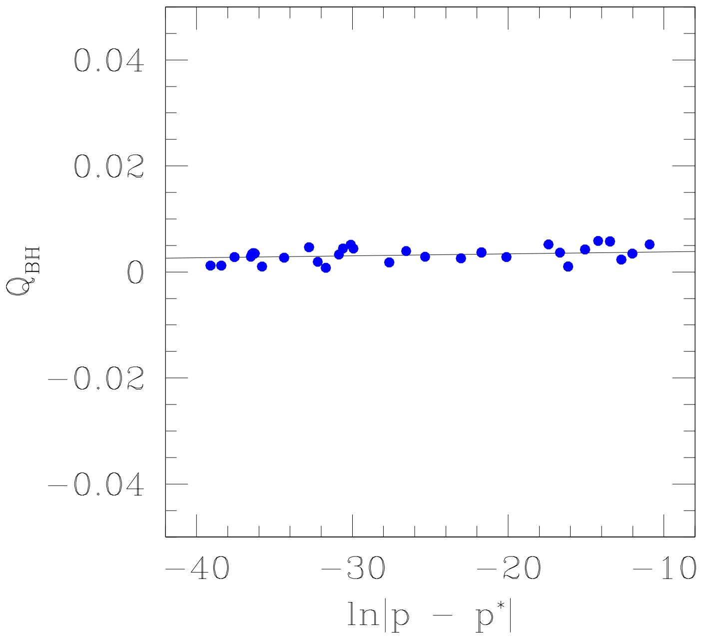

Figure 3.16: Minimum charge of (supercritical) black hole solutions for $e = 1.0$, $m_\Phi = 1.0$ Maxwell-Klein-Gordon fields evolved from initial data family F. The average charge of black holes formed from slightly supercritical data remains fairly constant about $Q_{\rm BH} \approx 0.0032$ as $p \to p^*$. The best fit line is shown for reference.

independent, and without knowledge, of those eventually published in [92]. Figure 3.17 shows $\max(2m(t,r)/r)$ and $|\Phi(t,0)|$ in time for the slightly subcritical evolution of family F with $e = 1.0$ and $m_\Phi = 1.0$. Meanwhile, Figure 3.18 shows $\max(2m(t,r)/r)$ and $|\Phi(t,0)|$ in time for the slightly subcritical evolution of family F with $e = 0.0$ and $m_\Phi = 1.0$. In both cases, the displayed evolution is for a state with $|p - p^*| \sim 10^{-16}$. Observe how the solution with $e = 1.0$ enters its critical phase of evolution from $140 \lesssim t \lesssim 450$ before attempting dispersal. The solution then attempts recollapse and $\max(2m(t,r)/r)$ peaks at $t \approx 660$. The charged scalar field attempts a second dispersal, but then undergoes complete gravitational collapse at $t \approx 960$. Also observe how the high frequency oscillations with period $\approx 4t$ persist throughout the evolution. Furthermore, note the correlation between the high frequency oscillations of $|\Phi(t,0)|$ and those of $\max(2m(t,r)/r)$, and how the amplitude $|\Phi(t,0)|$ drops to nearly zero with each oscillation period $\approx 4t$ from the beginning to the end of evolution. Meanwhile, Figure 3.18 demonstrates how the slightly subcritical evolution of for $e = 0.0$ enters the critical phase of evolution which lasts from $140 \lesssim t \lesssim 250$ before attempting a seemingly infinite series of attempted dispersals and collapses. The high frequency oscillations of period $\approx 4t$ are again observed throughout evolution in both $\max(2m(t,r)/r)$ and $|\Phi(t,0)|$. While the $|\Phi(t,0)|$ drops to nearly zero with each oscillation, the cycle averaged value of $|\Phi(t,0)|$ shows direct correlation with the cycle averaged value of $\max(2m(t,r)/r)$. Finally, with each attempted dispersal and contraction on the scale of $\approx 230t$ (similar to that found in [92]), the value of $\max(2m(t,r)/r)$ asymptotes towards a value ≈ 0.14. Similar behaviour is seen in $|\Phi(t,0)|$ as its peak values tend to approach ≈ 0.04. While only presented for family F initial conditions, similar behaviour can be observed for periodic solutions of all families A through F when $m_\Phi = 1.0$ and $0.0 \leq e \leq 1.0$.

3.3.4 Code Testing

Finally, the adaptive mesh code I use to obtain the results is demonstrably convergent to second order, and through convergence of conserved quantities can be shown to be accurate to well within a percent for a typical evolution. Also, the suitability of the approximate Sommerfeld boundary condition was briefly investigated and found to contribute an error on the order of a percent in worst case scenarios. Detailed investigation of these boundary condition effects is certainly of interest in future calculation.

In conclusion I provide in Figure 3.19 an explicit demonstration that the code, being convergent, generates lifetime scaling exponents that asymptote towards a specific value. In this figure are plotted the lifetime of the nearly critical periodic solutions for family F when $e = 1.0$ and $m_\Phi = 1.0$. The lifetimes were calculated using the adaptive code, but with the mesh refinement effectively disabled by setting a large solution error tolerance.[16] Results were thus obtained on fixed finite difference meshes with $J = 1601$, $J = 801$ and $J = 401$ grid points. Since the critical parameter value p^* is resolution dependent, this required recalculation of the critical parameter value for each of the three resolutions. Fitting a liner function to the results at each resolution generates values of $\gamma_\tau \approx 12.5$ for $J = 1601$, $\gamma_\tau \approx 13.0$ for $J = 801$ and $\gamma_\tau \approx 17.5$ for $J = 401$. Clearly, as resolution is increased, the lifetime scaling exponent approaches the value $\gamma_\tau \approx 12.3$ obtained using the adaptive code. Of course, this behaviour is entirely expected.

[16] See Appendix C for discussion of the adaptive algorithm and refinement by solution error.

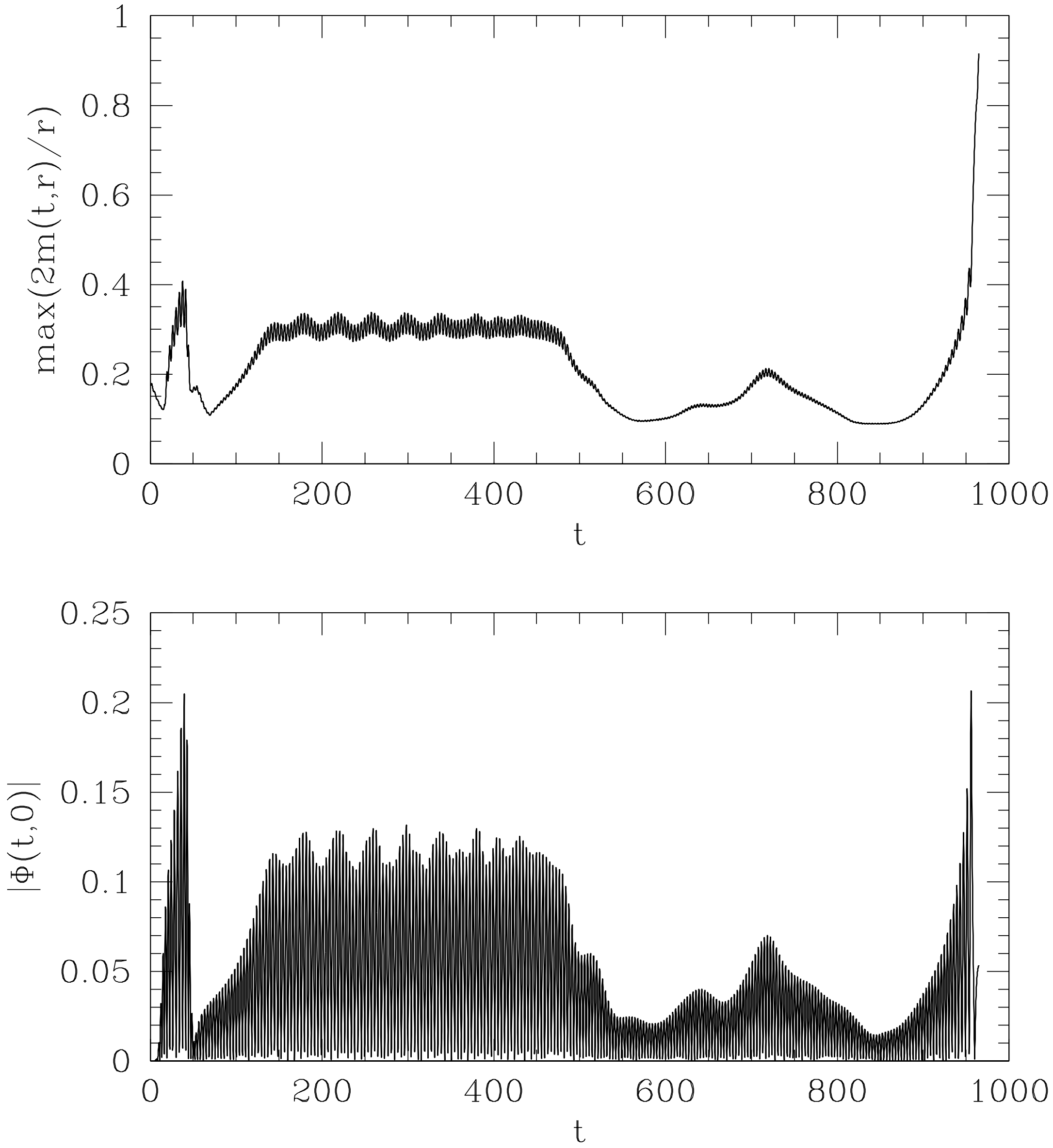

Figure 3.17: $\max(2m(t,r)/r)$ and $|\Phi(t,0)|$ in coordinate time t for the $e = 1.0$, $m_\Phi = 1.0$ fields for slightly subcritical initial data family F, specifically $|p - p^*| \sim 10^{-16}$. After the critical phase of evolution $140 \lesssim t \lesssim 450$, the charged massive scalar field attempts dispersal twice before eventually collapsing to form a black hole at $t \approx 960$. The high frequency oscillations of period $\approx 4t$ are apparent throughout evolution for both $\max(2m(t,r)/r)$ and $|\Phi(t,0)|$, and $|\Phi(t,0)|$ drops to nearly zero with each of these oscillations.

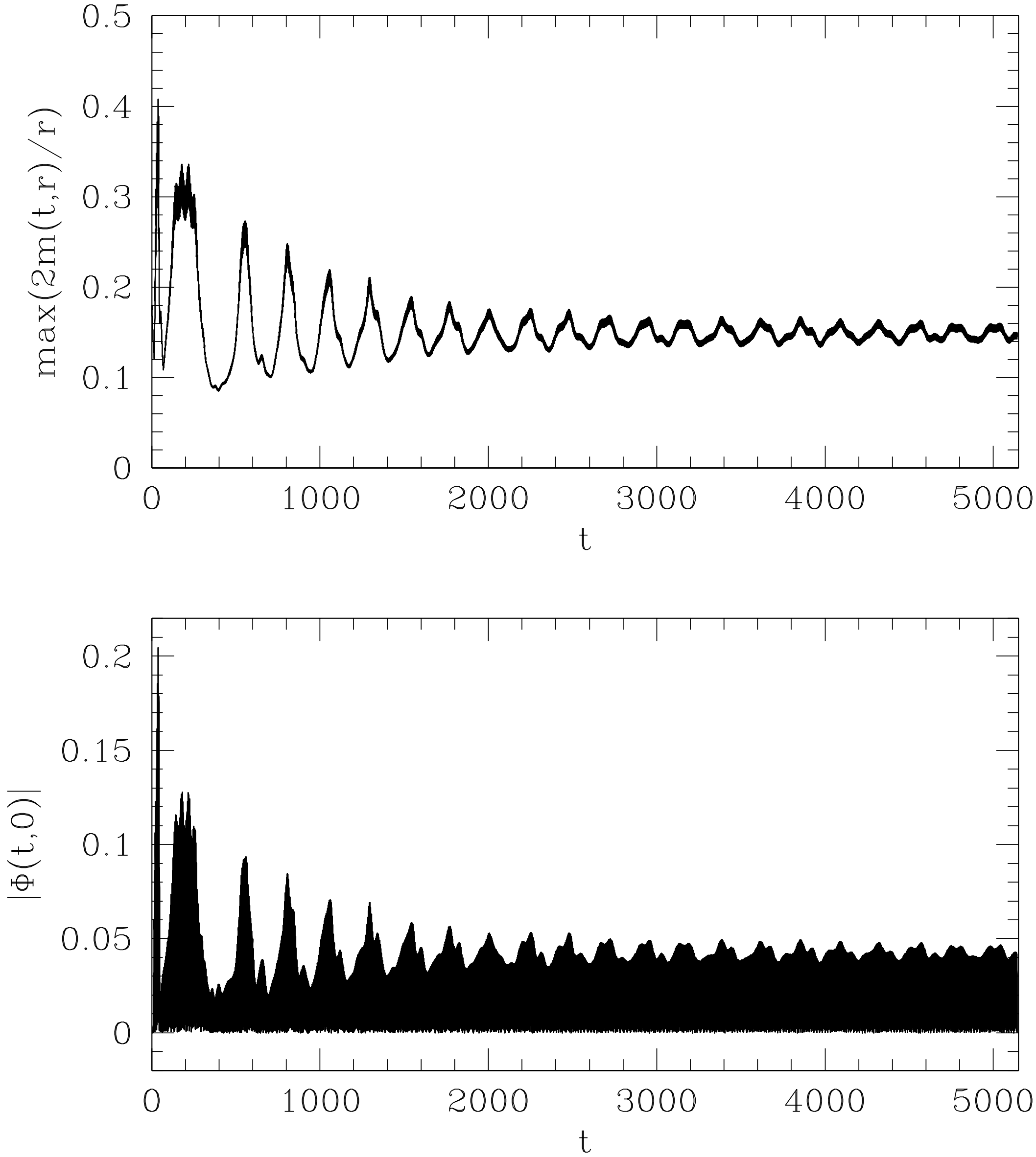

Figure 3.18: $\max(2m(t,r)/r)$ and $|\Phi(t,0)|$ in coordinate time t for the $e = 0.0$, $m_\Phi = 1.0$ fields for slightly subcritical initial data family F, specifically $|p - p^*| \sim 10^{-16}$. The massive scalar field exits its critical period of evolution and undergoes an apparently infinite series of dispersals and contractions. The high frequency oscillations of period $\approx 4t$ are apparent throughout evolution for both $\max(2m(t,r)/r)$ and $|\Phi(t,0)|$, and $|\Phi(t,0)|$ drops to nearly zero for each of these oscillations. It appears that $\max(2m(t,r)/r)$ and $|\Phi(t,0)|$ gradually relax to a less excited state as the evolution proceeds.

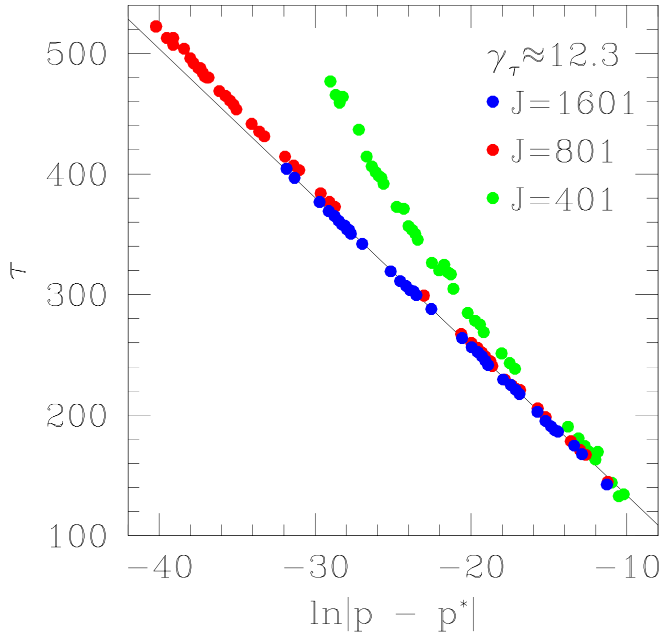

Figure 3.19: Lifetime of the critical periodic state for $e = 1.0$, $m_\Phi = 1.0$ Maxwell-Klein-Gordon fields evolved from initial data family F on three successive grid resolutions. The lifetime scaling exponent of the nearly critical solution on a grid of $J = 401$ points is $\gamma_\tau \approx 17.5$, on a grid of $J = 801$ points is $\gamma_\tau \approx 13.0$, and on a grid of $J = 1601$ points is $\gamma_\tau \approx 12.5$. With increase in resolution, the scaling exponent thus approaches a value near $\gamma_\tau \approx 12.3$ as found with the adaptive code.

CHAPTER 4

CHARGED SCALAR ACCRETION

To summarize, Chapter 1 introduced and motivated the research and results to be presented in this dissertation, Chapter 2 covered the physical formalism to be used in the investigations of following chapters, and Chapter 3 provided discussion and results for the critical gravitational collapse of spherically symmetric charged massive scalar fields. This chapter will cover the scattering and accretion of axially symmetric charged massive scalar fields in Kerr spacetime. The length of this chapter warrants outline of the physics to be investigated and results obtained through numerical solution. Table 4.1 has also been provided for reference and summary.

In this chapter, I first provide discussion of theory and previous work on the subject of $s = 0$ (scalar) and $s = 1$ (electromagnetic) perturbations of black hole spacetimes. Specifically, §4.1.1 outlines the effective potential formulation for Schwarzschild spacetime, the trapping of massive scalar perturbations in the effective potential formulation, and the scattering of both scalar and electromagnetic perturbations from the effective potential perspective. §4.1.2 outlines the physics of glories and orbiting resonances in Schwarzschild spacetime from the perspective of the effective potential formulation. §4.1.3 outlines the effective potential formulation of $s = 0$ and $s = 1$ perturbations in Kerr spacetime, and §4.1.4 covers the physics of superradiant scattering and some related topics. §4.1.5 and §4.1.6 close discussion of the underlying theory by respectively covering the topic of black hole perturbation decay at late time and reviewing related work in the area of charged scalar perturbations. Table 4.1 references these subsections in the context of physics investigated through numerical simulation as presented later in the chapter.

Following the theory is a section which details the system of equations to be used in numerical simulation. This includes discussion of the Kerr spacetime (§4.2.1), the matter Lagrangian and equations of motion (§4.2.2 and §4.2.3), physical fields and conserved quantities (§4.2.4). The section ends by discussing some aspects of the numerical solution method, including regularity, boundary conditions and dissipation (§4.2.5), and then strategies for adaptive mesh refinement and parallel computation (§4.2.6).

The remainder of this chapter presents numerical solution of the equations presented in §4.2 to investigate the theory of §4.1. Specifically, §4.3.1 outlines the prescription of initial data, §4.3.2 presents results for orbiting resonances and mode trapping of massive $s = 0$ perturbations and §4.3.3 presents results displaying orbiting resonance and superradiant scattering of $s = 1$ perturbations. §4.3.4, §4.3.5 and §4.3.6 then present solutions for electromagnetically coupled $s = 0$ and $s = 1$ perturbations which display orbiting resonance, charge separation, dynamo-like behaviour and collimation along the axis of black hole rotation. Again, Table 4.1 provides quick and convenient summary of the observed physics in relation to predictions from the theory of black hole perturbations. The last few subsections of the chapter provide validation of the numerical solutions through convergence testing (§4.3.7) and independent residual testing (§4.3.8) the numerical implementation, and by testing the approximate outgoing radiation boundary condition used throughout (§4.3.9).

s	phenomenon, subsection(s)	m_Φ,	e,	a/M	detail(s)
0	orbiting resonance, §4.1.1, §4.1.2, §4.1.3, §4.3.2	0.0,	0.0,	≥ 0.0	orbital period $\approx 70t$, orbital attenuation $\sim 10^{-1}$, $\log(T) \sim -kt$, $k \approx 1 \times 10^{-2}$
	mode trapping, §4.1.1, §4.1.3, §4.3.2	0.3,	0.0,	≥ 0.0	$\log(T) \sim -kt$, $k \approx 5 \times 10^{-3}$
	rapid infall, §4.1.1, §4.1.3, §4.3.2	2.4,	0.0,	≥ 0.0	$\log(T) \sim -kt$, $k \approx 7 \times 10^{-2}$
	energy collimation, §4.3.2	0.3,	0.0,	≥ 0.0	$\int \rho_T(t,r,0)dtdr$ $\approx \int \rho_T(t,r,\pi)dtdr$ $\gg \int \rho_T(t,r,\pi/2)dtdr$
1	orbiting resonance, §4.1.1, §4.1.2, §4.1.3, §4.3.3	0.0,	0.0,	≥ 0.0	orbital period $\approx 70t$, orbital attenuation $\sim 10^{-1}$, $\log(T) \sim -kt$, $k \approx 1 \times 10^{-2}$
	superradiant scattering, §4.1.3, §4.1.4, §4.3.3	0.0,	0.0,	0.8	amplification $\approx 0.05\%$
		0.0,	0.0,	0.98	amplification $\approx 1.3\%$
		0.0,	0.0,	≥ 0.998	amplification $\approx 1.6\%$
0, 1	orbiting resonance, §4.1.1, §4.1.2, §4.1.3, §4.3.4, §4.3.5	0.0,	≤ 0.6,	≥ 0.0	orbital period $\approx 70t$, orbital attenuation $\sim 10^{-1}$, $\log(T) \sim -kt$, $k \approx 1 \times 10^{-2}$
	orbiting resonance, §4.1.1, §4.1.2, §4.1.3, §4.3.6	0.6,	0.6,	≥ 0.0	orbital period $\approx 70t$, orbital attenuation $\sim 10^{-1}$, $\log(T) \sim -kt$, $k \approx 6 \times 10^{-3}$
	charge separation, §4.3.4, §4.3.5, §4.3.6	≥ 0.0,	> 0.0,	≥ 0.0	$\partial_t \rho_Q(t,r,\theta) \neq 0$ for $t \geq 0$
	dynamo-like behaviour, §4.3.4, §4.3.5, §4.3.6	≥ 0.0,	> 0.0,	≥ 0.0	$\partial_t J_\phi(t,r,\theta) \neq 0$ for $t \geq 0$
	energy collimation, §4.3.6	0.3,	0.6,	≥ 0.0	$\int \rho_T(t,r,0)dtdr$ $\approx \int \rho_T(t,r,\pi)dtdr$ $\gg \int \rho_T(t,r,\pi/2)dtdr$, $\int \rho_{T(\Phi)}(t,r,0)dtdr$ $\gg \int \rho_{T(A)}(t,r,0)dtdr$ $\gg \int \rho_{T(\Phi A)}(t,r,0)dtdr$

Table 4.1: Predicted and observed physics of the $s = 0$ (scalar) and $s = 1$ (electromagnetic) perturbations in Kerr spacetime. The second column lists phenomena which arise and chapter subsections covering the relevant theory and numerical solutions. The third column specifies the scalar field mass parameter m_Φ, the fourth lists the value of electromagnetic coupling parameter e, and the fifth column lists a/M where M is the black hole mass and a is the black hole angular momentum per unit mass. The sixth column summarizes some of the most significant details from numerical simulation. This table is to be treated as an index, and the reader is referred back to the listed chapter subsections for notation, detail and complete discussion.

4.1 Scattering and the Physics of Black Hole Perturbations

4.1.1 The Effective Potential Formulation for Schwarzschild Spacetime

The programme of quasi-normal mode analysis has provided insight that, in part, helps explain the early and intermediate time behaviour in the scattering phenomena I study. Consider a perturbation $\Psi = \Psi(t, r, \theta, \phi)$ in the form of a massless, uncharged Klein-Gordon field in Schwarzschild spacetime. Recall this spacetime is described by the line element

$$ds^2 = -\left(1 - \frac{2M}{r}\right) dt^2 + \left(1 - \frac{2M}{r}\right)^{-1} dr^2 + r^2 d\Omega^2 \tag{4.1}$$

in the usual (t, r, θ, ϕ) Schwarzschild coordinates, where M determines the black hole mass and

$$d\Omega^2 = d\theta^2 + \sin^2\theta d\phi^2 \ . \tag{4.2}$$

By instead choosing to use the (t, r_*, θ, ϕ) radial tortoise coordinate system, defined in relation to the (t, r, θ, ϕ) coordinates by

$$\frac{d}{dr_*} = \left(1 - \frac{2M}{r}\right) \frac{d}{dr} \ , \tag{4.3}$$

and expanding the perturbing field in spherical harmonics $Y_{lm}(\theta, \phi)$ as per

$$\Psi(t, r, \theta, \phi) = \sum_{l,m} \frac{\psi_l(t, r)}{r} Y_{lm}(\theta, \phi) \ , \tag{4.4}$$

the radial equation of motion for the perturbing field is simply

$$\left(\frac{\partial^2}{\partial r_*^2} - \frac{\partial^2}{\partial t^2} - V_l(r)\right) \psi_l(t, r) = 0 \ , \tag{4.5}$$

where $V_l(r)$ is the *effective* or *Regge-Wheeler* potential (cf. [132])

$$V_l(r) = \left(1 - \frac{2M}{r}\right) \left(\frac{l(l+1)}{r^2} + \frac{2M}{r^3}\right) \ . \tag{4.6}$$

Furthermore, if a harmonic time decomposition

$$\psi_l(t, r) = \int \widetilde{\psi}_l(\omega, r) e^{-i\omega t} d\omega \tag{4.7}$$

is assumed, then equation (4.5) becomes the ordinary differential equation

$$\left(\frac{d^2}{dr_*^2} + \omega^2 - V_l(r)\right) \widetilde{\psi}_l(\omega, r) = 0 \ , \tag{4.8}$$

where V_l is again given by (4.6). More generally, for axial perturbations (i.e., those which transform as $(-1)^{l+1}$ under a change of parity)

$$V_l(r) = \left(1 - \frac{2M}{r}\right) \left(\frac{l(l+1)}{r^2} + \frac{2(1-s^2)M}{r^3}\right) \ , \tag{4.9}$$

where $s = 0, 1, 2$ is the spin of the perturbing field. For massless Klein-Gordon fields $s = 0$, for electromagnetic radiation perturbations $s = 1$, and for gravitational perturbations $s = 2$. The term $2M/r$ is interpreted as the Newtonian contribution, $l(l+1)/r^2$ is the so-called centrifugal barrier,

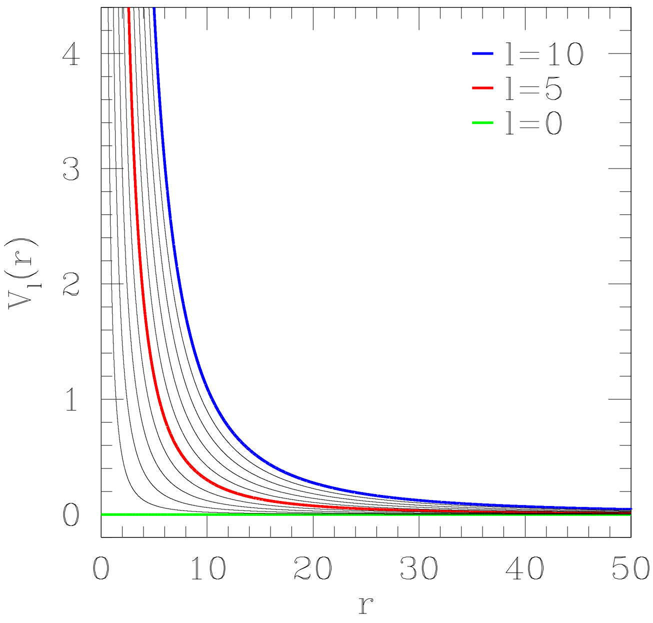

Figure 4.1: The effective (Regge-Wheeler) potential for massless scalar perturbations in $M = 0$ Minkowski spacetime. Displayed is the potential for modes $l = 0$ through $l = 10$. $l = 0$, $l = 5$ and $l = 10$ are highlighted for reference. Since $M = 0$, only the centrifugal barrier contributes to scattering of scalar perturbations. This indicates scalar modes cannot be trapped in the Minkowski spacetime.

and $2(1-s^2)M/r^3$ is the additional term from relativistic effects. Notice how the relativistic term is dominant for sufficiently small r. Purely radial modes are those with $l = 0$. Equations (4.6) and (4.9) show the effective potential has a peak near $r = 3M$ (corresponding with the unstable circular photon orbit from the null geodesic equations). Figures 4.1, 4.2 and 4.3 show the effective potential for scalar modes $l = 0$ through $l = 10$ for $M = 0$, $M = 1$ and $M = 5$ spacetimes, respectively. Except for the case $M = 0$, it is clear that a change in black hole mass M rescales the V_l, but leaves them otherwise unchanged. In the exceptional $M = 0$ case, only the centrifugal barrier contributes. Figure 4.4 displays the effective potential for electromagnetic modes $l = 0$ through $l = 10$. Besides the vanishing $l = 0$ mode, the electromagnetic effective potential is similar to that for scalar perturbations. Because the effective potential has at most a single extremum (in this case a maximum) massless scalar and electromagnetic perturbations are expected to scatter without becoming trapped.

Now, allowing for massive scalar perturbations in Schwarzschild spacetime, the effective potential becomes

$$V_l(r) = \left(1 - \frac{2M}{r}\right)\left(\frac{l(l+1)}{r^2} + \frac{2(1-s^2)M}{r^3} + \frac{(1-s)(2-s)m_\Psi^2}{2}\right), \tag{4.10}$$

m_Ψ being the mass parameter of the perturbing scalar field. Figures 4.5 and 4.6 show the effective potential for scalar modes $l = 0$ through $l = 10$ in a spacetime with $M = 5$, respectively for

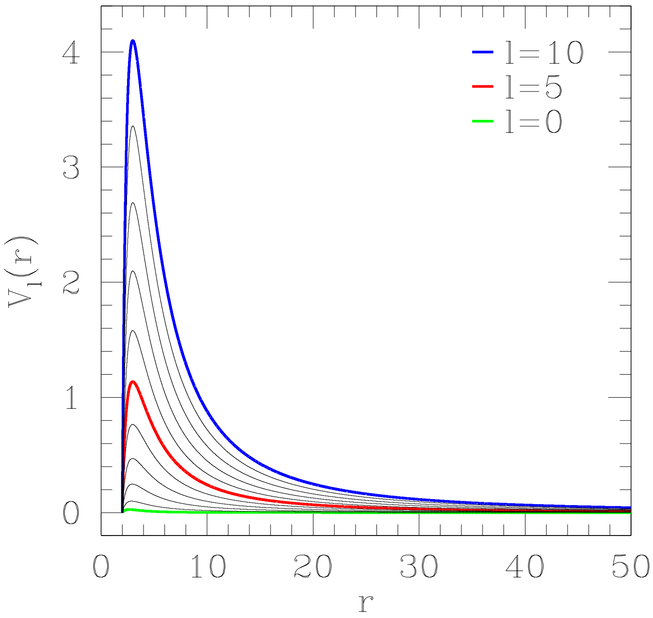

Figure 4.2: The effective (Regge-Wheeler) potential for massless scalar perturbations in Schwarzschild spacetime with $M = 1$. Displayed is the potential for modes $l = 0$ through $l = 10$. $l = 10$. $l = 0$, $l = 5$ and $l = 10$ are highlighted for reference. Scalar perturbations can scatter off the centrifugal barrier and also off the peak near $r = 3M$, but cannot be trapped in the spacetime.

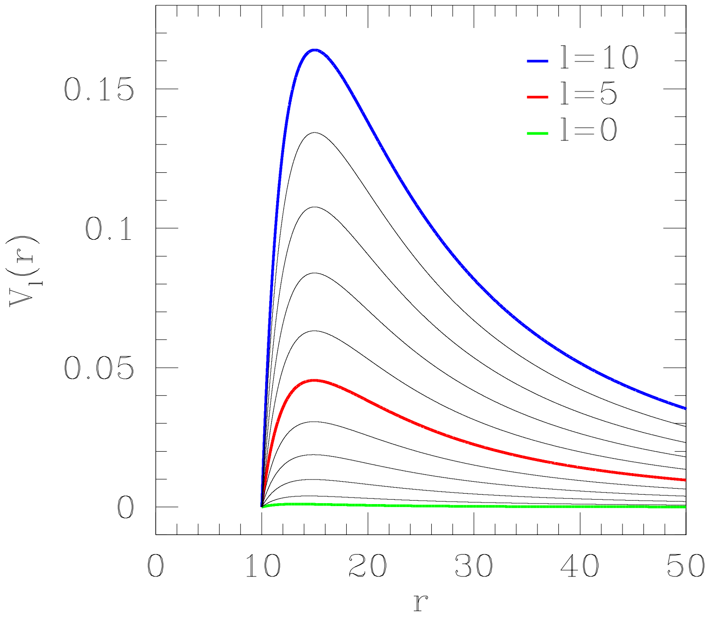

Figure 4.3: The effective potential for massless scalar perturbations in Schwarzschild spacetime with $M = 5$. Displayed is the potential for modes $l = 0$ through $l = 10$. $l = 10$. $l = 0$, $l = 5$ and $l = 10$ are highlighted for reference. Again, while scalar perturbations scatter off both the centrifugal barrier and potential peak near $r = 3M$, they do not experience trapping in the spacetime. The change in black hole mass simply shifts the location of the potential maximum to larger radii.

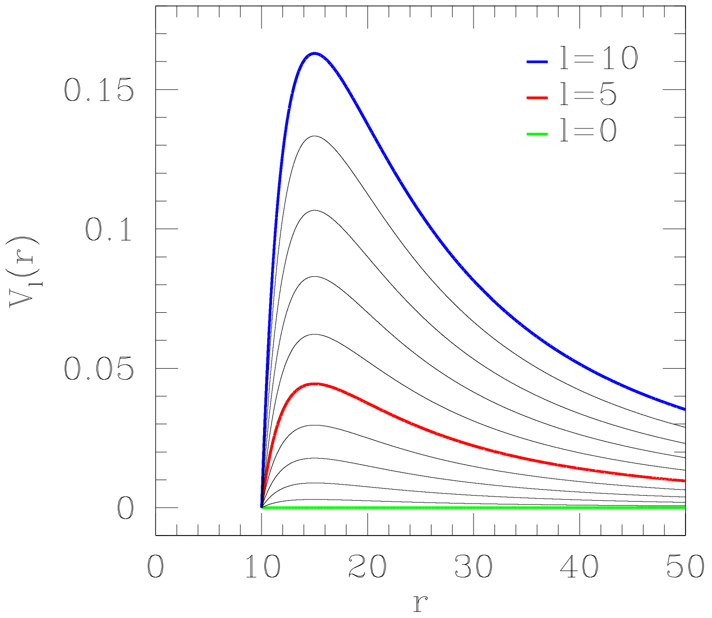

Figure 4.4: The effective potential for electromagnetic perturbations in Schwarzschild spacetime with $M = 5$. Displayed is the potential for modes $l = 0$ through $l = 10$. $l = 10$. $l = 0$, $l = 5$ and $l = 10$ are highlighted for reference. As in the case of scalar perturbations, scattering off the centrifugal barrier and potential peak near $r = 3M$ does not allow the possibility of mode trapping.

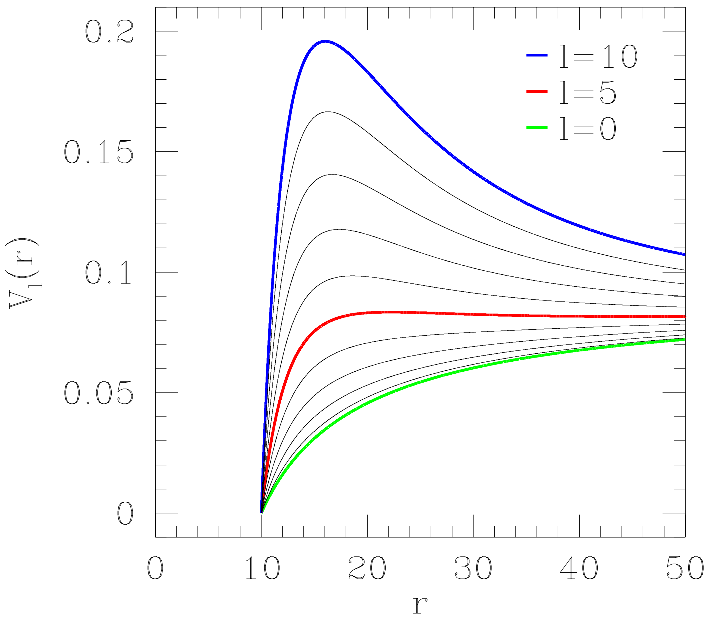

Figure 4.5: The effective potential for $m_\Psi = 0.3$ massive scalar perturbations in Schwarzschild spacetime with $M = 5$. Displayed is the potential for modes $l = 0$ through $l = 10$. $l = 10$. $l = 0$, $l = 5$ and $l = 10$ are highlighted for reference. The nonzero scalar perturbation mass introduces a local minimum of potential about which perturbations can be trapped.

$m_\Psi = 0.3$ and $m_\Psi = 0.6$. This shows the scalar field mass parameter can modify the effective potential by either removing the maximum, or shifting its location to larger radii and possibly introducing a local minimum. The details depend on the black hole mass, the mode number, and the scalar field mass parameter. Figures 4.7 and 4.8 show the effective potential for the scalar modes with local minima for $m_\Psi = 0.3$ and $m_\Psi = 0.6$ respectively. For the case $m_\Psi = 0.3$ the minimum occurs near $r = 45$ for mode $l = 5$, and for $m_\Psi = 0.6$ it occurs near $r = 35$ for $l = 10$. Since the effective potential possess a local minimum, massive scalar perturbations of an appropriate mode and energy can become trapped and persist indefinitely in a region of spacetime not far from the black hole. The effect is like that of mirrors reflecting the modes back and forth between two radii straddling the potential minimum. Also note that trapping does not occur in the $M = 0$ Minkowski limit, since then the only contributions to the potential are a positive term $l(l+1)/r^2$, and a constant m_Ψ^2.

Deeper analysis of the effective potential reveals interesting behaviour. The effort is simplified if one considers high or low frequency limits for scattered perturbations. In these cases closed form approximations can be obtained. The results for massless scalar and electromagnetic perturbations clearly indicate that, in the high frequency limit $\omega M \to \infty$, perturbations are hardly affected by the effective potential barrier. This means that such incident perturbations are almost completely absorbed by the black hole (it has a large transmission amplitude, $A_{\rm tran}$, and small reflection amplitude, $A_{\rm ref}$). The opposite is true in the low frequency limit $\omega M \to 0$. In that case, almost all

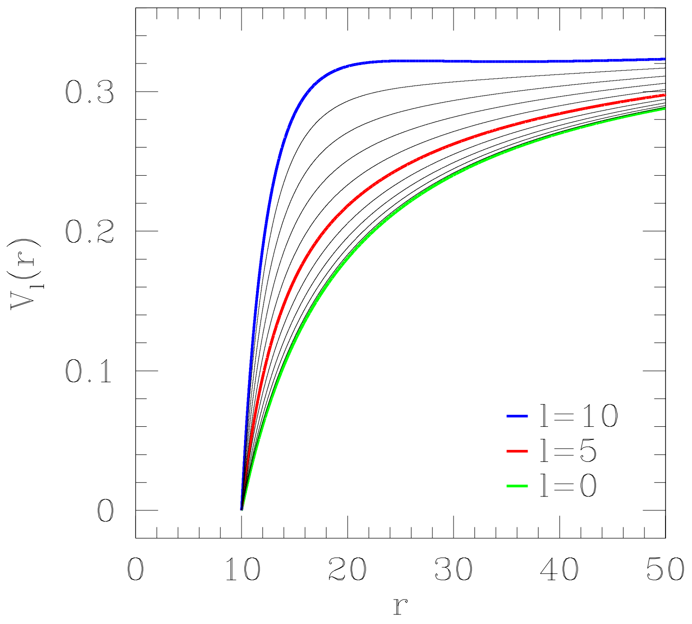

Figure 4.6: The effective potential for $m_\Psi = 0.6$ massive scalar perturbations in Schwarzschild spacetime with $M = 5$. Displayed is the potential for modes $l = 0$ through $l = 10$. $l = 10$. $l = 0$, $l = 5$ and $l = 10$ are highlighted for reference. Again, the scalar perturbation mass gives rise to a local minimum of potential where perturbations can be trapped. Furthermore, the location of this minimum changes with perturbation mass.

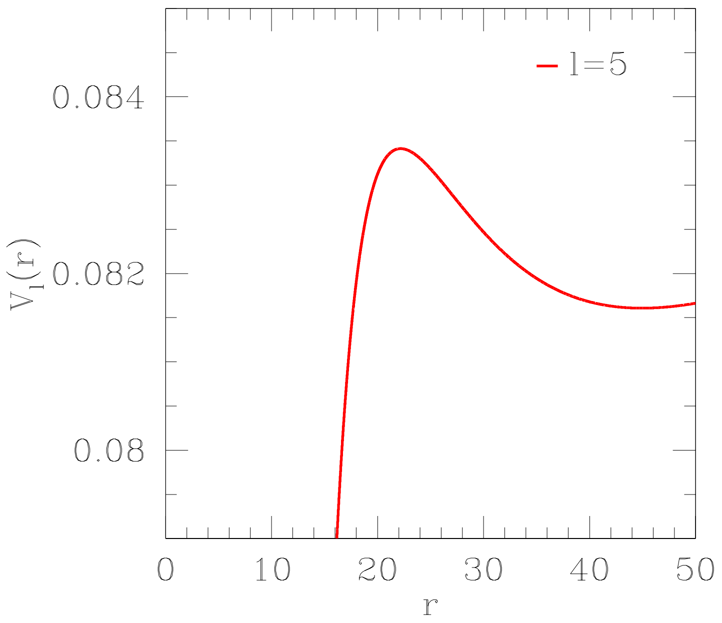

Figure 4.7: The $l = 5$ effective potential for $m_\Psi = 0.3$ massive scalar perturbations in Schwarzschild spacetime with $M = 5$. This figure details the potential for $l = 5$ scalar modes. These modes exhibit the deepest local minimum of potential and should therefore experience the greatest trapping in the $M = 5$ spacetime. The local minimum is in this case located near $r = 45$.

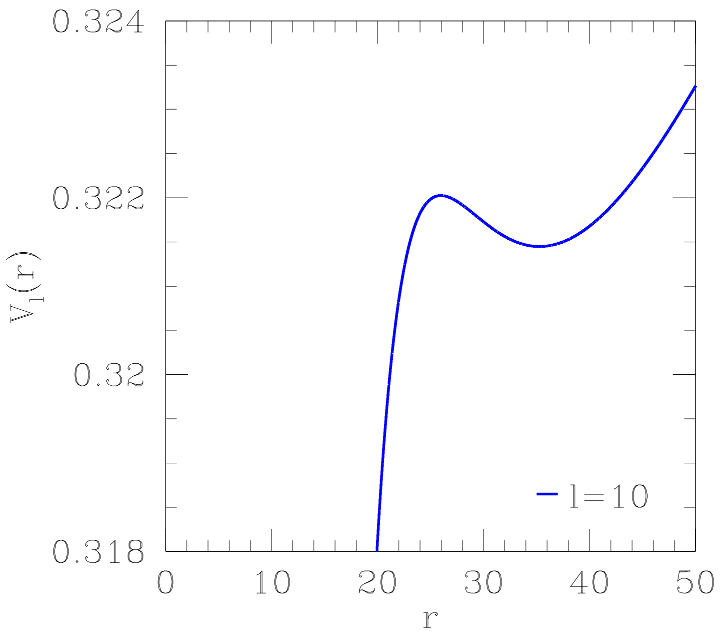

Figure 4.8: The $l = 10$ effective potential for $m_\Psi = 0.6$ massive scalar perturbations in Schwarzschild spacetime with $M = 5$. The $l = 10$ modes experience the deepest local minimum for the $M = 5$ spacetime. The minimum is located near $r = 35$ for this choice of perturbation mass. This designates the location about which $m_\Psi = 0.6$ perturbations are likely to be trapped.

of the incident perturbation is scattered off the potential barrier (A_{tran} is low, and A_{ref} is high). The analysis is well documented, and I refer the reader to [49], [51] and references contained therein. Finally, it should be clear from this discussion that the radial profile of an ingoing perturbation will have an effect on the transmission and reflection amplitudes. Specifically, steep gradients in the radial profile imply rapid changes in amplitude as the perturbation moves past a fixed radius. This means the high frequency content of such a perturbation will be relatively large. The converse is true with perturbations possessing a relatively flat radial profile. This effectively means sharply peaked distributions will have smaller A_{tran} (and larger A_{ref}) that those with a flatter profile. For demonstrative purposes, I have computed the scattering of initially ingoing massless scalar perturbations from a Schwarzschild black hole in spherical symmetry. The radial profile of the scalar perturbation is specified at initial time with a Gaussian

$$\Psi(t=0,r) = a_\Psi \exp\left[-\left(\frac{r-r_\Psi}{\delta_\Psi}\right)^2\right] , \tag{4.11}$$

where a_Ψ is the Gaussian amplitude, r_Ψ determines the center of the Gaussian profile, and δ_Ψ sets its width. As expected, the transmission increases (and reflection decreases) with decreasing δ_Ψ, as such profiles have steeper radial gradients. Denoting the energy of the set of ingoing modes T_{in} and the energy of that set upon reflection T_{out}, the fractional transmitted energy, $Z+1$, is

$$Z+1 = \frac{T_{\mathrm{out}}}{T_{\mathrm{in}}} , \tag{4.12}$$

Figure 4.9 shows this fractional transmitted energy as a function of $0 \le \delta_\Psi/M \le 25$.

4.1.2 The Glory Effect and Orbiting Resonances

The phenomena of glories and orbiting resonances can also be obtained as limiting cases in the analysis of (4.10). The details are again summarized in [49] and [51], while a more recent and rather thorough investigation of scalar glories for both Schwarzschild and Kerr spacetime has been presented in [54]. The *glory* is a diffraction phenomenon that happens when a differential scattering cross-section diverges in either the forwards or backwards directions. The phenomenon is known to occur in optics, quantum mechanics, and also in the scattering of perturbations off a black hole, among others. In the case of black hole scattering, glories arise as a consequence of strong gravitational interaction of high frequency perturbations through angles near $\Theta = k\pi$, k being an integer. The generic relationship between total scattering angle Θ and impact parameter $b = b(\Theta)$ for massless perturbations of this sort is [38], [39], [102],

$$b \approx 3\sqrt{3}M + 3.48M\exp(-\Theta) , \tag{4.13}$$

providing $b \sim 2M$. The impact parameter for the first backwards glory $\Theta = \pi$ is thus $b = b_{\mathrm{glory}} \approx 5.35M$. Figure 4.10 depicts scattering trajectories for angles near $\Theta = \pi$. The differential scattering cross-section for massless perturbations of arbitrary spin near angles $\Theta = k\pi$ is given by [43], [155]

$$\left.\frac{d\sigma}{d\Omega}\right| \approx 2\pi\omega b^2 \left|\frac{db}{d\Theta}\right| J_{2s}^2\left(\omega b \sin\Theta\right) , \tag{4.14}$$

where $b = b(\Theta)$ is provided by (4.13), s is the perturbation spin, and $J_{2s}\left(\omega b \sin\Theta\right)$ is the standard Bessel function with argument $\omega b \sin\Theta$. From (4.14), it is apparent that glories constructively interfere for massless ($s=0$) scalar fields, but destructively interfere for ($s=1$) electromagnetic and ($s=2$) gravitational perturbations.

The phenomenon known as *orbiting resonance* occurs when a perturbation scatters through an angle $\Theta \ge 2\pi$. The perturbations can be deflected through several multiples of 2π before escaping to

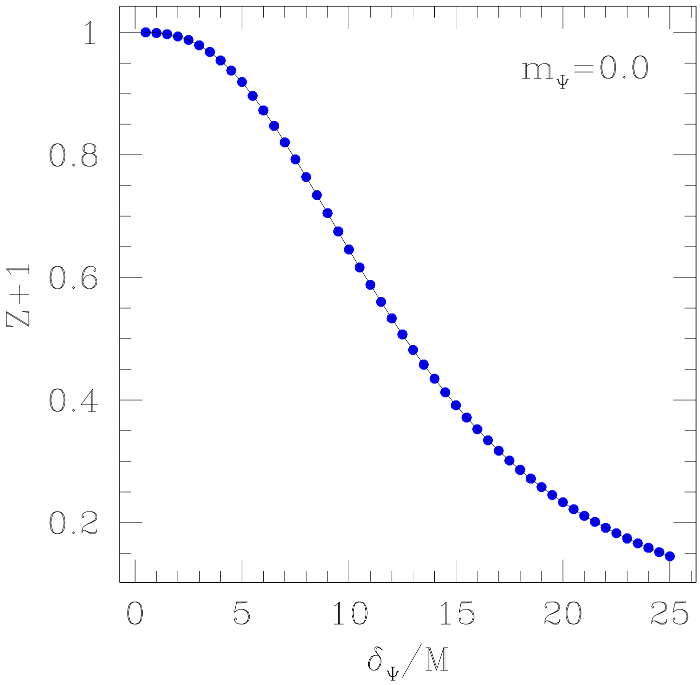

Figure 4.9: Fractional transmitted energy, $Z + 1$, for spherically symmetric massless scalar perturbations scattering off a Schwarzschild black hole. The profile is an initially ingoing Gaussian profile of width δ_Ψ. The fractional transmitted energy is plotted as a function of δ_Ψ/M, where M is the black hole mass.

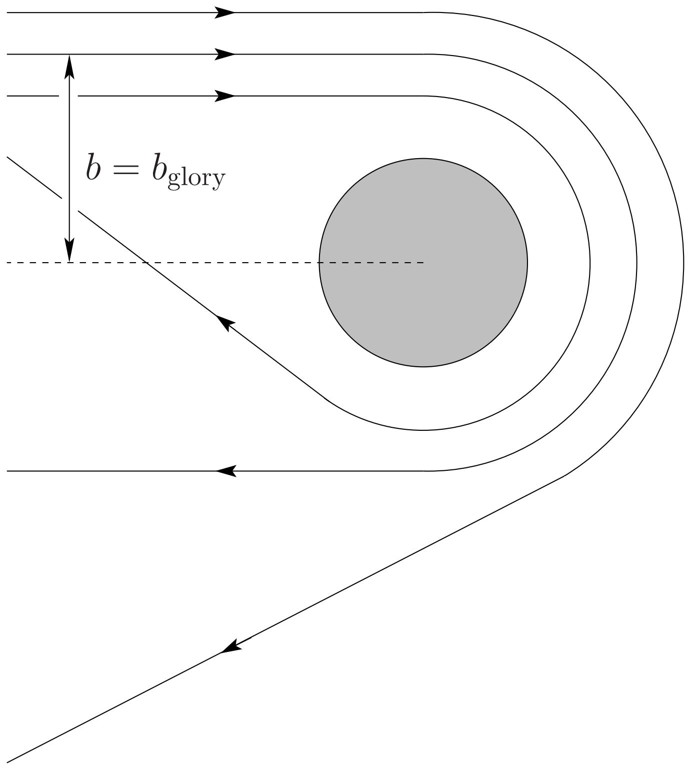

Figure 4.10: In the glory effect, perturbations with impact parameters $b = b_{\text{glory}}$ deflect through an angle of $\Theta = \pi$. Impact parameters larger that b_{glory} scatter through smaller angles, while smaller impact parameters scatter through angles larger than $\Theta = \pi$. This figure depicts scattering trajectories for angles near $\Theta = \pi$.

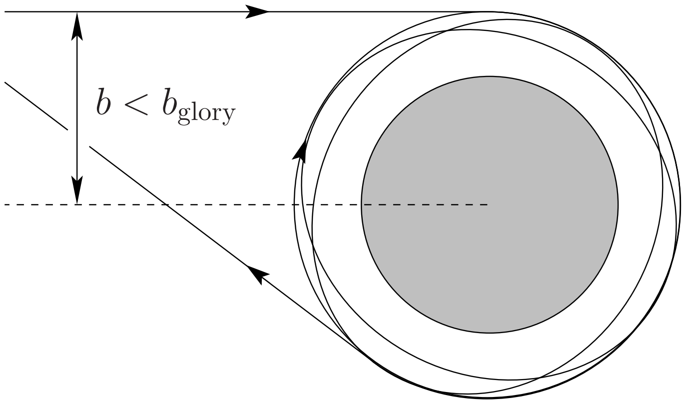

Figure 4.11: Orbiting resonances require impact parameters, b, smaller than those for a glory, b_{glory}. In an orbiting resonance, the total scattering angle is $\Theta = 2\pi$ or larger. This figure depicts the trajectory for a resonance which orbits the black hole several times before escaping to large distances.

distances much larger than $r \sim 2M$. However, the cross-section observes approximately exponential decay in Θ. For example, equation (4.14) shows that a second backwards glory (scattered through angle $\Theta = 3\pi$) is suppressed by at least $\exp(-2\pi)$ relative to the first backwards glory (with scattering angle $\Theta = \pi$). An resonance of several orbits is depicted in Figure 4.11.

4.1.3 The Effective Potential Formulation for Kerr Spacetime

The calculations become further complicated when considering rotating black hole spacetimes. In the simplest case of Kerr spacetime[1], the perturbation equations can be separated into radial and angular parts if, rather than spherical harmonics, the expansion of the perturbing field is performed in terms of the spin-weighted spheroidal harmonics $S_{lm}(\theta)$ as per

$$\Psi(t,r,\theta,\phi) = \sum_{l,m} \frac{\psi_{lm}(t,r)}{\sqrt{2\pi}} S_{lm}(\theta) e^{-im\phi} \ . \tag{4.20}$$

Then, assuming a harmonic time decomposition

$$\psi_{lm}(t,r) = \int \widetilde{\psi}_{lm}(\omega, r) e^{-i\omega t} d\omega \ , \tag{4.21}$$

[1] Recall the line element for Kerr spacetime in (t,r,θ,ϕ) Boyer-Lindquist coordinates is

$$ds^2 = -\left(1 - \frac{2Mr}{\Sigma}\right) dt^2 - \frac{4Mra\sin^2\theta}{\Sigma} dt d\phi + \frac{\Sigma}{\Delta} dr^2 + \Sigma d\theta^2 + \frac{A\sin^2\theta}{\Sigma} d\phi^2 \ , \tag{4.15}$$

where

$$\Sigma \equiv r^2 + a^2\cos^2\theta \ , \tag{4.16}$$
$$\Delta \equiv r^2 - 2Mr + a^2 \ , \tag{4.17}$$
$$A \equiv \left(r^2 + a^2\right)^2 - a\Delta\sin^2\theta \ , \tag{4.18}$$

and

$$a \equiv \frac{J}{M} \tag{4.19}$$

is the black hole angular momentum per unit mass, J designating the black hole angular momentum.

and using the (t, r_*, θ, ϕ) tortoise coordinate system related to the standard (t, r, θ, ϕ) Boyer-Lindquist coordinates through

$$\frac{d}{dr_*} = \frac{\Delta}{r^2 + a^2}\frac{d}{dr} \ , \tag{4.22}$$

the radial part of the perturbation equation becomes

$$\left[\frac{d^2}{dr_*^2} + \frac{K^2 - 2is(r-M)K + \Delta\left(4ir\omega s - \lambda - r^2(1-s)(2-s)m_\Psi^2/2\right)}{(r^2+a^2)^2} - G^2 - \frac{dG}{dr_*}\right]\widetilde{\chi}_{lm}(\omega, r) = 0 \ , \tag{4.23}$$

where

$$\begin{aligned} K &\equiv (r^2 + a^2)\omega - am \ , && (4.24)\\ \lambda &\equiv E - s(s+1) + a^2\omega^2 - 2am\omega \ , && (4.25)\\ G &\equiv \frac{s(r-M)}{r^2+a^2} + \frac{r\Delta}{(r^2+a^2)^2} \ , && (4.26)\\ \widetilde{\chi}_{lm} &\equiv (r^2+a^2)^{1/2}\Delta^{s/2}\psi_{lm} \ , && (4.27) \end{aligned}$$

E being the separation constant

$$E \equiv l\,(l+1) - \frac{2ma\omega s^2}{l\,(l+1)} + \mathcal{O}\left(a^2 m_\Psi^2\left(1 - \frac{\omega^2}{m_\Psi^2}\right)\right) \ , \tag{4.28}$$

$\Delta \equiv r^2 - 2Mr + a^2$, M is the black hole mass, a is the black hole angular momentum per unit mass, s is again the spin of the perturbing field, and m_Ψ is the mass parameter of the scalar ($s = 0$) perturbations. It is clear from (4.23) the effective potential is now dependent on the perturbation frequency, and that it reduces to the expected Schwarzschild form (4.10) in the limit $a \to 0$. All the scattering phenomena previously presented will therefore play a role in Kerr spacetime.

4.1.4 Polarization, Superradiance, and the Black Hole Bomb

Two new scattering effects are present for perturbations on Kerr spacetime which are absent from the Schwarzschild black hole scenario discussed in subsection 4.1. They are polarization and superradiant scattering of the incident perturbation. Both electromagnetic and gravitational perturbations can be partially polarized by scattering off a rotating black hole. [98] and [99] present the first calculations demonstrating this polarization effect for electromagnetic perturbations in Kerr spacetime. The calculations are involved, but essentially different polarization states scatter differently in the rotating black hole spacetime. It should, in principle, be possible to observe these effects in the numerical evolutions I present.

The superradiant scattering effect should also play a role in my computations. In *superradiant scattering* an incident perturbation is amplified as it scatters off the black hole, the additional energy being drawn from the rotation of the black hole. Some of the earliest studies of superradiant scattering were [151], [152], [153], [5], [101], [124], [137], [138] and [141]. The appearance of superradiant scattering is intimately connected with the change of character of Killing vector $t^a = (1, 0, 0, 0)$ in different regions of the Kerr spacetime. For radii $r > r_s = M + \sqrt{M^2 - a^2\cos^2\theta}$, t^a is timelike. However, t^a becomes spacelike for $r < r_s$. This implies energy densities ρ_T can be negative within the ergoregion, defined by $r < r_s$. Under these circumstances an incident perturbation can carry negative energy into the black hole, leaving a reflected component with greater amplitude and energy than that which was incident. From analysis of (4.23) the incident perturbation will carry negative energy when

$$0 < \omega < m\Omega_{\rm H} \ , \tag{4.29}$$

$\Omega_{\rm H}$ being the *horizon angular velocity*

$$\Omega_{\rm H} = \frac{a}{r_+^2 + a^2} \ , \tag{4.30}$$

where $r_+ = M + \sqrt{M^2 - a^2}$ marks the location of the event horizon. Equation is known as the *superradiance condition*, since it can be shown that superradiance must occur the condition is met. Clearly, this requires the perturbations be prograde ($\omega > 0$), and also that mode numbers satisfy $m > 0$. [141] found this superradiant amplification is maximal for $a = M$, and drops sharply with decreasing a, or with increasing mode numbers l and m. Denoting the energy of an ingoing mode $T_{\rm in}$ and the energy of that mode upon reflection $T_{\rm out}$, [141] numerically determined the maximum of fractional energy change, Z, given by

$$Z = \frac{T_{\rm out}}{T_{\rm in}} - 1 \ , \tag{4.31}$$

for a single mode is 1.38 for ($s = 2$) gravitational perturbations, and 1.044 for ($s = 1$) electromagnetic perturbations. The maximal value of Z was calculated at 1.003 for ($s = 0$) massless scalar perturbations in [124]. More recent investigations have shown that the maximal value of Z can be increased to near 1.07 for scalar perturbations confined to a toroidal wedge in the equatorial plane of the Kerr black hole [142], [1]. For the same geometry, Z decreases to approximately 1.003 in the case of confined electromagnetic perturbations [1]. Confinement of plasma in a toroidal ring by magnetospheric dynamics was the motivation for these two investigations.

Because massive scalar perturbations are dispersive, it is difficult to define notions of purely ingoing and outgoing modes when $m_\Psi > 0$. None the less, modes can be reflected superradiantly. The superradiant condition is again (4.29). It was pointed out to me by [48] that such massive perturbation modes possess growing mode instabilities when they become trapped by the effective potential of the black hole spacetime. If modes are trapped, then superradiant scattering can amplify the trapped modes over and over, thereby leading to a growing mode instability. The effect is analogous to the so-called *black hole bomb* first discussed by Press and Teukolsky [124]. The first work to note this instability for massive scalar perturbations was [37]. Later studies include [156], [41], [50] and [140]. One implication is that through this mechanism, a black hole can, in principle lose all of its angular momentum. However, these unstable massive scalar modes are slowly growing, with a growth times similar to the age of the universe for solar mass black holes. These instabilities are thus not expected to play a role in my calculations (which cover significantly shorter timescales). Recalling that scalar field models can represent the pions, note how this time scale is also quite large relative to π^0, π^+ and π^- lifetimes of 8.4×10^{-17}s and 2.6×10^{-8}s respectively. Furthermore, for typical π^0, π^+ and π^- masses of $m_\Psi \simeq 2.4 - 2.5 \times 10^{-28}$kg, the growth rate is found to be maximal for black hole masses $M \ll 10^{15}$kg. Such black holes are far less massive than solar mass stars, where $M = M_\odot \simeq 2.0 \times 10^{30}$kg.

4.1.5 Late Time Decay, and the Coupling of Electromagnetic and Gravitational Perturbations

Perturbations are known to exhibit exponential amplitude decay at sufficiently late time. Like the intermediate phase of evolution, these asymptotic late time dynamics also originate from the spacetime curvature. From analysis of (4.10), it has been shown that decay rates of massless ($s = 0$) scalar, ($s = 1$) electromagnetic, and ($s = 2$) gravitational perturbation amplitudes in Schwarzschild spacetime observe the late-time relationship

$$|\Psi(t,r)| \sim t^{-(2l+P+1)} \ , \tag{4.32}$$

where $P = 1$ if the field is initially static, and $P = 2$ otherwise [130], [131]. Meanwhile, it was found by [89] that, for massive Klein-Gordon perturbations, the late-time decay rate is independent of the mode number and adopts the form

$$|\Psi(t,r)| \sim t^{-5/6} \ . \tag{4.33}$$

While the authors of [89] have studied the massive scalar problem in detail in [88] and [90], the first to begin investigation of this system were Novikov and Starobinski [139], and Burko [14].

While, it was shown in [15] that (4.33) also holds for sufficiently late times in Kerr spacetime, regardless of the black hole angular momentum, the power-law decay of massless scalar, electromagnetic, and gravitational perturbations differ from (4.32) when the black hole rotates. Specifically, [74] [75] and [76] studied the $r|\omega| \ll 1$ and $a|\omega| \ll 1$ limits of massless perturbations. It was found the decay of massless ($s = 0$) scalar perturbations at timelike infinity obeys

$$|\Psi(t,r)| \sim t^{-(2l+3)} \ , \tag{4.34}$$

when $|m| \leq l \leq |m| + 1$, and

$$|\Psi(t,r)| \sim t^{-(l+|m|+P+1)} \ , \tag{4.35}$$

when $|m| + 2 \leq l$, where $P = 0$ if $l - |m|$ is even and $P = 1$ otherwise. Meanwhile, electromagnetic and gravitational perturbations were found to obey

$$|\Psi(t,r)| \sim t^{-(2\max(|m|,s)+3)} \ , \tag{4.36}$$

when $\max(|m|, s) \leq l \leq \max(|m|, s) + 1$, and

$$|\Psi(t,r)| \sim t^{-(l+\max(|m|,s)+1)} \ , \tag{4.37}$$

when $\max(|m|, s) + 2 \leq l$. While results (4.34) through (4.37) hold for perturbations consisting of a single mode l, [74] demonstrated that when a perturbation is initially a superposition of many modes, the decay law becomes

$$|\Psi(t,r)| \sim t^{-(2\max(|m|,s)+3)} \ , \tag{4.38}$$

for all s. These results contradict the previously widely held belief that late time decay of perturbations in gravitational collapse is universal (i.e., independent of s), and are presumably a consequence of the coupling of modes with different l for rotating black hole spacetimes. Furthermore, these results demonstrate the possibility of slower decay rates than in the non-rotating case. In a more general pair of studies [3] and [55] found the decay rate of massless scalar perturbations reduces to

$$|\Psi(t,r)| \sim t^{-1} \ , \tag{4.39}$$

for a maximally rotating black hole (i.e., $a = M$). This slower decay rate is apparently the result of superradiant scattering.

In principle, all these late time relations for scalar and electromagnetic perturbations should be observable for the system I study in this dissertation. However, since my numerical evolutions are relatively short, I do not expect to get good estimates of any power law decay. Furthermore, since the chosen computational domain only covers finite radii, the results obtained for asymptotically large distances will not be attainable. Spatial compactification would be one way to correct this second restriction.

4.1.6 Charged Scalar Perturbations in Static and Stationary Spacetimes

Finally, the effective potential formulation of black hole perturbations has been studied for charged scalar fields in static and stationary spacetime. The analysis was performed in the context of weakly charged perturbations about a Reissner-Norström black hole in [69], [70], [86], [87]. In [37] and [50] analysis was also carried out for weakly charged perturbations, but their spacetime was Kerr-Newman (i.e., the charged analogue of Kerr). In all these studies it was assumed the scalar perturbations carry test charge in the sense that while they could be electromagnetically affected by the charge of the black hole, they themselves did not contribute to electric or magnetic fields. These charged perturbations did not electromagnetically self-interact. In the limit where the black hole charge vanishes, this system is thus exactly that of uncharged scalar perturbations in Schwarzschild spacetime. It is through this approximation the equations of a charged scalar perturbation become linear and allow an effective potential formulation.[2]

The system I study—described in the next section—assumes a fundamentally different approximation. The scalar perturbations are massive and electromagnetically self-interacting. But while self-interacting, this system assumes the charge carried by these perturbations doesn't influence the curvature of the spacetime in which they evolve. However, this does not imply weak electromagnetic interaction, or even limitation to a regime in which electromagnetic interaction is subordinate to all gravitational effects—consider a common crystalline substance where electromagnetic binding energy is orders of magnitude stronger than gravitational attraction. Furthermore, the system assumes the field mass is likewise too small to affect the curvature of spacetime. Since the influence of charge and mass on spacetime must be through the stress-energy tensor, the assumptions are essentially a statement that the local energy density of the field must be small. The notion of small can be roughly quantified through comparison with the Schwarzschild solution. Since the Schwarzschild radius is $R_{\mathrm{S}} = 2M$, the average energy density of the black hole is $\rho_{T\mathrm{S}} \sim M/(\frac{4}{3}\pi R_{\mathrm{S}}^3) = 3/(32\pi M^2)$. Therefore, the assumption that the perturbation energy density ρ_T is small means $\rho_T/\rho_{T\mathrm{S}} \sim 3\rho_T/(32\pi M^2) \ll 1$. For the results presented in section 4.3, where $M = 5$, the maximum energy densities are $\rho_T \approx 1$–10, so the assumption $\rho_T/\rho_{T\mathrm{S}} \ll 1$ holds.

The system of equations for these perturbations are nonlinear and so cannot be cast in the form of an effective potential problem. Being nonlinear, the system must be solved numerically. To my knowledge, the only other work that has analysed the nonlinear problem is [71], where the authors investigated the late-time decay of massless charged scalar perturbations in a dynamic spherically symmetric spacetime. Investigation of the nonlinear charged model in rotating spacetime has until now been lacking—the results I present are the first of their kind.

[2] The effective potential formulation for charged spacetime backgrounds is known to couple electromagnetic and gravitational perturbations. A purely electromagnetic incident perturbation can by this mechanism scatter as a purely gravitational perturbation. This could lead to interesting consequences for both superradiant scattering and eventually gravitational wave detection. The effect is apparently dependent on the existence of a background electric field, which is not the case for the system I investigate. However, some of the earliest works on this topic are [18], [154], [104], [53], [105], [19] and [118].

4.2 System of Equations for Charged Scalar Accretion

4.2.1 The Spacetime Metric

The rotating black hole spacetime is described by the Kerr metric. In (t, r, θ, ϕ) Kerr-Schild coordinates the line element takes the form

$$\begin{aligned} ds^2 \quad = \quad & -\left(1 - \frac{2Mr}{\Sigma}\right) dt^2 + \left(1 + \frac{2Mr}{\Sigma}\right) dr^2 + \Sigma d\theta^2 + \sin^2\theta \left(r^2 + a^2 + \frac{2Mra^2\sin^2\theta}{\Sigma}\right) d\phi^2 \\ & + \left(\frac{4Mr}{\Sigma}\right) dtdr - \left(\frac{4Mra\sin^2\theta}{\Sigma}\right) dtd\phi - 2a\sin^2\theta \left(1 + \frac{2Mr}{\Sigma}\right) drd\phi \ , \end{aligned} \tag{4.40}$$

where

$$\Sigma \equiv r^2 + a^2\cos^2\theta \ , \tag{4.41}$$

$$a \equiv \frac{J}{M} \ , \tag{4.42}$$

t is the temporal coordinate, and r, θ and ϕ are respectively the radial and angular spatial coordinates, M represents the total mass of the black hole spacetime and J its total angular momentum. The metric (4.40) diverges at $\Sigma = 0$ and the scalar invariant $R_{abcd}R^{abcd}$ indicates the root $r = a\cos\theta$ is a true curvature singularity. The singularity is a ring of radius a. Because the form (4.40) is horizon penetrating, it doesn't immediately reveal the existence of other special surfaces in the spacetime such as $\Delta = 0$, where

$$\Delta \equiv r^2 + a^2 - 2Mr \ . \tag{4.43}$$

When $a^2 \leq M^2$ the root $r = r_+ = M + \sqrt{M^2 - a^2}$ marks the location of the event horizon. It is geometrically a sphere in the given coordinates. The second root $r = r_- = M - \sqrt{M^2 - a^2}$ is a Cauchy horizon.[3] When $a^2 > M^2$ there is no event horizon and the ring singularity is naked. Since in this instance there is no event horizon, the metric does not describe a black hole spacetime. Such a spacetime would be in violation of the *Cosmic Censor Conjecture* as put forth by [123] which states no such singularities should be visible to any observer. The spacetime (4.40) possesses two Killing vector fields $t^a = (1, 0, 0, 0)$ and $s^a = (0, 0, 0, 1)$. t^a is timelike and s^a spacelike in the portion of spacetime where $r > r_\mathrm{s} = M + \sqrt{M^2 - a^2\cos^2\theta}$. However, when $r_+ < r < r_\mathrm{s}$ the Killing vector field t^a becomes spacelike. The region $r_+ < r < r_\mathrm{s}$ is known as the *ergosphere*. From the perspective of a stationary observer at infinity, a timelike orbit cannot remain stationary within the ergosphere, but must rotate in the direction of rotation of the black hole. $r = r_\mathrm{s}$ is thus called a *stationary limit surface* in this strong example of the *frame-dragging effect*. Figure 4.12 depicts the rotating Kerr black hole spacetime, and Figure 4.13 displays its causal structure.

Finally, the future-directed unit-norm spatial hypersurface orthogonal vector is

$$n^a = \left(\sqrt{g_{rr}}, -\frac{g_{tr}}{\sqrt{g_{rr}}}, 0, 0\right) \tag{4.44}$$

[3]Based upon arguments that an observer crossing $r = r_-$ will see entire histories evolved from a Cauchy surface of the Kerr spacetime in a finite period of time, the Cauchy horizon at $r = r_-$ is thought to be unstable, as first put forth by Penrose in [122]. However, definitive results, numerical or otherwise, detailing the formation and evolution of the Kerr Cauchy horizon are apparently lacking. But if the results known for horizons of charged spherically symmetric black holes carry over, then perturbations of the Kerr spacetime could lead to the formation of null singularities which then merge with the Cauchy horizon. However, as in the charged spherically symmetric case, this null singularity may still be traversable by observers willing to suffer finite tidal forces. While the Kerr metric may not accurately describe the interior of a black hole formed by the collapse of matter with angular momentum, it is assumed to accurately depict the exterior spacetime after a stationary state has been achieved. Since my interest is with the dynamics of fields outside the event horizon $r = r_+$, I can excise the portion of spacetime $r < r_+$ without additional concern.

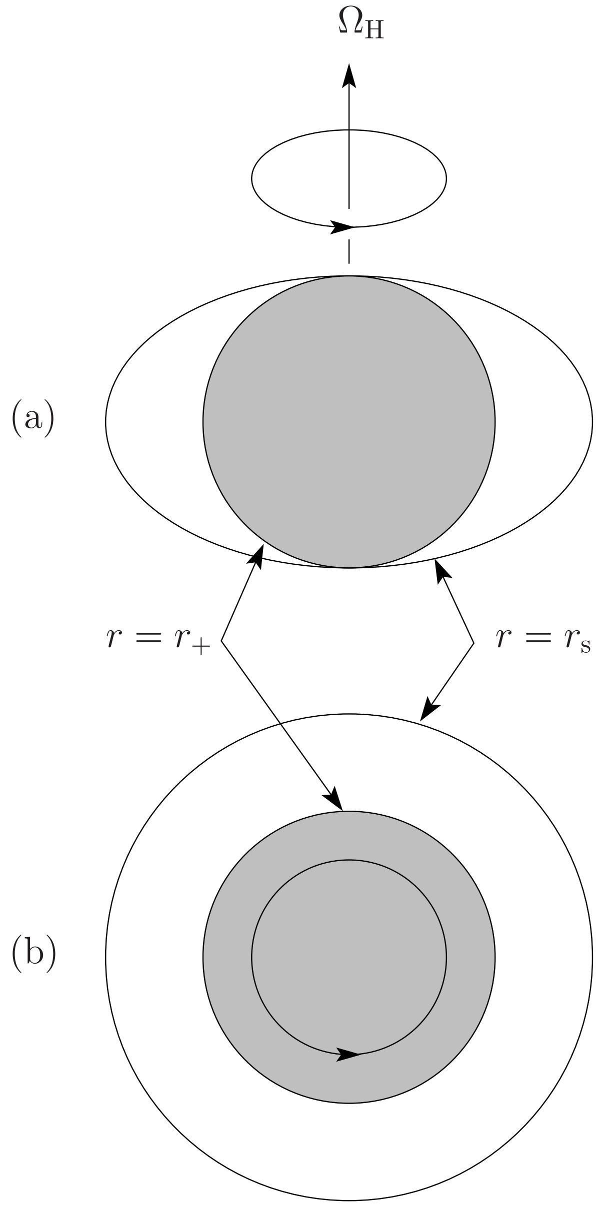

Figure 4.12: Horizons of Kerr spacetime: side view (a) and top view (b). $r = r_+$ marks the event horizon, $r = r_{\rm s}$ is the stationary limit surface, and $\Omega_{\rm H}$ is the horizon angular velocity. The ergosphere is the region $r_+ < r < r_{\rm s}$. The ring singularity is shrouded by the event horizon.

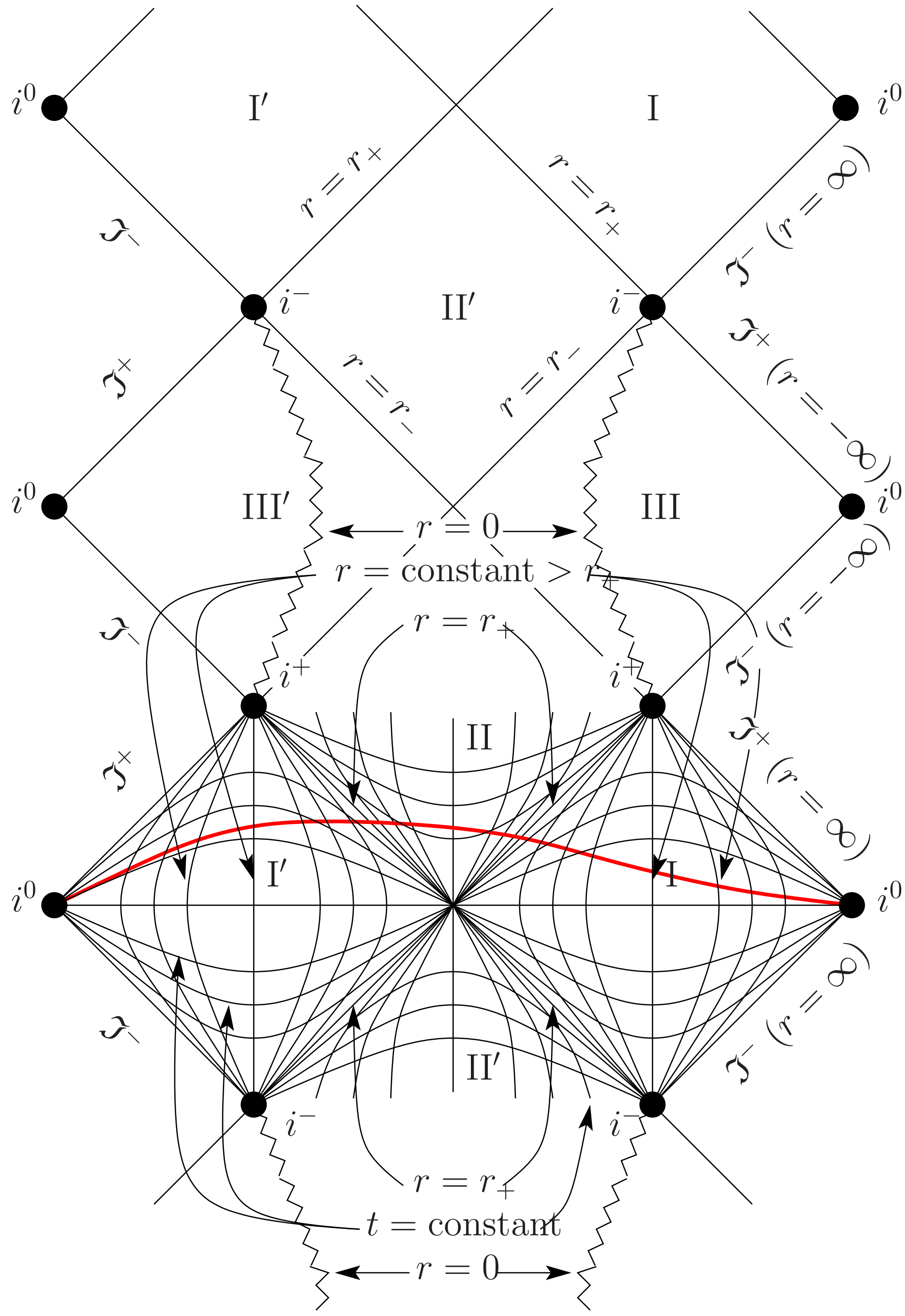

Figure 4.13: Penrose diagram showing causal structure of Kerr spacetime (cf. [62]). I and I' depict asymptotically flat regions of the spacetime outside the black hole. II and II' are interior to the event horizon at $r = r_+$, while interior regions III and III' are separated from II and II' by the Cauchy horizons at $r = r_-$. $\mathfrak{I}^+$ represents future null infinity and $\mathfrak{I}^-$ past null infinity, while i^- represents past timelike infinity, i^+ future timelike infinity and i^0 spacelike infinity. The singularity at $r = 0$ is timelike, and can thus be avoided by a timelike trajectory originating on the Cauchy surface (red).

where

$$g_{tr} = \left(\frac{2Mr}{\Sigma}\right) \ , \tag{4.45}$$

$$g_{rr} = \left(1 + \frac{2Mr}{\Sigma}\right) \ , \tag{4.46}$$

and the spatial metric is encapsulated by the hypersurface line element

$$\begin{aligned} d\sigma^2 &= \left(1+\frac{2Mr}{\Sigma}\right) dr^2 + \Sigma d\theta^2 + \sin^2\theta \left(r^2 + a^2 + \frac{2Mra^2\sin^2\theta}{\Sigma}\right) d\phi^2 \\ &- 2a\sin^2\theta\left(1+\frac{2Mr}{\Sigma}\right) dr d\phi \ . \end{aligned} \tag{4.47}$$

4.2.2 The Matter Lagrangian and Equations of Motion

The Lagrangian for a massive electromagnetically coupled complex scalar field is again

$$\mathcal{L}_{\mathcal{M}} = \sqrt{-g}[-(\nabla_a\Phi - ieA_a\Phi)(\nabla^a\Phi^* + ieA^a\Phi^*) - \frac{1}{4}F^{ab}F_{ab} - m_\Phi^2\Phi^*\Phi] \ , \tag{4.48}$$

where m_Φ is the scalar field mass parameter, e sets the strength of electromagnetic coupling between the real and imaginary components of complex scalar field $\Phi = \Phi(t,r,\theta)$ (respectively $\phi_1 = \phi_1(t,r,\theta)$ and $\phi_2 = \phi_2(t,r,\theta)$), the symbol * denotes complex conjugation, $A_a = A_a(t,r,\theta)$ is the electromagnetic vector potential, and F_{ab} is the antisymmetric electromagnetic field strength tensor. The set of Euler-Lagrange equations for the system described by (4.48) yields equations of motion

$$\nabla^a\nabla_a\Phi^* + 2ie(\nabla_a\Phi^*)A^a - e^2\Phi^*A_aA^a + ie\Phi^*\nabla_aA^a - m_\Phi^2\Phi^* = 0 \ , \tag{4.49}$$

$$\nabla^a\nabla_a\Phi - 2ie(\nabla_a\Phi)A^a - e^2\Phi A_aA^a - ie\Phi\nabla_aA^a - m_\Phi^2\Phi = 0 \ , \tag{4.50}$$

$$\nabla^a F_{ab} - ie(\Phi^*\nabla_b\Phi - \Phi\nabla_b\Phi^*) - 2e^2\Phi\Phi^*A_b = 0 \ . \tag{4.51}$$

where (4.49) and (4.50) are completely equivalent. I also choose the Lorentz gauge condition

$$\nabla_a A^a = 0 \ , \tag{4.52}$$

the conserved current is

$$-J^b \equiv \nabla_a F^{ab} = ie(\Phi^*\nabla^b\Phi - \Phi\nabla^b\Phi^*) + 2e^2\Phi\Phi^*A^b, \tag{4.53}$$

and the stress-energy tensor is once again

$$\begin{aligned} T_{ab} &= \frac{1}{2}\left(\nabla_a\Phi\nabla_b\Phi^* + \nabla_b\Phi\nabla_a\Phi^*\right) - \frac{1}{2}ie\left[\left(\Phi\nabla_b\Phi^* - \Phi^*\nabla_b\Phi\right)A_a + \left(\Phi\nabla_a\Phi^* - \Phi^*\nabla_a\Phi\right)A_b\right] \\ &+e^2\Phi\Phi^*A_aA_b + \frac{1}{2}F_{ac}F_{bd}g^{cd} - \frac{1}{2}g_{ab}[(\nabla_c\Phi - ieA_c\Phi)(\nabla^c\Phi^* + ieA^c\Phi^*) + \frac{1}{4}F^{cd}F_{cd} \\ &+m_\Phi^2\Phi^*\Phi] \ . \end{aligned} \tag{4.54}$$

4.2.3 Matter Equations in First-Order Form

Equation of motion (4.50) can be rewritten as

$$\nabla^a\left(\nabla_a\Phi - ieA_a\Phi\right) - ieA^a\left(\nabla_a\Phi - ieA_a\Phi\right) - m_\Phi^2\Phi = 0 \ . \tag{4.55}$$

Computing covariant derivatives with respect to metric (4.40), the equation of motion adopts a rather complicated form. I choose to rewrite (4.55) in terms of first-order temporal and spatial derivatives. To recast it in a more tractable form I first define field variables

$$\begin{aligned}
\Pi_\Phi(t,r,\theta) &\equiv n^a\sqrt{-g}\,(\nabla_a\Phi - ieA_a\Phi)\ , &(4.56)\\
\Phi_r(t,r,\theta) &\equiv \partial_r\Phi\ , &(4.57)\\
\Phi_\theta(t,r,\theta) &\equiv \partial_\theta\Phi\ , &(4.58)\\
A_{tr}(t,r,\theta) &\equiv \partial_r A_t\ , &(4.59)\\
A_{t\theta}(t,r,\theta) &\equiv \partial_\theta A_t\ , &(4.60)\\
A_{rr}(t,r,\theta) &\equiv \partial_r A_r\ , &(4.61)\\
A_{r\theta}(t,r,\theta) &\equiv \partial_\theta A_r\ , &(4.62)\\
A_{\theta r}(t,r,\theta) &\equiv \partial_r A_\theta\ , &(4.63)\\
A_{\theta\theta}(t,r,\theta) &\equiv \partial_\theta A_\theta\ , &(4.64)\\
A_{\phi r}(t,r,\theta) &\equiv \partial_r A_\phi\ , &(4.65)\\
A_{\phi\theta}(t,r,\theta) &\equiv \partial_\theta A_\phi\ , &(4.66)
\end{aligned}$$

and auxiliary metric functions

$$\begin{aligned}
f_{t\phi}(t,r,\theta) &\equiv \frac{g_{t\phi}}{\sin\theta}\ , &(4.67)\\
f_{\phi\phi}(t,r,\theta) &\equiv \frac{g_{\phi\phi}}{\sin\theta}\ , &(4.68)\\
e_{t\phi}(t,r,\theta) &\equiv \frac{g_{t\phi}}{\sin^2\theta}\ , &(4.69)\\
e_{\phi\phi}(t,r,\theta) &\equiv \frac{g_{\phi\phi}}{\sin^2\theta}\ , &(4.70)
\end{aligned}$$

where

$$g_{t\phi} = -\frac{2Mra\sin^2\theta}{\Sigma}\ , \tag{4.71}$$

$$g_{\phi\phi} = \sin^2\theta\left(r^2 + a^2 + \frac{2Mra^2\sin^2\theta}{\Sigma}\right)\ , \tag{4.72}$$

and

$$g = -\frac{\left(g_{tr}^2 g_{\phi\phi} - g_{t\phi}^2 g_{rr}\right)^2}{g_{tr}^4\sin^2\theta}\ . \tag{4.73}$$

Under these transformations equation of motion (4.55) becomes the set

$$
\begin{aligned}
\dot{\Pi}_\Phi \quad = \quad & e^2\left(-\frac{f_{\phi\phi}}{g_{rr}^{3/2}}A_r^2+2\frac{f_{t\phi}}{g_{tr}\sqrt{g_{rr}}}A_rA_\phi-\frac{\sin\theta}{\sqrt{g_{rr}}}A_\theta^2-\frac{1}{\sin\theta\sqrt{g_{rr}}}A_\phi^2\right)\Phi+ie\left[\left(\frac{\left(\partial_r g_{rr}\right)f_{\phi\phi}}{g_{rr}^{5/2}}A_r\right.\right.\\
& -\frac{\left(\partial_r f_{\phi\phi}\right)}{g_{rr}^{3/2}}A_r-\frac{f_{\phi\phi}}{g_{rr}^{3/2}}A_{rr}-\frac{\cos\theta}{\sqrt{g_{rr}}}A_\theta-\frac{\sin\theta}{\sqrt{g_{rr}}}A_{\theta\theta}-\frac{\left(\partial_r g_{tr}\right)f_{t\phi}}{\sqrt{g_{rr}}g_{tr}^2}A_\phi+\frac{\left(\partial_r f_{t\phi}\right)}{\sqrt{g_{rr}}g_{tr}}A_\phi\\
& \left.+\frac{f_{t\phi}}{\sqrt{g_{rr}}g_{tr}}A_{\phi r}\right)\Phi-\left(2\frac{f_{\phi\phi}}{g_{rr}^{3/2}}A_r-2\frac{f_{t\phi}}{\sqrt{g_{rr}}g_{tr}}A_\phi\right)\Phi_r-\left(2\frac{\sin\theta}{\sqrt{g_{rr}}}A_\theta\right)\Phi_\theta+\Big(A_t\cdot\\
& \left.\left.-\frac{g_{tr}}{g_{rr}}A_r\right)\Pi_\Phi\cdot\right]+m_\Phi^2\left(\frac{g_{t\phi}\sqrt{g_{rr}}f_{t\phi}}{g_{tr}^2}-\frac{f_{\phi\phi}}{\sqrt{g_{rr}}}\right)\Phi-\left(\frac{\left(\partial_r g_{rr}\right)f_{\phi\phi}}{g_{rr}^{5/2}}-\frac{\left(\partial_r f_{\phi\phi}\right)}{g_{rr}^{3/2}}\right)\Phi_r\\
& +\frac{f_{\phi\phi}}{g_{rr}^{3/2}}\left(\partial_r\Phi_r\right)+\frac{\cos\theta}{\sqrt{g_{rr}}}\Phi_\theta+\frac{\sin\theta}{\sqrt{g_{rr}}}\left(\partial_\theta\Phi_\theta\right)-\left(\frac{1}{2}\frac{g_{tr}\left(\partial_r g_{rr}\right)}{g_{rr}^2}-\frac{\left(\partial_r g_{tr}\right)}{g_{rr}}\right)\Pi_\Phi+\frac{g_{tr}}{g_{rr}}\left(\partial_r\Pi_\Phi\right)\ ,
\end{aligned}
\tag{4.74}
$$

$$\dot{\Phi}_r=\partial_r\left[ie\left(A_t-\frac{g_{tr}}{g_{rr}}A_r\right)\Phi+\frac{g_{tr}}{g_{rr}}\Phi_r+\frac{g_{tr}^2}{\sqrt{g_{rr}}\left(g_{tr}^2f_{\phi\phi}-g_{t\phi}f_{t\phi}g_{rr}\right)}\Pi_\Phi\right] \tag{4.75}$$

$$\dot{\Phi}_\theta=\partial_\theta\left[ie\left(A_t-\frac{g_{tr}}{g_{rr}}A_r\right)\Phi+\frac{g_{tr}}{g_{rr}}\Phi_r+\frac{g_{tr}^2}{\sqrt{g_{rr}}\left(g_{tr}^2f_{\phi\phi}-g_{t\phi}f_{t\phi}g_{rr}\right)}\Pi_\Phi\right] \tag{4.76}$$

$$\dot{\Phi}=ie\left(A_t-\frac{g_{tr}}{g_{rr}}A_r\right)\Phi+\frac{g_{tr}}{g_{rr}}\Phi_r+\frac{g_{tr}^2}{\sqrt{g_{rr}}\left(g_{tr}^2f_{\phi\phi}-g_{t\phi}f_{t\phi}g_{rr}\right)}\Pi_\Phi \tag{4.77}$$

where the overdot, $\dot{}$, again designates differentiation with respect to coordinate t.

I similarly choose to evolve the four-vector potential equations of motion (4.51) in first-order form. For this purpose I define auxiliary variables

$$\Pi_r(t,r,\theta) \quad\equiv\quad n^a\sqrt{-g}\left(\nabla_r A_a-\nabla_a A_r\right)\ , \tag{4.78}$$

$$\Pi_\theta(t,r,\theta) \quad\equiv\quad n^a\sqrt{-g}\left(\nabla_\theta A_a-\nabla_a A_\theta\right)\ , \tag{4.79}$$

$$\Pi_\phi(t,r,\theta) \quad\equiv\quad n^a\sqrt{-g}\left(\nabla_\phi A_a-\nabla_a A_\phi\right)\ , \tag{4.80}$$

under which (4.51) become

$$
\begin{aligned}
\dot{\Pi}_r \quad = \quad & -\frac{1}{\left(g_{tr}^2 e_{\phi\phi} - f_{t\phi}^2 g_{rr}\right)} \left(\frac{g_{tr}^2 \left(\partial_\theta g_{rr}\right) e_{\phi\phi} \sin\theta}{g_{rr}^{3/2}} - \frac{g_{tr}^2 e_{\phi\phi} \cos\theta}{\sqrt{g_{rr}}} + \frac{\left(\partial_\theta g_{tr}\right) f_{t\phi}^2 \sqrt{g_{rr}} \sin\theta}{g_{tr}} \right. \\
& \left. - \left(\partial_\theta g_{t\phi}\right) e_{t\phi} \sqrt{g_{rr}} \sin\theta - \frac{f_{t\phi}^2 \left(\partial_\theta g_{rr}\right) \sin\theta}{\sqrt{g_{rr}}} + f_{t\phi}^2 \sqrt{g_{rr}} \cos\theta \right) A_{r\theta} + \frac{\sin\theta}{\sqrt{g_{rr}}} \left(\partial_\theta A_{r\theta}\right) \\
& + \frac{1}{\left(g_{tr}^2 e_{\phi\phi} - f_{t\phi}^2 g_{rr}\right)} \left(\frac{g_{tr}^2 \left(\partial_\theta g_{rr}\right) e_{\phi\phi} \sin\theta}{g_{rr}^{3/2}} - \frac{g_{tr}^2 e_{\phi\phi} \cos\theta}{\sqrt{g_{rr}}} + \frac{\left(\partial_\theta g_{tr}\right) f_{t\phi}^2 \sqrt{g_{rr}} \sin\theta}{g_{tr}} \right. \\
& \left. - \frac{f_{t\phi}^2 \left(\partial_\theta g_{rr}\right) \sin\theta}{\sqrt{g_{rr}}} + f_{t\phi}^2 \sqrt{g_{rr}} \cos\theta - \left(\partial_\theta g_{t\phi}\right) e_{t\phi} \sqrt{g_{rr}} \sin\theta \right) A_{\theta r} - \frac{\sin\theta}{\sqrt{g_{rr}}} \left(\partial_\theta A_{\theta r}\right) \\
& - \frac{f_{t\phi} \left(\partial_r g_{rr}\right)}{g_{tr} g_{rr}^{3/2}} A_{\phi r} + \frac{f_{t\phi}}{g_{tr} \sqrt{g_{rr}}} \left(\partial_r A_{\phi r}\right) + \frac{\sqrt{g_{rr}}}{\left(g_{tr}^2 e_{\phi\phi} - f_{t\phi}^2 g_{rr}\right)} \left(g_{tr} \left(\partial_{\cos\theta} g_{t\phi}\right)\right. \\
& \left. - \left(\partial_{\cos\theta} g_{tr}\right) g_{t\phi}\right) A_{\phi\theta} - \frac{1}{\left(g_{tr}^2 e_{\phi\phi} - f_{t\phi}^2 g_{rr}\right)} \left(\frac{1}{2} \frac{g_{tr}^3 \left(\partial_t g_{rr}\right) e_{\phi\phi}}{g_{rr}^2} - \frac{3}{2} \frac{g_{tr} f_{t\phi}^2 \left(\partial_r g_{rr}\right)}{g_{rr}} \right. \\
& \left. - g_{tr} f_{t\phi} \left(\partial_r f_{t\phi}\right) + 2 \left(\partial_r g_{tr}\right) f_{t\phi}^2 \cdot \right) \Pi_r + \frac{g_{tr}}{g_{rr}} \left(\partial_r \Pi_r\right) + \frac{g_{tr}^2}{g_{rr} \left(g_{tr}^2 e_{\phi\phi} - f_{t\phi}^2 g_{rr}\right)} \left(g_{tr} \left(\partial_\theta g_{rr}\right)\right. \\
& \left. - \left(\partial_\theta g_{tr}\right) g_{rr}\right) \Pi_\theta - \frac{g_{tr}}{g_{rr} \left(g_{tr}^2 e_{\phi\phi} - f_{t\phi}^2 g_{rr}\right)} \left(g_{tr} e_{t\phi} \left(\partial_r g_{rr}\right) + g_{tr} \left(\partial_r e_{t\phi}\right) g_{rr}\right. \\
& \left. - 2 \left(\partial_r g_{tr}\right) e_{t\phi} g_{rr}\right) \Pi_\phi + \frac{\left(g_{tr}^2 f_{\phi\phi} - g_{t\phi} f_{t\phi} g_{rr}\right)}{g_{tr}^2 \sqrt{g_{rr}}} J_r \ ,
\end{aligned}
\tag{4.81}
$$

$$
\begin{aligned}
\dot{\Pi}_\theta \quad = \quad & -\frac{f_{\phi\phi}}{g_{rr}^{3/2}}\left(\partial_\theta A_{rr}\right)+\frac{1}{\left(g_{tr}^2 e_{\phi\phi}-f_{t\phi}^2 g_{rr}\right)}\left(\frac{g_{tr}^2\left(\partial_r g_{rr}\right) f_{\phi\phi} e_{\phi\phi}}{g_{rr}^{5/2}}+2\frac{\left(\partial_r g_{tr}\right) g_{t\phi} f_{t\phi} e_{\phi\phi}}{g_{tr}\sqrt{g_{rr}}}\right. \\
& \left.-2\frac{g_{t\phi} f_{t\phi}\left(\partial_r g_{rr}\right) e_{\phi\phi}}{g_{rr}^{3/2}}+\frac{g_{t\phi} f_{t\phi}\left(\partial_r e_{\phi\phi}\right)}{\sqrt{g_{rr}}}-\frac{2\left(\partial_r g_{t\phi}\right) f_{t\phi} e_{\phi\phi}}{\sqrt{g_{rr}}}\right) A_{r\theta} \\
& -\frac{1}{\left(g_{tr}^2 e_{\phi\phi}-f_{t\phi}^2 g_{rr}\right)}\left(\frac{g_{tr}^2\left(\partial_r g_{rr}\right) f_{\phi\phi} e_{\phi\phi}}{g_{rr}^{5/2}}+2\frac{\left(\partial_r g_{tr}\right) g_{t\phi} f_{t\phi} e_{\phi\phi}}{g_{tr}\sqrt{g_{rr}}}-2\frac{g_{t\phi} f_{t\phi}\left(\partial_r g_{rr}\right) e_{\phi\phi}}{g_{rr}^{3/2}}\right. \\
& \left.+\frac{f_{t\phi} e_{t\phi}\left(\partial_r g_{\phi\phi}\right)}{\sqrt{g_{rr}}}-2\frac{\left(\partial_r g_{t\phi}\right) f_{t\phi} e_{\phi\phi}}{\sqrt{g_{rr}}}\right) A_{\theta r}+\frac{f_{\phi\phi}}{g_{rr}^{3/2}}\left(\partial_r A_{\theta r}\right)+\frac{f_{t\phi}}{g_{tr}\sqrt{g_{rr}}}\left(\partial_\theta A_{\phi r}\right) \\
& -\frac{1}{\left(g_{tr}^2 e_{\phi\phi}-f_{t\phi}^2 g_{rr}\right)}\left(\frac{g_{tr} e_{t\phi}\left(\partial_r f_{\phi\phi}\right)}{\sqrt{g_{rr}}}-\frac{g_{tr}\left(\partial_r f_{t\phi}\right) e_{\phi\phi}}{\sqrt{g_{rr}}}+\frac{\left(\partial_r g_{tr}\right) f_{t\phi}^3\sqrt{g_{rr}}}{g_{tr}^2}\right. \\
& \left.+\frac{\left(\partial_r g_{tr}\right) f_{t\phi} e_{\phi\phi}}{\sqrt{g_{rr}}}-\frac{f_{t\phi}^3\left(\partial_r g_{rr}\right)}{g_{tr}\sqrt{g_{rr}}}-\frac{f_{t\phi}^2\left(\partial_r f_{t\phi}\right)\sqrt{g_{rr}}}{g_{tr}}\right) A_{\phi\theta} \\
& -\frac{1}{\left(g_{tr}^2 e_{\phi\phi}-f_{t\phi}^2 g_{rr}\right)}\left(\frac{1}{2}\frac{g_{tr}^3\left(\partial_r g_{rr}\right) e_{\phi\phi}}{g_{rr}^2}+\frac{g_{tr}^3\left(\partial_r e_{\phi\phi}\right)}{g_{rr}}-\frac{g_{tr}^2\left(\partial_r g_{tr}\right) e_{\phi\phi}}{g_{rr}}-\frac{3}{2}\frac{g_{tr} f_{t\phi}^2\left(\partial_r g_{rr}\right)}{g_{rr}}\right. \\
& \left.-2 g_{tr} f_{t\phi}\left(\partial_r f_{t\phi}\right)+3\left(\partial_r g_{tr}\right) f_{t\phi}^2\cdot\right)\Pi_\theta+\frac{g_{tr}}{g_{rr}}\left(\partial_r \Pi_\theta\right)+\frac{\left(g_{tr}^2 f_{\phi\phi}-g_{t\phi} f_{t\phi} g_{rr}\right)}{g_{tr}^2\sqrt{g_{rr}}} J_\theta\ , \qquad (4.82)
\end{aligned}
$$

$$\begin{aligned}
\dot{\Pi}_\phi &= -\frac{1}{\sqrt{g_{rr}}\left(g_{tr}^2 e_{\phi\phi} - f_{t\phi}^2 g_{rr}\right)}\left(\frac{g_{tr} g_{t\phi}\left(\partial_\theta g_{rr}\right) f_{\phi\phi}}{g_{rr}} - g_{tr} f_{t\phi}\left(\partial_\theta g_{\phi\phi}\right) + g_{tr}\left(\partial_\theta g_{t\phi}\right) f_{\phi\phi}\right. \\
&\left. - \left(\partial_\theta g_{tr}\right) g_{t\phi} f_{\phi\phi} \cdot\right) A_{r\theta} + \frac{1}{\sqrt{g_{rr}}\left(g_{tr}^2 e_{\phi\phi} - f_{t\phi}^2 g_{rr}\right)}\left(\frac{g_{tr} g_{t\phi}\left(\partial_\theta g_{rr}\right) f_{\phi\phi}}{g_{rr}} - g_{tr} f_{t\phi}\left(\partial_\theta g_{\phi\phi}\right)\right. \\
&\left. + g_{tr}\left(\partial_\theta g_{t\phi}\right) f_{\phi\phi} - \left(\partial_\theta g_{tr}\right) g_{t\phi} f_{\phi\phi} \cdot\right) A_{\theta r} - \frac{\left(\partial_r g_{rr}\right) f_{\phi\phi}}{g_{rr}^{5/2}} A_{\phi r} + \frac{f_{\phi\phi}}{g_{rr}^{3/2}}\left(\partial_r A_{\phi r}\right) \\
&+ \frac{1}{\left(g_{tr}^2 e_{\phi\phi} - f_{t\phi}^2 g_{rr}\right)}\left(\frac{g_{tr}^2 e_{\phi\phi}\cos\theta}{\sqrt{g_{rr}}} + \frac{g_{tr}^2\left(\partial_{\cos\theta} g_{\phi\phi}\right)}{\sqrt{g_{rr}}} - \frac{\left(\partial_\theta g_{tr}\right) f_{t\phi}^2 \sqrt{g_{rr}}\sin\theta}{g_{tr}}\right. \\
&\left. - f_{t\phi}^2\sqrt{g_{rr}}\cos\theta + \frac{f_{t\phi}^2\left(\partial_\theta g_{rr}\right)\sin\theta}{\sqrt{g_{rr}}} + \left(\partial_\theta g_{t\phi}\right) e_{t\phi}\sqrt{g_{rr}}\sin\theta\right) A_{\phi\theta} + \frac{\sin\theta}{\sqrt{g_{rr}}}\left(\partial_\theta A_{\phi\theta}\right) \\
&+ \frac{g_{tr}^2}{g_{rr}\left(g_{tr}^2 e_{\phi\phi} - f_{t\phi}^2 g_{rr}\right)}\left(e_{t\phi}\left(\partial_r g_{\phi\phi}\right) - \left(\partial_r g_{t\phi}\right) e_{\phi\phi}\right)\Pi_r \\
&+ \frac{g_{tr} g_{t\phi}}{g_{rr}\left(g_{tr}^2 e_{\phi\phi} - f_{t\phi}^2 g_{rr}\right)}\left(g_{tr}\left(\partial_\theta g_{rr}\right) - \left(\partial_\theta g_{tr}\right) g_{rr}\right)\Pi_\theta \\
&+ \frac{1}{\left(-g_{tr}^2 e_{\phi\phi} + f_{t\phi}^2 g_{rr}\right)}\left(\frac{1}{2}\frac{g_{tr}^3\left(\partial_r g_{rr}\right) e_{\phi\phi}}{g_{rr}^2} + \frac{g_{tr}^3\left(\partial_r e_{\phi\phi}\right)}{g_{rr}} - \frac{g_{tr}^2\left(\partial_r g_{tr}\right) e_{\phi\phi}}{g_{rr}}\right. \\
&\left. - \frac{1}{2}\frac{g_{tr} f_{t\phi}^2\left(\partial_r g_{rr}\right)}{g_{rr}} - g_{tr}\left(\partial_r g_{t\phi}\right) + \left(\partial_r g_{tr}\right) f_{t\phi}^2\right)\Pi_\phi + \frac{g_{tr}}{g_{rr}}\left(\partial_r \Pi_\phi\right) \\
&+ \frac{\left(g_{tr}^2 f_{\phi\phi} - g_{t\phi} f_{t\phi} g_{rr}\right)}{g_{tr}^2\sqrt{g_{rr}}} J_\phi \ , \qquad (4.83)
\end{aligned}$$

$$\dot{A}_{rr} = \partial_r\left[A_{tr} + \frac{g_{tr}^2}{\sqrt{g_{rr}}\,(g_{tr}^2 f_{\phi\phi} - g_{t\phi} f_{t\phi} g_{rr})}\Pi_r\right] \ , \qquad (4.84)$$

$$\dot{A}_{\theta r} = \partial_r\left[A_{t\theta} - \frac{g_{tr}}{g_{rr}}A_{r\theta} + \frac{g_{tr}}{g_{rr}}A_{\theta r} + \frac{g_{tr}^2}{\sqrt{g_{rr}}\,(g_{tr}^2 f_{\phi\phi} - g_{t\phi} f_{t\phi} g_{rr})}\Pi_\theta\right] \ , \qquad (4.85)$$

$$\dot{A}_{\phi r} = \partial_r\left[\frac{g_{tr}}{g_{rr}}A_{\phi r} + \frac{g_{tr}^2}{\sqrt{g_{rr}}\,(g_{tr}^2 f_{\phi\phi} - g_{t\phi} f_{t\phi} g_{rr})}\Pi_\phi\right] \ , \qquad (4.86)$$

$$\dot{A}_{r\theta} = \partial_\theta\left[A_{tr} + \frac{g_{tr}^2}{\sqrt{g_{rr}}\,(g_{tr}^2 f_{\phi\phi} - g_{t\phi} f_{t\phi} g_{rr})}\Pi_r\right] \ , \qquad (4.87)$$

$$\dot{A}_{\theta\theta} = \partial_\theta\left[A_{t\theta} - \frac{g_{tr}}{g_{rr}}A_{r\theta} + \frac{g_{tr}}{g_{rr}}A_{\theta r} + \frac{g_{tr}^2}{\sqrt{g_{rr}}\,(g_{tr}^2 f_{\phi\phi} - g_{t\phi} f_{t\phi} g_{rr})}\Pi_\theta\right] \ , \qquad (4.88)$$

$$\dot{A}_{\phi\theta} = \partial_\theta\left[\frac{g_{tr}}{g_{rr}}A_{\phi r} + \frac{g_{tr}^2}{\sqrt{g_{rr}}\,(g_{tr}^2 f_{\phi\phi} - g_{t\phi} f_{t\phi} g_{rr})}\Pi_\phi\right] \ , \qquad (4.89)$$

$$\dot{A}_r = A_{tr} + \frac{g_{tr}^2}{\sqrt{g_{rr}}\left(g_{tr}^2 f_{\phi\phi} - g_{t\phi} f_{t\phi} g_{rr}\right)} \Pi_r \ , \tag{4.90}$$

$$\dot{A}_\theta = A_{t\theta} - \frac{g_{tr}}{g_{rr}} A_{r\theta} + \frac{g_{tr}}{g_{rr}} A_{\theta r} + \frac{g_{tr}^2}{\sqrt{g_{rr}}\left(g_{tr}^2 f_{\phi\phi} - g_{t\phi} f_{t\phi} g_{rr}\right)} \Pi_\theta \ , \tag{4.91}$$

$$\dot{A}_\phi = \frac{g_{tr}}{g_{rr}} A_{\phi r} + \frac{g_{tr}^2}{\sqrt{g_{rr}}\left(g_{tr}^2 f_{\phi\phi} - g_{t\phi} f_{t\phi} g_{rr}\right)} \Pi_\phi \ , \tag{4.92}$$

where from (4.53)

$$J_r = -ie(\Phi^*\Phi_r - \Phi\Phi_r^*) - 2e^2\Phi\Phi^* A_r \ , \tag{4.93}$$

$$J_\theta = -ie(\Phi^*\Phi_\theta - \Phi\Phi_\theta^*) - 2e^2\Phi\Phi^* A_\theta \ , \tag{4.94}$$

$$J_\phi = -2e^2\Phi\Phi^* A_\phi \ , \tag{4.95}$$

and I have used the chain rule to rewrite some partial derivatives with respect to θ.[4] Finally, the Lorentz gauge condition (which evolves component A_t) is already in the first order form

$$\begin{aligned}
\dot{A}_t = & \frac{1}{\left(g_{tr}^2 e_{\phi\phi} - f_{t\phi}^2 g_{rr}\right)} \left(\frac{g_{tr}^3 \left(\partial_r e_{\phi\phi}\right)}{g_{rr}} + \frac{g_{tr}^2 \left(\partial_r g_{tr}\right) e_{\phi\phi}}{g_{rr}} - \frac{g_{tr} f_{t\phi}^2 \left(\partial_r g_{rr}\right)}{g_{rr}} - 2 g_{tr} \left(\partial_r g_{t\phi}\right) e_{t\phi} \right. \\
& \left. + \left(\partial_r g_{tr}\right) f_{t\phi}^2 \cdot \right) A_t + 2 \frac{g_{tr}}{g_{rr}} A_{tr} + \frac{1}{\left(g_{tr}^2 e_{\phi\phi} - f_{t\phi}^2 g_{rr}\right)} \left(\frac{g_{tr}^4 \left(\partial_r g_{rr}\right) e_{\phi\phi}}{g_{rr}^3} - \frac{g_{tr}^4 \left(\partial_r e_{\phi\phi}\right)}{g_{rr}^2} \right. \\
& \left. - 2 \frac{g_{tr}^3 \left(\partial_r g_{tr}\right) e_{\phi\phi}}{g_{rr}^2} + 2 \frac{g_{tr}^2 \left(\partial_r g_{t\phi}\right) e_{t\phi}}{g_{rr}} - \frac{g_{tr}^2 \left(\partial_r g_{rr}\right) e_{\phi\phi}}{g_{rr}^3} + \frac{g_{tr}^2 \left(\partial_r e_{\phi\phi}\right)}{g_{rr}^2} \right) A_r \\
& - \frac{g_{tr}^2}{g_{rr}^2 \left(g_{tr}^2 e_{\phi\phi} - f_{t\phi}^2 g_{rr}\right)} \left(g_{tr}^2 e_{\phi\phi} - f_{t\phi}^2 g_{rr} - e_{\phi\phi}\right) A_{rr} - \frac{g_{tr}^2 \left(\partial_{\cos\theta} \sin\theta\right)}{g_{rr} \left(g_{tr}^2 e_{\phi\phi} - f_{t\phi}^2 g_{rr}\right)} A_\theta \\
& + \frac{g_{tr}^2}{g_{rr} \left(g_{tr}^2 e_{\phi\phi} - f_{t\phi}^2 g_{rr}\right)} A_{\theta\theta} - \frac{1}{g_{rr} \left(g_{tr}^2 e_{\phi\phi} - f_{t\phi}^2 g_{rr}\right)} \left(g_{tr} \left(\partial_r e_{t\phi}\right) - \left(\partial_r g_{tr}\right) e_{t\phi}\right) A_\phi \\
& - \frac{g_{tr} e_{t\phi}}{g_{rr} \left(g_{tr}^2 e_{\phi\phi} - f_{t\phi}^2 g_{rr}\right)} A_{\phi r} + \frac{g_{tr}^3}{g_{rr}^{3/2} \left(g_{tr}^2 f_{\phi\phi} - g_{t\phi} f_{t\phi} g_{rr}\right)} \Pi_r \ .
\end{aligned} \tag{4.98}$$

4.2.4 Physical and Conserved Quantities

In axial symmetry, none of the components E_a or B_a generically vanish.[5] This differs from the spherically symmetric case presented in Chapter 3 where E_r was the only nonzero component. Explicitly, using definitions

$$E_a = F_{ab} n^b \tag{4.99}$$

[4]Applying the chain rule

$$\frac{\partial f}{\partial \theta} = \frac{\partial \cos\theta}{\partial \theta} \frac{\partial f}{\partial \cos\theta} = -\sin\theta \frac{\partial f}{\partial \cos\theta} \tag{4.96}$$

transforms numerically unsuitable forms at $\theta = 0$ or $\theta = \pi$ such as

$$\frac{1}{\sin\theta} \frac{\partial f}{\partial \theta} = -\frac{\partial f}{\partial \cos\theta}. \tag{4.97}$$

[5]Regularity will, however, require E_θ, E_ϕ, B_θ and B_ϕ to vanish on the axis of symmetry (i.e., along $\theta = 0$ and $\theta = \pi$).

and

$$B_a = -\frac{1}{2}\epsilon_{ab}{}^{cd}F_{cd}n^b \tag{4.100}$$

for an observer with four-velocity n^a,

$$E_r = -\frac{g_{tr}^2}{(g_{tr}^2 f_{\phi\phi} - g_{t\phi}f_{t\phi}g_{rr})}\Pi_r \ , \tag{4.101}$$

$$E_\theta = -\frac{g_{tr}^2}{(g_{tr}^2 f_{\phi\phi} - g_{t\phi}f_{t\phi}g_{rr})}\Pi_\theta \ , \tag{4.102}$$

$$E_\phi = -\frac{g_{tr}^2}{(g_{tr}^2 f_{\phi\phi} - g_{t\phi}f_{t\phi}g_{rr})}\Pi_\phi \ , \tag{4.103}$$

$$B_r = \frac{g_{tr}\sqrt{g_{rr}}}{\left(g_{tr}^2 e_{\phi\phi} - f_{t\phi}^2 g_{rr}\right)}\left(g_{tr}\left(\partial_{\cos\theta}A_\phi\right) + f_{t\phi}A_{r\theta} - f_{t\phi}A_{\theta r}\right) \ , \tag{4.104}$$

$$B_\theta = -\frac{1}{\sqrt{g_{rr}}\sin\theta}A_{\phi r} \ , \tag{4.105}$$

and

$$B_\phi = \frac{g_{tr}}{\sqrt{g_{rr}}\left(g_{tr}^2 e_{\phi\phi} - f_{t\phi}^2 g_{rr}\right)}\left(g_{tr}f_{\phi\phi}A_{r\theta} - g_{tr}f_{\phi\phi}A_{\theta r} - f_{t\phi}g_{rr}A_{\phi\theta}\right) \ . \tag{4.106}$$

Meanwhile, the temporal component of the current four-vector is

$$J_t = -ie\frac{g_{tr}}{g_{rr}}\left(\Phi^*\Phi_r - \Phi\Phi_r^*\right) - ie\frac{g_{tr}^2}{\sqrt{g_{rr}}\left(g_{tr}^2 f_{\phi\phi} - g_{t\phi}f_{t\phi}g_{rr}\right)}\left(\Phi^*\Pi_\Phi - \Phi\Pi_\Phi^*\right) - 2e^2\frac{g_{tr}}{g_{rr}}\Phi\Phi^*A_r \ , \tag{4.107}$$

and the conserved electric charge density can be expressed

$$\rho_Q = ie\frac{g_{tr}^2}{\left(g_{tr}^2 f_{\phi\phi} - g_{t\phi}f_{t\phi}g_{rr}\right)}\left(\Phi^*\Pi_\Phi - \Phi\Pi_\Phi^*\right) \ . \tag{4.108}$$

Contracting the stress-energy tensor T_{ab} of (4.54) with n^a from (4.44) and $t^a = (1,0,0,0)$ obtains a conserved energy density,

$$\rho_T = \rho_{T(\Phi)} + \rho_{T(A)} + \rho_{T(\Phi A)} \ , \tag{4.109}$$

where $\rho_{T(\Phi)}$ is the contribution from the scalar field terms of T_{ab}, $\rho_{T(A)}$ is the contribution from electromagnetic field variable terms, and $\rho_{T(\Phi A)}$ is the contribution from terms involving the interaction of Φ and A_a through coupling constant e.[6] In detail,

$$\begin{aligned}
\rho_{T(\Phi)} &= e^2\left(\frac{1}{2}\sqrt{g_{rr}}A_t^2 - \frac{g_{tr}}{\sqrt{g_{rr}}}A_tA_r + \frac{1}{2}\frac{g_{tr}^2}{g_{rr}^{3/2}}A_r^2\right)\Phi\Phi^* + \frac{ie}{2}\left[\left(\frac{g_{tr}}{\sqrt{g_{rr}}}A_t - \frac{g_{tr}^2}{g_{rr}^{3/2}}A_r\right)(\Phi\Phi_r^*\right. \\
&\quad -\Phi^*\Phi_r) + \left.\left(\frac{g_{tr}^2}{(g_{tr}^2 f_{\phi\phi} - g_{t\phi}f_{t\phi}g_{rr})}A_t - \frac{g_{tr}^3}{g_{rr}(g_{tr}^2 f_{\phi\phi} - g_{t\phi}f_{t\phi}g_{rr})}A_r\right)(\Phi\Pi_\Phi^* - \Phi^*\Pi_\Phi)\cdot\right] \\
&\quad +\frac{m_\Phi^2}{2}\frac{1}{\sqrt{g_{rr}}}\Phi\Phi^* + \frac{1}{2}\frac{g_{tr}^2 e_{\phi\phi}}{g_{rr}^{3/2}(g_{tr}^2 e_{\phi\phi} - f_{t\phi}^2 g_{rr})}\Phi_r\Phi_r^* + \frac{1}{2}\frac{g_{tr}^2}{\sqrt{g_{rr}}(g_{tr}^2 e_{\phi\phi} - f_{t\phi}^2 g_{rr})}\Phi_\theta\Phi_\theta^* \\
&\quad +\frac{1}{2}\frac{g_{tr}^3}{g_{rr}(g_{tr}^2 f_{\phi\phi} - g_{t\phi}f_{t\phi}g_{rr})}(\Phi_r\Pi_\Phi^* + \Phi_r^*\Pi_\Phi) + \frac{1}{2}\frac{g_{tr}^4}{\sqrt{g_{rr}}(g_{tr}^2 f_{\phi\phi} - g_{t\phi}f_{t\phi}g_{rr})^2}\Pi_\Phi\Pi_\Phi^*\ ,
\end{aligned} \tag{4.111}$$

[6] Before substituting auxiliary variables, $\rho_{T(\Phi)}$ has the form

$$\begin{aligned}
\rho_{T(\Phi)} &= \frac{m_\Phi^2}{2}\frac{1}{(g_{tr}^2 g_{\phi\phi} - g_{t\phi}^2 g_{rr})}\left(\frac{g_{tr}^2 g_{\phi\phi}}{\sqrt{g_{rr}}} - g_{t\phi}^2\sqrt{g_{rr}}\right)\Phi\Phi^* + \frac{1}{2}\frac{\sqrt{g_{rr}}}{(g_{tr}^2 g_{\phi\phi} - g_{t\phi}^2 g_{rr})}\left(g_{tr}^2 g_{\phi\phi} - g_{t\phi}^2 g_{rr}\right)\dot{\Phi}\dot{\Phi}^* \\
&\quad -\frac{1}{2}\frac{g_{tr}^2}{(g_{tr}^2 g_{\phi\phi} - g_{t\phi}^2 g_{rr})}\left(\frac{g_{tr}^2 g_{\phi\phi}}{g_{rr}^{3/2}} - \frac{g_{\phi\phi}}{g_{rr}^{3/2}} - \frac{g_{t\phi}^2}{\sqrt{g_{rr}}}\right)\Phi_r\Phi_r^* + \frac{1}{2}\frac{g_{tr}^2\sin^2\theta}{\sqrt{g_{rr}}(g_{tr}^2 g_{\phi\phi} - g_{t\phi}^2 g_{rr})}\Phi_\theta\Phi_\theta^*\ .
\end{aligned} \tag{4.110}$$

$$
\begin{aligned}
\rho_{T(A)} \;=\;& \frac{1}{4}\frac{g_{tr}^4 e_{\phi\phi}}{g_{rr}^{3/2}(g_{tr}^2 e_{\phi\phi}-f_{t\phi}^2 g_{rr})^2}A_{r\theta}^2 - \frac{1}{2}\frac{g_{tr}^4 e_{\phi\phi}}{g_{rr}^{3/2}(g_{tr}^2 e_{\phi\phi}-f_{t\phi}^2 g_{rr})^2}A_{r\theta}A_{\theta r}\\
&-\frac{1}{2}\frac{g_{tr}^3 e_{t\phi}}{\sqrt{g_{rr}}(g_{tr}^2 e_{\phi\phi}-f_{t\phi}^2 g_{rr})^2}A_{r\theta}A_{\phi\theta} + \frac{1}{4}\frac{g_{tr}^4 e_{\phi\phi}}{g_{rr}^{3/2}(g_{tr}^2 e_{\phi\phi}-f_{t\phi}^2 g_{rr})^2}A_{\theta r}^2\\
&+\frac{1}{2}\frac{g_{tr}^3 e_{t\phi}}{\sqrt{g_{rr}}(g_{tr}^2 e_{\phi\phi}-f_{t\phi}^2 g_{rr})^2}A_{\theta r}A_{\phi\theta} - \frac{1}{4}\frac{g_{tr}^2}{g_{rr}^{3/2}(g_{tr}^2 g_{\phi\phi}-g_{t\phi}^2 g_{rr})}A_{\phi r}^2\\
&+\frac{1}{4}\frac{g_{tr}^4}{\sqrt{g_{rr}}(g_{tr}^2 e_{\phi\phi}-f_{t\phi}^2 g_{rr})^2}\left(\partial_{\cos\theta}A_\phi\right)^2 + \frac{1}{2}\frac{g_{tr}^5}{g_{rr}(g_{tr}^2 e_{\phi\phi}-f_{t\phi}^2 g_{rr})^2}\left(\partial_{\cos\theta}A_r\right)\Pi_\theta\\
&+\frac{1}{2}\frac{g_{tr}^5}{g_{rr}(g_{tr}^2 f_{\phi\phi}-g_{t\phi}f_{t\phi}g_{rr})(g_{tr}^2 e_{\phi\phi}-f_{t\phi}^2 g_{rr})}A_{\theta r}\Pi_\theta\\
&-\frac{1}{2}\frac{g_{tr}^4 e_{t\phi}}{g_{rr}(g_{tr}^2 f_{\phi\phi}-g_{t\phi}f_{t\phi}g_{rr})(g_{tr}^2 e_{\phi\phi}-f_{t\phi}^2 g_{rr})}A_{\phi r}\Pi_r\\
&+\frac{1}{2}\frac{g_{tr}^5}{g_{rr}(g_{tr}^2 g_{\phi\phi}-g_{t\phi}^2 g_{rr})(g_{tr}^2 f_{\phi\phi}-g_{t\phi}f_{t\phi}g_{rr})}A_{\phi r}\Pi_\phi\\
&+\frac{1}{4}\frac{g_{tr}^6 e_{\phi\phi}}{g_{rr}^{3/2}(g_{tr}^2 f_{\phi\phi}-g_{t\phi}f_{t\phi}g_{rr})^2(g_{tr}^2 e_{\phi\phi}-f_{t\phi}^2 g_{rr})}\Pi_r^2\\
&-\frac{1}{2}\frac{g_{tr}^5 e_{t\phi}}{\sqrt{g_{rr}}(g_{tr}^2 f_{\phi\phi}-g_{t\phi}f_{t\phi}g_{rr})^2(g_{tr}^2 e_{\phi\phi}-f_{t\phi}^2 g_{rr})}\Pi_r\Pi_\phi\\
&+\frac{1}{4}\frac{g_{tr}^6}{\sqrt{g_{rr}}(g_{tr}^2 f_{\phi\phi}-g_{t\phi}f_{t\phi}g_{rr})^2(g_{tr}^2 e_{\phi\phi}-f_{t\phi}^2 g_{rr})}\Pi_\theta^2\\
&+\frac{1}{4}\frac{g_{tr}^6}{\sqrt{g_{rr}}(g_{tr}^2 g_{\phi\phi}-g_{t\phi}^2 g_{rr})(g_{tr}^2 f_{\phi\phi}-g_{t\phi}f_{t\phi}g_{rr})^2}\Pi_\phi^2\ ,
\end{aligned}
\tag{4.112}
$$

$$
\begin{aligned}
\rho_{T(\Phi A)} \;=\;& e^2\left[\frac{1}{2}\frac{g_{tr}^2}{g_{rr}^{3/2}}\left(\frac{e_{\phi\phi}}{(g_{tr}^2 e_{\phi\phi}-f_{t\phi}^2 g_{rr})}-1\right)A_r^2 - \frac{g_{tr}e_{t\phi}}{\sqrt{g_{rr}}(g_{tr}^2 e_{\phi\phi}-f_{t\phi}^2 g_{rr})}A_rA_\phi + \frac{g_{tr}}{\sqrt{g_{rr}}}A_rA_t\right.\\
&\left.+\ \frac{1}{2}\frac{g_{tr}^2}{\sqrt{g_{rr}}(g_{tr}^2 e_{\phi\phi}-f_{t\phi}^2 g_{rr})}A_\theta^2 + \frac{1}{2}\frac{g_{tr}^2}{\sqrt{g_{rr}}(g_{tr}^2 g_{\phi\phi}-g_{t\phi}^2 g_{rr})}A_\phi^2 - \frac{1}{2}\sqrt{g_{rr}}A_t^2\right]\Phi\Phi^*\\
&-\frac{ie}{2}\left\{\left[\frac{g_{tr}^2}{g_{rr}^{3/2}}\left(\frac{e_{\phi\phi}}{(g_{tr}^2 e_{\phi\phi}-f_{t\phi}^2 g_{rr})}-1\right)A_r - \frac{g_{tr}e_{t\phi}}{\sqrt{g_{rr}}(g_{tr}^2 e_{\phi\phi}-f_{t\phi}^2 g_{rr})}A_\phi\right.\right.\\
&\left.+\ \frac{g_{tr}}{\sqrt{g_{rr}}}A_t\right](\Phi\Phi_r^*-\Phi^*\Phi_r) + \frac{g_{tr}^2}{\sqrt{g_{rr}}(g_{tr}^2 e_{\phi\phi}-f_{t\phi}^2 g_{rr})}A_\theta(\Phi\Phi_\theta^*-\Phi^*\Phi_\theta)\\
&\left.+\ \frac{g_{tr}^2}{(g_{tr}^2 f_{\phi\phi}-g_{t\phi}f_{t\phi}g_{rr})}A_t(\Phi\Pi_\Phi^*-\Phi^*\Pi_\Phi)\right\}\ .
\end{aligned}
\tag{4.113}
$$

Similarly, contracting T_{ab} with n^a and $s^a = (0,0,0,1)$ yields the conserved angular momentum density

$$\rho_S = \rho_{S(A)} + \rho_{S(\Phi A)}\ , \tag{4.114}$$

where

$$\begin{aligned}\rho_{S(A)} &= \frac{1}{2}\frac{g_{tr}^4 f_{\phi\phi}}{g_{rr}(g_{tr}^2 f_{\phi\phi} - g_{t\phi}f_{t\phi}g_{rr})^2}A_{\phi r}\Pi_r \\ &- \frac{1}{2}\frac{g_{tr}^3 f_{t\phi}}{(g_{tr}^2 f_{\phi\phi} - g_{t\phi}f_{t\phi}g_{rr})^2}A_{\phi r}\Pi_\phi \\ &+ \frac{1}{2}\frac{g_{tr}^4 \sin\theta}{(g_{tr}^2 f_{\phi\phi} - g_{t\phi}f_{t\phi}g_{rr})^2}A_{\phi\theta}\Pi_\theta\end{aligned} \tag{4.115}$$

is the electromagnetic field contribution, and

$$\rho_{S(\Phi A)} = \frac{ie}{2}\frac{g_{tr}^2}{(g_{tr}^2 f_{\phi\phi} - g_{t\phi}f_{t\phi}g_{rr})}A_\phi(\Phi\Pi_\Phi^* - \Phi^*\Pi_\Phi) \tag{4.116}$$

is from the coupling of scalar and electromagnetic fields. Then, from (2.104), the total charge

$$Q = \int_{\phi=0}^{2\pi}\int_{\theta=0}^{\pi}\int_{r=0}^{\infty}\rho_Q\frac{\sqrt{g_{rr}}\left(g_{tr}^2 f_{\phi\phi} - g_{t\phi}f_{t\phi}g_{rr}\right)}{g_{tr}^2}drd\theta d\phi\ , \tag{4.117}$$

from (2.108), the total energy

$$T = \int_{\phi=0}^{2\pi}\int_{\theta=0}^{\pi}\int_{r=0}^{\infty}\rho_T\frac{\sqrt{g_{rr}}\left(g_{tr}^2 f_{\phi\phi} - g_{t\phi}f_{t\phi}g_{rr}\right)}{g_{tr}^2}drd\theta d\phi \tag{4.118}$$

and, from (2.109), the total angular momentum

$$S = \int_{\phi=0}^{2\pi}\int_{\theta=0}^{\pi}\int_{r=0}^{\infty}\rho_S\frac{\sqrt{g_{rr}}\left(g_{tr}^2 f_{\phi\phi} - g_{t\phi}f_{t\phi}g_{rr}\right)}{g_{tr}^2}drd\theta d\phi \tag{4.119}$$

will all be constant, providing t^a is timelike everywhere the densities ρ_Q, ρ_T and ρ_S are non-zero.

4.2.5 Regularity, Boundary Conditions and Dissipation

From the definitions of section 2.4 (cf. [6], [45]), regularity for the functions listed above requires Φ, Φ_r, A_r, A_{rr}, J_r, $A_{\theta\theta}$, Π_θ, A_ϕ, $A_{\phi r}$, J_ϕ, A_t, A_{tr}, E_r, E_ϕ, B_r, B_ϕ, J_t, ρ_Q, ρ_T and ρ_S be, to leading order, even in θ on axis (i.e., at $\theta = 0$ and $\theta = \pi$). In addition to being even, Π_θ, A_ϕ, $A_{\phi r}$, J_ϕ, E_ϕ and B_ϕ must also vanish along the axis of symmetry (i.e., they are at least quadratic in θ on axis). Meanwhile, remaining variables Φ_θ, Π_Φ, $A_{r\theta}$, Π_r, A_θ, $A_{\theta r}$, J_θ, $A_{\phi\theta}$, Π_ϕ, $A_{t\theta}$, E_θ and B_θ are, to leading order, odd. For the leading-order-even variables I enforce regularity on grid points corresponding to $\theta = 0$ and $\theta = \pi$ by applying a quadratic fix as listed in Appendix C. I also apply interpolation in the direction of θ on the next-to-axis points for these variables using a 3rd order Lagrange interpolant as discussed in Appendix C. Numerical testing shows the additional interpolation helps ensure smooth and stable evolution along the axis of symmetry. Variables Π_θ, A_ϕ, $A_{\phi r}$, J_ϕ, E_ϕ and B_ϕ are exceptional cases. I enforce regularity by setting them equal to zero on the axis and imposing a quadratic fix on the next-to-axis points. Meanwhile, regularity of the leading-order-odd variables is enforced by setting the functions equal to zero at the degenerate point. As with the leading-order-even variables, interpolation is applied next-to-axis.

Because their counterparts in the massless electromagnetically uncoupled (i.e., $e = 0$) theory can be expressed as wave equations, I apply the (approximate) Sommerfeld outgoing radiation condition to Φ, A_r, A_θ, A_ϕ and A_t. As discussed in Chapter 2, the condition can here be written

$$\partial_t(ru) + \left(\frac{-2Mr/\Sigma + 1}{1 + 2Mr/\Sigma}\right) \partial_r(ru) = 0 \ , \tag{4.120}$$

where $u = u(t, r, \theta)$ are one of Φ, A_r, A_θ, A_ϕ or A_t. The condition is applied on the outermost grid points (i.e., at the points corresponding to the largest value of radial coordinate $r = r_{\max}$) with the exception of those lying on the axis of symmetry ($\theta = 0$ or $\theta = \pi$) and those next-to-axis (i.e., at $\theta = \Delta\theta$ or $\theta = \pi - \Delta\theta$). Therefore, a backwards spatial differencing operator is used to implement ∂_r. The Sommerfeld condition for Φ provides an algebraic equation for boundary values of Π_Φ as well. Fields E_r, E_θ and E_ϕ can similarly be rewritten as a set of wave equations. Sommerfeld conditions for the electric field components provide outer boundary conditions for Π_r, Π_θ and Π_ϕ, which are again applied at all points $r = r_{\max}$ except those on axis or next-to-axis. Backwards difference operators are similarly used at $r = r_{\max}$ for Φ_r, A_{rr}, $A_{\theta r}$, $A_{\phi r}$ and A_{tr}, while Φ_θ, $A_{r\theta}$, J_r, $A_{\theta\theta}$, J_θ, $A_{\phi\theta}$, J_ϕ, $A_{t\theta}$, E_r, E_θ, E_ϕ, B_r, B_θ, B_ϕ, J_t, ρ_Q, ρ_T and ρ_S require no special treatment.

I avoid both the Cauchy horizon at $r = r_-$ and ring singularity at $r = a\cos\theta$ by excising grid points within a surface of constant $r = r_{\text{ex}}$, $r_- < r_{\text{ex}} < r_+$, from the computational domain. I have found that numerical evolution is stable and smooth if I apply a mixture of extrapolation (in coordinate r) and interpolation (in θ) to the time-dependent grid functions $u(t, r, \theta)$. Formally, I use the linear combination

$$u(t + \Delta t, r, \theta) = \frac{\Delta\theta}{\Delta r + \Delta\theta}\left(P_{2,r}^{t+\Delta t}\right) + \frac{\Delta r}{\Delta r + \Delta\theta}\left(P_{3,\theta}^{t+\Delta t}\right) \ , \tag{4.121}$$

where

$$P_{2,r}^{t+\Delta t} = 3u(t + \Delta t, r + \Delta r, \theta) - 3u(t + \Delta t, r + 2\Delta r, \theta) + u(t + \Delta t, r + 3\Delta r, \theta) \tag{4.122}$$

is the 2nd order extrapolating polynomial in r,

$$P_{3,\theta}^{t+\Delta t} = -\frac{1}{6}u(t+\Delta t, r, \theta-2\Delta\theta)+\frac{2}{3}u(t+\Delta t, r, \theta-\Delta\theta)+\frac{2}{3}u(t+\Delta t, r, \theta+\Delta\theta)-\frac{1}{6}u(t+\Delta t, r, \theta+2\Delta\theta) \tag{4.123}$$

is the 3rd order Lagrange interpolating polynomial in θ, Δt designating the interval in coordinate t, Δr the interval in r and Δ the interval in θ. Factors

$$\frac{\Delta\theta}{\Delta r + \Delta\theta} \ , \tag{4.124}$$

and

$$\frac{\Delta r}{\Delta r + \Delta\theta} \tag{4.125}$$

provide weights adjusted to differences in intervals $\Delta\theta$ and Δr. This weighted combination of interpolation and extrapolation is applied at all points $r = r_{\text{ex}}$ which are neither on axis nor next-to-axis.

I employ Kreiss-Oliger dissipation as outlined and summarized in Appendix C. Dissipation is added to all equations of motion explicitly involving partial derivatives with respect to t. This set of functions is Φ, Φ_r, Φ_θ, Π_Φ, A_r, A_{rr}, $A_{r\theta}$, Π_r, A_θ, $A_{\theta r}$, $A_{\theta\theta}$, Π_θ, A_ϕ, $A_{\phi r}$, $A_{\phi\theta}$, Π_ϕ and A_t. The Kreiss-Oliger dissipation operators have stencils five points wide. For coordinate r they can then be applied only at locations two grid points from the boundaries $r = r_{\text{ex}}$ and $r = r_{\max}$. Similarly, dissipation in coordinate θ can be applied only when, at minimum, two grid points away from boundaries $\theta = 0$ and $\theta = \pi$. Therefore, dissipation in both r and θ is applied only in the bulk of the computational domain—where $r_{\text{ex}} + 2\Delta r \le r \le r_{\max} - 2\Delta r$ and $2\Delta\theta \le \theta \le \pi - 2\Delta\theta$—while dissipation in θ alone is applied at $r = r_{\text{ex}} + \Delta r$ and $r \ge r_{\max} - \Delta r$. Formally, if $u = u(t, r, \theta)$

is one of the functions whose equation contains an explicit derivative in time, then, using the Crank-Nicholson scheme without dissipation, its expression will be

$$\frac{u(t+\Delta t,r,\theta)-u(t,r,\theta)}{\Delta t}=\frac{1}{2}\left[R(t+\Delta t,r,\theta)+R(t,r,\theta)\right] \ , \tag{4.126}$$

where the left hand side is—to $\mathcal{O}\left((\Delta t)^2\right)$ accuracy—the time derivative of u centered between times t and $t+\Delta t$, and the right hand side represents—to $\mathcal{O}\left((\Delta r)^2\right)$ and $\mathcal{O}\left((\Delta \theta)^2\right)$—all other terms in the equation time averaged between steps t and $t+\Delta t$. Then, Kreiss-Oliger dissipation is implemented by adding specific terms on the right hand side of equation (4.126). In this case,

$$\begin{aligned}\frac{u(t+\Delta t,r,\theta)-u(t,r,\theta)}{\Delta t} &= \frac{1}{2}\left[R(t+\Delta t,r,\theta)+R(t,r,\theta)\right]\\ &+\frac{1}{2}\left[D_r(t+\Delta t,r,\theta)+D_r(t,r,\theta)\right]\\ &+\frac{1}{2}\left[D_\theta(t+\Delta t,r,\theta)+D_\theta(t,r,\theta)\right]\end{aligned} \tag{4.127}$$

when $r_{\rm ex}+2\Delta r\leq r\leq r_{\max}-2\Delta r$ and $2\Delta\theta\leq\theta\leq\pi-2\Delta\theta$, and

$$\begin{aligned}\frac{u(t+\Delta t,r,\theta)-u(t,r,\theta)}{\Delta t} &= \frac{1}{2}\left[R(t+\Delta t,r,\theta)+R(t,r,\theta)\right]\\ &+\frac{1}{2}\left[D_\theta(t+\Delta t,r,\theta)+D_\theta(t,r,\theta)\right]\end{aligned} \tag{4.128}$$

when $2\Delta\theta\leq\theta\leq\pi-2\Delta\theta$ and $r=r_{\rm ex}+\Delta r$ or $r\geq r_{\max}-\Delta r$, where

$$\begin{aligned}D_r(t,r,\theta) &= -\frac{\epsilon_r}{16\Delta t}\left[u(t,r+2\Delta r,\theta)-4u(t,r+\Delta r,\theta)+6u(t,r,\theta)\right.\\ &\left.-4u(t,r-\Delta r,\theta)+u(t,r-2\Delta r,\theta)\right] \ ,\end{aligned} \tag{4.129}$$

$$\begin{aligned}D_\theta(t,r,\theta) &= -\frac{\epsilon_\theta}{16\Delta t}\left[u(t,r,\theta+2\Delta\theta)-4u(t,r,\theta+\Delta\theta)+6u(t,r,\theta)\right.\\ &\left.-4u(t,r,\theta-\Delta\theta)+u(t,r,\theta-2\Delta\theta)\right] \ ,\end{aligned} \tag{4.130}$$

and $0\leq\epsilon_r<1$ and $0\leq\epsilon_\theta<1$ are adjustable parameters. I use values $\epsilon_r=0.5$ and $\epsilon_\theta=0.5$ for the adjustable dissipation parameters in directions r and θ, respectively. Using a Courant factor

$$\lambda=\frac{\Delta t}{\sqrt{\frac{1}{2}\left((\Delta r)^2+(\Delta\theta)^2\right)}}\simeq 0.25 \ , \tag{4.131}$$

this system of equations evolves stably under the Crank-Nicholson iterative solution scheme.

4.2.6 Strategies for AMR and Parallel Computation

I have three functional numerical implementations that solve the dynamics of the Maxwell-Klein-Gordon system: (1) a uniprocessor unigrid code; (2) a multiprocessor unigrid code; and (3) a uniprocessor adaptive mesh code.[7] The uniprocessor unigrid code was written with the aid of RNPL

[7]While I attempted to incorporate a multiprocessor adaptive code, I was unable to find conditions at once compatible with the regularity conditions and processor distribution process. Specifically, all tested implementations were found to introduce high frequency errors during the adaptive regridding process. It is suspected this problem could be easily resolved by switching to another coordinate system where regularity is not at issue.

([94], [95], [96], [97]), and was used exclusively in obtaining results for the uncharged Maxwell-Klein-Gordon equations. My multiprocessor unigrid code and uniprocessor adaptive mesh codes make use of the PAMR ([128], [129]) library. While I use the multiprocessor unigrid code extensively in solving the electromagnetically coupled dynamics, I have not found mesh refinement very beneficial. This is discussed below.

In the parallel implementation it is necessary to ensure the computational domain is properly distributed among the compute nodes. While PAMR takes care of the processor distribution and information passing processes, I must manually specify the ghost region[8] widths. For the example given in Appendix C, a ghost width of a single point was appropriate. However, in the present case, the chosen difference equations involve not only Kreiss-Oliger dissipation operators, but also interpolation and extrapolation operators. Simple counting reveals these operator stencils can extend as many as 3 points in each grid direction from their centers. This means ghost regions at least 3 points wide are required for complete information communication. However, more than 3 ghost points are not required. Using a wider ghost region is therefore unnecessary and will only decrease computational efficiency. I exclusively use ghost regions with exactly 3 points in each grid direction for this reason. Furthermore, it is important to use no more processors than necessary. Specifically, since there is a cost associated with inter-node communication from the transfer of data on ghost regions, choosing too many compute nodes could result in a total ghost point count comparable to the number of points on the global domain itself. I have found that 64 processors is typically a good choice for global domains having a total of 3.2×10^5 grid points or more.

The uniprocessor adaptive mesh code uses the modified Berger and Oliger time stepping algorithm as discussed in Appendix C, and implementation again uses the PAMR libraries. Central to this algorithm is the relative solution error that compares results on successive levels of resolution. It is important to consider appropriate grid functions in this measure of error. A good choice for the system includes the functions representing physical fields Φ, E_a, B_a and J_a, and conserved densities ρ_T, ρ_S and ρ_Q. Auxiliary fields and vector potential components could always be included in the measure of error, but the physical fields and conserved densities are ultimately the quantities of interest to physics, so ensuring they are properly resolved through the measure should be sufficient. Forming the measure and from these quantities and using a number of different error tolerances, I have tested the adaptive implementation by evolving massive electromagnetically coupled Maxwell-Klein-Gordon perturbations on an $a = M = 5$ Kerr spacetime. While evolution was smooth and otherwise well behaved, I have found the regions of adaptive refinement quickly grow and cover the greatest proportion of the computational domain, indicating the resolutional requirements become nearly uniform across most of the domain. This behaviour is depicted in Figure 4.14 for a maximum of four allowed levels of resolution. Considering the computational overhead of the adaptive refinement procedure, it is not clear that long term advantages can be gained from this implementation. The efficiency and cost is likely comparable to that of the parallel implementation where I simply evolve on a grid of sufficient uniform resolution. While the adaptive measure of solution error could probably be optimized, the improvement will probably not be great for the choice of spatial domain, typical initial conditions and parameter values e and m_Φ. I have therefore not investigated mesh refinement in any more detail.[9]

[8]Effectively, the *ghost region* of a parallel finite difference code is that set of grid points whose values must be communicated between processors. The size and form of a ghost region is determined by the computational domain of dependence, which is itself established through the choice of specific finite difference approximations and thus stencils. Details and discussion can be found in Appendix C.

[9]Of course, if the evolutionary details were known ahead of time, a non-uniform grid could be used in lieu of adaptive mesh refinement. Clearly, these non-uniform grids would have to be chosen on a case by case basis to accommodate resolutional requirements of the unfolding dynamics. So while much simpler to implement than adaptive refinement, the case-specific nature of non-uniform grid methods pose a serious limitation for the technique.

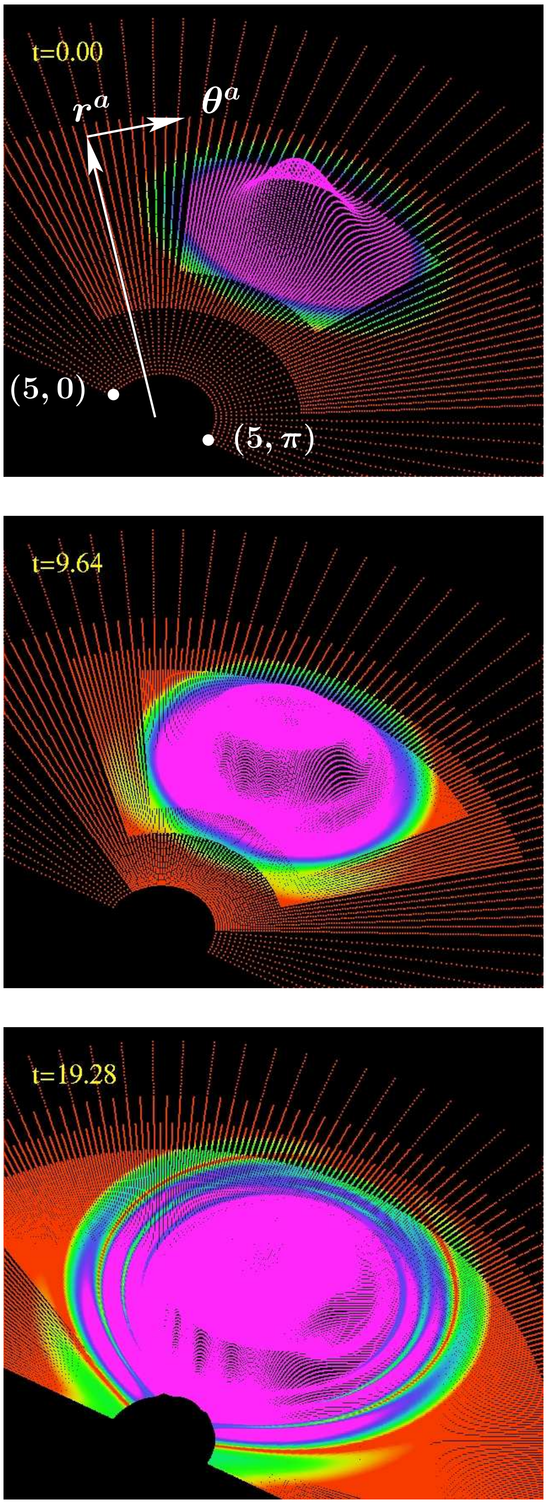

Figure 4.14: Adaptive mesh refinement (to a maximum of four levels) of the energy density for massive electromagnetically coupled perturbations in for $a = M = 5$ Kerr spacetime. The directions of coordinate vectors $r^a \sim (0, 1, 0, 0)$ and $\theta^a \sim (0, 0, 1, 0)$ are shown in the first frame. The computational domain covers the range $5 \leq r \leq 50$ and $0 \leq \theta \leq \pi$, and the corners of the domain are labelled with their (r, θ) ordinate values. The amplitude is scaled linearly and the colour gradient is scaled logarithmically. Refined regions quickly grow to cover a large proportion of the computational domain.

4.3 Results

4.3.1 Initial Data

The initial value problem for the Maxwell-Klein-Gordon system in Kerr spacetime amounts to specification of all the variables in a manner consistent with regularity and gauge conditions, and satisfying the electromagnetic constraint equation

$$D^a E_a = \rho_Q \ , \tag{4.132}$$

where D^a is the spatial covariant derivative operator, and ρ_Q, is, according to equation (4.108),

$$\rho_Q = ie \frac{g_{tr}^2}{(g_{tr}^2 f_{\phi\phi} - g_{t\phi} f_{t\phi} g_{rr})} \left(\Phi^* \Pi_\Phi - \Phi \Pi_\Phi^*\right) \ . \tag{4.133}$$

Following the procedure of section 2.2.1, I decompose E_a into its longitudinal and transverse parts, respectively L_a and T_a, to obtain

$$E_a = L_a + T_a \ . \tag{4.134}$$

Then introducing the scalar potential, $U = U(r, \theta)$, as per

$$D_a U = L_a \ , \tag{4.135}$$

(4.132) becomes

$$D^a D_a U = D^a E_a = \rho_Q \ , \tag{4.136}$$

where the left hand side is explicitly

$$\begin{aligned} D^a D_a U \quad = \quad & \frac{1}{2} \frac{g_{tr}^2}{g_{rr}^2 \left(g_{tr}^2 e_{\phi\phi} - f_{t\phi}^2 g_{rr}\right)} \left[2 g_{rr} (\partial_r e_{\phi\phi})(\partial_r U) - (\partial_r g_{rr}) e_{\phi\phi} (\partial_r U) + 2 g_{rr} e_{\phi\phi} (\partial_{rr} U)\right. \\ & \left. + g_{rr} (\partial_\theta g_{rr})(\partial_\theta U) - 2 g_{rr}^2 \cos\theta (\partial_{\cos\theta} U) + 2 g_{rr}^2 (\partial_{\theta\theta} U)\right] \ . \end{aligned} \tag{4.137}$$

After solving (4.136) using the methods of Appendix C, I reconstruct the longitudinal electric field components, which are, from (4.135),

$$L_r = \partial_r U \ , \tag{4.138}$$

$$L_\theta = \partial_\theta U \ , \tag{4.139}$$

$$L_\phi = 0 \ . \tag{4.140}$$

I can then specify any divergenceless set of components for the transverse part T_a. For simplicity, I choose

$$T_r = 0 \ , \tag{4.141}$$

$$T_\theta = 0 \ , \tag{4.142}$$

$$T_\phi = 0 \ . \tag{4.143}$$

The completely reconstructed electric field at initial time is then

$$E_r = \partial_r U \ , \tag{4.144}$$

$$E_\theta = \partial_\theta U \ , \tag{4.145}$$

$$E_\phi = 0 \ . \tag{4.146}$$

Having solved for E_a, the final step is to then initialize Π_r, Π_θ and Π_ϕ in accordance with (4.101), (4.102) and (4.103), meaning

$$\Pi_r = -\frac{g_{tr}^2 f_{\phi\phi} - g_{t\phi} f_{t\phi} g_{rr}}{g_{tr}^2} E_r \ , \tag{4.147}$$

$$\Pi_\theta = -\frac{g_{tr}^2 f_{\phi\phi} - g_{t\phi} f_{t\phi} g_{rr}}{g_{tr}^2} E_\theta \ , \tag{4.148}$$

$$\Pi_\phi = -\frac{g_{tr}^2 f_{\phi\phi} - g_{t\phi} f_{t\phi} g_{rr}}{g_{tr}^2} E_\phi \ . \tag{4.149}$$

Having satisfied the initial data constraint, I can freely specify the remaining variables in accordance with their definitions and regularity conditions. For simplicity I choose Gaussian profiles for the complex components of $\Phi(t,r,\theta) = \phi_1(t,r,\theta) + i\phi_2(t,r,\theta)$, $\Pi_\Phi(t,r,\theta) = \Pi_1(t,r,\theta) + i\Pi_2(t,r,\theta)$, and the vector potential components $A_a(t,r,\theta)$.[10] That is,

$$\phi_1(0,r,\theta) = a_1 \exp\left(-((r-r_1)/\delta_{r1})^2\right) \exp\left(-((\theta-\theta_1)/\delta_{\theta 1})^2\right) \ , \tag{4.150}$$

$$\phi_2(0,r,\theta) = a_2 \exp\left(-((r-r_2)/\delta_{r2})^2\right) \exp\left(-((\theta-\theta_2)/\delta_{\theta 2})^2\right) \ , \tag{4.151}$$

$$\Pi_1(0,r,\theta) = a_3 \exp\left(-((r-r_3)/\delta_{r3})^2\right) \exp\left(-((\theta-\theta_3)/\delta_{\theta 3})^2\right) \ , \tag{4.152}$$

$$\Pi_2(0,r,\theta) = a_4 \exp\left(-((r-r_4)/\delta_{r4})^2\right) \exp\left(-((\theta-\theta_4)/\delta_{\theta 4})^2\right) \ , \tag{4.153}$$

$$A_t(0,r,\theta) = a_r \exp\left(-((r-r_t)/\delta_{rt})^2\right) \exp\left(-((\theta-\theta_t)/\delta_{\theta t})^2\right) \ , \tag{4.154}$$

$$A_r(0,r,\theta) = a_r \exp\left(-((r-r_r)/\delta_{rr})^2\right) \exp\left(-((\theta-\theta_r)/\delta_{\theta r})^2\right) \ , \tag{4.155}$$

$$A_\theta(0,r,\theta) = a_\theta \exp\left(-((r-r_\theta)/\delta_{r\theta})^2\right) \exp\left(-((\theta-\theta_\theta)/\delta_{\theta\theta})^2\right) \ , \tag{4.156}$$

$$A_\phi(0,r,\theta) = a_\phi \exp\left(-((r-r_\phi)/\delta_{r\phi})^2\right) \exp\left(-((\theta-\theta_\phi)/\delta_{\theta\phi})^2\right) \ , \tag{4.157}$$

where a_1, a_2, a_3, a_4, a_t, a_r, a_θ and a_ϕ are constants setting the initial amplitudes, r_1, r_2, r_3, r_4, r_t, r_r, r_θ and r_ϕ determine the Gaussian peaks in the radial direction, θ_1, θ_2, θ_3, θ_4, θ_t, θ_r, θ_θ and θ_ϕ determine the Gaussian peaks in the θ coordinate direction, δ_{r1}, δ_{r2}, δ_{r3}, δ_{r4}, δ_{rt}, δ_{rr}, $\delta_{r\theta}$ and $\delta_{r\phi}$ determine the Gaussian widths in coordinate r, and $\delta_{\theta 1}$, $\delta_{\theta 2}$, $\delta_{\theta 3}$, $\delta_{\theta 4}$, $\delta_{\theta t}$, $\delta_{\theta r}$, $\delta_{\theta\theta}$ and $\delta_{\theta\phi}$ determine widths in θ. All remaining variables are initialized according to definitions in sections

[10] From equations (4.93) and (4.94), nonzero electric current components J_r and J_θ require e, Φ and Φ^* to all be nonzero. The condition for nonzero J_r additionally requires that either A_r, Φ_r or Φ_r^* be nonzero. Similarly, the condition for nonzero J_θ additionally requires that either A_θ, Φ_θ or Φ_θ^* be nonzero. Clearly, the chosen initial data (4.150)–(4.162) satisfies the nonzero conditions for both J_r and J_θ when $e \neq 0$. Therefore, it can be said charge separation begins at $t = 0$ for this specification of the Maxwell-Klein-Gordon system.

4.2.3 and 4.2.4. Unless otherwise specified, I use values

$$a_1 = a_2 = a_3 = a_4 = a_t = a_r = a_\theta = a_\phi = 1.0 \ , \tag{4.158}$$

$$r_1 = r_2 = r_3 = r_4 = r_t = r_r = r_\theta = r_\phi = 25.0 \ , \tag{4.159}$$

$$\theta_1 = \theta_2 = \theta_3 = \theta_4 = \theta_t = \theta_r = \theta_\theta = \theta_\phi = \pi/2 \ , \tag{4.160}$$

$$\delta_{r1} = \delta_{r2} = \delta_{r3} = \delta_{r4} = \delta_{rt} = \delta_{rr} = \delta_{r\theta} = \delta_{r\phi} = 5.0 \ , \tag{4.161}$$

$$\delta_{\theta 1} = \delta_{\theta 2} = \delta_{\theta 3} = \delta_{\theta 4} = \delta_{\theta t} = \delta_{\theta r} = \delta_{\theta\theta} = \delta_{\theta\phi} = 0.3 \ . \tag{4.162}$$

The chosen Kerr spacetime is exclusively mass $M = 5$ with variable angular momentum per unit mass, a. Finally, the computational domain always covers the coordinate range $5 \leq r \leq 50$ and $0 \leq \theta \leq \pi$.

Finally, while the form of metric (4.40) suggests symmetry about the equatorial plane ($\theta = \pi/2$), this symmetry is for the spacetime metric and not for matter evolving in the background spacetime. Since the Maxwell-Klein-Gordon fields are here treated as perturbations not affecting the spacetime, they are free to evolve in a manner which is not symmetric about the equatorial plane. Observe how the equations of motion and constraint have been written in a general form consistent with the assumption of axial symmetry and therefore allow a more generic evolution—one that need not respect any symmetry about the equatorial plane.[11] As shown in section 4.3.3, the choice of initial conditions (4.132), (4.147)–(4.149), and (4.154)–(4.157) do not generate electromagnetic fields with covariant components all symmetric about $\theta = \pi/2$. Furthermore, since the difference approximations used are accurate to only $\mathcal{O}\left((\Delta\theta)^2\right)$, slight asymmetries about the equatorial plane will be expected throughout evolution regardless of how initial conditions are chosen.

4.3.2 Klein-Gordon Dynamics: Orbiting Resonances and Massive Mode Trapping for $s = 0$ Perturbations

With initial data specified as discussed above, I evolve massive $s = 0$ perturbations on a Kerr spacetime. The black hole mass is set to $M = 5$, and the angular momentum per unit mass is chosen to be either $a = 0$ or $a = M$. I vary the Klein-Gordon mass parameter $m_\Phi \equiv m_\Psi$ between $m_\Phi = 0.0$ and $m_\Phi = 2.4$. The computational domain covers radial coordinate range $5 \leq r \leq 50$ and angular coordinates $0 \leq \theta \leq \pi$. The computational domain has $J = 401$ points radially and $K = 201$ points in the θ angular direction. The numerical evolutions span the range of coordinate time $0 \leq t \lesssim 200$.

For $a = M = 5$, $m_\Phi = 0.0$ evolution, perturbations clearly display the glory effect and orbiting resonances. Figure 4.15 displays the normalized energy density within $5 \leq r \leq 50$, $0 \leq \theta \leq \pi$ and $0 \leq \phi \leq 2\pi$ by a sequence of steps from the evolution beginning at $t = 0$ and leading to a final step at $t = 77.11$ shown in Figure 4.16. The orbit resonance period is $\approx 70t$ and each successive orbit is attenuated by a factor of $\sim 10^{-1}$. Note how the orbital frequency $\approx 1/(70t)$ is more than twice that of the unstable circular photon orbits occurring at $r = 3M$.[12] While strong gravitational

[11] While an equatorially symmetric code could be written for the Maxwell-Klein-Gordon system, it would not allow study of any physics unique to the non-equatorially symmetric system.

[12] The innermost stable circular orbit of the Schwarzschild spacetime described by (4.1) occurs at radius $r = 6M$, while the innermost unstable circular orbit occurs at $r = 3M$. From the study of timelike geodesics in Schwarzschild spacetime it can be shown that circular orbits in the equatorial plane are given by

$$\frac{\partial\phi}{\partial\tau} = \frac{L}{r^2} \ , \tag{4.163}$$

where τ is proper time and L is the angular momentum per unit rest mass as measured by a static observer at infinity. The proper time for the innermost stable circular orbit of an $M = 5$ Schwarzschild spacetime is therefore $\frac{1800\pi}{L}$, while the proper time for the innermost unstable circular orbit in the same spacetime is $\frac{450\pi}{L}$. More cannot be said about the orbital period without specifying a value for L. Instead consider the null geodesics of Schwarzschild interaction is observable in the form of orbiting resonances, neither mode trapping nor superradiant scattering are apparent from the calculations. While mode trapping is expected only for massive scalar perturbations, superradiant scattering could, in fact, be present for any scalar perturbation mass. However, the effect is expected to be only on the order of a fraction of a percent [124]. Figure 4.17 displays the integrated normalized energy density within the computational domain for $0 \leq t \lesssim 200$ for both $a = 0$ and $a = M$. Clearly, the addition of black hole angular momentum has but a small effect on the scalar perturbation evolution.[13] Predominantly, addition of black hole angular momentum decreases the perturbation energy flux through surfaces $r = 5$ and $r = 50$. While not exact for either $a = 0$ or $a = M$, the late time decay of integrated normalized energy, T, is approximately a power law of form

$$\log(T) \sim -kt \ , \tag{4.165}$$

with constant of proportionality $k \approx 1 \times 10^{-2}$. A local maximum in this integrated energy density would be sufficient for identification of superradiant scattering. But since scalar perturbations are flowing out of the computational domain at both the $r = 5$ excision surface and the $r = 50$ outer boundary, a better test would also incorporate the energy flux through the surface $r = 50$. A local maximum in the integrated energy within the computational domain plus that of the outflowing flux would constitute a necessary condition for superradiant scattering. So while not apparent in the data shown, superradiant scattering may, in fact, be occurring in the evolution of the massless scalar perturbations. Finally, Figure 4.18 displays the normalized energy density at $t = 53.98$. Results presented in section 4.3.3 show a superradiant scattering peak for $s = 1$ electromagnetic perturbations at this time (cf. Figures 4.29 and 4.30).

spacetime. It is known there are no stable circular orbits and just a single unstable circular orbit at $r = 3M$ whose equation in the equatorial plane is

$$\frac{\partial \phi}{\partial t} = \left(\frac{r - 2M}{r^3} \right)^{1/2} \ . \tag{4.164}$$

The period in coordinate time of a unstable circular photon orbit in $M = 5$ Schwarzschild spacetime is therefore $\sqrt{330}\pi \simeq 163.24$.

[13] In fact, a comparison of the normalized energy densities reveals that $a = 0$ and $a = M$ evolutions are morphologically nearly identical.

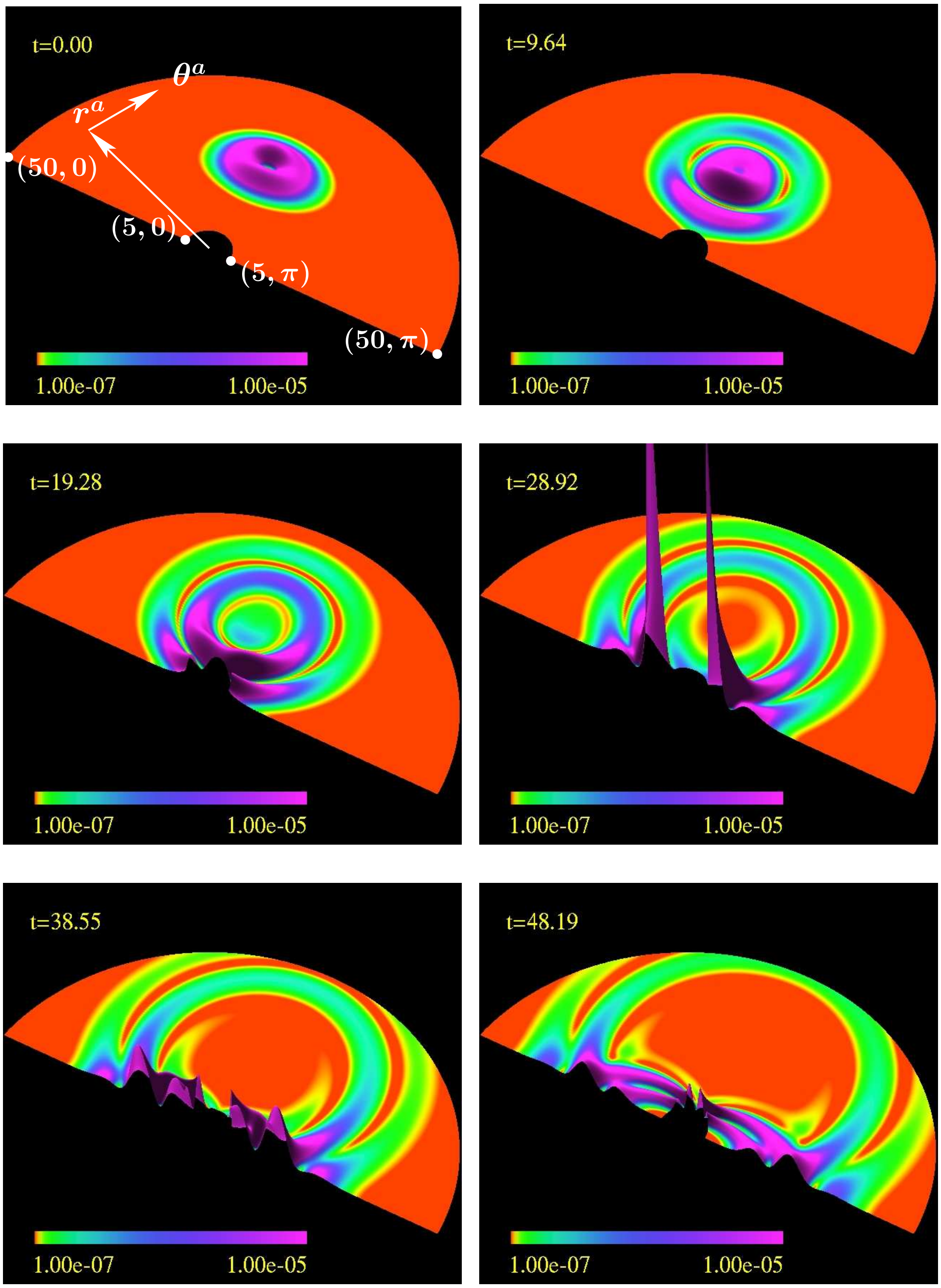

Figure 4.15: The glory effect and orbiting resonances for $a = M = 5$, $m_\Phi = 0.0$ scalar perturbations. The figure displays the normalized energy density in a sequence of steps. The directions of coordinate vectors $r^a \sim (0, 1, 0, 0)$ and $\theta^a \sim (0, 0, 1, 0)$ are shown in the first frame. The computational domain covers the range $5 \leq r \leq 50$ and $0 \leq \theta \leq \pi$, and the corners of the domain are labelled with their (r, θ) ordinate values. The amplitude is scaled linearly, while the scale of the colour gradient is logarithmic.

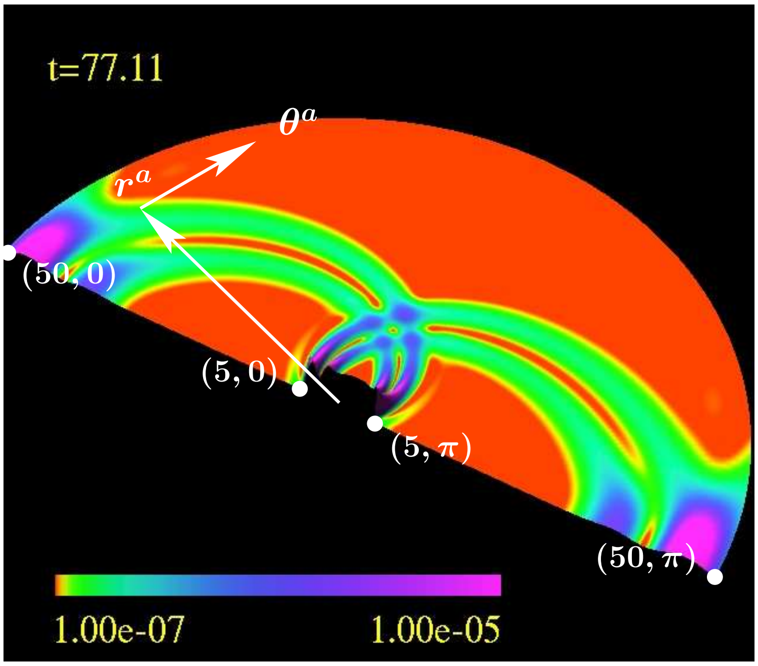

Figure 4.16: The glory effect and orbiting resonances for $a = M = 5$, $m_\Phi = 0.0$ scalar perturbations at late time. The figure displays the normalized energy density at a final step of the evolution. The directions of coordinate vectors $r^a \sim (0, 1, 0, 0)$ and $\theta^a \sim (0, 0, 1, 0)$ are shown, the computational domain covers the range $5 \leq r \leq 50$ and $0 \leq \theta \leq \pi$, and the corners of the domain are labelled with their (r, θ) ordinate values. The amplitude is again scaled linearly and the colour gradient logarithmically. An MPEG animation showing orbiting resonance through normalized energy density for the period $0 \leq t \lesssim 108$ is available at `http://$WWW/People/petryk/animations/2.mpeg` where `$WWW` is currently `laplace.physics.ubc.ca` .

As discussed in section 4.1, setting the scalar perturbation mass to nonzero values may permit mode trapping in the minimum of the effective gravitational potential. The details depend on the specific mode, and the magnitude of the perturbation mass, m_Φ, relative to the mass of the black hole, M. Specifically, Figures 4.5 and 4.7 demonstrate that $l = 5$ can be the only trapped mode of perturbation mass $m_\Phi = 0.3$ in a spacetime with $a = 0$ and $M = 5$. From equation (4.10) it can be deduced that, for $r \leq 50$, all modes with $l < 5$ experience only a potential well centered within the event horizon. The only well for modes $l > 5$ is again within the event horizon, but now additional scattering is observed because of a local maximum in the potential near $r = 3M$. Comparing with Figures 4.3, 4.6 and 4.8 it is clear that, for a given spacetime, trapping of low l modes occurs for smaller values of m_Φ, and trapping of higher l modes takes place for larger m_Φ. Furthermore, if m_Φ is sufficiently large, all lower l modes are expected to experience only a deep potential well and therefore fall into the black hole. Figure 4.19 displays the integrated normalized energy density for $m_\Phi = 0.0, 0.3, 0.6, 1.2$, and 2.4 massive scalar perturbations in an $a = M = 5$ Kerr spacetime. $m_\Phi = 0.3$ perturbations experience the greatest trapping and persist longest on the computational domain, while the $m_\Phi = 2.4$ perturbation total energy decays most rapidly. At late time, $t \approx 200$, the total energy of $m_\Phi = 0.6$ perturbations most closely matches that of the $m_\Phi = 0.0$ perturbations. Superradiant scattering peaks are not observed for any of these cases,

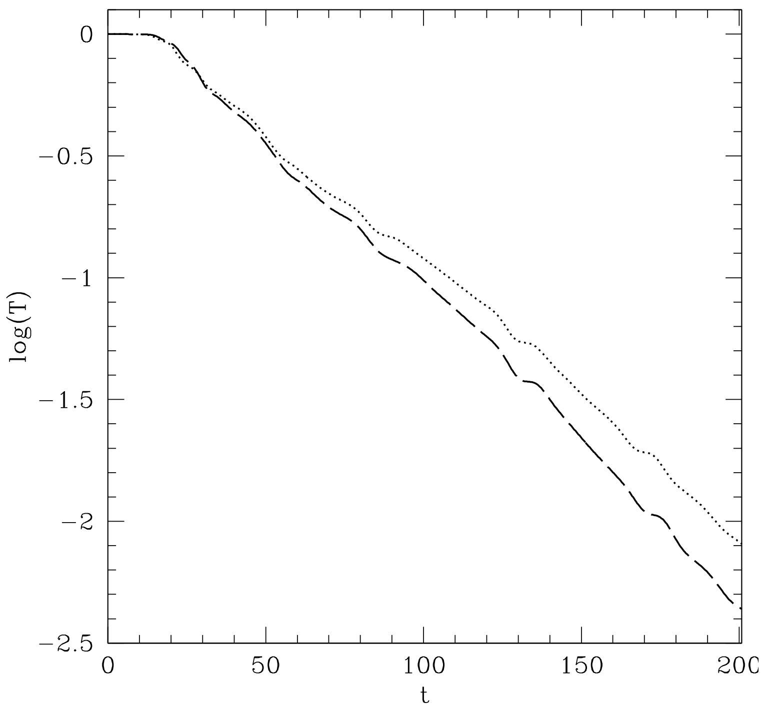

Figure 4.17: Integrated normalized energy density for massless scalar perturbations. Plotted is $\log(T)$, the logarithm of the total energy contained within $5 \leq r \leq 50$, $0 \leq \theta \leq \pi$ and $0 \leq \phi \leq 2\pi$, as a function of coordinate time t. The dashed line represents data for $a/M = 0/5 = 0$ and the dotted line data for $a/M = 5/5 = 1$. The decay rate of integrated energy is approximately a power law at late time. A local maximum signalling superradiant scattering is not observable for either evolution. Black hole angular momentum effectively decreases the overall decay rate of these massless scalar perturbations. Note the decrease in time of this quantity results from the energy flux across surfaces $r = 5$ and $r = 50$, and thus out of the computational domain.

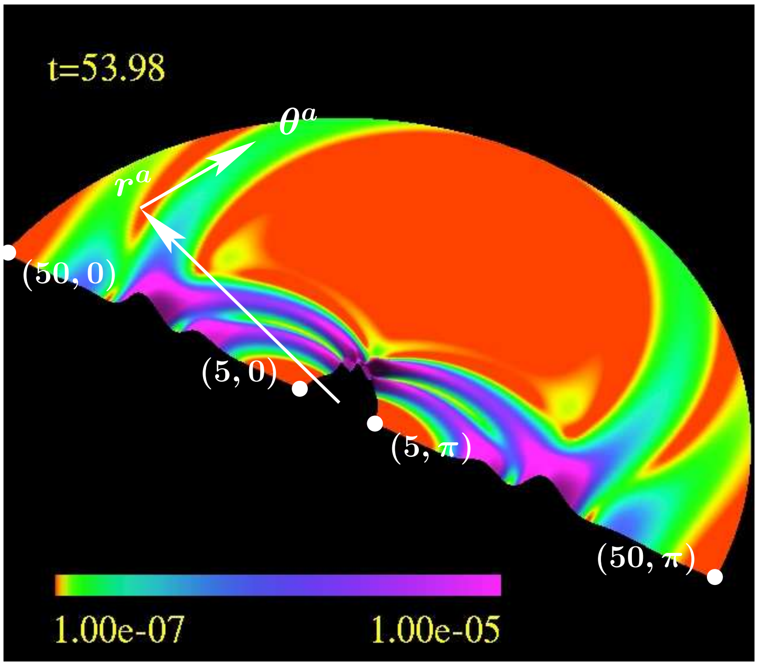

Figure 4.18: Normalized energy density at $t = 53.98$ for $a = M = 5$, $m_\Phi = 0.0$ scalar perturbations. It is at this time that superradiant scattering peaks are seen for electromagnetic perturbations (cf. Figures 4.29 and 4.30), but here there is no evidence of superradiance for the massless scalar perturbations. The directions of coordinate vectors $r^a \sim (0, 1, 0, 0)$ and $\theta^a \sim (0, 0, 1, 0)$ are shown, the computational domain covers the range $5 \leq r \leq 50$ and $0 \leq \theta \leq \pi$, and the (r, θ) ordinate values at the domain corners are provided. The amplitude is again scaled linearly and the colour gradient logarithmically.

but this test is again sufficient but not necessary for superradiance.

The detailed structure of massive scalar perturbation evolution in $a = M = 5$ Kerr spacetime is displayed for $m_\Phi = 0.3$ in Figures 4.20 and 4.21, and for $m_\Phi = 2.4$ in Figure 4.22. Figures 4.20 and 4.21 reveal a rather detailed (normalized) energy density distribution as the $m_\Phi = 0.3$ perturbations evolve on the computational domain. While the evolution markedly different from that of $m_\Phi = 0.0$, there is still some evidence of orbiting resonances very near the excision surface at $r = 5$, but it is not possible to provide a reasonable estimate for either the resonance orbit period or their attenuation. However, the perturbations now persist for a extended period of time in the vicinity of the black hole. Furthermore, there is some evidence of additional energy density concentration along the axis of black hole rotation. Meanwhile, Figure 4.22 shows how the $m_\Phi = 2.4$ scalar perturbations remain localized throughout evolution as they become tidally distorted and consumed by the black hole within a relatively short period of time. The evolution of $m_\Phi = 1.2$ perturbations (not displayed) are very much similar in these respects. Finally, as expected. the effect of black hole angular momentum are small for $(s = 0)$ scalar perturbations. Morphologically, the $a = 0$ and $a = M$ evolutions are nearly identical for $m_\Phi = 0.3$ and also for $m_\Phi = 2.4$. Figures 4.23 and 4.24 compare $a = 0$ and $a = M$ integrated normalized energy densities for the respective $m_\Phi = 0.3$ and $m_\Phi = 2.4$ evolutions. The results again show little difference in the total energy within $5 \leq r \leq 50$, $0 \leq \theta \leq \pi$ and $0 \leq \phi \leq 2\pi$ as a function of time between $a = 0$ and $a = M$ spacetimes. The approximation of total integrated energy, T, to a power law of form

$$\log(T) \sim -kt \tag{4.166}$$

is worse than for the massless perturbations. However, if a power law is assumed at late time, the decay constant would be $k \approx 5 \times 10^{-3}$ for $m_\Phi = 0.3$ perturbations, and $k \approx 7 \times 10^{-2}$ for $m_\Phi = 2.4$ perturbations. The lower decay rate for m_Φ perturbations results from mode trapping about a local potential minimum, and the increased decay rate for $m_\Phi = 2.4$ perturbations derives from the rapid infall of perturbations in a steeper potential well. These results differ from the case of $(s = 1)$ electromagnetic perturbations presented below.

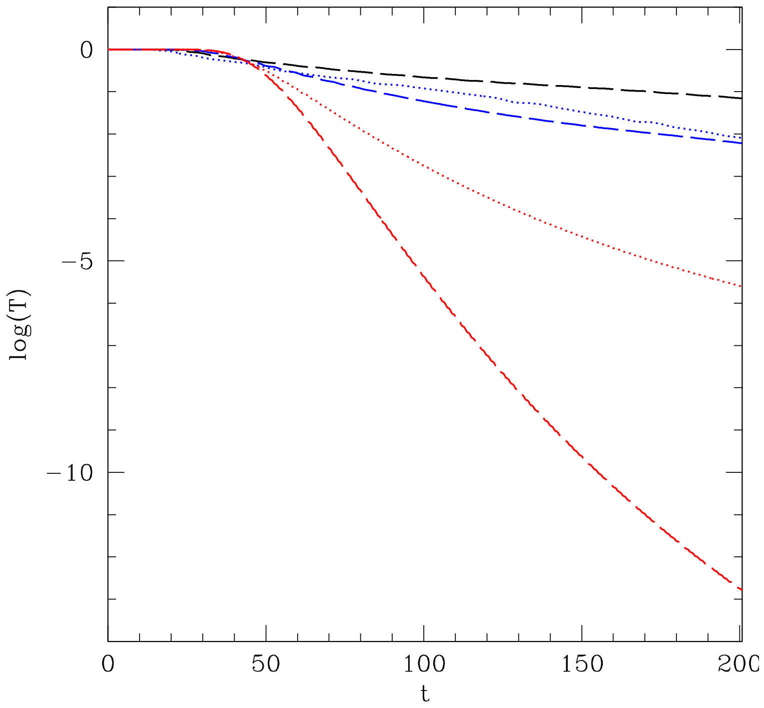

Figure 4.19: Integrated normalized energy density for massive scalar perturbations. Plotted is $\log(T)$, the logarithm of the total energy contained within $5 \leq r \leq 50$, $0 \leq \theta \leq \pi$ and $0 \leq \phi \leq 2\pi$, as a function of coordinate time t. All data is for the $a/M = 5/5 = 1$ Kerr spacetime. The dashed red line is for $m_\Phi = 2.4$, the dotted red line is for $m_\Phi = 1.2$, the dashed blue line is $m_\Phi = 0.6$, the dotted blue line is $m_\Phi = 0.0$, and the dashed black line is $m_\Phi = 0.3$. Clearly, $m_\Phi = 0.3$ perturbations experience the greatest trapping and persist longest on the computational domain. In none of the cases is a local maximum signalling superradiant scattering apparent. The decrease in time of this quantity results from the energy flux across surfaces $r = 5$ and $r = 50$, and thus out of the computational domain.

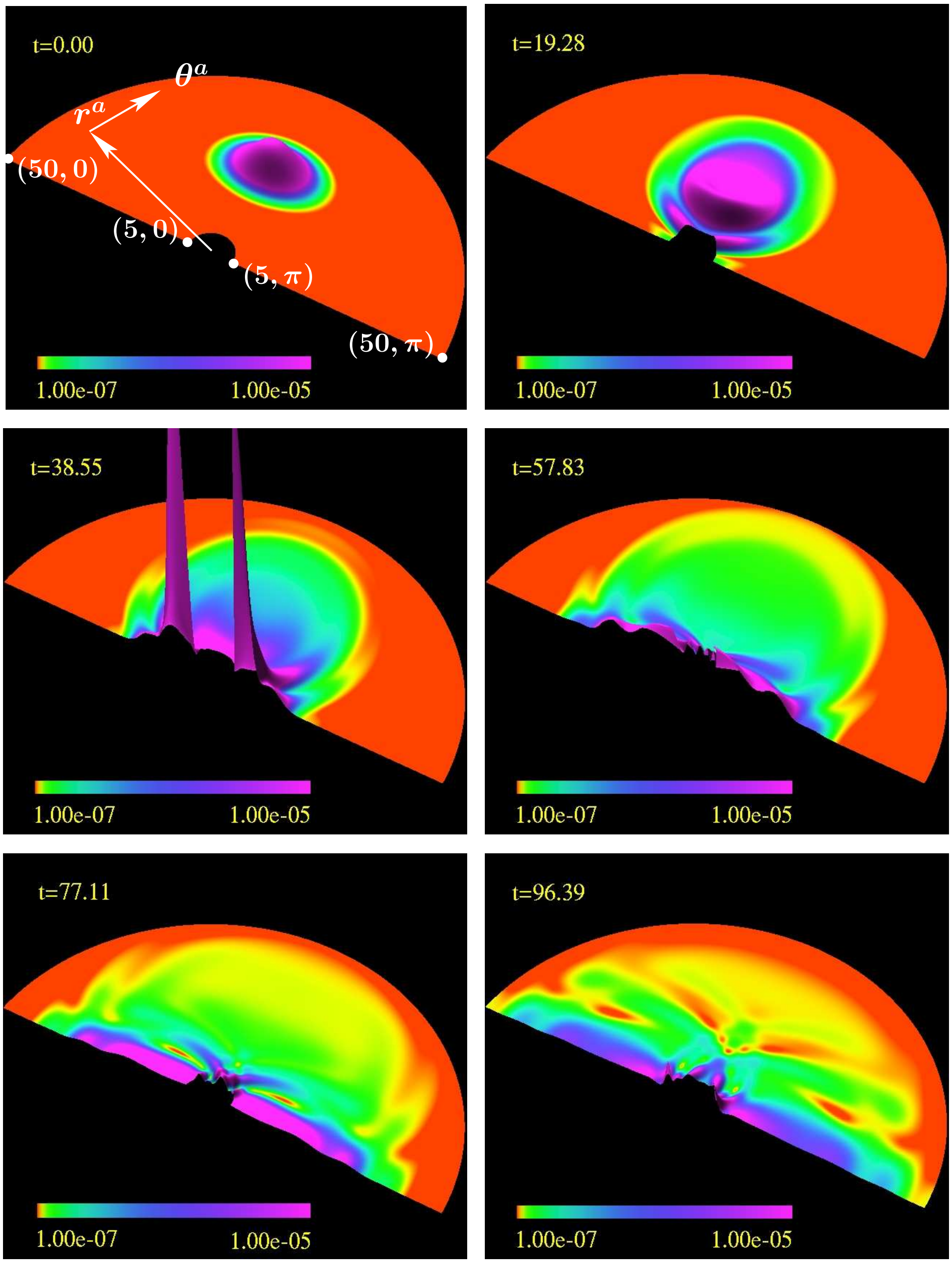

Figure 4.20: Mode trapping and orbiting resonances for $a = M = 5$, $m_\Phi = 0.3$ scalar perturbations. The figure displays the normalized energy density evolution in a sequence of steps. The directions of coordinate vectors $r^a \sim (0, 1, 0, 0)$ and $\theta^a \sim (0, 0, 1, 0)$ are shown, the computational domain covers the range $5 \leq r \leq 50$ and $0 \leq \theta \leq \pi$, and the corners of the domain are labelled with their (r, θ) ordinate values. The amplitude is again scaled linearly and the colour gradient logarithmically. An MPEG animation of the evolution over the period $0 \leq t \lesssim 108$ is available at `http://$WWW/People/petryk/animations/3.mpeg` where `$WWW` is currently `laplace.physics.ubc.ca`.

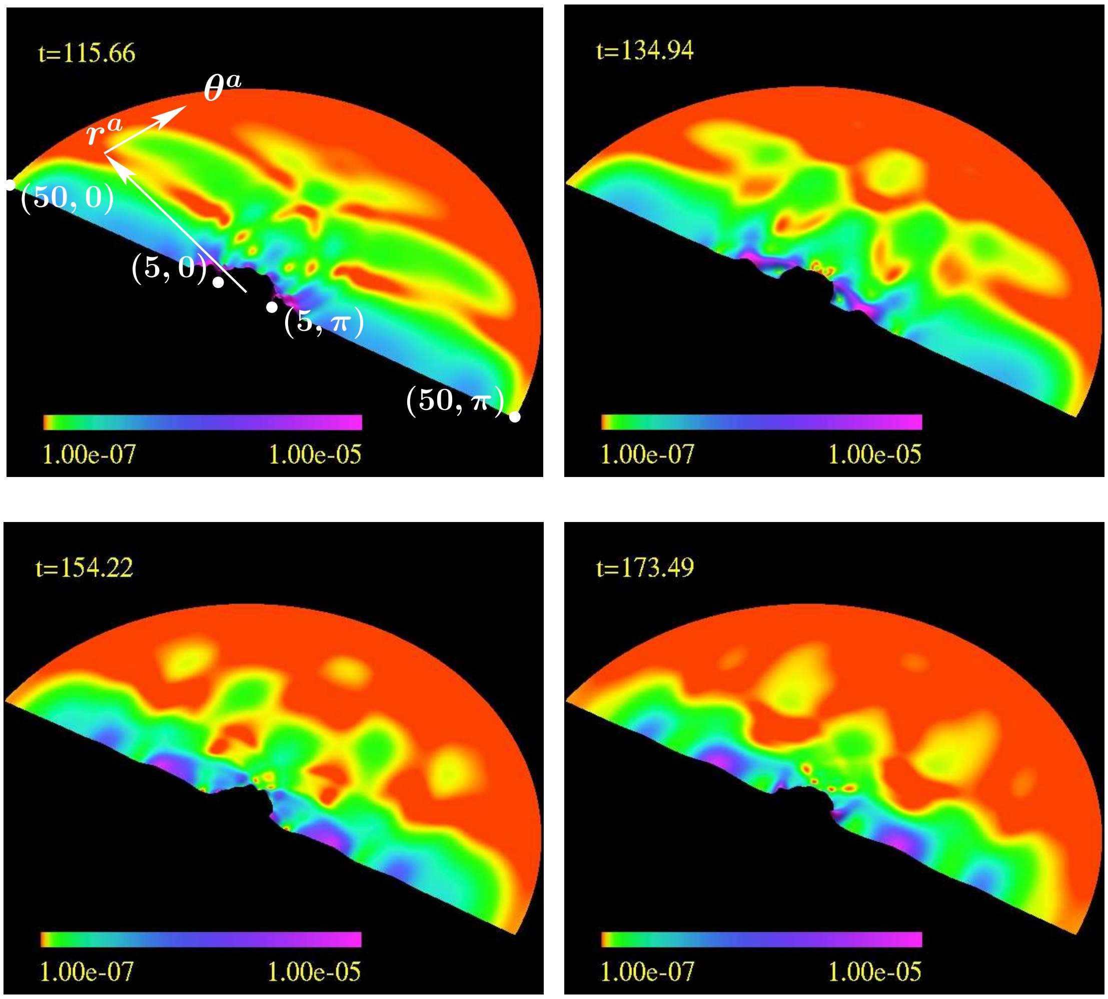

Figure 4.21: Mode trapping and orbiting resonances for $a = M = 5$, $m_\Phi = 0.3$ scalar perturbations at late time. The figure displays the normalized energy density evolution in a sequence of steps. The directions of coordinate vectors $r^a \sim (0, 1, 0, 0)$ and $\theta^a \sim (0, 0, 1, 0)$ are again shown, the computational domain again covers the range $5 \leq r \leq 50$ and $0 \leq \theta \leq \pi$, and the corners of the domain are labelled with their (r, θ) ordinate values. The amplitude is again scaled linearly and the colour gradient logarithmically.

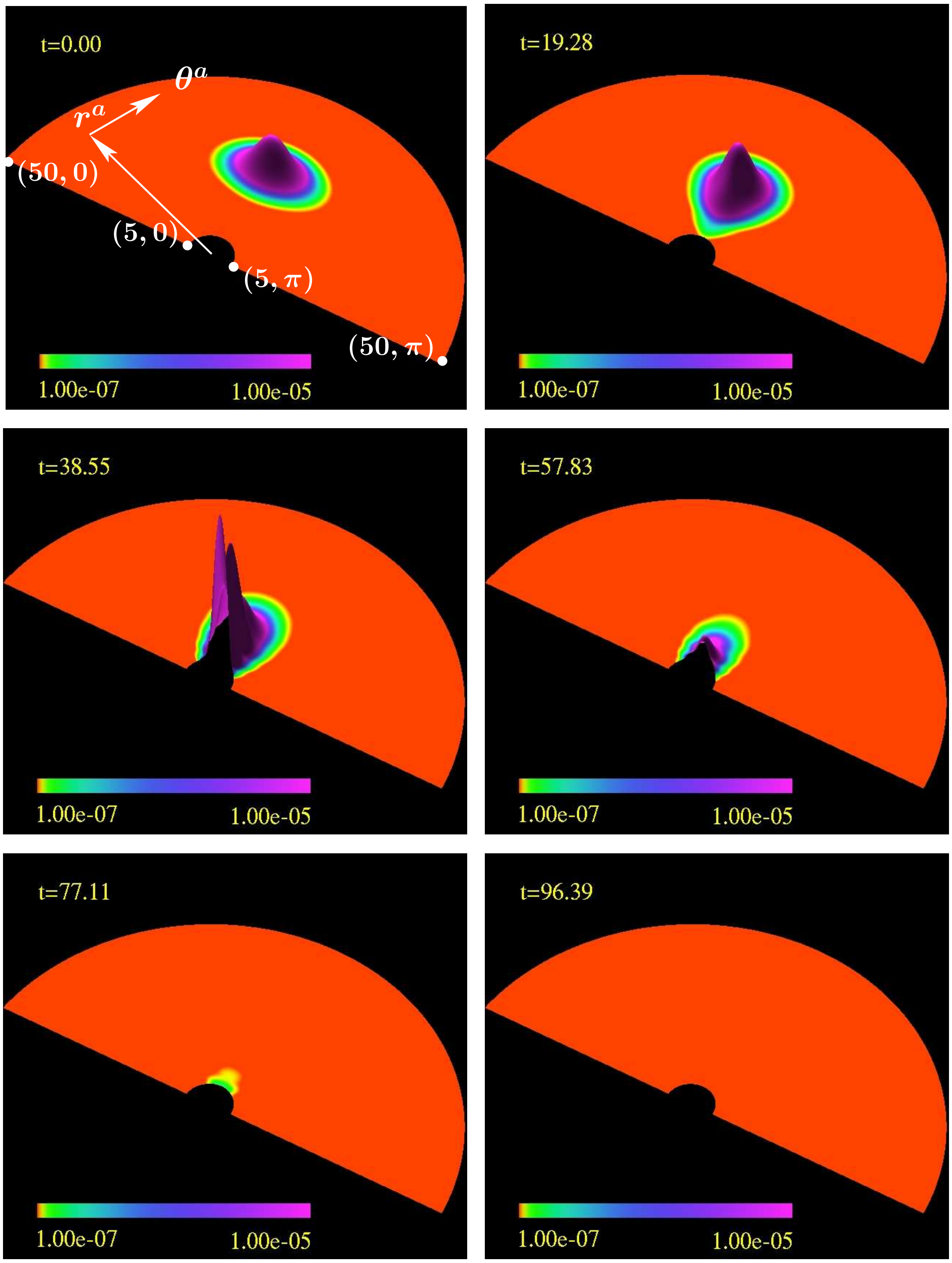

Figure 4.22: Localization, tidal distortion, and rapid decay of $m_\Phi = 2.4$ scalar perturbations in $a = M = 5$ Kerr spacetime. The figure displays the normalized energy density evolution in a sequence of steps. The directions of coordinate vectors $r^a \sim (0, 1, 0, 0)$ and $\theta^a \sim (0, 0, 1, 0)$ are shown, the computational domain covers the range $5 \leq r \leq 50$ and $0 \leq \theta \leq \pi$, and the corners of the domain are labelled with their (r, θ) ordinate values. The amplitude is again scaled linearly and the colour gradient logarithmically. An MPEG animation of the evolution over the period $0 \leq t \lesssim 108$ is available at `http://$WWW/People/petryk/animations/4.mpeg` where `$WWW` is currently `laplace.physics.ubc.ca`.

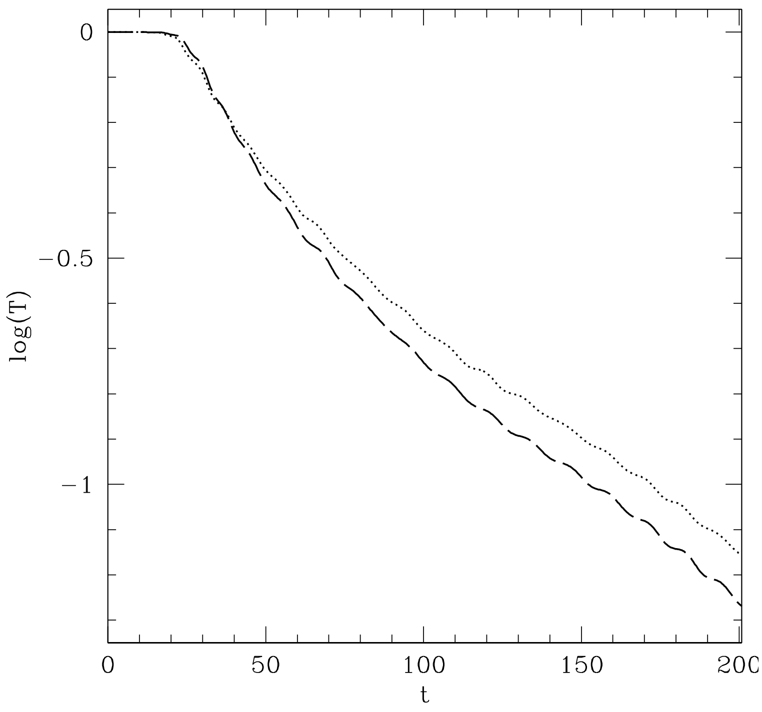

Figure 4.23: Integrated normalized energy density for $m_\Phi = 0.3$ scalar perturbations. Plotted is $\log(T)$, the logarithm of the total energy contained within $5 \le r \le 50$, $0 \le \theta \le \pi$ and $0 \le \phi \le 2\pi$, as a function of coordinate time t. The dashed line represents data for $a/M = 0/5 = 0$ and the dotted line data for $a/M = 5/5 = 1$. Black hole angular momentum decreases the overall decay rate for these massive scalar perturbations. The decrease in time of this quantity results from the energy flux across surfaces $r = 5$ and $r = 50$, and thus out of the computational domain.

4.3.3 Maxwell Equation Dynamics: Orbiting Resonances and Superradiance for $s = 1$ Perturbations

With initial data again specified according to section 4.3.1, I evolve $s = 1$ perturbations on a Kerr spacetime. The black hole mass is again set to $M = 5$, and the angular momentum per unit mass is chosen somewhere in the range $a = 0$ through $a = M$. The computational domain again covers radial coordinate range $5 \le r \le 50$ and angular coordinates $0 \le \theta \le \pi$. The computational domain has $J = 401$ points radially and $K = 201$ points in the θ angular direction and numerical evolutions span the range of coordinate time $0 \le t \lesssim 200$. In terms of physical fields, the chosen initial data amounts to an everywhere vanishing electric field and a non-vanishing nontrivial magnetic field at $t = 0$. For example, in the case $a = M$, the initial magnetic field components are distributed as shown in Figure 4.25. The resulting energy density distribution is shown in the first frame of Figure 4.28. While the electric field components are initially vanishing, their time derivatives—and also those of the magnetic field components—are not, implying nontrivial evolution.

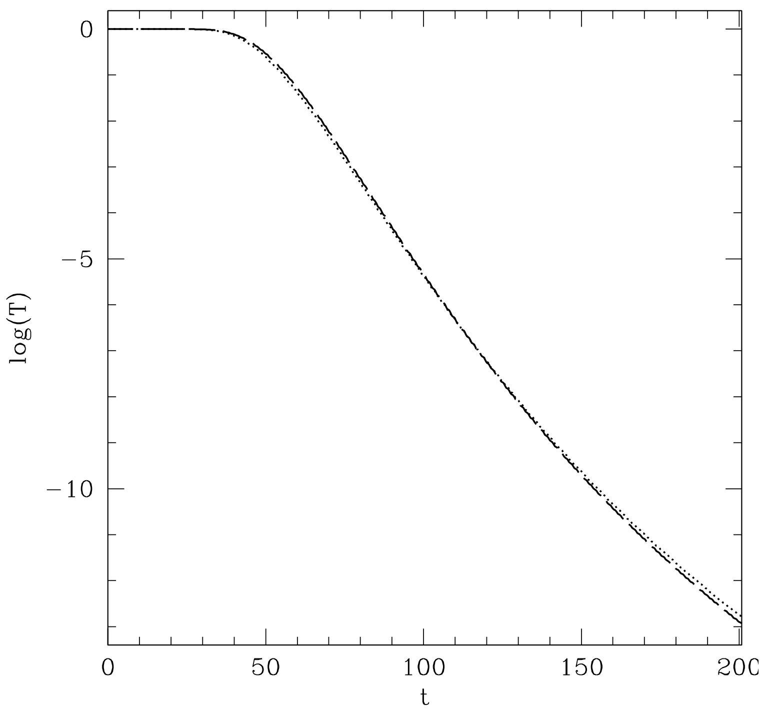

Figure 4.24: Integrated normalized energy density for $m_\Phi = 2.4$ scalar perturbations. Plotted is $\log(T)$, the logarithm of the total energy contained within $5 \leq r \leq 50$, $0 \leq \theta \leq \pi$ and $0 \leq \phi \leq 2\pi$, as a function of coordinate time t. The dashed line represents data for $a/M = 0/5 = 0$ and the dotted line data for $a/M = 5/5 = 1$. Black hole angular momentum has little effect on the evolution of these massive scalar perturbations. Again, decreases in time of this quantity result from the energy flux across surfaces $r = 5$ and $r = 50$, and thus out of the computational domain.

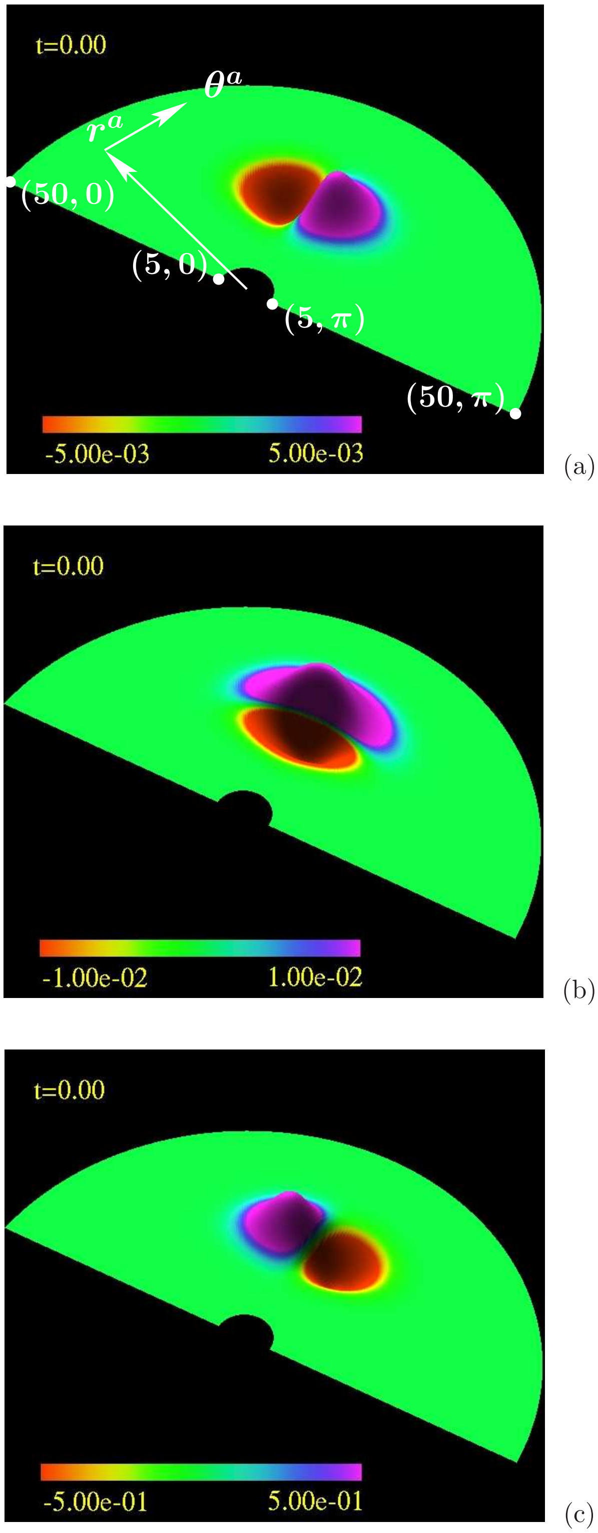

Figure 4.25: Initial magnetic field distribution for $a = M = 5$, electromagnetic perturbations. (a) displays B_r, (b) displays B_θ, and (c) shows B_ϕ. The directions of coordinate vectors $r^a \sim (0, 1, 0, 0)$ and $\theta^a \sim (0, 0, 1, 0)$ are shown in (a). The computational domain covers the range $5 \leq r \leq 50$ and $0 \leq \theta \leq \pi$, and the corners of the domain are labelled with their (r, θ) ordinate values. The amplitude and colour gradient are both scaled linearly.

For evolutions $a = 0$ through $a = M$, electromagnetic perturbations clearly display the glory effect and orbiting resonances. Figure 4.26 displays the normalized energy density within $5 \leq r \leq 50$, $0 \leq \theta \leq \pi$ and $0 \leq \phi \leq 2\pi$ by a sequence of steps from the evolution beginning at $t = 0$ and leading to a final step at $t = 77.11$ shown in Figure 4.27. Strong gravitational interaction is clearly manifest in the form of orbiting resonances. Similar to the case of massless scalar perturbations, the resonance orbit period is $\approx 70t$, corresponding to an orbital frequency more than twice that the unstable circular photon orbit at $r = 3M$ (cf. equation (4.164) and related discussion). Furthermore, the attenuation between successive orbits is again $\sim 10^{-1}$. While an effect akin to mode trapping is not expected for electromagnetic perturbations, superradiant scattering could be present, depending on the initial data and value of angular momentum parameter a. The maximum superradiant amplification is expected to be on the order of four percent in an $a = M$ spacetime. Figure 4.28 displays the integrated normalized energy density within the computational domain for $0 \leq t \lesssim 200$ for $a = 0, 0.8M$ and $a = M$. Clearly, the addition of black hole angular momentum has a measurable effect on the evolution of electromagnetic perturbations. At late time the total integrated energy, T, can be roughly approximated by the power law

$$\log(T) \sim -kt \ , \tag{4.167}$$

where the decay constant is $k \approx 1 \times 10^{-2}$. Generally, the decay constant decreases with increasing black hole angular momentum. However, the total integrated energies are nearly identical for all $a \geq 0.998$. Figure 4.29 displays the integrated normalized energy densities for $a = 0, 0.8M, 0.98M, 0.998M$ and $a = M$ for $47.5 \leq t \leq 57.5$. The local maxima of the integrated energy densities for $a = 0.8M, 0.98M, 0.998M$ and $a = M$ at $t = 53.98$ are signals of superradiant scattering. From the data I deduce a lower estimate on the superradiant amplification in the amount of $\approx 0.05\%$ for $a = 0.8M$, $\approx 1.3\%$ for $a = 0.98M$ and $\approx 1.6\%$ for $a \geq 0.998M$. Observe how the largest value measured here is $\approx 1/3$ the maximal value of 4.4% calculated in the study of $s = 1$ perturbations by Teukolsky and Press [141]. Again, since perturbations are flowing out of the computational domain at the $r = 50$ outer boundary, a better estimate for the total superradiant amplification would also incorporate the energy flux through that surface. The superradiant amplification could thus be a couple percent larger than given by these lower estimates. For reference, Figure 4.30 displays the normalized energy density at the maximum of the superradiant scattering peak for the $a = M$ spacetime perturbations. The concentration of energy density in the plane $\theta = \pi/2$ within the ergosphere near the excision surface is markedly different from the case of scalar perturbations at $t = 53.98$ as depicted in Figure 4.18. Apart from the resonance and superradiant scattering amplitudes, the energy densities are quite similar for electromagnetic perturbation evolutions in $a = 0, 0.8M, 0.98M$ and $0.998M \leq a \leq M$ spacetimes.

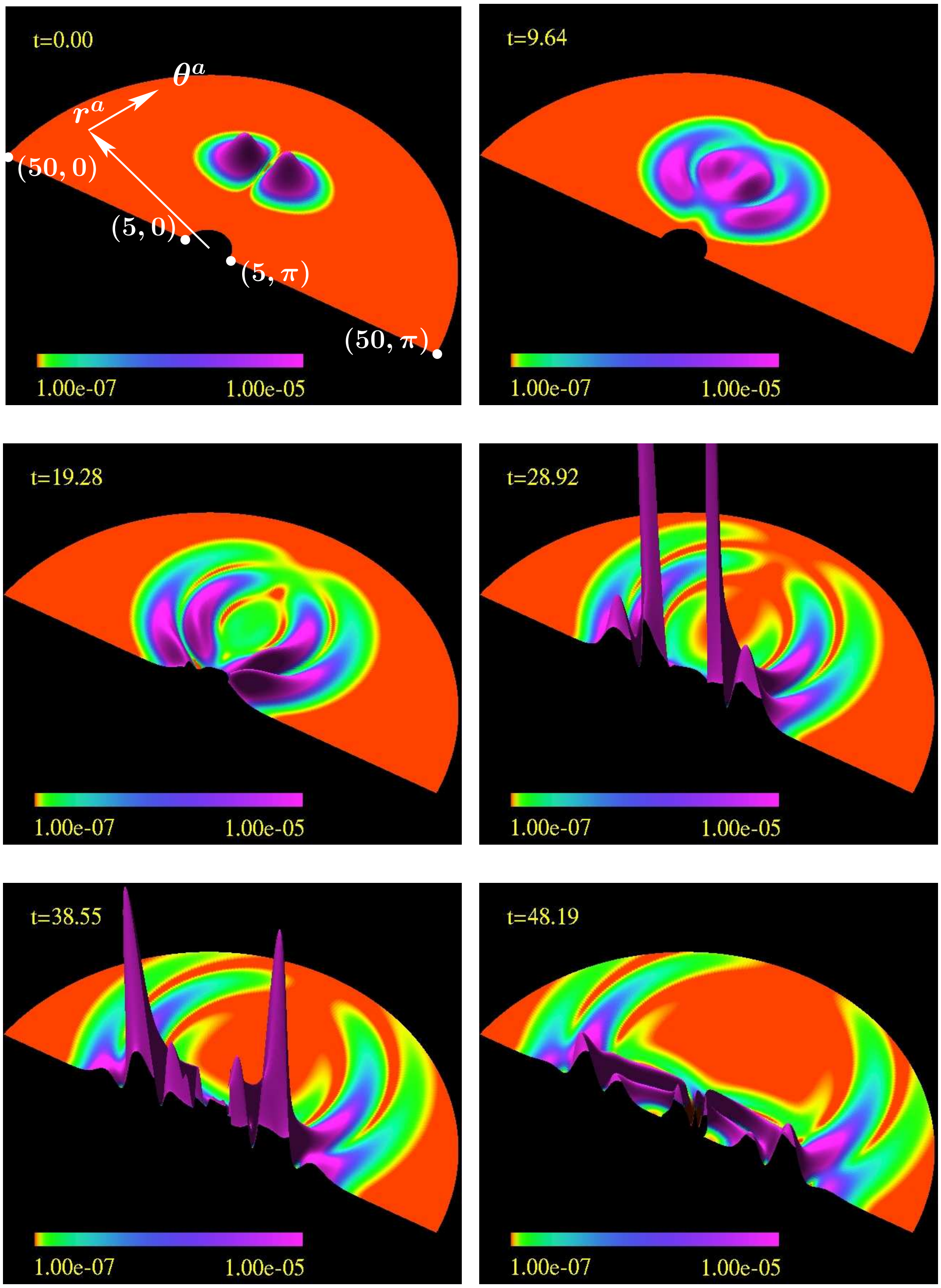

Figure 4.26: The glory effect and orbiting resonances for $a = M = 5$, electromagnetic perturbations. The figure displays the normalized energy density in a sequence of steps. The directions of coordinate vectors $r^a \sim (0, 1, 0, 0)$ and $\theta^a \sim (0, 0, 1, 0)$ are shown in the first frame. The computational domain covers the range $5 \leq r \leq 50$ and $0 \leq \theta \leq \pi$, and the corners of the domain are labelled with their (r, θ) ordinate values. The amplitude is scaled linearly, while the scale of the colour gradient is logarithmic.

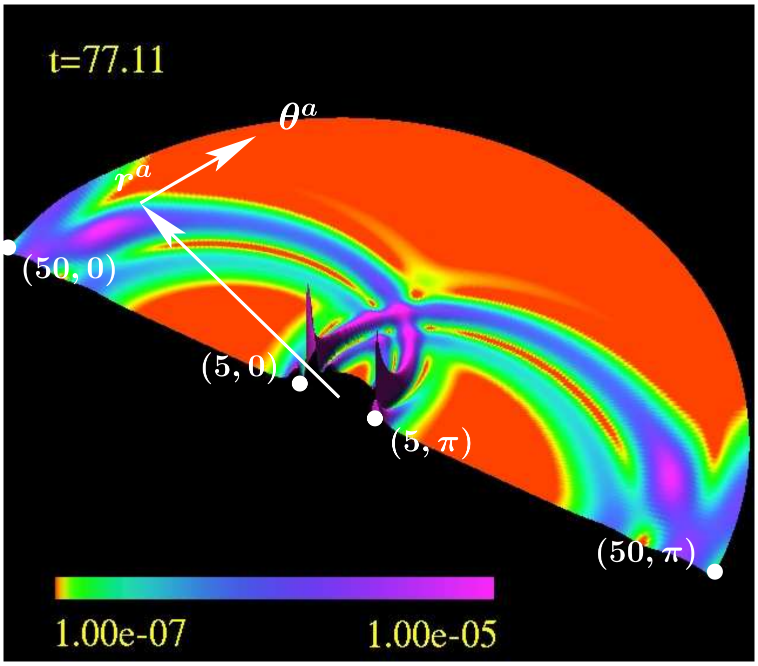

Figure 4.27: The glory effect and orbiting resonances for $a = M = 5$, electromagnetic perturbations at late time. The figure displays the normalized energy density at a final step of the evolution. The directions of coordinate vectors $r^a \sim (0, 1, 0, 0)$ and $\theta^a \sim (0, 0, 1, 0)$ are shown, the computational domain covers the range $5 \leq r \leq 50$ and $0 \leq \theta \leq \pi$, and the corners of the domain are labelled with their (r, θ) ordinate values. The amplitude is again scaled linearly and the colour gradient logarithmically. An MPEG animation showing orbiting resonance through normalized energy density for the $s = 1$ perturbations over period $0 \leq t \lesssim 108$ is available at `http://$WWW/People/petryk/animations/5.mpeg` where `$WWW` is currently `laplace.physics.ubc.ca` .

For an understanding of the magnetic and electric field dynamics, I compose the products $B_a B^a$ and $E_a E^a$ for the $a = M = 5$ spacetime evolution. Figure 4.31 displays the square of the magnetic field at times $t = 0$, 19.28, 38.55, 53.98, 57.83 and $t = 77.11$. Similarly, Figure 4.32 displays the square of the electric field at $t = 0$, 19.28, 38.55, 53.98, 57.83 and $t = 77.11$. Observe that while the $B_a B^a$ is essentially zero in the equatorial plane $\theta = \pi/2$ outside the ergoregion, the quantity $E_a E^a$ is not. This indicates that the energy density outside the ergosphere about the equatorial disk is carried predominantly by the electric field. Furthermore, the magnetic field amplitude is substantially smaller than the electric field amplitude along the axis of symmetry where $\theta = 0$ or $\theta = \pi$. However, note that, in curved spacetime, $E_a E^a$ and $B_a B^a$ are merely proportional to the contributions from electric and magnetic fields. The relationship between these squares and the energy density is only made an equality through inclusion of multiplicative factors that include metric components. Therefore, the sum of squares $\frac{1}{4}\left(E_a E^a + B_a B^a\right)$ is not generally a conserved quantity. The identification between this specific function and a conserved density can only be made in the exceptional case of flat spacetime. Furthermore, Figure 4.33 plots the integrated squares over the computational domain,

$$B^2 \equiv \int_{\phi=0}^{2\pi} \int_{\theta=0}^{\pi} \int_{r=5}^{50} B_a B^a \frac{\sqrt{g_{rr}}\left(g_{tr}^2 f_{\phi\phi} - g_{t\phi} f_{t\phi} g_{rr}\right)}{g_{tr}^2} dr d\theta d\phi \ , \tag{4.168}$$

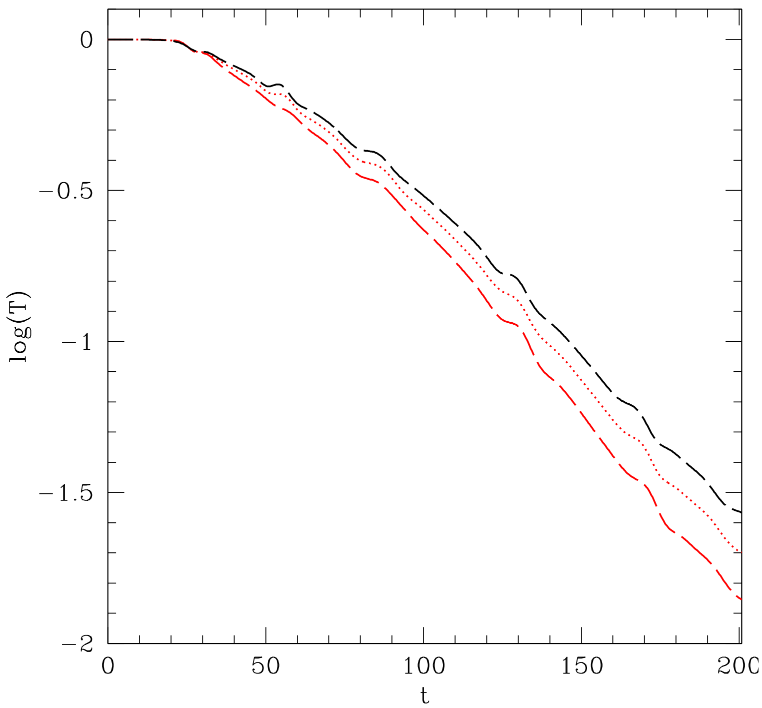

Figure 4.28: Integrated normalized energy density for electromagnetic perturbations in $M = 5$ Kerr spacetime. Plotted is $\log(T)$, the logarithm of the total energy contained within $5 \le r \le 50$, $0 \le \theta \le \pi$ and $0 \le \phi \le 2\pi$, as a function of coordinate time t. The dashed red line represents data for $a/M = 0$, the dotted red line data for $a/M = 0.8$, and the dashed black line data for $a/M = 1$. Clearly, black hole angular momentum decreases the overall decay rate of electromagnetic perturbations. Any decrease in time of the energy results from the flux across surfaces $r = 5$ and $r = 50$, and thus out of the computational domain.

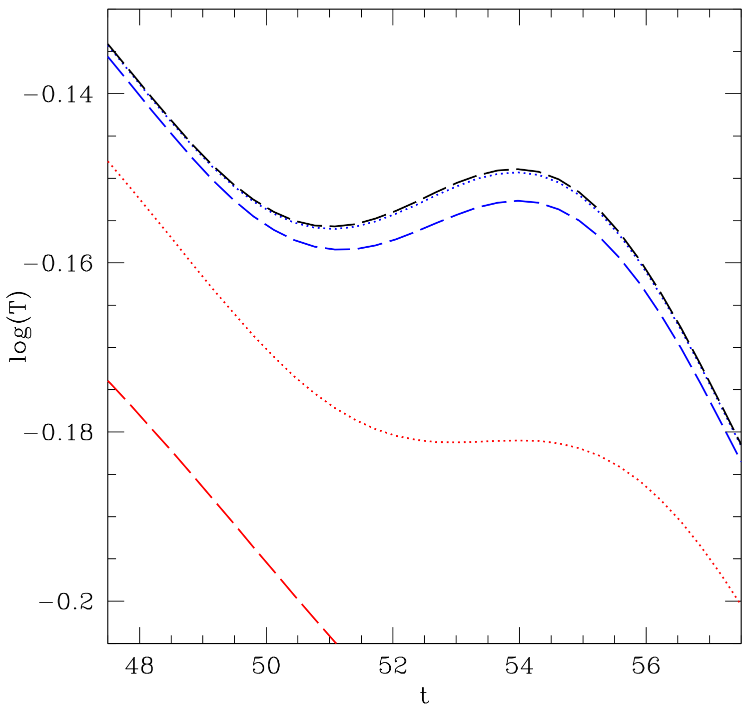

Figure 4.29: Integrated normalized energy density for electromagnetic perturbations in $M = 5$ Kerr spacetime. Plotted is $\log(T)$, the logarithm of the total energy contained within $5 \leq r \leq 50$, $0 \leq \theta \leq \pi$ and $0 \leq \phi \leq 2\pi$, as a function of coordinate time t. The dashed red line represents data for $a/M = 0$, the dotted red line data for $a/M = 0.8$, the dashed blue line data for $a/M = 0.98$, the dotted blue line (nearly coincident with the dashed black line) data for $a/M = 0.998$, and the dashed black line data for $a/M = 1$. The peaks in integrated energy densities at $t = 53.98$ for $a \geq 0.8M$ are a mark of superradiant scattering.

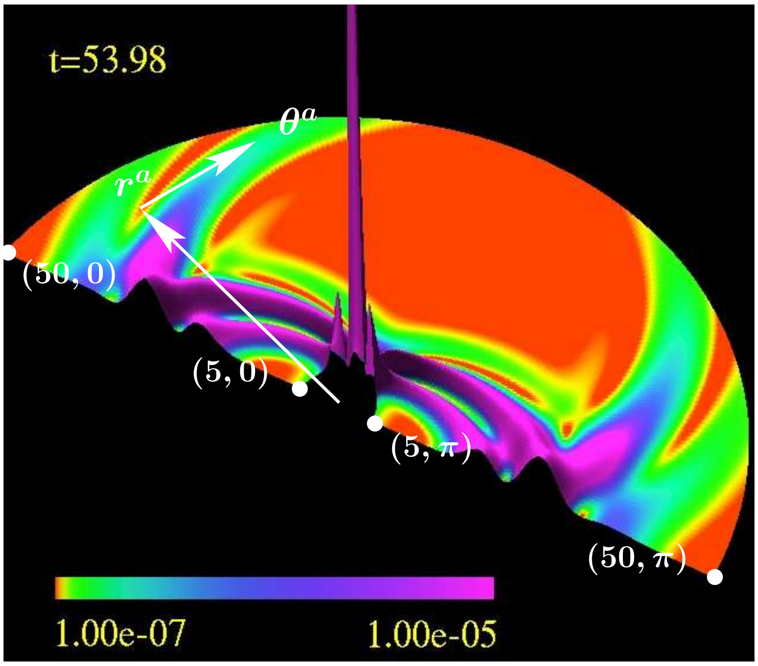

Figure 4.30: Normalized energy density at the superradiant scattering peak time $t = 53.98$ for electromagnetic perturbations in an $a = M = 5$ Kerr spacetime. The directions of coordinate vectors $r^a \sim (0, 1, 0, 0)$ and $\theta^a \sim (0, 0, 1, 0)$ are shown, the computational domain covers the range $5 \leq r \leq 50$ and $0 \leq \theta \leq \pi$, and the (r, θ) ordinate values at the domain corners are provided. The amplitude is scaled linearly and the colour gradient logarithmically. A concentration of energy density in the plane $\theta = \pi/2$ within the ergosphere near the excision surface is the manifestation of superradiant scattering.

and

$$E^2 \equiv \int_{\phi=0}^{2\pi} \int_{\theta=0}^{\pi} \int_{r=5}^{50} E_a E^a \frac{\sqrt{g_{rr}} \left(g_{tr}^2 f_{\phi\phi} - g_{t\phi} f_{t\phi} g_{rr} \right)}{g_{tr}^2} dr d\theta d\phi \ . \tag{4.169}$$

After an initial period of oscillation where magnetic fields convert to electric fields, and vice-versa, the integrated amplitudes become closely matched. At late time, the decay rates can be roughly approximated by the power laws

$$\log(B^2) \sim -kt \ , \tag{4.170}$$

and

$$\log(E^2) \sim -kt \ , \tag{4.171}$$

where $k \approx 1 \times 10^{-2}$ in both (4.170) and (4.171). Finally, except for the lack of superradiant amplification and even smaller $B_a B^a$ contribution along the axis of symmetry, evolution of $B_a B^a$ and $E_a E^a$ are very similar in the $a = 0$ and $a = M$ spacetimes. The integrated densities B^2 and E^2 are also similar in the cases $a = 0$ and $a = M$.

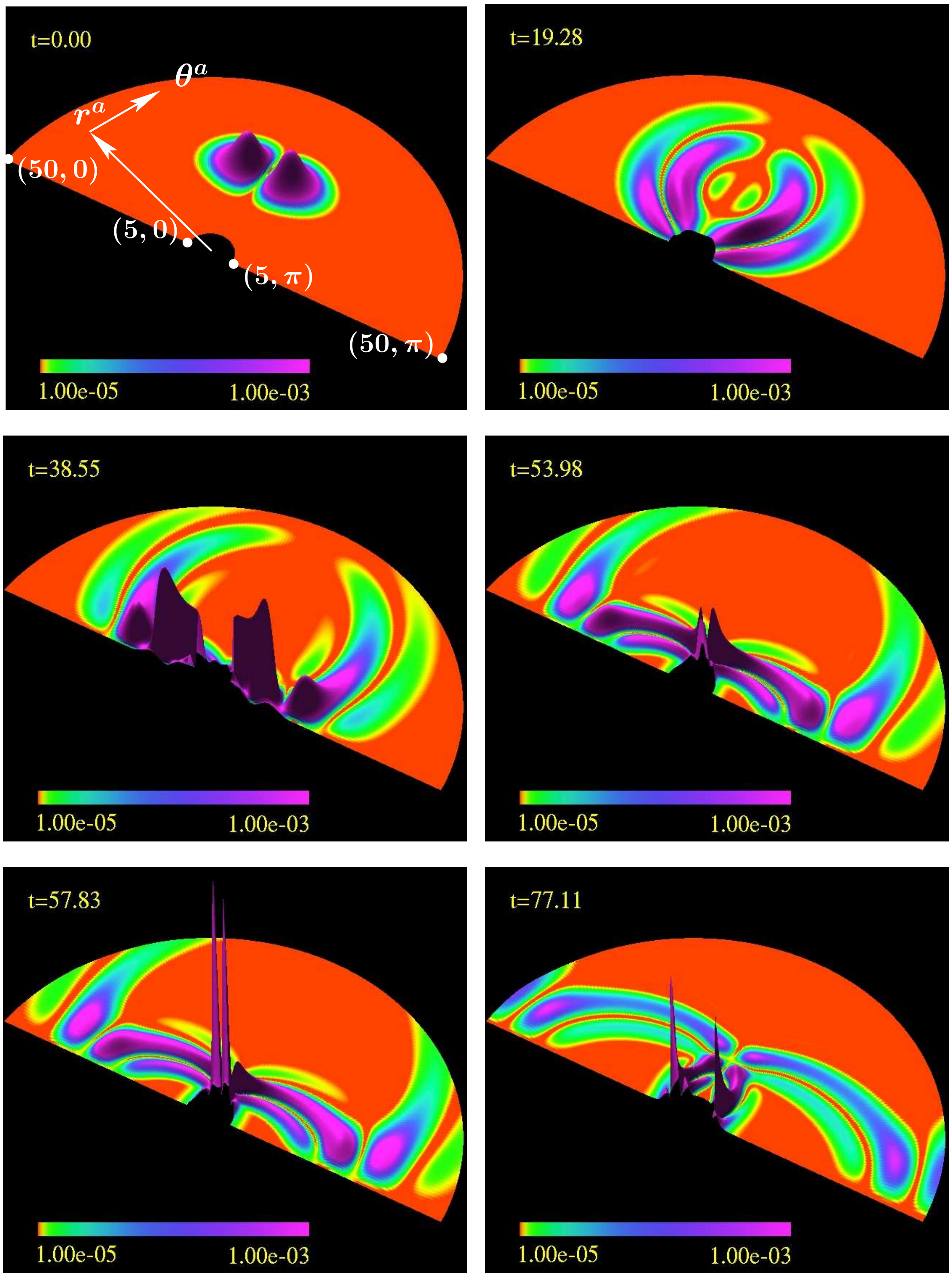

Figure 4.31: $B_a B^a$ for $a = M = 5$, electromagnetic perturbations. The figure displays the square of the magnetic field in a sequence of steps including the superradiant scattering peak at $t = 53.98$. The computational domain covers the range $5 \leq r \leq 50$ and $0 \leq \theta \leq \pi$, and the corners of the domain are labelled with their (r, θ) ordinate values. The amplitude is scaled linearly, while the scale of the colour gradient is logarithmic. The magnetic field amplitude is negligible outside the ergoregion in the plane $\theta = \pi/2$, and much smaller than the electric field along the axis of symmetry where $\theta = 0$ and $\theta = \pi$ (cf. Figure 4.32).

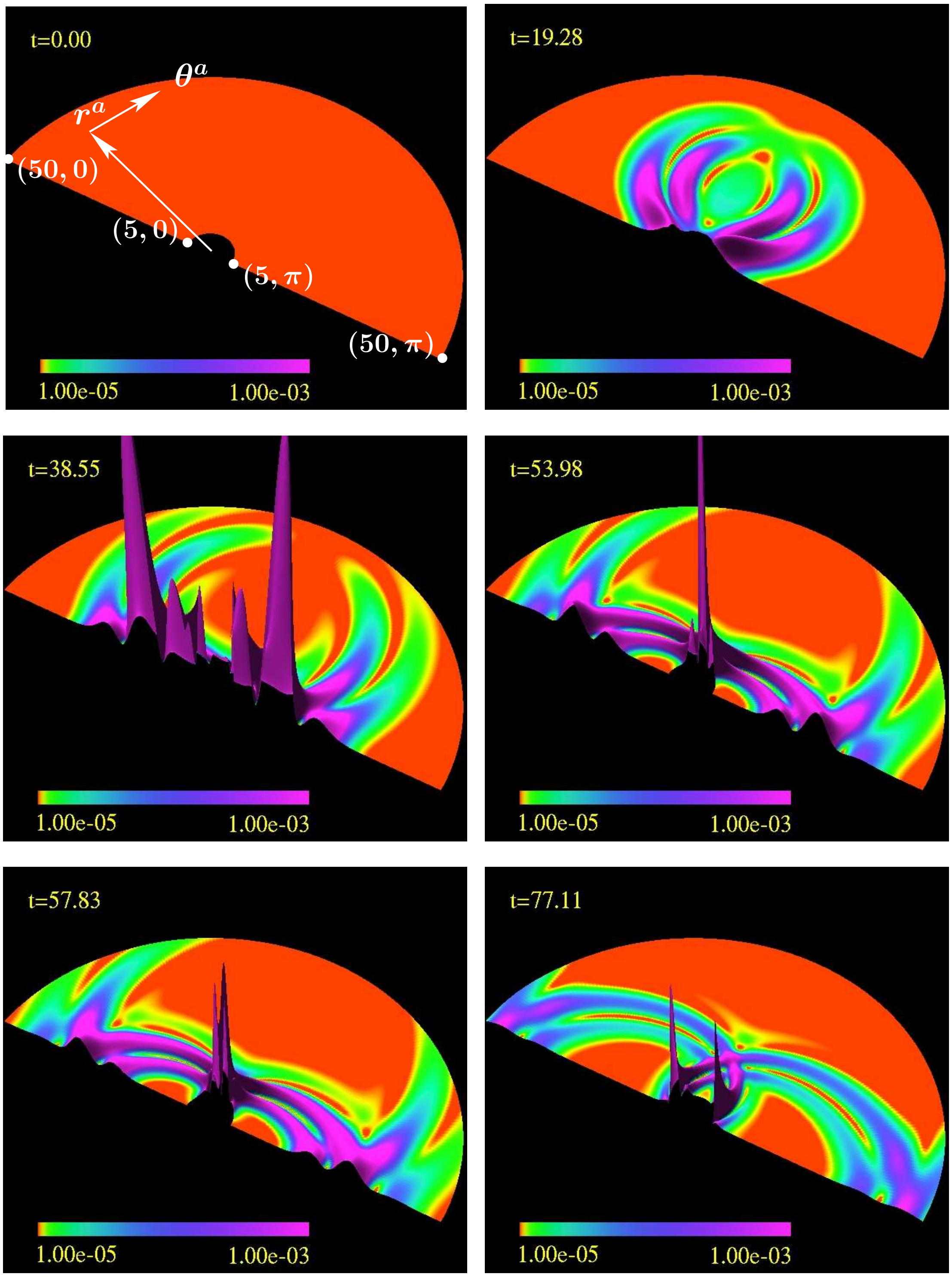

Figure 4.32: E_aE^a for $a = M = 5$, electromagnetic perturbations. The figure displays the square of the electric field in a sequence of steps including the superradiant scattering peak at $t = 53.98$. The directions of coordinate vectors $r^a \sim (0, 1, 0, 0)$ and $\theta^a \sim (0, 0, 1, 0)$ are shown in the first frame. The computational domain covers the range $5 \leq r \leq 50$ and $0 \leq \theta \leq \pi$, and the corners of the domain are labelled with their (r, θ) ordinate values. The amplitude is scaled linearly, while the scale of the colour gradient is logarithmic. The electric field amplitude is substantially larger than the magnetic field amplitude along the axis of black hole rotation (cf. Figure 4.31).

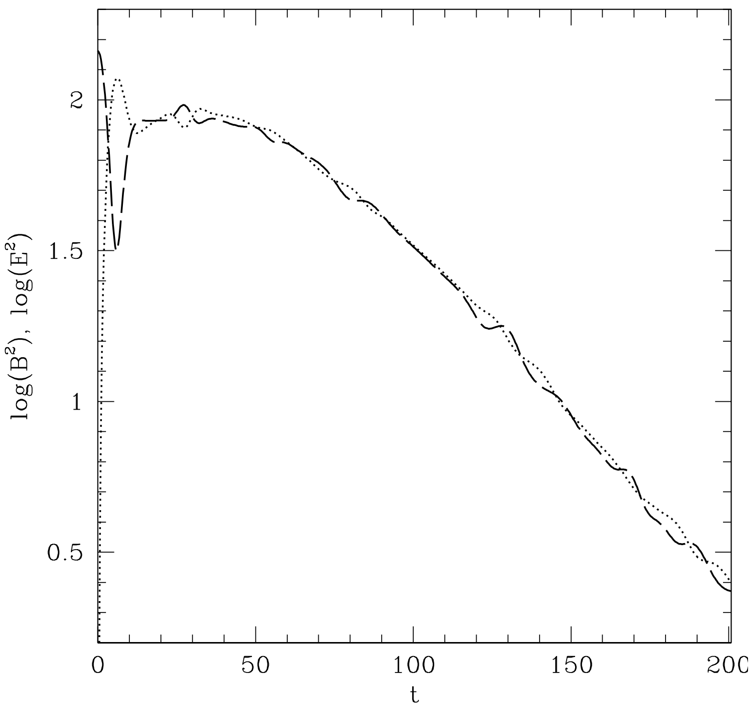

Figure 4.33: Integrated squares of electric and magnetic fields in $a = M = 5$ Kerr spacetime. Plotted are $\log(B^2)$ and $\log(E^2)$, the logarithm of the integrated squares contained within $5 \leq r \leq 50$, $0 \leq \theta \leq \pi$ and $0 \leq \phi \leq 2\pi$, as a function of coordinate time t. The dashed black line represents $\log(B^2)$, and the dotted black line $\log(E^2)$. Initially, the field amplitudes undergo substantial oscillation, but the decay of integrated electric and magnetic amplitudes become closely matched at intermediate and late time.

The effects of black hole rotation are more strongly manifest in the evolution of electromagnetic angular momentum. The angular momentum density for electromagnetic perturbations is given by equation (4.115). Figure 4.34 displays the evolution for $a = M$ in a sequence of steps, beginning at $t = 0$, and leading to the final displayed step at $t = 77.11$ in Figure 4.35.[14] Meanwhile, Figure 4.37 shows the evolution sequence for $a = 0$, leading to the final displayed frame in Figure 4.38. Observe how the $a = M$ density has much larger amplitude and steeper gradients than the $a = 0$ data. Furthermore, Figures 4.36 and 4.39 respectively display the angular momentum densities at the superradiant scattering peak time $t = 53.98$ for $a = M$ and $a = 0$. It is there evident how strongly the electromagnetic perturbation angular momentum is affected by the black hole rotation. Finally, Figure 4.40 shows the angular momentum density integrated over the computational domain as a function of time for the $M = 5$ spacetimes with $a = 0$, $a = 0.8M$ and $a = M$. Also, Figure 4.41 shows the integrated angular momentum for $a = 0, 0.8M, 0.98M, 0.998M$ and $a = M$ for $47.5 \leq t \leq 57.5$. Notice that, while highly variable for $a \geq 0.8M$ spacetimes, the total angular

[14]This nontrivial evolution of electromagnetic perturbation angular momentum introduces an interesting possibility for black hole formation. Namely, not only can black holes be formed from pure electromagnetic radiation, but such black holes can also carry angular momentum. This makes it possible to generically study black hole angular momentum scaling in critical phenomena at the threshold of black hole formation in both axial symmetry and in four dimensional spacetimes without symmetries.

momentum, S, tends towards $S = 0$.

In the standard picture of superradiant scattering, amplification of incident perturbations occurs at the expense of black hole rotational energy, and therefore at the expense of black hole angular momentum [151], [152], [153], [5], [101], [124], [137], [138] and [141]. A net flux of angular momentum should thus be observed from a black hole during superradiant scattering events. Figure 4.36 shows there is very large angular momentum density in the region of the event horizon and ergosphere, and negligible angular momentum density at the $r = 50$ outer boundary, when $t = 53.98$ in the $a = M = 5$ Kerr spacetime. Meanwhile, Figure 4.39 similarly shows negligible angular momentum density at the $r = 50$ domain boundary, and a small (but not insignificant) density near the event horizon at $t = 53.98$ in the $a = 0$, $M = 5$ spacetime. Any substantial changes of total angular momentum in these spacetimes around $t = 53.98$ will then be due to flux to or from the black hole itself. Figures 4.40 and 4.41 show marked increases in total angular momentum for the $0.8 \leq a/M \leq 1$, $M = 5$ spacetimes around $t = 53.98$, but insignificant change in angular momentum for the $a = 0$, $M = 5$ spacetime around the same period. But $t = 53.98$ is precisely the time when total electromagnetic energy within $r = 50$ in the $0.8 \leq a/M \leq 1$, $M = 5$ spacetimes show their largest increase in value (cf. Figure 4.29). Then, according to the standard picture, the marked increases of electromagnetic angular momentum around $t = 53.98$ in these spacetimes are the direct result of superradiant amplification drawn from the rotation of the black hole itself.

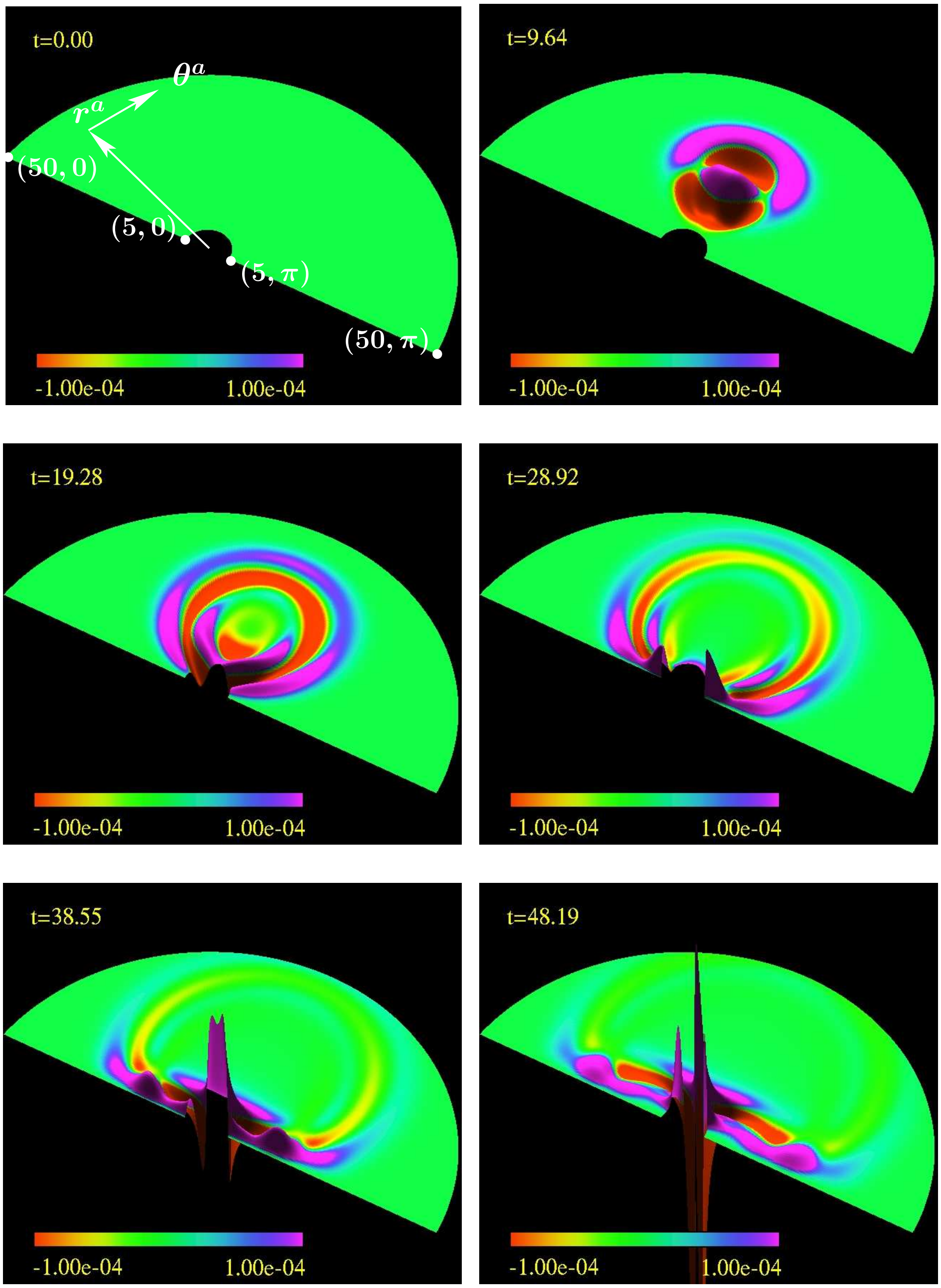

Figure 4.34: Angular momentum density for electromagnetic perturbations in $a = M = 5$ Kerr spacetime. The figure displays angular momentum density density in a sequence of steps. The directions of coordinate vectors $r^a \sim (0, 1, 0, 0)$ and $\theta^a \sim (0, 0, 1, 0)$ are shown in the first frame. The computational domain covers the range $5 \leq r \leq 50$ and $0 \leq \theta \leq \pi$, and the corners of the domain are labelled with their (r, θ) ordinate values. The amplitude and colour gradient are both scaled linearly.

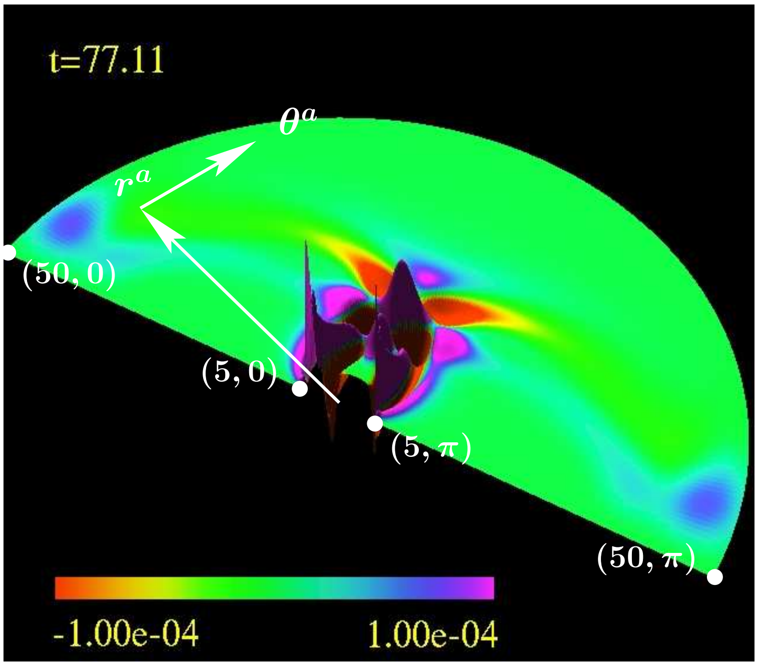

Figure 4.35: Angular momentum density for electromagnetic perturbations at late time in $a = M = 5$ Kerr spacetime. The figure displays angular momentum density density at a final step of the evolution. The directions of coordinate vectors $r^a \sim (0, 1, 0, 0)$ and $\theta^a \sim (0, 0, 1, 0)$ are shown, the computational domain covers the range $5 \leq r \leq 50$ and $0 \leq \theta \leq \pi$, and the corners of the domain are labelled with their (r, θ) ordinate values. The amplitude and colour gradient are again scaled linearly.

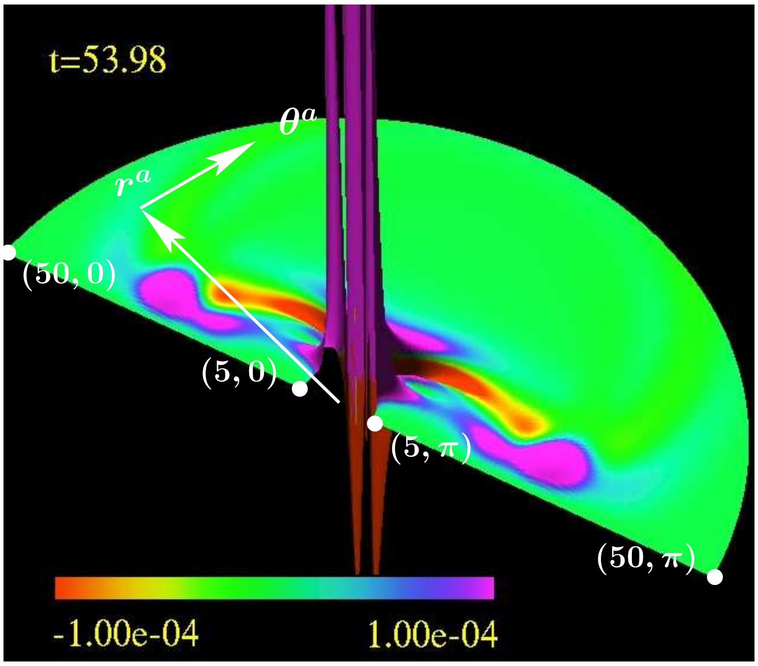

Figure 4.36: Angular momentum density for electromagnetic perturbations at superradiant scattering peak time $t = 53.98$ in $a = M = 5$ Kerr spacetime. The directions of coordinate vectors $r^a \sim (0, 1, 0, 0)$ and $\theta^a \sim (0, 0, 1, 0)$ are shown, the computational domain covers the range $5 \leq r \leq 50$ and $0 \leq \theta \leq \pi$, and the corners of the domain are labelled with their (r, θ) ordinate values. The amplitude and colour gradient are again scaled linearly.

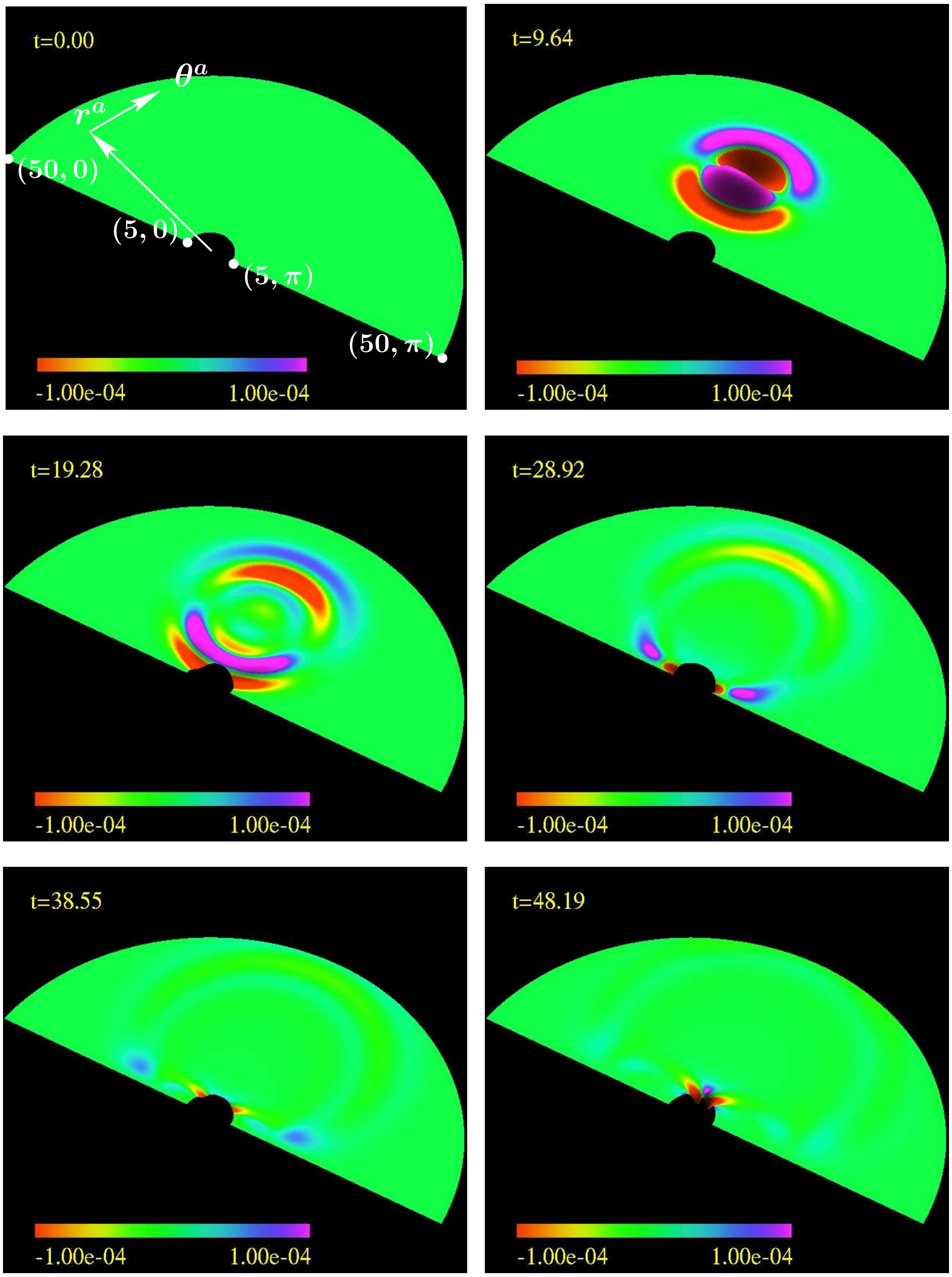

Figure 4.37: Angular momentum density for electromagnetic perturbations in $a = 0$, $M = 5$ Kerr spacetime. The figure displays angular momentum density density in a sequence of steps. Notice the general decay in electromagnetic angular momentum relative to that of the case $a = M$. The directions of coordinate vectors $r^a \sim (0, 1, 0, 0)$ and $\theta^a \sim (0, 0, 1, 0)$ are shown in the first frame. The computational domain covers the range $5 \leq r \leq 50$ and $0 \leq \theta \leq \pi$, and the corners of the domain are labelled with their (r, θ) ordinate values. The amplitude and colour gradient are both scaled linearly.

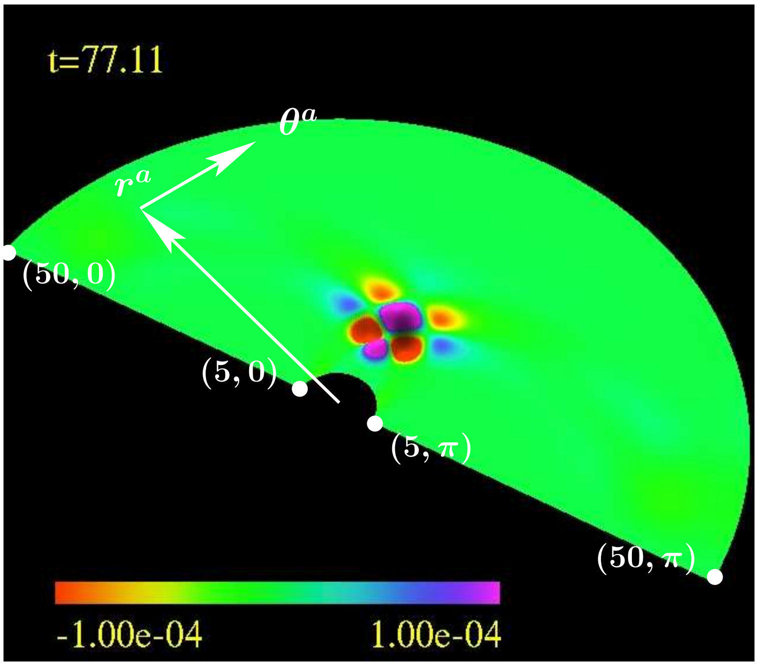

Figure 4.38: Angular momentum density for electromagnetic perturbations at late time in $a = 0$, $M = 5$ Kerr spacetime. The figure displays angular momentum density density at a final step of the evolution. Notice how the angular momentum density distribution here differs from that of the case $a = M$. The directions of coordinate vectors $r^a \sim (0, 1, 0, 0)$ and $\theta^a \sim (0, 0, 1, 0)$ are shown, the computational domain covers the range $5 \leq r \leq 50$ and $0 \leq \theta \leq \pi$, and the corners of the domain are labelled with their (r, θ) ordinate values. The amplitude and colour gradient are again scaled linearly.

4.3.4 Massless Maxwell-Klein-Gordon Equation Dynamics I: Orbiting Resonances, Charge Separation and Dynamo-Like Behaviour for $e = 0.6$ Electromagnetically Coupled $s = 0$ and $s = 1$ Perturbations

I again specify initial data according to section 4.3.1, but here I evolve $m_\Phi = 0.0$ electromagnetically coupled $s = 0$ and $s = 1$ perturbations on a Kerr spacetime by specifying nonzero charge coupling constant e. The black hole mass is set to $M = 5$, and the angular momentum per unit mass is again chosen somewhere in the range $a = 0$ through $a = M$. As before, the computational domain covers radial coordinate range $5 \leq r \leq 50$ and angular coordinates $0 \leq \theta \leq \pi$, but now resolutional requirements demand a computational domain with $J = 801$ radial points and $K = 401$ points in the θ angular direction. Because of the computational demands, these calculations were performed in parallel across 64 processors with processor overlap regions being 3 grid points wide. The numerical evolutions again span the range of coordinate time $0 \leq t \lesssim 200$. Since I choose the charge coupling parameter $e = 0.6$ in a following analysis of charged massive scalar fields, I focus discussion mostly on the $e = 0.6$ case but later compare these results to the evolution of both $e < 0.6$ and $e > 0.6$ coupling parameter data. In terms of physical electromagnetic fields, the chosen initial data again amounts to an everywhere vanishing electric field and a non-vanishing nontrivial magnetic field at $t = 0$. For the case $a = M$, the initial magnetic field components are distributed as shown in previous Figure 4.25. However, the coupling between scalar and electromagnetic fields now gives rise to a nontrivial four-current distribution at initial time. The nonlinear dynamics are

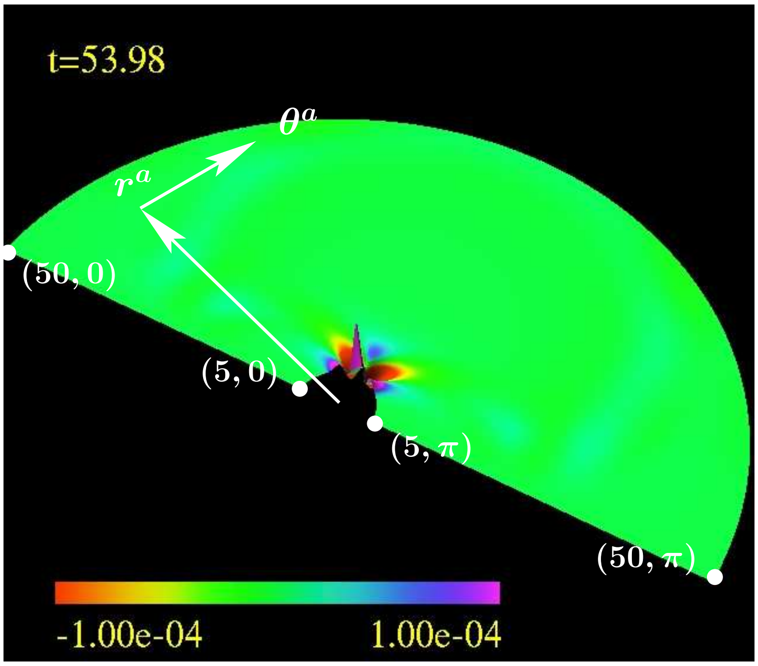

Figure 4.39: Angular momentum density for electromagnetic perturbations at $t = 53.98$ in $a = 0$, $M = 5$ Kerr spacetime. The density distribution has significantly smaller gradients than in the case $a = M$ The directions of coordinate vectors $r^a \sim (0, 1, 0, 0)$ and $\theta^a \sim (0, 0, 1, 0)$ are shown, the computational domain covers the range $5 \leq r \leq 50$ and $0 \leq \theta \leq \pi$, and the corners of the domain are labelled with their (r, θ) ordinate values. The amplitude and colour gradient are again scaled linearly.

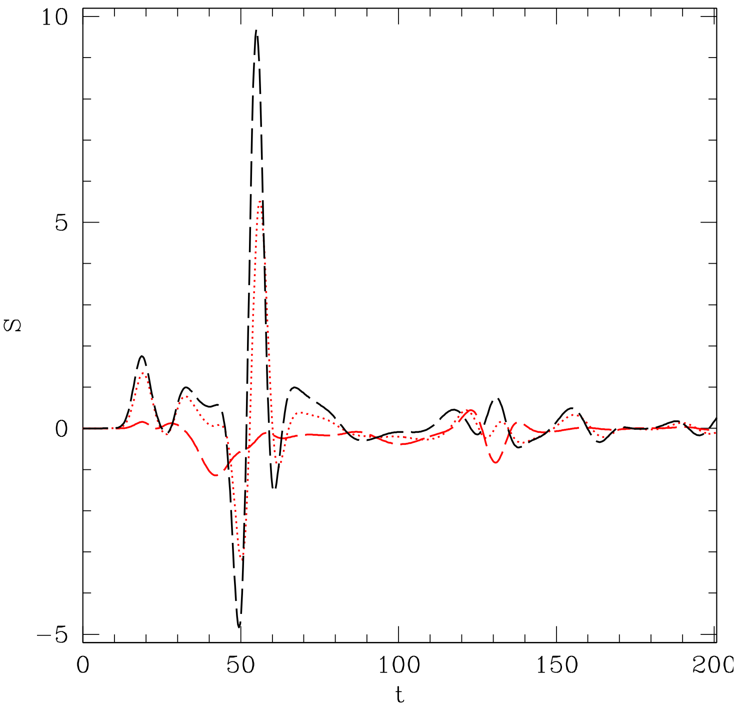

Figure 4.40: Integrated angular momentum density for electromagnetic perturbations in $M = 5$ Kerr spacetime. Plotted is S, the total angular momentum contained within $5 \leq r \leq 50$, $0 \leq \theta \leq \pi$ and $0 \leq \phi \leq 2\pi$, as a function of coordinate time t. The dashed red line represents data for $a/M = 0$, the dotted red line data for $a/M = 0.8$, and the dashed black line data for $a/M = 1$. Clearly, perturbation angular momentum is highly variable in rotating black hole spacetimes, but tends towards $S = 0$ at late time.

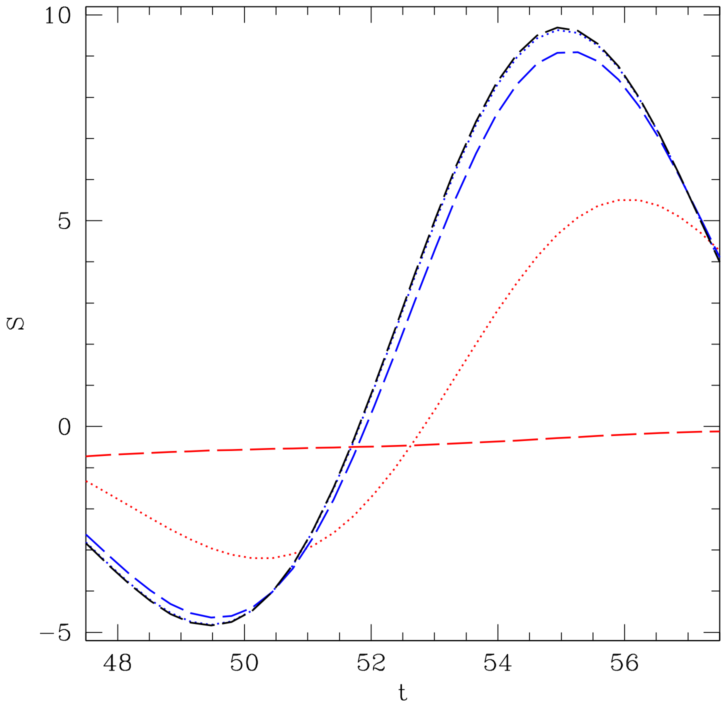

Figure 4.41: Integrated angular momentum density for electromagnetic perturbations in $M = 5$ Kerr spacetime. Plotted is S, the total angular momentum contained within $5 \leq r \leq 50$, $0 \leq \theta \leq \pi$ and $0 \leq \phi \leq 2\pi$, as a function of coordinate time t. The dashed red line represents data for $a/M = 0$, the dotted red line data for $a/M = 0.8$, the dashed blue line data for $a/M = 0.98$, the dotted blue line (nearly coincident with the dashed black line) data for $a/M = 0.998$, and the dashed black line data for $a/M = 1$. The differences between $a = 0$ and $a > 0$ data are significant.

rather detailed as discussed below. In addition to orbiting resonances, I find the electromagnetically coupled fields display both charge separation and dynamo-like behaviour.

Starting with $e = 0.6$, $a = M = 5$ initial data, the total normalized energy within the computational domain is displayed as a sequence of steps starting at $t = 0$ in Figure 4.42 with a final displayed time at $t = 77.11$ as shown in Figure 4.43. Gravitational interaction in the form of orbiting resonances are again observed, and the resonance period is again $\approx 70t$, corresponding to an orbital frequency more than twice that the unstable circular photon orbit at $r = 3M$ (cf. equation (4.164) and related discussion). Furthermore, the attenuation between the first two successive orbits is again $\sim 10^{-1}$. Mode trapping is not apparent and neither is superradiant scattering[15]. Figure 4.44 shows the total normalized energy within the computational domain for $0 \leq t \lesssim 150$ for $a = 0, 0.8M$ and $a = M$ spacetimes.[16] It is there apparent how black hole angular momentum decreases the decay rate of electromagnetically coupled perturbations. Furthermore, at late time, the decay of perturbations in the $a = M$ spacetime can be approximated as the power law

$$\log(T) \sim -kt \ , \tag{4.172}$$

with decay constant $k \approx 1 \times 10^{-2}$, similar to the cases of $s = 1$ and massless $s = 0$ perturbations. The evolution of energy densities are otherwise similar in the $a = 0, 0.8M$ and $a = M$ spacetimes.

[15] Again, while this test does not compensate for flux lost through the outer boundary $r = 50$, some superradiant amplification could still be present

[16] While the evolution was extended to $t \approx 200$, a very slowly growing instability is manifest some time after $t = 175$ at $r = 50$ for cases $a = 0.8M$ and $a = M$. I therefore limit examination to the shorter time interval.

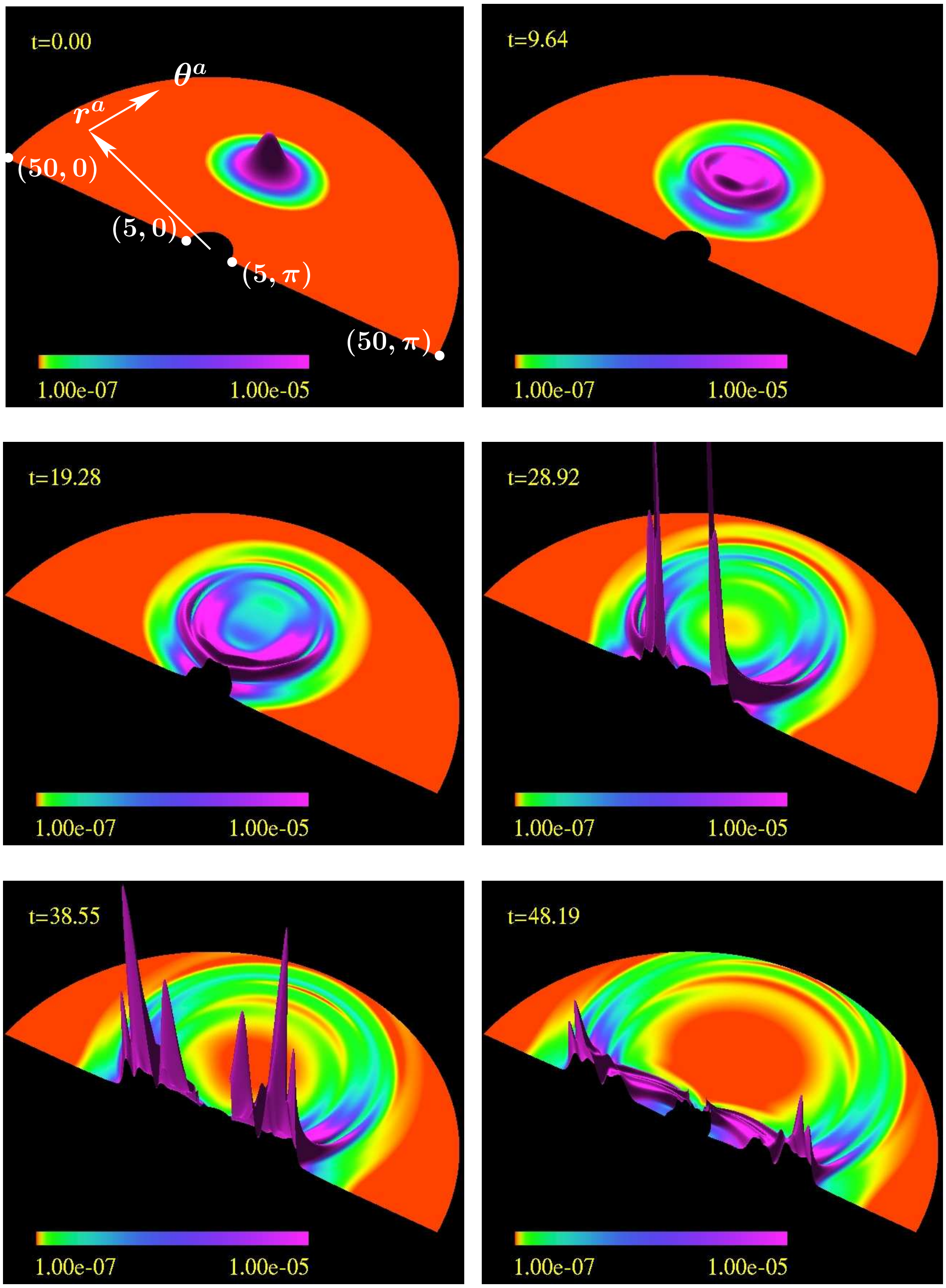

Figure 4.42: The glory effect and orbiting resonances for $a = M = 5$, $m_\Phi = 0.0$, $e = 0.6$ coupled perturbations. The figure displays the total normalized energy density in a sequence of steps. The directions of coordinate vectors $r^a \sim (0, 1, 0, 0)$ and $\theta^a \sim (0, 0, 1, 0)$ are shown in the first frame. The computational domain covers the range $5 \leq r \leq 50$ and $0 \leq \theta \leq \pi$, and the corners of the domain are labelled with their (r, θ) ordinate values. The amplitude is scaled linearly, while the scale of the colour gradient is logarithmic.

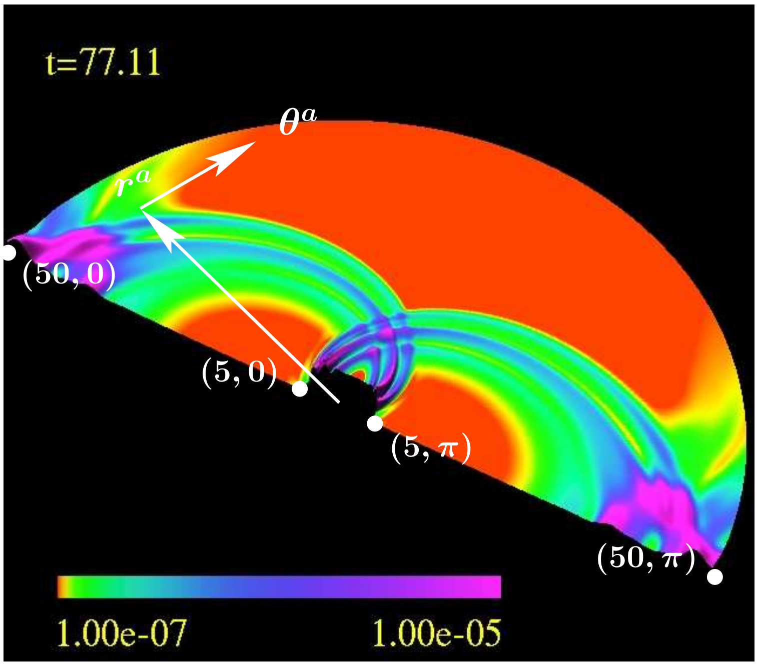

Figure 4.43: The glory effect and orbiting resonances for $a = M = 5$, $m_\Phi = 0.0$, $e = 0.6$ coupled perturbations at late time. The figure displays the total normalized energy density at a final step of the evolution. The directions of coordinate vectors $r^a \sim (0, 1, 0, 0)$ and $\theta^a \sim (0, 0, 1, 0)$ are shown, the computational domain covers the range $5 \leq r \leq 50$ and $0 \leq \theta \leq \pi$, and the corners of the domain are labelled with their (r, θ) ordinate values. The amplitude is again scaled linearly and the colour gradient logarithmically.

According to equations (4.109) through (4.113), the total conserved energy density can be decomposed into two terms independent of couping parameter e plus one dependent on e. The e-independent terms are the energy density of purely scalar contributions, $\rho_{T(\Phi)}$, and the energy density of purely electromagnetic field contributions, $\rho_{T(A)}$. The e-dependent term, $\rho_{T(\Phi A)}$, couples the scalar and electromagnetic fields. While the total

$$\rho_T = \rho_{T(\Phi)} + \rho_{T(A)} + \rho_{T(\Phi A)} \tag{4.173}$$

is a conserved quantity, the individual components are not. In fact, the coupling term $\rho_{T(\Phi A)}$ isn't even strictly positive in flat spacetime. Figures 4.45. 4.46, and 4.47 respectively depict sequences of evolution of $\rho_{T(\Phi)}$, $\rho_{T(A)}$ and $\rho_{T(\Phi A)}$. Observe how the purely scalar contribution is the dominant contributor for the displayed phase of evolution. Also note how purely electromagnetic contributions increase rapidly at very early time and then remain fairly large in amplitude for the remaining evolution. Furthermore, the coupling term $\rho_{T(\Phi A)}$ is small in amplitude throughout evolution, except along $\theta = 0$ and $\theta = \pi$ at the time when perturbations first scatter off the steep gravitational potential near the black hole event horizon. Figure 4.48 displays the total normalized energy contained in the computational domain, T, and also the three components $T(\Phi)$, $T(A)$, and $T(\Phi A)$ contributing to the total. It is there apparent that $T(\Phi)$ is the dominant contributor until $t \approx 90$, after which $T(A)$ dominates. It is also clear that $T(\Phi A)$ is sometimes positive, and at other times negative. Finally, there appears to be a strong correlation between $T(\Phi)$ and $T(\Phi A)$ during the period $20 \lesssim t \lesssim 40$, corresponding to the first perturbation scattering from the steep

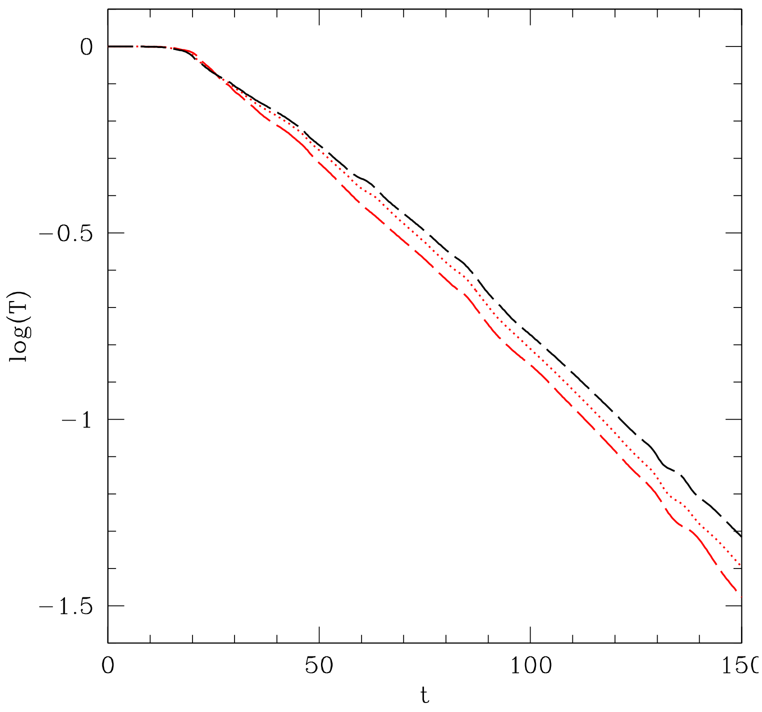

Figure 4.44: Integrated normalized energy density for $e = 0.6$ coupled massless perturbations in $M = 5$ Kerr spacetime. Plotted is $\log(T)$, the logarithm of the total energy contained within $5 \leq r \leq 50$, $0 \leq \theta \leq \pi$ and $0 \leq \phi \leq 2\pi$, as a function of coordinate time t. The dashed red line represents data for $a/M = 0$, the dotted red line data for $a/M = 0.8$, and the dashed black line data for $a/M = 1$. Clearly, black hole angular momentum decreases the overall decay rate of electromagnetic perturbations. Any decrease in time of the energy results from the flux across surfaces $r = 5$ and $r = 50$, and thus out of the computational domain.

gravitational potential. The correlation between the electromagnetic component $T(A)$ and $T(\Phi A)$ appears to be rather weak during this event.

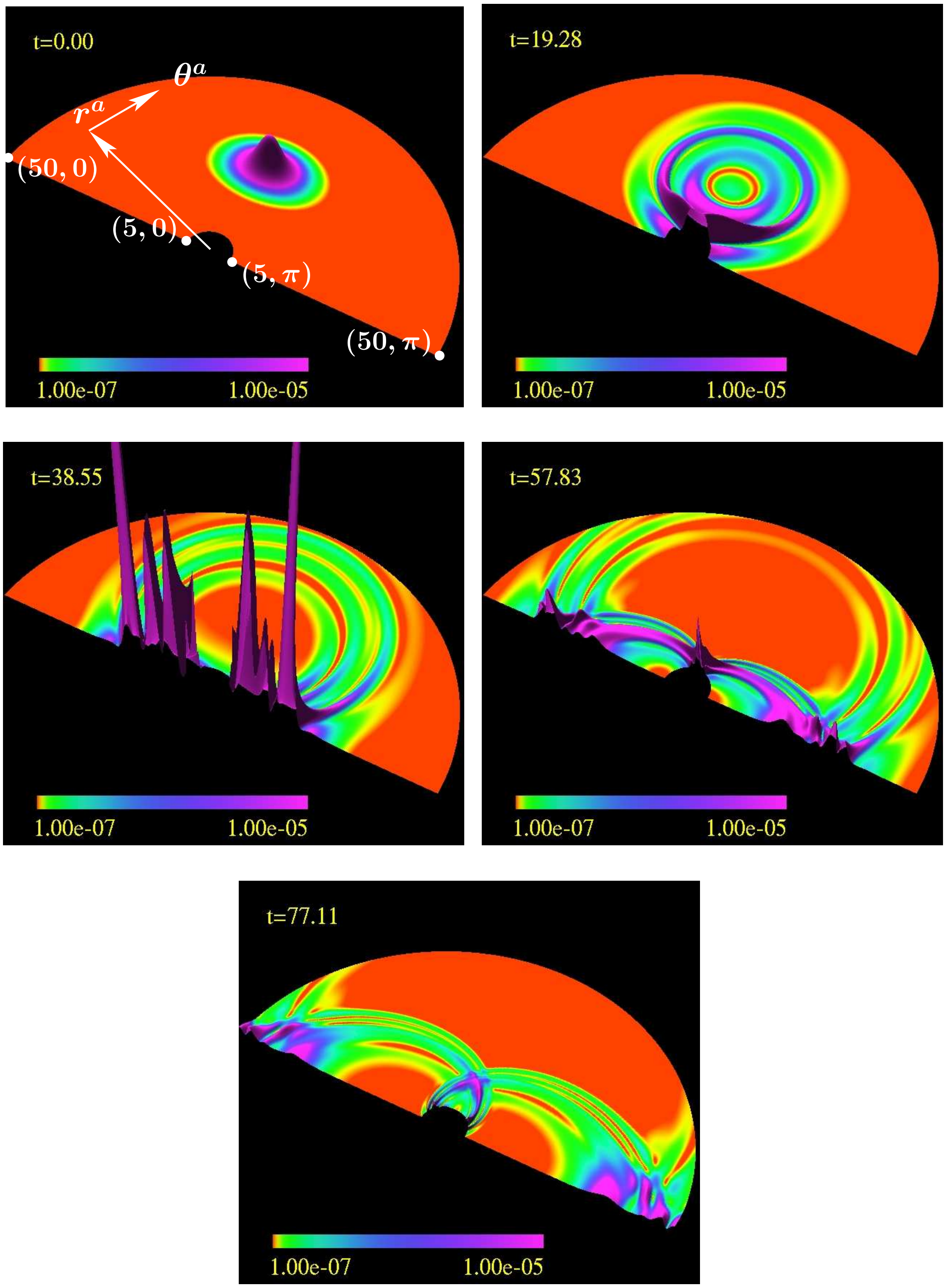

Figure 4.45: Evolution of the scalar contribution to the total energy for $a = M = 5$, $m_\Phi = 0.0$, $e = 0.6$ coupled perturbations. The figure displays the normalized scalar contribution to the energy density in a sequence of steps. The directions of coordinate vectors $r^a \sim (0, 1, 0, 0)$ and $\theta^a \sim (0, 0, 1, 0)$ are shown in the first frame. The computational domain covers the range $5 \leq r \leq 50$ and $0 \leq \theta \leq \pi$, and the corners of the domain are labelled with their (r, θ) ordinate values. The amplitude is scaled linearly, while the scale of the colour gradient is logarithmic.

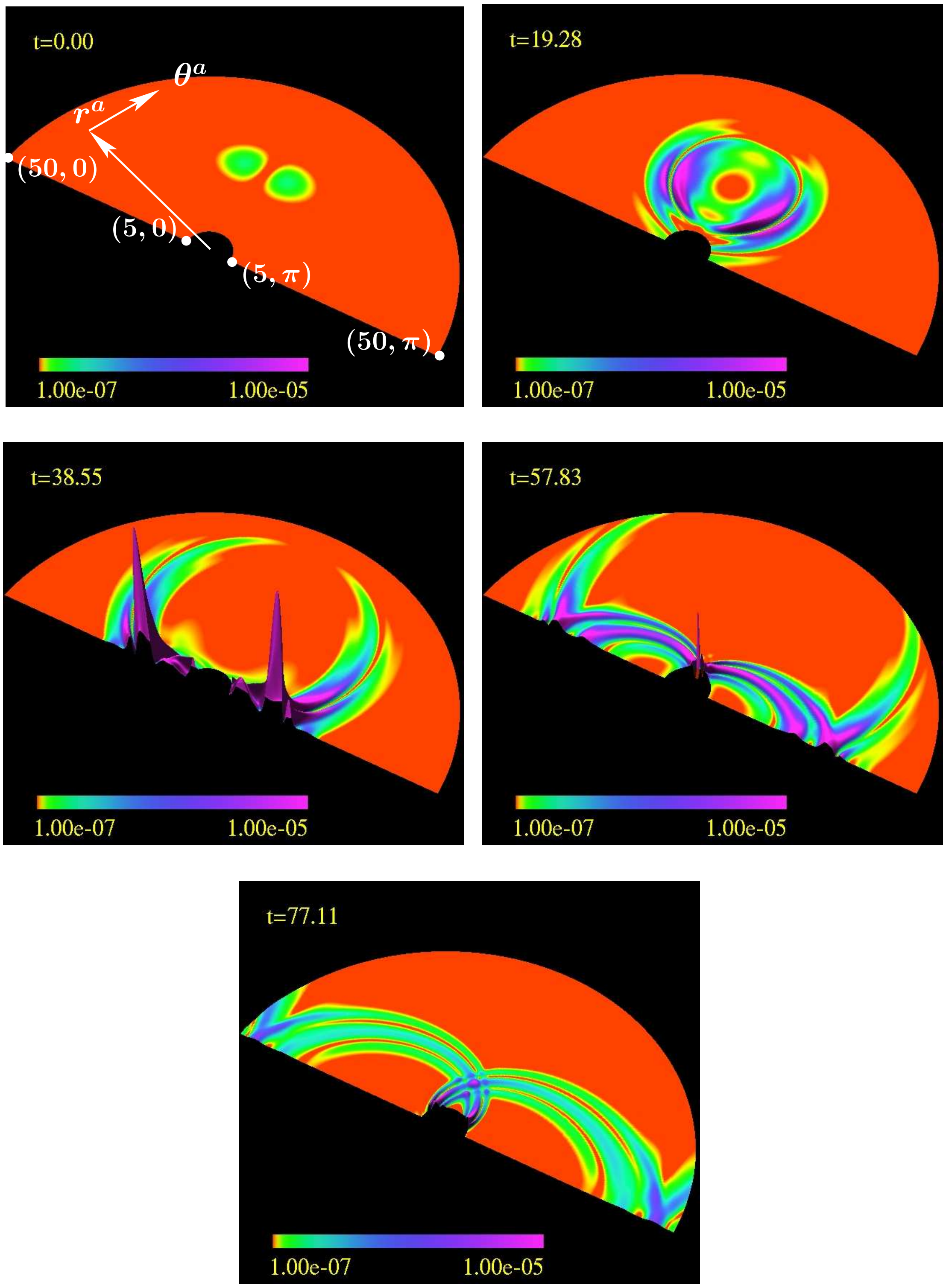

Figure 4.46: Evolution of the electromagnetic contribution to the total energy for $a = M = 5$, $m_\Phi = 0.0$, $e = 0.6$ coupled perturbations. The figure displays the normalized electromagnetic contribution to the energy density in a sequence of steps. The directions of coordinate vectors $r^a \sim (0, 1, 0, 0)$ and $\theta^a \sim (0, 0, 1, 0)$ are shown in the first frame. The computational domain covers the range $5 \leq r \leq 50$ and $0 \leq \theta \leq \pi$, and the corners of the domain are labelled with their (r, θ) ordinate values. The amplitude is scaled linearly, while the scale of the colour gradient is logarithmic.

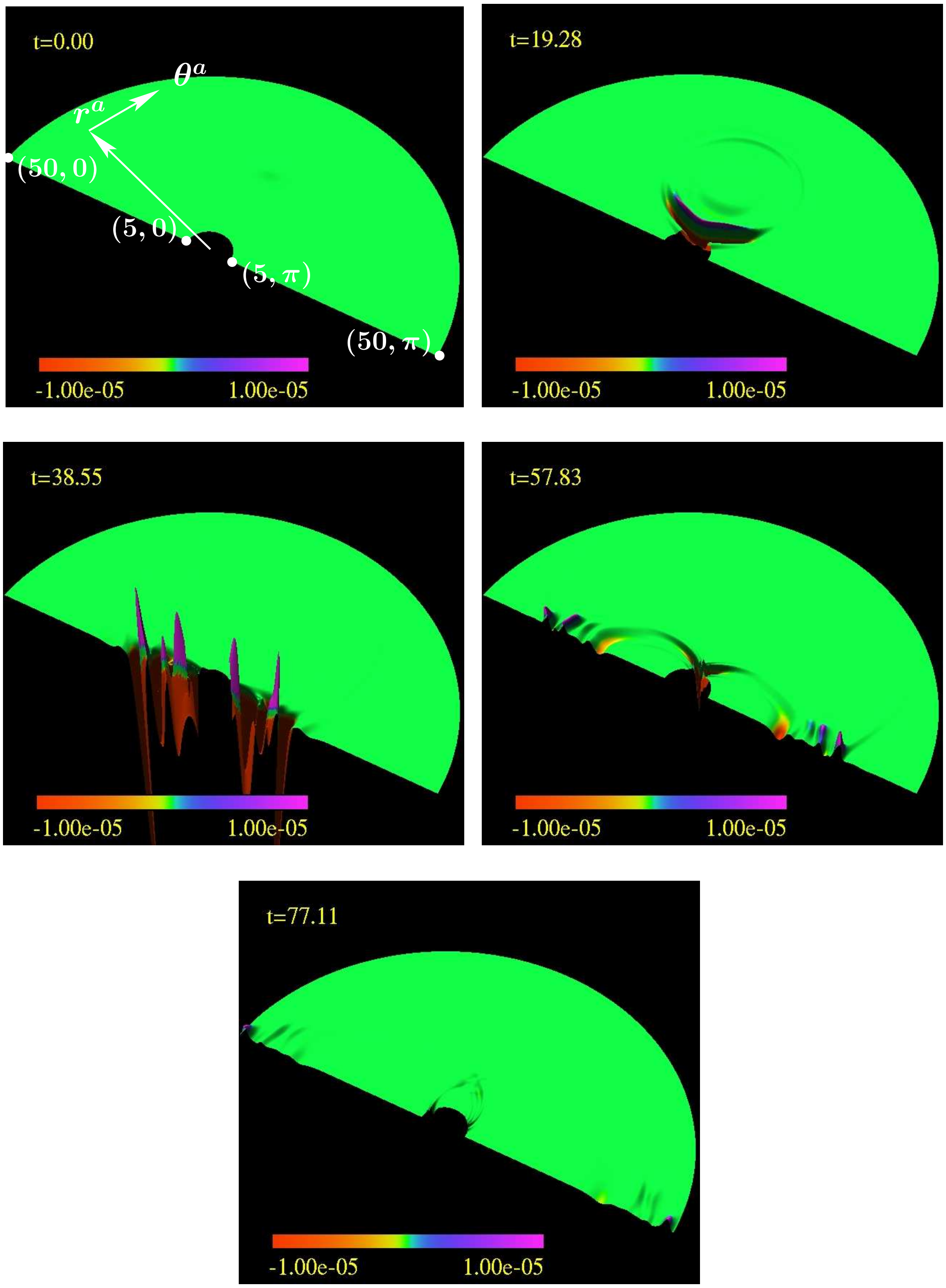

Figure 4.47: Evolution of the coupling terms contributing to the total energy for $a = M = 5$, $m_\Phi = 0.0$, $e = 0.6$ perturbations. The figure displays the normalized coupling contribution to the energy in a sequence of steps. The directions of coordinate vectors $r^a \sim (0, 1, 0, 0)$ and $\theta^a \sim (0, 0, 1, 0)$ are shown in the first frame. The computational domain covers the range $5 \leq r \leq 50$ and $0 \leq \theta \leq \pi$, and the corners of the domain are labelled with their (r, θ) ordinate values. The amplitude is scaled linearly, while the scale of the colour gradient is logarithmic.

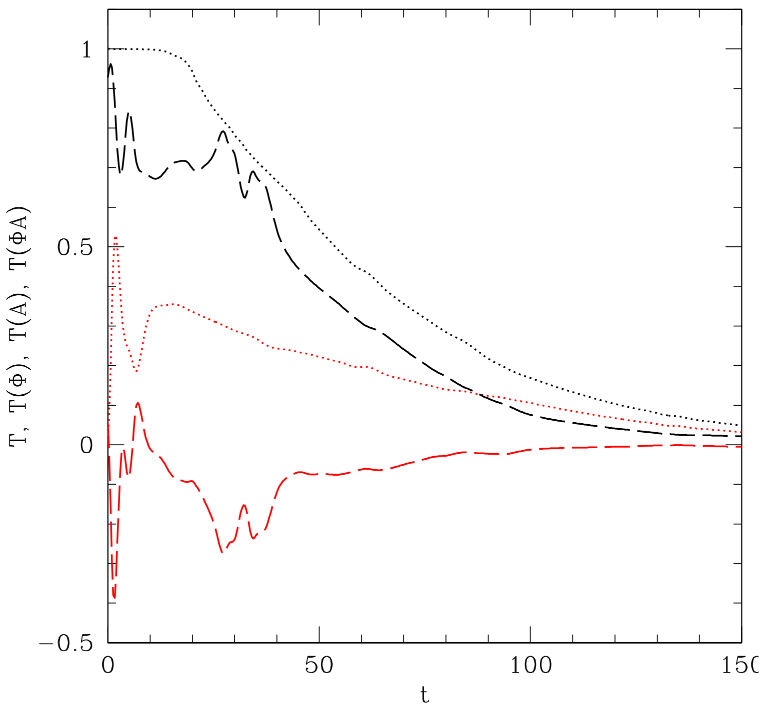

Figure 4.48: Decomposition of integrated normalized energy density for $e = 0.6$ coupled massless perturbations in $a = M = 5$ Kerr spacetime. Plotted are the total energy and contributions to the total contained within $5 \leq r \leq 50$, $0 \leq \theta \leq \pi$ and $0 \leq \phi \leq 2\pi$, as a function of coordinate time t. The dotted black line represents the total normalized energy, the dashed black line represents the normalized scalar field contribution, the dotted red line is the normalized electromagnetic contribution and the dashed red line the normalized contribution from electromagnetic coupling terms.

I again analyze the magnetic and electric field dynamics through analysis of $B_a B^a$ and $E_a E^a$. Figure 4.49 displays $B_a B^a$, while Figure 4.50 shows $E_a E^a$. As in the case of pure electromagnetic perturbations, the magnetic field norm is substantially smaller than that of the electric field in the equatorial plane ($\theta = \pi/2$) and along the axis of symmetry ($\theta = 0$ and $\theta = \pi$). The integrals of these norms are displayed in Figure 4.51. After undergoing substantial change at early time, these integrated amplitudes become comparable and very roughly decay according to

$$\log(B^2) \sim -kt \ , \tag{4.174}$$

and

$$\log(E^2) \sim -kt \ , \tag{4.175}$$

where $k \approx 1 \times 10^{-2}$ similar to the case of pure electromagnetic perturbations. Finally, the evolution of $B_a B^a$ and $E_a E^a$ are qualitatively very similar in both $a = 0$ and $a = M$ spacetimes.

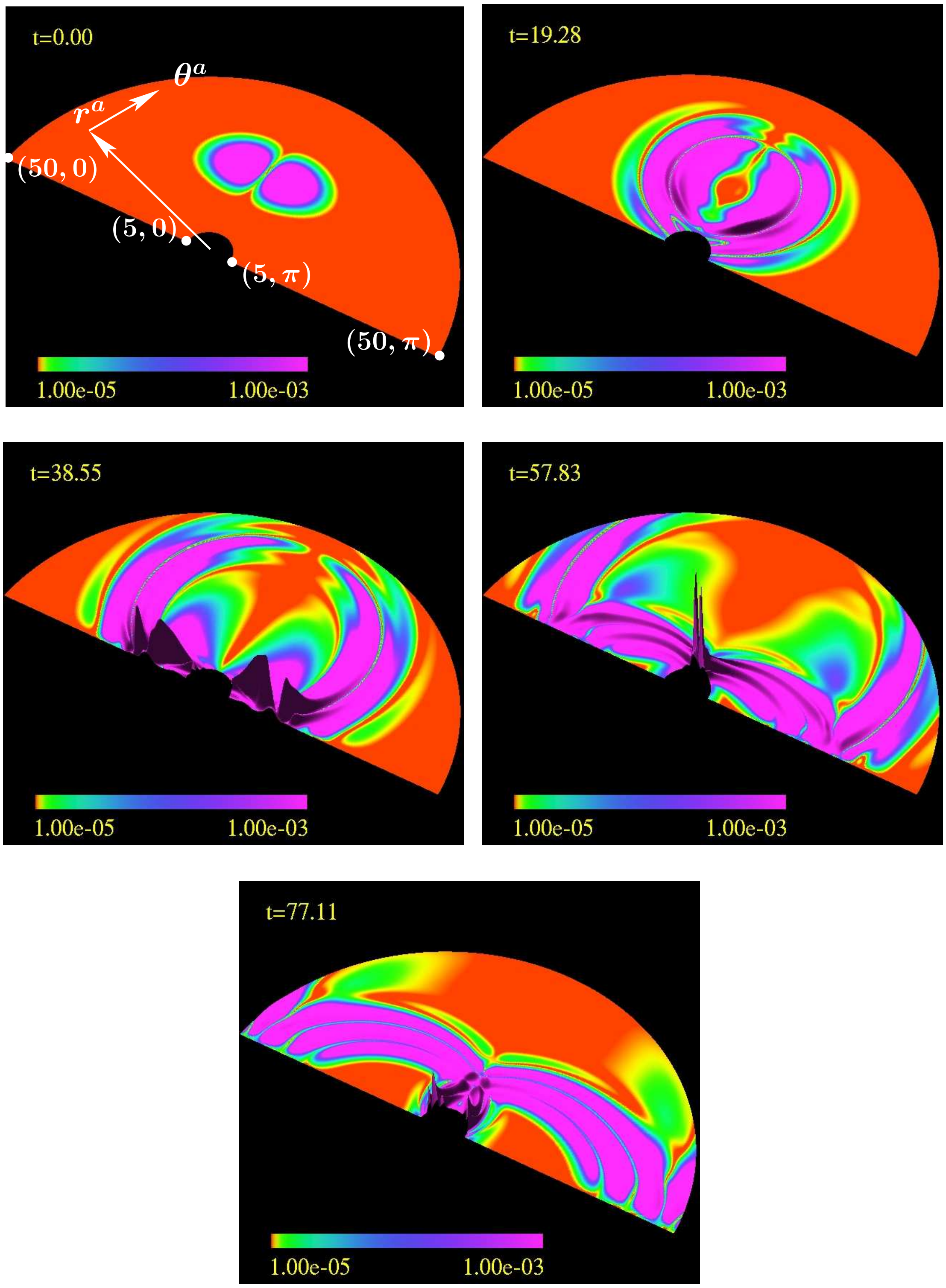

Figure 4.49: $B_a B^a$ for $a = M = 5$, $e = 0.6$ coupled perturbations. The figure displays the square of the magnetic field in a sequence of steps. The directions of coordinate vectors $r^a \sim (0, 1, 0, 0)$ and $\theta^a \sim (0, 0, 1, 0)$ are shown in the first frame. The computational domain covers the range $5 \leq r \leq 50$ and $0 \leq \theta \leq \pi$, and the corners of the domain are labelled with their (r, θ) ordinate values. The amplitude is scaled linearly, while the scale of the colour gradient is logarithmic. The magnetic field amplitude is negligible outside the ergoregion in the plane $\theta = \pi/2$.

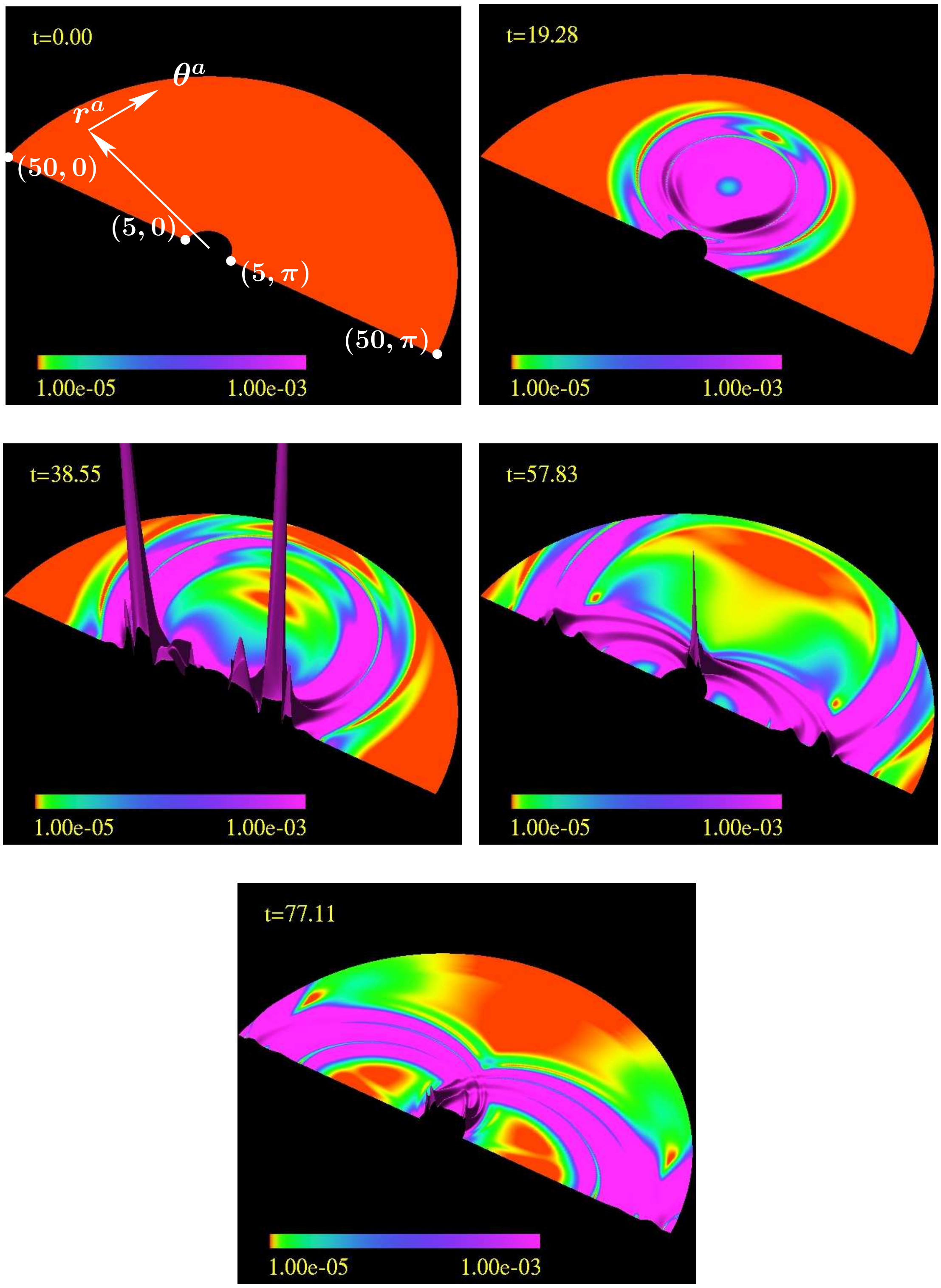

Figure 4.50: $E_a E^a$ for $a = M = 5$, $e = 0.6$ coupled perturbations. The figure displays the square of the electric field in a sequence of steps. The directions of coordinate vectors $r^a \sim (0, 1, 0, 0)$ and $\theta^a \sim (0, 0, 1, 0)$ are shown in the first frame. The computational domain covers the range $5 \leq r \leq 50$ and $0 \leq \theta \leq \pi$, and the corners of the domain are labelled with their (r, θ) ordinate values. The amplitude is scaled linearly, while the scale of the colour gradient is logarithmic.

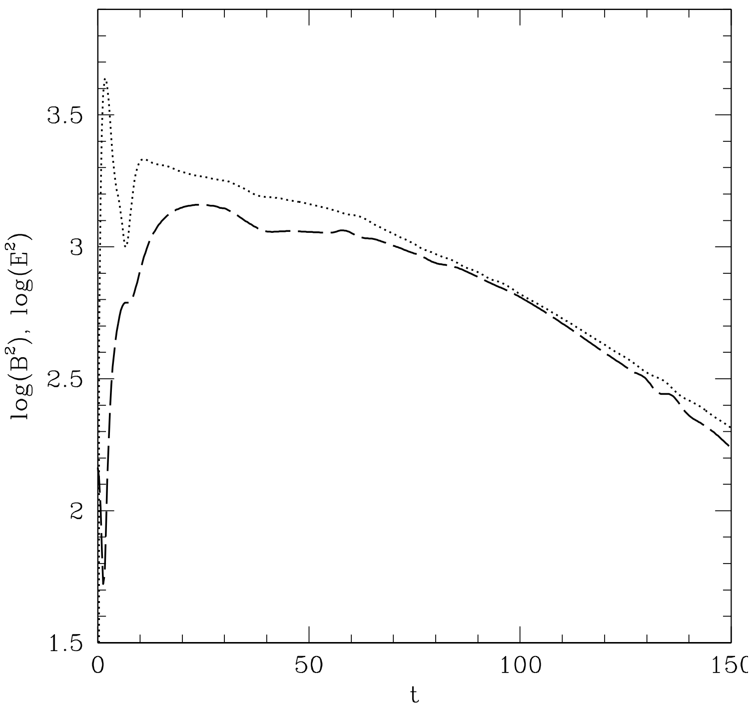

Figure 4.51: Integrated squares of electric and magnetic fields in $a = M = 5$ Kerr spacetime for $e = 0.6$ coupled perturbations. Plotted are $\log(B^2)$ and $\log(E^2)$, the logarithm of the integrated squares contained within $5 \leq r \leq 50$, $0 \leq \theta \leq \pi$ and $0 \leq \phi \leq 2\pi$, as a function of coordinate time t. The dashed black line represents $\log(B^2)$, and the dotted black line $\log(E^2)$. Initially, the field amplitudes undergo substantial change, but the decay of integrated electric and magnetic amplitudes become comparable at later time.

Before analyzing the physics of charge separation and dynamo-like behaviour unique to electromagnetically coupled $s = 0$ and $s = 1$ perturbations I now include discussion of angular momentum density evolution. I display the conserved angular momentum density in the sequence of steps shown in Figure 4.52. Similar to the case of purely electromagnetic perturbations, the chosen initial data is for zero net the angular momentum at all point in the computational domain. However, the distribution becomes nontrivial in short order as shown. Furthermore, as seen in the case of uncoupled electromagnetic perturbations, the distribution becomes sharply peaked in the ergoregion at intermediate time before evolving to a somewhat less dynamic scenario. Also observe that the local angular momentum density amplitudes are enhanced by an order of magnitude over those of the uncoupled electromagnetic perturbations. This effect is clearly due to the addition of charge coupling. Furthermore, in Figure 4.53, I display the same evolution sequence in $a = 0$ spacetime. There it is clear that the black hole rotation amplifies the angular momentum density amplitude. This is again similar to the situation observed for uncoupled electromagnetic perturbations. To conclude, I display the integrated angular momentum density for $a = 0, 0.8M$ and $a = M$ spacetimes in Figure 4.54. It is there evident that the total angular momentum is especially variable for $a \geq 0.8M$ spacetimes during the evolutionary period $40 \lesssim t \lesssim 70$.

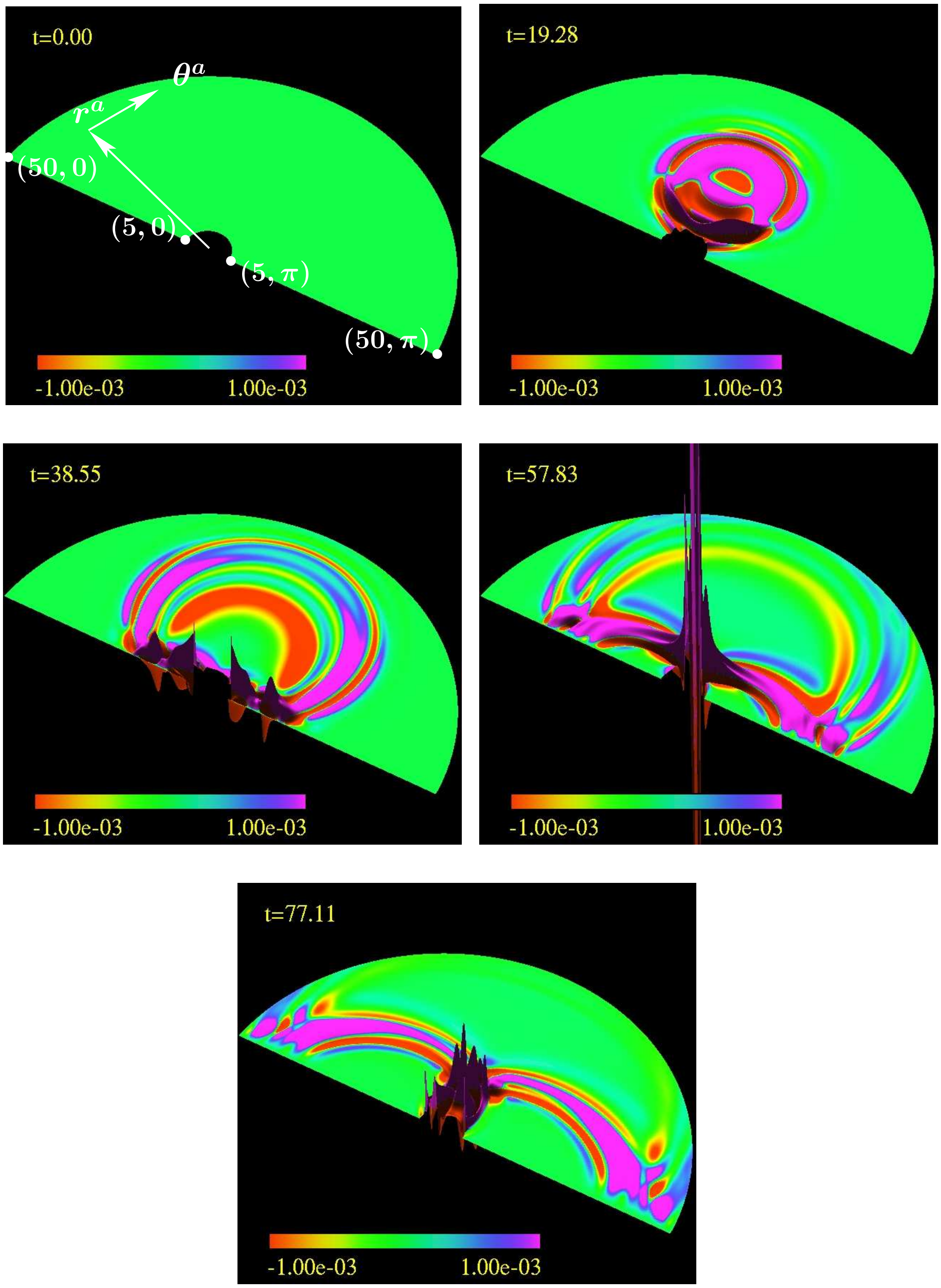

Figure 4.52: Angular momentum density for $a = M = 5$, $e = 0.6$ coupled perturbations in a sequence of steps. The directions of coordinate vectors $r^a \sim (0, 1, 0, 0)$ and $\theta^a \sim (0, 0, 1, 0)$ are shown in the first frame. The computational domain covers the range $5 \leq r \leq 50$ and $0 \leq \theta \leq \pi$, and the corners of the domain are labelled with their (r, θ) ordinate values. The amplitude and colour gradient are both scaled linearly.

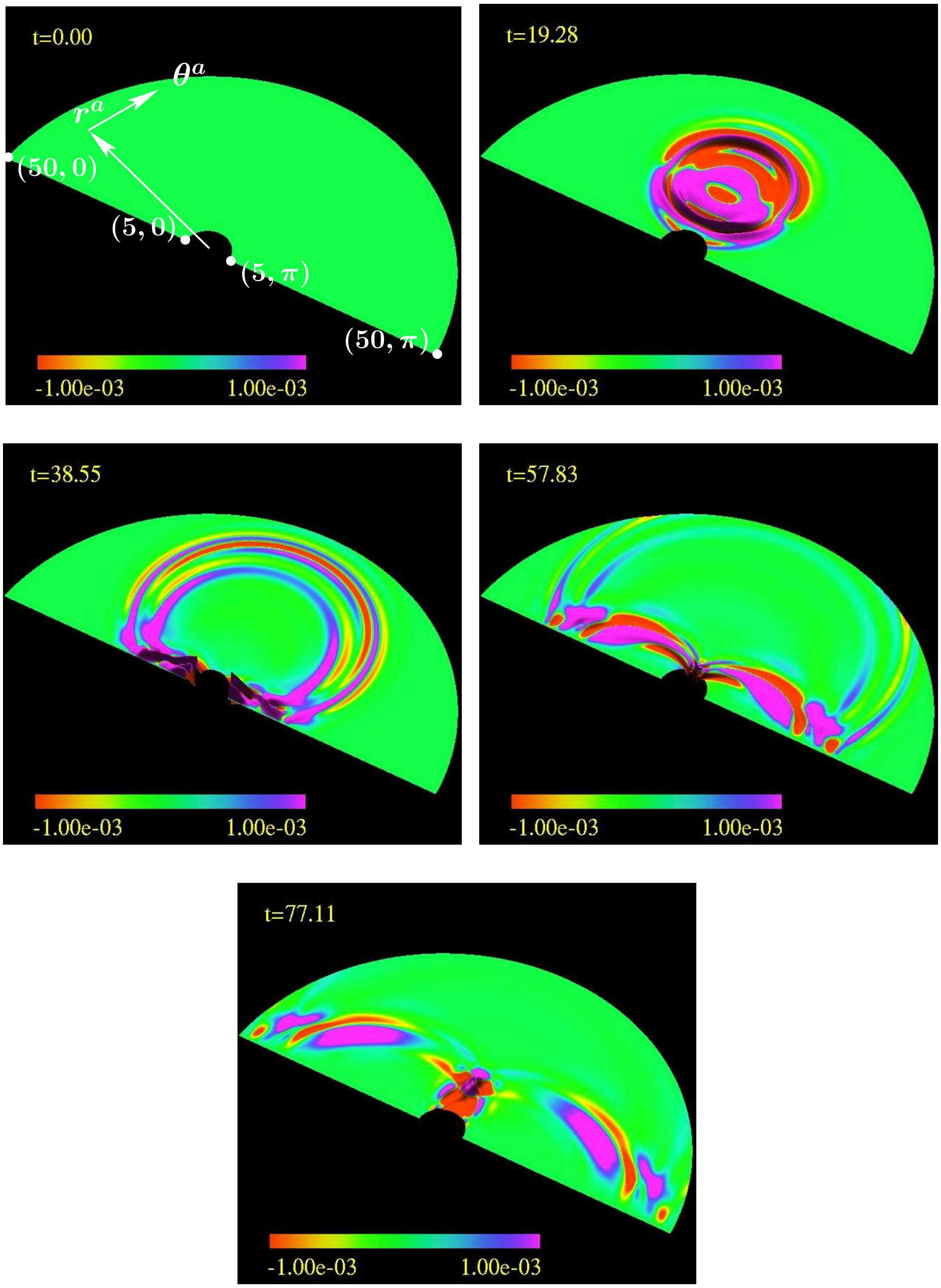

Figure 4.53: Angular momentum density for $a = 0$, $e = 0.6$ coupled perturbations in a sequence of steps. The directions of coordinate vectors $r^a \sim (0, 1, 0, 0)$ and $\theta^a \sim (0, 0, 1, 0)$ are shown in the first frame. The computational domain covers the range $5 \leq r \leq 50$ and $0 \leq \theta \leq \pi$, and the corners of the domain are labelled with their (r, θ) ordinate values. The amplitude and colour gradient are both scaled linearly.

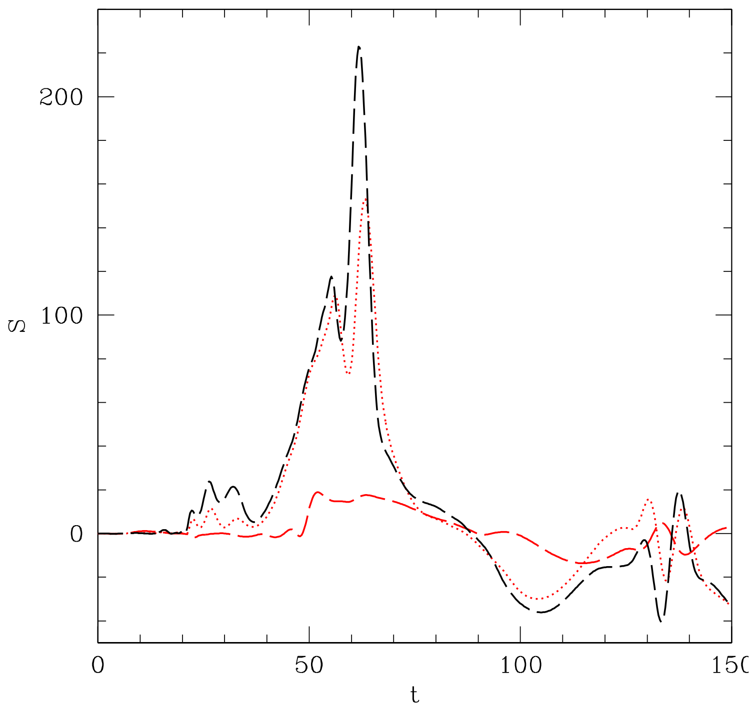

Figure 4.54: Integrated angular momentum density for $e = 0.6$ coupled massless perturbations in $M = 5$ Kerr spacetime. Plotted is S, the total angular momentum contained within $5 \leq r \leq 50$, $0 \leq \theta \leq \pi$ and $0 \leq \phi \leq 2\pi$, as a function of coordinate time t. The dashed red line represents data for $a/M = 0$, the dotted red line data for $a/M = 0.8$, and the dashed black line data for $a/M = 1$. The total angular momentum is especially variable for $a \geq 0.8M$ spacetimes during $40 \lesssim t \lesssim 70$.

In this subsection I have so far discussed the dynamics of energy and angular momentum for the coupled $s = 0$ and $s = 1$ perturbations on Kerr spacetime. It is fair to say that, while quantitatively different, the energy and angular momentum dynamics are in many ways similar to those of uncoupled perturbations previously discussed. Because the electromagnetically coupled perturbations carry charge, two physically unique features appear in the field dynamics—the separation of electric charge and dynamo-like behaviour of electric current. The evolution of electric charge density in $a = M = 5$ spacetime is displayed as a sequence in Figure 4.55. There it is seen how an everywhere zero net charge density quickly evolves into regions of separated net positive and negative charge. Note that this process is not particular to rotating black hole spacetimes. For comparison, I display the analogous sequence for $a = 0$, $M = 5$ spacetime in Figure 4.56. The early dynamics of ρ_Q are nearly identical for $a = M$ and $a = 0$, and only significantly deviate in magnitude after the initial scattering from the steep gravitational potential. For further comparison I plot the total charge contained in the computational domain, Q, for $a = 0, 0.8M$ and $a = M$ spacetimes in Figure 4.57, where it is observed how closely the total charges agree at early time for all black hole angular momenta. In addition, observe how the choice of initial data prefers to transfer positive charge through the event horizon and outer computational boundary for $40 \lesssim t \lesssim 50$ and transfer negative charge for $70 \lesssim t \lesssim 100$.

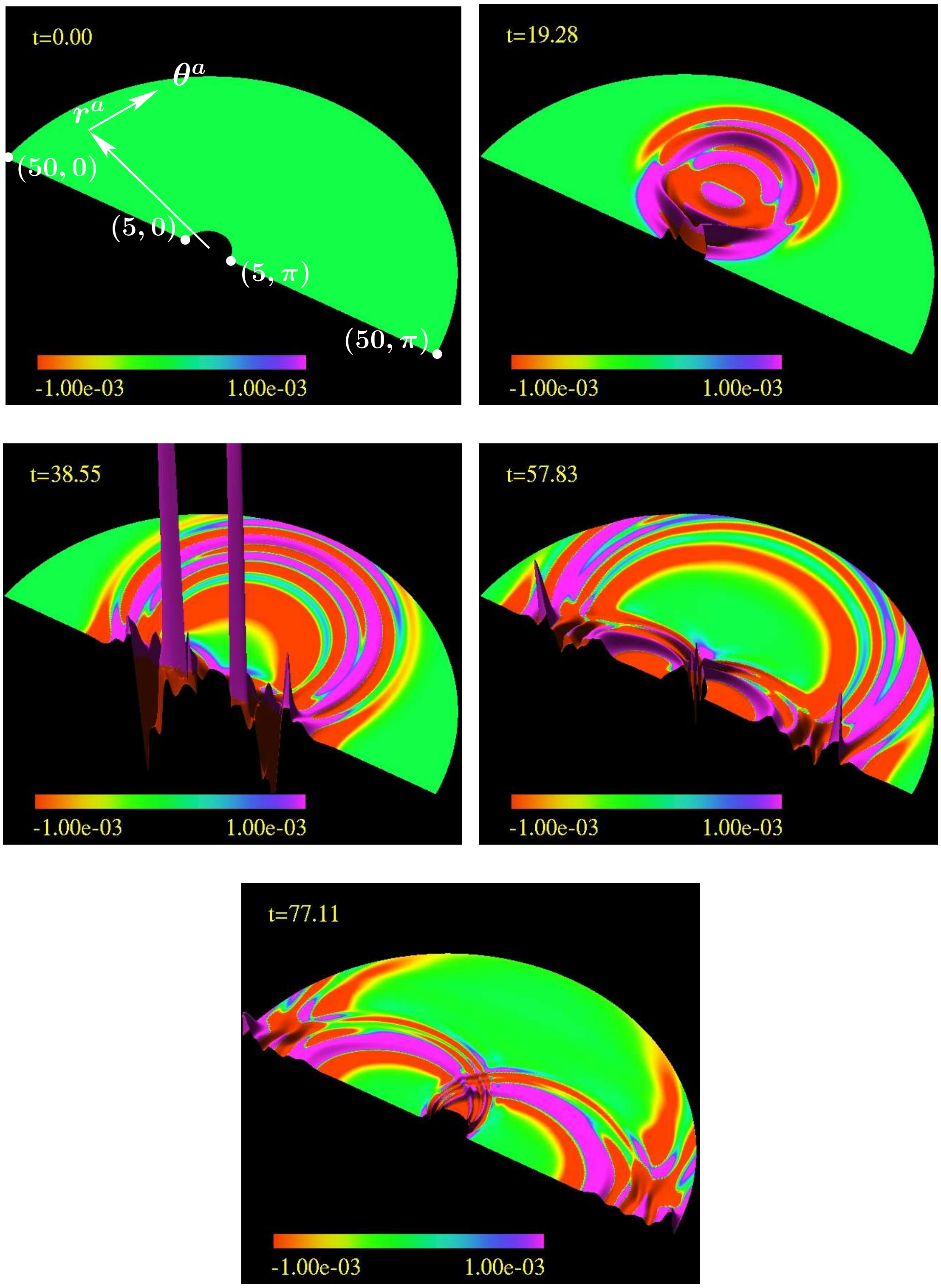

Figure 4.55: Charge density showing separation in the $a = M = 5$ spacetime for $e = 0.6$ perturbations. Both amplitude and colour gradient are scaled linearly. The directions of coordinate vectors $r^a \sim (0, 1, 0, 0)$ and $\theta^a \sim (0, 0, 1, 0)$ are shown in the first frame. The computational domain covers the range $5 \leq r \leq 50$ and $0 \leq \theta \leq \pi$, and the corners of the domain are labelled with their (r, θ) ordinate values.

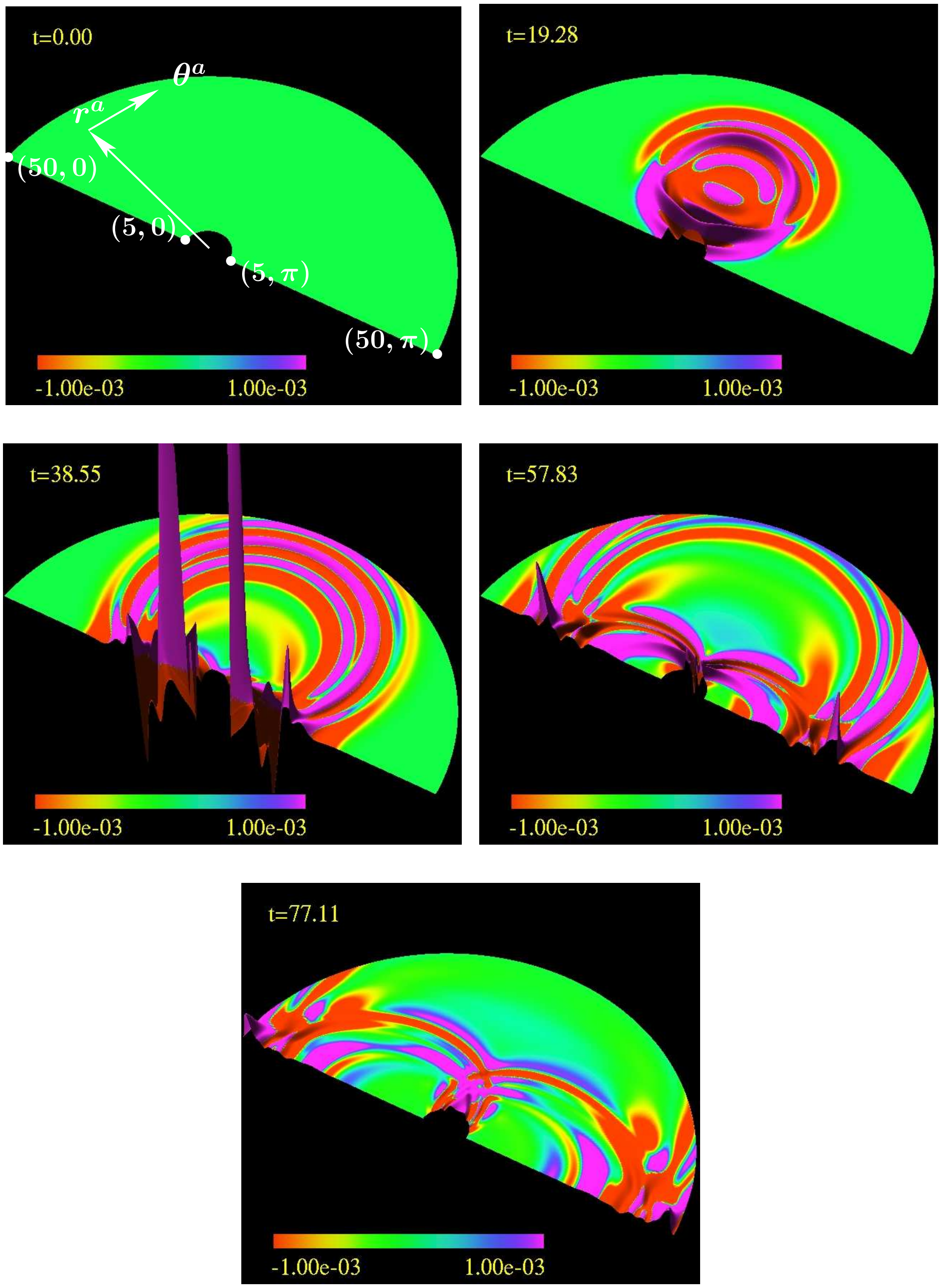

Figure 4.56: Charge density showing separation in the $a = 0$, $M = 5$ spacetime for $e = 0.6$ perturbations. The amplitude and colour gradient are again scaled linearly. The directions of coordinate vectors $r^a \sim (0, 1, 0, 0)$ and $\theta^a \sim (0, 0, 1, 0)$ are shown in the first frame. The computational domain covers the range $5 \leq r \leq 50$ and $0 \leq \theta \leq \pi$, and the corners of the domain are labelled with their (r, θ) ordinate values.

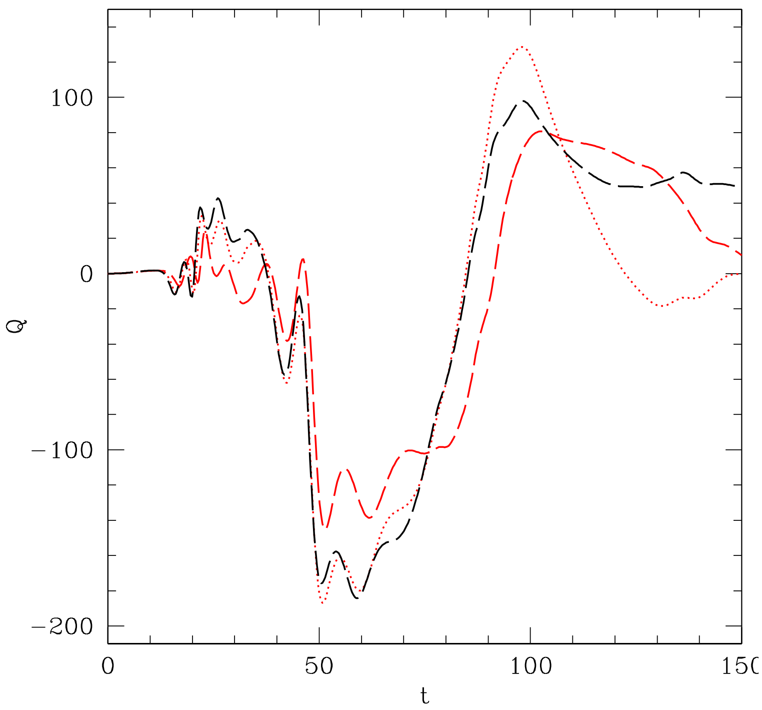

Figure 4.57: Integrated charge density for $e = 0.6$ coupled massless perturbations in $M = 5$ Kerr spacetime. Plotted is Q, the total charge contained within $5 \le r \le 50$, $0 \le \theta \le \pi$ and $0 \le \phi \le 2\pi$, as a function of coordinate time t. The dashed red line represents data for $a/M = 0$, the dotted red line data for $a/M = 0.8$, and the dashed black line data for $a/M = 1$. The choice of initial data preferentially transfers positive charge through the event horizon and outer computational boundary for $40 \lesssim t \lesssim 50$ and negative charge for $70 \lesssim t \lesssim 100$.

As the coupled perturbations carrying charge and momentum display interesting dynamics, it is also surmised the electric current should reveal behaviour worth studying. While the evolution of ρ_Q encapsulates information regarding current components J_r and J_θ, it doesn't completely reveal the behaviour of the axial current component J_ϕ. For this reason I plot an evolutionary sequence for J_ϕ in $a = M = 5$ Kerr spacetime in Figure 4.58. Most generally, I consider the *dynamo-like behaviour* to be the dynamic interplay of electric current and electromagnetic field, converting between kinetic and non-kinetic contributions of the system's total energy. As there is no outside mechanism to constrain the axial current of the coupled perturbations, they must necessarily display dynamo-like behaviour. However, observe how J_ϕ undergoes directional reversal throughout evolution. The choice of initial conditions clearly disallows a single persistent current loop.[17] Instead, the loop oscillates in a nontrivial manner lacking a regular period of oscillation.

[17] This behaviour can be simply explained as a manifestation of Faraday's Law. Recall the differential form of Faraday's law in flat spacetime can be expressed

$$\vec{\nabla} \times \vec{E} + \frac{\partial \vec{B}}{\partial t} = 0 \, , \tag{4.176}$$

which shows that a time dependent magnetic field induces an electric field. The electric field, then, will induce a current (or change in current) in a direction to counteract the change in magnetic field. In the case examined here, The same is true for evolution in $a = 0$, $M = 5$ spacetime as shown in Figure 4.59. This is substantiated in part by Figures 4.60 and 4.61 which respectively display the global maxima and minima of J_ϕ for $a = 0$ and $a = M$ spacetimes. While $a = 0$ perturbations have larger global maxima at early time, these maxima quickly decay and the $a = M$ becomes dominant. Especially note how the maximum, $\max(J_\phi)$, peaks during the period $20 \lesssim t \lesssim 50$. Meanwhile, the global minima, $\min(J_\phi)$, evolve with comparable amplitude for early time until $a = M$ perturbations begin dominating when $40 \lesssim t \lesssim 80$. The global maxima and minima were also analyzed for $a = 0.8M$ (not displayed) and were found to be qualitatively similar to those of the $a = M$ spacetime. It can therefore be concluded that while black hole angular momentum initially suppresses the evolution of J_ϕ, it later acts to amplify this axial current density.

there is an axial current loop at initial time as shown in Figure 4.58. There is also a magnetic field at initial time, whose square is shown in Figure 4.49. Note how this initial magnetic field distribution—the same as that studied in section 4.3.3—has a nonzero time derivative. As this magnetic field changes in time it induces an electric field as supported by results shown in Figures 4.50 and 4.51. Of course, the resulting induced change in current by the electric field must be in the direction opposing the change in magnetic flux.

Now consider the scenario where a stationary charged disk generates a current loop around a black hole and persists indefinitely unless acted on by an external agent. If an electromagnetic wave passes through part of the loop, a current fluctuation will then be induced in order to oppose the change in magnetic flux enclosed by the loop. And so it is by this mechanism that one could imagine electromagnetic radiation destabilizing a stationary charged accretion flow in the spacetime of a black hole. Note there was no appeal to a property unique to black holes in this destabilization mechanism, and to the argument should also hold for other gravitating celestial objects like stars.

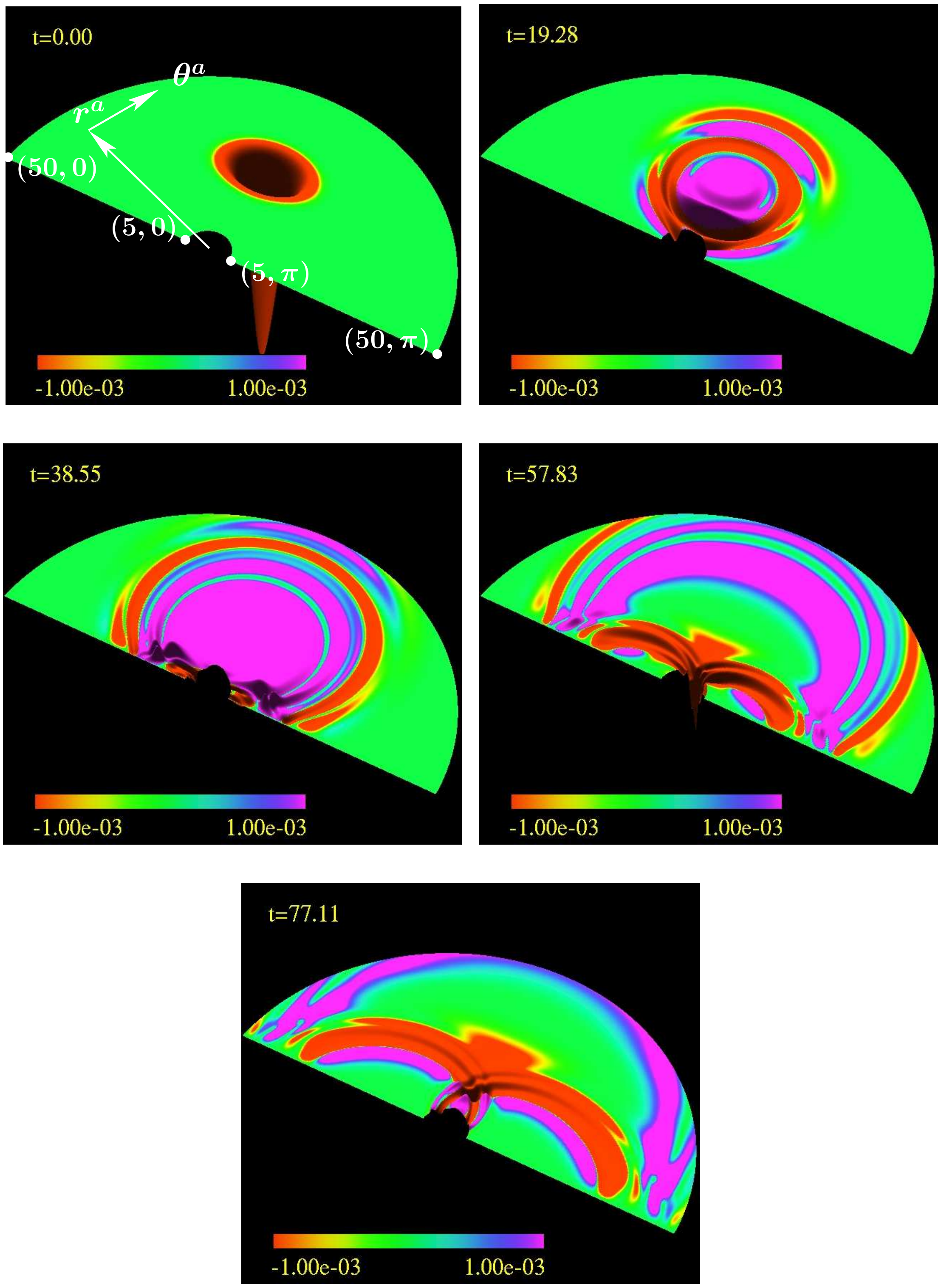

Figure 4.58: Displayed is the axial current, J_ϕ, oscillation in $a = M = 5$ Kerr spacetime for $e = 0.6$ coupled perturbations. Both amplitude and colour gradient are scaled linearly. The directions of coordinate vectors $r^a \sim (0, 1, 0, 0)$ and $\theta^a \sim (0, 0, 1, 0)$ are shown in the first frame. The computational domain covers the range $5 \leq r \leq 50$ and $0 \leq \theta \leq \pi$, and the corners of the domain are labelled with their (r, θ) ordinate values.

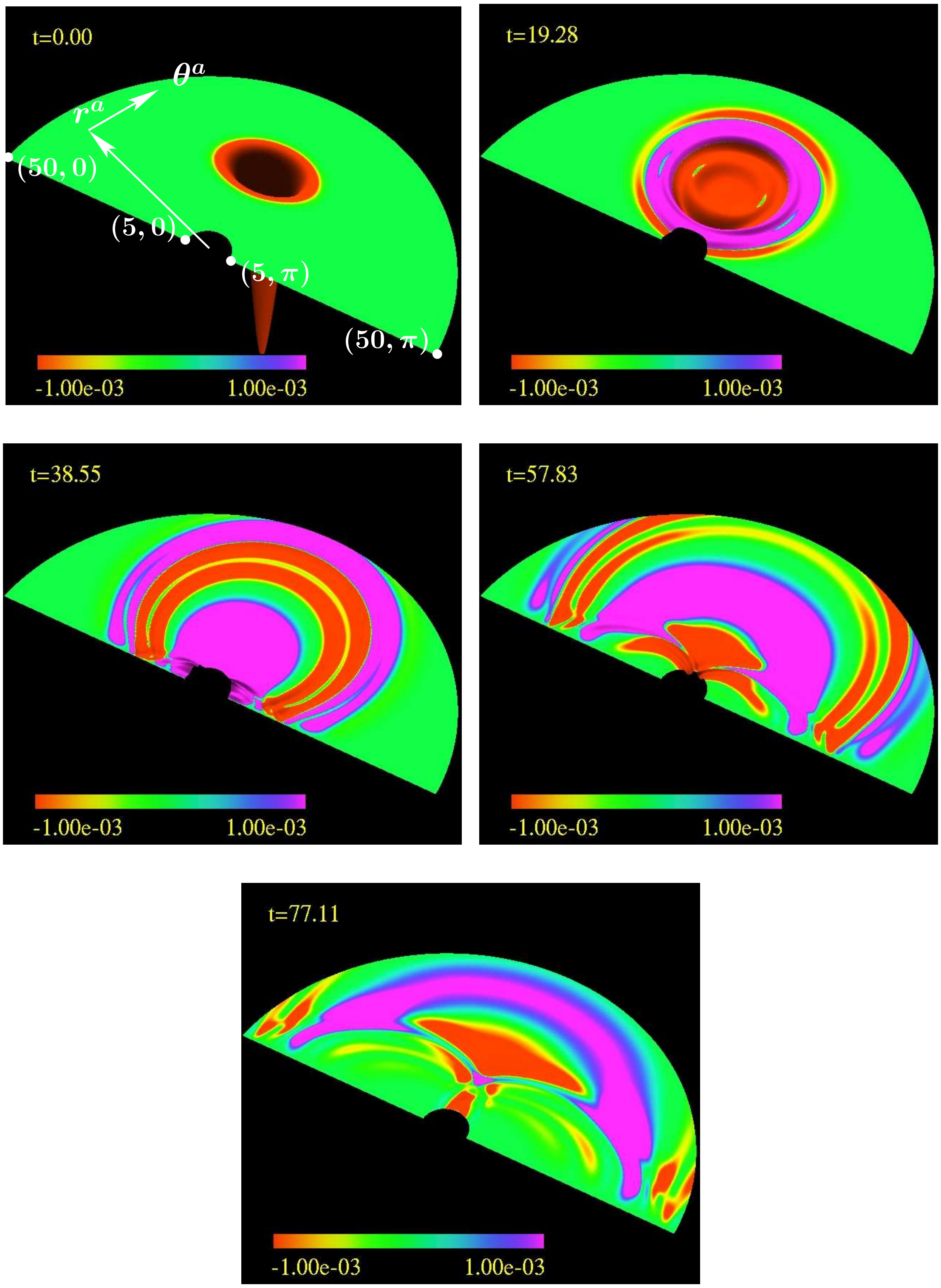

Figure 4.59: Displayed is the axial current, J_ϕ, oscillating in $a = 0$, $M = 5$ Kerr spacetime for $e = 0.6$ coupled perturbations. Both amplitude and colour gradient are scaled linearly. The directions of coordinate vectors $r^a \sim (0, 1, 0, 0)$ and $\theta^a \sim (0, 0, 1, 0)$ are shown in the first frame. The computational domain covers the range $5 \leq r \leq 50$ and $0 \leq \theta \leq \pi$, and the corners of the domain are labelled with their (r, θ) ordinate values.

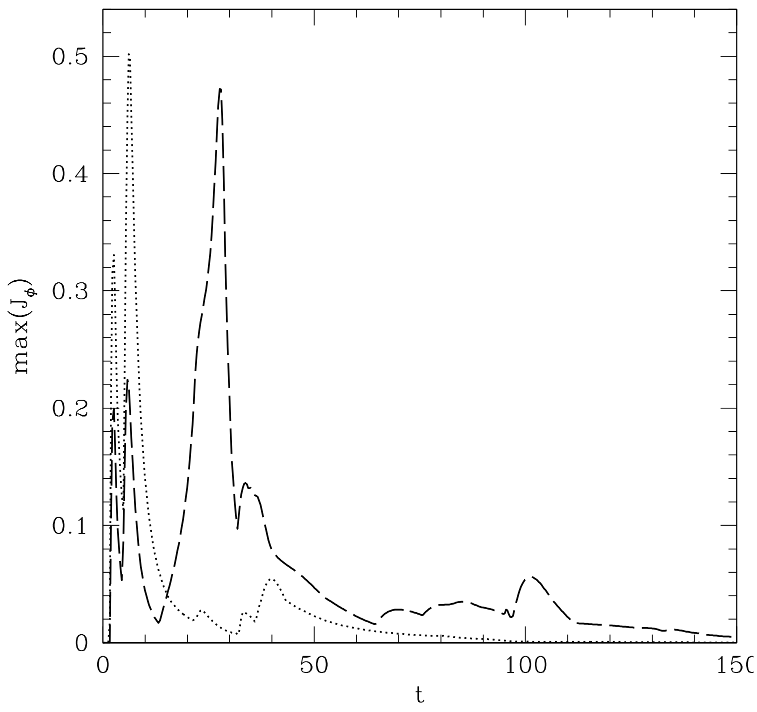

Figure 4.60: Global maxima of J_ϕ in the computational domain, $\max(J_\phi)$, as a function of t for $e = 0.6$ coupled massless perturbations in $M = 5$ Kerr spacetime. The dotted black line represents data for $a/M = 0$ and the dashed black line data for $a/M = 1$.

To gain additional insight on the nature of charge and current in this model, consider the ratios ρ_Q/e and J_a/e. From equation (4.108), the first of the ratios is

$$\frac{\rho_Q}{e} = i\frac{g_{tr}^2}{(g_{tr}^2 f_{\phi\phi} - g_{t\phi} f_{t\phi} g_{rr})}\left(\Phi^* \Pi_\Phi - \Phi \Pi_\Phi^*\right) \ , \tag{4.177}$$

and may be interpreted as a conserved scalar field density. However, recall that charge density can be both positive and negative. The proper interpretation of ρ_Q/e is therefore the density of the scalar field carrying charge with sign $e/|e|$. Negative values of ρ_Q/e simply indicate the scalar field is carrying charge of opposite sign at those locations. Furthermore, comparing ρ_Q of (4.108) to $\rho_{S(\Phi A)}$ from (4.116) obtains

$$\rho_Q = -\frac{2}{A_\phi}\rho_{S(\Phi A)} \ , \tag{4.178}$$

revealing the connection between charge density and the angular momentum contribution from the coupling of scalar and electromagnetic fields. Meanwhile, (4.93) and (4.94) obtain the quantities

$$\frac{J_r}{e} = -i\left(\Phi^* \Phi_r - \Phi \Phi_r^*\right) - 2e\Phi\Phi^* A_r \tag{4.179}$$

and

$$\frac{J_\theta}{e} = -i\left(\Phi^* \Phi_\theta - \Phi \Phi_\theta^*\right) - 2e\Phi\Phi^* A_\theta \ , \tag{4.180}$$

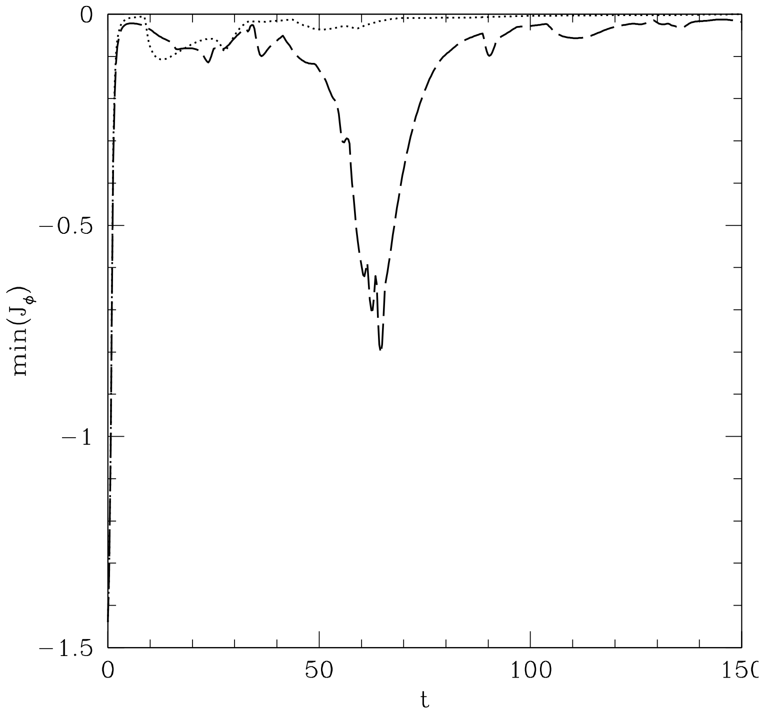

Figure 4.61: Global minima of J_ϕ in the computational domain, $\min(J_\phi)$, as a function of t for $e = 0.6$ coupled massless perturbations in $M = 5$ Kerr spacetime. The dotted black line represents data for $a/M = 0$ and the dashed black line data for $a/M = 1$.

which represent scalar field velocities in the r and θ coordinate directions. Now, from (4.95),

$$\frac{J_\phi}{e} = -2e\Phi\Phi^* A_\phi \ , \tag{4.181}$$

which represents a scalar field velocity in the axial direction—specifically, the axial velocity of scalar field carrying charge of sign $e/|e|$.

From (4.56), the quantity Π_Φ appearing in (4.177) is

$$\Pi_\Phi = n^a \sqrt{-g}\left(\nabla_a \Phi - ieA_a\Phi\right) \ , \tag{4.182}$$

where, from (4.73),

$$\sqrt{-g} = \frac{g_{tr}^2 f_{\phi\phi} - g_{t\phi} f_{t\phi} g_{rr}}{g_{tr}^2} \ . \tag{4.183}$$

Substituting (4.182) and (4.183) into (4.177) and taking the limit $e \to 0$ obtains

$$\lim_{e\to 0} \frac{\rho_Q}{e} = -n^a i\left(\Phi^* \nabla_a \Phi - \Phi \nabla_a \Phi^*\right) \ . \tag{4.184}$$

Similarly, taking the $e \to 0$ limits of (4.179)–(4.181) yields

$$\lim_{e\to 0} \frac{J_r}{e} = -i\left(\Phi^* \Phi_r - \Phi \Phi_r^*\right) \ , \tag{4.185}$$

$$\lim_{e\to 0} \frac{J_\theta}{e} = -i\left(\Phi^* \Phi_\theta - \Phi \Phi_\theta^*\right) \ , \tag{4.186}$$

and

$$\lim_{e\to 0} \frac{J_\phi}{e} = 0 \ . \tag{4.187}$$

Observe how, consistent with the assumptions of axial symmetry, the scalar field velocity in the axial direction vanishes in the limit $e \to 0$. Furthermore, the relationship between the Noether current of a (massless and uncharged) complex scalar field,

$$\mathcal{J}_a = -i\left(\Phi^* \nabla_a \Phi - \Phi \nabla_a \Phi^*\right) \ , \tag{4.188}$$

and the quantities appearing in (4.184)–(4.187) is clear.

Of course, ρ_Q, J_r, J_θ and J_ϕ are observer dependent quantities. As far as that goes, so are E_a, B_a, ρ_T, and ρ_S. But it is well known from both special and general relativity that densities and electromagnetic quantities are dependent on the frame in which they are measured. This discussion concludes subsection 4.3.4.

4.3.5 Massless Maxwell-Klein-Gordon Equation Dynamics II: Comparing Electromagnetically Coupled $s = 0$ and $s = 1$ Perturbations With Different Values of Parameter e

Having examined the effects of charge coupling $e = 0.6$ in the massless Maxwell-Klein-Gordon system for different values of the black hole angular momentum parameter a, I now investigate how changing e alters the observed dynamics in $a = M = 5$ Kerr spacetime. Specifically, I investigate $e = 0.0, 0.3, 0.6, 1.2$ and $e = 2.4$. The computational domain again spans $5 \leq r \leq 50$ and $0 \leq \theta \leq \pi$, and the initial data is specified as in the preceding subsection. For $e = 0.0, 0.3$ and $e = 0.6$ I use a finite difference grid with resolution $J = 801$ radial points and $K = 401$ angular points. This provides an accuracy to within $\approx 1\%$ before the perturbations first cross the ergosphere and then the excision surface at $r = 5$. For $e = 1.2$ a resolution of $J = 1601$ radial points and $K = 801$ angular points is used to provide the same level of accuracy. For $e = 2.4$, a resolution of at least $J = 3201$ radial and $K = 1601$ angular points is required before this order of accuracy is achieved.[18] The computational requirements are thus very large for $e = 1.2$ and $e = 2.4$, and so I compute the evolution just past the first excision surface crossing for these two coupling parameter values.[19] Finally, the calculations for $0.0 \leq e \leq 1.2$ are performed in parallel across 64 processors with processor overlap regions 3 grid points wide, and the calculations for $e = 2.4$ are performed across 256 processors with overlap regions 3 points wide.

While computational demands have restricted the length of high e evolutions, I have complete data for $e = 0.0, 0.3$, and $e = 0.6$ over $0 \leq t \lesssim 150$ for the $a = M = 5$ Kerr spacetime. The data for $e = 0.0$ are essentially the sum of results from sections 4.3.2 and 4.3.3. Furthermore, the case $e = 0.6$ has already been discussed in section 4.3.4. While the results for $e = 0.3$ should display behaviour between those of $e = 0.0$ and $e = 0.6$, I quantify the similarities and differences through the total normalized energy, total angular momentum and charge contained in the computational domain. Figure 4.62 displays the energy, Figure 4.63 the angular momentum, and Figure 4.64 the charge. While proportionately greater energy persists over time for for $e = 0.3$ and $e = 0.6$ than for $e = 0.0$, there is reasonably close agreement between the cases $e = 0.3$ and $e = 0.6$. While the differences are small, it can still be argued that addition of modest charge coupling

[18] The need for higher accuracy when e is large can be inferred from equation of motion (4.50),

$$\nabla^a \nabla_a \Phi - 2ie(\nabla_a \Phi)A^a - e^2 \Phi A_a A^a - ie\Phi \nabla_a A^a - m_\Phi^2 \Phi = 0 \ . \tag{4.189}$$

For simplicity, consider solutions of this equation in a flat spacetime with one spatial dimension and one temporal dimension. Points in this spacetime are designated by the value of spatial coordinate x and the value of temporal coordinate t. Furthermore, consider solutions of equation (4.189) of the form

$$\Phi = a_\Phi \exp i(kx - \omega t) \ , \tag{4.190}$$

where a_Φ is the amplitude, k is the wavenumber and ω is the solution frequency. When $e = m_\Phi = 0$, equation (4.189) becomes

$$\nabla^a \nabla_a \Phi = 0 \ . \tag{4.191}$$

The dispersion relation obtained by substituting (4.190) into (4.191) is simply

$$\omega^2 = k^2 \ . \tag{4.192}$$

When $e = 0$ and $m_\Phi \neq 0$, equation (4.189) becomes

$$\nabla^a \nabla_a \Phi - m_\Phi^2 \Phi = 0 \ . \tag{4.193}$$

Assuming (4.193) has solutions of the form (4.190), the dispersion relation becomes

$$\omega^2 = k^2 + m_\Phi^2 \ . \tag{4.194}$$

This shows large values for m_Φ result in correspondingly large values of ω for a given wavenumber k. Numerically, this implies a need for higher resolution to obtain a solution with the same accuracy as in the case $m_\Phi = 0$. Similarly, the need for high resolution can be inferred when $m_\Phi = 0$ and $e \neq 0$ is large. Using the Lorentz gauge condition $\nabla_a A^a = 0$ and assuming $m_\Phi = 0$, equation (4.189) becomes

$$\nabla^a \nabla_a \Phi - 2ie(\nabla_a \Phi)A^a - e^2 A_a A^a \Phi = 0 \ . \tag{4.195}$$

Solutions (4.190) then obtain a dispersion relation

$$\omega^2 + 2eA^t \omega = k^2 + 2eA^r k + e^2 A_a A^a \ . \tag{4.196}$$

Comparing with (4.193) and (4.194), the quantity $\left(e^2 A_a A^a\right)^{1/2}$ plays a role similar to that of a t and r dependent scalar field mass. Furthermore, it is clear from (4.196) that increasing e correspondingly increases the solution frequency ω for a given wavenumber k. This, in turn, suggests the need for higher resolution to numerically obtain the same solution accuracy as in the case $e = 0$.

[19] Finally, while adaptive mesh refinement is not clearly beneficial for the evolution of $e \leq 0.6$ perturbations from the specified initial conditions on the given computational domain (as discussed in preceding section 4.2.6), cases with sufficiently large coupling may benefit from the technique. Specifically, my results demonstrate how (at least for the early phase of evolution) a relatively high resolution is required in a proportionately small region of the computational domain for cases such as $e = 2.4$. The utility of adaptive mesh refinement was, however, not investigated in any more detail.

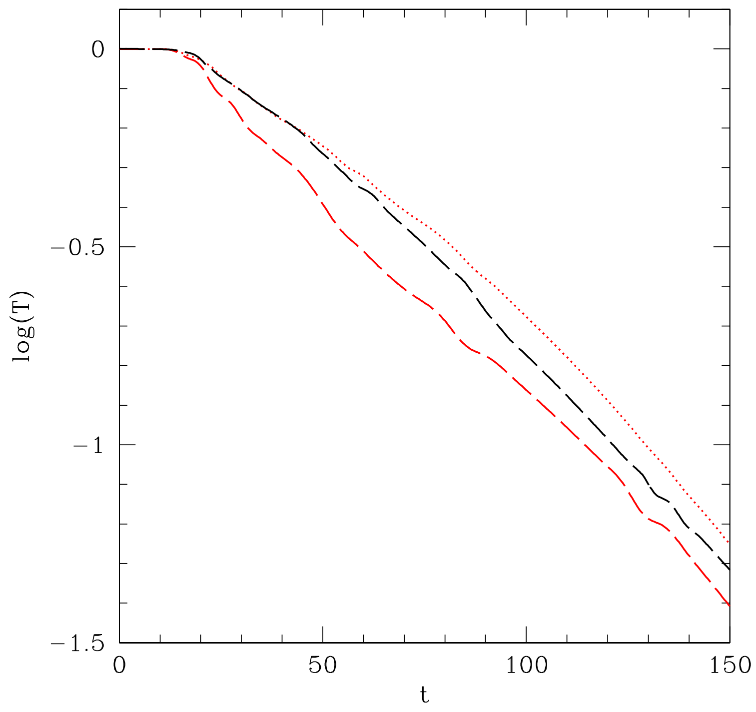

Figure 4.62: Total normalized energy for the massless electromagnetically coupled perturbations in $a = M = 5$ Kerr spacetime. The dashed red line represents data for $e = 0.0$, the dotted red line data for $e = 0.3$ and the dashed black line data for $e = 0.6$. The decay rates of charged perturbations are smaller than for the case $e = 0.0$. Any decrease in time of this quantity results from the energy flux across surfaces $r = 5$ and $r = 50$, and thus out of the computational domain.

decreases the overall decay rate of total perturbation energy.[20] Meanwhile, note that only the $s = 1$ component of perturbations contributes to the total angular momentum of the $e = 0.0$ data. However, an additional coupling term contributes with the introduction of nonzero e. It is clear from Figure 4.63 how the addition of electromagnetic coupling increases the amplitude of angular momentum remaining in the computational domain as evolution progresses. Furthermore, the maximum amplitude of this total angular momentum increases with parameter e. Finally, while the case $e = 0.0$ has zero charge density, I still display the $e = 0.0$ data along with those of $e = 0.3$ and $e = 0.6$ in Figure 4.64. The charge remaining in the computational domain varies in time, and the difference between the cases is more significantly affected by parameter e than by black hole angular momentum a as discussed in section 4.3.4. Also note that it cannot be determined in advance whether net positive of negative charge will preferentially leave the domain. Rather, the details must be determined through numerical evolution. Overall, the effect of changing e is notable over the period of evolution.

[20]It is not possible to definitively conclude what trends in decay rate will arise with increased electromagnetic coupling parameter without further computation. From the data of Figure 4.62 it is clear that energy decay rates are not ordered according to the value of e. A similar trend was observed in the massive uncharged perturbation decay rates of Figure 4.19, where the value $m_\Phi = 0.3$ gave rise to mode trapping, and $m_\Phi \geq 1.2$ resulted in rapid energy decay by infall onto the black hole. It is possible that the behaviour displayed in Figure 4.62 is the beginning of a similar trend with the electromagnetic coupling parameter.

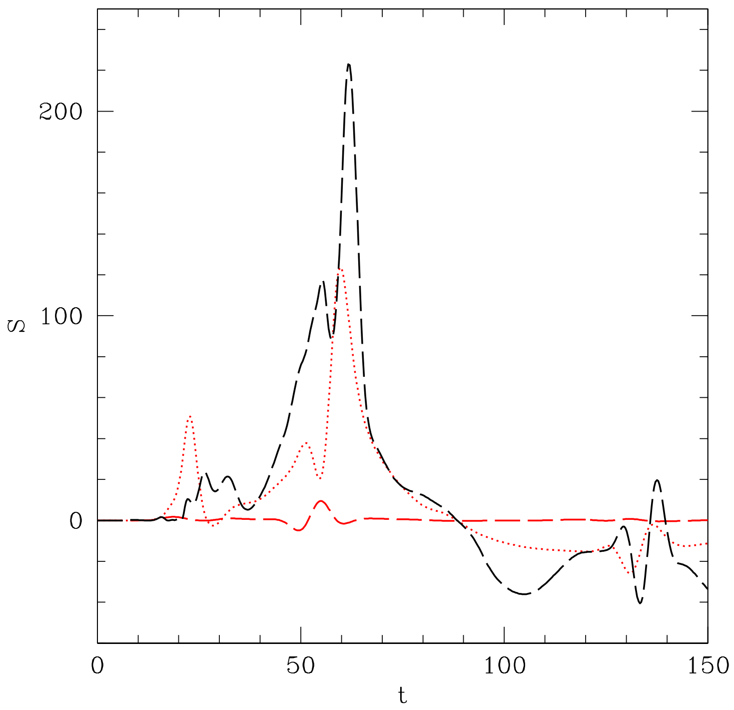

Figure 4.63: Total angular momentum for the massless electromagnetically coupled perturbations in $a = M = 5$ Kerr spacetime. The dashed red line represents data for $e = 0.0$, the dotted red line data for $e = 0.3$ and the dashed black line data for $e = 0.6$. The total angular momenta are more dynamic for charged perturbations than for $e = 0.0$.

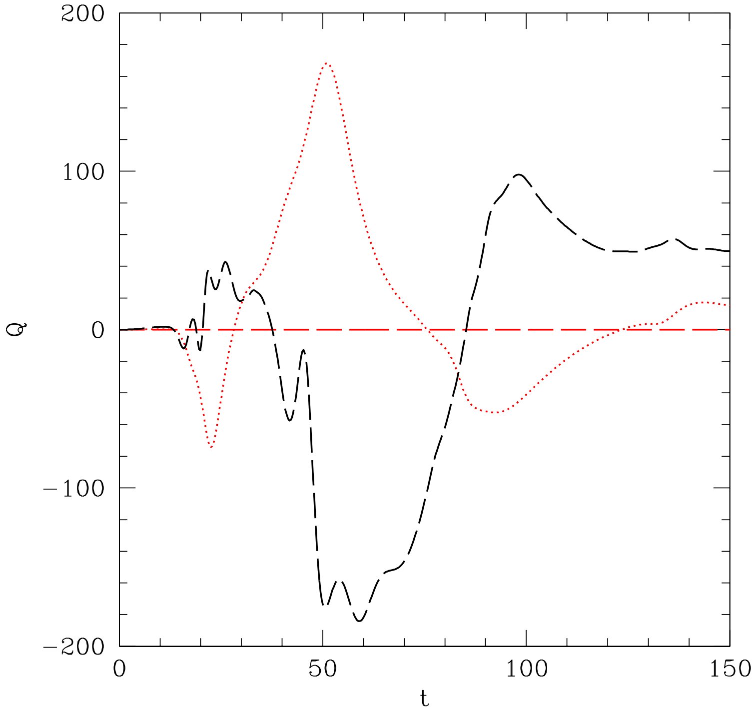

Figure 4.64: Total charge for the massless electromagnetically coupled perturbations in $a = M = 5$ Kerr spacetime. The dashed red line represents data for $e = 0.0$, the dotted red line data for $e = 0.3$ and the dashed black line data for $e = 0.6$.

Investigating the evolution of high e perturbations it is further apparent that dynamics of large e fields are much richer than those with small e. Figure 4.65 displays the total normalized energy density of $e = 2.4$ in a sequence of steps from $t = 0$ through $t = 16.06$.[21] To emphasize, I provide an enlarged view of time step $t = 16.06$ in Figure 4.66. Comparing with the results of sections 4.3.2, 4.3.3 and 4.3.4 it is clear how the morphology changes and the density gradient increases with charge coupling. There is also a tendency is for density amplitudes to grow with increasing e. Furthermore, notice how early evolution of the $e = 2.4$ data would suggest perturbations with large coupling are likely to persist in the computational domain for an extended period of time. That is, the rate at which large e perturbations are likely to decay—either by passing through the $r = 5$ excision surface or escaping through the $r = 50$ outer boundary—is probably smaller than for small or vanishing e. This, in turn, suggests the possibility of an effect similar to mode trapping for massless electromagnetically coupled perturbations. However, the origins of such a phenomenon would have to be investigated by evolving the fields in spacetimes with differing black hole mass and angular momentum. The rich dynamics are also manifest in quantities like the angular momentum density of Figures 4.67 and 4.68, and the charge density of Figures 4.69 and 4.70. Again, comparing with previous results it is clear how the dynamics are enriched as both the density gradients and amplitudes increase with e.

[21] The evolutionary dynamics for $e = 0.3$ lie between those of $e = 0.0$ and $e = 0.6$, and the dynamics of $e = 1.2$ lie between those of $e = 0.6$ and $e = 2.4$. Neither $e = 0.3$ nor $e = 1.2$ are displayed.

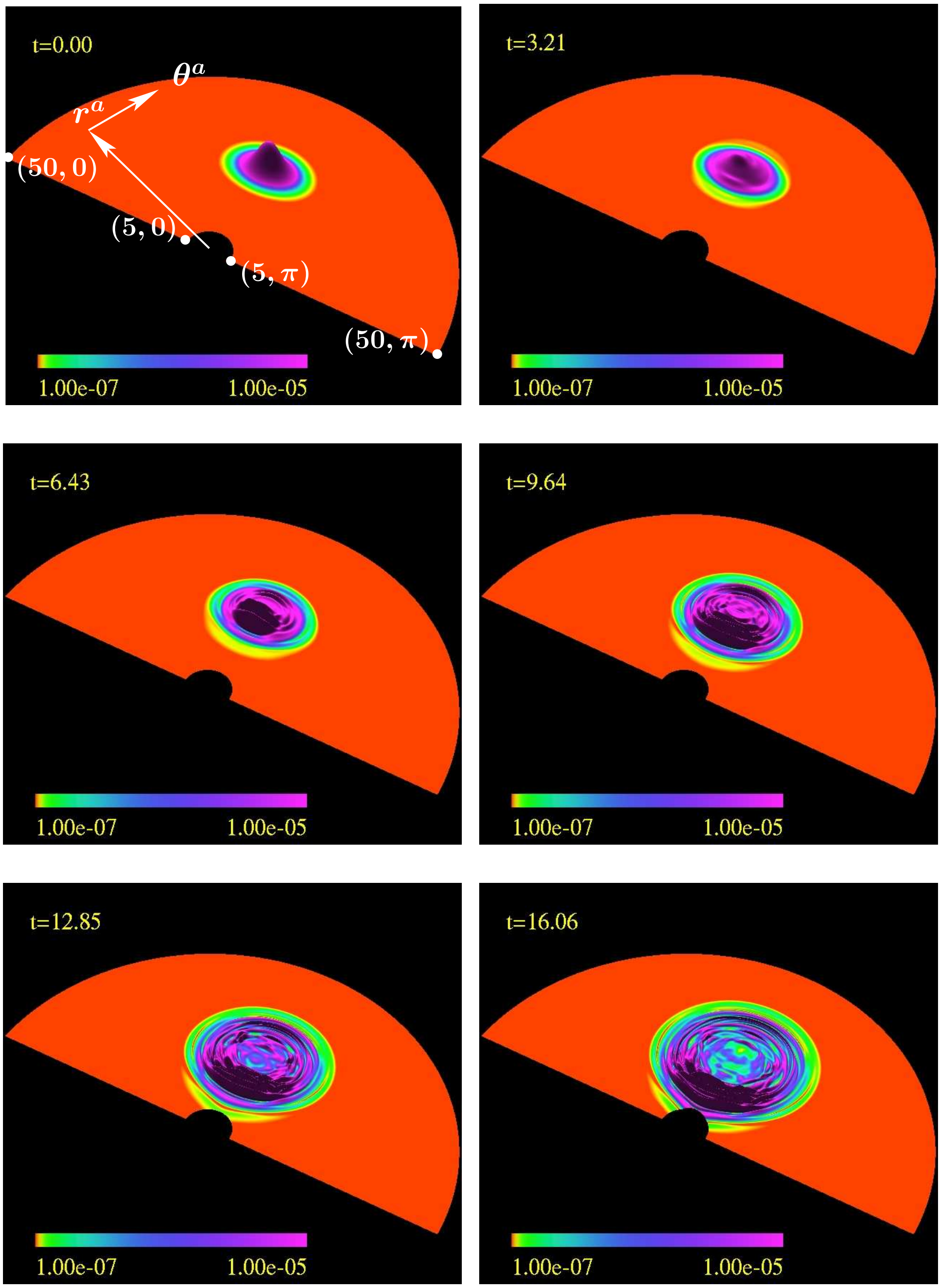

Figure 4.65: Displayed is the total normalized energy density in $a = M = 5$ Kerr spacetime for $e = 2.4$ massless perturbations for the early phase of evolution. Amplitude is scaled linearly and the colour gradient logarithmically. The directions of coordinate vectors $r^a \sim (0, 1, 0, 0)$ and $\theta^a \sim (0, 0, 1, 0)$ are shown in the first frame. The computational domain covers the range $5 \leq r \leq 50$ and $0 \leq \theta \leq \pi$, and the corners of the domain are labelled with their (r, θ) ordinate values.

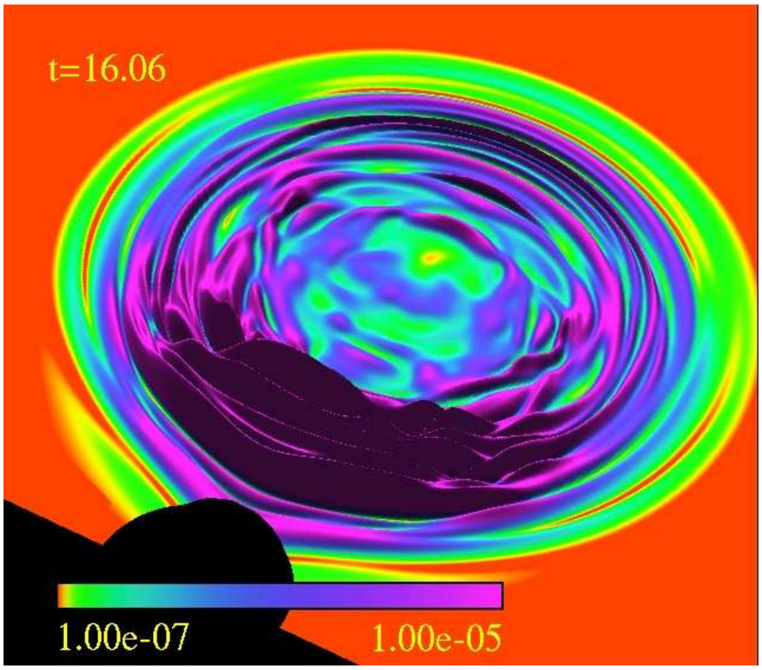

Figure 4.66: Displayed is a closer view of the total normalized energy density at $t = 16.06$ in $a = M = 5$ Kerr spacetime for $e = 2.4$ massless perturbations. Amplitude is again scaled linearly and the colour gradient logarithmically. The computational domain and coordinate vectors would be the same as those shown in Figure 4.65.

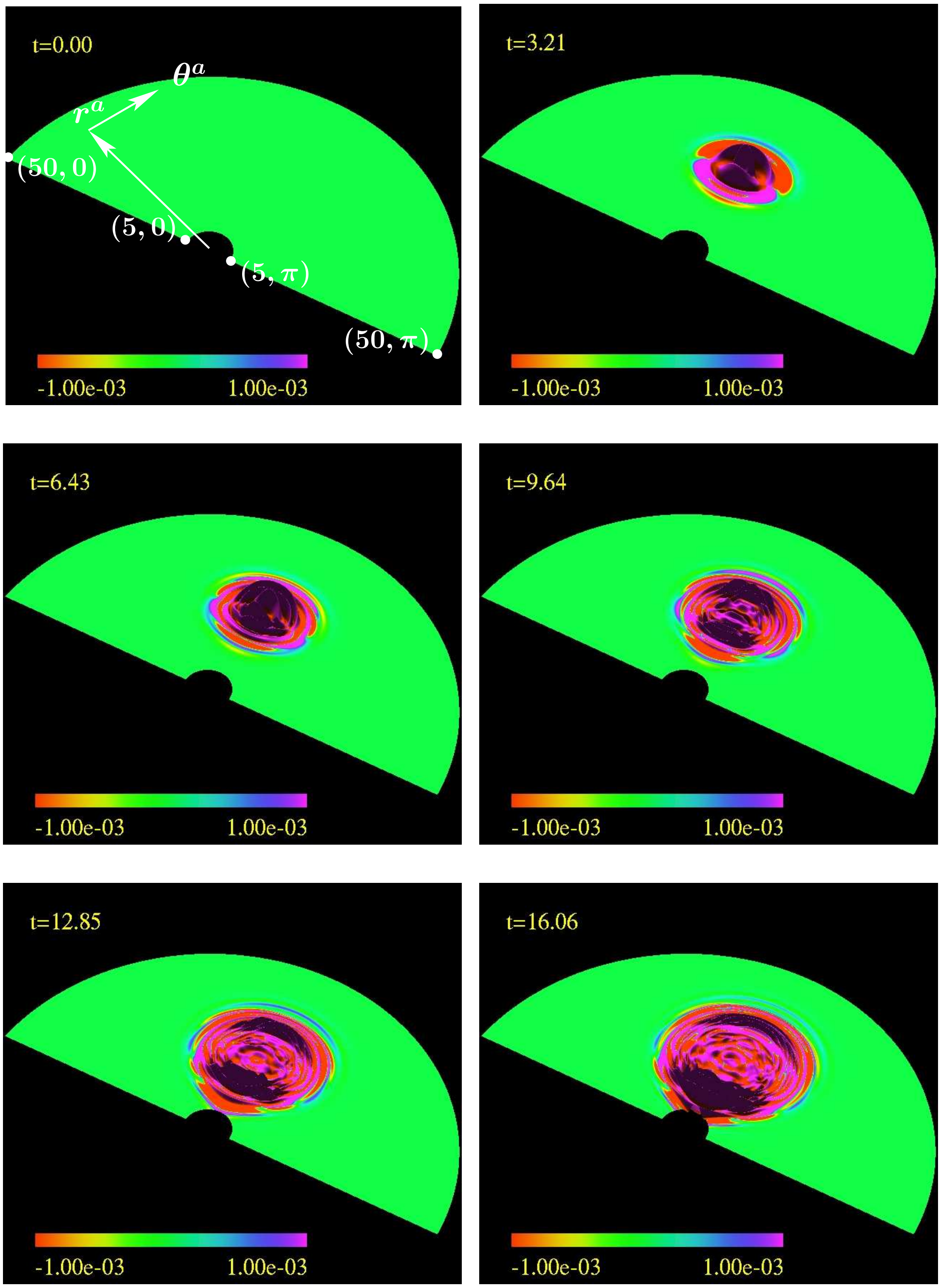

Figure 4.67: Displayed is the total angular momentum density in $a = M = 5$ Kerr spacetime for $e = 2.4$ massless perturbations for the early phase of evolution. Both amplitude and colour gradient are scaled linearly. The directions of coordinate vectors $r^a \sim (0, 1, 0, 0)$ and $\theta^a \sim (0, 0, 1, 0)$ are shown in the first frame. The computational domain covers the range $5 \leq r \leq 50$ and $0 \leq \theta \leq \pi$, and the corners of the domain are labelled with their (r, θ) ordinate values.

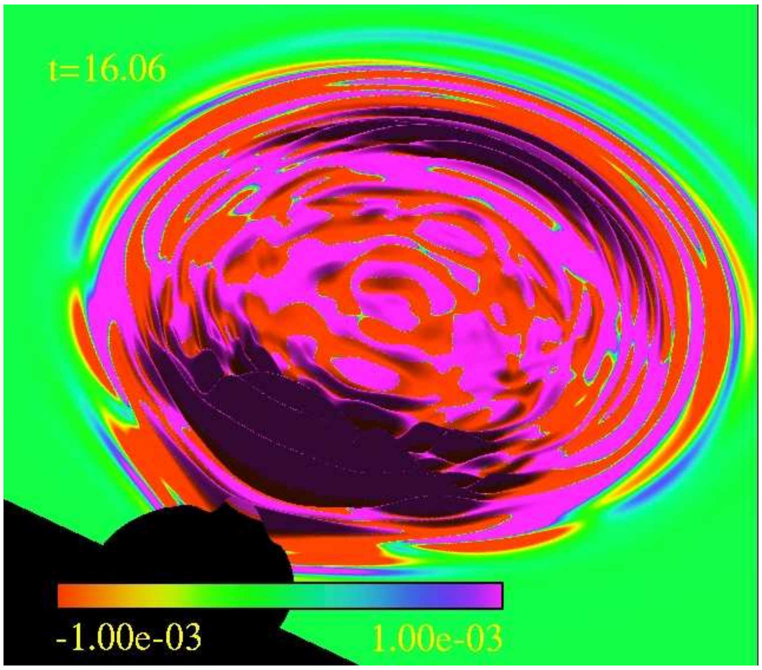

Figure 4.68: Displayed is a closer view of the total angular momentum density at $t = 16.06$ in $a = M = 5$ Kerr spacetime for $e = 2.4$ massless perturbations. Amplitude and colour gradient are both scaled linearly. The computational domain and coordinate vectors would be the same as those shown in Figure 4.67.

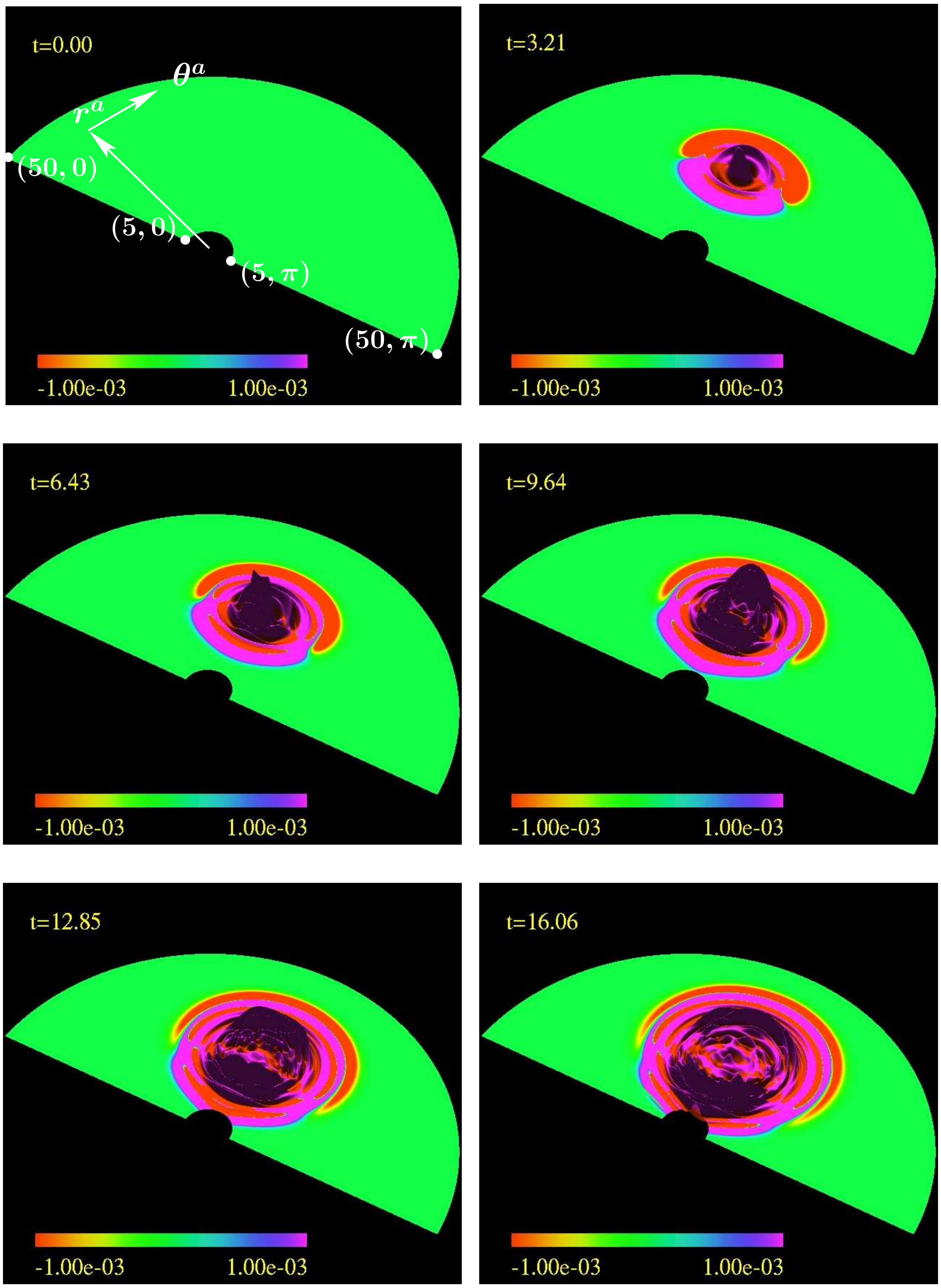

Figure 4.69: Displayed is the charge density in $a = M = 5$ Kerr spacetime for $e = 2.4$ massless perturbations for the early phase of evolution. Both amplitude and colour gradient are scaled linearly. The directions of coordinate vectors $r^a \sim (0, 1, 0, 0)$ and $\theta^a \sim (0, 0, 1, 0)$ are shown in the first frame. The computational domain covers the range $5 \le r \le 50$ and $0 \le \theta \le \pi$, and the corners of the domain are labelled with their (r, θ) ordinate values.

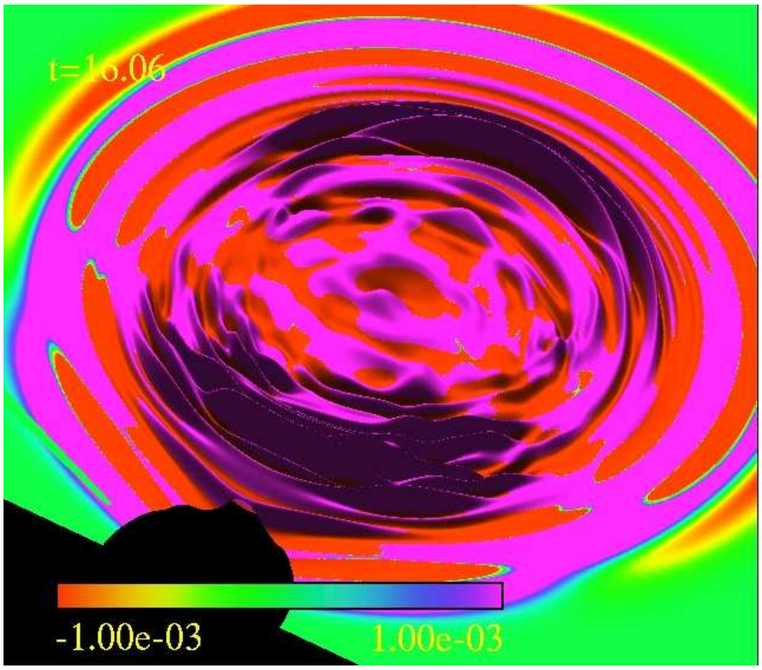

Figure 4.70: Displayed is a closer view of the charge density at $t = 16.06$ in $a = M = 5$ Kerr spacetime for $e = 2.4$ massless perturbations. Amplitude and colour gradient are again scaled linearly, and the computational domain and coordinate vectors would be the same as those shown in Figure 4.69.

4.3.6 Massive Charged Maxwell-Klein-Gordon Equation Dynamics: Collimation, Orbiting Resonances and Decay of $m_\Phi = 0.3$, $e = 0.6$ Electromagnetically Coupled $s = 0$ and $s = 1$ Perturbations

Now that I have examined massless coupled and uncoupled $s = 0$ and $s = 1$ perturbations in sufficient detail, I am in a position to examine the physics of massive coupled perturbations in $M = 5$ Kerr spacetime. To summarize preceding results, massless $s = 0$ perturbations display the effect of orbiting resonance, while massive $s = 0$ perturbations display mode trapping. Furthermore, for the value $m_\Phi = 0.3$ which displays the strongest trapping, the $s = 0$ perturbations appear to display preferential scattering along the axis of black hole rotation. While $s = 1$ perturbations also exhibit orbiting resonance, they do not display either trapping or preferential scattering in the spacetime. However, there is evidence in the form of total energy increase and angular momentum flux from the black hole to support superradiant scattering of the $s = 1$ perturbations. Finally, while massless electromagnetically coupled $s = 0$ and $s = 1$ perturbations display orbiting resonance, charge separation, and dynamo-like behaviour, neither trapping, preferential scattering, nor superradiant amplification are in evidence from analysis of the choice $e = 0.6$.

I now demonstrate how a choice of nonzero mass and charge coupling parameter together lead to new dynamics. The natural choice for mass parameter is $m_\Phi = 0.3$—since that is the value at which mode trapping is greatest (for the given initial conditions), it is hypothesized the choice will provide a substantial period over which the perturbations will persist and interact electromagnetically in the black hole spacetime. The choice for charge coupling parameter is not as obvious. While values as large as $e = 2.4$ may be desired, the resulting intricate dynamics would require very high resolution and correspondingly large computational resources. However, the intermediate choice $e = 0.6$

has demonstrated sufficient coupling for interesting electromagnetic effects while requiring modest finite difference grid resolution. I therefore compute the evolution for $m_\Phi = 0.3$ perturbations with $e = 0.6$ on $M = 5$ Kerr spacetimes of rotation $a = 0, 0.8M$ and $a = M$. The computational domain spans the coordinate range $5 \leq r \leq 50$, $0 \leq \theta \leq \pi$, and the period $0 \leq t \lesssim 200$. The data is computed in parallel across 64 processors with overlap regions 3 grid points wide. The finite difference grid itself has $J = 801$ radial and $K = 401$ angular points, providing sufficient resolution to maintain an accuracy of $\approx 1\%$ until perturbations first cross the ergosphere.

Examining first the total normalized energy density of Figures 4.71 and 4.72, it is apparent that evolution in the $a = M = 5$ spacetime displays behaviour different from that seen in the other choices for m_Φ and e. Except for the case $m_\Phi = 0.3$, there was previously no evidence for preferential scattering along the axis of black hole rotation. In the present case, addition of charge coupling results in somewhat different focusing of the energy density and greater collimation. To understand contributions to the observed dynamics, I also display the normalized scalar energy density, $\rho_{T(\Phi)}$ (Figures 4.73 and 4.74), and the electromagnetic contribution, $\rho_{T(A)}$ (Figures 4.75 and 4.76). For completeness, I also display the corresponding evolutionary sequence for $\rho_{T(\Phi A)}$ (see Figures 4.77 and 4.78). From $\rho_{T(\Phi)}$ and $\rho_{T(A)}$ it is apparent how the scalar component accounts for the greatest contribution to the collimated energy density. I then conclude that while electromagnetic coupling has an effect on the collimation of energy, it does not seem to be more significant in this regard than the effect of massive mode scattering from the black hole potential. One case where electromagnetism could have a profound influence is in the collimation of large m_Φ scalar fields that would otherwise not reflect off the spacetime potential barrier. This hypothesis will have be be tested with future computation. Finally, in Figure 4.79 I display the total normalized energy in the computational domain, T, along with individual contributions $T(\Phi)$, $T(A)$ and $T(\Phi A)$. It is there obvious that $T(\Phi)$ is the dominant component throughout evolution. $T(A)$ is initially very small, but quickly increases by orders of magnitude at early time. During this phase both $T(\Phi)$ and $T(\Phi A)$ decrease sharply. Afterwards, $T(A)$ remains large, and $T(\Phi A)$ increases at the expense of $T(\Phi)$. After $t = 20$ the changes in each of the components are less dramatic. Again, $T(\Phi A)$ takes on both positive and negative values during evolution. Before proceeding, note also the presence of orbiting resonances as displayed in the data, and notice how $\rho_{T(A)}$ is the principal contributor. As in the case of massless $e = 0.6$ perturbations, the period between the first two orbits is $\approx 70t$ and the attenuation is $\sim 10^{-1}$. Again, the orbital period here corresponds to a frequency more than twice that of unstable circular photon orbits at $r = 3M$ (cf. equation (4.164) and related discussion).

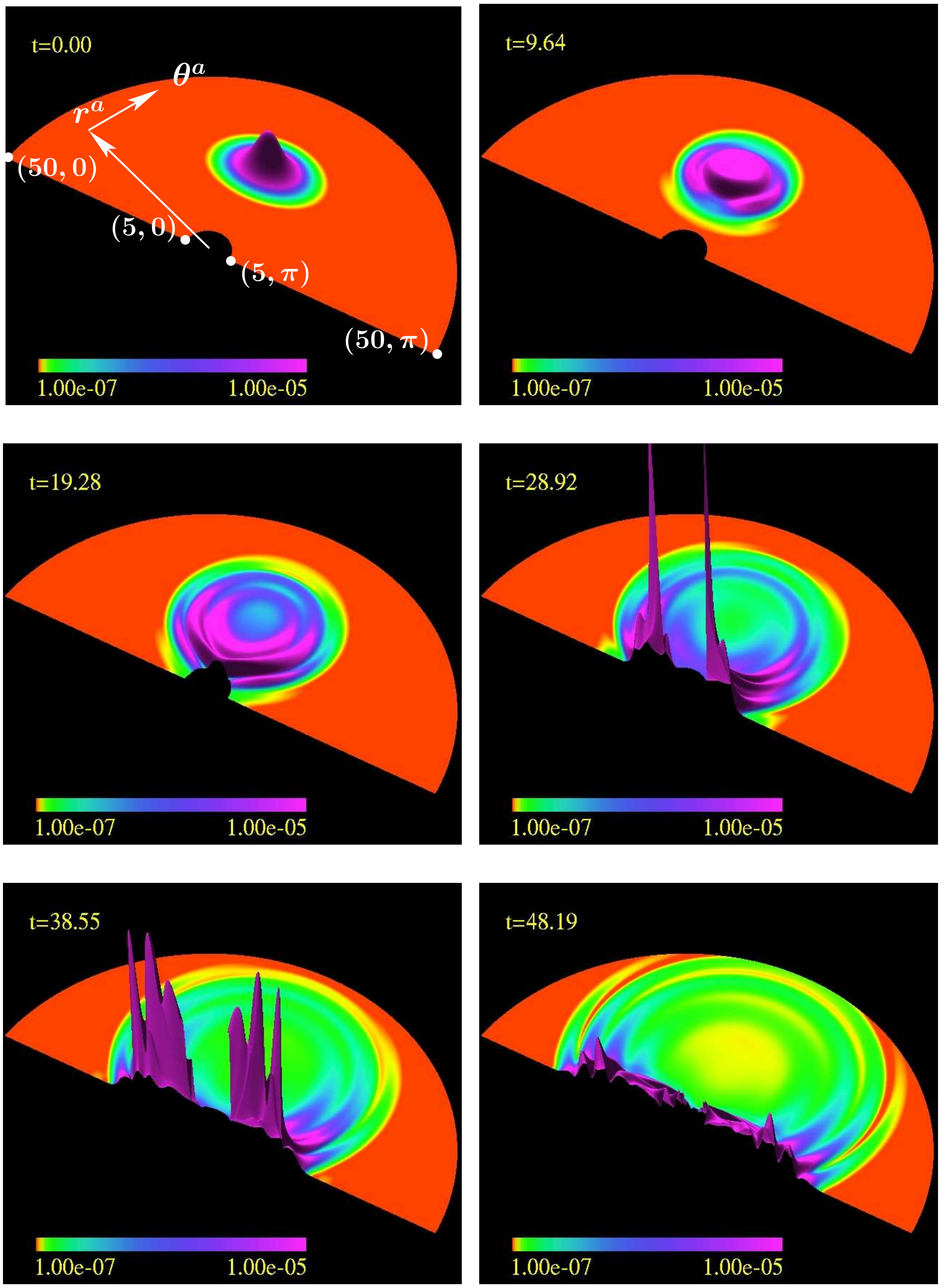

Figure 4.71: Displayed is the total normalized energy density in $a = M = 5$ Kerr spacetime for $e = 0.6$, $m_\Phi = 0.3$ perturbations. The amplitude is scaled linearly and the colour gradient is scaled logarithmically. The directions of coordinate vectors $r^a \sim (0, 1, 0, 0)$ and $\theta^a \sim (0, 0, 1, 0)$ are shown in the first frame. The computational domain covers the range $5 \leq r \leq 50$ and $0 \leq \theta \leq \pi$, and the corners of the domain are labelled with their (r, θ) ordinate values.

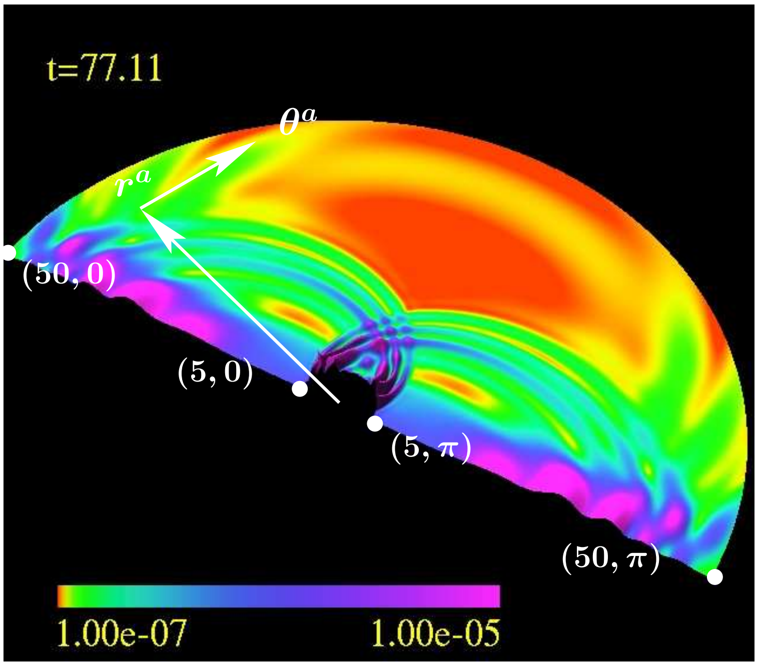

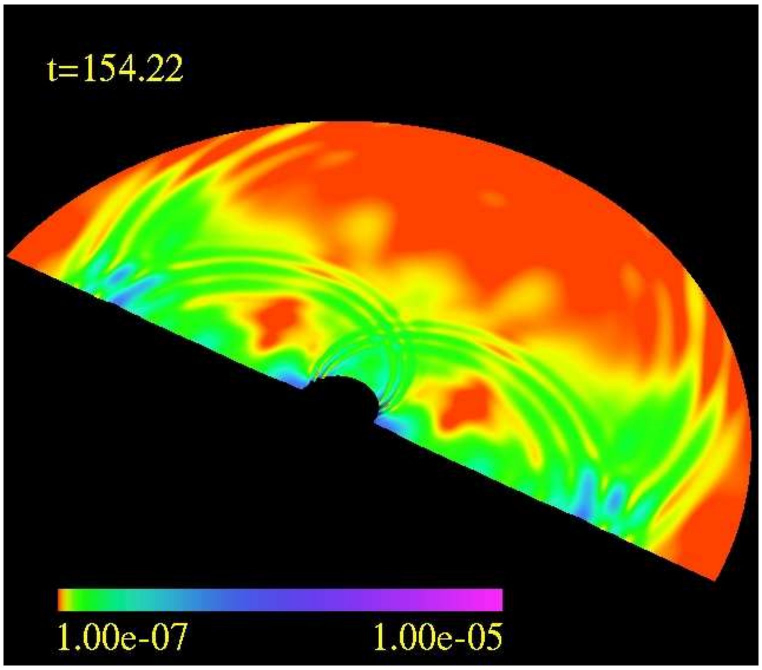

Figure 4.72: Displayed is the total normalized energy density at $t = 77.11$ and $t = 154.22$ in $a = M = 5$ Kerr spacetime for $e = 0.6$, $m_\Phi = 0.3$ perturbations. The amplitude is scaled linearly and the colour gradient is scaled logarithmically. The directions of coordinate vectors $r^a \sim (0, 1, 0, 0)$ and $\theta^a \sim (0, 0, 1, 0)$ are shown in the first frame. The computational domain covers the range $5 \le r \le 50$ and $0 \le \theta \le \pi$, and the corners of the domain are labelled with their (r, θ) ordinate values. An MPEG animation showing evolution of normalized energy density for $e = 0.6$, $m_\Phi = 0.3$ perturbations over the period $0 \le t \lesssim 154$ is available at `http://$WWW/People/petryk/animations/6.mpeg` where `$WWW` is currently `laplace.physics.ubc.ca` .

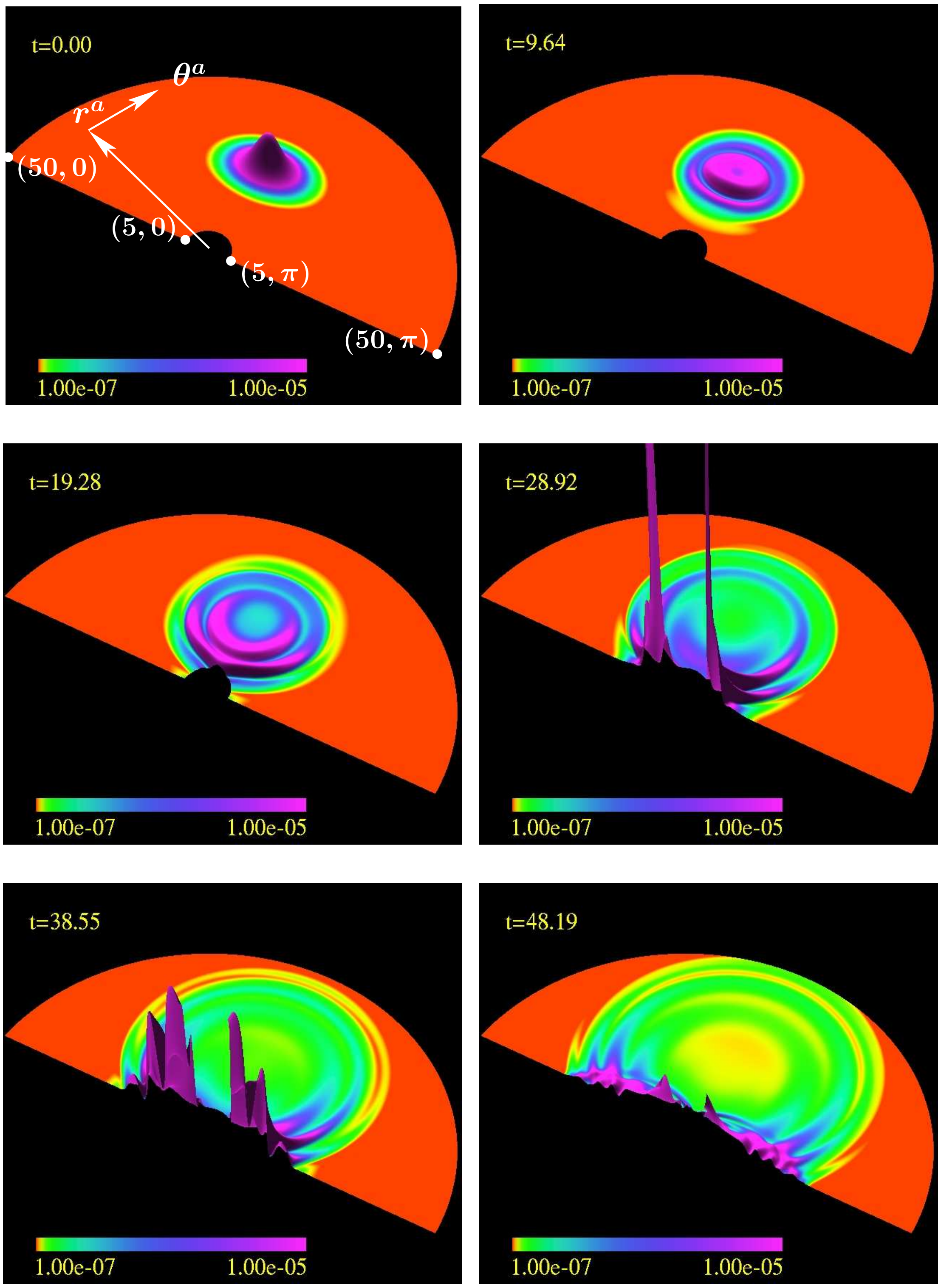

Figure 4.73: Displayed is the normalized scalar energy density in $a = M = 5$ Kerr spacetime for $e = 0.6$, $m_\Phi = 0.3$ perturbations. The amplitude is scaled linearly and the colour gradient is scaled logarithmically. The directions of coordinate vectors $r^a \sim (0, 1, 0, 0)$ and $\theta^a \sim (0, 0, 1, 0)$ are shown in the first frame. The computational domain covers the range $5 \leq r \leq 50$ and $0 \leq \theta \leq \pi$, and the corners of the domain are labelled with their (r, θ) ordinate values.

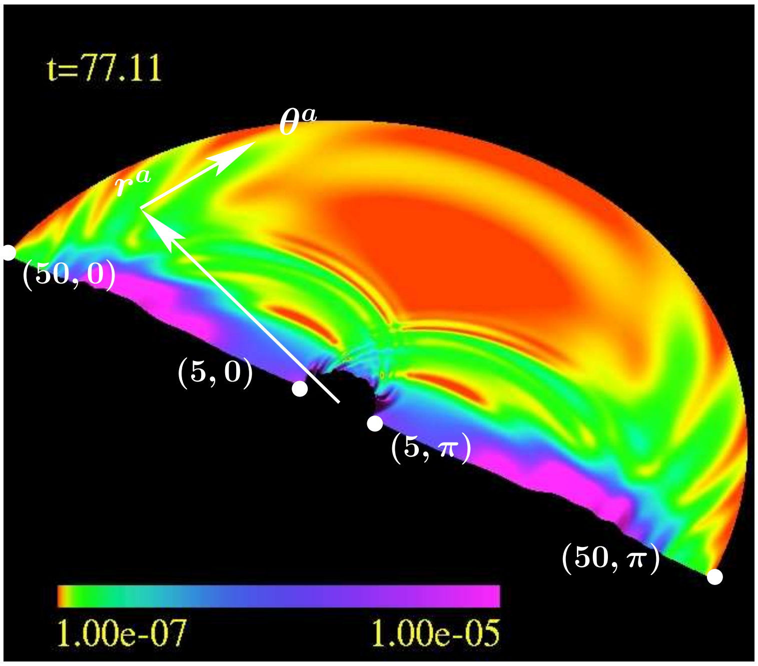

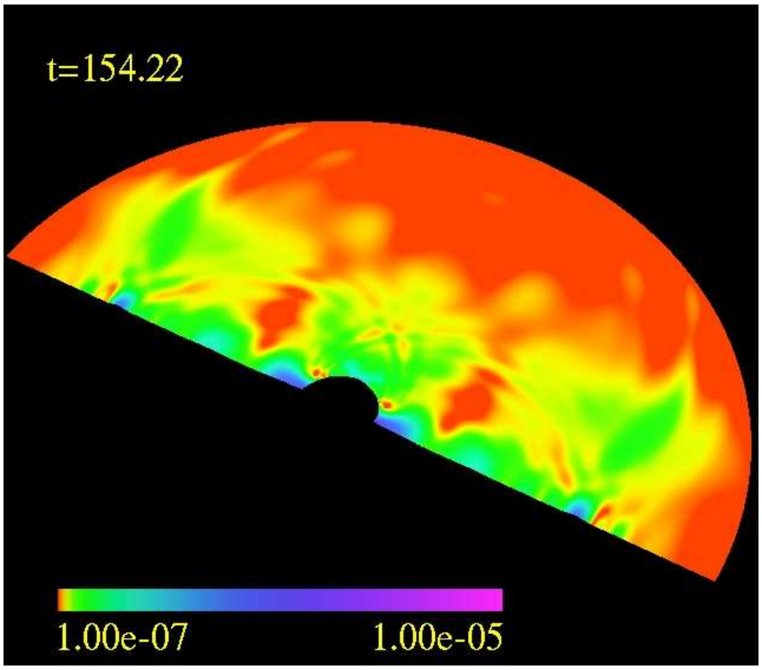

Figure 4.74: Displayed is the normalized scalar energy density at $t = 77.11$ and $t = 154.22$ in $a = M = 5$ Kerr spacetime for $e = 0.6$, $m_\Phi = 0.3$ perturbations. The amplitude is scaled linearly and the colour gradient is scaled logarithmically. The directions of coordinate vectors $r^a \sim (0, 1, 0, 0)$ and $\theta^a \sim (0, 0, 1, 0)$ are shown in the first frame. The computational domain covers the range $5 \leq r \leq 50$ and $0 \leq \theta \leq \pi$, and the corners of the domain are labelled with their (r, θ) ordinate values.

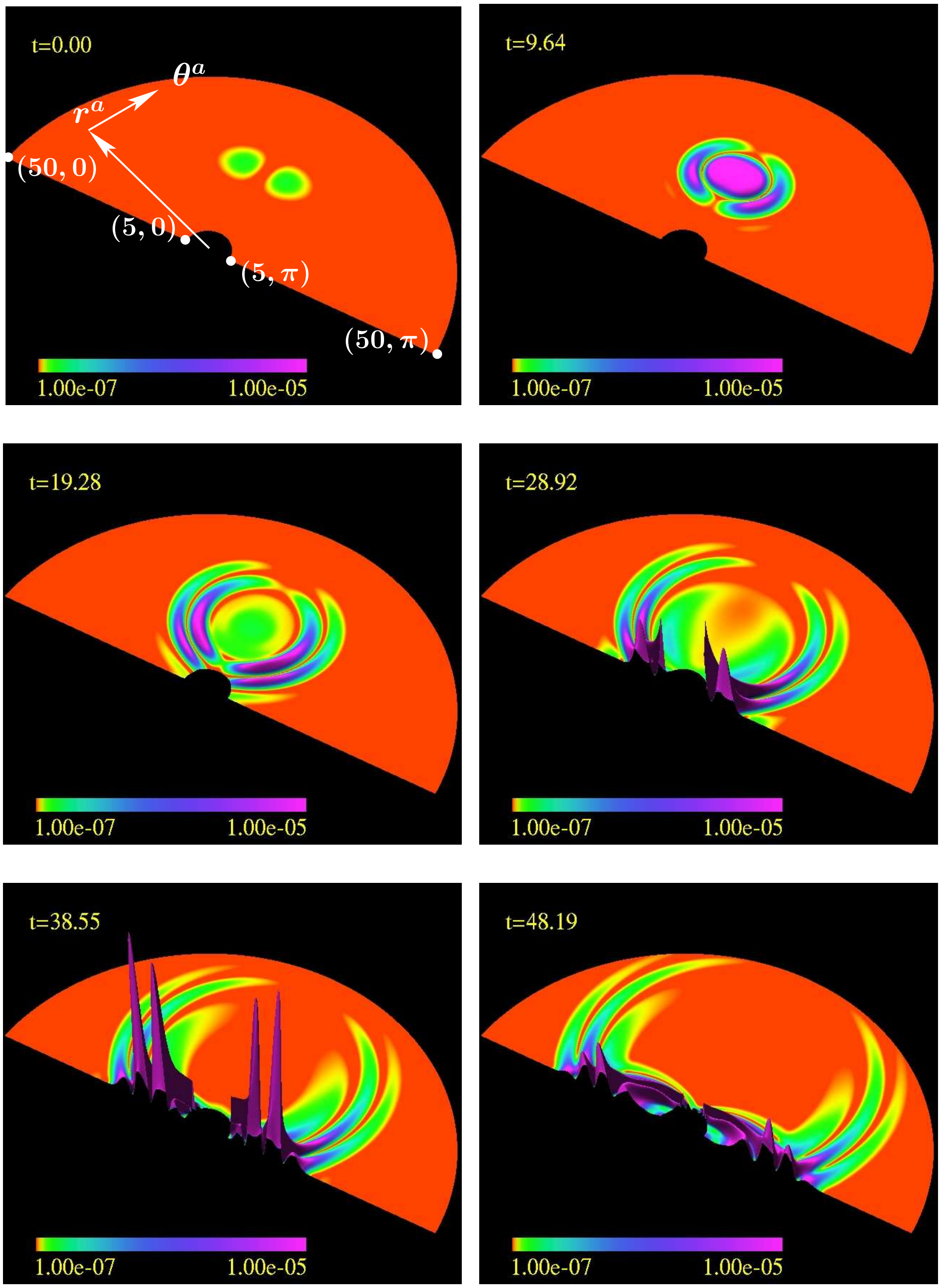

Figure 4.75: Displayed is the normalized electromagnetic energy density in $a = M = 5$ Kerr spacetime for $e = 0.6$, $m_\Phi = 0.3$ perturbations. The amplitude is scaled linearly and the colour gradient is scaled logarithmically. The directions of coordinate vectors $r^a \sim (0, 1, 0, 0)$ and $\theta^a \sim (0, 0, 1, 0)$ are shown in the first frame. The computational domain covers the range $5 \leq r \leq 50$ and $0 \leq \theta \leq \pi$, and the corners of the domain are labelled with their (r, θ) ordinate values.

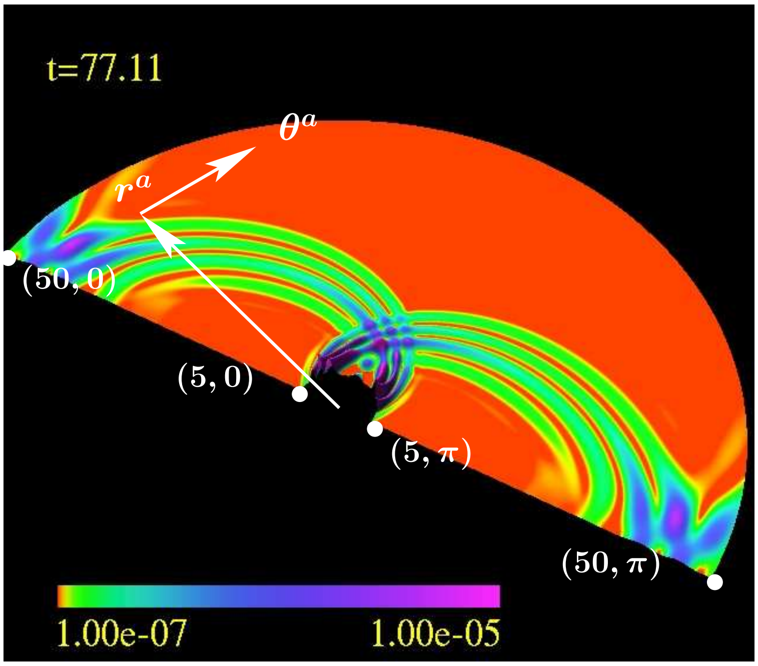

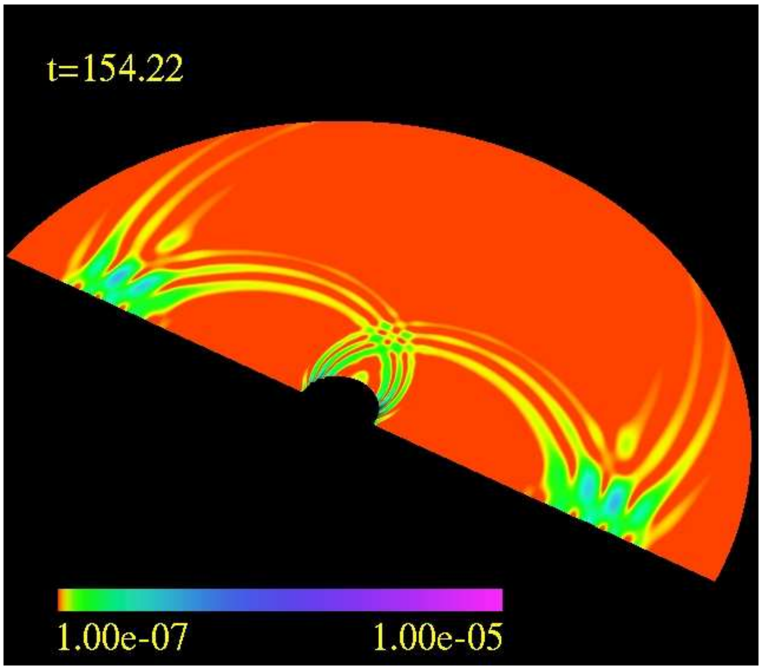

Figure 4.76: Displayed is the normalized electromagnetic energy density at $t = 77.11$ and $t = 154.22$ in $a = M = 5$ Kerr spacetime for $e = 0.6$, $m_\Phi = 0.3$ perturbations. The amplitude is scaled linearly and the colour gradient is scaled logarithmically. The directions of coordinate vectors $r^a \sim (0, 1, 0, 0)$ and $\theta^a \sim (0, 0, 1, 0)$ are shown in the first frame. The computational domain covers the range $5 \le r \le 50$ and $0 \le \theta \le \pi$, and the corners of the domain are labelled with their (r, θ) ordinate values.

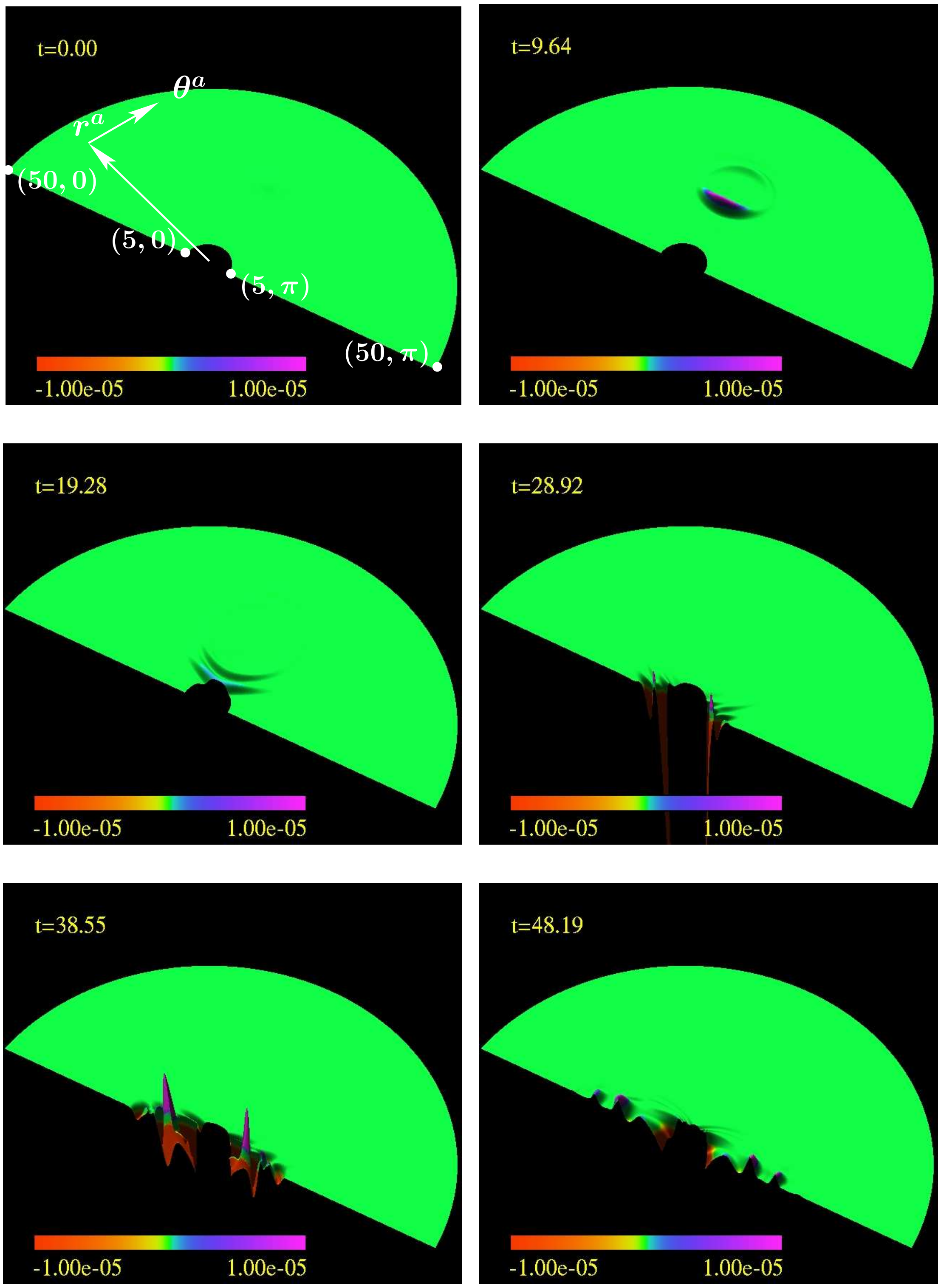

Figure 4.77: Displayed is the normalized coupling energy density in $a = M = 5$ Kerr spacetime for $e = 0.6$, $m_\Phi = 0.3$ perturbations. The amplitude is scaled linearly and the colour gradient is scaled logarithmically. The directions of coordinate vectors $r^a \sim (0, 1, 0, 0)$ and $\theta^a \sim (0, 0, 1, 0)$ are shown in the first frame. The computational domain covers the range $5 \leq r \leq 50$ and $0 \leq \theta \leq \pi$, and the corners of the domain are labelled with their (r, θ) ordinate values.

To determine how much effect black hole rotation has on collimation I also evolve the $m_\Phi = 0.3$, $e = 0.6$ perturbations in $M = 5$ Kerr spacetimes with $a = 0$ and $a = 0.8M$. The results are nearly identical in all respects to the case $a = M$. I simply display the total normalized energy density at $t = 77.11$ for $a = 0$ in Figure 4.80. To further quantify similarities I plot the total normalized energy, T, contained in the computational domain for $0 \leq t \lesssim 200$ for $a = 0, 0.8M$ and $a = M$ in Figure 4.81. It is there seen that black hole angular momentum has a rather small effect in the evolution of the coupled massive perturbations. However, while the differences are small, it can still be seen that black hole rotation decreases the perturbation energy decay rate at intermediate and late time. At late time, this decay rate can be approximated with the power law

$$\log(T) \sim -kt \ , \tag{4.197}$$

with the decay constant $k \approx 6 \times 10^{-3}$. The proximity of this value to $k \approx 5 \times 10^{-3}$ measured for uncoupled $m_\Phi = 0.3$ perturbations in $a = M = 5$ Kerr spacetime further supports the conclusion that massive scalar effects have a dominant influence in the dynamics.

Detailed analysis of the remaining conserved quantities (angular momentum and charge) and axial current component are not especially illuminating since their behaviour can be largely deduced from the results of preceding sections. It is almost sufficient to state they evolve in a nontrivial and morphologically unique manner for $e = 0.6$, $m_\Phi = 0.3$ perturbations. For completeness, I provide just a few steps of each evolution. Figure 4.82 depicts the angular momentum density at $t = 0, 77.11$ and $t = 154.22$ for black hole parameter values $a = M = 5$. As in the case of massless electromagnetically coupled perturbations, the initial angular momentum density is zero everywhere, but quickly evolves in a rather detailed manner. The complexity of its dynamics lies somewhere between those of massless perturbations with $e = 0.6$ and those with $e = 2.4$ (cf. Figures 4.52, 4.67 and 4.68). At both intermediate and late time there is noticeable correlation between the angular momentum and orbiting resonances seen in the energy density distributions of Figure 4.72. To analyze the effects of black hole rotation I have also evolved perturbations on the $a = 0$ and $a = 0.8M$ spacetimes. As in the case of massless $e = 0.6$ perturbations, comparison reveals the black hole rotation has a noticeable effect on the evolution. Figure 4.83 shows the angular momentum density at $t = 77.11$ in $a = 0$, $M = 5$ spacetime. Comparing with Figure 4.82, it is evident that black hole rotation dramatically amplifies the density and its gradients. This is especially true in the ergoregion and surrounding spacetime at intermediate times near $t = 77.11$. For further analysis I display the total integrated angular momentum in Figure 4.84 for the period $0 \leq t \lesssim 200$ for $a = 0, 0.8M$ and $a = M$ Kerr spacetimes. Also similar to the massless $e = 0.6$ solutions is the high variability of total angular momentum over an intermediate phase of the evolution (cf. Figure 4.54). In the present case, this variability peaks during $50 \lesssim t \lesssim 80$ when the electromagnetic component is largely concentrated in the ergoregion (cf. Figure 4.76). Thus, the total angular momentum is strongly affected by black hole angular momentum, predominantly associated with the electromagnetic perturbations, and not dramatically altered by simply increasing m_Φ from zero to $m_\Phi = 0.3$.

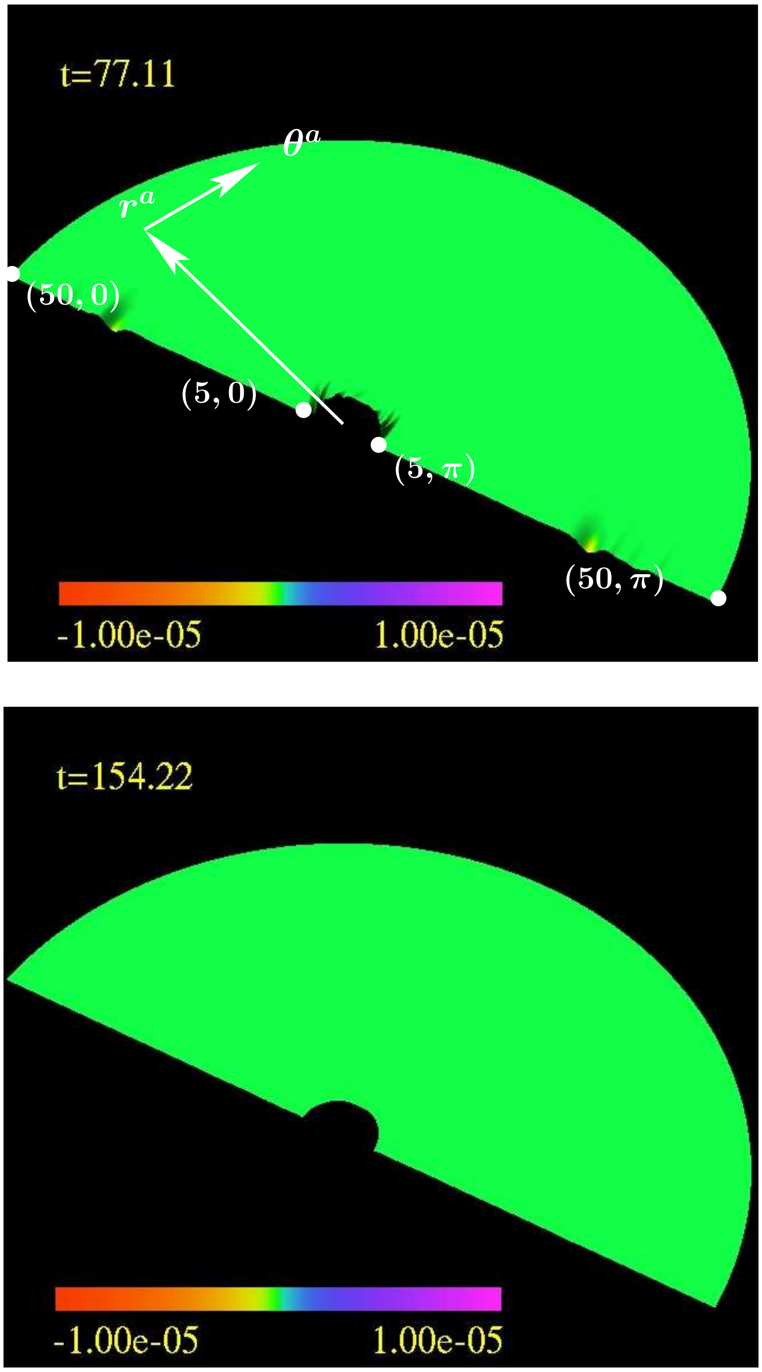

Figure 4.78: Displayed is the normalized coupling energy density at $t = 77.11$ in $a = M = 5$ Kerr spacetime for $e = 0.6$, $m_\Phi = 0.3$ perturbations. The amplitude is scaled linearly and the colour gradient is scaled logarithmically. The directions of coordinate vectors $r^a \sim (0, 1, 0, 0)$ and $\theta^a \sim (0, 0, 1, 0)$ are shown in the first frame. The computational domain covers the range $5 \leq r \leq 50$ and $0 \leq \theta \leq \pi$, and the corners of the domain are labelled with their (r, θ) ordinate values.

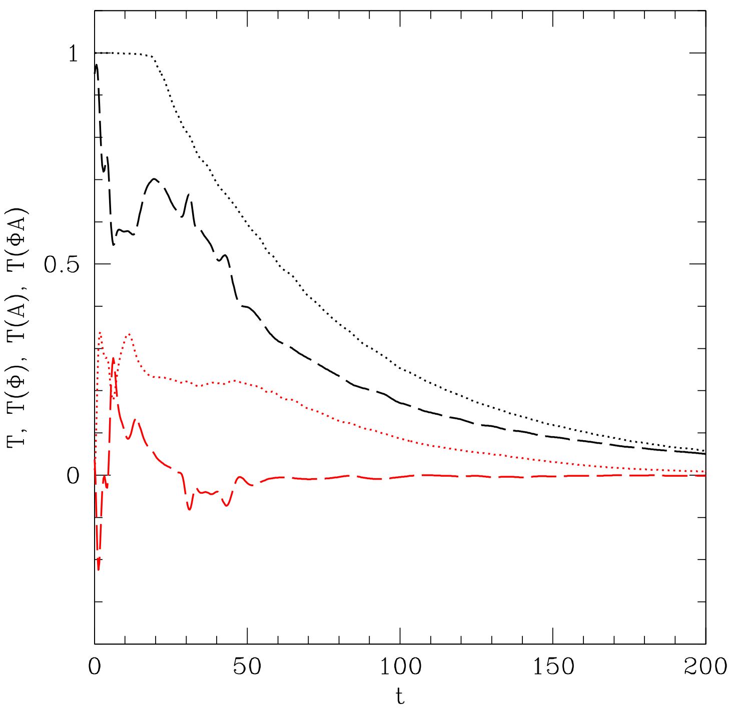

Figure 4.79: Decomposition of integrated normalized energy density for $m_\Phi = 0.3$, $e = 0.6$ perturbations in $a = M = 5$ Kerr spacetime. Plotted are the total energy and contributions to the total contained within $5 \leq r \leq 50$, $0 \leq \theta \leq \pi$ and $0 \leq \phi \leq 2\pi$, as a function of coordinate time t. The dotted black line represents the total normalized energy, the dashed black line represents the normalized scalar field contribution, the dotted red line is the normalized electromagnetic contribution and the dashed red line the normalized contribution from coupling terms.

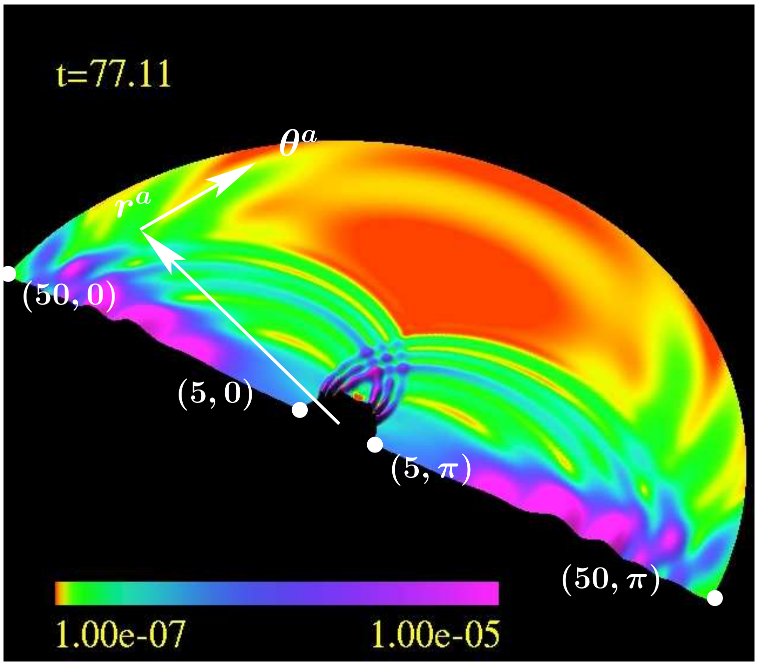

Figure 4.80: Displayed is the normalized total energy density at $t = 77.11$ in $a = 0$, $M = 5$ Kerr spacetime for $e = 0.6$, $m_\Phi = 0.3$ perturbations. Observe how closely the $a = 0$ data matches that of $a = M$ shown in Figure 4.72. The amplitude is scaled linearly and the colour gradient is scaled logarithmically. The directions of coordinate vectors $r^a \sim (0, 1, 0, 0)$ and $\theta^a \sim (0, 0, 1, 0)$ are shown in the first frame. The computational domain covers the range $5 \leq r \leq 50$ and $0 \leq \theta \leq \pi$, and the corners of the domain are labelled with their (r, θ) ordinate values.

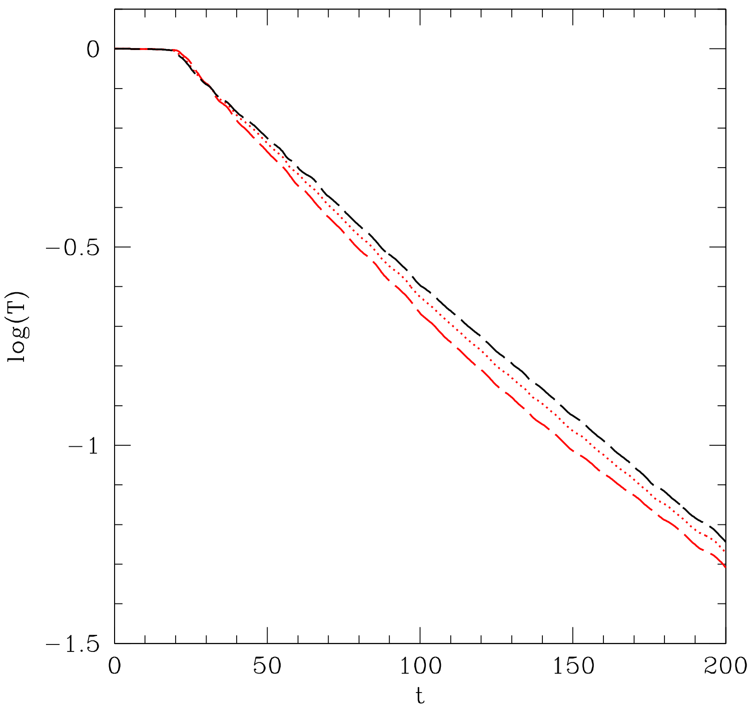

Figure 4.81: Integrated normalized energy density for $m_\Phi = 0.3$, $e = 0.6$ perturbations in $M = 5$ Kerr spacetime. Plotted is $\log(T)$, the logarithm of the total energy contained within $5 \leq r \leq 50$, $0 \leq \theta \leq \pi$ and $0 \leq \phi \leq 2\pi$, as a function of coordinate time t. The dashed red line represents data for $a/M = 0$, the dotted red line data for $a/M = 0.8$, and the dashed black line data for $a/M = 1$. Observe how black hole angular momentum decreases the overall decay rate of electromagnetic perturbations. Again, the decrease of energy over time results from the flux across surfaces $r = 5$ and $r = 50$, and thus out of the computational domain.

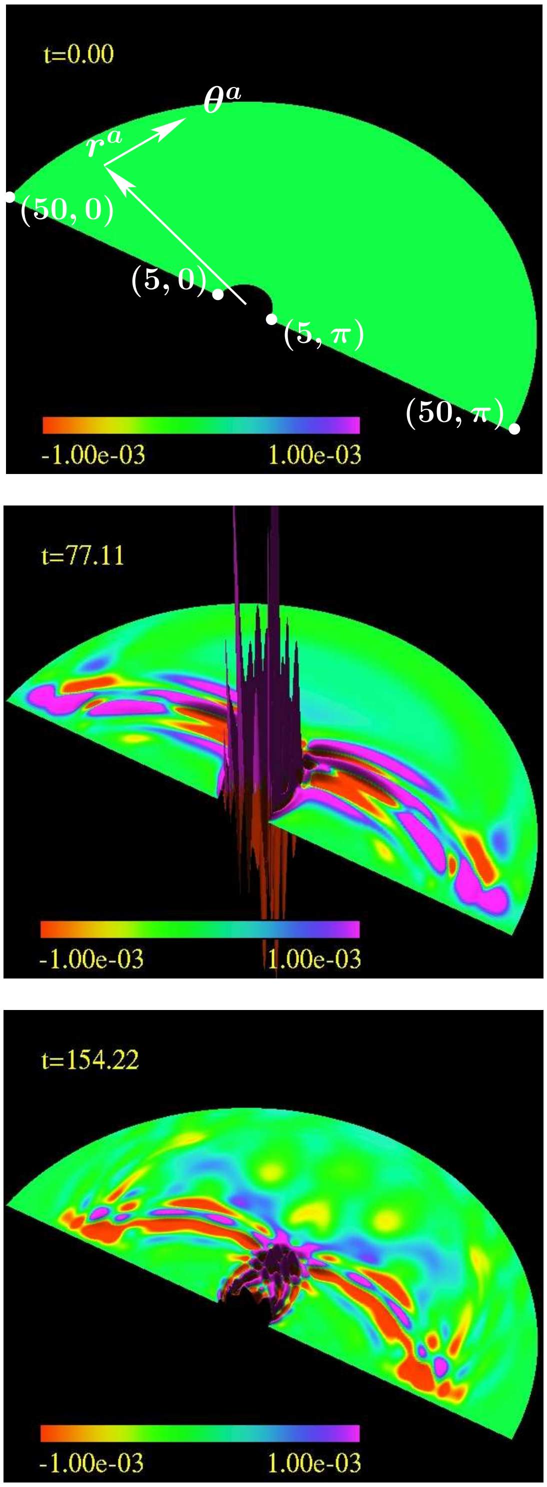

Figure 4.82: Angular momentum density at $t = 0, 77.11, 154.22$ for $e = 0.6$, $m_\Phi = 0.3$ perturbations in $a = M = 5$ Kerr spacetime. The directions of coordinate vectors $r^a \sim (0,1,0,0)$ and $\theta^a \sim (0,0,1,0)$ are shown in the first frame. The computational domain covers the range $5 \leq r \leq 50$ and $0 \leq \theta \leq \pi$, and the corners of the domain are labelled with their (r, θ) ordinate values. The amplitude and colour gradient are both scaled linearly. An MPEG animation showing evolution over $0 \leq t \lesssim 154$ is available at `http://$WWW/People/petryk/animations/7.mpeg` where `$WWW` is currently `laplace.physics.ubc.ca` .

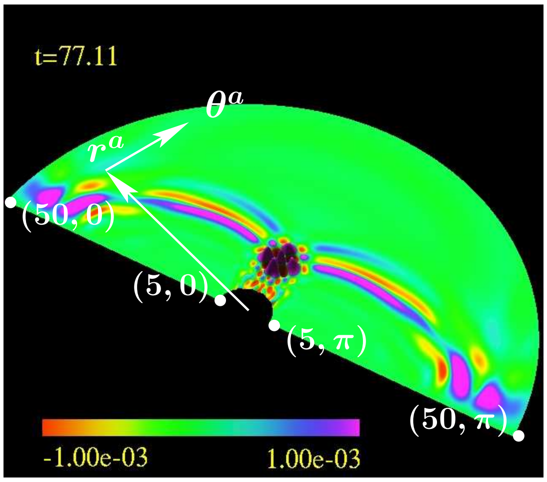

Figure 4.83: Angular momentum density at $t = 77.11$ for $e = 0.6$, $m_\Phi = 0.3$ perturbations in $a = 0$, $M = 5$ Kerr spacetime. The directions of coordinate vectors $r^a \sim (0, 1, 0, 0)$ and $\theta^a \sim (0, 0, 1, 0)$ are shown in the first frame. The computational domain covers the range $5 \le r \le 50$ and $0 \le \theta \le \pi$, and the corners of the domain are labelled with their (r, θ) ordinate values. The amplitude and colour gradient are both scaled linearly. Observe how small these angular momentum density gradients are in comparison to those at $t = 77.11$ in $a = M$ Kerr spacetime as shown in Figure 4.82.

Examining the charge density depicted in Figure 4.85 for time steps $t = 0, 77.11$ and $t = 154.22$ for the $e = 0.6$, $m_\Phi = 0.3$ perturbations in $a = M = 5$ spacetime, I observe nontrivial evolution beginning from a zero net charge density initial data profile and leading to dynamic charge separation for all $t > 0$. While somewhat more intricate than the corresponding evolution of massless $e = 0.6$ perturbations (cf. Figure 4.55), the dynamics are certainly not as rich as those of massless $e = 2.4$ perturbations (cf. Figures 4.69 and 4.70). It therefore appears that addition of a nonzero mass parameter has a significant effect on the details of the evolution of charge density. Comparing with the $t = 77.11$ time step of $e = 0.6$, $m_\Phi = 0.3$ perturbation evolution in $a = 0$, $M = 5$ spacetime as shown in Figure 4.86, it is clear that while slightly different in detail, the degree of charge separation is comparable in rotating and nonrotating black hole backgrounds. The comparison is further investigated in Figure 4.87 where I display the total charge integrated over the computational domain for $0 \le t \lesssim 200$ in $a = 0, 0.8M$ and $a = M$ backgrounds. This figure shows how the total charge is in very close agreement for each of the spacetimes throughout evolution. It is thus obvious that while a modest change in the value of m_Φ has a substantial effect on charge separation, the evolution of charge density from the given initial conditions is only slightly dependent on black hole angular momentum for $e = 0.6$ perturbations (cf. Figures 4.55, 4.56 and 4.57).

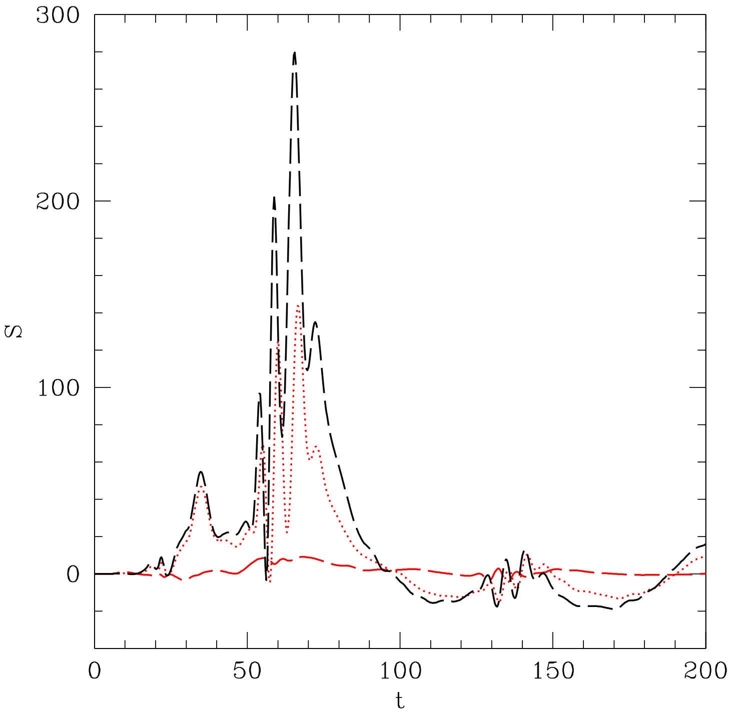

Figure 4.84: Integrated angular momentum density for $e = 0.6$, $m_\Phi = 0.3$ perturbations in $M = 5$ Kerr spacetime. Plotted is S, the total angular momentum contained within $5 \leq r \leq 50$, $0 \leq \theta \leq \pi$ and $0 \leq \phi \leq 2\pi$, as a function of coordinate time t. The dashed red line represents data for $a/M = 0$, the dotted red line data for $a/M = 0.8$, and the dashed black line data for $a/M = 1$. Clearly, perturbation angular momentum is especially variable in rotating black hole spacetimes over $50 \lesssim t \lesssim 80$, but tends towards $S = 0$ at late time.

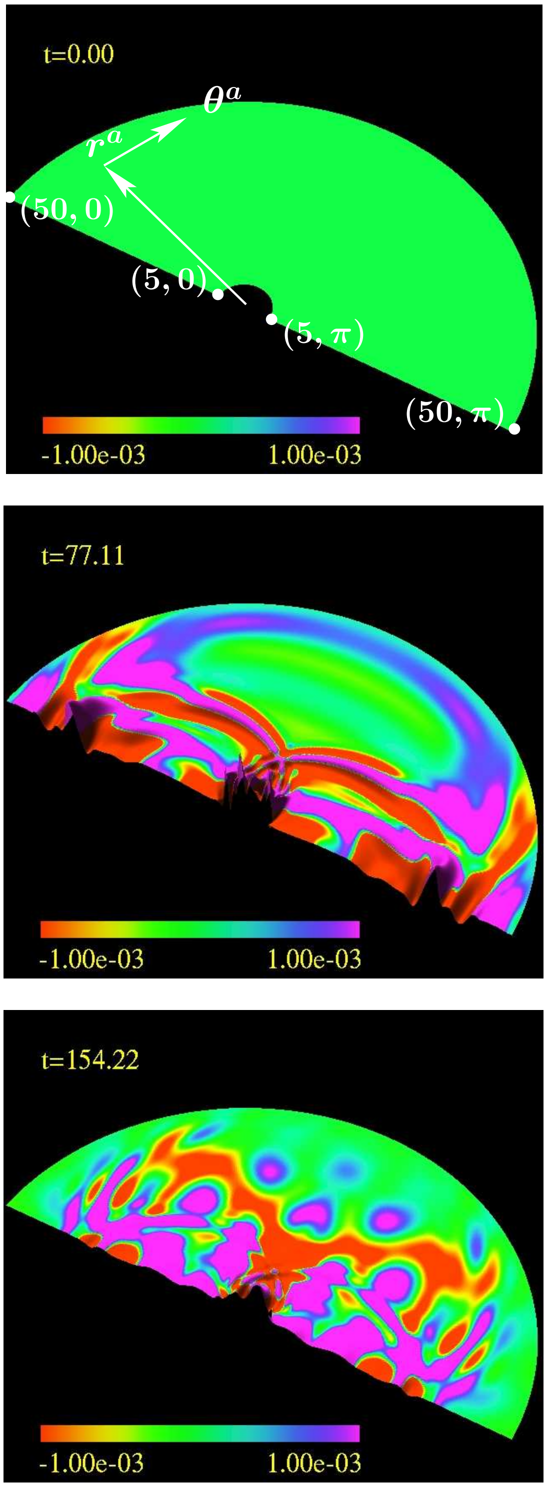

Figure 4.85: Charge density at $t = 0, 77.11, 154.22$ for $e = 0.6$, $m_\Phi = 0.3$ perturbations in $a = M = 5$ Kerr spacetime. The directions of coordinate vectors $r^a \sim (0,1,0,0)$ and $\theta^a \sim (0,0,1,0)$ are shown in the first frame. The computational domain covers the range $5 \le r \le 50$ and $0 \le \theta \le \pi$, and the corners of the domain are labelled with their (r,θ) ordinate values. The amplitude and colour gradient are both scaled linearly. An MPEG animation showing evolution over $0 \le t \lesssim 154$ is available at `http://$WWW/People/petryk/animations/8.mpeg` where `$WWW` is currently `laplace.physics.ubc.ca`.

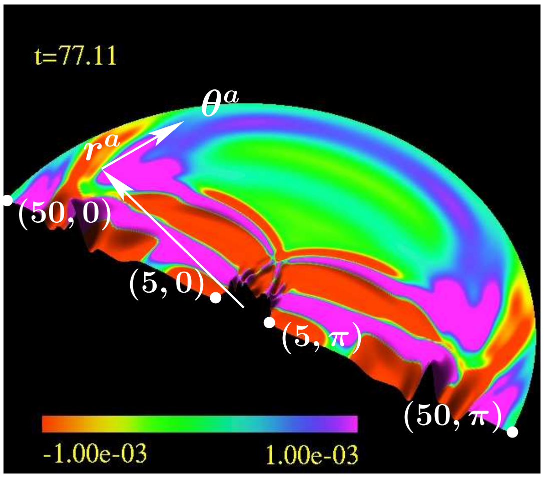

Figure 4.86: Charge density at $t = 77.11$ for $e = 0.6$, $m_\Phi = 0.3$ perturbations in $a = 0$, $M = 5$ Kerr spacetime. The directions of coordinate vectors $r^a \sim (0, 1, 0, 0)$ and $\theta^a \sim (0, 0, 1, 0)$ are shown in the first frame. The computational domain covers the range $5 \leq r \leq 50$ and $0 \leq \theta \leq \pi$, and the corners of the domain are labelled with their (r, θ) ordinate values. The amplitude and colour gradient are both scaled linearly. Comparing with Figure 4.85, it is clear that charge density distributions at $t = 77.11$ are affected by the value of black hole rotation parameter a, but not very strongly.

As could have been deduced from the preceding study of angular momentum evolution—and also from earlier investigation of angular momentum for the massless $e = 0.6$ perturbations—the effects of black hole rotation on the axial component of current, J_ϕ, are significant. Figure 4.88 displays J_ϕ at $t = 0, 77.11$ and $t = 154.22$ for the $e = 0.6$, $m_\Phi = 0.3$ perturbations in $a = M = 5$ spacetime. From a relatively simple profile at $t = 0$, the axial component evolves in a nontrivial manner. The current oscillates in direction and amplitude, indicating dynamo-like behaviour. Furthermore, the distribution displays large amplitude and steep gradients at $t = 77.11$ before relaxing at late time. As shown in Figure 4.82, the angular momentum density of the $e = 0.6$, $m_\Phi = 0.3$ perturbations also evolved from a simple distribution at $t = 0$ to a state with steep gradients in the ergoregion at $t = 77.11$ before settling down to some degree at late time. To determine the effects of black hole rotation on the axial component of the current, I evolve the $e = 0.6$, $m_\Phi = 0.3$ perturbations evolved in an $a = 0$, $M = 5$ Kerr spacetime. The distribution of J_ϕ at $t = 77.11$ is displayed in Figure 4.89. Comparing the small amplitudes and gradients of J_ϕ at $t = 77.11$ for the $a = 0$, $M = 5$ spacetime to the profile of J_ϕ at $t = 77.11$ for the $a = M = 5$ Kerr spacetime of Figure 4.82 it is clear that black hole rotation leads to significant amplification of J_ϕ in the ergoregion and surrounding space. To examine the effects of black hole rotation in more detail, I display the global maxima of J_ϕ evolved in $a = 0$ and $a = M$ spacetimes in Figure 4.90. The corresponding global minima are shown in Figure 4.91. As in the data of massless $e = 0.6$ perturbations (cf. Figures 4.61 and 4.60), $\max(J_\phi)$ for $a = M$ dominates over that of $a = 0$ after an early phase of evolution. The same is observed in the development of $\min(J_\phi)$. Therefore, while black hole rotation initially suppresses J_ϕ, its effect is to amplify the axial component of current after $t \approx 20$.

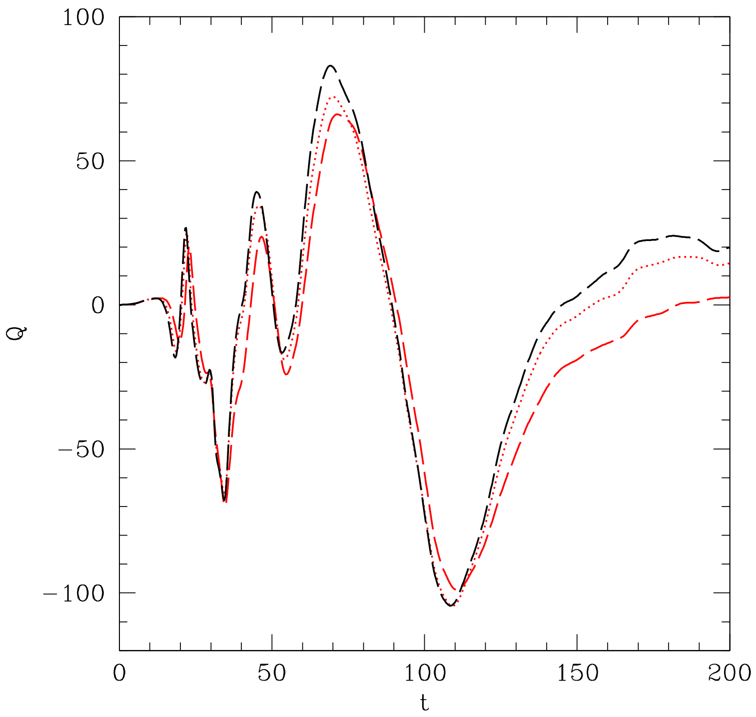

Figure 4.87: Integrated charge density for $e = 0.6$, $m_\Phi = 0.3$ perturbations in $M = 5$ Kerr spacetime. Plotted is Q, the total charge contained within $5 \le r \le 50$, $0 \le \theta \le \pi$ and $0 \le \phi \le 2\pi$, as a function of coordinate time t. The dashed red line represents data for $a/M = 0$, the dotted red line data for $a/M = 0.8$, and the dashed black line data for $a/M = 1$.

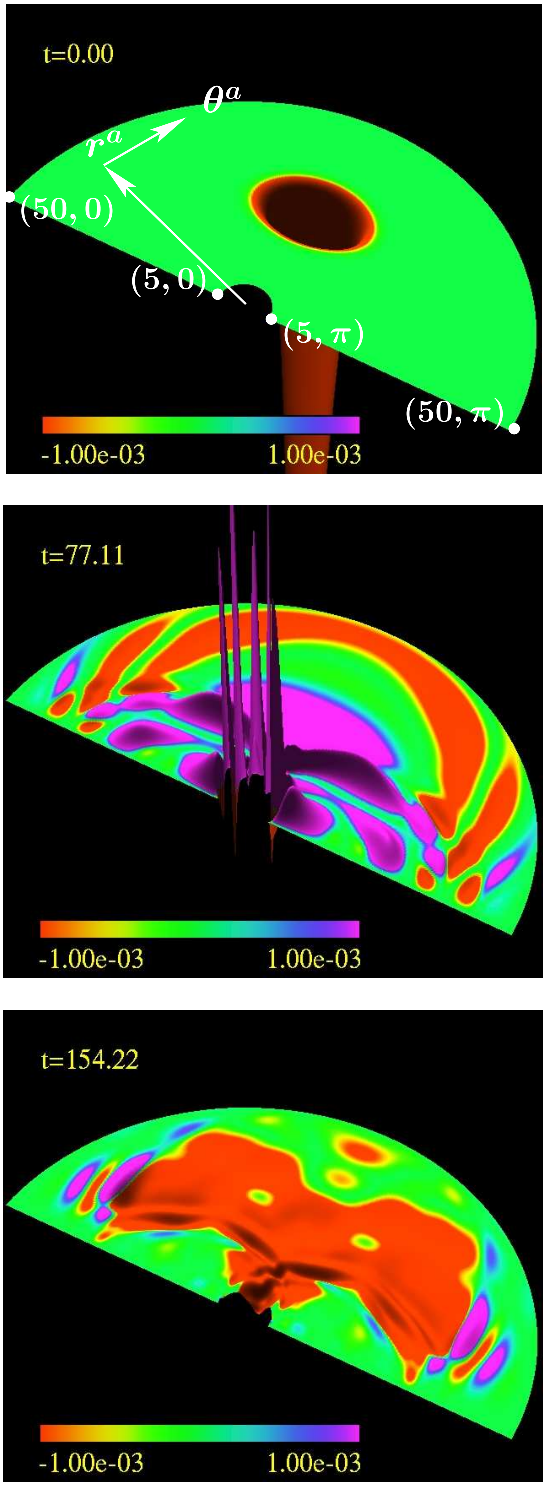

Figure 4.88: Axial current component, J_ϕ, at $t = 0, 77.11, 154.22$ for $e = 0.6$, $m_\Phi = 0.3$ perturbations in $a = M = 5$ Kerr spacetime. The directions of coordinate vectors $r^a \sim (0, 1, 0, 0)$ and $\theta^a \sim (0, 0, 1, 0)$ are shown in the first frame. The computational domain covers the range $5 \leq r \leq 50$ and $0 \leq \theta \leq \pi$, and the corners of the domain are labelled with their (r, θ) ordinate values. The amplitude and colour gradient are both scaled linearly. An MPEG animation showing evolution over $0 \leq t \lesssim 154$ is available at `http://$WWW/People/petryk/animations/9.mpeg` where `$WWW` is currently `laplace.physics.ubc.ca` .

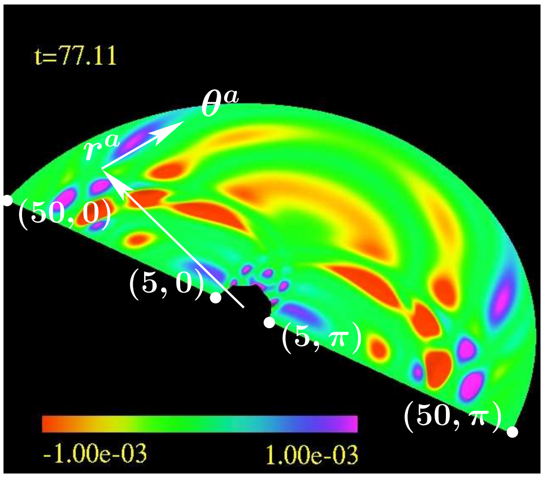

Figure 4.89: Axial current component, J_ϕ, at $t = 77.11$ for $e = 0.6$, $m_\Phi = 0.3$ perturbations in $a = 0$, $M = 5$ Kerr spacetime. The directions of coordinate vectors $r^a \sim (0, 1, 0, 0)$ and $\theta^a \sim (0, 0, 1, 0)$ are shown in the first frame. The computational domain covers the range $5 \leq r \leq 50$ and $0 \leq \theta \leq \pi$, and the corners of the domain are labelled with their (r, θ) ordinate values. The amplitude and colour gradient are both scaled linearly. Observe how small the amplitude and gradients are when compared to those at $t = 77.11$ in $a = M$ Kerr spacetime shown in Figure 4.88.

Before concluding discussion of the results, a brief analysis of electric and magnetic field amplitudes is in order. Again, the details can be deduced from preceding results. As in the case of massless $e = 0.6$ perturbations, the magnetic field square, B_aB^a, is very small in the equatorial plane ($\theta = \pi/2$) and also along the axis of black hole rotation ($\theta = 0$ and $\theta = \pi$) as depicted in Figure 4.92. Meanwhile, Figure 4.93 shows how the electric field square E_aE^a begins evolution from a state of zero initial amplitude and displays significant amplitude along both the axis of rotation and equatorial plane at later time. The integrals of the magnetic and electric field norms (respectively B^2 and E^2) are shown in Figure 4.94. After an initial phase of rapid change the amplitudes take on comparable magnitudes. Also note how the most significant increases in B^2 and E^2 take place well before time $t \approx 40$ at which collimation of energy density becomes apparent (cf. Figures 4.71 and 4.72). This suggests electromagnetic fields likely play a secondary role in collimating the perturbations along the axis of black hole rotation ($\theta = 0$ and $\theta = \pi$). Also note how the late time decay of B^2 and E^2 can be approximated by

$$\log(B^2) \sim -kt \; , \tag{4.198}$$

and

$$\log(E^2) \sim -kt \; , \tag{4.199}$$

where $k \approx 1 \times 10^{-2}$. This decay rate is comparable to those for the massless cases with $e = 0.0$ and $e = 0.6$ (cf. Figures 4.33 and 4.51). Finally, the evolution of B_aB^a, E_aE^a, B^2 and E^2 in the $a = 0$ spacetime (figures not provided) are qualitatively similar to those in the $a = M$ black hole spacetime.

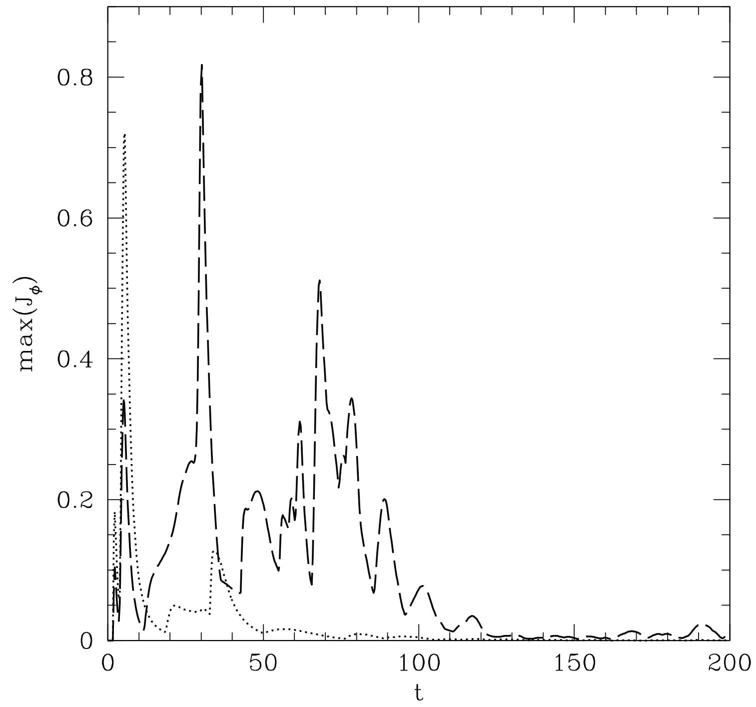

Figure 4.90: Global maxima of J_ϕ in the computational domain, $\max(J_\phi)$, as a function of t for $e = 0.6$ coupled massive perturbations in $M = 5$ Kerr spacetime. The dotted black line represents data for $a/M = 0$ and the dashed black line data for $a/M = 1$. The global maximum value of J_ϕ for $a/M = 1$ spacetime is substantially larger than those of $a/M = 0$ spacetime at intermediate and late time, providing evidence that black hole rotation amplifies the axial current.

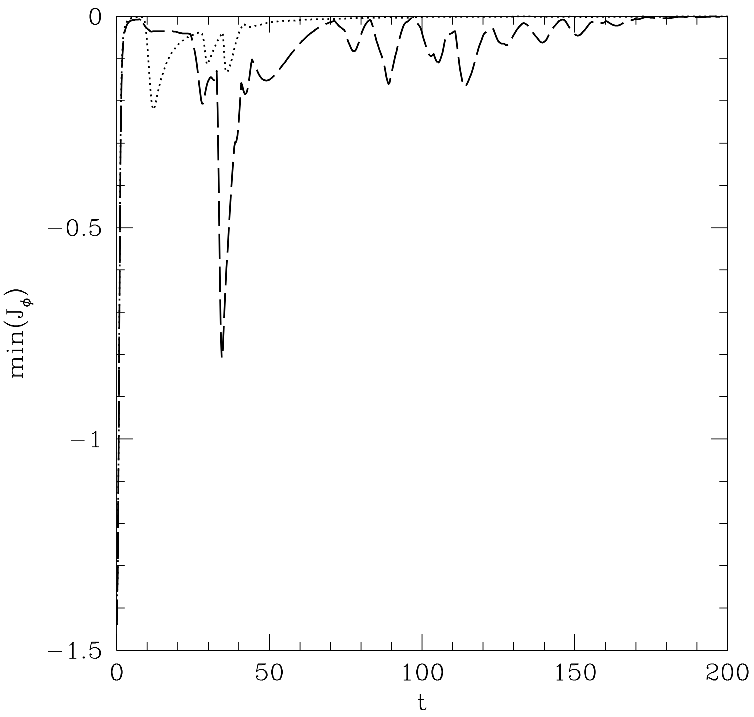

Figure 4.91: Global minima of J_ϕ in the computational domain, $\min(J_\phi)$, as a function of t for $e = 0.6$ coupled massive perturbations in $M = 5$ Kerr spacetime. The dotted black line represents data for $a/M = 0$ and the dashed black line data for $a/M = 1$. The global minimum value of J_ϕ for $a/M = 1$ spacetime is substantially larger than those of $a/M = 0$ spacetime at intermediate and late time, providing further evidence that black hole rotation amplifies the axial component of the electric current.

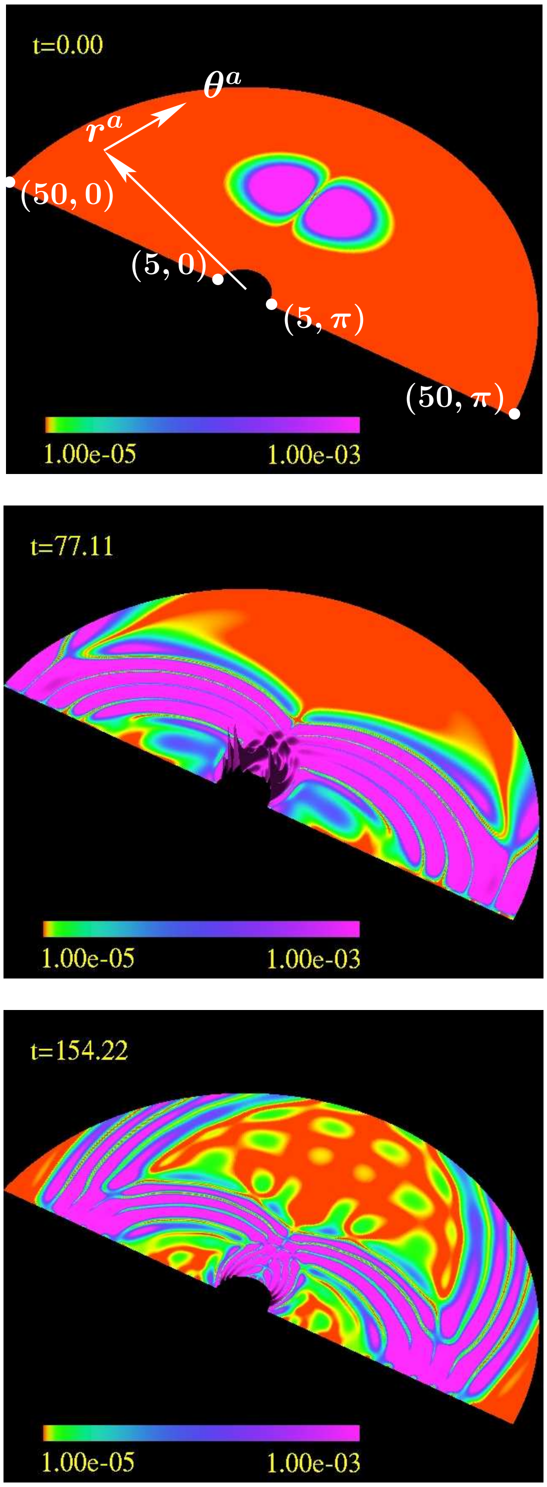

Figure 4.92: The figure displays the square of the magnetic field, $B_a B^a$, at $t = 0, 77.11, 154.22$ for $e = 0.6$, $m_\Phi = 0.3$ perturbations in $a = M = 5$ Kerr spacetime. The directions of coordinate vectors $r^a \sim (0, 1, 0, 0)$ and $\theta^a \sim (0, 0, 1, 0)$ are shown in the first frame. The computational domain covers the range $5 \leq r \leq 50$ and $0 \leq \theta \leq \pi$, and the corners of the domain are labelled with their (r, θ) ordinate values. The amplitude is scaled linearly, while the colour gradient is logarithmic. Observe how the magnetic field square is relatively small in the equatorial plane ($\theta = \pi/2$) and along the axis of black hole rotation ($\theta = 0$ and $\theta = \pi$).

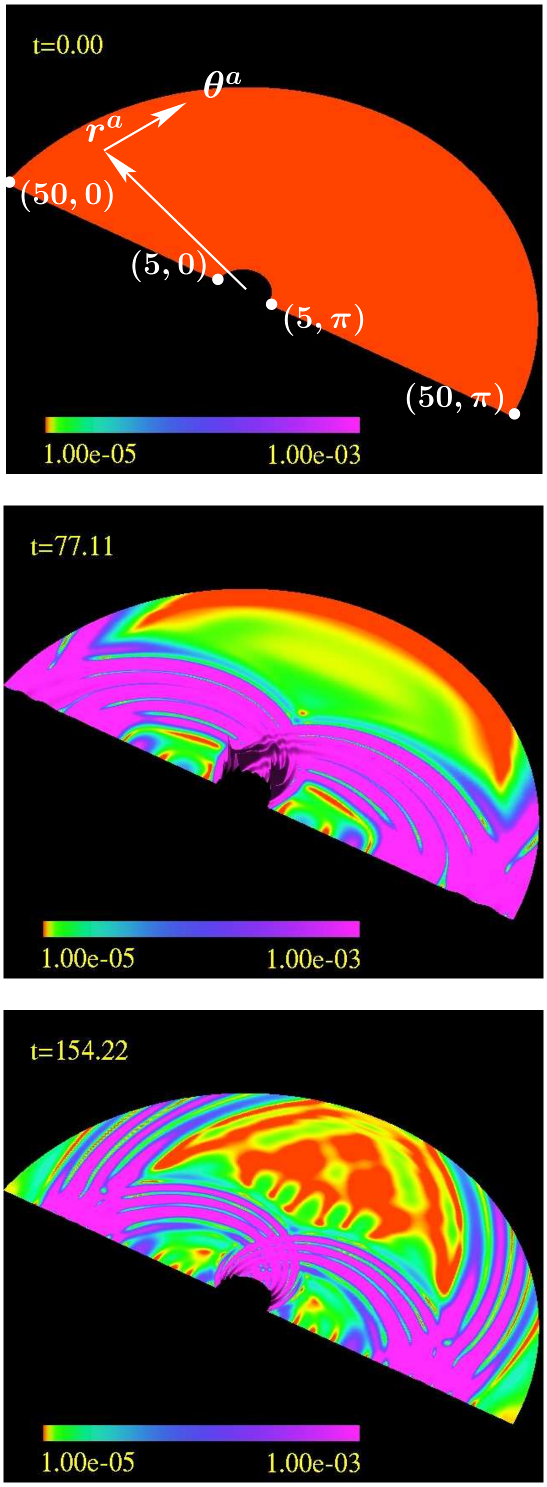

Figure 4.93: The figure displays the square of the electric field, $E_a E^a$, at $t = 0, 77.11, 154.22$ for $e = 0.6$, $m_\Phi = 0.3$ perturbations in $a = M = 5$ Kerr spacetime. The directions of coordinate vectors $r^a \sim (0, 1, 0, 0)$ and $\theta^a \sim (0, 0, 1, 0)$ are shown in the first frame. The computational domain covers the range $5 \leq r \leq 50$ and $0 \leq \theta \leq \pi$, and the corners of the domain are labelled with their (r, θ) ordinate values. The amplitude is scaled linearly, while the colour gradient is logarithmic. Note how the electric field square in the equatorial plane ($\theta = \pi/2$) and along the axis of black hole rotation ($\theta = 0$ and $\theta = \pi$) are comparable to the square along other surfaces of constant θ.

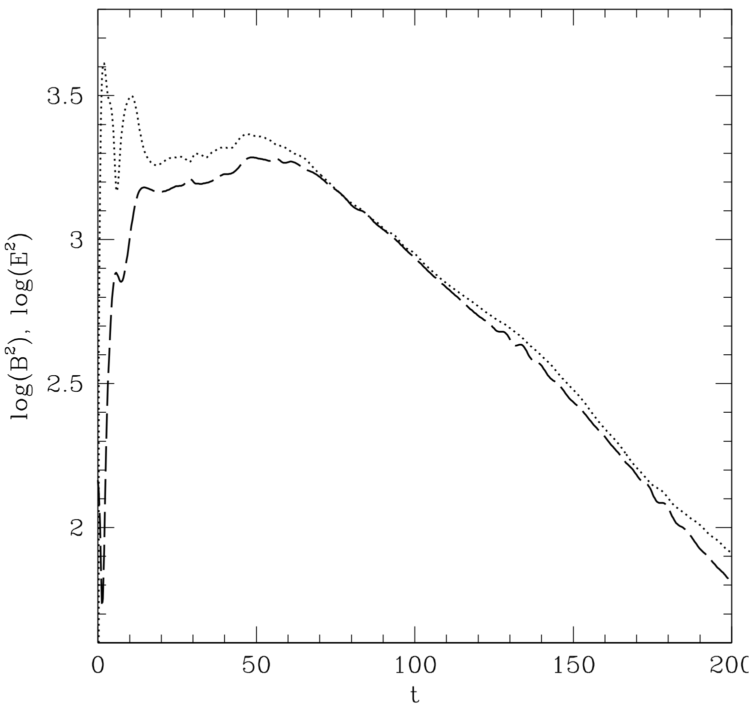

Figure 4.94: Plotted are $\log(B^2)$ and $\log(E^2)$, the logarithm of the integrated squares contained within $5 \leq r \leq 50$, $0 \leq \theta \leq \pi$ and $0 \leq \phi \leq 2\pi$, as a function of coordinate time t. The results are for $e = 0.6$, $m_\Phi = 0.3$ perturbations in $a = M = 5$ Kerr spacetime. The dashed black line represents $\log(B^2)$, and the dotted black line $\log(E^2)$. Initially, the field amplitudes undergo substantial oscillation, but the decay of integrated electric and magnetic amplitudes become closely matched at intermediate and late time.

4.3.7 Convergence of Conserved Quantities

I examine the convergence and accuracy of my code by examining the evolution of $e = 0.6$, $m_\Phi = 0.3$ perturbations (initial data specified as above) in the $a = M = 5$ spacetime. As discussed, the implemented solution scheme incorporates second-order finite difference methods, and the results I have presented are typically accurate to $\approx 1\%$ over the period $0 \leq t \lesssim 12$—the time at which perturbations begin crossing the excision surface at $r = 5$—as demonstrated by the invariance of conserved quantities over this period. The conserved quantity values are expected to vary after $t \approx 10$ as perturbations cross the ergosphere and then flow out of the computational domain at the $r = 5$ excision surface. After $t \approx 17$ there will be additional change as they also begin flowing through the $r = 50$ outer boundary. Figures 4.95, 4.96 and 4.97 respectively display the total normalized energy, total angular momentum and total charge within the computational domain $5 \leq r \leq 50$, $0 \leq \theta \leq \pi$ over the period $0 \leq t \leq 10$ for three levels of grid resolution. The lowest resolution grid has $J = 801$ radial points and $K = 401$ angular points, the intermediate resolution grid has $J = 1601$ radial points and $K = 801$ angular points, and the grid with highest resolution has $J = 3201$ radial and $K = 1601$ angular points. All data was computed in parallel across 64

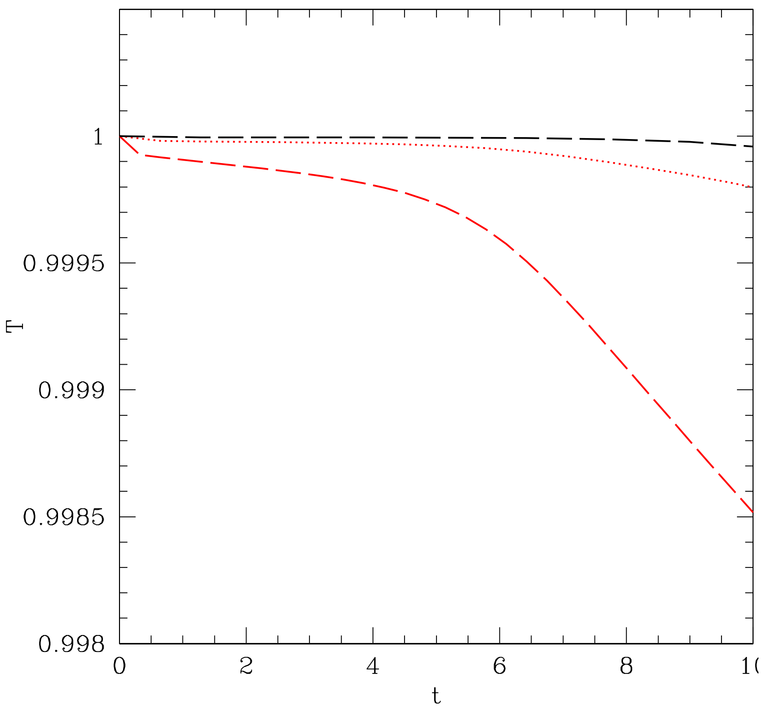

Figure 4.95: Convergence of total normalized energy, T, for $e = 0.6$, $m_\Phi = 0.3$ perturbations in $a = M = 5$ Kerr spacetime. The dashed red line represents data for a finite difference grid with $J = 801$ radial points and $K = 401$ angular points, the dotted red line represents data for a grid with $J = 1601$ radial and $K = 801$ angular points, and the dashed black line represents data for a grid with $J = 3201$ radial and $K = 1601$ angular points.

processors. Clearly, the conserved quantities display convergence.[22] Furthermore, the convergence factor, time averaged over the period $0 \lesssim t \lesssim 24$, is $C \approx 7.7$ for the total normalized energy, $C \approx 3.7$ for the total angular momentum and $C \approx 8.6$ for the total charge of the system. This is somewhat better than the $C \simeq 4$ I would expect for a completely centered second-order convergent scheme. However, some deviation is expected, as the operators I use near the computational boundaries are not completely centered. At any rate, the convergence factors may still approach values closer to 4 as resolution is further increased.

While the second-order convergence of a conserved density implies the second order convergence of its integral (providing the numerical integration scheme is itself at least second-order), it may still be useful to display the convergence factor for the density itself. I calculate the convergence factors for the total angular momentum density ρ_S, the total energy density ρ_T and the charge density ρ_Q as displayed in Figure 4.98. It is there shown how the convergence factors for energy density and charge remain near $C \simeq 4$ for the evolution. However, while still convergent, the result is not as good for the angular momentum density. Averaged over time, $C \approx 4.9$ for the energy density, $C \approx 4.1$ for the angular momentum density and $C \approx 5.0$ for the charge density.

[22] Convergent invariance of conserved quantities indicates I am numerically approximating the true solutions of the system. Technically, it is then not necessary to perform independent residual evaluations as discussed in Appendix C. I can for this reason justifiably omit independent residual testing of the code.

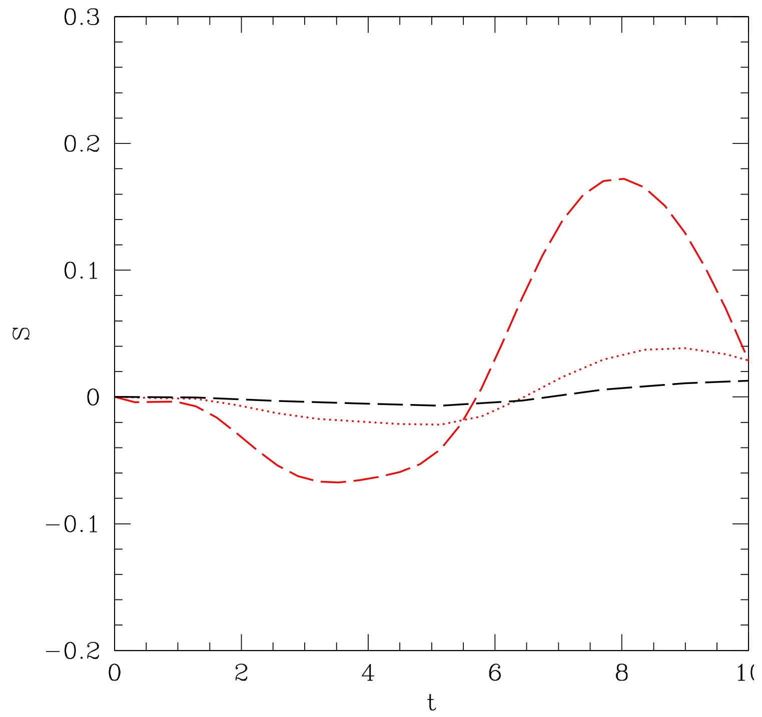

Figure 4.96: Convergence of total angular momentum, S, for $e = 0.6$, $m_\Phi = 0.3$ perturbations in $a = M = 5$ Kerr spacetime. The dashed red line represents data for a finite difference grid with $J = 801$ radial points and $K = 401$ angular points, the dotted red line represents data for a grid with $J = 1601$ radial and $K = 801$ angular points, and the dashed black line represents data for a grid with $J = 3201$ radial and $K = 1601$ angular points.

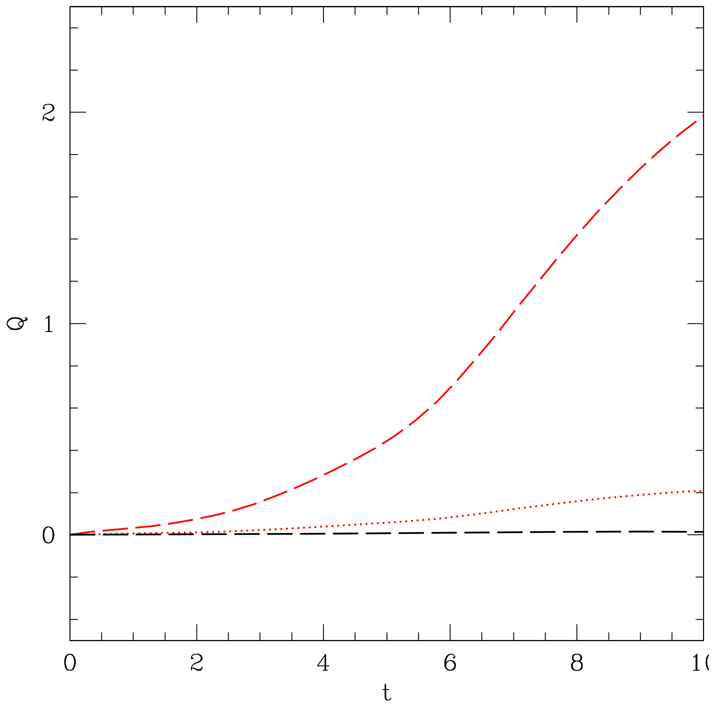

Figure 4.97: Convergence of total charge, Q, for $e = 0.6$, $m_\Phi = 0.3$ perturbations in $a = M = 5$ Kerr spacetime. The dashed red line represents data for a finite difference grid with $J = 801$ radial points and $K = 401$ angular points, the dotted red line represents data for a grid with $J = 1601$ radial and $K = 801$ angular points, and the dashed black line represents data for a grid with $J = 3201$ radial and $K = 1601$ angular points.

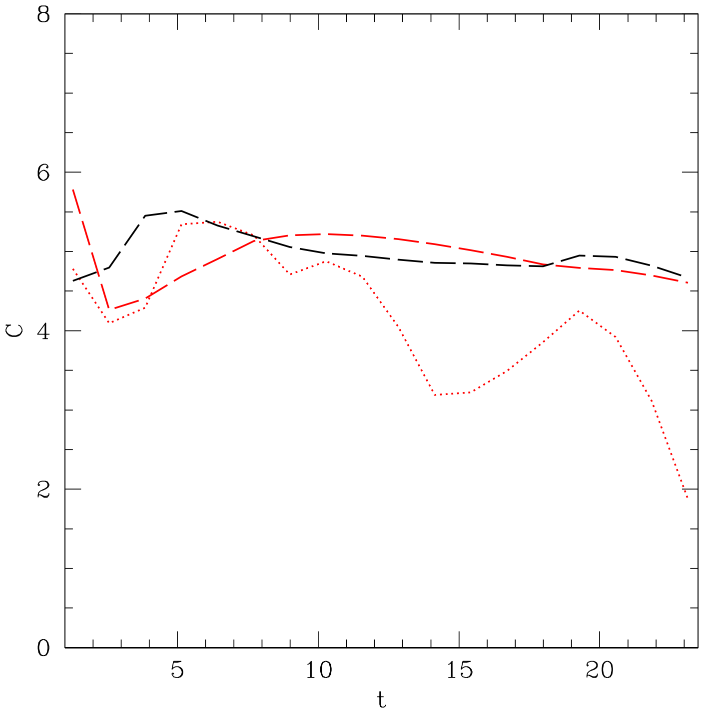

Figure 4.98: Convergence factors for energy density (dashed red line), angular momentum density (dotted red line) and charge density (dashed black line) for $e = 0.6$, $m_\Phi = 0.3$ perturbations in $a = M = 5$ Kerr spacetime. The convergence factors are based on a comparison of functions evolved on finite difference grids with $J = 801$ radial points and $K = 401$ angular points, $J = 1601$ radial and $K = 801$ angular points, and $J = 3201$ radial and $K = 1601$ angular points.

Again, deviations from the expected value of $C \simeq 4$ are likely due to points near the computational boundary where non-centered operators are employed. Since, given the initial conditions, at least some amount of perturbation should evolve to the computational domain boundaries by $t \approx 24$, convergence testing over the period $0 \lesssim t \lesssim 24$ should be adequate. To verify the results, testing over a longer period of evolution could be performed at a later date.

4.3.8 Independent Residual Testing Dynamical Variables

Having shown convergence of conserved quantities over the period $0 \lesssim t \lesssim 24$, further validation of the code is provided by independent residual testing as described in Appendix D. Recall that a properly implemented finite difference scheme will not only be convergent, but also drive the residual

$$r^h \equiv L^h \tilde{u}^h - f^h \tag{4.200}$$

to zero, where L^h is the discretized difference operator, f^h is the discretized source function, and $\tilde{u}^h$ is the approximate solution obtained by the scheme. In an independent residual test a second (independent) discretization $\tilde{L}^h$ is applied to the approximate solution, and it is verified whether the residual-like quantity

$$\tilde{r}^h \equiv \tilde{L}^h \tilde{u}^h - f^h \tag{4.201}$$

approaches zero as the scale of discretization h approaches zero. If it does, then quantity $\tilde{u}^h$ has been verified a true approximation of the solution u to differential equation

$$Lu - f = 0\ . \tag{4.202}$$

In obtaining solutions presented in this chapter, equations of motion for Φ, A_r, A_θ and A_ϕ are discretized using the Crank-Nicholson scheme with centered spatial derivatives when $r_{\min} + \Delta r \leq r \leq r_{\max} - \Delta r$ and $2\Delta\theta \leq \theta \leq \pi - 2\Delta\theta$. Approximate solutions of auxiliary variables Φ_r, Φ_θ, A_{rr}, $A_{\theta r}$, $A_{\phi r}$, $A_{r\theta}$, $A_{\theta\theta}$ and $A_{\phi\theta}$ are thus obtained. A suitable independent residual test then involves substituting the approximate solutions into respective equations (4.75), (4.76), (4.84), (4.85), (4.86), (4.87), (4.88) and (4.89), where partial derivatives in time and space are replaced by independent difference approximations. Formally, if $u = u(t, r, \theta)$ represents an auxiliary variable and $R = R(t, r, \theta)$ the operand on the right hand side of differential equation

$$\dot{u} = \partial_r R\ , \tag{4.203}$$

then a suitable independent difference approximation for (4.203) is

$$\begin{aligned}&\frac{1}{2}\left(\frac{u(t+\Delta t, r+\Delta r, \theta) - u(t-\Delta t, r+\Delta r, \theta)}{2\Delta t} + \frac{u(t+\Delta t, r, \theta) - u(t-\Delta t, r, \theta)}{2\Delta t}\right)\\ &= \frac{R(t, r+\Delta r, \theta) - R(t, r, \theta)}{\Delta r}\ ,\end{aligned} \tag{4.204}$$

where a leap-frog style centered difference scheme is used to approximate the derivative in t, and the difference scheme approximating the derivative in r is centered about the virtual spatial point $r+\frac{1}{2}\Delta r$ in analogy to Crank-Nicholson. Observe how the left hand side of (4.204) has been averaged in space between r and $r + \Delta r$ so that it too is centered about virtual point $r + \frac{1}{2}\Delta r$. Similarly, a suitable independent difference approximation for

$$\dot{u} = \partial_\theta R\ , \tag{4.205}$$

is

$$\begin{aligned}&\frac{1}{2}\left(\frac{u(t+\Delta t, r, \theta+\Delta\theta) - u(t-\Delta t, r, \theta+\Delta\theta)}{2\Delta t} + \frac{u(t+\Delta t, r, \theta) - u(t-\Delta t, r, \theta)}{2\Delta t}\right)\\ &= \frac{R(t, r, \theta+\Delta\theta) - R(t, r, \theta)}{\Delta\theta}\ ,\end{aligned} \tag{4.206}$$

which is now centered about the virtual point $\theta + \frac{1}{2}\Delta\theta$. Rewriting (4.205) and (4.206) in the form (4.201), and substituting in approximate solutions $\tilde{u}$ and $\tilde{R}$, I thus compute independent residuals from the equations for $\dot{A}_{rr}$, $\dot{A}_{r\theta}$, $\dot{A}_{\theta r}$, $\dot{A}_{\theta\theta}$, $\dot{A}_{\phi r}$, $\dot{A}_{\phi\theta}$, $\dot{\Phi}_r$ and $\dot{\Phi}_\theta$, and then calculate the l_2 norms $||\tilde{r}^h||_2$. The independent residuals are computed in parallel across 64 processors on difference meshes of $J = 210$ radial and $K = 101$ angular points, $J = 401$ radial and $K = 201$ angular points, $J = 801$ radial and $K = 401$ angular points, and $J = 1601$ radial and $K = 801$ angular points. Figure 4.99 displays $||\tilde{r}^h||_2$ from the equations $\dot{A}_{rr}$, $\dot{A}_{\theta r}$ and $\dot{A}_{\phi r}$ at three subsequent resolutions. Similarly, Figure 4.100 displays $||\tilde{r}^h||_2$ from the equations for $\dot{\Phi}_{th}$ at three different subsequent levels of resolution. The decrease of $||\tilde{r}^h||_2$ with h is proof the solutions obtained are true approximations of the system of differential equations.

4.3.9 Testing The Sommerfeld Boundary Condition

The Sommerfeld boundary condition is only approximate for the fields evolved in my computations. A test of its suitability is therefore required, especially for the case when the fields have both nonzero

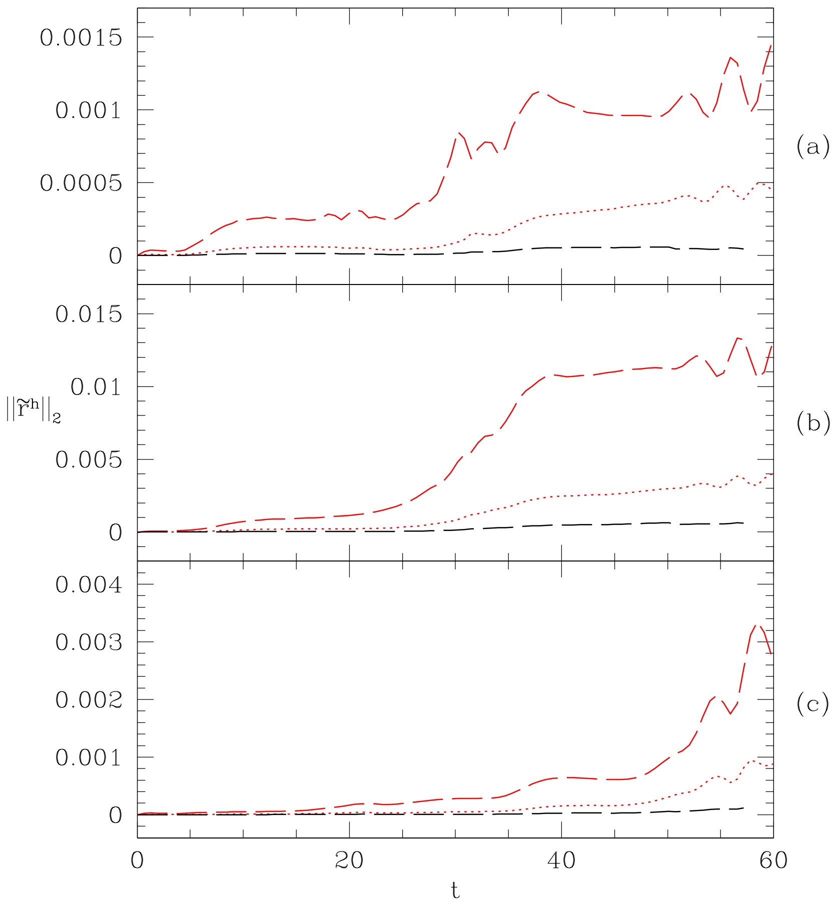

Figure 4.99: Independent residual norms $||\tilde{r}^h||_2$ from the equation (4.84) for $\dot{A}_{rr}$, equation (4.85) for $\dot{A}_{\theta r}$ and equation (4.86) for $\dot{A}_{\phi r}$. Frame (a) represents the independent residual norm associated with $\dot{A}_{rr}$, frame (b) the independent residual norm associated with $\dot{A}_{\theta r}$, and (c) represents the same for $\dot{A}_{\phi r}$. The $\tilde{r}^h$ have been computed for difference grids with $J = 401$ radial and $K = 201$ angular points (dashed red line), $J = 801$ radial and $K = 401$ angular points (dotted red line), and $J = 1601$ radial and $K = 801$ angular points (dashed black line). As expected of a correctly implemented scheme, the independent residual norm decreases with increased resolution.

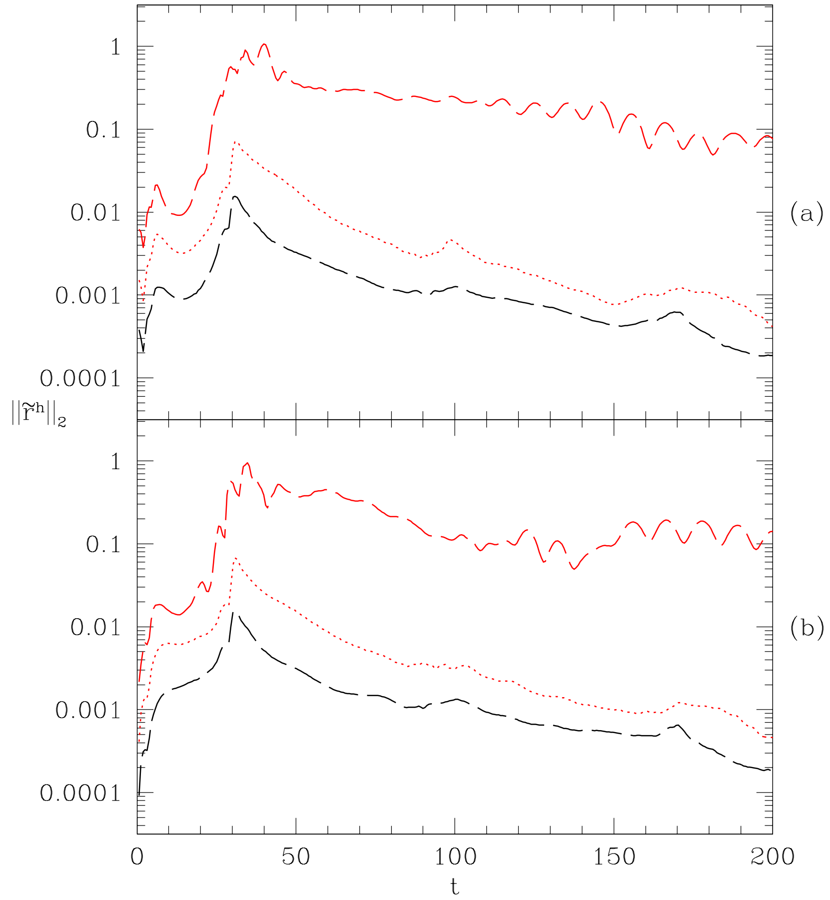

Figure 4.100: Independent residual norms $||\tilde{r}^h||_2$ from equation (4.76) for $\dot{\Phi}_\theta$. Recall that $\Phi = \phi_1 + i\phi_2$, and so $\dot{\Phi}_\theta = \dot{\phi}_{1\theta} + i\dot{\phi}_{2\theta}$. Frame (a) displays the independent residual norm associated with $\dot{\phi}_{1\theta}$ while frame (b) displays the same for $\dot{\phi}_{2\theta}$. Note the logarithmic scaling of the vertical axes. The $\tilde{r}^h$ have been computed for difference grids with $J = 201$ radial and $K = 101$ angular points (dashed red line), $J = 401$ radial and $K = 201$ angular points (dotted red line), and $J = 801$ radial and $K = 401$ angular points (dashed black line). The decrease in $||\tilde{r}^h||_2$ with h provides evidence the numerical implementation is correct.

mass and electromagnetic coupling parameters. I test this suitability by comparing the results of evolution for $m_\Phi = 0.3$, $e = 0.6$ perturbations in $a = M = 5$ Kerr spacetime on a finite difference grid with resolution and initial conditions identical to these used in above, but now covering the larger computational domain $5 \leq r \leq 95$, $0 \leq \theta \leq \pi$. The grid of this larger computational domain is therefore composed of $J = 1601$ radial and $K = 401$ angular points. I again compute across 64 processors, but division of the computational domain across processors now differs from that used for the smaller grid.[23]

In detail, comparison is through the relative errors of conserved quantities. For example, the relative error of energy density, $\delta\rho_T/\rho_T$, is given by

$$\delta\rho_T/\rho_T = \frac{||\widetilde{\rho}_T - \rho_T||_2}{||\widetilde{\rho}_T||_2} \ , \tag{4.207}$$

where $\widetilde{\rho}_T$ is the solution for energy density on the large computational domain, and $||\cdot||_2$ represents the l_2 norm. While the solution $\widetilde{\rho}_T$ is treated as exact, it is known to deviate from the ideal solution after perturbations evolve to its boundary. This is because the approximate Sommerfeld condition is also applied on the larger computational domain. For this reason, calculation of $\delta\rho_T/\rho_T$ should be limited to the period $0 \leq t \lesssim 65$. However, I extend calculation to $0 \leq t \leq 77.11$ for good measure. I similarly calculate relative errors for the angular momentum density, $\delta\rho_S/\rho_S$, and charge density, $\delta\rho_Q/\rho_Q$. The results are displayed in Figure 4.101. It is there apparent how relative errors of all three conserved densities are on the order of a percent. Considering that these densities are known to be conserved to $\approx 1\%$ for the early stages of evolution, the Sommerfeld boundary condition has produced surprisingly good results. So while only approximate, the Sommerfeld condition is likely sufficient for the results presented above. While a quantitatively better approximation is desirable, I have not implemented one for the evolution of Maxwell-Klein-Gordon fields on Kerr spacetime. However, a different treatment is included in Appendix D, where I provide results on Minkowski spacetime for comparison.

An alternate test (the one I use in Appendix D) is through the error of the integrated conserved densities. For example, the error in total normalized energy, δT, is given by

$$\delta T = ||\widetilde{T} - T||_2 \ , \tag{4.208}$$

where T is the total charge in the smaller computational domain, $\widetilde{T}$ is that in the large domain, and $||\cdot||_2$ again represents the l_2 norm. T and $\widetilde{T}$ are obtained through integration over a common region of space. I again calculate this quantity over the period $0 \leq t \leq 77.11$. The result is displayed in Figure 4.102 along with the analogous errors for angular momentum (δS) and charge (δQ). Comparing these results with the relative errors presented above, it is apparent how the true quality of the boundary condition is obfuscated by the amplitudes of the functions under considered.

[23]This comparison will therefore also test whether parallel distribution between the processors has a significant influence on the computed results.

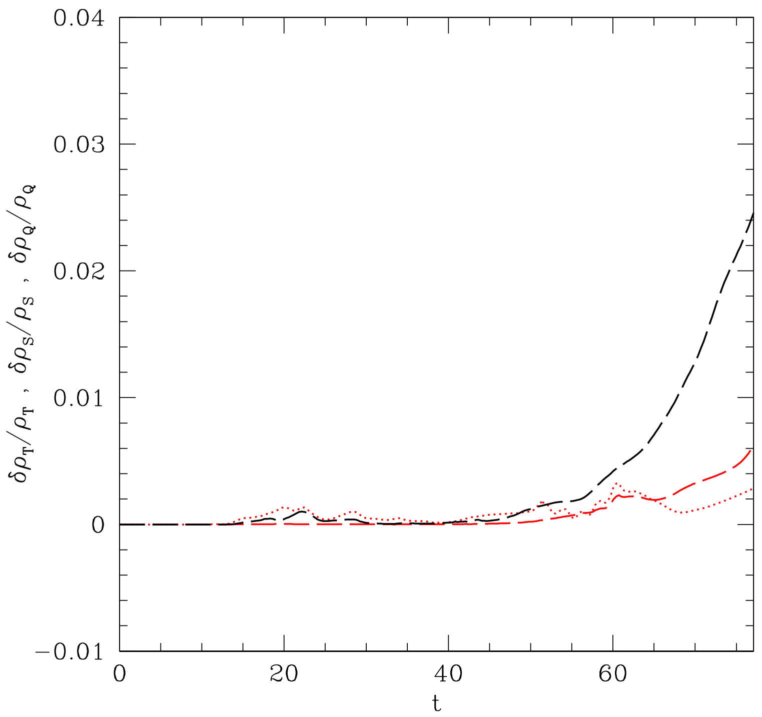

Figure 4.101: Displayed are the relative errors for energy density ($\delta\rho_T/\rho_T$, dashed red line), angular momentum density ($\delta\rho_S/\rho_S$, dotted red line), and charge density ($\delta\rho_Q/\rho_Q$, dashed black line) for $e = 0.6$, $m_\Phi = 0.3$ perturbations in $a = M = 5$ Kerr spacetime. The relative errors are based on the comparison of functions evolved on domains covering ranges $5 \leq r \leq 50$ and $5 \leq r \leq 95$.

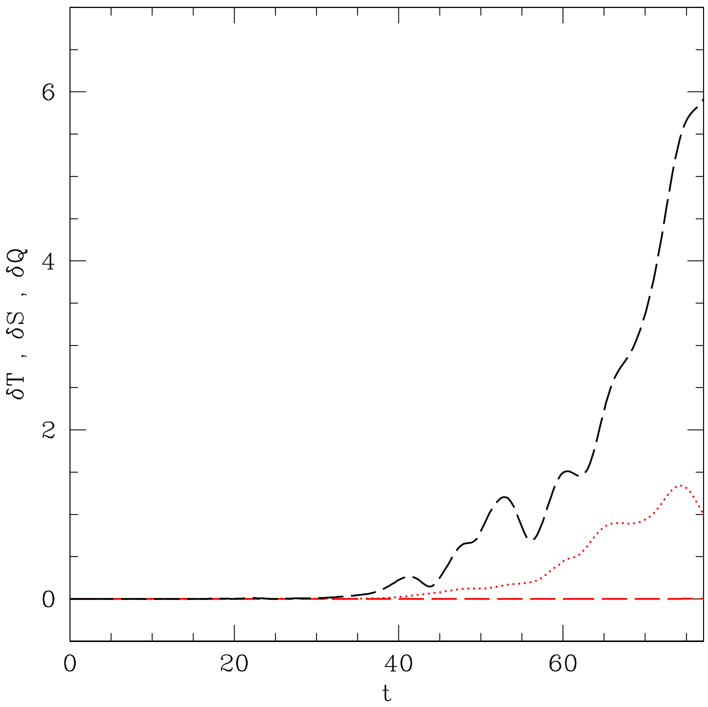

Figure 4.102: Displayed are the errors for normalized integrated energy (δT, dashed red line), integrated angular momentum (δS, dotted red line) and integrated charge (δQ, dashed black line) of $e = 0.6$, $m_\Phi = 0.3$ perturbations in $a = M = 5$ Kerr spacetime. The errors are based on the comparison of functions evolved on domains covering ranges $5 \leq r \leq 50$ and $5 \leq r \leq 95$.

CHAPTER 5

CONCLUSIONS AND FUTURE WORK

I have thus investigated critical solutions for massive charged scalar fields and the detailed evolutionary dynamics of Maxwell-Klein-Gordon perturbations on a Kerr spacetime background. The studies were numerical, based on finite difference techniques, and have made use of adaptive mesh refinement and parallel computation.

In Chapter 3, I have obtained the critical solutions at black hole threshold for massive charged scalar fields in spherical symmetry. For the case of sufficiently small mass parameter, the solutions are discretely self-similar and exhibit Type II scaling in both the black hole mass and charge. When the mass parameter is sufficiently large, a new critical solution is obtained. In this case it is periodic and resembles a perturbed charged boson star. These new periodic solutions exhibit behaviour typical of Type I phenomena, and their lifetimes exhibit a well-defined scaling relation.

In Chapter 4, I have studied Maxwell-Klein-Gordon perturbations on a Kerr spacetime background and have discovered that: (1) gravitational interaction effects are strongly manifest as orbiting resonances for weakly coupled perturbations; (2) massive Klein-Gordon perturbations display mode trapping and a tendency for scattering along the axis of symmetry for intermediate mass parameter values, but are quickly overcome by attraction to the black hole when the values are large; (3) there is evidence for superradiant scattering of purely electromagnetic perturbations in rotating black hole spacetimes; (4) electromagnetic coupling introduces the phenomena of charge separation and dynamo-like behaviour; (5) the complexity of the observed dynamics tends to increase with charge coupling parameter and black hole rotation; and finally, (6) there is strong evidence for energy collimation along the axis of rotation for an appropriate choice of mass and charge coupling parameters, but it is not clear that either rotational or electromagnetic effects are the strongest contributors to this phenomenon. For comparison, Appendix D provides results for the dynamics of Maxwell-Klein-Gordon fields in Minkowski spacetime. That appendix also describes the utility of Monotonically Increasingly Boosted coordinates in treating outer boundary conditions during numerical evolution of the field equations.

In future study, it would be useful to complete the investigation of critical phenomena, specifically investigating the possibility of new solutions details with a sufficiently large charge coupling. In particular, it would be interesting to see if Type I solutions can be obtained for the massless Maxwell-Klein-Gordon system when $e \gg 1$. It would also be interesting to study critical phenomena and compact object formation for a plasma-like matter (i.e., one where positive charge can be associated with a distribution of energetic heavy particles and negative charge associated with a corresponding distribution of light particles). The Einstein-Vlasov-Maxwell system (see [109], [110], [111], [112], [113]) appears to be a good candidate and should be investigated in detail for this purpose.

As well, the study of Maxwell-Klein-Gordon perturbations in axial symmetry should be extended to include evolution of the charged case when the mass parameter m_Φ is very large—it seems possible that electromagnetic interactions could balance or overcome the tendency for the otherwise rapid plunge into the black hole. Furthermore, investigation should be extended to the case with very large electromagnetic coupling parameter e where new physics like mode trapping is likely to occur. It would also be worth investigating initial conditions more closely resembling a stationary accretion disk. From such initial conditions it would then be possible to study the possible destabilization of stationary disks through interaction with electromagnetic waves.

Finally, in light of the availability of gravitationally backreacting codes and computational infrastructure, it is rather surprising that neither black hole formation nor critical gravitational collapse have been studied for pure electromagnetic radiation.[1] The evolution of electromagnetic radiation is not overly complicated and yet it carries a nontrivial angular momentum distribution. The effects and scaling of angular momentum could thus be studied in general by this most realistic of fields.

[1]The study of geons [147] and their formation is another exciting possibility for self-gravitating Maxwell field simulation.

BIBLIOGRAPHY

[1] A. N. Aguirre, "On the Superradiance of Spin-1 Waves in an Equatorial Wedge around a Kerr Hole," *Astrophys. J.* **529**, L9 (2000).

[2] E. Anderson, Z. Bai, C. Bischof, S. Blackford, J. Demmel, J. Dongarra, J. Du Croz, A. Greenbaum, S. Hammarling, A. McKenney and D. Sorensen, *LAPACK User's Guide*, 3rd edition, SIAM, Philadelphia (1999).

[3] N. Andersson and K. Glampedakis, "A Superradiance Resonance Cavity Outside Rapidly Rotating Black Holes," *Phys. Rev. Lett.* **84**, 4537 (2000).

[4] R. Arnowitt, S. Deser and C. W. Misner, "The Dynamics of General Relativity," in *Gravitation: An Introduction to Current Research*, ed. L. Witten, Wiley, New York (1962).

[5] J. M. Bardeen, W. H. Press and S. A. Teukolsky, "Rotating Black Holes: Locally Nonrotating Frames, Energy Extraction, and Scalar Synchrotron Radiation," *Astrophys. J.* **178**, 347 (1972).

[6] J. M. Bardeen and T. Piran, "General Relativistic Axisymmetric Rotating Systems: Coordinates and Equations," *Phys. Rep.* **96**, No. 4, 205 (1983).

[7] M. J. Berger and J. Oliger, "Adaptive Mesh Refinement for Hyperbolic Partial Differential Equations," *J. Comp. Phys.* **53**, 484 (1984).

[8] M. J. Berger and I. Rigoustos, "An Algorithm for Point Clustering and Grid Generation," *IEEE Trans. Vol. 21* **No. 5**, (1991).

[9] P. Bizon and T. Chmaj, "Critical Collapse of Skyrmions," *Phys. Rev. D* **58**, 041501 (1998).

[10] P. Bizon, T. Chmaj and Z. Tabor, "On Equivalence of Critical Collapse of Non-Abelian Fields," *Phys. Rev. D* **59**, 104003 (1999).

[11] D. Boulware, "Naked Singularities, Thin Shells, and the Reissner-Nordström Metric," *Phys. Rev. D* **8**, 2363 (1973).

[12] P. R. Brady, C. M. Chambers and S. M. C. V. Goncalves, "Phases of Massive Scalar Field Collapse," *Phys. Rev. D* **56**, 6057 (1997).

[13] A. Brandt, "Multi-level Adaptive Solutions to Boundary Value Problems," *Math. Comp.* **31**, 333 (1977).

[14] L. M. Burko, "Late-time Behavior of Massive Scalar Field Collapse," talk given at the *15th International Conference on General Relativity and Gravitation*, Pune (1997).

[15] L. M. Burko and G. Khanna, "Universality of Massive Scalar Field Late-time Tails in Black-hole Spacetimes," *Phys. Rev. D* **70**, 044018 (2004).

[16] C. M. Chambers, P. R. Brady and S. M. C. Goncalves, "A Critical Look at Massive Scalar Field Collapse," arXiv:gr-qc/9710014 (currently `http://arxiv.org/gr-qc/9710014`) (1997).

[17] S. Chandrasekhar, *The Mathematical Theory of Black Holes*, Oxford University Press, New York (1983).

[18] D. M. Chitre, R. H. Price and V. D. Sandberg, "Electromagnetic Radiation from an Unmoving Charge," *Phys. Rev. Lett.* **31**, 1018 (1973).

[19] D. M. Chitre, "Electromagnetic Radiation Generated by Gravitational Perturbations of a Charged Rotating Black Hole," *Phys. Rev. D* **11**, 760 (1975).

[20] M. W. Choptuik, *A Study of Numerical Techniques for the Initial Value Problem of General Relativity*, M. Sc. Dissertation, The University of British Columbia (1982).

[21] M. W. Choptuik, *A Study of Numerical Techniques for Radiative Problems in General Relativity*, Ph. D. Dissertation, The University of British Columbia (1986).

[22] M. W. Choptuik, "Consistency of Finite-Difference Solutions of Einstein's Equations," *Phys. Rev. D* **44**, 3124 (1991).

[23] M. W. Choptuik, "Universality and Scaling in Gravitational Collapse of a Massless Scalar Field," *Phys. Rev. Lett.* **70**, 9 (1993).

[24] M. W. Choptuik, "Critical Behavior in Scalar Field Collapse," in *Deterministic Chaos in General Relativity*, eds. D. W. Hobill, A. Burd and A. A. Coley, Plenum Press, New York (1994).

[25] M. W. Choptuik, "ad: An Implementation of the Berger-Oliger Mesh Refinement Algorithm for the Wave Equation in Spherical Symmetry," `ftp://$WWW/pub/ad/doc/ad.ps` (`$WWW` is currently `laplace.physics.ubc.ca`) (1994).

[26] M. W. Choptuik, T. Chmaj and P. Bizon, "Critical Behavior in Gravitational Collapse of a Yang-Mills Field," *Phys. Rev. Lett.* **77**, 424 (1996).

[27] M. W. Choptuik, "The 3+1 Einstein Equations," `http://$WWW/People/matt/Teaching/98Spring/Phy387N/Doc/3+1.ps` (`$WWW` is currently `laplace.physics.ubc.ca`) (1998).

[28] M. W. Choptuik, "The (Unstable) Threshold of Black Hole Formation," arXiv:gr-qc/9803075 (currently `http://arxiv.org/gr-qc/9803075`) (1998).

[29] M. W. Choptuik, E. W. Hirschmann and R. L. Marsa, "New Critical Behavior in Einstein-Yang-Mills Collapse," *Phys. Rev. D* **60**, 124011 (1999).

[30] M. W. Choptuik, "The 3+1 Einstein Equations," `http://$WWW/People/matt/Teaching/99Mexico/lecture.ps` (`$WWW` is currently `laplace.physics.ubc.ca`) (1998).

[31] M. W. Choptuik, personal communication (2001).

[32] M. W. Choptuik, personal communication (2003).

[33] Y. Choquet-Bruhat, "The Cauchy Problem" in *Gravitation: An Introduction to Current Research*, ed. L. Witten, New York, Wiley (1962).

[34] Y. Choquet-Bruhat and R. P. Gerooch, "Global Aspects of the Cauchy Problem in General Relativity," *Commun. Math. Phys.* **14**, 329 (1969).

[35] Y. Choquet-Bruhat and J. W. York, Jr., "The Cauchy Problem" in *General Relativity and Gravitation: One Hundred Years After the Birth of Albert Einstein*, ed. A. Held, Plenum Press, New York (1980).

[36] D. Christodoulou, personal communication to M. W. Choptuik (1987).

[37] T. Damour, N. Deruelle and R. Ruffini, “On Quantum Resonances in Stationary Geometries,” *Lettere al Nuovo Cimento* **15**, 257 (1976).

[38] C. Darwin, “The Gravity Field of a Particle, I,” *Proc. R. Soc. Lond. A* **249**, 180 (1959).

[39] C. Darwin, “The Gravity Field of a Particle, II,” *Proc. R. Soc. Lond. A* **263**, 39 (1961).

[40] F. De Felice and C. J. S. Clarke, *Relativity on Curved Manifolds*, Cambridge University Press, New York (1990).

[41] S. Detweiler, “Klein-Gordon Equation and Rotating Black Holes,” *Phys. Rev. D* **22**, 2323 (1980).

[42] J. P. De Villiers, J. F. Hawley, J. H. Krolik and S. Hirose, “Magnetically Driven Accretion in the Kerr Metric III: Unbound Outflows,” *Astrophys. J.* **620**, 878 (2005).

[43] C. DeWitt-Morette and B. L. Nelson, “Glories—and Other Degenerate Points of the Action,” *Phys. Rev. D* **29**, 1663 (1984).

[44] K. Eppley, “Evolution of Time-symmetric Gravitational Waves: Initial Data and Apparent Horizons,” *Phys. Rev. D* **16**, 1609 (1977).

[45] C. R. Evans, *A Method for Numerical Relativity: Simulation of Axisymmetric Gravitational Collapse and Gravitational Radiation Generation*, Ph. D. Dissertation, The University of Texas at Austin (1984).

[46] C. R. Evans and J. S. Coleman, “Observation of Critical Phenomena and Self-similarity in the Gravitational Collapse of Radiation Fluid,” *Phys. Rev. Lett.* **72**, 1782 (1994).

[47] Y. Fourès-Bruhat, *J. Rational Mech. Anal.* **5**, 951 (1956) (text in French).

[48] J. Friedman, personal communication (2004).

[49] V. P. Frolov and I. D. Novikov, *Black Hole Physics: Basic Concepts and New Developments*, Kluwer Academic Press, Boston (1998).

[50] H. Furuhashi and Y. Nambu, “Instability of Massive Scalar Fields in Kerr-Newman Spacetime,” *Prog. Theor. Phys.* **112**, 983 (2004).

[51] J. A. H. Futterman, F. A. Handler and R. A. Matzner, *Scattering From Black Holes*, Cambridge University Press, New York (1988).

[52] D. Garfinkle, “Choptuik Scaling in Null Coordinates,” *Phys. Rev. D* **51**, 5558 (1995).

[53] U. H. Gerlach, “Beat Frequency Oscillations near Charged Black Holes and Other Electrovacuum Geometries,” *Phys. Rev. Lett.* **32**, 1023 (1974).

[54] K. Glampedakis and N. Andersson, “Scattering of Scalar Waves by Rotating Black Holes,” *Class. Quant. Grav.* **18**, 1939 (2001).

[55] K. Glampedakis and N. Andersson, “Late-time Dynamics of Rapidly Rotating Black Holes,” *Phys. Rev. D* **64**, 104021 (2001).

[56] D. Grumiller and W. Kummer, “Absolute Conservation Law for Back Holes,” *Phys. Rev. D* **61**, 064006 (2000).

[57] C. Gundlach and J. M. Martin-Garcia, “Charge Scaling and Universality in Critical Collapse,” *Phys. Rev. D* **54** , 7353 (1996).

[58] C. Gundlach, "Understanding Critical Collapse of a Scalar Field," *Phys. Rev. D* **55**, 695 (1997).

[59] C. Gundlach, "Critical Phenomena in Gravitational Collapse - Living Reviews," *Living Rev. Rel.* **2**, (currently `http://www.livingreviews.org/lrr-1999-4`) (1999).

[60] C. Gundlach, "Critical Phenomena in Gravitational Collapse," *Phys. Rept.* **376**, 339 (2003).

[61] B. Gustafsson, H. O. Kreiss and J. Oliger, *Time Dependent Problems and Difference Methods*, Wiley, New York (1995).

[62] S. W. Hawking and G. F. R. Ellis, *The Large Scale Structure of Space-time*, Cambridge University Press, New York (1995).

[63] S. H. Hawley and M. W. Choptuik, "Boson Stars Driven to the Brink of Black Hole Formation," *Phys. Rev. D* **62**, 104024 (2000).

[64] S. H. Hawley, *Scalar Analogues of Compact Astrophysical Systems*, Ph. D. Dissertation, The University of Texas at Austin (2000).

[65] S. H. Hawley and M. W. Choptuik, "Critical Phenomena Associated with Boson Stars," arXiv:gr-qc/0103019 (currently `http://arxiv.org/gr-qc/0103019`) (2001).

[66] S. Hod, M. Sc. Dissertation, The Hebrew University of Jerusalem (1995) (text in Hebrew).

[67] S. Hod and T. Piran, "Fine-structure of Choptuik's Mass-scaling Relation," *Phys. Rev. D* **55**, 440 (1997).

[68] S. Hod and T. Piran, "Critical Behaviour and Universality in Gravitational Collapse of a Charged Scalar Field," *Phys. Rev. D* **55**, 3485 (1997).

[69] S. Hod and T. Piran, "Late-time Evolution of Charged Gravitational Collapse and Decay of Charged Scalar Hair. I," *Phys. Rev. D* **58**, 024017 (1998).

[70] S. Hod and T. Piran, "Late-time Evolution of Charged Gravitational Collapse and Decay of Charged Scalar Hair. II," *Phys. Rev. D* **58**, 024018 (1998).

[71] S. Hod and T. Piran, "Late-time Evolution of Charged Gravitational Collapse and Decay of Charged Scalar Hair. III: Nonlinear Analysis," *Phys. Rev. D* **58**, 024019 (1998).

[72] S. Hod and T. Piran, "Mass Inflation in Dynamical Gravitational Collapse of a Charged Scalar Field," *Phys. Rev. Lett.* **81**, 1554 (1998).

[73] S. Hod and T. Piran, "The Inner Structure of Black Holes," *Gen. Rel. Grav.* **30**, 1555 (1998).

[74] S. Hod, "Mode-coupling in Realistic Rotating Gravitational Collapse," arXiv:gr-qc/9902073 (currently `http://arxiv.org/gr-qc/9902073`) (1999).

[75] S. Hod, "Mode-coupling in Rotating Gravitational Collapse of a Scalar Field," *Phys. Rev. D* **61**, 024033 (2000).

[76] S. Hod, "The Radiative Tail of Realistic Gravitational Collapse," *Phys. Rev. Lett.* **84**, 10 (2000).

[77] E. P. Honda, *Resonant Dynamics Within the Nonlinear Klein-Gordon Equation: Much ado About Oscillons*, Ph. D. Dissertation, The University of Texas at Austin (2000).

[78] E. Honda and M. W. Choptuik, "Fine Structure of Oscillons in the Spherically Symmetric ϕ^4 Klein-Gordon Model," *Phys. Rev. D* **65**, 084037 (2002).

[79] P. Jetzer and J. J. Van Der Bij, "Charged Boson Stars," *Phys. Lett. B* **227**, 341 (1989).

[80] P. Jetzer, "Stability of Charged Boson Stars," *Phys. Lett. B* **231**, 433 (1989).

[81] P. Jetzer, "Boson Stars," *Phys. Rept.* **220**, 163 (1992).

[82] Y. Kato, S. Mineshige and K. Shibata, "Magnetohydrodynamical Accretion Flows: Formation of Magnetic Tower Jet and Subsequent Quasi-Steady State," *Astrophys. J.* **605**, 307 (2004).

[83] S. Koide, D. L. Meier, K. Shibata and T. Kudoh, "General Relativistic Simulations of Jet Formation by a Rapidly Rotating Black Hole," arXiv:/astro-ph/9907434 (currently `http://arxiv.org/astro-ph/9907434`) (1999).

[84] S. Koide, D. L. Meier, K. Shibata and T. Kudoh, "General Relativistic Simulations of Early Jet Formation in a Rapidly Rotating Black Hole Magnetosphere," *Astrophys. J.* **536**, 668 (2000).

[85] K. D. Kokkotas and B. G. Schmidt, "Quasi-Normal Modes of Stars and Black Holes," *Living Rev. Relativity* **2**, (currently `http://www.livingreviews.org/lrr-1999-2`) (1999).

[86] R. A. Konoplya, "Decay of Charged Scalar Field Around a Black Hole: Quasinormal Modes of R-N, R-N-AdS and Dilaton Black Hole," *Phys. Rev. D* **66**, 084007 (2002).

[87] R. A. Konoplya, "Massive Charged Scalar Field in a Reissner-Nordström Black Hole Background: Quasinormal Ringing," *Phys. Lett. B* **550**, 117 (2002).

[88] H. Koyama and A. Tomimatsu, "Asymptotic Power-law Tails of Massive Scalar Fields in Reissner-Nordström Background," *Phys. Rev. D* **63**, 064032 (2001).

[89] H. Koyama and A. Tomimatsu, "Asymptotic Tails of Massive Scalar Fields in Schwarzschild Background," *Phys. Rev. D* **64**, 044014 (2001).

[90] H. Koyama and A. Tomimatsu, "Slowly Decaying Tails of Massive Scalar Fields in Spherically Symmetric Spacetimes," *Phys. Rev. D* **65**, 084031 (2002).

[91] H. O.Kreiss and J. Oliger, *Methods for the Approximate Solution of Time Dependent Problems*, World Meteorological Organization [and] International Council of Scientific Unions, Geneva (1973).

[92] C. W. Lai, *A Numerical Study of Boson Stars*, Ph. D. Dissertation, The University of British Columbia (2004).

[93] S. L. Liebling, *Nonlinear Field Dynamics in General Relativity: Black Hole Critical Phenomena and Topological Defects*, Ph. D. Dissertation, The University of Texas at Austin (1998).

[94] R. L. Marsa, *Radiative Problems in Black Hole Spacetimes*, Ph. D. Dissertation, The University of Texas at Austin (1995).

[95] R. L. Marsa, "The RNPL Reference Manual," `http://$WWW/People/marsa/rnpl/refman/refman.html` (`$WWW` is currently `laplace.physics.ubc.ca`) (1995).

[96] R. L. Marsa, "The RNPL User's Guide," `http://$WWW/People/marsa/rnpl/users_guide/users_guide.html` (`$WWW` is currently `laplace.physics.ubc.ca`) (1995).

[97] R. L. Marsa, "New Features in RNPL," `http://$WWW/People/matt/Rnpl/newfeatures.html` (`$WWW` is currently `laplace.physics.ubc.ca`) (1998).

[98] B. Mashoon, “Scattering of Electromagnetic Radiation from a Black Hole,” *Phys. Rev. D* **7**, 2807 (1973).

[99] B. Mashoon, “Electromagnetic Scattering from a Black Hole and the Glory Effect,” *Phys. Rev. D* **10**, 1059 (1974).

[100] R. A. Matzner, N. Zamorano and V. D. Sandberg, “Instability of the Cauchy Horizon of Reissner-Nordström Black Holes,” *Phys. Rev. D* **19**, 2821 (1979).

[101] C. W. Misner, “Interpretation of Gravitational-Wave Observations,” *Phys. Rev. Lett.* **28**, 994 (1972).

[102] C. W. Misner, K. S. Thorne and J. A. Wheeler, *Gravitation*, Wiley, New York (1973).

[103] A. R. Mitchell and D. F. Griffiths, *The Finite Difference Method in Partial Differential Equations*, New York, Wiley (1980).

[104] V. Moncrief, “Odd-parity Stability of a Reissner-Nordström Black Hole,” *Phys. Rev. D* **9**, 2707 (1974).

[105] V. Moncrief, “Stability of Reissner-Nordström Black Holes,” *Phys. Rev. D* **10**, 1057 (1974).

[106] D. W. Neilsen, *Extremely Relativistic Fluids in Strong-Field Gravity*, Ph. D. Dissertation, The University of Texas at Austin (1999).

[107] K. I. Nishikawa, G. Richardson, S. Koide, K. Shibata, T. Kudoh, P. Hardee and G. J. Fishman, “A General Relativistic Magnetohydrodynamic Simulation of Jet Formation,” *Astrophys. J.* **625**, 60 (2005).

[108] S. C. Noble, *A Numerical Study of Relativistic Fluid Collapse*, Ph. D. Dissertation, The University of Texas at Austin (2003).

[109] P. Noundjeu, N. Noutchegueme and A. D. Rendall, “Existence of Initial Data Satisfying the Constraints for the Spherically Symmetric Einstein-Vlasov-Maxwell System,” *J. Math. Phys.* **45**, 668 (2004).

[110] P. Noundjeu and N. Noutchegueme, “Local Existence and Continuation Criterion for Solutions of the Spherically Symmetric Einstein-Vlasov-Maxwell System,” *Gen. Rel. Grav.* **36**, 1373 (2004).

[111] P. Noundjeu, “On a Regularity Theorem for Solutions of the Spherically Symmetric Einstein-Vlasov-Maxwell System,” arXiv:gr-qc/0406021 (currently `http://arxiv.org/gr-qc/0406021`) (2004).

[112] P. Noundjeu, “The Einstein-Vlasov-Maxwell(EVM) System with Spherical Symmetry,” *Class. Quant. Grav.* **22**, 5365 (2005).

[113] P. Noundjeu, “On the Non-relativistic Limit of the Spherically Symmetric Einstein-Vlasov-Maxwell System,” arXiv:gr-qc/0508078 (currently `http://arXiv.org/gr-qc/0508078`) (2005).

[114] J. Novak, “Velocity-induced Collapses of Stable Neutron Stars,” *Astron. Astrophys.* **376**, 606 (2001).

[115] I. D. Novikov, *Pis'ma Zh. Teor. Eksp. Fiz.* **3**, 223 (1966) (text in Russian); I. D. Novikov, “Change of Relativistic Collapse into Anticollapse and Kinematics of a Charged Sphere,” *Sov. Phys.—JETP Lett.* **3**, 142 (1966) (English translation).

[116] I. D. Novikov, "The Physics of Black Holes" in *Theory of Black Hole Accretion Disks*, ed. M. A. Abramowicz, G. Björnsson and J. E. Pringle, Cambridge University Press, New York (1998).

[117] I. Olabarrieta, *Relativistic Hydrodynamics and Other Topics in Numerical Relativity*, Ph. D. Dissertation, The University of British Columbia (2004).

[118] D. W. Olson and W. G. Unruh, "Conversion of Electromagnetic to Gravitational Radiation by Scattering from a Charged Black Hole," *Phys. Rev. Lett.* **33**, 1116 (1974).

[119] Y. Oren and T. Piran, "On the Collapse of Charged Scalar Fields," *Phys. Rev. D* **68**, 044013 (2003).

[120] A. Ori, "Inner Structure of a Charged Black Hole: An Exact Mass-inflation Solution," *Phys. Rev. Lett.* **67**, 789 (1991).

[121] A. Ori, "Structure of the Singularity Inside a Realistic Rotating Black Hole," *Phys. Rev. Lett.* **68**, 2117 (1992).

[122] R. Penrose, "Structure of Spacetime" in *Battelle Recontres*, ed. C. M. de Witt and J. A. Wheeler, Benjamin, New York (1968).

[123] R. Penrose, "Singularities and Time Asymmetry" in *General Relativity*, ed. S. W. Hawking and W. Israel, Cambridge University Press, Cambridge (1979).

[124] W. H. Press and S. A. Teukolsky "Floating Orbits, Super-Radiant Scattering and the Black-Hole Bomb," *Nature* **238**, 211 (1972).

[125] W. H. Press, S. A. Teukolsky, W. T. Vetterling and B. P. Flannery, *Numerical Recipes in C: The Art of Scientific Computing*, 2nd edition, Cambridge University Press, Cambridge (1992).

[126] W. H. Press, S. A. Teukolsky, W. T. Vetterling and B. P. Flannery, *Numerical Recipes in Fortran 77: The Art of Scientific Computing*, 2nd edition, Cambridge University Press, Cambridge (1992).

[127] F. Pretorius, *Numerical Simulations of Gravitational Collapse*, Ph. D. Dissertation, The University of British Columbia (2002).

[128] F. Pretorius, "PAMR Reference Manual," `http://$WWW/Doc/pamr/PAMR_ref.ps` (`$WWW` is currently `laplace.physics.ubc.ca`) (2004).

[129] F. Pretorius, "AMRD Reference Manual," `http://$WWW/Doc/pamr/AMRD_ref.ps` (`$WWW` is currently `laplace.physics.ubc.ca`) (2004).

[130] R. H. Price, "Nonspherical Perturbations of Relativistic Gravitational Collapse. I. Scalar and Gravitational Perturbations," *Phys. Rev. D* **5**, 2419 (1972).

[131] R. H. Price, "Nonspherical Perturbations of Relativistic Gravitational Collapse. II. Integer-Spin, Zero-Rest-Mass Fields," *Phys. Rev. D* **5**, 2439 (1972).

[132] T. Regge and J. A. Wheeler, "Stability of a Schwarzschild Singularity," *Phys. Rev.* **108**, 1063 (1957).

[133] L. F. Richardson, "The Approximate Arithmetical Solution by Finite Differences of Physical Problems Involving Differential Equations, with an Application to the Stresses in a Masonry Dam," *Phil. Trans. Roy. Soc.* **210**, 307 (1910).

[134] R. D. Richtmeyer and K. W. Morton, *Difference Methods for Initial-Value Problems*, Interscience, New York (1967).

[135] A. Sommerfeld, *Partial Differential Equations in Physics*, Academic Press, New York (1949).

[136] A. Sommerfeld, *Lectures on Theoretical Physics*, Academic Press, New York (1964).

[137] A. A. Starobinsky, *Zh. Eksp. Teor. Fiz.* **64**, 48 (1973) (text in Russian); A. A. Starobinsky, "Amplification of Waves During Reflection From a Rotating Black-Hole," *Sov. Phys.—JETP* **37**, 28 (1973) (English translation).

[138] A. A. Starobinsky and S. M. Churilov, *Zh. Eksp. Teor. Fiz.* **65**, 3 (1974) (text in Russian); A. A. Starobinsky and S. M. Churilov, "Amplification of Electromagnetic and Gravitational Waves Scattered by a Rotating Black-Hole," *Sov. Phys.—JETP* **38**, 1 (1974) (English translation).

[139] A. A. Starobinski, personal communication to L. M. Burko and G. Khanna (1997).

[140] M. J. Strafuss and G. Khanna, "Massive Scalar Field Instability in Kerr Spacetime," *Phys. Rev. D* **71**, 024034 (2005).

[141] S. A. Teukolsky and W. H. Press, "Perturbations of a Rotating Black Hole. III—Interaction of the Hole with Gravitational and Electromagnetic Radiation," *Astrophys. J.* **193**, 443 (1974).

[142] M. H. P. M. van Putten, "Superradiance in a Torus Magnetosphere around a Black Hole," *Science* **284**, 115 (1999).

[143] R. S. Varga, *Matrix Iterative Analysis*, Springer Verlag, New York (2000).

[144] J. F. Ventrella, *A Numerical Treatment of Spin-$\frac{1}{2}$ Fields Coupled to Gravity*, Ph. D. Dissertation, The University of Texas at Austin (2002).

[145] R. M. Wald, *General Relativity*, The University of Chicago Press, Chicago (1992).

[146] P. Wesseling, *An Introduction to Multigrid Methods*, John Wiley & Sons, New York (1992).

[147] J. A. Wheeler, "Geons," *Phys. Rev.* **97**, 511 (1957).

[148] J. W. York, Jr., " Kinematics and Dynamics of General Relativity" in *Sources of Gravitational Radiation*, ed. L. Smarr, Cambridge University Press, Seattle (1979).

[149] J. W. York and T. Piran, " The Initial Value Problem and Beyond" in *Spacetime and Geometry: The Alfred Schild Lectures*, ed. R. A. Matzner and L. C. Shipley, University of Texas Press, Austin (1982).

[150] D. M. Young, *Iterative Solution of Large Linear Systems*, Academic Press, New York (1971).

[151] Ya. B. Zel'dovich, *Pis'ma v. Eksp. Teor. Fiz.* **12**, 443 (1970) (text in Russian); Ya. B. Zel'dovich, "Particle Production in Cosmology," *Sov. Phys.—JETP Lett.* **12**, 307 (1970) (English translation).

[152] Ya. B. Zel'dovich, *Pis'ma v. Eksp. Teor. Fiz.* **14**, 270 (1971) (text in Russian); Ya. B. Zel'dovich, "Generation of Waves by a Rotating Body," *Sov. Phys.—JETP Lett.* **14**, 180 (1971) (English translation).

[153] Ya. B. Zel'dovich, *Zh. Eksp. Teor. Fiz.* **62**, 2076 (1972) (text in Russian); Ya. B. Zel'dovich, "Amplification of Cylindrical Waves Reflected from a Rotating Body," *Sov. Phys.—JETP* **35**, 1085 (1972) (English translation).

[154] F. J. Zerilli, "Perturbation Analysis for Gravitational and Electromagnetic Radiation in a Reissner-Nordström Geometry," *Phys. Rev. D* **9**, 860 (1974).

[155] T. R. Zhang and C. DeWitt-Morette, "WKB Cross-Section for Polarized Glories of Massless Waves in Curved Space-Times," *Phys. Rev. Lett.* **52**, 2313 (1984).

[156] T. J. M. Zouros and D. M. Eardley, "Instabilities of Massive Scalar Perturbations of a Rotating Black Hole," *Annals Phys.* **118**, 139 (1979).

APPENDIX A

GLOSSARY OF NOTATION

This appendix tabulates some notation used throughout the dissertation, if not explicitly defined in the text.

notation	definition
$A \equiv B$	A defined to be B
$A \Rightarrow B$	A implies B
$A \rightarrow B$	A approaches B
$A \in B$	A is a member of B
$\{A\}$	set of objects similar to A
$\|A\|$	modulus of object A
$\|\|A\|\|$	arbitrary norm of object A
$\|\|A\|\|_2$	l_2 norm of object A
$\|\|A\|\|_\infty$	l_∞ norm of object A
$(A_a)_m$	component m of vector A_a
$(A_a)_{mn}$	component mn of matrix A_a
$\mathrm{Tr}A$	trace of matrix A
Ω	n-dimensional domain Ω
$\partial\Omega$	$n-1$-dimensional boundary of domain Ω
$\mathbb{Z}$	the set of integers
$\mathbb{Z}^+$	the set of positive integers

Table A.1: Mathematical miscellanea.

notation	definition
$T^{abc\ldots}_{def\ldots}$	components of tensor T
$T^{a(bc)\ldots}_{def\ldots}$	symmetrization of tensor T in components b and c
$T^{abc\ldots}_{d(ef)\ldots}$	symmetrization of tensor T in components e and f
$T^{a[bc]\ldots}_{def\ldots}$	antisymmetrization of tensor T in components b and c
$T^{abc\ldots}_{d[ef]\ldots}$	antisymmetrization of tensor T in components e and f
δ^a_b	Kronecker delta where $\delta^a_b = 1$ if $a = b$ and $\delta^a_b = 0$ if $a \neq b$
ϵ_{abcd}	totally antisymmetric tensor of positive orientation where $\epsilon_{0123} = 1$

Table A.2: Tensor notation.

notation	definition
$\frac{\partial}{\partial x^g} T^{abc\ldots}_{def\ldots}, \partial_g T^{abc\ldots}_{def\ldots}\ T^{abc\ldots}_{def\ldots,g}$	partial derivative of tensor $T^{abc\ldots}_{def\ldots}$ with respect to coordinate x^g
$\pounds_A T^{abc\ldots}_{def\ldots}$	Lie derivative of tensor $T^{abc\ldots}_{def\ldots}$ along vector A
$\nabla_g T^{abc\ldots}_{def\ldots},\ T^{abc\ldots}_{def\ldots;g}$	covariant derivative of tensor $T^{abc\ldots}_{def\ldots}$ with respect to coordinate x^g
∇^2	the Laplacian operator

Table A.3: Derivative notation.

notation	definition
$\mathcal{M}$	n-dimensional manifold $\mathcal{M}$
$\partial\mathcal{M}$	$n-1$-dimensional boundary of manifold $\mathcal{M}$
$(\mathcal{M}, g_{ab})$	n-dimensional manifold $\mathcal{M}$ with metric g_{ab} and Christoffel connection
R_{abcd}	Riemann tensor
R_{ab}	Ricci tensor
R	curvature scalar

Table A.4: Manifolds and Riemannian spaces.

notation	definition
$\mathfrak{I}^-$	past null infinity
$\mathfrak{I}^+$	future null infinity
i^-	past timelike infinity
i^0	spatial infinity
i^+	future timelike infinity

Table A.5: Causal structure of spacetime.

APPENDIX B

DIFFERENCE AND DISCRETE OPERATORS

This appendix tabulates the FDAs and other discrete operators used in the dissertation.

B.1 Finite Difference Operators

This section tabulates the FDAs used in the thesis. In the tables below I use the same notation as introduced in Appendix C, except now all difference operators are given for the case of two spatial dimensions and one temporal dimension, and spacetime coordinates given by the ordered triple (t, r, θ). That is, $u^n_{i,j}$ labels a point in the finite difference mesh with ordinates (t, r, θ), $u^n_{i+1,j}$ labels a point with ordinates $(t, r + \Delta r, \theta)$, et cetera. Furthermore, r_{i-1} and r_{i+1} respectively designate coordinate values $r - \Delta r$ and $r + \Delta r$. Also as before, $\left(u^n_{i,j}\right)_{,r}$ designates the partial derivative of $u(t, r, \theta)$ with respect to coordinate r and evaluated at (t, r, θ), $\left(u^n_{i,j}\right)_{,rr}$ the second partial derivative of $u(t, r, \theta)$ with respect to r at (t, r, θ), and so on. The special case is $\left(u^{n+\frac{1}{2}}_{i,j}\right)_{,t}$, which designates the partial derivative of $u(t, r, \theta)$ with respect to t and is centered at the virtual time step $t + \frac{1}{2}$. All the listed FDAs are 2-nd order accurate in grid spacings Δr, $\Delta\theta$ and time interval Δt, and approach the corresponding continuum limit PDE as grid spacings and time interval approach zero.

PDE		FDA
$\left(u^n_{i,j}\right)_{,r}$	$\Rightarrow$	$\dfrac{u^n_{i+1,j} - u^n_{i-1,j}}{2\Delta r}$
$\left(u^n_{i,j}\right)_{,rr}$	$\Rightarrow$	$\dfrac{u^n_{i+1,j} - 2u^n_{i,j} + u^n_{i-1,j}}{(\Delta r)^2}$
$\left(u^n_{i,j}\right)_{,r^2}$	$\Rightarrow$	$\dfrac{u^n_{i+1,j} - u^n_{i-1,j}}{r^2_{i+1} - r^2_{i-1}}$
$\left(u^n_{i,j}\right)_{,r^3}$	$\Rightarrow$	$\dfrac{u^n_{i+1,j} - u^n_{i-1,j}}{r^3_{i+1} - r^3_{i-1}}$
$\left(u^n_{i,j}\right)_{,\theta}$	$\Rightarrow$	$\dfrac{u^n_{i,j+1} - u^n_{i,j-1}}{2\Delta\theta}$
$\left(u^n_{i,j}\right)_{,\theta\theta}$	$\Rightarrow$	$\dfrac{u^n_{i,j+1} - 2u^n_{i,j} + u^n_{i,j-1}}{(\Delta\theta)^2}$
$\left(u^n_{i,j}\right)_{,\cos\theta}$	$\Rightarrow$	$\dfrac{u^n_{i,j+1} - u^n_{i,j-1}}{\cos\theta_{j+1} - \cos\theta_{j-1}}$
$\left(u^n_{i,j}\right)_{,t}$	$\Rightarrow$	$\dfrac{u^{n+1}_{i,j} - u^{n-1}_{i,j}}{2\Delta t}$
$\left(u^{n+\frac{1}{2}}_{i,j}\right)_{,t}$	$\Rightarrow$	$\dfrac{u^{n+1}_{i,j} - u^n_{i,j}}{\Delta t}$

Table B.1: Centered difference operators.

PDE	FDA
$\left(u^n_{i,j}\right)_{,r}$	$\Rightarrow \dfrac{-u^n_{i+2,j}+4u^n_{i+1,j}-3u^n_{i,j}}{2\Delta r}$
$\left(u^n_{i,j}\right)_{,\theta}$	$\Rightarrow \dfrac{-u^n_{i,j+2}+4u^n_{i,j+1}-3u^n_{i,j}}{2\Delta \theta}$

Table B.2: Forward difference operators.

PDE	FDA
$\left(u^n_{i,j}\right)_{,r}$	$\Rightarrow \dfrac{3u^n_{i,j}-4u^n_{i-1,j}+u^n_{i-2,j}}{2\Delta r}$
$\left(u^n_{i,j}\right)_{,\theta}$	$\Rightarrow \dfrac{3u^n_{i,j}-4u^n_{i,j-1}+u^n_{i,j-2}}{2\Delta \theta}$

Table B.3: Backward difference operators.

B.2 Other Discrete Operators

In this section of the appendix I list other discrete operators used in the finite difference schemes of the dissertation.

B.2.1 Quadratic Fix Operators

Quadratic fix operators are used on functions in regions of the finite difference grid which correspond to locations in space where those functions are known to be quadratic. Typically, these regions will be at the point of spherical symmetry or along the line of axial symmetry. The quadratic fix operators are derived from the Forwards and backwards difference operators for $u_{,r}$ or $u_{,\theta}$.

If a function is quadratic at the point of spherical symmetry, $r = 0$, then its first derivative is known to vanish there. Using the forwards difference operator for $u_{,r}$ obtains the expression

$$0 = -u^n_{i+2,j} + 4u^n_{i+1,j} - 3u^n_{i,j}, \tag{B.1}$$

which is used to update the value of the function at the point of spherical symmetry. When the function is quadratic about the line of axial symmetry, the forwards and backwards difference forms for $u_{,\theta}$ are used to obtain the quadratic fix operators

$$0 = -u^n_{i,j+2} + 4u^n_{i,j+1} - 3u^n_{i,j} \tag{B.2}$$

to be applied along axis when $\theta = 0$, and

$$0 = 3u^n_{i,j} - 4u^n_{i,j-1} + u^n_{i,j-2} \tag{B.3}$$

which is used to update points along $\theta = \pi$. These results are tabulated below.

quadratic fix operator
$u^n_{i,j} = \frac{1}{3}\left(-u^n_{i+2,j} + 4u^n_{i+1,j}\right)$
$u^n_{i,j} = \frac{1}{3}\left(-u^n_{i,j+2} + 4u^n_{i,j+1}\right)$
$u^n_{i,j} = \frac{1}{3}\left(-4u^n_{i,j-1} + u^n_{i,j-2}\right)$

Table B.4: Quadratic fix operators.

Alternately, it is sometimes useful to use the (B.1), (B.2) and (B.3) to update grid points adjacent to the those at which the functions are known to be quadratic in coordinate θ. Under these circumstances, the quadratic fix operators will be expressed as in Table B.5.

quadratic fix operator
$u^n_{i,j} = \frac{1}{4}\left(u^n_{i,j+1} + 3u^n_{i,j-1}\right)$
$u^n_{i,j} = \frac{1}{4}\left(3u^n_{i,j+1} + u^n_{i,j-1}\right)$

Table B.5: Adjacent quadratic fix operators.

B.2.2 Interpolation and Extrapolation Operators

For function $u^n_{i,j}$, the mth degree Lagrange polynomial in coordinate r, $P^n_{m,r}(r,\theta)$, is

$$P^n_{m,r}(r,\theta) \equiv \sum_{i=1}^{m} P^n_i(r,\theta), \tag{B.4}$$

where

$$P^n_i(r,\theta) \equiv u^n_{i,j} \prod_{\substack{l=1 \\ l\neq i}}^{m} \frac{r - r_l}{r_i - r_l}. \tag{B.5}$$

Similarly, the mth Lagrange polynomial in coordinate θ, $P^n_{m,\theta}(r,\theta)$, is

$$P^n_{m,\theta}(r,\theta) \equiv \sum_{j=1}^{m} P^n_j(r,\theta), \tag{B.6}$$

where

$$P^n_j(r,\theta) \equiv u^n_{i,j} \prod_{\substack{l=1 \\ l\neq j}}^{m} \frac{\theta - \theta_l}{\theta_j - \theta_l}. \tag{B.7}$$

At times I use these Lagrange polynomials to update values of $u^n_{i,j}$ from its values at neighbouring points by extrapolating in coordinate r or interpolating in coordinate θ. Since high degree Lagrange polynomials generally produce poor results when used as extrapolants, especially for points far from those upon which they are based, I use only the 2nd degree Polynomial to *extrapolate* for smaller r as per

$$u^n_{i,j} = \left(u^n_{i+3,j} - 3u^n_{i+2,j} + 3u^n_{i+1,j}\right). \tag{B.8}$$

Interpolation from Lagrange polynomials is, however, much more reliable. When I *interpolate* in coordinate θ I use 3rd degree Lagrange polynomials. I alternately use the Lagrange polynomial in a centered fashion as per

$$u^n_{i,j} = \left(-\frac{1}{6}u^n_{i,j+2} + \frac{2}{3}u^n_{i,j+1} + \frac{2}{3}u^n_{i,j-1} - \frac{1}{6}u^n_{i,j-2}\right), \tag{B.9}$$

and at other times in an off-center fashion as per

$$u^n_{i,j} = \left(\frac{1}{4}u^n_{i,j+3} - u^n_{i,j+2} + \frac{3}{2}u^n_{i,j+1} + \frac{1}{4}u^n_{i,j-1}\right) \tag{B.10}$$

or

$$u^n_{i,j} = \left(\frac{1}{4}u^n_{i,j+1} + \frac{3}{2}u^n_{i,j-1} - u^n_{i,j-2} + \frac{1}{4}u^n_{i,j-3}\right), \tag{B.11}$$

depending on the distribution of available grid points. Finally note the *time-averaging operator* of the Crank-Nicholson scheme

$$u^{n+\frac{1}{2}}_{i,j} = \frac{1}{2}\left(u^{n+1}_{i,j} + u^n_{i,j}\right) \tag{B.12}$$

is itself an interpolant based upon a 2nd degree Lagrange polynomial in temporal coordinate t. These results are all summarized in Table B.6.

interpolation/extrapolation operator
$u^n_{i,j} = \left(u^n_{i+3,j} - 3u^n_{i+2,j} + 3u^n_{i+1,j}\right)$
$u^n_{i,j} = \left(-\frac{1}{6}u^n_{i,j+2} + \frac{2}{3}u^n_{i,j+1} + \frac{2}{3}u^n_{i,j-1} - \frac{1}{6}u^n_{i,j-2}\right)$
$u^n_{i,j} = \left(\frac{1}{4}u^n_{i,j+3} - u^n_{i,j+2} + \frac{3}{2}u^n_{i,j+1} + \frac{1}{4}u^n_{i,j-1}\right)$
$u^n_{i,j} = \left(\frac{1}{4}u^n_{i,j+1} + \frac{3}{2}u^n_{i,j-1} - u^n_{i,j-2} + \frac{1}{4}u^n_{i,j-3}\right)$
$u^{n+\frac{1}{2}}_{i,j} = \frac{1}{2}\left(u^{n+1}_{i,j} + u^n_{i,j}\right)$

Table B.6: Interpolation and extrapolation operators.

B.2.3 Kreiss-Oliger Dissipation Operators

I designate the Kreiss-Oliger dissipation operator in coordinate r for an FDA acting on $u^n_{i,j}$ by $\mathrm{s}_r u^n_{i,j}$, the dissipation operator in coordinate θ by $\mathrm{s}_\theta u^n_{i,j}$, and dissipation operator in both coordinates r and θ by $\mathrm{s}_{r\theta} u^n_{i,j}$. The following table provides a listing of these operators.

dissipation operator
$s_r u^n_{i,j} = \frac{\epsilon_r}{16}\left(u^n_{i-2,j} - 4u^n_{i-1,j} + 6u^n_{i,j} - 4u^n_{i+1,j} + u^n_{i+2,j}\right)$
$s_\theta u^n_{i,j} = \frac{\epsilon_\theta}{16}\left(u^n_{i,j-2} - 4u^n_{i,j-1} + 6u^n_{i,j} - 4u^n_{i,j+1} + u^n_{i,j+2}\right)$
$s_{r\theta} u^n_{i,j} = \frac{\epsilon_{r\theta}}{16}\left(\left(u^n_{i-2,j} - 4u^n_{i-1,j} + 6u^n_{i,j} - 4u^n_{i+1,j} + u^n_{i+2,j}\right)\right.$
$\left. + \left(u^n_{i,j-2} - 4u^n_{i,j-1} + 6u^n_{i,j} - 4u^n_{i,j+1} + u^n_{i,j+2}\right)\right)$

Table B.7: Kreiss-Oliger dissipation operators.

B.2.4 Integration Rules

The following table lists two integration rules for equally spaced abscissae. The second in the list is the trapezoidal rule used in calculations presented throughout this dissertation.

integration rule
$\int_{r_i}^{r_J} u(r)dr = \sum_{j=i}^{J} u_j \Delta r + \mathcal{O}\left((\Delta r)^2\right)$
$\int_{r_i}^{r_J} u(r)dr = \sum_{j=i}^{J-1} \left(\frac{1}{2}u_j + \frac{1}{2}u_{j+1}\right) \Delta r + \mathcal{O}\left((\Delta r)^3\right)$

Table B.8: Integration rules for equally spaced abscissae.

APPENDIX C
NUMERICS

C.1 Finite Difference Techniques and Approximations

Of the numerical techniques available, finite difference methods are chosen to solve the equations of constraint and evolution presented in this thesis. Finite difference methods are well-established and understood, and the notion of the finite difference approximation on which they are based is simple and intuitive. This makes them a natural choice for numerical relativists, especially when solving the systems similar to those in this thesis.[1] Good references for the topics in this section are [91], [103], [61], [134], along with the summary [30]. Furthermore, [21] and [22] are useful references for finite difference techniques as applied to the equations of general relativity.

The key element of finite difference methods is the *finite difference approximation* (FDA). Essentially, an FDA is what one obtains when a continuous differential equation is replaced with a discrete difference equation. The discrete difference equation is based on the notion of a grid of points at which functions are evaluated, and thus is an approximation to the continuum solution one aims to solve. In the subsections that follow the concept of the FDA is discussed in the context of consistency, accuracy, stability and convergence of a finite difference scheme. Another topic covered is dissipation in finite difference methods, as it plays a vital role in the computation of solutions to equations presented in later chapters.

C.1.1 Basic Definitions and Concepts

This dissertation considers FDAs to systems of partial differential equations (PDEs) on a mesh or grid of *spacing* h, and will therefore be vitally interested in the behaviour of the FDAs and their solution schemes in the *continuum limit* as the grid spacing tends to zero, $h \to 0$. It is expected that, for a correctly implemented finite difference scheme, the error of the approximation to approach zero in the continuum limit. Following discussion will begin with the introduction of some notation.

Let a differential equation be denoted by

$$Lu = f, \tag{C.1}$$

where L is a *difference operator*, u is the *unknown function* to be solved, and f is some *source function*. f will generally be a function of the variables on which u also depends. The discretized operators, variables and functions will be denoted with a superscript ^{h}. The discretization of the system (C.1) is thus denoted

$$L^h u^h = f^h, \tag{C.2}$$

or

$$L^h u^h - f^h = 0. \tag{C.3}$$

where L^h is the *discretized difference operator*, u^h the *discrete unknown function*, and f^h the *discretized source function*. All functions of the discrete system are evaluated at points on the finite difference mesh. If h is the only discretization scale in the problem the FDA is said to be

[1] Other commonly used methods are spectral and finite element, and they should be used where appropriate. However, finite difference methods are typically simpler, especially when solving systems of equations with regular domain boundaries, as is the case in this thesis.

convergent if and only if

$$u^h \to u \quad \text{as} \quad h \to 0. \tag{C.4}$$

For obvious reasons, all FDAs are desired to be convergent. The *solution error*, e^h, of the FDA is defined

$$e^h \equiv u - u^h. \tag{C.5}$$

So if the FDA is convergent, then $e^h \to 0$ as $h \to 0$.

Another type of error in the subject of FDAs will now be developed. The *truncation error*, τ^h, of the FDA is given by

$$\tau^h \equiv L^h u - f^h. \tag{C.6}$$

So while the solution error is a measure of how well the FDA solution approximates the solution of the PDE, the truncation error is a measure of how closely the finite difference equation approximates the PDE whose solutions are sought. Assume the FDA again has a single discretization scale h. Then, if for the FDA

$$\tau^h \to 0 \quad as \quad h \to 0 \tag{C.7}$$

holds, it is called *consistent*. Consistency is therefore required if the FDA is to be convergent. If, furthermore,

$$\lim_{h\to 0} \tau^h = \mathcal{O}\left(h^p\right) \tag{C.8}$$

for positive integer p (i.e., $p \in \mathbb{Z}^+$), then the FDA is said to be *pth order accurate*. A useful result pertaining to FDA truncation errors is the observation that

$$\tau^h = \mathcal{O}\left(h^p\right). \tag{C.9}$$

This was first noted in [133] and is based on the *Richardson ansatz*, that if an FDA is completely centered[2] and is based upon a mesh uniform in a single scale parameter h, then u^h has the expansion

$$u^h = u + h^2 e_2 + h^4 e_4 + \cdots \tag{C.10}$$

in the limit as $h \to 0$, where e_2, e_4, ... are functions independent of h.[3]

Finally, the concept of the residual of an FDA is defined. The form (C.3) leads us to the definition that if $\tilde{u}^h$ is an approximation to the true solution u^h of (C.3), then the *residual* of the FDA, r^h, is given by

$$r^h \equiv L^h \tilde{u}^h - f^h. \tag{C.12}$$

Essentially, the residual is the degree to which finite difference solutions fail to satisfy the FDA. The aim therefore is to find a convergent process by which the residual of the FDA is driven to zero.

C.1.2 Convergence Testing and Independent Residual Evaluation

From (C.10) the notion of the convergence test can be developed. Suppose an FDA is solved three times, each time beginning from the same initial data set, but each time using a different grid spacing. For the sake of argument, assume the grid spacings are h, $2h$, and $4h$. Furthermore, assume the three finite difference grids overlap in the sense that the $4h$ grid points are subsets of the $2h$ grid points, and that the $2h$ grid points are a subset of the h grid points. Finally, assume the FDAs are completely centered, and that h, $2h$ and $4h$ are respectively the only scale parameters

[2] An FDA is said to be *centered* if L^h is symmetric about the grid point where u^h is evaluated.

[3] If the scheme is not completely centered then (C.10) is modified as per

$$u^h = u + he_1 + h^2 e_2 + \cdots. \tag{C.11}$$

in the problem. Then investigating how solutions u^h, u^{2h}, and u^{4h} differ provides information about the convergence of the chosen FDA. The Richardson ansatz (C.10) for a completely centered scheme then provides

$$u^h = u + h^2 e_2 + h^4 e_4 + \cdots, \tag{C.13}$$

$$u^{2h} = u + (2h)^2 e_2 + (2h)^4 e_4 + \cdots, \tag{C.14}$$

and

$$u^{4h} = u + (4h)^2 e_2 + (4h)^4 e_4 + \cdots. \tag{C.15}$$

Then for some suitable spatial norm $||\cdot||$ such as the l_2 norm

$$||u^h||_2 = \left(J^{-1} \sum_{i=1}^{J} \left(u_i^h\right)^2 \right)^{\frac{1}{2}}, \tag{C.16}$$

u_i^h being the ith component of vector u^h, a quantity called the *convergence factor*, $C(t)$, is defined

$$C(t) \equiv \frac{||u^{4h} - u^{2h}||}{||u^{2h} - u^h||}, \tag{C.17}$$

where argument t designates comparing u^h, u^{2h} and u^{4h} at the same time, or step, in the evolution. Using (C.13), (C.14) and (C.15), and providing the system is convergent, it should then observed

$$\lim_{h\to 0} C(t) = 4. \tag{C.18}$$

A *convergence test* using discretizations h, $2h$ and $4h$ would then amount to verification that (C.18) holds. Furthermore, having confirmed convergence of the FDA, the solution error between any two discretizations can explicitly be calculated as per

$$u^{2h} - u^h = \left(u + (2h)^2 e_2 + (2h)^4 e_4 + \cdots\right) - \left(u + h^2 e_2 + h^4 e_4 + \cdots\right) = 3h^2 e_2 + \mathcal{O}\left(h^4\right) \tag{C.19}$$

or

$$u^{4h} - u^{2h} = \left(u + (4h)^2 e_2 + (4h)^4 e_4 + \cdots\right) - \left(u + (2h)^2 e_2 + (2h)^4 e_4 + \cdots\right) = 12h^2 e_2 + \mathcal{O}\left(h^4\right). \tag{C.20}$$

Suppose a convergence test has been performed as outlined above and find the finite difference evolution is in fact converging to some continuum solution. The problem then to resolve is whether the evolution is approaching the correct continuum solution. For example, it is entirely possible the FDA is convergent, but incorrectly implemented, and so a closely related (but different) system is now being solved. If the system possesses conservation laws, perhaps the best way to test whether (C.1) is being correctly solved is to ensure the associated conserved quantities are converging to constant values in the expected manner. In the absence of conservation laws, or simply to check the FDA in another manner, an *independent residual test* can be used. This test is also based upon the Richardson ansatz (C.10) for u^h, but additionally upon the observation that for a pth order FDA L^h of L, L^h can always be expanded in powers of the mesh spacing according to

$$L^h = L + h^p E_p + \mathcal{O}\left(h^{2p}\right), \tag{C.21}$$

where E_p is a differential operator involving higher order derivatives in L. Then if $\tilde{L}^h$ is another FDA for L, but this time is 2nd order, expression

$$\tilde{L}^h = L + h^2 \tilde{E}_2 + \mathcal{O}\left(h^4\right) \tag{C.22}$$

is obtained, where $\tilde{E}_2$ is another differential operator involving higher order derivatives in L. Since

$$u^h = u + h^2 e_2 + \mathcal{O}\left(h^4\right), \tag{C.23}$$

applying $\tilde{L}^h$ to u^h expression

$$\tilde{L}^h u^h = \left(\left(L + h^2 \tilde{E}_2 + \mathcal{O}\left(h^4\right)\right)\left(u + h^2 e_2 + \mathcal{O}\left(h^4\right)\right)\right) = Lu + \mathcal{O}\left(h^2\right) \tag{C.24}$$

is obtained. It is then concluded $\tilde{L}^h u^h$ is of the form of a residual and converges to Lu as $h \to 0$.

Now suppose the solution scheme has been incorrectly implemented but convergence is still observed as per

$$\lim_{h\to 0} C\left(t\right) = 4. \tag{C.25}$$

The expansion of u^h instead would have to be of form

$$u^h = u + e_0 + h^2 e_2 + \mathcal{O}\left(h^2\right), \tag{C.26}$$

and thus would have an $\mathcal{O}\left(h^0\right)$ error, e_0 being an independent function of h. Calculating $\tilde{L}^h u^h$ now would yield

$$\tilde{L}^h u^h = \left(\left(L + h^2 \tilde{E}_2 + \mathcal{O}\left(h^4\right)\right)\left(u + e_0 + h^2 e_2 + \mathcal{O}\left(h^2\right)\right)\right) = Lu + \mathcal{O}\left(h^0\right), \tag{C.27}$$

and so the *independent residual*, $\tilde{r}^h$,

$$\tilde{r}^h \equiv \tilde{L}^h u^h \tag{C.28}$$

would approach a finite value as $h \to 0$. Such a result would indicate that either the implementation of the solution scheme, or the independent residual evaluation, is somehow flawed. Since this sort of independent residual test is applied after the finite difference solution is obtained, it typically adds negligible computational work overall.

C.1.3 Deriving Finite Difference Formulae

The basic element of a finite difference scheme is the FDA. FDAs for a PDE are obtained rather simply using Taylor series expansions of the function u on the finite difference grid. It is now outlined how to obtain FDAs for PDEs in one spatial and one temporal dimension. The generalization to greater than one spatial dimension is straightforward and so will be omitted from the discussion. Finally, Appendix B tabulates all FDAs used in the dissertation, including all those derived in this subsection.

Consider the finite difference grid shown in Figure C.1. Here, spacetime coordinates are given by the ordered pair (t, r), grid spacing in the spatial dimension is characterized by a single parameter $\Delta r = h$, and the temporal interval is characterized by parameter Δt. Furthermore, grid points are labelled by spatial indices $...i-1, i, i+1, ...$ and temporal indices $...n-1, n, n+1, ...$ The discretized function u^h at ordinates $(t, r - \Delta r)$ will be labelled u^n_{i-1}, at ordinates (t, r) by u^n_i, at $(t, r + \Delta r)$ by u^n_{i+1}, at $(t + \Delta t, r)$ by u^{n+1}_i, and so on. The Taylor expansions of $u(t, r - 2\Delta r)$, $u(t, r - \Delta r)$, $u(t, r)$ $u(t, r + \Delta r)$, and $u(t, r + 2\Delta r)$ evaluated at (t, r) are thus

$$u^n_{i-2} = u^n_i - 2\Delta r \left(u^n_i\right)_{,r} + \frac{1}{2}\left(2\Delta r\right)^2\left(u^n_i\right)_{,rr} - \frac{1}{6}\left(2\Delta r\right)^3\left(u^n_i\right)_{,rrr} + \mathcal{O}\left(\left(\Delta r\right)^4\right), \tag{C.29}$$

$$u^n_{i-1} = u^n_i - \Delta r \left(u^n_i\right)_{,r} + \frac{1}{2}\left(\Delta r\right)^2\left(u^n_i\right)_{,rr} - \frac{1}{6}\left(\Delta r\right)^3\left(u^n_i\right)_{,rrr} + \mathcal{O}\left(\left(\Delta r\right)^4\right), \tag{C.30}$$

$$u^n_i = u^n_i, \tag{C.31}$$

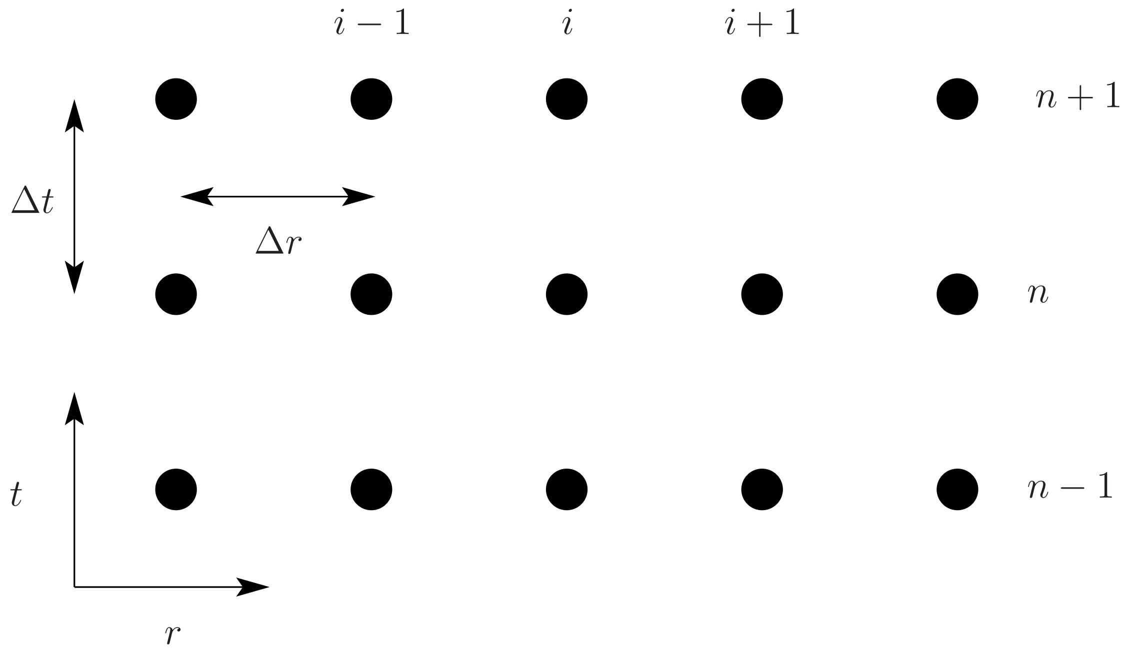

Figure C.1: A schematic representation of the finite difference grid in one spatial and one temporal dimension. Spacetime coordinates are given by the ordered pair (t, r), grid spacing in the spatial dimension is characterized by a single parameter Δr, and the temporal interval is characterized by parameter Δt. Grid points are labelled by spatial indices $...i-1, i, i+1, ...$ and temporal indices $...n-1, n, n+1, ...$

$$u^n_{i+1} = u^n_i + \Delta r \left(u^n_i\right)_{,r} + \frac{1}{2}\left(\Delta r\right)^2 \left(u^n_i\right)_{,rr} + \frac{1}{6}\left(\Delta r\right)^3 \left(u^n_i\right)_{,rrr} + \mathcal{O}\left(\left(\Delta r\right)^4\right), \tag{C.32}$$

$$u^n_{i+2} = u^n_i + 2\Delta r \left(u^n_i\right)_{,r} + \frac{1}{2}\left(2\Delta r\right)^2 \left(u^n_i\right)_{,rr} + \frac{1}{6}\left(2\Delta r\right)^3 \left(u^n_i\right)_{,rrr} + \mathcal{O}\left(\left(\Delta r\right)^4\right), \tag{C.33}$$

where subscript notation $\left(u^n_i\right)_{,r}$ designates the partial derivative of $u(t, r)$ with respect to coordinate r evaluated at point (t, r), $\left(u^n_i\right)_{,rr}$ the second partial derivative of $u(t, r)$ with respect to r at (t, r), and so on.

Then, as an example, to find the centered $\mathcal{O}\left(\left(\Delta r\right)^2\right)$ approximation for the FDA $\left(u^n_i\right)_{,r}$, solve the linear system of three equations (C.30), (C.31), (C.32). The solution in this case is simply

$$\left(u^n_i\right)_{,r} = \frac{u^n_{i+1} - u^n_{i-1}}{2\Delta r} + \mathcal{O}\left(\left(\Delta r\right)^2\right). \tag{C.34}$$

Using this technique, the centered $\mathcal{O}\left(\left(\Delta r\right)^2\right)$ approximation for FDA $\left(u^n_i\right)_{,rr}$ could also be obtained. It is given by

$$\left(u^n_i\right)_{,rr} = \frac{u^n_{i+1} - 2u^n_i + u^n_{i-1}}{\left(\Delta r\right)^2} + \mathcal{O}\left(\left(\Delta r\right)^2\right). \tag{C.35}$$

Analogous expressions hold for FDAs involving derivatives of t. For example, the centered FDA for the first derivative in time is

$$\left(u^n_i\right)_{,t} = \frac{u^{n+1}_i - u^{n-1}_i}{2\Delta t} + \mathcal{O}\left(\left(\Delta t\right)^2\right). \tag{C.36}$$

Notice the similarity between these FDAs and a centered limit definition of the derivative,

$$\frac{\partial u}{\partial r} \equiv \lim_{\Delta r \to 0} \frac{u(r+\Delta r) - u(r-\Delta r)}{2\Delta r}. \tag{C.37}$$

As another example, consider the one-sided $\mathcal{O}\left((\Delta r)^2\right)$ approximation for $\left(u_i^n\right)_{,r}$ which makes use of u_i^n, u_{i+1}^n, and u_{i+2}^n. Solving (C.31), (C.32), and (C.33) obtains

$$\left(u_i^n\right)_{,r} = \frac{-u_{i+2}^n + 4u_{i+1}^n - 3u_i^n}{2\Delta r} + \mathcal{O}\left((\Delta r)^2\right). \tag{C.38}$$

This so-called *forwards difference* operator allows me to evaluate $\left(u_i^n\right)_{,r}$ at the point on the finite difference grid with smallest value of coordinate r. Similarly, the *backwards difference* operator for $\left(u_i^n\right)_{,r}$ can be obtained by solving the system (C.29), (C.30) and (C.31). This operator allows me to evaluate $\left(u_i^n\right)_{,r}$ at the largest value of coordinate r and has form

$$\left(u_i^n\right)_{,r} = \frac{u_{i-2}^n - 4u_{i-1}^n + 3u_i^n}{2\Delta r} + \mathcal{O}\left((\Delta r)^2\right). \tag{C.39}$$

C.1.4 The Leap-Frog and Crank-Nicholson Schemes

As an example PDE consider the *advection equation*

$$\frac{\partial u}{\partial t} = v\frac{\partial u}{\partial r}, \tag{C.40}$$

which represents the passive advection of scalar field u carried along by a flow of constant speed v. Since later chapters of this dissertation deal almost exclusively with PDEs first order in both time and space, the advection equation is a useful prototype. Using the results of the previous subsection, this PDE could be represented with FDA

$$\frac{u_i^{n+1} - u_i^{n-1}}{2\Delta t} + \mathcal{O}\left((\Delta t)^2\right) = v\left(\frac{u_{i+1}^n - u_{i-1}^n}{2\Delta r}\right) + \mathcal{O}\left((\Delta r)^2\right). \tag{C.41}$$

The *stencil* of an FDA is defined as the discrete set of spacetime points on which the FDA depends. Since this FDA employs values u_i^{n-1}, u_{i-1}^n, u_{i+1}^n and u_i^{n+1}, it has a four-point stencil as represented in Figure C.2. This scheme is known as *leap-frog* and is one of the more common finite difference schemes used in solving PDEs. Since the value of u in the future, u_i^{n+1}, is determined entirely from values of u in its past, this scheme is *explicit*. Being explicit, the value of u_i^{n+1} can be obtained in a single step.

Instead of the leap-frog scheme, iterative Crank-Nicholson will be used to obtain the majority of results presented in this dissertation. The principle reasons for this alternate choice are initial data and stability. While the leap-frog scheme must be initialized with data from two time steps, u_{i-1}^n, u_{i+1}^n and u_i^{n-1}, the Crank-Nicholson scheme is initialized from values at a single time step, u_{i-1}^n and u_{i+1}^n. Second, the Crank-Nicholson scheme is known to be stable[4] for a wide range of FDAs, given grid spacing Δr and temporal interval Δt.

The *Crank-Nicholson* scheme is defined by modifying the temporal derivative operator to be centered at the virtual time step $t + \frac{1}{2}\Delta t$. A straightforward derivation obtains

$$\left(u_i^{n+\frac{1}{2}}\right)_{,t} = \frac{u_i^{n+1} - u_i^n}{\Delta t} + \mathcal{O}\left((\Delta t)^2\right), \tag{C.42}$$

[4]The issue of stability of a solution scheme is briefly discussed in subsection C.1.5.

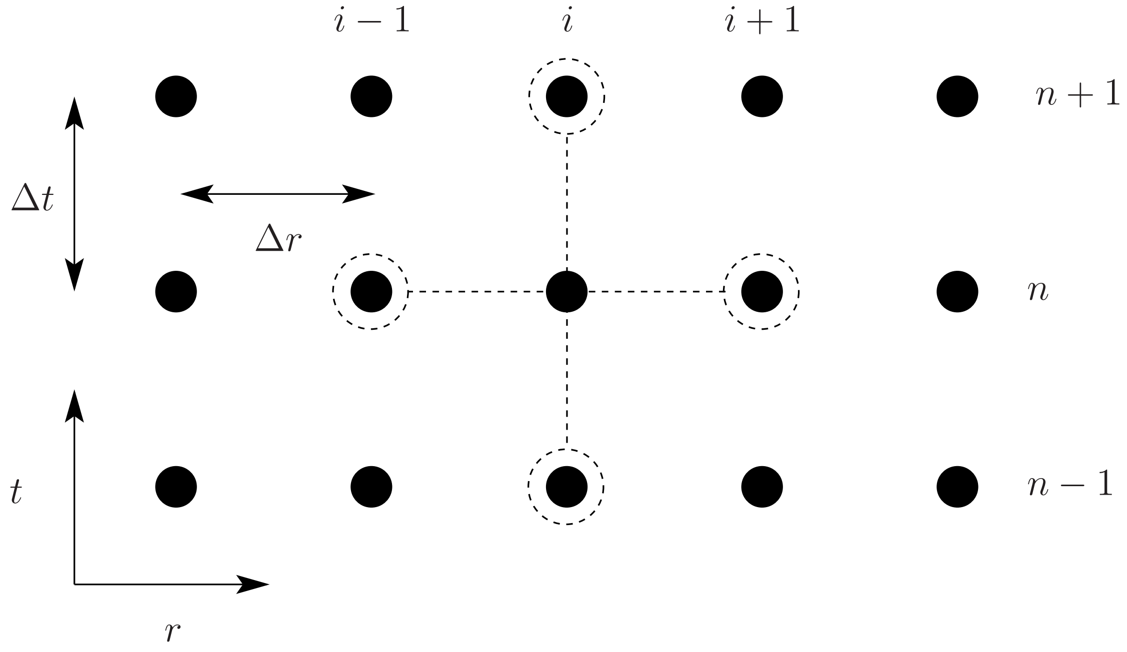

Figure C.2: The four-point stencil of the leap-frog scheme for the advection equation. The stencil is marked by dashed lines and circles. Grid points are labelled by spatial indices $...i-1, i, i+1, ...$ and temporal indices $...n-1, n, n+1, ...$. The scheme employs values u_i^{n-1}, u_{i-1}^n, u_{i+1}^n and u_i^{n+1} of function u. Spacetime coordinates are given by the ordered pair (t, r), grid spacing in the spatial dimension is characterized by a single parameter Δr, and the temporal interval is characterized by parameter Δt.

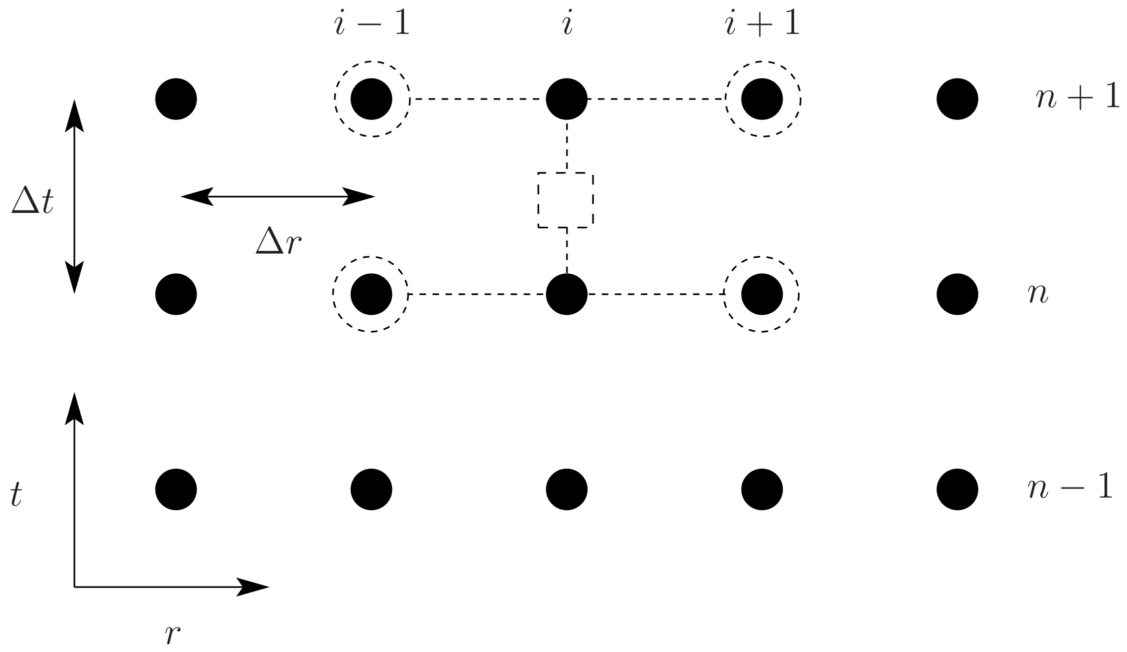

Figure C.3: The four-point stencil of the Crank-Nicholson scheme for the advection equation. The stencil is marked by dashed lines and circles, and is centered about the virtual point marked with a dashed square. Grid points are labelled by spatial indices $...i-1, i, i+1, ...$ and temporal indices $...n-1, n, n+1, ...$ The scheme employs values u_{i-1}^n, u_{i+1}^n, u_{i-1}^{n+1} and u_{i+1}^{n+1} of function u. Spacetime coordinates are given by the ordered pair (t, r), grid spacing in the spatial dimension is characterized by a single parameter Δr, and the temporal interval is characterized by parameter Δt.

where $u_i^{n+\frac{1}{2}}$ designates the value of u centered spatially at point labelled i and temporally at a virtual point between n and $n+1$. The expression of advection equation (C.40) as an FDA is then accomplished by evaluating spatial derivatives at this intermediate time step through a temporal average. The FDA thus becomes

$$\frac{u_i^{n+1} - u_i^n}{\Delta t} + \mathcal{O}\left((\Delta t)^2\right) = \frac{v}{2}\left(\frac{u_{i+1}^n - u_{i-1}^n}{2\Delta r} + \frac{u_{i+1}^{n+1} - u_{i-1}^{n+1}}{2\Delta r}\right) + \mathcal{O}\left((\Delta r)^2\right). \tag{C.43}$$

This scheme has a four-point stencil as displayed in Figure C.3. Since this scheme couples values at the future time step, u_{i-1}^{n+1} and u_{i-1}^{n+1}, it is called *implicit*. Being implicit, values of u in the future cannot be obtained in a single step. Rather, they must be obtained with an iterative procedure.

C.1.5 Stability

As mentioned in the previous subsection, one reason for choosing the implicit Crank-Nicholson scheme is because it tends to minimize instabilities for many PDEs. Since a detailed discussion of stability for finite difference schemes is beyond the scope of this dissertation, the conditions for stability will not be explicitly calculated for the PDEs used in this thesis, but instead will introduce the concept of stability at a heuristic level and mention an important result known as the CFL condition. Technical aspects and detailed discussions of stability can be found in [91], [103], [61], [134], and [30].

It is entirely possible to correctly implement a finite difference scheme for a time dependent problem, yet have the solutions plagued by floating point overflows at some point in the evolution. Providing there are no instabilities in the PDE being solved, the overflow will be as a consequence of the nature of the finite difference scheme itself—some schemes are inherently unstable for a given class of problem while others can be conditionally unstable.

As an example, consider the previously discussed advection equation (C.40) with periodic boundary conditions. A property of the advection equation is that a norm of the solution will not change significantly in time. That is to say,

$$||u(t,r)|| \sim ||u(t+\Delta t,r)|| \sim ||u(t+2\Delta t,r)|| \sim \cdots . \tag{C.44}$$

Equation (C.44) will be the working definition of *stability*. In fact, a system would be considered stable even if solutions grew as a polynomial in $||u(t,r)||$. However, exponential growth in the norm is certainly considered *unstable*. If the FDA to the PDE exhibiting property (C.44) is convergent, the discrete solution is expected to exhibit the analogous behaviour

$$||u_i^n|| \sim ||u_i^{n+1}|| \sim ||u_i^{n+2}|| \sim \cdots . \tag{C.45}$$

It would then be hoped solutions obtained from a scheme such as leap-frog,

$$u_i^{n+1} = v\frac{\Delta t}{\Delta r}\left(u_{i+1}^n - u_{i-1}^n\right) + u_i^{n-1} + \mathcal{O}\left((\Delta t)^2\right) + \mathcal{O}\left((\Delta r)^2\right), \tag{C.46}$$

would exhibit property (C.46). As it turns out, there are values of the *Courant factor*,

$$\lambda \equiv \frac{\Delta t}{\Delta r}, \tag{C.47}$$

for which (C.45) is violated. In fact, (C.46) is unstable for all

$$\lambda > \frac{1}{|v|}. \tag{C.48}$$

Now, if instead of leap-frog, the Crank-Nicholson scheme

$$u_i^{n+1} = \frac{v}{4}\frac{\Delta t}{\Delta r}\left(u_{i+1}^n - u_{i-1}^n + u_{i+1}^{n+1} - u_{i-1}^{n+1}\right) + u_i^n + \mathcal{O}\left((\Delta t)^2\right) + \mathcal{O}\left((\Delta r)^2\right) \tag{C.49}$$

is implemented, stability will be observed for all values λ. It is in this sense that Crank-Nicholson is considered *unconditionally stable*, in support of the previous claim that the Crank-Nicholson scheme tends to result in an FDA with improved stability.

To obtain the preceding stability conditions one needs to consider more detailed study of the *heuristic stability condition*, or alternately perform a *von-Neumann stability analysis*. Such analyses become complicated for nontrivial (i.e., nonlinear) PDEs like those used in later chapters of this thesis. The complexity of the analyses is further increased when nontrivial boundary conditions beyond periodic or Dirichlet, typical in systems of interest to numerical relativity, are applied to the PDEs. The reader is again referred to [91], [103], [61], [134], [30], [21] and [22].

In closing this discussion on the stability of finite difference schemes, it is worth mentioning one important result extracted from the von-Neumann stability analysis of (C.46)—the *CFL condition*, as derived by Courant, Friedrichs and Lewy in 1928. The condition is a statement that all $\lambda > 1$ are unstable for an explicit scheme, and carries the interpretation that the physical domain of dependence of a PDE must be entirely contained within the numerical domain of dependence if the scheme is to be stable. That is, Courant factor, λ, must be adjusted for the PDE under consideration, and it must certainly be less than unity. Note that since an implicit scheme couples values at the future time step, they do not possess similar interpretation for a single iteration.

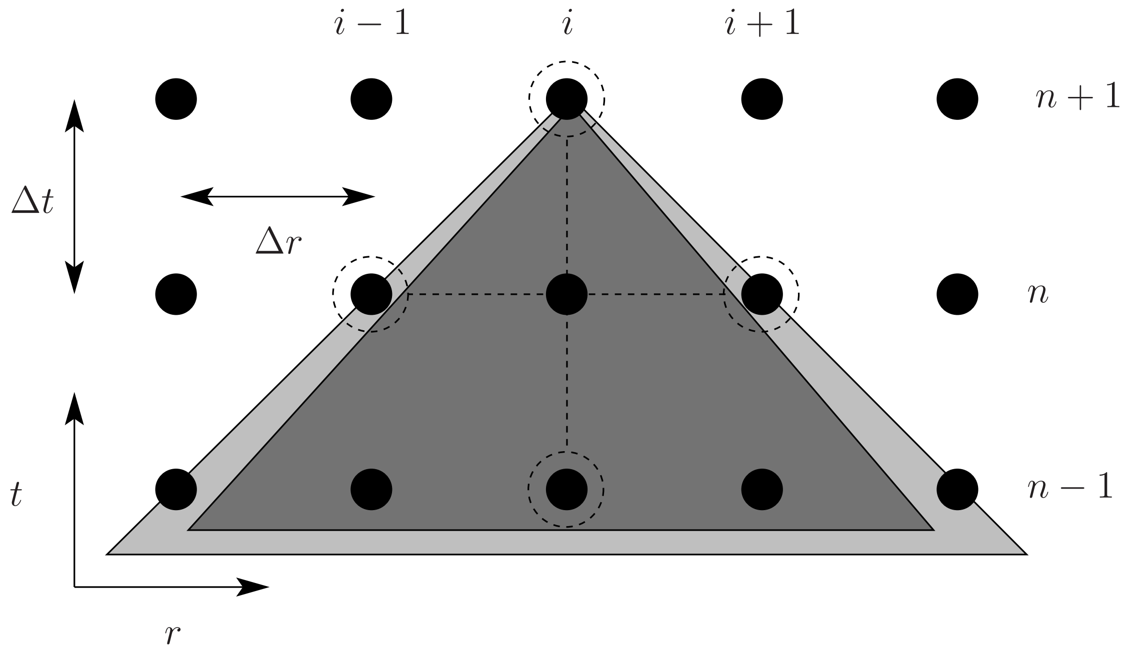

Figure C.4: The CFL condition for a stable leap-frog scheme. Grid points are labelled by spatial indices $...i-1, i, i+1, ...$ and temporal indices $...n-1, n, n+1, ...$. Spacetime coordinates are given by the ordered pair (t, r), grid spacing in the spatial dimension is characterized by a single parameter Δr, and the temporal interval is characterized by parameter Δt. The physical domain of dependence is shaded dark grey, while the numerical domain of dependence is shaded light grey. Note the physical domain of dependence is entirely contained by the numerical domain of dependence.

The CFL condition is represented pictorially for the leap-frog scheme of the advection equation in Figure C.4.

C.1.6 Kreiss-Oliger Dissipation Operators

This section on finite difference techniques will now be ended with discussion of Kreiss-Oliger dissipation operators. To start, note that the advection equation (C.40) admits normal mode solutions

$$u(t, r) \sim e^{ik(r+vt)} \tag{C.50}$$

with wavenumber k, which do not change in time. The solutions thus are said to be *non-dissipative*. Some FDAs possess similar non-dissipative character, while others do not. The leap-frog scheme in particular is non-dissipative. The dissipative character of finite difference schemes is considered because, especially for nonlinear PDEs, propagation and growth of high frequency components of a difference solution can lead to instabilities. It is therefore advantageous to ensure the scheme employs some form of dissipation to stabilize the solutions. The key point is to do so in a way that affects only the high frequency components, thereby mimicking the behaviour of a low-pass filter.

Again revert to discussion of the leap frog-scheme (C.46). If (C.46) is modified as per

$$u_i^{n+1} = v\frac{\Delta t}{\Delta r}\left(u_{i+1}^n - u_{i-1}^n\right) + u_i^{n-1} - \frac{\epsilon}{16}\left(u_{i+2}^n - 4u_{i+1}^n + 6u_i^n - 4u_{i-1}^n + u_{i-2}^n\right) + \mathcal{O}\left((\Delta t)^2\right) + \mathcal{O}\left((\Delta r)^2\right), \tag{C.51}$$

for adjustable parameter $0 \leq \epsilon < 1$, the additional terms do not modify the truncation error to leading order. The new scheme, does, however modify the amplification of modes with wave number $\xi \equiv k\Delta x$ to be

$$1 - \epsilon \sin^4 \frac{\xi}{2}. \tag{C.52}$$

The addition of *Kreiss-Oliger dissipation operator*

$$-\frac{\epsilon}{16}\left(u^n_{i+2} - 4u^n_{i+1} + 6u^n_i - 4u^n_{i-1} + u^n_{i-2}\right), \tag{C.53}$$

to the scheme thus acts as a low-pass filter with relatively sharp cutoff as $\xi \rightarrow \pi$.

For brevity, Kreiss-Oliger dissipation will not be discussed in more detail, but will note that since it does not modify truncation error at second order, it can be safely employed for all second-order accurate schemes. In particular, Kreiss-Oliger dissipation is used everywhere PDEs are solved in this dissertation with the Crank-Nicholson scheme. solve are nonlinear, there is significant likelihood that instability from high frequency modes would be an issue. Instead of explicitly determining the conditions for stability of the chosen FDAs, an experimental approach as adopted where some choice is made for $\lambda < 1$ and $\epsilon < 1$ and evolve the system. If the solutions blow up then λ and ϵ are adjusted until the system evolves in a stable manner. Once stability is achieved the values of these adjustable parameters are left unchanged for future evolutions. The advantage to using adjustable dissipation, as per Kreiss-Oliger, is that the amount of dissipation can be increased to the desired amount without applying so much dissipation that physical (i.e., lower-frequency) modes of the solution will be affected.

C.1.7 Iterative Solution Scheme for Evolutionary Equations

An explicit scheme such as leap-frog is soluble in a single step. Implicit schemes, however, couple functions at adjacent spatial grid points at the future time step and must therefore be solved iteratively. The Crank-Nicholson scheme is an example. For demonstrative purposes, consider the Crank-Nicholson scheme for advection equation (C.40) with the addition of Kreiss-Oliger dissipation. The $\mathcal{O}\left((\Delta t)^2\right)$, $\mathcal{O}\left((\Delta r)^2\right)$ FDA is

$$u^{n+1}_i = \frac{v}{4}\frac{\Delta t}{\Delta r}\left(-u^n_{i+2} + 4u^n_{i+1} - 3u^n_i - u^{n+1}_{i+2} + 4u^{n+1}_{i+1} - 3u^{n+1}_i\right) + u^n_i \qquad \text{for} \quad i = 1, \tag{C.54}$$

$$u^{n+1}_i = \frac{v}{4}\frac{\Delta t}{\Delta r}\left(u^n_{i+1} - u^n_{i-1} + u^{n+1}_{i+1} - u^{n+1}_{i-1}\right) + u^n_i \qquad \text{for} \quad i = 2, \tag{C.55}$$

$$\begin{aligned} u^{n+1}_i = \frac{v}{4}\frac{\Delta t}{\Delta r}\left(u^n_{i+1} - u^n_{i-1} + u^{n+1}_{i+1} - u^{n+1}_{i-1}\right) + u^n_i \quad &- \quad \frac{\epsilon}{32}\left(u^{n+1}_{i+2} - 4u^{n+1}_{i+1} + 6u^{n+1}_i - 4u^{n+1}_{i-1} + u^{n+1}_{i-2}\right) \\ &- \quad \frac{\epsilon}{32}\left(u^n_{i+2} - 4u^n_{i+1} + 6u^n_i - 4u^n_{i-1} + u^n_{i-2}\right) \\ &\text{for} \quad 3 \leq i \leq J-2, \end{aligned} \tag{C.56}$$

$$u^{n+1}_i = \frac{v}{4}\frac{\Delta t}{\Delta r}\left(u^n_{i+1} - u^n_{i-1} + u^{n+1}_{i+1} - u^{n+1}_{i-1}\right) + u^n_i \qquad \text{for} \quad i = J-1, \tag{C.57}$$

$$u^{n+1}_i = \frac{v}{4}\frac{\Delta t}{\Delta r}\left(u^n_{i-2} - 4u^n_{i-1} + 3u^n_i + u^{n+1}_{i-2} - 4u^{n+1}_{i-1} + 3u^{n+1}_i\right) + u^n_i \qquad \text{for} \quad i = J, \tag{C.58}$$

where the dissipation operator has been time averaged. The strategy of the iterative solution scheme begins with a specification of initial data u^n_i for $1 \leq i \leq J$, and an initial guess for u^{n+1}_i where again $1 \leq i \leq J$. (C.55) through (C.58) are then employed to obtain the first iterate of solution u_i^{n+1}. Designating the kth iterate of u_i^{n+1} as $u_i^{n+1(k)}$, a proper iterative scheme generates a sequence of iterates $u_i^{n+1(0)}$, $u_i^{n+1(1)}$, $u_i^{n+1(2)}$, ..., $u_i^{n+1(k)}$, converging upon the solution u_i^{n+1} in the limit $k \to \infty$. Two issues need further discussion: (1) the initial guess; and (2) the generation of the sequence of iterates. For evolutionary equations it is usually valid to assume the solution undergoes little change between the nth and $(n+1)$th time steps. So without prior knowledge of the evolution, a reasonable choice is simply to use the values from the step in the immediate past as an initial guess. That is,

$$u_i^{n+1(0)} = u_i^n, \tag{C.59}$$

the iteration count of the past time step being omitted from the notation. This resolves the first issue. The second item now warrants discussion.

In the most trivial scheme known as *Jacobi iterative*, the sequence of iterates is defined entirely from values of the preceding iterate. However, it can be shown that faster convergence can be obtained if the method uses the most recent iterates as they become available. This is the essence of a *Gauss-Seidel* iterative scheme. For example, assuming the order of updates proceeds $i = 3, ..., J-2$, the sequence of Gauss-Seidel iterates for equation (C.56) will be generated according to

$$\begin{aligned}
u_i^{n+1(k)} + \frac{\epsilon}{32}\left(6u_i^{n+1(k)}\right) &= \frac{v}{4}\frac{\Delta t}{\Delta r}\left(u_{i+1}^n - u_{i-1}^n + u_{i+1}^{n+1(k-1)} - u_{i-1}^{n+1(k)}\right) + u_i^n \\
&- \frac{\epsilon}{32}\left(u_{i+2}^{n+1(k-1)} - 4u_{i+1}^{n+1(k-1)} - 4u_{i-1}^{n+1(k)} + u_{i-2}^{n+1(k)}\right) \\
&- \frac{\epsilon}{32}\left(u_{i+2}^n - 4u_{i+1}^n + 6u_i^n - 4u_{i-1}^n + u_{i-2}^n\right).
\end{aligned} \tag{C.60}$$

While alternatives such as Newton's method converge more rapidly, they typically require a more accurate initial guess $u_i^{n+1(k)}$, and are somewhat more difficult to implement. Gauss-Seidel is found to be a sufficient method and is used in obtaining all results presented in this thesis. This method has been implemented using the Rapid Numerical Prototyping Language (RNPL) [94], [95], [96], [97]. In brief, RNPL is a high-level language which can be used to handle many details common to most numerical codes. For example, RNPL can be used to manage parameter fetching and memory allocation, along with input, output and update routines, allowing the user to focus efforts on aspects more interesting to physics and numerical relativity. After the user specifies (in the RNPL syntax) parameter names and types, a coordinate system, grid structure, grid function names and types, finite difference operators, evolutionary equations and an initialization scheme, RNPL can be used to generate an essentially complete FORTAN or C code. In the case of an iterative scheme, RNPL automatically implements Gauss-Seidel. The user thereby is saved from expending time on everything except for those aspects of greatest interest to the typical numerical relativist. Refer to [94], [95], [96], [97] for details and examples of RNPL's capabilities and limitations. But one important issue to note by design is RNPL's lack of support for the solution schemes appropriate to elliptic equations. Therefore, users are required to implement their own methods for solving constraint equations.

C.2 Constraint Equations

Constraint conditions typically form systems consisting of a elliptic equation to be solved in a domain with boundary conditions and sources in its interior. Boundary conditions are typically *Dirichlet* (the boundary value of the unknown function is specified), *Neumann* (the normal derivative of the function is specified) or *Robin* (an algebraic equation is given which relates the value of the unknown function to its normal derivative on the domain boundary). The canonical example of a constraint condition is the *Poisson* equation

$$\nabla^2 u = \rho, \tag{C.61}$$

where ∇^2 is the Laplacian operator, and u is to be solved on a domain Ω with specified source function ρ and where conditions for u are given on the boundary $\partial\Omega$. The Laplacian operator is a second-order PDE in the spatial coordinates. For example, the flat space Laplacian on u in spherical polar coordinates (r, θ, ϕ) is given by

$$\nabla^2 u = \frac{1}{r^2}\frac{\partial}{\partial r}\left(r^2 \frac{\partial u}{\partial r}\right) + \frac{1}{r^2 \sin\theta}\frac{\partial}{\partial \theta}\left(\sin\theta \frac{\partial u}{\partial \theta}\right) + \frac{1}{r^2 \sin^2\theta}\frac{\partial^2 u}{\partial \phi^2}. \tag{C.62}$$

Finally, notice that the Poisson equation is linear in u. Depending on the symmetries involved, this linearity in u results in an FDA which can be solved by direct or indirect methods as mentioned below. [125] and [126] form the set of references for direct methods, and the primary set of references for discussion of iterative methods also includes [150], [143] and [146].

C.2.1 The Poisson Equation in Spherical Symmetry

Restricting the system to spherical symmetry, $u = u(r)$, (C.62) becomes

$$\nabla^2 u = \frac{1}{r^2}\frac{\partial}{\partial r}\left(r^2 \frac{\partial u}{\partial r}\right) = \frac{2}{r}\frac{\partial u}{\partial r} + \frac{\partial^2 u}{\partial r^2}. \tag{C.63}$$

Then using the FDAs of subsection C.1.3, the derivatives in (C.62) can be expressed to 2nd order accuracy using three-point stencils. Then, using the established notation, the one-dimensional finite difference equation

$$\nabla^2 u_i^n = \frac{2}{r_i}\left(\frac{u_{i+1}^n - u_{i-1}^n}{2\Delta r}\right) + \left(\frac{u_{i+1}^n - 2u_i^n + u_{i-1}^n}{(\Delta r)^2}\right) + \mathcal{O}\left((\Delta r)^2\right) \tag{C.64}$$

is obtained. Substituting (C.64) into (C.61) the elliptic to be solved becomes

$$\frac{2}{r_i}\left(\frac{u_{i+1}^n - u_{i-1}^n}{2\Delta r}\right) + \left(\frac{u_{i+1}^n - 2u_i^n + u_{i-1}^n}{(\Delta r)^2}\right) = \rho_i^n. \tag{C.65}$$

Then if coordinate r in the computational domain Ω ranges $[r_1, r_J]$ over a grid of J points, (C.65) forms a tridiagonal system linear in u in the interior of Ω. However, boundary conditions still need to be specified before the full system can be solved. If the boundary conditions were Dirichlet at both $r = r_1$ and $r = r_J$, the complete system of equations would be

$$u_1^n = b_1^n, \tag{C.66}$$

$$\frac{2}{r_i}\left(\frac{u_{i+1}^n - u_{i-1}^n}{2\Delta r}\right) + \left(\frac{u_{i+1}^n - 2u_i^n + u_{i-1}^n}{(\Delta r)^2}\right) = \rho_i^n \qquad \text{for} \quad 2 \le i \le J-1, \tag{C.67}$$

$$u_J^n = b_J^n, \tag{C.68}$$

where b_1^n and b_J^n are specified boundary values.

However, outside of cases where spacetime has been compactified so that computational boundaries correspond to spatial infinity, systems of interest to numerical relativity seldom possess constraints with Dirichlet boundary conditions. Neumann and Robin conditions are far more prevalent. For instance, where constraint equation (C.61) represents the Gauss' law electromagnetic constraint, outside of a localized charge distribution, the electric potential will possess a Coulombic dependence in spherical symmetry. This means the form of u will there be

$$u = \frac{u_{-1}}{r} + u_0, \tag{C.69}$$

where u_{-1} and u_0 are constants. The choice of u_0 amounts to choosing a convenient location for the zero of the potential. Typically, u_0 is chosen so that either $u = 0$ at $r = 0$ or $u = 0$ at $r = \infty$. Then if $r = r_J$ is external to sources, the choice $u_0 = 0$ there amounts to setting the zero of potential at $r = \infty$. Equation (C.69) then reduces to

$$u = \frac{u_{-1}}{r}. \tag{C.70}$$

Differentiating (C.70) with respect to r then yields

$$\frac{\partial u}{\partial r} = -\frac{u_{-1}}{r^2} = -\frac{1}{r}u, \tag{C.71}$$

or, in finite difference form,

$$\left(\frac{3u_J^n - 4u_{J-1}^n + u_{J-2}^n}{2\Delta r}\right) = -\frac{1}{r_J}u_J^n, \tag{C.72}$$

where the backwards difference expression for the derivative has been used. Then solving (C.72) for u_{J-2}^n obtains

$$u_{J-2}^n = -\left(\frac{2\Delta r}{r_J} + 3\right)u_J^n + 4u_{J-1}^n, \tag{C.73}$$

which, substituted into (C.65) for $i = J - 1$ yields

$$\left(\frac{2}{r_J r_{J-1}} - \frac{2}{r_J \Delta r} + \frac{4}{r_{J-1}\Delta r} - \frac{2}{(\Delta r)^2}\right)u_J^n + \left(-\frac{4}{r_{J-1}\Delta r} + \frac{2}{(\Delta r)^2}\right)u_{J-1}^n = \rho_{J-1}^n, \tag{C.74}$$

the boundary condition to be applied at $r = r_J$.

To obtain a realistic boundary condition at $r = r_1$, notice that for a smooth spherically symmetric distribution, the charge density ρ will be expansible in powers of radial coordinate r near $r = 0$ with even leading order. That is,

$$\rho = \rho_0 + \rho_2 r^2 + \rho_4 r^4 + \mathcal{O}\left(r^6\right), \tag{C.75}$$

where ρ_0, ρ_2, and ρ_4 are appropriately chosen constants. Integrating over ρ to find q_{encl}, the amount charge enclosed by a small sphere of radius R centered at $r = 0$ obtains

$$\begin{aligned}
q_{encl} &= \int_{r=0}^{r=R}\int_{\phi=0}^{\phi=2\pi}\int_{\theta=0}^{\theta=\pi}\left(\rho_0 + \rho_2 r^2 + \rho_4 r^4 + \mathcal{O}\left(r^6\right)\right)r^2 \sin\theta d\theta d\phi dr \\
&= 4\pi\int_{r=0}^{r=R}\left(\rho_0 + \rho_2 r^2 + \rho_4 r^4 + \mathcal{O}\left(r^6\right)\right)r^2 dr \\
&= 4\pi\left(\rho_0\frac{R^3}{3} + \rho_2\frac{R^5}{5} + \rho_4\frac{R^7}{7} + \mathcal{O}\left(R^9\right)\right).
\end{aligned} \tag{C.76}$$

Then, using (C.75) or (C.76), straightforward integration obtains the amplitude of the electric field, E, at $r = R$ as

$$E = \left(\rho_0\frac{R}{3} + \rho_2\frac{R^3}{5} + \rho_4\frac{R^5}{7} + \mathcal{O}\left(R^7\right)\right), \tag{C.77}$$

and the value of the electric potential, u, at $r = R$ as

$$u = u_0 - \left(\rho_0 \frac{R^2}{6} + \rho_2 \frac{R^4}{20} + \rho_4 \frac{R^6}{42} + \mathcal{O}\left(R^8\right)\right), \tag{C.78}$$

where u_0 is a constant of integration, chosen so that (C.70) and (C.78) agree at the outer boundary of charge density ρ. However, it is not necessary to solve for u_0. Instead, the required boundary condition can be derived by simply by noting that u is an even function of r near $r = 0$, and so its derivative with respect to r must vanish. Thus, using the 2nd order forwards difference approximation, obtains

$$\frac{-u_3^n + 4u_2^n - 3u_1^n}{2\Delta r} = 0, \tag{C.79}$$

and thus

$$u_3^n = 4u_2^n - 3u_1^n. \tag{C.80}$$

Then, substituting (C.80) into (C.65) for $i = 2$ yields

$$-\left(\frac{4}{r_2 \Delta r} + \frac{2}{(\Delta r)^2}\right) u_1^n + \left(\frac{4}{r_2 \Delta r} + \frac{2}{(\Delta r)^2}\right) u_2^n = \rho_2^n. \tag{C.81}$$

In summary, the complete system of equations has become

$$-\left(\frac{4}{r_2 \Delta r} + \frac{2}{(\Delta r)^2}\right) u_1^n + \left(\frac{4}{r_2 \Delta r} + \frac{2}{(\Delta r)^2}\right) u_2^n = \rho_2^n, \tag{C.82}$$

$$\frac{2}{r_i}\left(\frac{u_{i+1}^n - u_{i-1}^n}{2\Delta r}\right) + \left(\frac{u_{i+1}^n - 2u_i^n + u_{i-1}^n}{(\Delta r)^2}\right) = \rho_i^n \qquad \text{for} \quad 2 \le i \le J-1, \tag{C.83}$$

$$\begin{aligned} &\left(\frac{2}{r_J r_{J-1}} - \frac{2}{r_J \Delta r} + \frac{4}{r_{J-1} \Delta r} - \frac{2}{(\Delta r)^2}\right) u_J^n \\ &\qquad + \left(-\frac{4}{r_{J-1} \Delta r} + \frac{2}{(\Delta r)^2}\right) u_{J-1}^n = \rho_{J-1}^n. \end{aligned} \tag{C.84}$$

The elliptic system is again linear and still can be written in tridiagonal matrix form, even with nontrivial boundary conditions. However, while being able to rewrite the system in tridiagonal form will simplify computations presented in later chapters, the key feature here is the linearity of the system of equations. Being linear, direct solution schemes such as Gauss-Jordan elimination, Gaussian elimination or LU decomposition can be applied to solve for unknowns u_i^n. Being elementary techniques and well documented in the literature, The reader is simply referred to [125] and [126] for detailed discussion. Finally, it is sufficient to state that, after reducing the electromagnetic constraint equation of Chapter 3 to linear tridiagonal form, it is solved using Gaussian elimination[5] followed by back-substitution with routines provided by the LAPACK software suite [2].

[5] A common source of error with systems requiring many operations is the accumulation or roundoff errors. While an elimination scheme will return a result under such circumstances, the solution will be incorrect by some degree, as can be checked by substituting the result back into the original system. To correct this problem the *iterative improvement* technique is used as outlined in [125], [126].

C.2.2 The Poisson Equation in Axial Symmetry

Now consider the Poisson equation in axial symmetry. Being dependent on just the two coordinate dimensions r and θ, it will be expressed

$$\frac{1}{r^2}\frac{\partial}{\partial r}\left(r^2\frac{\partial u}{\partial r}\right)+\frac{1}{r^2\sin\theta}\frac{\partial}{\partial\theta}\left(\sin\theta\frac{\partial u}{\partial\theta}\right)=\nabla^2 u=\rho. \tag{C.85}$$

Off boundary, (C.85) can be written as the second order FDA

$$\begin{aligned}&\frac{2}{r_i}\left(\frac{u^n_{i+1,j}-u^n_{i-1,j}}{2\Delta r}\right)+\left(\frac{u^n_{i+1,j}-2u^n_{i,j}+u^n_{i-1,j}}{(\Delta r)^2}\right)\\&+\frac{1}{r_i^2}\left(\frac{\cos\theta_j}{\sin\theta_j}\right)\left(\frac{u^n_{i,j+1}-u^n_{i,j-1}}{2\Delta\theta}\right)+\frac{1}{r_i^2}\left(\frac{u^n_{i,j+1}-2u^n_{i,j}+u^n_{i,j-1}}{(\Delta\theta)^2}\right)=\rho^n_{i,j}\qquad\text{for}\quad 2\le i\le J-1,\\&\qquad\qquad\qquad\qquad\qquad\qquad\qquad\qquad\qquad\qquad\qquad\qquad 2\le j\le K-1,\end{aligned} \tag{C.86}$$

the indices i for coordinate r being a member of the positive integer set $\{1,2,\cdots,J\}$, indices j for θ being a member of $\{1,2,\cdots,K\}$, the grid spacing in the direction of coordinate r being Δr, and spacing in the direction of θ being $\Delta\theta$. A comma-separated subscript notation has been adopted for grid functions to avoid confusion in situations the likes of $u^n_{11,2}$. If the boundary conditions (C.82) and (C.84) are assumed for coordinate direction r, and furthermore $u^n_{i,j}$ is assumed to be an even function in θ along the line of axial symmetry ($\theta=0$ and $\theta=\pi$), the complete FDA can be expressed

$$
\begin{aligned}
&-\frac{2}{r_i^2}\left(\left(\frac{\cos\theta_2}{\sin\theta_2}\right)\frac{1}{\Delta\theta}+\frac{1}{(\Delta\theta)^2}\right)u_{i,1}^n \\
&+\frac{2}{r_i^2}\left(\left(\frac{\cos\theta_2}{\sin\theta_2}\right)\frac{1}{\Delta\theta}+\frac{1}{(\Delta\theta)^2}\right)u_{i,2}^n=\rho_{i,2}^n \qquad \text{for} \quad 1\le i\le J \\
&\qquad\qquad \text{at boundary } j=1,
\end{aligned} \tag{C.87}
$$

$$
-\left(\frac{4}{r_2\Delta r}+\frac{2}{(\Delta r)^2}\right)u_{1,j}^n+\left(\frac{4}{r_2\Delta r}+\frac{2}{(\Delta r)^2}\right)u_{2,j}^n=\rho_{2,j}^n \qquad \text{for} \quad 2\le j\le K-1 \quad \text{at boundary } i=1, \tag{C.88}
$$

$$
\begin{aligned}
&\frac{2}{r_i}\left(\frac{u_{i+1,j}^n-u_{i-1,j}^n}{2\Delta r}\right)+\left(\frac{u_{i+1,j}^n-2u_{i,j}^n+u_{i-1,j}^n}{(\Delta r)^2}\right) \\
&+\frac{1}{r_i^2}\left(\frac{\cos\theta_j}{\sin\theta_j}\right)\left(\frac{u_{i,j+1}^n-u_{i,j-1}^n}{2\Delta\theta}\right)+\frac{1}{r_i^2}\left(\frac{u_{i,j+1}^n-2u_{i,j}^n+u_{i,j-1}^n}{(\Delta\theta)^2}\right)=\rho_{i,j}^n \qquad \text{for} \quad 2\le i\le J-1, \\
&\qquad\qquad 2\le j\le K-1,
\end{aligned} \tag{C.89}
$$

$$
\begin{aligned}
&\frac{2}{r_i^2}\left(\left(\frac{\cos\theta_{K-1}}{\sin\theta_{K-1}}\right)\frac{1}{\Delta\theta}-\frac{1}{(\Delta\theta)^2}\right)u_{i,K}^n \\
&+\frac{2}{r_i^2}\left(-\left(\frac{\cos\theta_{K-1}}{\sin\theta_{K-1}}\right)\frac{1}{\Delta\theta}+\frac{1}{(\Delta\theta)^2}\right)u_{i,K-1}^n=\rho_{i,K-1}^n \qquad \text{for} \quad 1\le i\le J \\
&\qquad\qquad \text{at boundary } j=K,
\end{aligned} \tag{C.90}
$$

$$
\begin{aligned}
&\left(\frac{2}{r_Jr_{J-1}}-\frac{2}{r_J\Delta r}+\frac{4}{r_{J-1}\Delta r}-\frac{2}{(\Delta r)^2}\right)u_{J,j}^n \\
&\left(-\frac{4}{r_{J-1}\Delta r}+\frac{2}{(\Delta r)^2}\right)u_{J-1,j}^n=\rho_{J-1,j}^n \qquad \text{for} \quad 2\le j\le K-1 \\
&\qquad\qquad \text{at boundary } i=J.
\end{aligned} \tag{C.91}
$$

As displayed in Figure C.5, this FDA has a five-point stencil utilizing grid points $u_{i,j}^n$, $u_{i-1,j}^n$, $u_{i+1,j}^n$, $u_{i,j-1}^n$, and $u_{i,j+1}^n$ when $2\le i\le J-1$ and $2\le j\le K-1$. The stencils on boundary are two-point. Stencils for boundary conditions (C.87) and (C.88) are respectively depicted in Figures C.6 and C.7.

This system of equations is amenable to any of a number of different solution schemes. Since it can be written in block tridiagonal form, it can be solved using *line successive over-relaxation* (LSOR)[6], which was a standard iterative method until the 1970s. Again, because it is well doc-

[6]Line successive over-relaxation is sometimes called *successive line over-relaxation* (SLOR) by other authors.

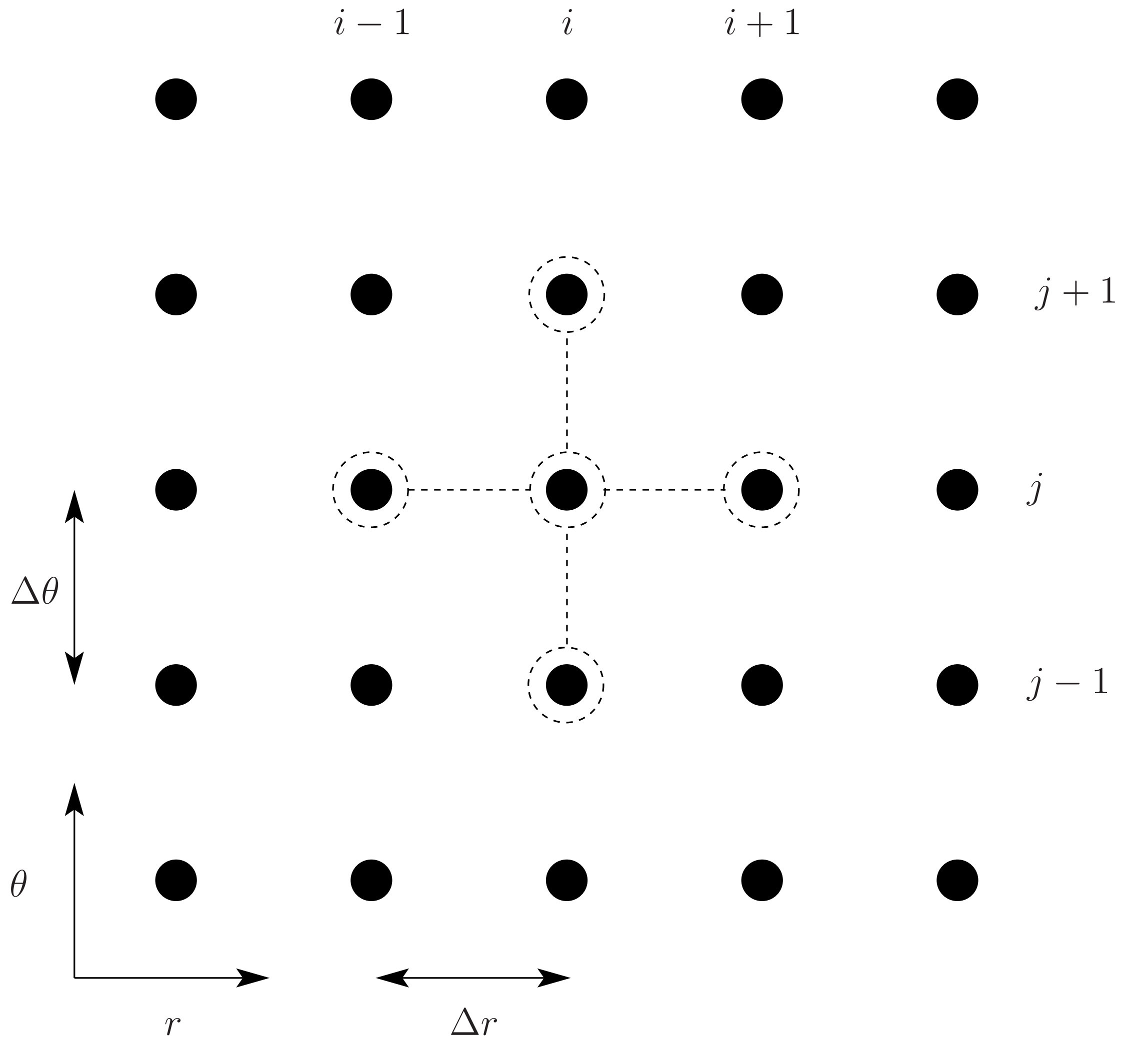

Figure C.5: The five-point stencil of the second order FDA for the Poisson equation off boundary in the two dimensions r and θ. The stencil is marked by dashed lines and circles. The stencil center lies on the range of indices $2 \leq i \leq J-1$ and $2 \leq j \leq K-1$. The scheme employs values $u^n_{i,j}$, $u^n_{i-1,j}$, $u^n_{i+1,j}$, $u^n_{i,j-1}$, and $u^n_{i,j+1}$ of function u. Coordinates are given by the ordered pair (r, θ), grid spacing in direction r is characterized by parameter Δr and in direction θ by parameter $\Delta\theta$.

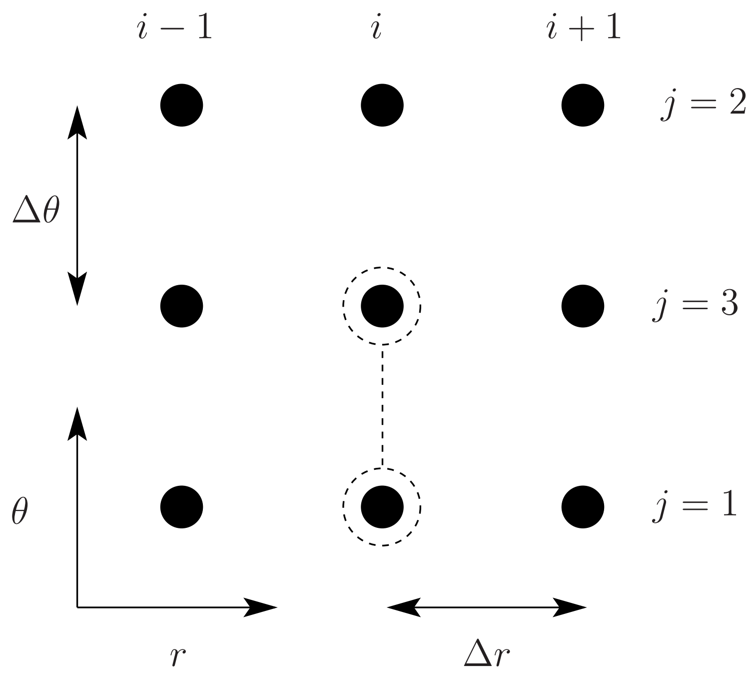

Figure C.6: The two-point stencil of the second order FDA for the Poisson equation in the two dimensions r and θ at boundary $\theta = 0$. The stencil is marked by dashed lines and circles. Stencil points cover the range of indices $1 \leq i \leq J$ and $1 \leq j \leq 2$. The scheme employs values $u^n_{i,1}$, and $u^n_{i,2}$ of function u. Grid spacing in direction θ is characterized by parameter $\Delta\theta$.

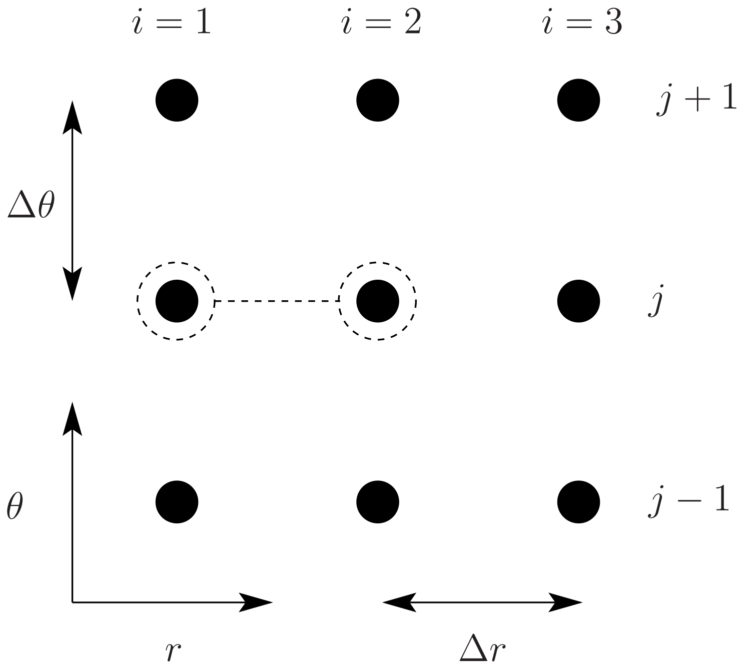

Figure C.7: The two-point stencil of the second order FDA for the Poisson equation in the two dimensions r and θ at boundary $r = 0$. The stencil is marked by dashed lines and circles. Stencil points cover the range of indices $1 \leq i \leq 2$ and $2 \leq j \leq K - 1$. The scheme employs values $u^n_{1,j}$, and $u^n_{2,j}$ of function u. Grid spacing in direction r is characterized by parameter Δr.

umented in the literature, The reader deferred to standard texts such as [143] and [150] for the details. In summary, the electromagnetic constraint equation in Chapter 4 is solved using LSOR with *zebra-stripe ordering* and *Chebyshev acceleration*.[7]

Having concluded discussion of finite difference difference schemes for evolutionary and constraint equations, the topics of adaptive mesh refinement for hyperbolic equations and parallel computation are now addressed, as they have played a crucial role in obtaining the results presented in this dissertation.

C.3 Adaptive Mesh Refinement

Adaptive mesh refinement (AMR) is important for finite difference schemes whose solutions unfold on a wide range of spatial and temporal scales. AMR solves resolutional problems associated with finite computational resources when solving such systems by adding resolution where needed and removing resolution when no longer required. AMR is especially important when resolution requirements are not known a priori, as would be the case in discovering new phenomena numerically.

In this thesis AMR is employed rather than a nonuniform mesh scheme, thereby circumventing both the problem of complicated FDA stencils and the requirement of a priori knowledge on resolution requirements during evolution. AMR is employed in both spherical symmetry and axial symmetry. In spherical symmetry AMR is implemented using a version of the *ad* code, developed by Choptuik [25], and first used in [23]. In axial symmetry AMR is implemented using the Parallel Adaptive Mesh Refinement (PAMR) code developed by Pretorius [128], [129]. With both the ad and PAMR codes, the user is provided the framework and utilities for AMR, but not the equations of motion for the systems of interest. In both cases it is up to the user to derive the equations and implement the associated FDAs.

Both ad and PAMR use an adaptive algorithm based on that of Berger and Oliger first introduced in 1984 [7]. The Berger and Oliger (B&O for short) algorithm is designed for general hyperbolic PDEs and based upon three key elements: (1) the AMR grid hierarchy; (2) a time stepping algorithm; and (3) dynamical regridding via relative solution error estimate. The modified B&0 algorithm is now described through its three key elements.

C.3.1 The Grid Hierarchy

AMR is implemented through a hierarchy of grids of different resolutions but uniform in each grid direction. Each level is assumed to be characterized by a single spatial discretization scale in each of these directions.[8] The mth level of the hierarchy, l_m, is defined as the set of grids of resolution h_m. In the set of levels, $\{l_m\}$, where m is a positive integer (i.e., $m \in \mathbb{Z}^+$), l_1 is the coarsest level,

[7] For many classes of problem, LSOR was eventually replaced with generally more efficient methods such as multigrid [13]. However, due to the complexity of multigrid methods and issues pertaining to the choice restriction and prolongation operators [125], [126], it can at times be difficult to code a convergent multigrid solver. This is especially true for nonlinear equations or those with much stronger coupling in one coordinate direction than another. When faced with the situation of either obtaining a solution with a somewhat inefficient solver or not obtaining a solution at all, it is better to sacrifice efficiency. This is the approach adopted in obtaining results presented in this dissertation. While a pointwise Gauss-Seidel multigrid scheme was implemented to solve the Poisson equation in Kerr spacetime, the scheme displayed poor convergence for many choices of black hole parameters $M_{\rm BH}$ and $a_{\rm BH}$. It was subsequently suggested by Choptuik [32] that the poor convergence was likely because the chosen pointwise relaxation scheme is an inadequate smoother for systems with a much stronger coupling in one coordinate direction than another. In such cases it is preferable to use a line iterative method, as in the line Gauss-Seidel multigrid algorithm implemented in [20]. Perhaps the first record of this issue were noted by Brandt in [13]. A complete discussion of the problem can be found in [146]. However, since a free evolution is performed for the electromagnetic variables, the Poisson equation needs to be solved just once during an evolution at the initial time step. Having written a demonstrably robust and relatively efficient LSOR solver, it was not necessary to revisit the multigrid problem. Implementing a line iterative multigrid scheme remains an avenue of future investigation.

[8] In the original B&O algorithm, grids could be nonuniform in a coordinate direction and thus characterized by more than a single spatial discretization scale.

$l_2 \leq l_m \leq l_{f-1}$ are intermediate resolution levels, and l_f is the level with the finest resolution. Successive levels of resolution are related via

$$h_m = \sigma_s h_{m+1}, \tag{C.92}$$

where σ_s is called the *spatial refinement ratio* and has properties $\sigma_s \in \mathbb{Z}^+$ and $\sigma_s \geq 2$. Additionally assume σ_s is the same in each coordinate direction and for all successive levels.[9] A grid at level l_m is called a *parent grid* and a grid at l_{m+1} a *child grid*. A child grid must be entirely contained by a parent grid. And finally, note that grids within a level may overlap.

The modified scheme used requires all grids to share the same coordinate system, and grid directions to be aligned with the coordinate directions. In addition, this modified scheme requires child grids be aligned so that, in their regions of overlap, all parent grid points are coincident with child grid points.[10] Finally, the modified algorithm assumes a single level l_1 grid called the *base grid* covers the entire computational domain. Figure C.8 displays a prototypical grid hierarchy for the case $l_f = l_3$ and $\sigma_s = 2$.

The next two subsections describe, in sequence, the time stepping algorithm used to advance solutions in the grid hierarchy, and the dynamical regridding procedure by which it is ensured solutions are adequately resolved at each time step in the evolution.

C.3.2 The Time-Stepping Algorithm

The core of a B&O-type AMR scheme is a recursive time-stepping algorithm in which functions on all parent grids are evolved before those on child grids. In this scheme, once functions on a parent grid in level l_m has been evolved into the future one time step Δt_m, the functions on child grids of level l_{m+1} are evolved into the future up to the same time through a sequence of σ_t time steps, where σ_t is the *temporal refinement ratio* with properties $\sigma_t \in \mathbb{Z}^+$ and $\sigma_t \geq 2$. A constant Courant factor across the hierarchy can be maintained by demanding

$$\Delta t_m = \sigma_t \Delta t_{m+1}. \tag{C.93}$$

This modified algorithm assumes σ_t is the same between each successive level.[11] Note that in order to ensure the CFL condition is satisfied, $\sigma_t \geq \sigma_s$ must be chosen.

Since functions update on parent grids before those on its children, values on the child grid boundaries off those of the base grid can be obtained by interpolating from function values on the parent grid. This avoids having to supply special conditions off the boundary of the base grid, and allows evolution only with the interior finite difference equations and solution scheme. Also, since the solution error of a function on the parent level near its child grid boundaries should be comparable to that on the child grid itself near those boundaries, the procedure of interpolating values on the child grid boundary from the parent grid solution will not result in increased solution error at these locations. Finally, once all functions on child grids have been updated to the future time step of their parents, the child grid function values are injected into the parent grids where their points coincide. This final step ensures the most accurate solution is available on all grids at all times.

C.3.3 Dynamical Regridding via Relative Solution Error

In B&O-type schemes, resolutional demands are periodically assessed and grids in the hierarchy are appropriately modified. The procedure of modifying grids is known as *regridding*. The period

[9] Historically, in B&O the spatial refinement ratio between two successive levels could be non-integer and different between different successive levels.

[10] The original B&O algorithm allows parent grids to be offset or rotated with respect to the children.

[11] As with the spatial refinement ratio, in the original B&O algorithm, the temporal refinement ratio between successive levels could differ of be non-integer.

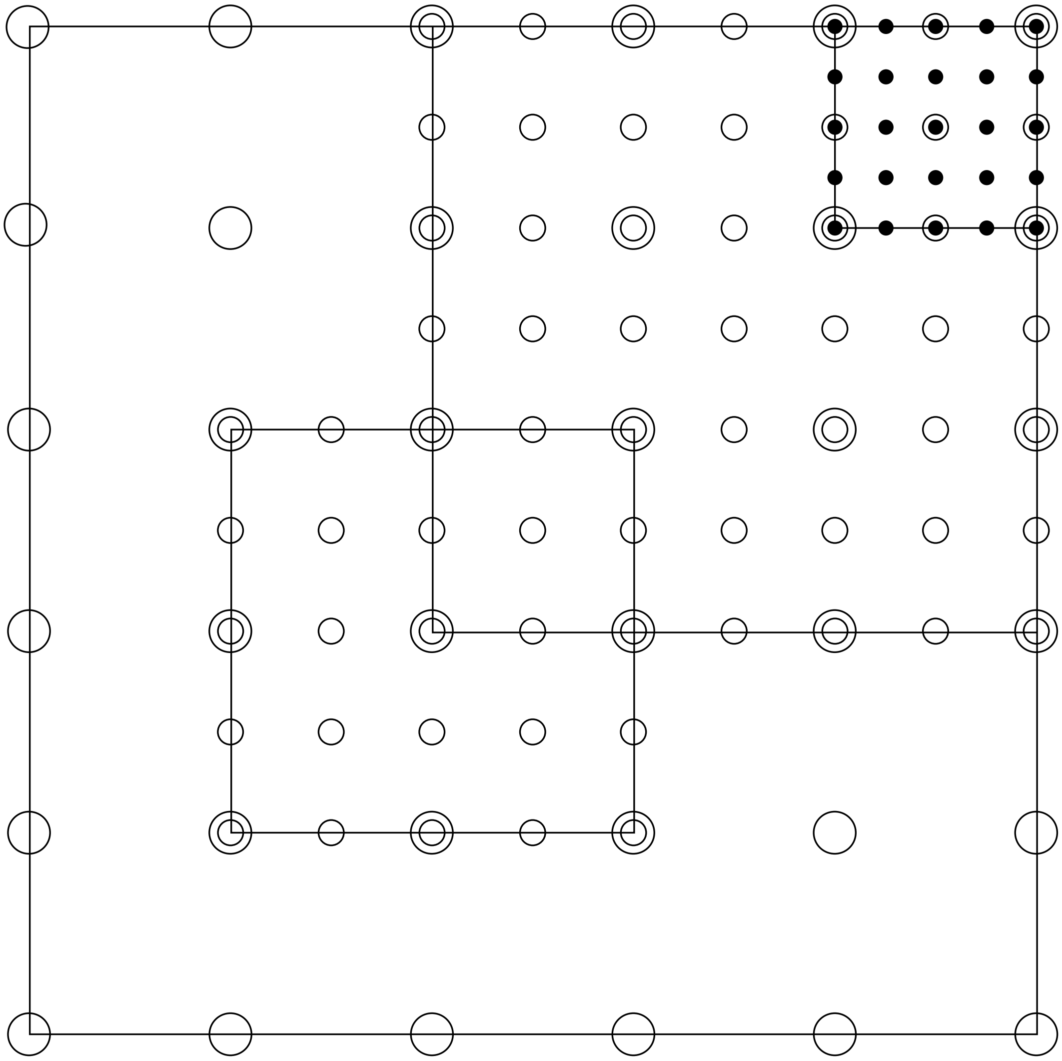

Figure C.8: A schematic representation of the AMR grid hierarchy in two spatial dimensions. Displayed are the base grid l_1 (large circles), along with prototypical levels l_2 (small circles) and l_3 (black dots) for the case $\sigma_s = 2$.

between resolutional assessments should be small enough to track all features of the solution. Since light speed, $c = 1$, is the upper limit of the speed at which information should propagate, requirements should be assessed at least every $\frac{c}{\lambda} = \frac{1}{\lambda}$ time steps, as this is the time in which a physical signal could spatially propagate a single grid point.

The key then is to set a criterion which determines when the resolutional requirements have changed. The approach outlined in [7] is employed by tying regridding to relative solution error estimates.[12] In order to establish the measure, each grid, g, at level l_m is first cloned and the clone labelled g^m. A second copy of g is then made and its number of grid points coarsened by factor σ_s. The second copy is labelled $g^{m-\sigma_s}$. The two new grids are evolved into the future until they are next coincident in time. Then comparing a discrete unknown solution on cloned grid copy g^m to that on coarsened grid copy $g^{m-\sigma_s}$ at the first coincident time the core of the measure becomes the *relative solution error*

$$e^{h_m}(u) = \left(u^{h_m} - u^{\sigma_s h_m}\right) + \mathcal{O}\left(h^p\right), \tag{C.94}$$

where u^{h_m} is the discrete solution on g^m, $u^{\sigma_s h_m}$ is the solution on $g^{m-\sigma_s}$, and $p \in \mathbb{Z}^+$ again being the order of the FD scheme. The criterion whether to regrid is then based on the magnitude of an appropriate point-by-point norm of the relative solution errors of some set of grid functions on each grid g. This point-by-point norm of the set of relative solution errors is denoted τ_g, and is formally

$$\tau_g = \sum_u ||e^{h_m}(u)||. \tag{C.95}$$

This is a measure that can be used dynamically during the time stepping procedure.

Once τ_g has been calculated for all grids in the hierarchy, the information is passed to a *clustering algorithm*. Essentially, the clustering algorithm begins by flagging points at which τ_g exceeds some predefined tolerance. The sets of flagged points then form the regions where child grids $g^{m+\sigma_s}$ are to be introduced. Conversely, the unflagged points (where τ_g falls below the tolerance value) define regions where the grid structure is to be coarsened by elimination of grids g^m. It is by this method that the grid hierarchy is refined. For more detail on clustering algorithms, and related topics of *buffer zones* and *filling factors* see [127] and [8]. Finally, after the grid points have been appropriately clustered and the hierarchy refined, function values are transferred from the old hierarchy to the new by appropriately interpolating grid functions from old parent grids, g^m, to new children, $g^{m-\sigma_s}$, and conversely by injecting grid function values from eliminated children onto their parent grids. This concludes discussion of the B&O-type AMR algorithms used in this thesis. For additional details the reader is referred to [7] and [127].

C.4 Parallel Computing

Programs traditionally have been written for *serial computation* defined as the sequential execution of an instruction set by a single central processing unit (CPU). Since the serial model allows just a single one-instruction execution at any moment in time, large calculations inevitably suffer from both both limited computer memory and long total execution time. The goal of an alternate computational model, such as parallel computation, is to delay, if not eliminate, the user experiencing the effects of these limitations. In the most basic form, the definition of *parallel computing* is the simultaneous use of multiple computing resources to solve a problem. Where required, the PAMR framework ([128], [129]) is adopted to parallelize codes used to obtain results for this dissertation.

[12] What has here been defined as the relative solution error historically has been referred to as the *local truncation error* (cf. [7]).

C.4.1 Parallel Program Design

PAMR provides support for managing load distribution and communication for codes dependent on a grid structure, thus providing a degree of automation for programmers wanting to parallelize finite difference codes. PAMR can divide a domain of grid points Ω with boundary $\partial\Omega$ into a specified number of subdomains Ω_1, Ω_2,... Ω_s with respective boundaries $\partial\Omega_1$, $\partial\Omega_2$,... $\partial\Omega_s$. Using this option for *domain decomposition*, PAMR assigns the subdomains in a manner that contain, as closely as possible, equal volumes of grid points with minimal area.[13] In the case where $s > 1$, PAMR attaches ghost regions of specified width to the interior subdomain grid boundaries. These *ghost regions* allow points within adjacent grids to maintain their couplings. For example, assuming the range of index i for coordinate r_i on Ω is $1 \leq i \leq J$, the centered three-point finite difference stencil for FDA

$$\left(u^n_{i,j}\right)_{,rr} = \frac{u^n_{i+1,j} - u^n_{i,j} + u^n_{i-1,j}}{\left(\Delta r\right)^2} \tag{C.96}$$

requires addition of a single grid point in the direction parallel to coordinate r_i for each subdomain boundary having $2 \leq i \leq J - 1$. An example grid decomposition is displayed in Figure C.9. Then, after being supplied with a modest set of additional information, PAMR can be used to compile a code for use on a set of s compute nodes, each subdomain being uniquely assigned to one of these nodes.[14]

Providing the program is not partitioned between so many nodes that inter-node communication becomes an execution bottleneck, considerable increase in performance can be obtained with a code parallelized as above. This concludes discussion of numerical methodology as it pertains to the work present in this dissertation.

[13]For AMR codes, PAMR can either partition each grid of each level into s subgrids and distribute them among the s compute nodes, or partition the set of all grids into s subgrids for distribution across the s nodes. The efficiency of either option will depend on the complete grid structure at a given time.

[14]Note that while PAMR uses domain decomposition, an alternate division is *functional decomposition* where the objective is to equally partition the work among nodes based on the cost of each function within the program.

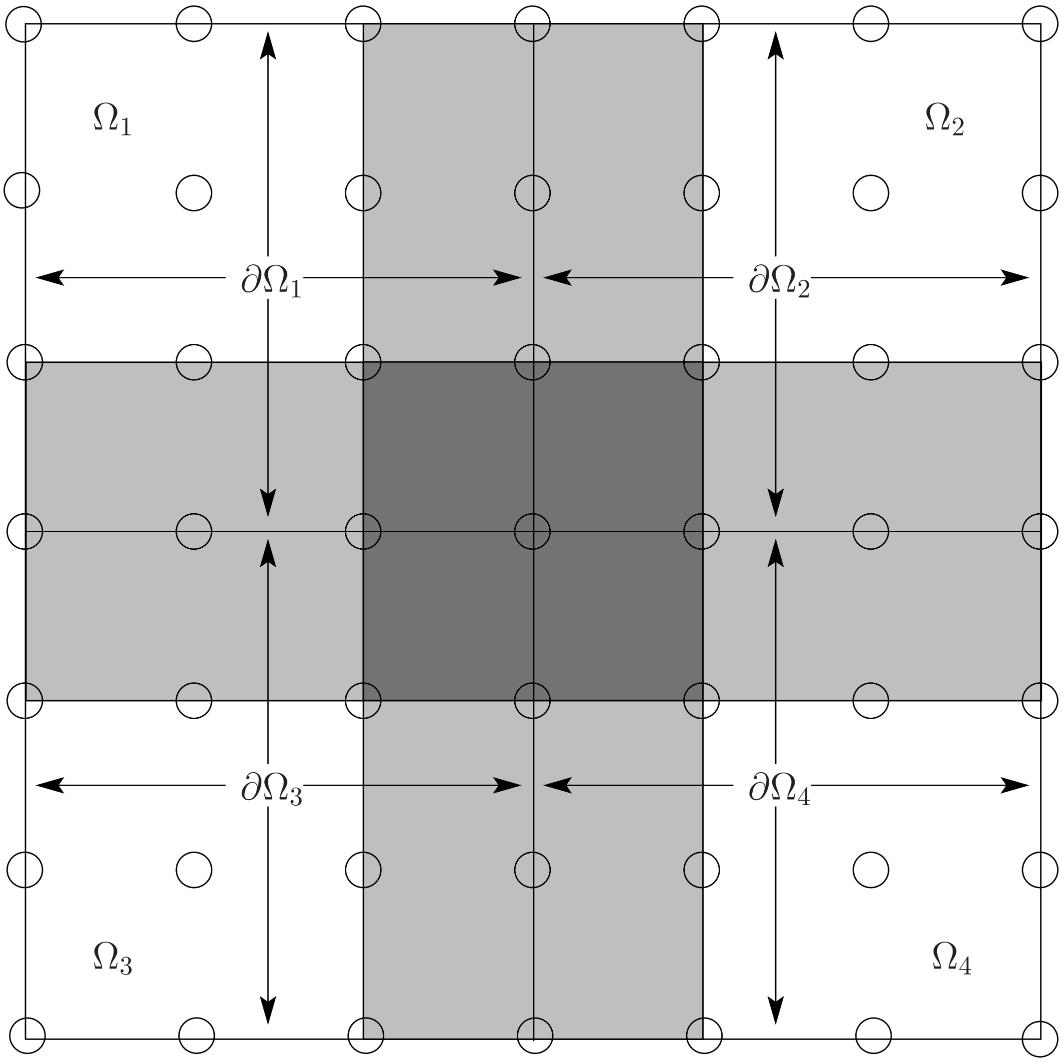

Figure C.9: Schematic representation of domain decomposition. The global domain Ω is divided into four subdomains Ω_1, Ω_2, Ω_3 and Ω_4. The boundaries $\partial\Omega_1$ $\partial\Omega_2$ $\partial\Omega_3$ $\partial\Omega_4$ are indicated with arrows. Ghost regions of a single grid point have been added to interior subdomain boundaries. Regions where two subdomains overlap is shaded light grey, and regions where four subdomains overlap is dark grey. Each of the subdomains contains an equal number of grid points, and is of minimal area.

APPENDIX D

MIB COORDINATES

D.1 The Monotonically Increasingly Boosted (MIB) Coordinate System

In this section I study boundary conditions for the massive electromagnetically coupled complex scalar field in flat axial symmetry. Again I employ the metric signature $(-,+,+,+)$ in accordance with Hawking and Ellis [62] and Wald [145]. Ultimately, to study a long numerical evolution of the electromagnetically coupled complex scalar field system on a finite coordinate domain, I must properly impose conditions on the computational outer boundary. Many techniques have been tried by others, but the most effective numerical treatment of the outer boundary on a finite computational domain perhaps is through the use of numerical dissipation in conjunction with the *Monotonically Increasingly Boosted* (MIB) coordinate system first introduced by Honda [77], and later published in [78]. The MIB coordinate system leaves the interior of the computational grid unchanged, but outwardly boosts the coordinates of points in an exterior region to approximately the speed of light with respect to the interior. While the MIB coordinates work to effectively freeze any radiation, numerical dissipation of the Kreiss-Oliger style can be added to quench this radiation. The problem of solution contamination by reflections off an outer boundary is thereby eliminated.

The Minkowski metric in the usual $\left(\tilde{t},\tilde{\rho},\tilde{\phi},\tilde{z}\right)$ cylindrical coordinate system is summarized by

$$ds^2 = -d\tilde{t}^2 + d\tilde{\rho}^2 + \tilde{\rho}^2 d\tilde{\phi}^2 + d\tilde{z}^2 \ . \tag{D.1}$$

The axially symmetric MIB coordinate transformations employed in [77] and [78] are

$$\tilde{t} = t \ , \ \tilde{\rho} = \rho + f(\rho)t \ , \ \tilde{\phi} = \phi \ , \ \tilde{z} = z + g(z)t \ , \tag{D.2}$$

where $f(\rho)$ is a monotonic function that interpolates between approximately 0 and 1 near a characteristic cutoff ρ_c, and $g(z)$ is a monotonic function that interpolates between approximately 0 and 1 near characteristic cutoff z_c and between approximately 0 and -1 near characteristic cutoff $-z_c$. That is,

$$f(\rho) \simeq \begin{Bmatrix} 0 & \text{for} & \rho \ll \rho_c \\ 1 & \text{for} & \rho \gg \rho_c \end{Bmatrix} \tag{D.3}$$

and

$$g(z) \simeq \begin{Bmatrix} -1 & \text{for} & z \ll -z_c \\ 0 & \text{for} & -z_c < z < z_c \\ 1 & \text{for} & z \gg z_c \end{Bmatrix} \ . \tag{D.4}$$

In these MIB coordinates the metric becomes

$$\begin{aligned} ds^2 &= (-1 + f(\rho)^2 + g(z)^2)dt^2 \\ &\quad +2f(\rho)(1 + \partial_\rho f(\rho)t)dtd\rho \\ &\quad +2g(z)(1 + \partial_z g(z)t)dtdz \\ &\quad +(1 + \partial_\rho f(\rho)t)^2 d\rho^2 \\ &\quad +(\rho + f(\rho)t)^2 d\phi^2 \\ &\quad +(1 + \partial_z g(z)t)^2 dz^2 \ , \end{aligned} \tag{D.5}$$

or, in the language of the $3+1$ formalism,

$$\begin{aligned} ds^2 &= (-\alpha^2 + \gamma_{\rho\rho}^2 \beta^{\rho 2} + \gamma_{zz}^2 \beta^{z2})dt^2 \\ &\quad +2\gamma_{\rho\rho}^2 \beta^\rho dtd\rho \\ &\quad +2\gamma_{zz}^2 \beta^z dtdz \\ &\quad +\gamma_{\rho\rho}^2 d\rho^2 \\ &\quad +\gamma_{\phi\phi}^2 d\phi^2 \\ &\quad +\gamma_{zz}^2 dz^2 \ , \end{aligned} \tag{D.6}$$

where

$$\begin{aligned} \alpha(t,\rho) &= 1 \ , & \beta^\rho(t,\rho) &= \frac{f(\rho)}{1 + \partial_\rho f(\rho)t} \ , \\ \beta^z(t,z) &= \frac{g(z)}{1 + \partial_z g(z)t} \ , & \gamma_{\rho\rho}(t,\rho) &= 1 + \partial_\rho f(\rho)t \ , \\ \gamma_{\phi\phi}(t,\rho) &= \rho + f(\rho)t \ , & \gamma_{zz}(t,z) &= 1 + \partial_z g(z)t \ . \end{aligned} \tag{D.7}$$

The unit-norm vector to spacelike hypersurfaces is

$$n^a = (1, -\beta^\rho, 0, -\beta^z) \ , \tag{D.8}$$

and the spatial metric is described by the hypersurface line element

$$d\sigma^2 = \gamma_{\rho\rho}^2 d\rho^2 + \gamma_{\phi\phi}^2 d\phi^2 + \gamma_{zz}^2 dz^2 \ . \tag{D.9}$$

The timelike Killing vector field of Minkowski spacetime is now $t^a = n^a$, $s_\phi^a = (0,0,1,0)$ is the axial Killing vector field, and $s_z^a = \left(0,0,0,\gamma_{zz}^{-1}\right)$ is the spacelike Killing vector field in the direction of coordinate z. Furthermore, I make use of the same interpolating functions as in [77] and [78],

$$f(\rho) = \frac{[1 + \tanh((\rho - \rho_c)/\delta_\rho)]}{2} - \frac{[1 + \tanh((-\rho_c)/\delta_\rho)]}{2} \ , \tag{D.10}$$

$$g(z) = \frac{\tanh((z - z_c)/\delta_z)}{2} + \frac{\tanh((z + z_c)/\delta_z)}{2} \ , \tag{D.11}$$

where parameters δ_ρ and δ_z set the length scales over which interpolation takes place. The interpolating functions $f(\rho)$ and $g(z)$ for this system are displayed in Figure D.1 and Figure D.2 respectively.

Clearly, the radially outgoing and ingoing null geodesics along $z = 0$ for spacetime metric (D.6)

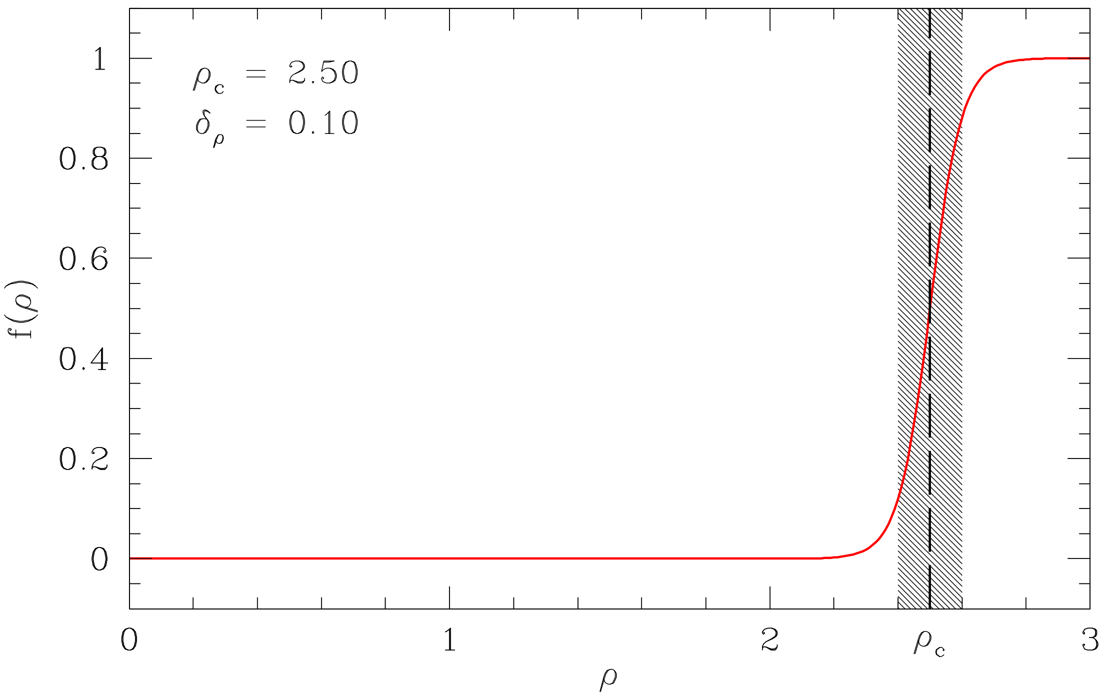

Figure D.1: MIB interpolating function $f(\rho)$. The shaded region represents $\rho_c \pm \delta_\rho$.

are given by

$$\lambda^{\rho}_{\pm}(t,\rho) = -\beta^{\rho} \pm \frac{\alpha}{\gamma_{\rho\rho}} \ , \tag{D.12}$$

while the axially outgoing and ingoing null geodesics along $\rho = 0$ are given by

$$\lambda^{z}_{\pm}(t,\rho) = -\beta^{z} \pm \frac{\alpha}{\gamma_{zz}} \ . \tag{D.13}$$

The null geodesics with $f(\rho)$ and $g(z)$ given by (D.10) and (D.11) are displayed in Figure D.3 through Figure D.6 below. Observe that, as desired,

$$\lambda^{\rho}_{\pm}(t,\rho) \simeq \begin{Bmatrix} \pm 1 & \text{for} & \rho \ll \rho_c \\ 0 & \text{for} & \rho \simeq \rho_c \end{Bmatrix} \ , \tag{D.14}$$

and

$$\lambda^{z}_{\pm}(t,\rho) \simeq \begin{Bmatrix} 0 & \text{for} & z \simeq -z_c \\ \pm 1 & \text{for} & -z_c < z < z_c \\ 0 & \text{for} & z \simeq z_c \end{Bmatrix} \ . \tag{D.15}$$

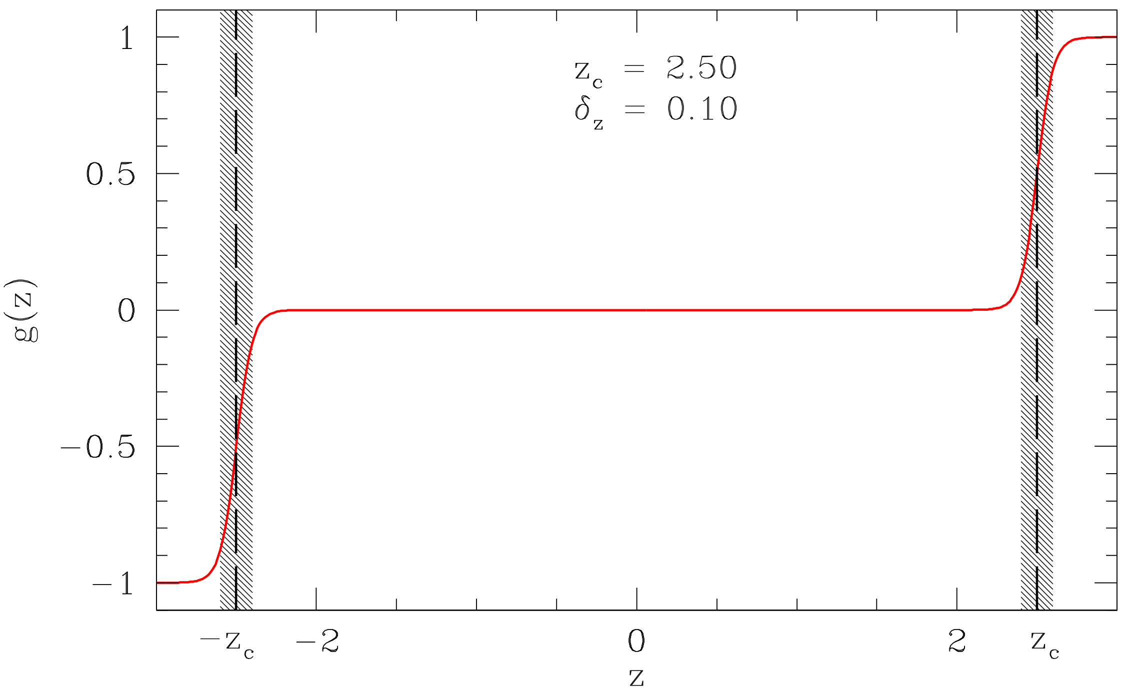

Figure D.2: MIB interpolating function $g(z)$. The shaded regions represent $z_c \pm \delta_z$ and $-z_c \pm \delta_z$.

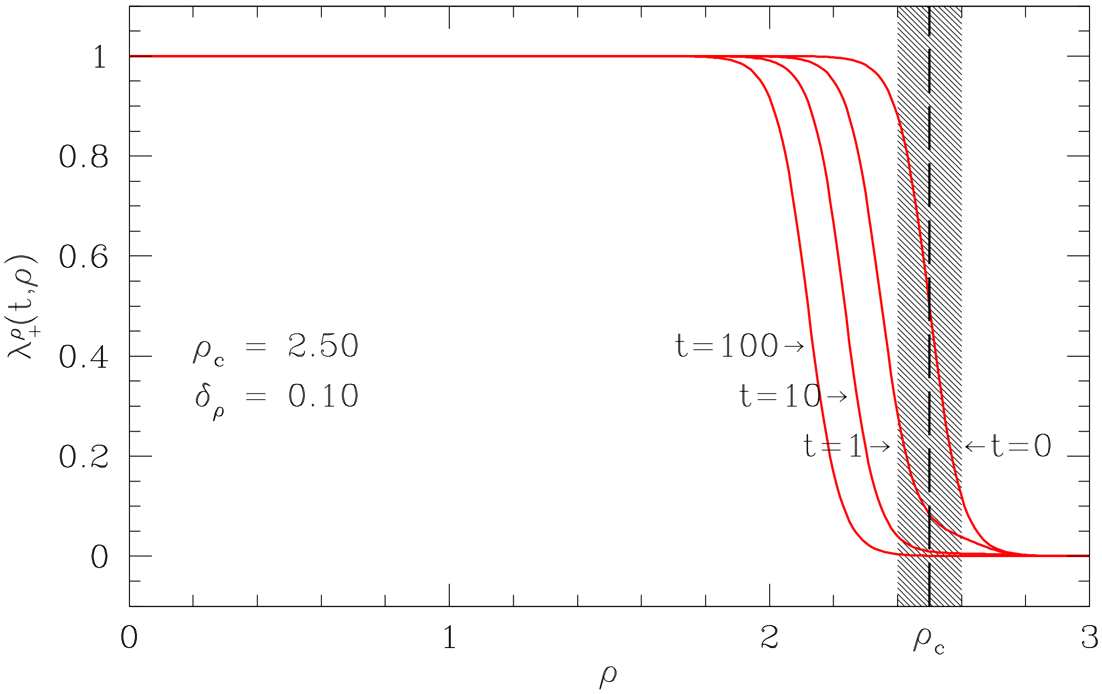

Figure D.3: Radially outgoing geodesic $\lambda_+^\rho(t,\rho)$ in the MIB coordinates at times $t = 0$, $t = 1$, $t = 10$, and $t = 100$. The shaded region represents $\rho_c \pm \delta_\rho$.

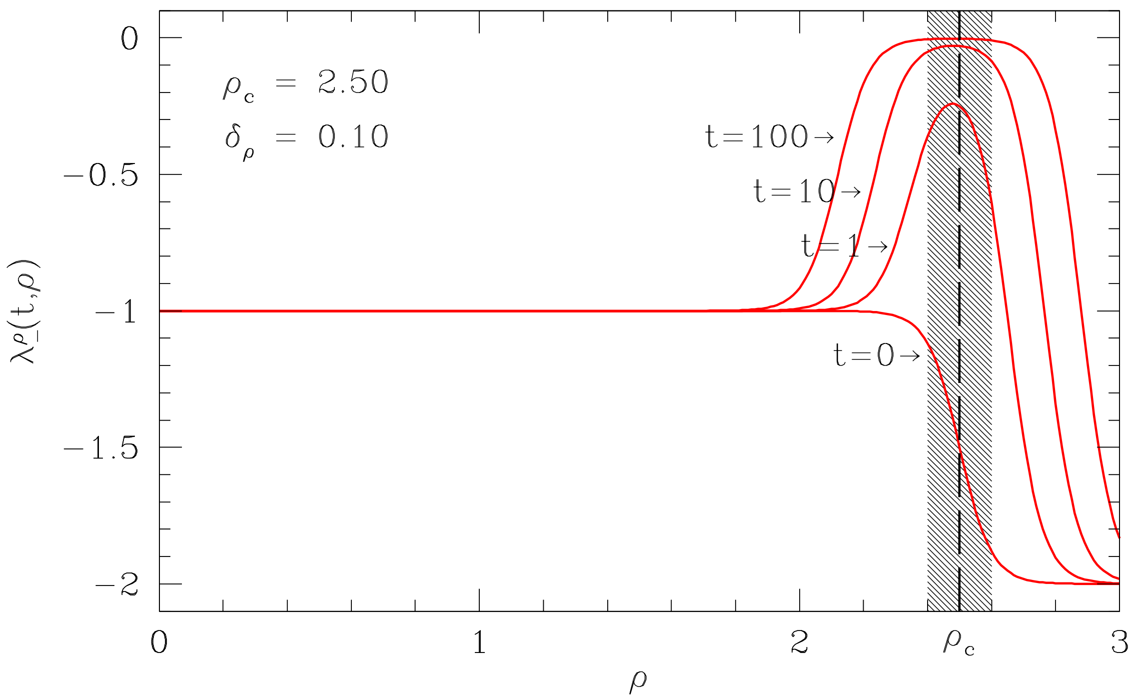

Figure D.4: Radially ingoing geodesic $\lambda^\rho_-(t,\rho)$ in the MIB coordinates at times $t = 0$, $t = 1$, $t = 10$, and $t = 100$. The shaded region represents $\rho_c \pm \delta_\rho$.

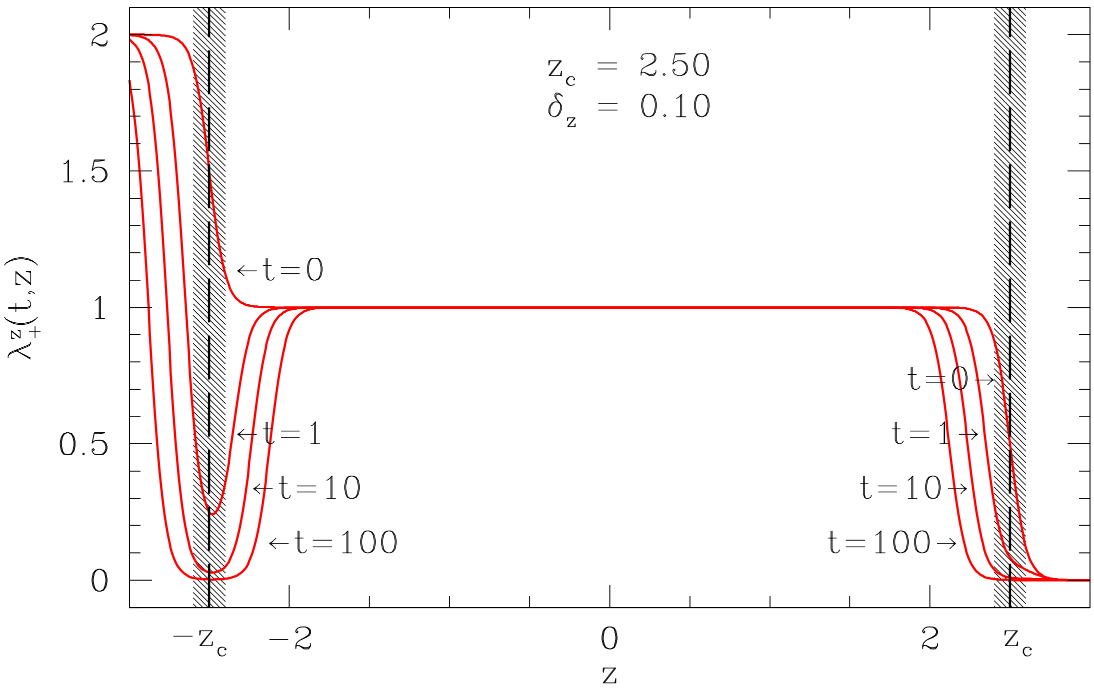

Figure D.5: Axially outgoing geodesic $\lambda^z_+(t,z)$ in the MIB coordinates at times $t = 0$, $t = 1$, $t = 10$, and $t = 100$. Shaded regions represent $z_c \pm \delta_z$ and $-z_c \pm \delta_z$.

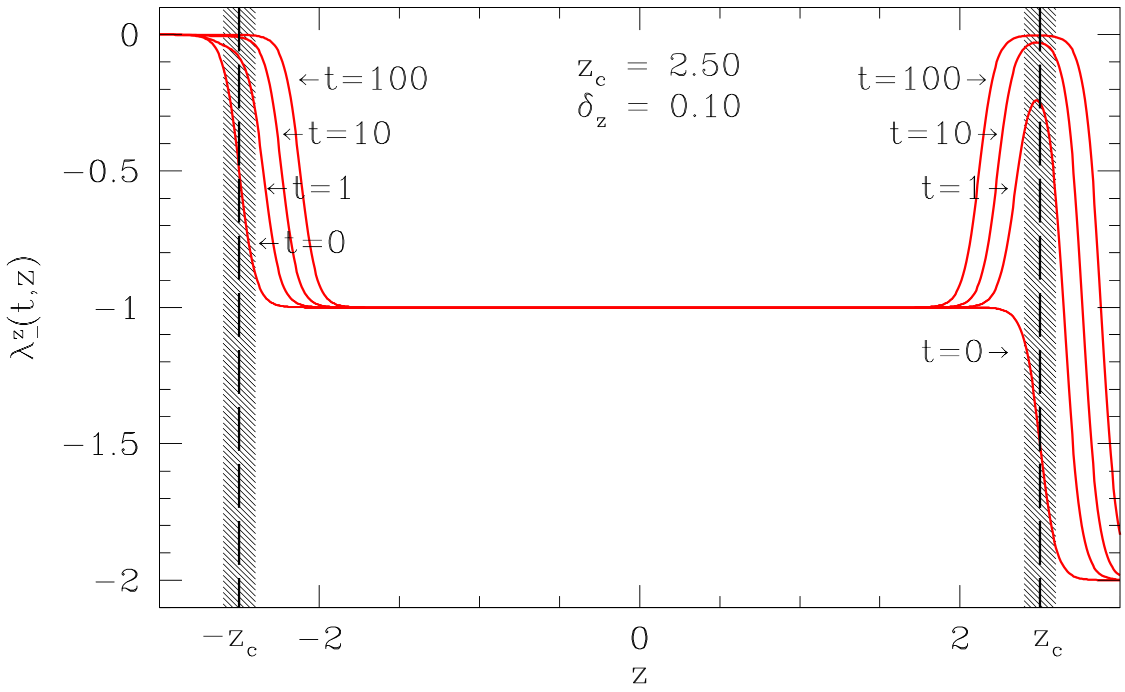

Figure D.6: Axially ingoing geodesic $\lambda^z_-(t,z)$ in the MIB coordinates at times $t = 0$, $t = 1$, $t = 10$, and $t = 100$. Shaded regions represent $z_c \pm \delta_z$ and $-z_c \pm \delta_z$.

D.2 Equations of Motion

The system described by Lagrangian

$$\mathcal{L}_{\mathcal{M}} = \sqrt{-g}[-(\nabla_a\Phi - ieA_a\Phi)(\nabla^a\Phi^* + ieA^a\Phi^*) - \frac{1}{4}F^{ab}F_{ab} - m_\Phi{}^2\Phi^*\Phi] \ , \tag{D.16}$$

yields equations of motion

$$\nabla^a\left(\nabla_a\Phi - ieA_a\Phi\right) - ieA^a\left(\nabla_a\Phi - ieA_a\Phi\right) - m_\Phi{}^2\Phi = 0 \tag{D.17}$$

for complex scalar field $\Phi = \Phi(t,\rho,z)$ (i.e., $\Phi = \phi_1 + i\phi_2$, where $\phi_1 = \phi_1(t,\rho,z)$ and $\phi_2 = \phi_2(t,\rho,z)$), and evolutionary equations

$$\nabla^a F_{ab} - ie(\Phi^*\nabla_b\Phi - \Phi\nabla_b\Phi^*) - 2e^2\Phi\Phi^*A_b = 0 \tag{D.18}$$

for four-vector potential $A_a = A_a(t,\rho,z)$. The Lorentz gauge condition

$$\nabla_a A^a = 0 \tag{D.19}$$

can be used to evolve the temporal component A_t. I continue to used the established notation where m_Φ is the scalar field mass parameter, e the electromagnetic coupling parameter, the symbol * denotes complex conjugation, and F_{ab} is the antisymmetric electromagnetic field strength tensor. Explicit calculation of (D.17), (D.18) and (D.19) for metric (D.5) obtains a fairly complicated set of expressions.

Defining auxiliary variables,

$$\Pi_\Phi(t,\rho,z) \equiv n^a\gamma_{\rho\rho}\gamma_{zz}\left(\nabla_a\Phi - ieA_a\Phi\right) \ , \tag{D.20}$$

$$\Phi_\rho(t,\rho,z) \equiv \partial_\rho\Phi \ , \tag{D.21}$$

$$\Phi_z(t,\rho,z) \equiv \partial_z\Phi \ , \tag{D.22}$$

and function

$$f_{\phi\phi}(t,\rho,z) \equiv \frac{\gamma_{\phi\phi}}{\rho} \ , \tag{D.23}$$

equation (D.17) can be recast in the first-order form[1]

$$\begin{aligned}\dot{\Pi}_\Phi \quad = \quad & 2\frac{1}{f_{\phi\phi}}\frac{\partial}{\partial(\rho^2)}\left[\gamma_{\phi\phi}\left(\beta^\rho\Pi_\Phi + \frac{\gamma_{zz}}{\gamma_{\rho\rho}}\left(\Phi_\rho - ieA_\rho\Phi\right)\right)\right] + \frac{\partial}{\partial z}\left(\beta^z\Pi_\Phi + \frac{\gamma_{\rho\rho}}{\gamma_{zz}}\left(\Phi_z - ieA_z\Phi\right)\right) \\ & -ie\left(\frac{\gamma_{zz}}{\gamma_{\rho\rho}}\left(\Phi_\rho - ieA_\rho\Phi\right)A_\rho + \frac{\gamma_{\rho\rho}}{\gamma_{zz}}\left(\Phi_z - ieA_z\Phi\right)A_z - \Pi_\Phi\left(A_t - \beta^\rho A_\rho - \beta^z A_z\right)\right. \\ & \left. -ie\frac{\gamma_{\rho\rho}\gamma_{zz}}{\gamma_{\phi\phi}^2}A_\phi^2\Phi\right) - \frac{\dot{\gamma}_{\phi\phi}}{\gamma_{\phi\phi}}\Pi_\Phi - \gamma_{\rho\rho}\gamma_{zz}m_\Phi^2\Phi \ ,\end{aligned} \tag{D.25}$$

$$\dot{\Phi}_\rho = \frac{\partial}{\partial\rho}\left(\frac{1}{\gamma_{\rho\rho}\gamma_{zz}}\Pi_\Phi + ieA_t\Phi + \beta^\rho\left(\Phi_\rho - ieA_\rho\Phi\right) + \beta^z\left(\Phi_z - ieA_z\Phi\right)\right) \ , \tag{D.26}$$

$$\dot{\Phi}_z = \frac{\partial}{\partial z}\left(\frac{1}{\gamma_{\rho\rho}\gamma_{zz}}\Pi_\Phi + ieA_t\Phi + \beta^\rho\left(\Phi_\rho - ieA_\rho\Phi\right) + \beta^z\left(\Phi_z - ieA_z\Phi\right)\right) \ , \tag{D.27}$$

[1] I use the chain rule

$$\frac{\partial}{\partial\rho} = 2\rho\frac{\partial}{\partial\left(\rho^2\right)} \tag{D.24}$$

to eliminate factors ρ^{-1} that would otherwise appear in expressions such as (D.25).

$$\dot{\Phi} = \frac{1}{\gamma_{\rho\rho}\gamma_{zz}}\Pi_\Phi + ieA_t\Phi + \beta^\rho\left(\Phi_\rho - ieA_\rho\Phi\right) + \beta^z\left(\Phi_z - ieA_z\Phi\right) \ , \tag{D.28}$$

where the overdot, $\dot{}$, again designates partial differentiation with respect to coordinate t. Similarly, defining

$$\begin{aligned}
\Pi_\rho(t,\rho,z) &\equiv n^a\gamma_{\rho\rho}\gamma_{zz}\left(\nabla_a A_\rho - \nabla_\rho A_a\right) \ , \\
\Pi_\phi(t,\rho,z) &\equiv n^a\gamma_{\rho\rho}\gamma_{zz}\left(\nabla_a A_\phi - \nabla_\phi A_a\right) \ , \\
\Pi_z(t,\rho,z) &\equiv n^a\gamma_{\rho\rho}\gamma_{zz}\left(\nabla_a A_z - \nabla_z A_a\right) \ ,
\end{aligned} \tag{D.29}$$

$$A_{t\rho}(t,\rho,z) \equiv \partial_\rho A_t \ , \tag{D.30}$$

$$A_{tz}(t,\rho,z) \equiv \partial_z A_t \ , \tag{D.31}$$

$$A_{\rho z}(t,\rho,z) \equiv \partial_z A_\rho \ , \tag{D.32}$$

$$A_{\phi\rho}(t,\rho,z) \equiv \partial_\rho A_\phi \ , \tag{D.33}$$

$$A_{\phi z}(t,\rho,z) \equiv \partial_z A_\phi \ , \tag{D.34}$$

$$A_{z\rho}(t,\rho,z) \equiv \partial_\rho A_z \ , \tag{D.35}$$

(D.18) can be rewritten

$$\begin{aligned}
\dot{\Pi}_\rho &= 2\frac{1}{f_{\phi\phi}}\frac{\partial}{\partial(\rho^2)}\left(\gamma_{\phi\phi}\beta^\rho\Pi_\rho\right) + \Pi_\rho\frac{\partial}{\partial\rho}\left(\beta^\rho\right) + \frac{\partial}{\partial z}\left(\beta^z\Pi_\rho + \frac{\gamma_{\rho\rho}}{\gamma_{zz}}\left(A_{\rho z} - A_{z\rho}\right)\right) - \frac{\dot{\gamma}_{\phi\phi}}{\gamma_{\phi\phi}}\Pi_\rho \\
&\quad + \gamma_{\rho\rho}\gamma_{zz}J_\rho \ ,
\end{aligned} \tag{D.36}$$

$$\dot{A}_{\rho z} = \frac{\partial}{\partial z}\left(\frac{1}{\gamma_{\rho\rho}\gamma_{zz}}\Pi_\rho + A_{t\rho} - \beta^z\left(A_{z\rho} - A_{\rho z}\right)\right) \ , \tag{D.37}$$

$$\dot{A}_\rho = \frac{1}{\gamma_{\rho\rho}\gamma_{zz}}\Pi_\rho + A_{t\rho} - \beta^z\left(A_{z\rho} - A_{\rho z}\right) \ , \tag{D.38}$$

$$\begin{aligned}
\dot{\Pi}_\phi &= -2\frac{\gamma_{zz}}{\gamma_{\rho\rho}f_{\phi\phi}}A_{\phi\rho}\frac{\partial}{\partial\left(\rho^2\right)}\left(\gamma_{\phi\phi}\right) + \gamma_{\phi\phi}\frac{\partial}{\partial\rho}\left(\frac{1}{\gamma_{\phi\phi}}\beta^\rho\Pi_\phi\right) + \gamma_{zz}\frac{\partial}{\partial\rho}\left(\frac{1}{\gamma_{\rho\rho}}A_{\phi\rho}\right) + \frac{\partial}{\partial z}\left(\beta^z\Pi_\phi\cdot\right. \\
&\quad \left. + \frac{\gamma_{\rho\rho}}{\gamma_{zz}}A_{\phi z}\right) + \frac{\dot{\gamma}_{\phi\phi}}{\gamma_{\phi\phi}}\Pi_\phi + \gamma_{\rho\rho}\gamma_{zz}J_\phi \ ,
\end{aligned} \tag{D.39}$$

$$\dot{A}_{\phi\rho} = \frac{\partial}{\partial\rho}\left(\frac{1}{\gamma_{\rho\rho}\gamma_{zz}}\Pi_\phi + \beta^\rho A_{\phi\rho} + \beta^z A_{\phi z}\right) \ , \tag{D.40}$$

$$\dot{A}_{\phi z} = \frac{\partial}{\partial z}\left(\frac{1}{\gamma_{\rho\rho}\gamma_{zz}}\Pi_\phi + \beta^\rho A_{\phi\rho} + \beta^z A_{\phi z}\right) \ , \tag{D.41}$$

$$\dot{A}_\phi = \frac{1}{\gamma_{\rho\rho}\gamma_{zz}}\Pi_\phi + \beta^\rho A_{\phi\rho} + \beta^z A_{\phi z} \ , \tag{D.42}$$

$$\begin{aligned}
\dot{\Pi}_z &= 2\frac{1}{f_{\phi\phi}}\frac{\partial}{\partial(\rho^2)}\left[\gamma_{\phi\phi}\left(\beta^\rho\Pi_z + \frac{\gamma_{zz}}{\gamma_{\rho\rho}}\left(A_{z\rho} - A_{\rho z}\right)\right)\right] + \frac{\partial}{\partial z}\left(\beta^z\Pi_z\right) + \Pi_z\frac{\partial}{\partial z}\left(\beta^z\right) - \frac{\dot{\gamma}_{\phi\phi}}{\gamma_{\phi\phi}}\Pi_z \\
&\quad + \gamma_{\rho\rho}\gamma_{zz}J_z \ ,
\end{aligned} \tag{D.43}$$

$$\dot{A}_{z\rho} = \frac{\partial}{\partial\rho}\left(\frac{1}{\gamma_{\rho\rho}\gamma_{zz}}\Pi_z + A_{tz} - \beta^\rho\left(A_{\rho z} - A_{z\rho}\right)\right) , \tag{D.44}$$

$$\dot{A}_{z} = \frac{1}{\gamma_{\rho\rho}\gamma_{zz}}\Pi_z + A_{tz} - \beta^\rho\left(A_{\rho z} - A_{z\rho}\right) , \tag{D.45}$$

where the conserved four-current, again defined

$$-J_a \equiv ie(\Phi^*\nabla_a\Phi - \Phi\nabla_a\Phi^*) + 2e^2\Phi\Phi^* A_a , \tag{D.46}$$

has spatial components

$$J_\rho = -ie(\Phi^*\Phi_\rho - \Phi\Phi^*_\rho) - 2e^2\Phi\Phi^* A_\rho , \tag{D.47}$$

$$J_\phi = -2e^2\Phi\Phi^* A_\phi , \tag{D.48}$$

$$J_z = -ie(\Phi^*\Phi_z - \Phi\Phi^*_z) - 2e^2\Phi\Phi^* A_z . \tag{D.49}$$

While (D.36), (D.39), (D.43) provide the equations of evolution of the spatial components of A_a, the value of A_t at future time can be obtained either by solving the electromagnetic constraint, or by solving the Lorentz gauge condition. Defining

$$\Omega_t(t,\rho,z) \equiv n^a\gamma_{\rho\rho}\gamma_{zz}A_a , \tag{D.50}$$

the Lorentz gauge condition can be recast as

$$\dot{\Omega}_t = 2\frac{1}{f_{\phi\phi}}\frac{\partial}{\partial(\rho^2)}\left(\gamma_{\phi\phi}\left(\beta^\rho\Omega_t + \frac{\gamma_{zz}}{\gamma_{\rho\rho}}A_\rho\right)\right) + \frac{\partial}{\partial z}\left(\beta^z\Omega_t + \frac{\gamma_{\rho\rho}}{\gamma_{zz}}A_z\right) - \frac{\dot{\gamma}_{\phi\phi}}{\gamma_{\phi\phi}}\Omega_t , \tag{D.51}$$

$$A_{t\rho} = \frac{\partial}{\partial\rho}\left(\frac{1}{\gamma_{\rho\rho}\gamma_{zz}}\Omega_t + \beta^\rho A_\rho + \beta^z A_z\right) , \tag{D.52}$$

$$A_{tz} = \frac{\partial}{\partial z}\left(\frac{1}{\gamma_{\rho\rho}\gamma_{zz}}\Omega_t + \beta^\rho A_\rho + \beta^z A_z\right) , \tag{D.53}$$

$$A_t = \frac{1}{\gamma_{\rho\rho}\gamma_{zz}}\Omega_t + \beta^\rho A_\rho + \beta^z A_z . \tag{D.54}$$

D.2.1 Physical and Conserved Quantities

While the preceding equations of motion have been written in terms of the four-vector potential A^a, the physical fields are themselves the electric field E_a and the magnetic field B_a. For an observer moving with four-velocity n^a, the measured electric field components are

$$E_\rho = -\frac{1}{\gamma_{\rho\rho}\gamma_{zz}}\Pi_\rho , \tag{D.55}$$

$$E_\phi = -\frac{1}{\gamma_{\rho\rho}\gamma_{zz}}\Pi_\phi , \tag{D.56}$$

$$E_z = -\frac{1}{\gamma_{\rho\rho}\gamma_{zz}}\Pi_z , \tag{D.57}$$

while the observed magnetic field is

$$B_\rho = -\frac{\gamma_{\rho\rho}}{\gamma_{\phi\phi}\gamma_{zz}} A_{\phi z} , \tag{D.58}$$

$$B_\phi = \frac{\gamma_{\phi\phi}}{\gamma_{\rho\rho}\gamma_{zz}} \left(A_{\rho z} - A_{z\rho}\right) , \tag{D.59}$$

$$B_z = \frac{\gamma_{zz}}{\gamma_{\rho\rho}\gamma_{\phi\phi}} A_{\phi\rho} . \tag{D.60}$$

The temporal component of the current four-vector is

$$\begin{aligned} J_t &= -ie\left(-\frac{1}{\gamma_{\rho\rho}\gamma_{zz}}\left(\Phi^*\Pi_\Phi - \Phi\Pi_\Phi^*\right) + \beta^\rho\left(\Phi^*\Phi_\rho - \Phi\Phi_\rho^*\right) + \beta^z\left(\Phi^*\Phi_z - \Phi\Phi_z^*\right)\right) \\ &\quad -2e^2\left(\beta^\rho\Phi\Phi^* A_\rho + \beta^z\Phi\Phi^* A_z\right) , \end{aligned} \tag{D.61}$$

and the observed charge density is

$$\rho_Q = -ie\frac{1}{\gamma_{\rho\rho}\gamma_{zz}}\left(\Phi^*\Pi_\Phi - \Phi\Pi_\Phi^*\right) . \tag{D.62}$$

The stress-energy tensor for the system described by (D.16) is

$$\begin{aligned} T_{ab} &= \frac{1}{2}\left(\nabla_a\Phi\nabla_b\Phi^* + \nabla_b\Phi\nabla_a\Phi^*\right) - \frac{1}{2}ie\left[\left(\Phi\nabla_b\Phi^* - \Phi^*\nabla_b\Phi\right)A_a + \left(\Phi\nabla_a\Phi^* - \Phi^*\nabla_a\Phi\right)A_b\right] \\ &\quad +e^2\Phi\Phi^* A_a A_b + \frac{1}{2}F_{ac}F_{bd}g^{cd} - \frac{1}{2}g_{ab}[(\nabla_c\Phi - ieA_c\Phi)(\nabla^c\Phi^* + ieA^c\Phi^*) + \frac{1}{4}F^{cd}F_{cd} \\ &\quad +m_\Phi^2\Phi^*\Phi] . \end{aligned} \tag{D.63}$$

Contracting T_{ab} with $n^a = (1, -\beta^\rho, 0, -\beta^z)$ and $t^a = n^a$ yields the conserved energy density

$$\rho_T = \rho_{T(\Phi)} + \rho_{T(A)} + \rho_{T(\Phi A)} , \tag{D.64}$$

$\rho_{T(\Phi)}$ being the contribution from scalar field terms, $\rho_{T(A)}$ the contribution from electromagnetic field variable terms, and $\rho_{T(\Phi A)}$ being the contribution from terms involving the electromagnetic interaction of Φ and A_a. Explicitly,

$$\begin{aligned} \rho_{T(\Phi)} &= e^2\left(\frac{1}{2}\left(\beta^\rho\right)^2 A_\rho^2 + \beta^\rho\beta^z A_\rho A_z - \beta^\rho A_\rho A_t + \frac{1}{2}\left(\beta^z\right)^2 A_z^2 - \beta^z A_z A_t + \frac{1}{2}A_t^2\right)\Phi\Phi^* \\ &\quad - \frac{ie}{2}\frac{1}{\gamma_{\rho\rho}\gamma_{zz}}\left(\beta^\rho A_\rho + \beta^z A_z - A_t\right)\left(\Phi\Pi_\Phi^* - \Phi^*\Pi_\Phi\right) + \frac{1}{2}m_\Phi^2\Phi\Phi^* + \frac{1}{2}\frac{1}{\gamma_{\rho\rho}^2}\Phi_\rho\Phi_\rho^* \\ &\quad + \frac{1}{2}\frac{1}{\gamma_{zz}^2}\Phi_z\Phi_z^* + \frac{1}{2}\frac{1}{\gamma_{\rho\rho}^2\gamma_{zz}^2}\Pi_\Phi\Pi_\Phi^* , \end{aligned} \tag{D.65}$$

$$\begin{aligned} \rho_{T(A)} &= \frac{1}{4}\frac{1}{\gamma_{\rho\rho}^2\gamma_{zz}^2}A_{\rho z}^2 - \frac{1}{2}\frac{1}{\gamma_{\rho\rho}^2\gamma_{zz}^2}A_{\rho z}A_{z\rho} + \frac{1}{4}\frac{1}{\gamma_{\rho\rho}^2\gamma_{\phi\phi}^2}A_{\phi\rho}^2 + \frac{1}{4}\frac{1}{\gamma_{\phi\phi}^2\gamma_{zz}^2}A_{\phi z}^2 + \frac{1}{4}\frac{1}{\gamma_{\rho\rho}^2\gamma_{zz}^2}A_{z\rho}^2 \\ &\quad + \frac{1}{4}\frac{1}{\gamma_{\rho\rho}^4\gamma_{zz}^2}\Pi_\rho^2 + \frac{1}{4}\frac{1}{\gamma_{\rho\rho}^2\gamma_{\phi\phi}^2\gamma_{zz}^2}\Pi_\phi^2 + \frac{1}{4}\frac{1}{\gamma_{\rho\rho}^2\gamma_{zz}^4}\Pi_z^2 , \end{aligned} \tag{D.66}$$

and

$$\begin{aligned}\rho_{T(\Phi A)} \;=\;& e^2\left[\frac{1}{2}\left(\frac{1}{\gamma_{\rho\rho}^2}-(\beta^\rho)^2\right)A_\rho^2-\beta^\rho\beta^z A_\rho A_z+\beta^\rho A_\rho A_t+\frac{1}{2}\frac{1}{\gamma_{\phi\phi}^2}A_\phi^2+\frac{1}{2}\left(\frac{1}{\gamma_{zz}^2}-(\beta^z)^2\right)A_z^2\right.\\ &\left.+\beta^z A_z A_t-\frac{1}{2}A_t^2\right]\Phi\Phi^*-\frac{ie}{2}\left(\frac{A_\rho}{\gamma_{\rho\rho}^2}(\Phi\Phi_\rho^*-\Phi^*\Phi_\rho)+\frac{A_z}{\gamma_{zz}^2}(\Phi\Phi_z^*-\Phi^*\Phi_z)\right.\\ &\left.-\frac{1}{\gamma_{\rho\rho}\gamma_{zz}}\left(\beta^\rho A_\rho+\beta^z A_z-A_t\right)\left(\Phi\Pi_\Phi^*-\Phi^*\Pi_\Phi\right)\right)\ . \end{aligned}\tag{D.67}$$

Similarly, contracting T_{ab} with n^a and $s_\phi^a=(0,0,1,0)$ yields the conserved angular momentum density

$$\rho_{S\phi}=\rho_{S\phi(A)}+\rho_{S\phi(\Phi A)}\ ,\tag{D.68}$$

where

$$\rho_{S\phi(A)}=-\frac{1}{2}\frac{1}{\gamma_{\rho\rho}^3\gamma_{zz}}A_{\phi\rho}\Pi_\rho-\frac{1}{2}\frac{1}{\gamma_{\rho\rho}\gamma_{zz}^3}A_{\phi z}\Pi_z\tag{D.69}$$

is the electromagnetic field contribution, and

$$\rho_{S\phi(\Phi A)}=-\frac{ie}{2}\frac{A_\phi}{\gamma_{\rho\rho}\gamma_{zz}}(\Phi\Pi_\Phi^*-\Phi^*\Pi_\Phi)\tag{D.70}$$

is from the coupling of scalar and electromagnetic fields. Finally, contracting T_{ab} with n^a and $s_z^a=(0,0,0,\gamma_{zz}^{-1})$ yields the conserved momentum density in the direction of coordinate z,

$$\rho_{Sz}=\rho_{Sz(\Phi)}+\rho_{Sz(A)}+\rho_{Sz(\Phi A)}\ ,\tag{D.71}$$

where

$$\rho_{Sz(\Phi)}=-\frac{ie}{2}\frac{1}{\gamma_{zz}}\left(\beta^\rho A_\rho+\beta^z A_z-A_t\right)\left(\Phi\Phi_z^*-\Phi^*\Phi_z\right)+\frac{1}{2}\frac{1}{\gamma_{\rho\rho}\gamma_{zz}^2}\left(\Phi_z\Pi_\Phi^*+\Phi_z^*\Pi_\Phi\right)\ ,\tag{D.72}$$

$$\rho_{Sz(A)}=\frac{1}{2}\frac{1}{\gamma_{\rho\rho}^3\gamma_{zz}^2}(A_{\rho z}-A_{z\rho})\Pi_\rho+\frac{1}{2}\frac{1}{\gamma_{\rho\rho}\gamma_{\phi\phi}^2\gamma_{zz}^2}A_{\phi z}\Pi_\phi\ ,\tag{D.73}$$

and

$$\rho_{Sz(\Phi A)}=\frac{ie}{2}\left(\frac{1}{\gamma_{zz}}(\beta^\rho A_\rho+\beta^z A_z-A_t)(\Phi\Phi_z^*-\Phi^*\Phi_z)-\frac{A_z}{\gamma_{\rho\rho}\gamma_{zz}^2}(\Phi\Pi_\Phi^*-\Phi^*\Pi_\Phi)\right)\ .\tag{D.74}$$

From (2.104), the total charge

$$Q=\int_{z=-\infty}^{\infty}\int_{\phi=0}^{2\pi}\int_{\rho=0}^{\infty}\rho_Q\left(\gamma_{\rho\rho}\gamma_{\phi\phi}\gamma_{zz}\right)d\rho d\phi dz\ ,\tag{D.75}$$

from (2.108), the total energy

$$T=\int_{z=-\infty}^{\infty}\int_{\phi=0}^{2\pi}\int_{\rho=0}^{\infty}\rho_T\left(\gamma_{\rho\rho}\gamma_{\phi\phi}\gamma_{zz}\right)d\rho d\phi dz\ ,\tag{D.76}$$

and from (2.109), the total angular momentum

$$S_\phi = \int_{z=-\infty}^{\infty} \int_{\phi=0}^{2\pi} \int_{\rho=0}^{\infty} \rho_{S\phi} \left(\gamma_{\rho\rho}\gamma_{\phi\phi}\gamma_{zz}\right) d\rho d\phi dz \tag{D.77}$$

and total momentum in direction of coordinate z

$$S_z = \int_{z=-\infty}^{\infty} \int_{\phi=0}^{2\pi} \int_{\rho=0}^{\infty} \rho_{Sz} \left(\gamma_{\rho\rho}\gamma_{\phi\phi}\gamma_{zz}\right) d\rho d\phi dz \tag{D.78}$$

all will be constant.

D.2.2 Regularity, Boundary Conditions and Dissipation

From section 2.4 (cf. [6], [45]), regularity for the evolved functions requires Φ, Φ_z, Π_Φ, A_ϕ, $A_{\phi z}$, Π_ϕ, A_z, Π_z, J_z, A_t, A_{tz}, Ω_t, J_ϕ, E_ϕ, E_z, B_ϕ, B_z, J_t, ρ_Q, ρ_T, $\rho_{S\phi}$ and ρ_{Sz} be, to leading order, even in ρ on axis (i.e., along $\rho = 0$). Furthermore, A_ϕ, $A_{\phi z}$, Π_ϕ, J_ϕ, E_ϕ and B_ϕ must also vanish on the axis of symmetry (i.e., they are at least quadratic in ρ on axis). Meanwhile, remaining variables Φ_ρ, A_ρ, $A_{\rho z}$, Π_ρ, J_ρ, $A_{\phi\rho}$, $A_{z\rho}$, $A_{t\rho}$, E_ρ and B_ρ are on axis odd in ρ to leading order. For the leading-order-even variables, I enforce regularity on grid points corresponding to $\rho = 0$ by applying a quadratic fix as listed in Appendix C. Also, I apply interpolation in the direction of ρ on the next-to-axis points using a 3rd order Lagrange interpolant as discussed in Appendix C. The additional interpolation helps ensure smooth and stable evolution along $\rho = 0$. Variables A_ϕ, $A_{\phi z}$, Π_ϕ, J_ϕ, E_ϕ and B_ϕ are the exceptional cases. For them, I enforce regularity by setting their values equal to zero on axis and imposing a quadratic fix on the next-to-axis points. Meanwhile, regularity of the leading-order-odd variables is enforced by setting the functions equal to zero at $\rho = 0$. As with the leading-order-even variables, I apply interpolation on the next-to-axis grid points.

Because their counterparts in the massless electromagnetically uncoupled (i.e., $e = 0$) theory can be expressed as wave equations, I could always apply the (approximate) Sommerfeld outgoing radiation condition to Φ, A_ρ, A_ϕ, A_z and A_t. The condition would be applied on the outermost grid points. The Sommerfeld condition for Φ would provide an algebraic equation for boundary values of Π_Φ as well. Fields E_ρ, E_ϕ and E_z similarly can be rewritten as a set of wave equations. The Sommerfeld condition for the electric field components, in turn, could provide outer boundary conditions for Π_ρ, Π_ϕ and Π_z. Meanwhile, backwards difference operators could be applied, as appropriate, to Φ_ρ, Φ_z, $A_{\rho z}$, $A_{\phi\rho}$, $A_{\phi z}$, $A_{z\rho}$, $A_{t\rho}$ and A_{tz}, while variables J_ρ, J_ϕ, J_z, Ω_t, E_ρ, E_ϕ, E_z, B_ρ, B_ϕ, B_z, J_t, ρ_Q, ρ_T, $\rho_{S\phi}$ and ρ_{Sz} would require no special treatment.

However, by using the MIB coordinates in conjunction with Kreiss-Oliger dissipation, radiation will be quenched before it propagates from the interior of the domain to the computational outer boundary. Providing the boundary conditions are appropriate to the initial value problem, their details should therefore be irrelevant. Thus, I choose to fix the boundary values of all the grid functions to what they were at initial time. As numerical evolution demonstrates in following sections, even such static boundary conditions work well in the MIB coordinate approach.

Kreiss-Oliger dissipation is applied as discussed in Appendix C. It is added to all functions whose equations of motion explicitly involve partial derivatives with respect to temporal coordinate t. They are Φ, Φ_ρ, Φ_z, Π_Φ, A_ρ, $A_{\rho z}$, Π_ρ, A_ϕ, $A_{\phi\rho}$, $A_{\phi z}$, Π_ϕ, A_z, $A_{z\rho}$, Π_z and Ω_t. Dissipation in both coordinate directions r and θ is applied throughout the bulk of the computational domain, where at least two grid points distant from the boundaries $\rho = 0$, $\rho = \rho_{\max}$, $z = z_{\min}$ and $z = z_{\max}$. However, because the operator stencils are five points wide, dissipation in coordinate ρ alone is applied $z = z_{\min} + \Delta z$ and $z = z_{\max} - \Delta z$. Meanwhile, dissipation in coordinate z alone is applied at $\rho = \rho_{\max} - \Delta\rho$. Formally, if $u = u(t, \rho, z)$ is one of the functions whose equation contains an explicit derivative in time, then, using the Crank-Nicholson scheme without dissipation, its expression will be

$$\frac{u(t+\Delta t,\rho,z)-u(t,\rho,z)}{\Delta t}=\frac{1}{2}\left[R(t+\Delta t,\rho,z)+R(t,\rho,z)\right]\ , \tag{D.79}$$

where the left hand side is—to $\mathcal{O}\left((\Delta t)^2\right)$ accuracy—the time derivative of u centered between times t and $t+\Delta t$, and the right hand side represents—to $\mathcal{O}\left((\Delta\rho)^2\right)$ and $\mathcal{O}\left((\Delta z)^2\right)$—all other terms in the equation time averaged between steps t and $t+\Delta t$. Then, Kreiss-Oliger dissipation is implemented by adding specific terms on the right hand side of equation (D.79). In this case,

$$\begin{aligned}\frac{u(t+\Delta t,\rho,z)-u(t,\rho,z)}{\Delta t} &= \frac{1}{2}\left[R(t+\Delta t,\rho,z)+R(t,\rho,z)\right]\\ &+\frac{1}{2}\left[D_\rho(t+\Delta t,\rho,z)+D_\rho(t,\rho,z)\right]\\ &+\frac{1}{2}\left[D_z(t+\Delta t,\rho,z)+D_z(t,\rho,z)\right]\end{aligned} \tag{D.80}$$

when $2\Delta\rho\le\rho\le\rho_{\max}-2\Delta\rho$ and $z_{\min}+2\Delta z\le z\le z_{\max}-2\Delta z$,

$$\begin{aligned}\frac{u(t+\Delta t,\rho,z)-u(t,\rho,z)}{\Delta t} &= \frac{1}{2}\left[R(t+\Delta t,\rho,z)+R(t,\rho,z)\right]\\ &+\frac{1}{2}\left[D_\rho(t+\Delta t,\rho,z)+D_\rho(t,\rho,z)\right]\end{aligned} \tag{D.81}$$

when $2\Delta\rho\le\rho\le\rho_{\max}-2\Delta\rho$ and $z=z_{\min}+\Delta z$ or $z=z_{\max}-\Delta z$, and

$$\begin{aligned}\frac{u(t+\Delta t,\rho,z)-u(t,\rho,z)}{\Delta t} &= \frac{1}{2}\left[R(t+\Delta t,\rho,z)+R(t,\rho,z)\right]\\ &+\frac{1}{2}\left[D_z(t+\Delta t,\rho,z)+D_z(t,\rho,z)\right]\end{aligned} \tag{D.82}$$

when $z_{\min}+2\Delta z\le z\le z_{\max}-2\Delta z$ and $\rho=\rho_{\max}-\Delta\rho$, where

$$\begin{aligned}D_\rho(t,\rho,z) &= -\frac{\epsilon_\rho}{16\Delta t}\left[u(t,\rho+2\Delta\rho,z)-4u(t,\rho+\Delta\rho,z)+6u(t,\rho,z)\right.\\ &\left.-4u(t,\rho-\Delta\rho,z)+u(t,\rho-2\Delta\rho,z)\right]\ ,\end{aligned} \tag{D.83}$$

$$\begin{aligned}D_z(t,\rho,z) &= -\frac{\epsilon_\theta}{16\Delta t}\left[u(t,\rho,z+2\Delta z)-4u(t,\rho,z+\Delta z)+6u(t,\rho,z)\right.\\ &\left.-4u(t,\rho,z-\Delta z)+u(t,\rho,z-2\Delta z)\right]\ ,\end{aligned} \tag{D.84}$$

and $0\le\epsilon_\rho<1$ and $0\le\epsilon_z<1$ are adjustable parameters. I use values $\epsilon_\rho=0.5$ and $\epsilon_z=0.5$ for the adjustable dissipation parameters in directions ρ and z, respectively. Using a Courant factor

$$\lambda=\frac{\Delta t}{\sqrt{\frac{1}{2}\left((\Delta\rho)^2+(\Delta z)^2\right)}}\simeq 0.25\ , \tag{D.85}$$

this system of equations evolves stably under the Crank-Nicholson iterative solution scheme.

D.3 Results

D.3.1 Initial Data

Again, the initial value problem for the Maxwell-Klein-Gordon system in a spacetime background requires specification of all the variables in a manner consistent with regularity and gauge conditions, and satisfying the electromagnetic constraint equation

$$D^a E_a = \rho_Q \ , \tag{D.86}$$

where D^a is the spatial covariant derivative operator, and ρ_Q, is, according to equation (D.62),

$$\rho_Q = -ie\frac{1}{\gamma_{\rho\rho}\gamma_{zz}}\left(\Phi^*\Pi_\Phi - \Phi\Pi_\Phi^*\right) \ . \tag{D.87}$$

Following the procedure of section 2.2.1, I again decompose E_a into its longitudinal and transverse parts, respectively L_a and T_a, to obtain

$$E_a = L_a + T_a \ . \tag{D.88}$$

Then introducing the scalar potential, $U = U(r, \theta)$, as per

$$D_a U = L_a \ , \tag{D.89}$$

(D.86) becomes

$$D^a D_a U = D^a E_a = \rho_Q \ , \tag{D.90}$$

where the left hand side is explicitly

$$\begin{aligned} D^a D_a U \quad = \quad & \frac{1}{\gamma_{\rho\rho}^3\gamma_{zz}^3}\left[\frac{2}{f_{\phi\phi}}\gamma_{\rho\rho}\gamma_{zz}^3(\partial_{\rho^2}\gamma_{\phi\phi})(\partial_\rho U) - (\partial_\rho\gamma_{\rho\rho})\gamma_{zz}^3(\partial_\rho U) + \gamma_{\rho\rho}\gamma_{zz}^3(\partial_{\rho\rho}U)\right. \\ & \left. -\gamma_{\rho\rho}^3(\partial_z\gamma_{zz})(\partial_z U) + \gamma_{\rho\rho}^3\gamma_{zz}(\partial_{zz}U)\cdot\right] \end{aligned} \tag{D.91}$$

After solving (D.90) using the methods of Appendix C, I reconstruct the longitudinal electric field components, which are, from (D.89),

$$L_\rho = \partial_\rho U \ , \tag{D.92}$$
$$L_z = \partial_z U \ , \tag{D.93}$$
$$L_\phi = 0 \ . \tag{D.94}$$

I then specify divergenceless components for the transverse component T_a. For simplicity, I again choose

$$T_\rho = 0 \ , \tag{D.95}$$
$$T_z = 0 \ , \tag{D.96}$$
$$T_\phi = 0 \ . \tag{D.97}$$

The completely reconstructed electric field at initial time is therefore

$$E_\rho = \partial_\rho U \ , \tag{D.98}$$

$$E_z = \partial_z U \ , \tag{D.99}$$

$$E_\phi = 0 \ . \tag{D.100}$$

Having solved for E_a, I then initialize Π_ρ, Π_z and Π_ϕ in accordance with (D.55), (D.56) and (D.57), meaning

$$\Pi_\rho = -\gamma_{\rho\rho}\gamma_{zz}E_\rho \ , \tag{D.101}$$

$$\Pi_\phi = -\gamma_{\rho\rho}\gamma_{zz}E_\phi \ , \tag{D.102}$$

$$\Pi_z = -\gamma_{\rho\rho}\gamma_{zz}E_z \ . \tag{D.103}$$

Having satisfied the initial data constraint, I then freely specify the remaining variables in accordance with their definitions and regularity conditions. For simplicity I again choose Gaussian profiles for the complex components of $\Phi(t,\rho,z) = \phi_1(t,\rho,z)+i\phi_2(t,\rho,z)$, $\Pi_\Phi(t,\rho,z) = \Pi_1(t,\rho,z)+i\Pi_2(t,\rho,z)$, and the vector potential components $A_a(t,r,\theta)$.[2] That is,

$$\phi_1(0,\rho,z) = a_1 \exp\left(-((\rho-\rho_1)/\delta_{\rho 1})^2\right)\exp\left(-((z-z_1)/\delta_{z1})^2\right) \ , \tag{D.104}$$

$$\phi_2(0,\rho,z) = a_2 \exp\left(-((\rho-\rho_2)/\delta_{\rho 2})^2\right)\exp\left(-((z-z_2)/\delta_{z2})^2\right) \ , \tag{D.105}$$

$$\Pi_1(0,\rho,z) = a_3 \exp\left(-((\rho-\rho_3)/\delta_{\rho 3})^2\right)\exp\left(-((z-z_3)/\delta_{z3})^2\right) \ , \tag{D.106}$$

$$\Pi_2(0,\rho,z) = a_4 \exp\left(-((\rho-\rho_4)/\delta_{\rho 4})^2\right)\exp\left(-((z-z_4)/\delta_{z4})^2\right) \ , \tag{D.107}$$

$$A_t(0,\rho,z) = a_r \exp\left(-((\rho-\rho_t)/\delta_{\rho t})^2\right)\exp\left(-((z-z_t)/\delta_{zt})^2\right) \ , \tag{D.108}$$

$$A_r(0,\rho,z) = a_r \exp\left(-((\rho-\rho_\rho)/\delta_{\rho\rho})^2\right)\exp\left(-((z-z_\rho)/\delta_{z\rho})^2\right) \ , \tag{D.109}$$

$$A_\theta(0,\rho,z) = a_\theta \exp\left(-((\rho-\rho_z)/\delta_{\rho z})^2\right)\exp\left(-((z-z_z)/\delta_{zz})^2\right) \ , \tag{D.110}$$

$$A_\phi(0,\rho,z) = a_\phi \exp\left(-((\rho-\rho_\phi)/\delta_{\rho\phi})^2\right)\exp\left(-((z-z_\phi)/\delta_{z\phi})^2\right) \ , \tag{D.111}$$

where a_1, a_2, a_3, a_4, a_t, a_ρ, a_z and a_ϕ are constants setting the initial amplitudes, ρ_1, ρ_2, ρ_3, ρ_4, ρ_t, ρ_ρ, r_z and ρ_ϕ determine the Gaussian peaks in the radial direction, z_1, z_2, z_3, z_4, z_t, z_ρ, z_z and z_ϕ determine the Gaussian peaks in the z coordinate direction, $\delta_{\rho 1}$, $\delta_{\rho 2}$, $\delta_{\rho 3}$, $\delta_{\rho 4}$, $\delta_{\rho t}$, $\delta_{\rho\rho}$, $\delta_{\rho z}$ and $\delta_{\rho\phi}$ determine the Gaussian widths in coordinate ρ, and δ_{z1}, δ_{z2}, δ_{z3}, δ_{z4}, δ_{zt}, $\delta_{z\rho}$, δ_{zz} and $\delta_{z\phi}$ determine widths in z. Finally, all remaining variables are initialized according to the definitions of section D.2.

D.3.2 Testing the Boundary Conditions

One of the principal reasons for studying evolution in the MIB coordinate system it to determine the utility of these coordinates in treating outer boundary effects (in specific, reflections). As discussed, grid points outside the MIB boosting region effectively propagate outwards at a rate approaching the speed of light. Any fields reaching this boosted region will be spatially compressed relative to the finite difference mesh. It is at that point that Kreiss-Oliger dissipation will quench these fields as their high-frequency components (relative to the mesh) grow. In principle, the quenching should

[2] From equations (D.47) and (D.49), nonzero electric current components J_ρ and J_z require e, Φ and Φ^* to all be nonzero. The condition for nonzero J_ρ additionally requires that either A_ρ, Φ_ρ or Φ^*_ρ be nonzero. Similarly, the condition for nonzero J_z additionally requires that either A_z, Φ_z or Φ^*_z be nonzero. Clearly, the chosen initial data (D.104)–(D.111) and (D.112)–(D.116) satisfies the nonzero conditions for both J_ρ and J_z when $e \neq 0$. Therefore, it can again be said charge separation begins at $t = 0$ for this specification of the Maxwell-Klein-Gordon system.

be sufficient to prevent any information from reaching the computational outer boundary.

To test the MIB system I evolve $m_\Phi = 1.0$, $e = 1.0$ Maxwell-Klein-Gordon fields in Minkowski spacetime with spatial domain $0 \leq \rho \leq 3$, $-3 \leq z \leq 3$ and compare the evolution to that on the larger domain having standard cylindrical coordinate range $0 \leq \widetilde{\rho} \leq 6$, $-6 \leq \widetilde{z} \leq 6$. The evolution with smaller computational domain using MIB coordinates employs parameter values $\rho_c = 2.50$, $\delta_\rho = 0.10$, $z_c = 2.50$ and $\delta_z = 0.10$, and contains $J = 201$ points in the ρ coordinate direction and $K = 401$ points in the direction of z. The larger computational domain has the same resolution and thus $\widetilde{J} = 401$ points in direction $\widetilde{\rho}$ and $\widetilde{K} = 801$ points in direction $\widetilde{z}$. Initial data is specified as discussed above for the choice of values

$$a_1 = a_2 = a_3 = a_4 = a_t = a_\rho = a_z = a_\phi = 1.00 \ , \tag{D.112}$$

$$\rho_1 = \rho_2 = \rho_3 = \rho_4 = \rho_t = \rho_\rho = \rho_z = \rho_\phi = 0.75 \ , \tag{D.113}$$

$$z_1 = z_2 = z_3 = z_4 = z_t = z_\rho = z_z = z_\phi = 0.00 \ , \tag{D.114}$$

$$\delta_{\rho 1} = \delta_{\rho 2} = \delta_{\rho 3} = \delta_{\rho 4} = \delta_{\rho t} = \delta_{\rho\rho} = \delta_{\rho z} = \delta_{\rho\phi} = 0.20 \ , \tag{D.115}$$

$$\delta_{z1} = \delta_{z2} = \delta_{z3} = \delta_{z4} = \delta_{zt} = \delta_{z\rho} = \delta_{zz} = \delta_{z\phi} = 0.20 \ . \tag{D.116}$$

The analogous choice is made for initial data on the standard cylindrical coordinate domain. Figure D.7 shows the evolution of charge density ρ_Q in a sequence of steps for the MIB coordinate system. Observe how the grid function is compressed and quenched in the boosting region, and how no signal reaches the outer boundary of the computational domain. An appropriate comparison between the MIB results and those of the larger computational domain is through the error of integrated conserved quantities. For example, I compute the error of total charge, δQ, as per

$$\delta Q = ||\widetilde{Q} - Q||_2 \ , \tag{D.117}$$

where Q is the total charge in the MIB domain, $\widetilde{Q}$ is that in the large domain, and $||\cdot||_2$ represents the l_2 norm. Q and $\widetilde{Q}$ are obtained through integration over a common region of space. Because of the location and growth of the boosting region I limit the region of integration to $0 \leq \rho \leq 1.5$, $-1.5 \leq z \leq 1.5$. I display these errors for total normalized energy (δT), angular momentum (δS) and charge (δQ) in Figures D.8, D.9, and D.10. To compare, these figures also display errors for the same system but using approximate Sommerfeld condition on a domain $0 \leq \widetilde{\rho} \leq 3$, $-3 \leq \widetilde{z} \leq 3$. It is clear that MIB coordinates together with dissipation are as good as an approximate Sommerfeld condition on the boundary. However, the useful spatial domain of the MIB system is effectively reduced in size due to the boosting regions. The errors of the MIB system results will likely drop significantly below those for the Sommerfeld condition when its interior (i.e., unboosted) region is increased to a comparable size. Furthermore, the choice $e = 1.0$, $m_\Phi = 1.0$ provides significantly stronger coupling than those used in following discussions of Maxwell-Klein-Gordon fields in Minkowski spacetime. Testing on a larger computational domain with weaker coupling would therefore be a useful future calculation.

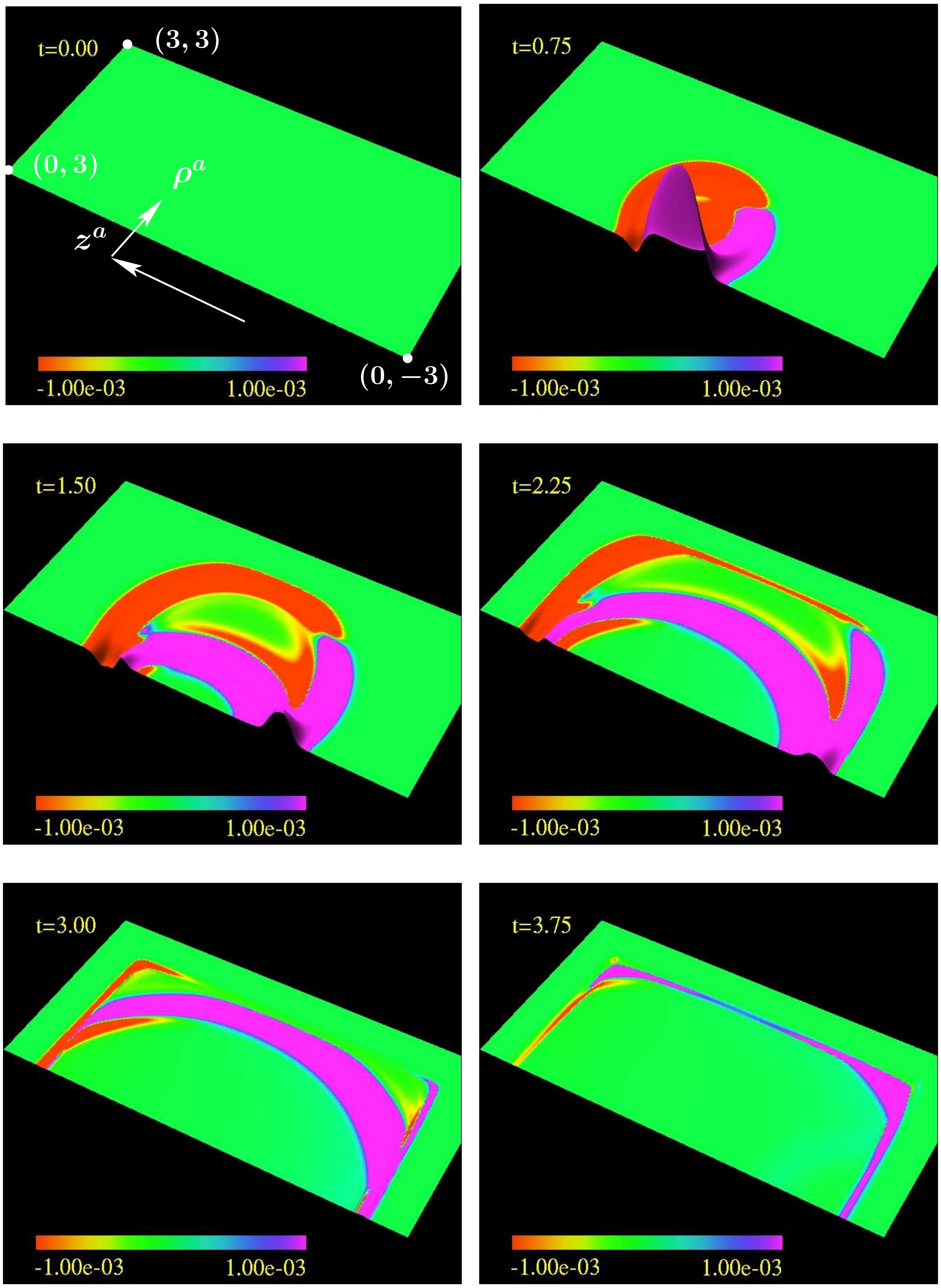

Figure D.7: MIB coordinates and dissipation acting on $m_\Phi = 1.0$, $e = 1.0$ Maxwell-Klein-Gordon fields. The figure displays the charge density in a sequence of steps. The directions of coordinate vectors $\rho^a \sim (0, 1, 0, 0)$ and $z^a \sim (0, 0, 1, 0)$ are shown in the first frame. The computational domain covers the range $0 \leq \rho \leq 3$ and $-3 \leq z \leq 3$, and the corners of the domain are labelled with their (ρ, z) ordinate values. The amplitude and colour gradient are both scaled linearly.

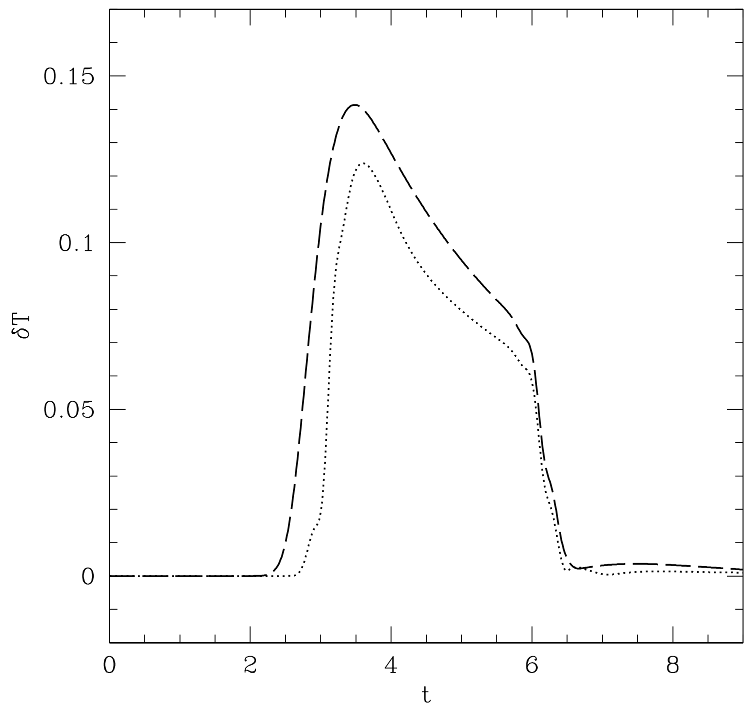

Figure D.8: Displayed is the error in total normalized energy for $e = 1.0$, $m_\Phi = 1.0$ Maxwell-Klein-Gordon fields in the MIB coordinate system (dashed black line), and in the standard cylindrical coordinates using an approximate Sommerfeld boundary condition (dotted black line).

D.3.3 Maxwell-Klein-Gordon Fields on a Flat Background

Having shown that MIB coordinates are as good as (and likely better than) the approximate Sommerfeld condition in treating the outer boundary of the computational domain, I now provide results which compare the Maxwell-Klein-Gordon dynamics on flat spacetime to those of chapter 4. Here and below I use a computational domain spanning the coordinate range $0 \leq \rho \leq 90$ and $-90 \leq z \leq 90$, and containing 401 points in the direction of coordinate ρ and 801 points in the direction of z. The relevant MIB coordinate parameters are $\rho_c = 80$, $\delta_\rho = 4$, $z_c = 80$ and $\delta_z = 4$. Finally, I specify initial data according to the outlined procedure for the choice of parameter values

$$a_1 = a_2 = a_3 = a_4 = a_t = a_\rho = a_z = a_\phi = 1.0 \ , \tag{D.118}$$

$$\rho_1 = \rho_2 = \rho_3 = \rho_4 = \rho_t = \rho_\rho = \rho_z = \rho_\phi = 25.0 \ , \tag{D.119}$$

$$z_1 = z_2 = z_3 = z_4 = z_t = z_\rho = z_z = z_\phi = 0.0 \ , \tag{D.120}$$

$$\delta_{\rho 1} = \delta_{\rho 2} = \delta_{\rho 3} = \delta_{\rho 4} = \delta_{\rho t} = \delta_{\rho\rho} = \delta_{\rho z} = \delta_{\rho\phi} = 5.0 \ , \tag{D.121}$$

$$\delta_{z1} = \delta_{z2} = \delta_{z3} = \delta_{z4} = \delta_{zt} = \delta_{z\rho} = \delta_{zz} = \delta_{z\phi} = 5.0 \ . \tag{D.122}$$

This provides initial conditions reasonably close to those used in evolving fields on the Kerr spacetime. To compare and contrast, it should be sufficient to present just the conserved quantities of this system.

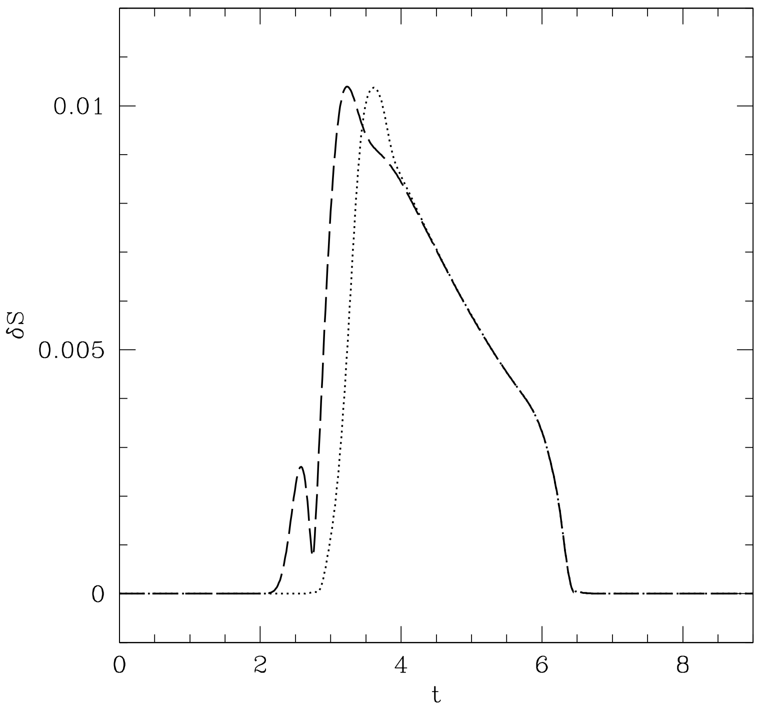

Figure D.9: Displayed is the error in angular momentum for $e = 1.0$, $m_\Phi = 1.0$ Maxwell-Klein-Gordon fields in the MIB coordinate system (dashed black line), and in the standard cylindrical coordinates using an approximate Sommerfeld boundary condition (dotted black line).

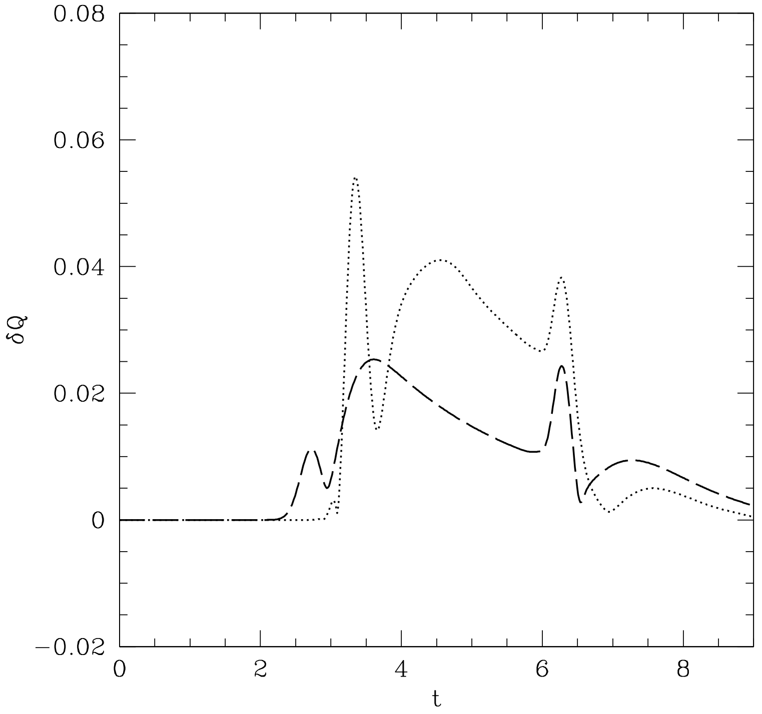

Figure D.10: Displayed is the error in charge for $e = 1.0$, $m_\Phi = 1.0$ Maxwell-Klein-Gordon fields in the MIB coordinate system (dashed black line), and in the standard cylindrical coordinates using an approximate Sommerfeld boundary condition (dotted black line).

Dynamics of Klein-Gordon Fields in Minkowski Spacetime

Beginning with the massive electromagnetically uncoupled fields I find: (1) orbiting resonances and other manifestations of gravitational interaction are never present; (2) the rate of field dissipation from the computational domain always decreases with increasing mass parameter; and (3) $m_\Phi = 0.3$ fields strongly display scattering concentrated along the axis of symmetry. These three facts are substantiated by simple comparison of the normalized energy densities shown in Figures D.11, D.12 and D.13, which respectively display the normalized energy densities for $m_\Phi = 0.0$. $m_\Phi = 0.3$ and $m_\Phi = 2.4$ Klein-Gordon fields.

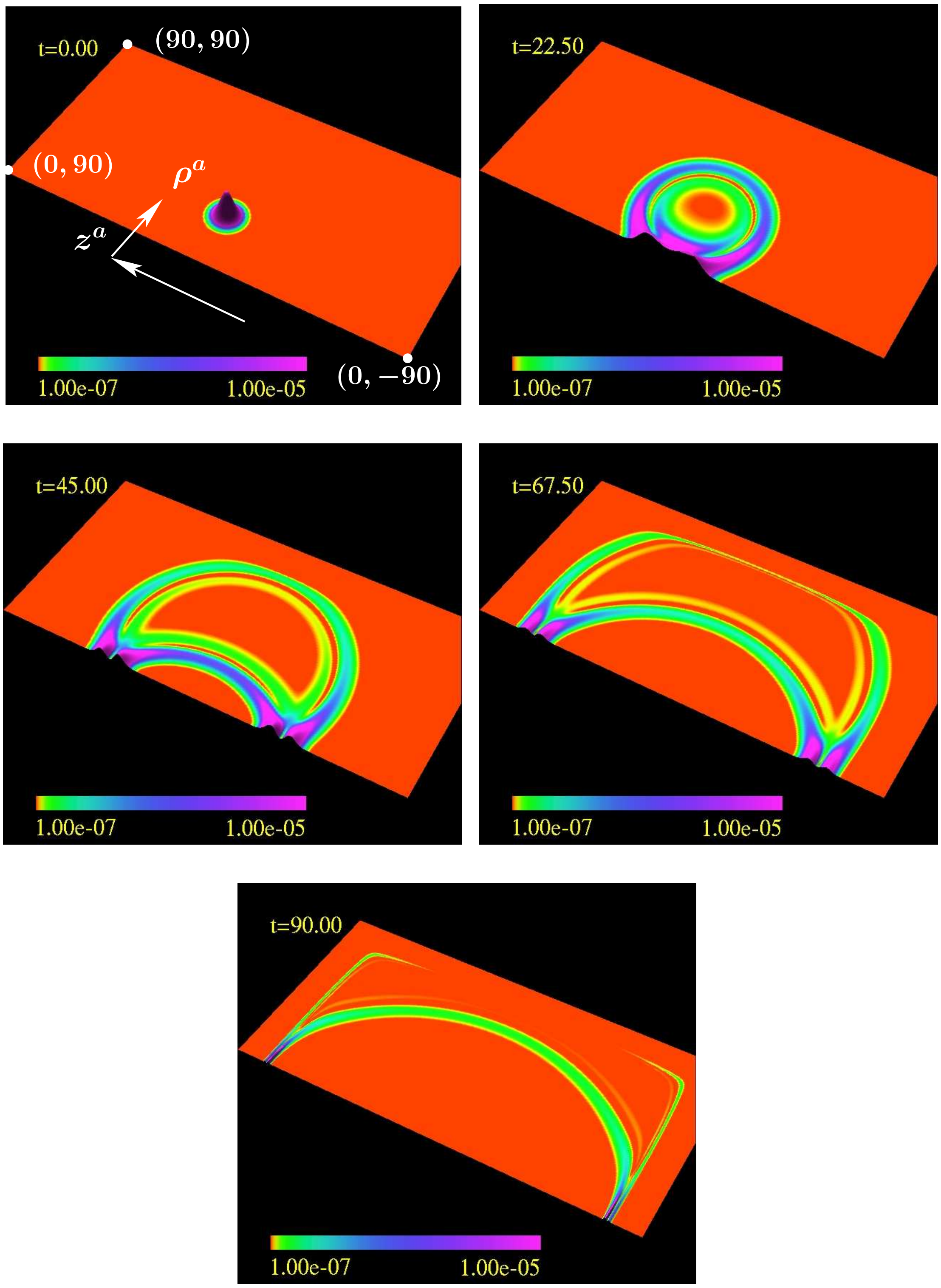

Figure D.11: $m_\Phi = 0.0$, $e = 0.0$ Klein-Gordon field dynamics in flat spacetime in terms of the normalized energy density. The directions of coordinate vectors $\rho^a \sim (0, 1, 0, 0)$ and $z^a \sim (0, 0, 1, 0)$ are shown in the first frame. The computational domain covers the range $0 \leq \rho \leq 90$ and $-90 \leq z \leq 90$, and the corners of the domain are labelled with their (ρ, z) ordinate values. The amplitude is scaled linearly while the colour gradient is scaled logarithmically.

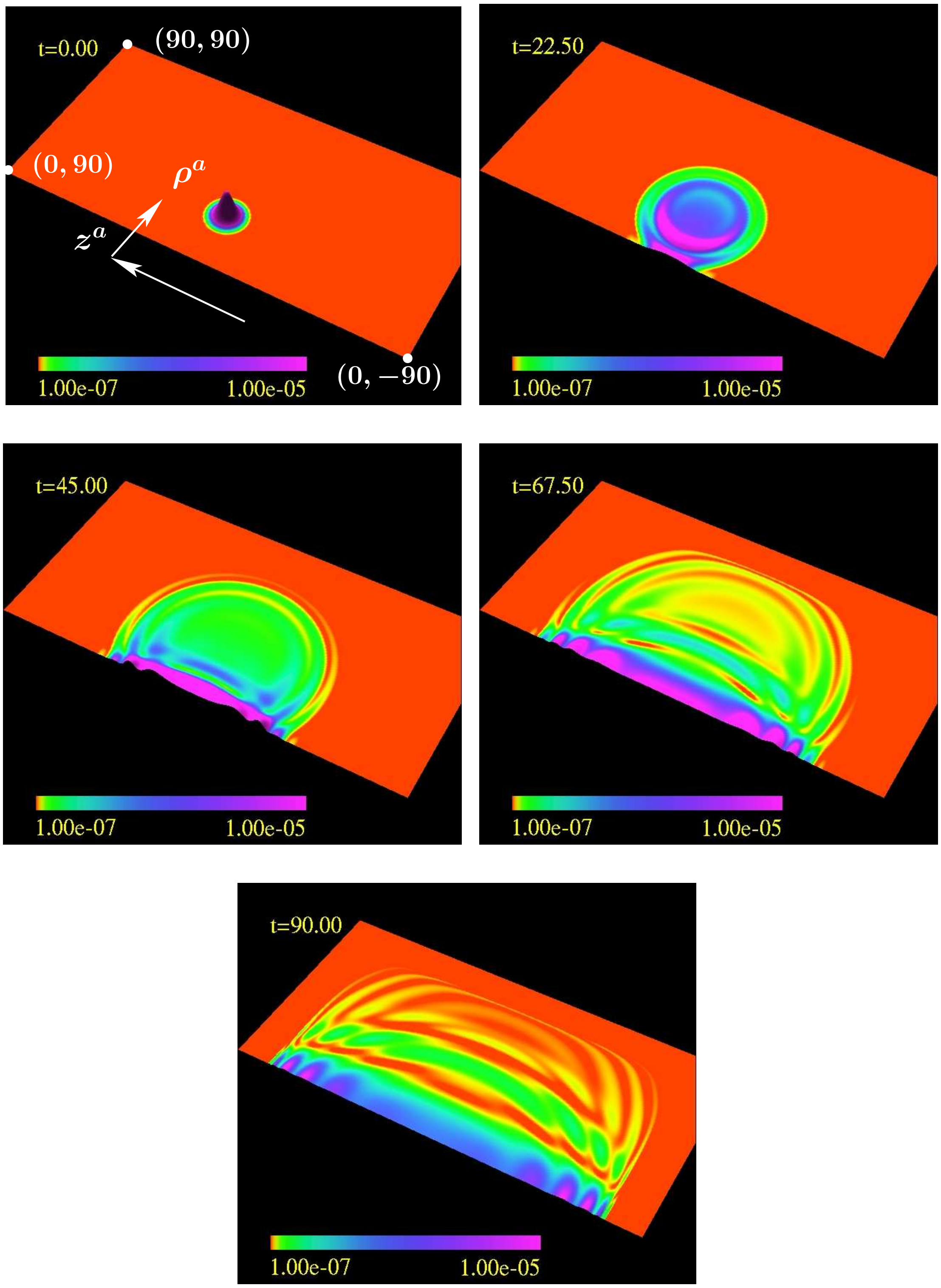

Figure D.12: $m_\Phi = 0.3$, $e = 0.0$ Klein-Gordon field dynamics in flat spacetime in terms of the normalized energy density. The directions of coordinate vectors $\rho^a \sim (0, 1, 0, 0)$ and $z^a \sim (0, 0, 1, 0)$ are shown in the first frame. The computational domain covers the range $0 \leq \rho \leq 90$ and $-90 \leq z \leq 90$, and the corners of the domain are labelled with their (ρ, z) ordinate values. The amplitude is scaled linearly while the colour gradient is scaled logarithmically.

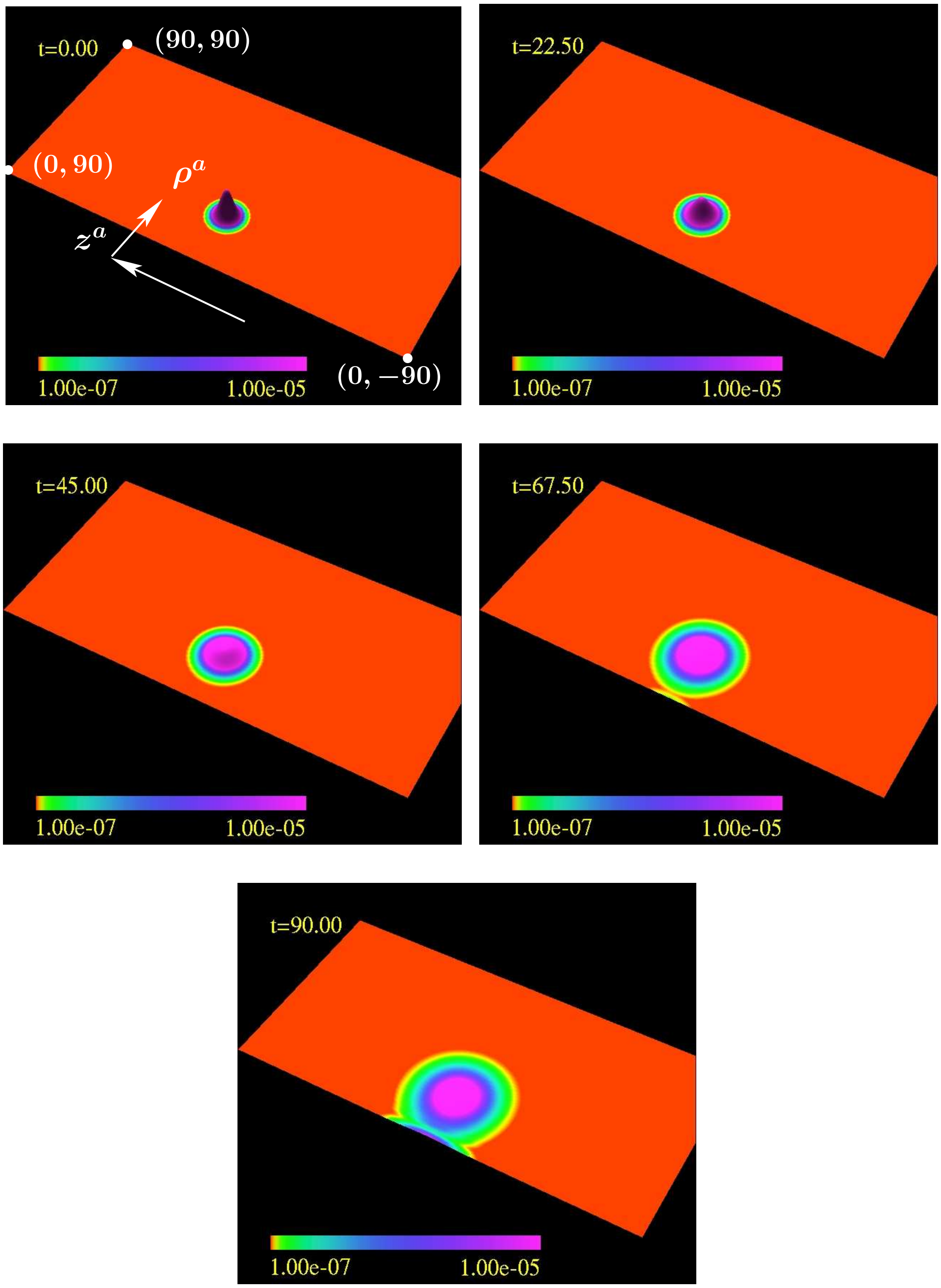

Figure D.13: $m_\Phi = 0.0$, $e = 2.4$ Klein-Gordon field dynamics in flat spacetime in terms of the normalized energy density. The directions of coordinate vectors $\rho^a \sim (0, 1, 0, 0)$ and $z^a \sim (0, 0, 1, 0)$ are shown in the first frame. The computational domain covers the range $0 \leq \rho \leq 90$ and $-90 \leq z \leq 90$, and the corners of the domain are labelled with their (ρ, z) ordinate values. The amplitude is scaled linearly while the colour gradient is scaled logarithmically.

Dynamics of Maxwell Fields in Minkowski Spacetime

Examining the conserved energy and angular momentum densities, respectively displayed in Figures D.14 and D.15, two facts are immediately clear: (1) effects resembling gravitational interaction are not present in flat spacetime; and (2) the electromagnetic angular momentum displays nontrivial evolution. The large amplitudes and steep gradients associated with scattering from the black hole spacetime are absent from the energy density. Furthermore, while the evolution of angular momentum density is nontrivial in Minkowski spacetime, the complexity observed in Kerr spacetime evolution is absent.

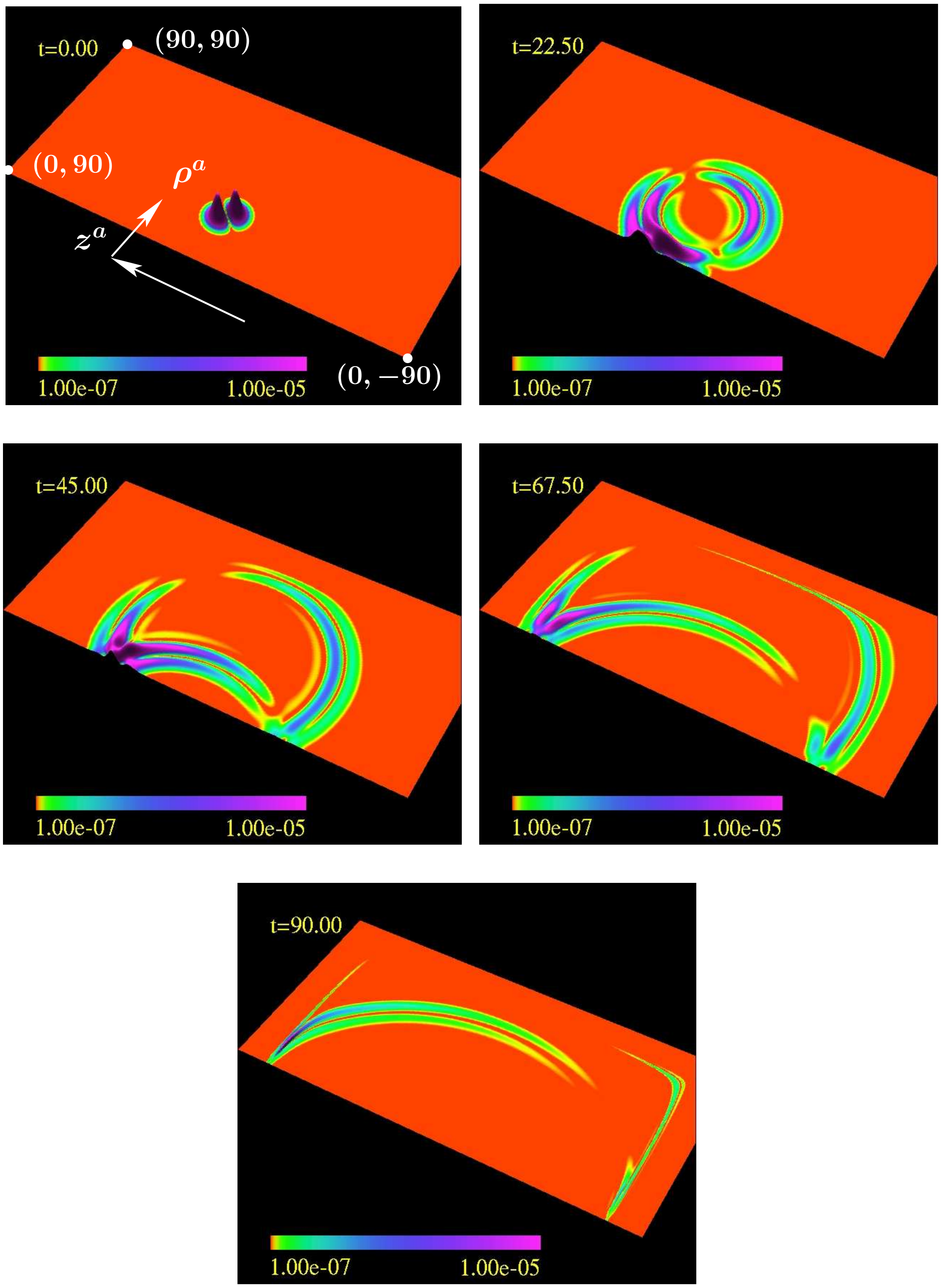

Figure D.14: Maxwell field dynamics in flat spacetime in terms of the normalized energy density. The directions of coordinate vectors $\rho^a \sim (0,1,0,0)$ and $z^a \sim (0,0,1,0)$ are shown in the first frame. The computational domain covers the range $0 \leq \rho \leq 90$ and $-90 \leq z \leq 90$, and the corners of the domain are labelled with their (ρ, z) ordinate values. The amplitude is scaled linearly while the colour gradient is scaled logarithmically.

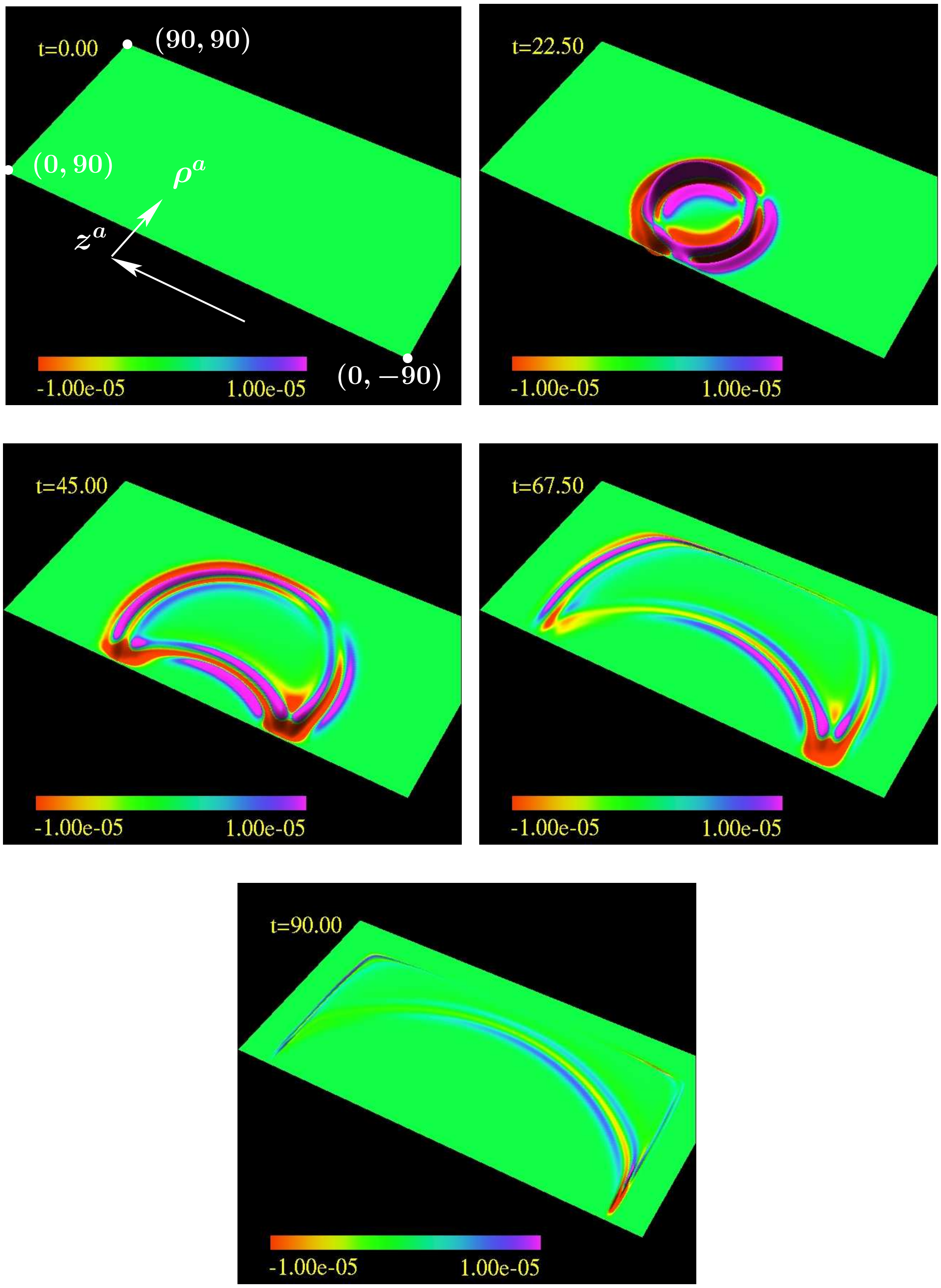

Figure D.15: Angular momentum of the Maxwell fields in flat spacetime. The directions of coordinate vectors $\rho^a \sim (0,1,0,0)$ and $z^a \sim (0,0,1,0)$ are shown in the first frame. The computational domain covers the range $0 \le \rho \le 90$ and $-90 \le z \le 90$, and the corners of the domain are labelled with their (ρ, z) ordinate values. The amplitude and colour gradient are both scaled linearly.

Dynamics of $e = 0.6$, $m_\Phi = 0.0$ Maxwell-Klein-Gordon Fields in Minkowski Spacetime

The conserved densities show that massless $e = 0.6$ Maxwell-Klein-Gordon fields in flat space: (1) do not display effects in any way resembling gravitational interaction; (2) have nontrivial angular momentum evolution; and (3) generically display charge separation. The normalized energy density of Figure D.16, angular momentum density of Figure D.17 and charge density of Figure D.18 provide the required evidence. The large amplitudes and steep gradients associated with scattering from the black hole spacetime are absent, and while the evolution of angular momentum density is nontrivial, the complexity observed in Kerr spacetime evolution is absent in flatspace. Furthermore, while gravitational effects are absent, the charge separation exhibited in flat space is still quite complex. Finally, from the evolution of angular momentum and charge density, dynamo-like behaviour can be deduced. It is sufficient to state this physics is manifest in the evolution of angular current J_ϕ (figures not provided).

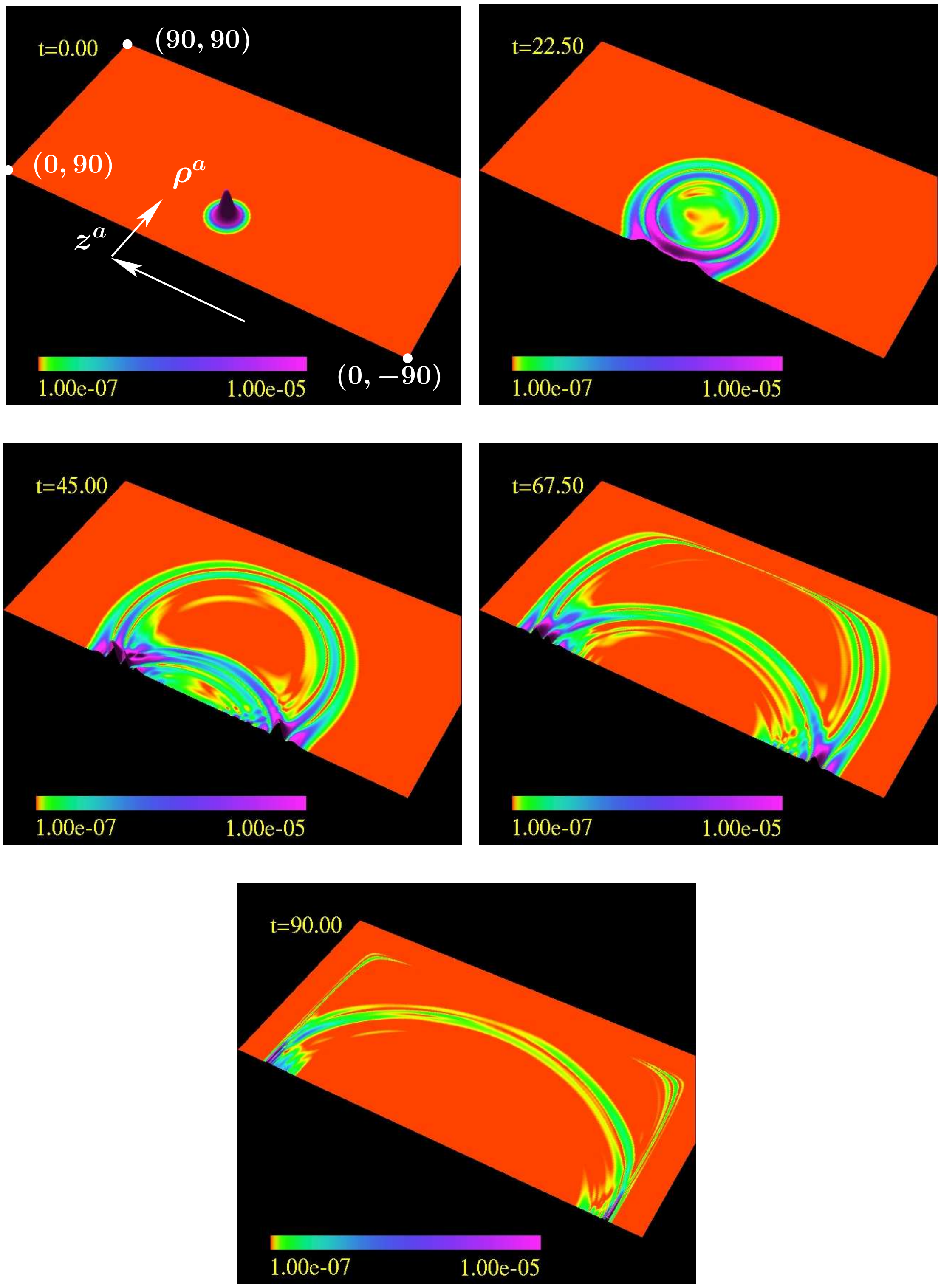

Figure D.16: Massless $e = 0.6$ Maxwell-Klein-Gordon field dynamics in flat spacetime in terms of the normalized energy density. The directions of coordinate vectors $\rho^a \sim (0, 1, 0, 0)$ and $z^a \sim (0, 0, 1, 0)$ are shown in the first frame. The computational domain covers the range $0 \leq \rho \leq 90$ and $-90 \leq z \leq 90$, and the corners of the domain are labelled with their (ρ, z) ordinate values. The amplitude is scaled linearly while the colour gradient is scaled logarithmically.

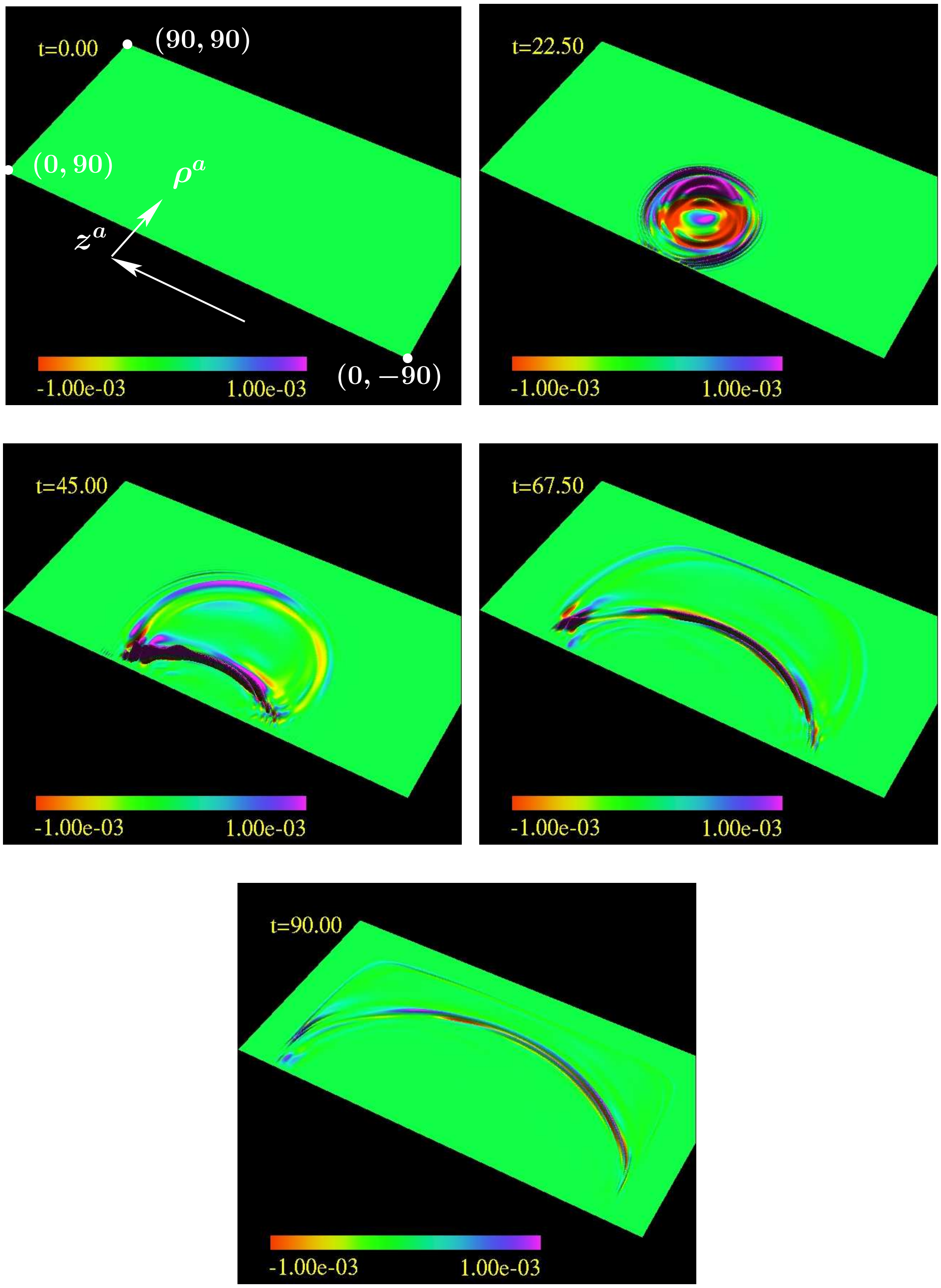

Figure D.17: Angular momentum of the massless $e = 0.6$ Maxwell-Klein-Gordon fields in flat spacetime. The directions of coordinate vectors $\rho^a \sim (0, 1, 0, 0)$ and $z^a \sim (0, 0, 1, 0)$ are shown in the first frame. The computational domain covers the range $0 \leq \rho \leq 90$ and $-90 \leq z \leq 90$, and the corners of the domain are labelled with their (ρ, z) ordinate values. The amplitude and colour gradient are both scaled linearly.

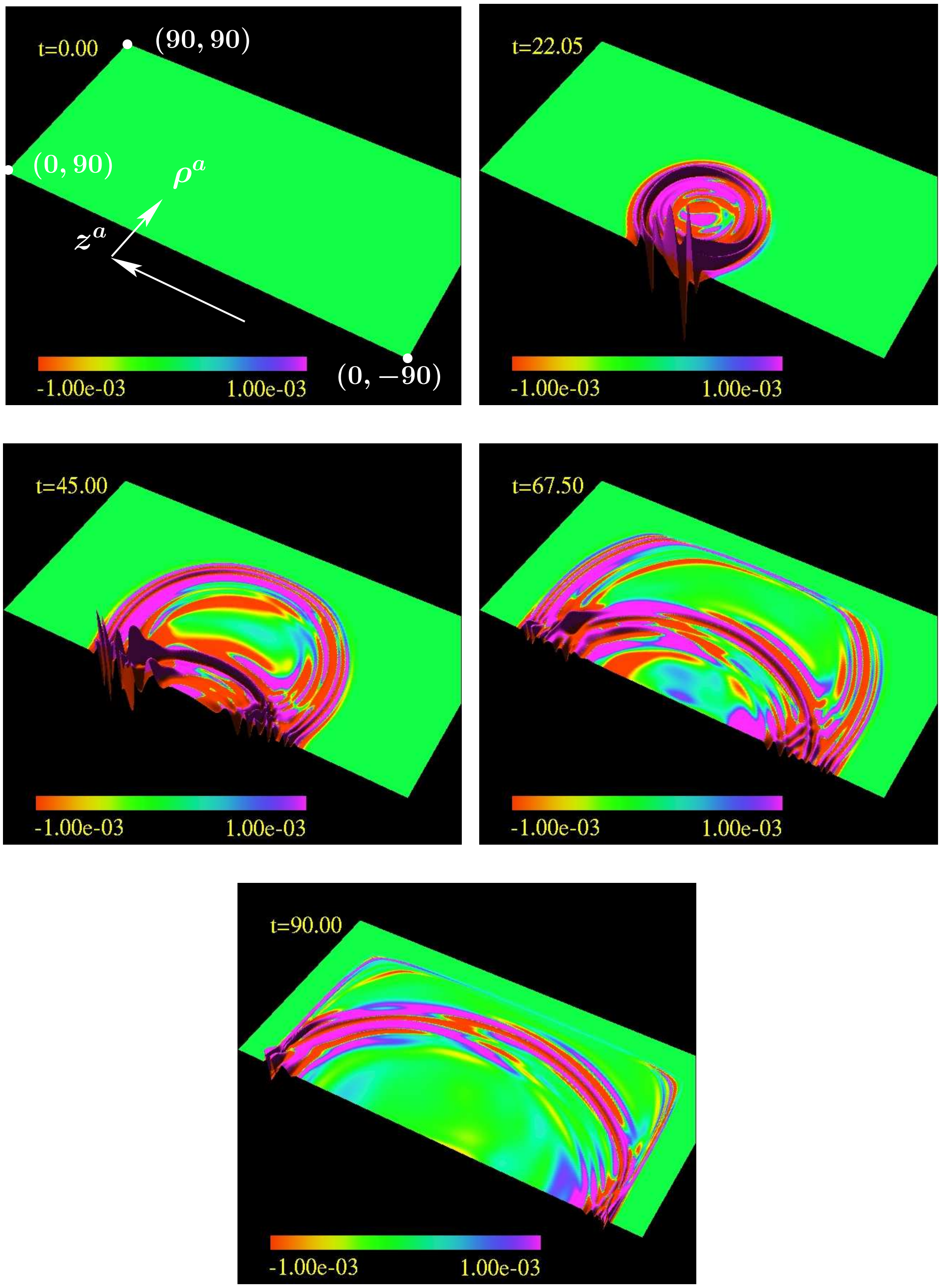

Figure D.18: Angular momentum of the massless $e = 0.6$ Maxwell-Klein-Gordon fields in flat spacetime. The directions of coordinate vectors $\rho^a \sim (0, 1, 0, 0)$ and $z^a \sim (0, 0, 1, 0)$ are shown in the first frame. The computational domain covers the range $0 \leq \rho \leq 90$ and $-90 \leq z \leq 90$, and the corners of the domain are labelled with their (ρ, z) ordinate values. The amplitude and colour gradient are both scaled linearly.

Dynamics of $e = 0.6$, $m_\Phi = 0.3$ Maxwell-Klein-Gordon Fields in Minkowski Spacetime

Finally, four facts can be stated for $m_\Phi = 0.3$, $e = 0.6$ (massive electromagnetically coupled) Maxwell-Klein-Gordon field dynamics in flat space: (1) effects resembling gravitational interaction are never observed; (2) there is only a slight preference for scattering along the axis of symmetry; (3) the evolution of angular momentum is again nontrivial; and (4) charge separation is again a generic feature of evolution. Figure D.19 displays the normalized energy density in support of the first two facts. Notice that while a slight collimation of energy along the axis is present, it is far less than observed for the scattering in $M = 5$ Kerr spacetime. The angular momentum density is presented in Figure D.20. While its evolution is again nontrivial, it here displays amplitudes and gradients far less than for the equivalent evolution in Kerr spacetime. While the amplitudes and gradients of charge density separation are comparable to those on the black hole background, Figure D.21 shows no evidence for morphology typical of the orbital effects seen on the curved spacetime calculations. Finally, as in the case of massless $e = 0.6$ evolution, the presence of dynamo-like behaviour can be deduced. This physics is again manifest in the evolution of angular current J_ϕ (figures not provided).

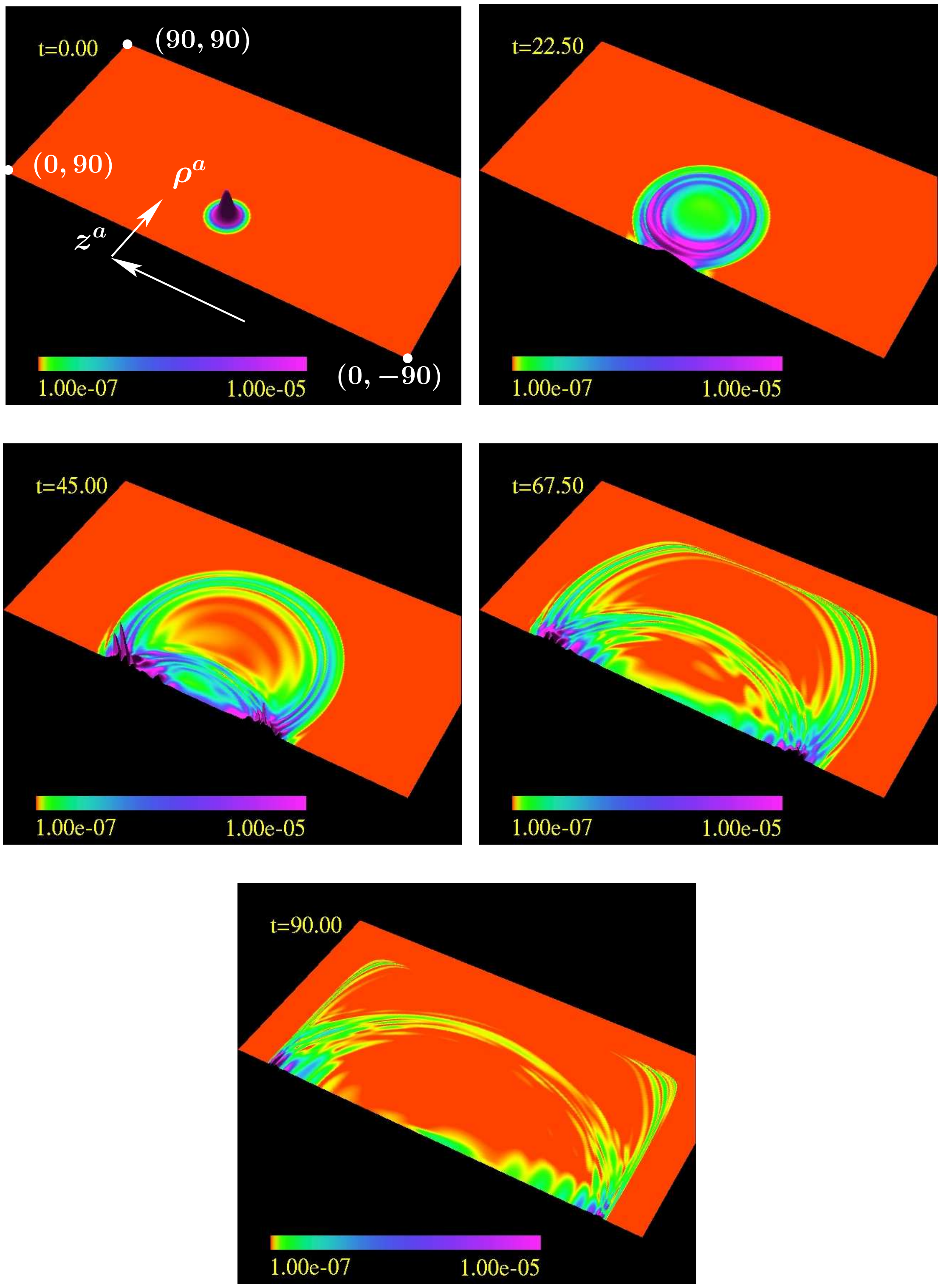

Figure D.19: $m_\Phi = 0.3$ $e = 0.6$ Maxwell-Klein-Gordon field dynamics in flat spacetime in terms of the normalized energy density. The directions of coordinate vectors $\rho^a \sim (0, 1, 0, 0)$ and $z^a \sim (0, 0, 1, 0)$ are shown in the first frame. The computational domain covers the range $0 \leq \rho \leq 90$ and $-90 \leq z \leq 90$, and the corners of the domain are labelled with their (ρ, z) ordinate values. The amplitude is scaled linearly while the colour gradient is scaled logarithmically.

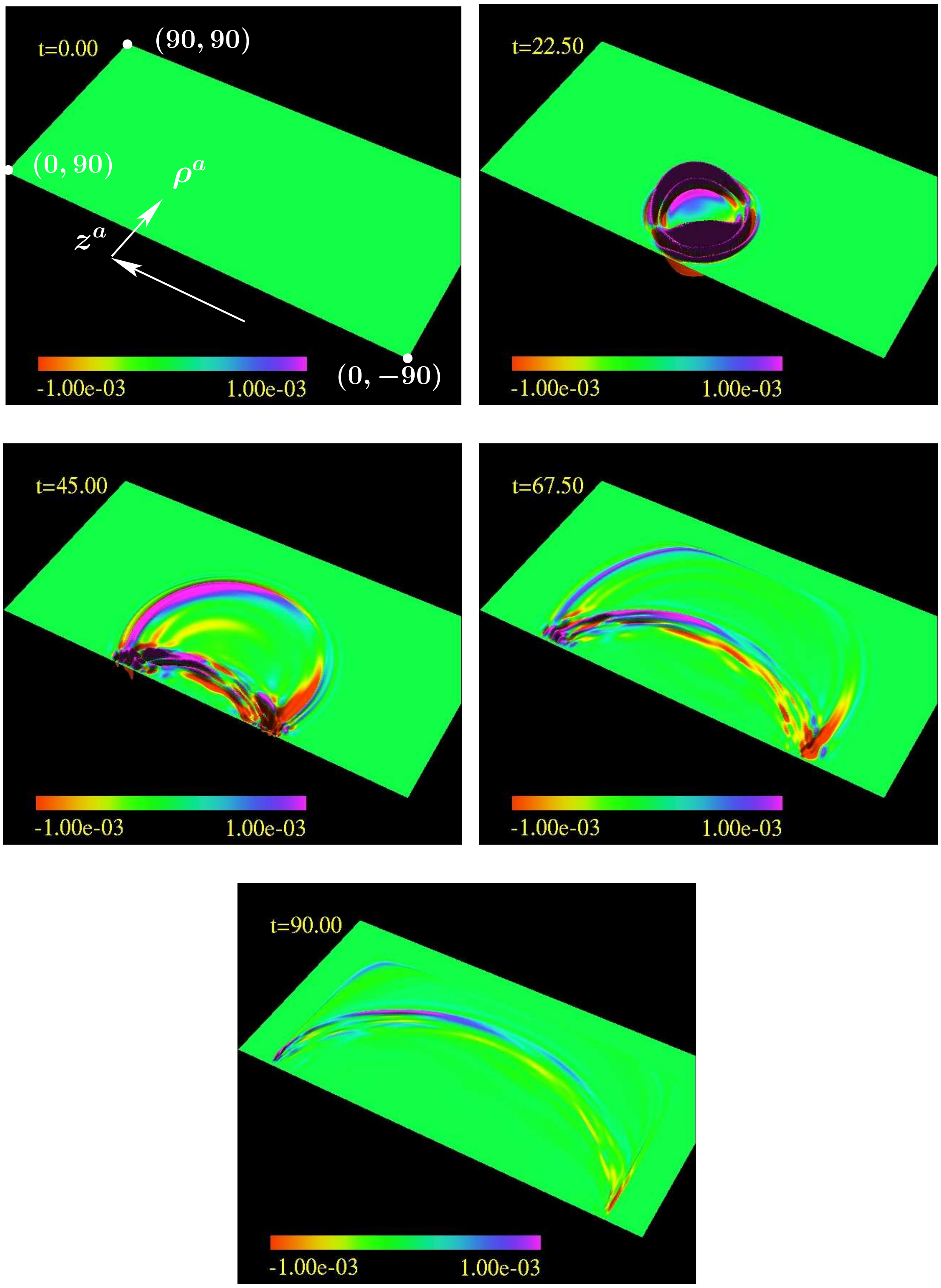

Figure D.20: Angular momentum of the $m_\Phi = 0.3$, $e = 0.6$ Maxwell-Klein-Gordon fields in flat spacetime. The directions of coordinate vectors $\rho^a \sim (0, 1, 0, 0)$ and $z^a \sim (0, 0, 1, 0)$ are shown in the first frame. The computational domain covers the range $0 \leq \rho \leq 90$ and $-90 \leq z \leq 90$, and the corners of the domain are labelled with their (ρ, z) ordinate values. The amplitude and colour gradient are both scaled linearly.

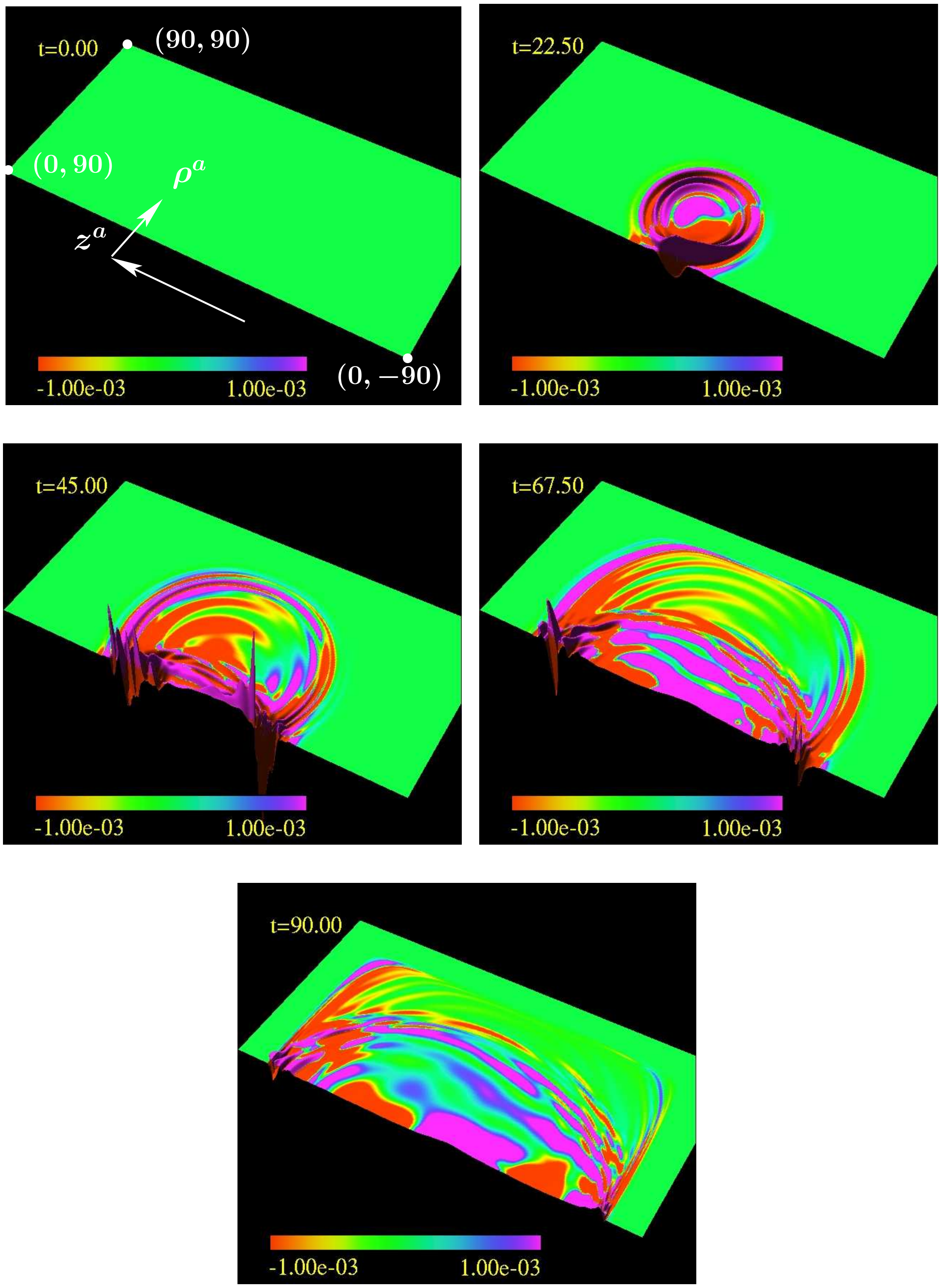

Figure D.21: Angular momentum of the $m_\Phi = 0.3$, $e = 0.6$ Maxwell-Klein-Gordon fields in flat spacetime. The directions of coordinate vectors $\rho^a \sim (0, 1, 0, 0)$ and $z^a \sim (0, 0, 1, 0)$ are shown in the first frame. The computational domain covers the range $0 \leq \rho \leq 90$ and $-90 \leq z \leq 90$, and the corners of the domain are labelled with their (ρ, z) ordinate values. The amplitude and colour gradient are both scaled linearly.

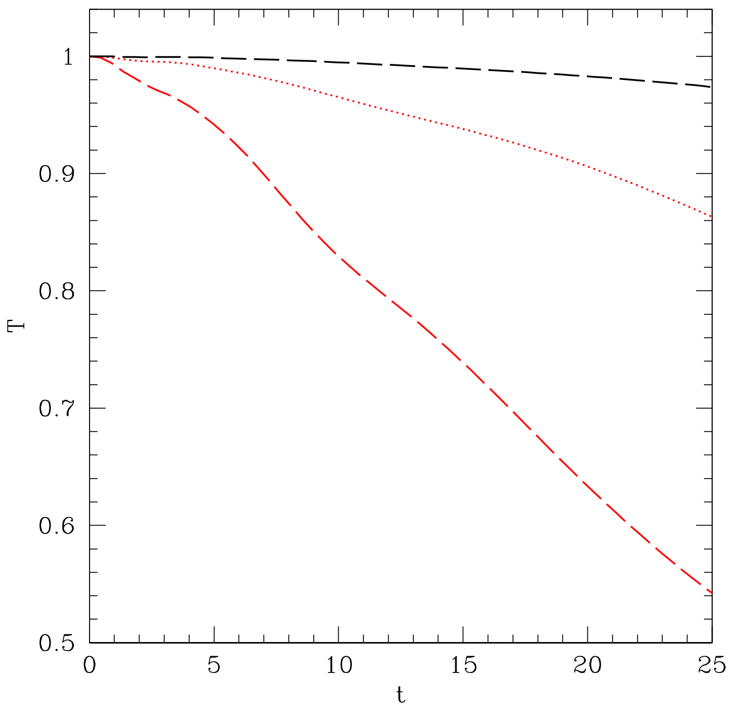

Figure D.22: Convergence of total normalized energy, T, for $e = 0.6$, $m_\Phi = 0.3$ fields in the MIB flat spacetime. The dashed red line represents data for a finite difference grid with $J = 101$ points in direction ρ and $K = 201$ points in direction z, the dotted red line represents data for a grid with $J = 201$ points in ρ and $K = 401$ points in z, and the dashed black line represents data for a grid with $J = 401$ points in ρ and $K = 801$ in z.

D.3.4 Convergence of Conserved Quantities

In concluding this appendix I provide evidence that the MIB coordinate code is both convergent and accurate. This is done by displaying convergence of the total energy, T, angular momentum, S and charge Q for $m_\Phi = 0.3$, $e = 0.6$ perturbations. Figure D.22 shows the convergence of energy, Figure D.23 the convergence of angular momentum, and Figure D.24 displays the results for charge. In each of the figures I show the total integrated quantity contained within coordinate range $0 \leq \rho \leq 50$, $-50 \leq z \leq 50$ for the period $0 \leq t \leq 25$. I use the reduced spatial domain because of the location and growth of the coordinate boosting regions, and a reduced period because fields will propagate past the reduced spatial domain at later times. The comparison is between grids with $J = 101$ points in ρ and $K = 201$ points in z, $J = 201$ points in ρ and $K = 401$ points in z, and $J = 401$ points in direction ρ and $K = 801$ in the direction of z. Based on the results of total energy conservation, the results for the massive charged fields are typically accurate to $\approx 2\%$ over the period $0 \leq t \leq 25$ on the grid with 401×801 points. Finally, the convergence factor, time averaged over the displayed period, is $C \approx 3.7$ for the total energy, $C \approx 3.1$ for angular momentum and $C \approx 5.1$ for the total charge of the system.

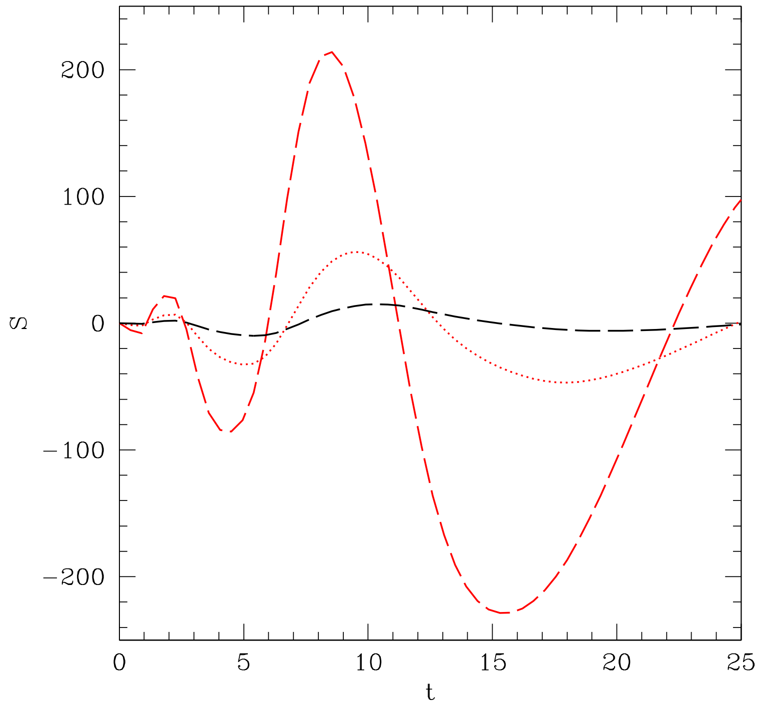

Figure D.23: Convergence of total angular momentum, S, for $e = 0.6$, $m_\Phi = 0.3$ fields in the MIB flat spacetime. The dashed red line represents data for a finite difference grid with $J = 101$ points in direction ρ and $K = 201$ points in direction z, the dotted red line represents data for a grid with $J = 201$ points in ρ and $K = 401$ points in z, and the dashed black line represents data for a grid with $J = 401$ points in ρ and $K = 801$ in z.

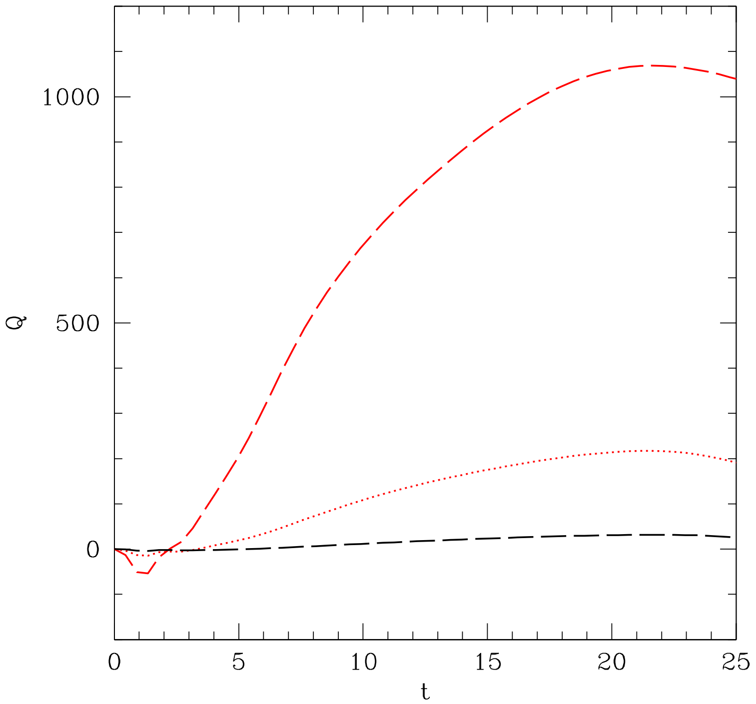

Figure D.24: Convergence of total charge, Q, for $e = 0.6$, $m_\Phi = 0.3$ fields in the MIB flat spacetime. The dashed red line represents data for a finite difference grid with $J = 101$ points in direction ρ and $K = 201$ points in direction z, the dotted red line represents data for a grid with $J = 201$ points in ρ and $K = 401$ points in z, and the dashed black line represents data for a grid with $J = 401$ points in ρ and $K = 801$ in z.